Engineering Dynamics and Life Sciences

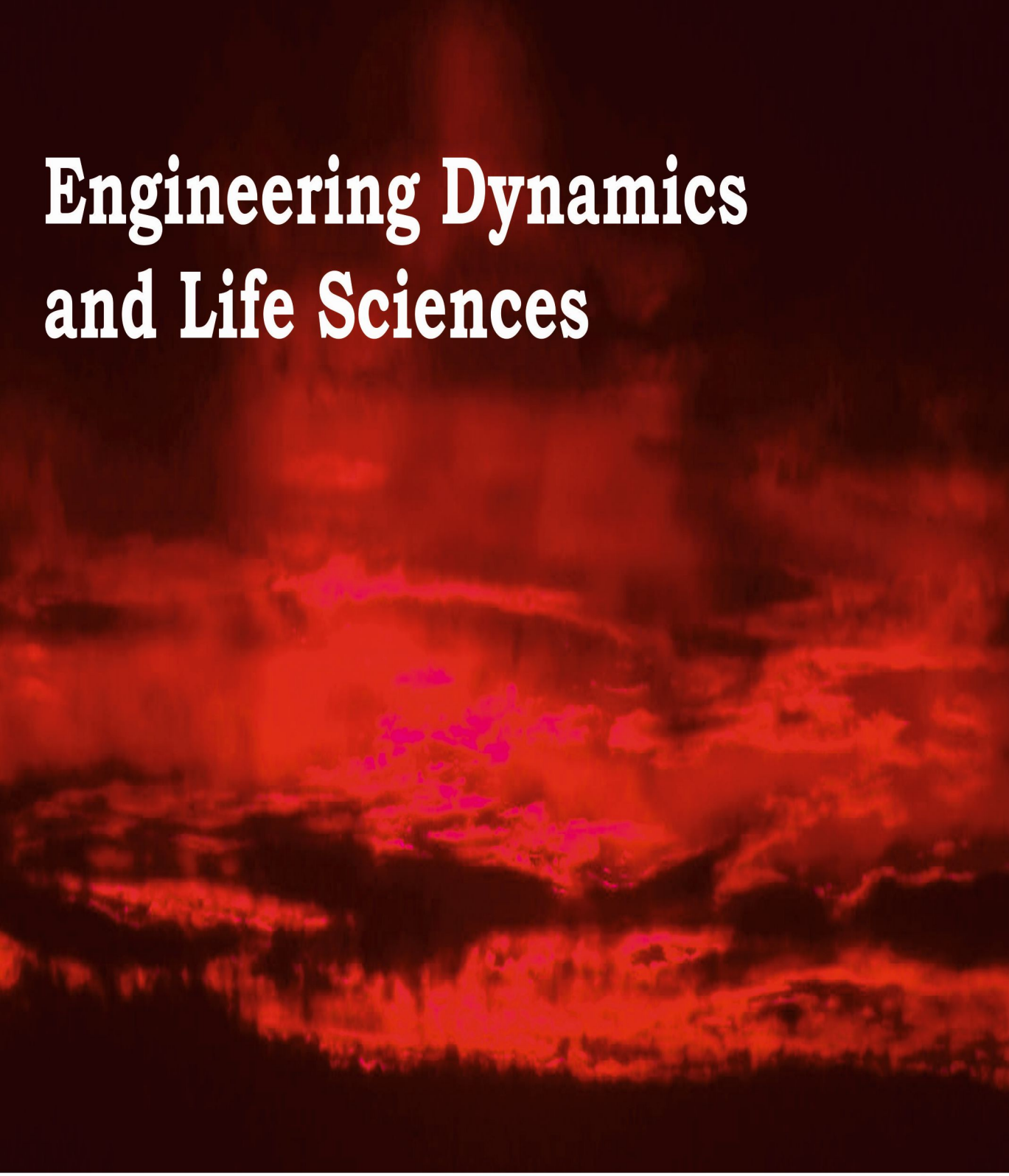

Editors
J. AWREJCEWICZ
M. KAŹMIERCZAK
J. MROZOWSKI
P. OLEJNIK

DSTA 2017

Engineering Dynamics and Life Sciences

Editors

JAN AWREJCEWICZ, MAREK KAŹMIERCZAK
JERZY MROZOWSKI, PAWEŁ OLEJNIK

ISBN 978-83-935312-4-0
10.34658/9788393531240
https://doi.org/10.34658/9788393531240

Cover design: Marek Kaźmierczak
Technical editor: Marek Kaźmierczak

Printed by:
ARSA Druk i Reklama
90-270 Łódź, ul. Piotrkowska 4
tel./fax (042) 633 02 52
marta@arsa.net.pl
www.arsa.net.pl

PREFACE

This is the fourteenth time when the conference “Dynamical Systems: Theory and Applications” gathers a numerous group of outstanding scientists and engineers, who deal with widely understood problems of theoretical and applied dynamics.

Organization of the conference would not have been possible without a great effort of the staff of the Department of Automation, Biomechanics and Mechatronics. The patronage over the conference has been taken by the Committee of Mechanics of the Polish Academy of Sciences and Ministry of Science and Higher Education of Poland.

It is a great pleasure that our invitation has been accepted by recording in the history of our conference number of people, including good colleagues and friends as well as a large group of researchers and scientists, who decided to participate in the conference for the first time. With proud and satisfaction we welcomed over **180** persons from **31** countries all over the world. They decided to share the results of their research and many years experiences in a discipline of dynamical systems by submitting many very interesting papers.

This year, the DSTA Conference Proceedings were split into three volumes entitled “Dynamical Systems” with respective subtitles: *Vibration, Control and Stability of Dynamical Systems*; *Mathematical and Numerical Aspects of Dynamical System Analysis* and *Engineering Dynamics and Life Sciences*. Additionally, there will be also published two volumes of Springer Proceedings in Mathematics and Statistics entitled “*Dynamical Systems in Theoretical Perspective”* and *“Dynamical Systems in Applications”.*

These books include the invited and regular papers covering the following topics:

- asymptotic methods in nonlinear dynamics,
- bifurcation and chaos in dynamical systems,
- control in dynamical systems,
- dynamics in life sciences and bioengineering,
- engineering systems and differential equations,
- non-smooth systems
- mathematical approaches to dynamical systems
- original numerical methods of vibration analysis,
- stability of dynamical systems,
- vibrations of lumped and continuous systems,
- other problems.

Proceedings of the 14th Conference „Dynamical Systems - Theory and Applications" summarize **168** and the Springer Proceedings summarize **80** best papers of university teachers and students, researchers and engineers from all over the world. The papers were chosen by the International Scientific Committee from **370** papers submitted to the conference. The reader thus obtains an overview of the recent developments of dynamical systems and can study the most progressive tendencies in this field of science.

Our previous experience shows that an extensive thematic scope comprising dynamical systems stimulates a wide exchange of opinions among researchers dealing with different branches of dynamics. We think that vivid discussions will influence positively the creativity and will result in effective solutions of many problems of dynamical systems in mechanics and physics, both in terms of theory and applications.

We do hope that DSTA 2017 will contribute to the same extent as all the previous conferences to establishing a new and tightening the already existing relations and scientific and technological cooperation between both Polish and foreign institutions.

On behalf of both
Scientific and Organizing Committees

Chairman
Professor Jan Awrejcewicz

CONTENTS

Model of dynamics of a knuckle-boom crane

Iwona Adamiec-Wójcik, Kamil Nadratowski, Łukasz Drąg, Stanisław Wojciech

Abstract: Multilink cranes are often used in offshore engineering due to their larger operational capabilities. The paper presents a 3D model of a crane with two booms and cylinders. The model takes into account their flexibilities. The rigid finite element method is used for discretization of the links. The flexibility of the rope system is also considered. Modelling of offshore cranes requires consideration of base motion, which is the movement of a vessel or platform caused by sea waves. In the paper it is assumed that this motion can be described by harmonic functions. Results of numerical simulations are presented. The model can also be used for simulation of an active overload protection system (AOPS).

1. Introduction

The off-shore equipment includes high performance cranes used for pipe handing mounted on vessels, platforms or drilling rigs. Manufacturers seek for more and more efficient designs with compact size and large capacity. Knuckle–boom cranes called also articulating cranes have two booms with a knuckle between them (see Fig.1). As a result the crane can be used in a restricted space and gives more options for the crane operator.

Figure 1. Knucle-boom crane (www.protea.pl)

Due to the low production and thus limited possibilities for building prototypes it is especially important for designers to develop and use simulation models enabling dynamic analysis. These models should be able to reflect the real system in the best possible manner yet with maximum numerical efficiency,

which enables fast and reliable decision making for the engineers. Modelling knuckle-boom cranes used in offshore applications have to take into account not only flexibilities of booms, cylinders and cables, but also base motion caused by the sea.

Much research has been carried out on the subject of modelling, simulation and control of various types of cranes. Modelling and simulation of offshore crane operations is presented in [1], while a knuckle boom crane is analyzed in [2-4]. For modelling flexible jibs of the crane the finite element method is usually used [1-3]. However, the finite segment method is also well known and often used in modelling of offshore slender structures [4-6].

The rigid finite element method [7] has been used for modelling different types of cranes and offshore structures [8]. This paper presents an application of a new formulation of the rigid finite element method [9] for modelling a knuckle boom crane produced by Protea. A special software package has been developed based on the model derived and it is used by Protea for calculations of statics and dynamics of the crane. Optimisation of winch drives of offshore cranes is discussed in [10, 11]. Proper choice of the drive torque of the winch ensures stabilisation of the load during its positioning.

2. Model of the crane

2.1. Kinematic structure

The crane considered is mounted either on vessels or platforms and thus the motion due to the sea waves has to be taken into account. This is defined using time functions describing the position and orientation of the base vessel (platform) as the following vector:

$$\mathbf{q}_b = \mathbf{q}_b(t) = [x_b(t) \quad y_b(t) \quad z_b(t) \quad \psi_b(t) \quad \theta_b(t) \quad \varphi_b(t)]^{\boldsymbol{T}} \tag{1}$$

where: $x_b(t), y_b(t), z_b(t)$ define the position of the base, $\psi_b(t), \theta_b(t), \varphi_b(t)$ are ZYX Euler angles describing the orientation of the base coordinate system $\{\tilde{x}, \tilde{y}, \tilde{z}\}$with respect to the inertial reference system $\{x, y, z\}$.

The scheme of the knuckle boom crane is presented in Fig.2. It is assumed that the jibs are flexible and their bending and torsional flexibilities are taken into account. Flexibility of the rope system as well as the longitudinal flexibility of cylinders are also considered. The load is treated as a lumped mass.

Booms are discretised by means of the rigid finite element method and the generalised coordinate are defined by the following vectors:

$$\mathbf{q}^{(s)} = \left[\mathbf{q}_0^{(s)^T} \quad \ldots \quad \mathbf{q}_i^{(s)^T} \quad \ldots \quad \mathbf{q}_{n_s}^{(s)^T}\right]^T \tag{2}$$

where n_s is the number of rigid elements (rfe), $\mathbf{q}_i^{(s)} = \left[x_i^{(s)} \quad y_i^{(s)} \quad z_i^{(s)} \quad \psi_i^{(s)} \quad \theta_i^{(s)} \quad \varphi_i^{(s)}\right]^T$ are generalized coordinates of each rfe, $x_i^{(s)}, y_i^{(s)}, z_i^{(s)}$ are the coordinates of the beginning of the local coordinate system assigned to rfe i, $\psi_i^{(s)}, \theta_i^{(s)}, \varphi_i^{(s)}$ are ZYX Euler angles describing the rotation of this local coordinate system with respect to system $\{\}^-$ (see Fig.2).

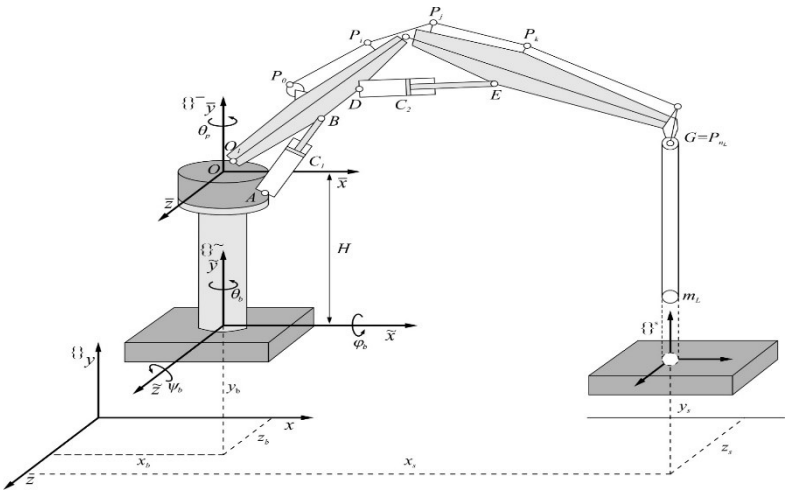

Figure 2. Model of the knuckle boom crane

The cylinders are modeled as two rigid finite elements connected by a spring damping elements. Assuming that torsion is omitted and including the longitudinal deflection, the generalized coordinates of one cylinder are the components of the vector:

$$\mathbf{q}_l^{(c)} = \left[x_l^{(c)} \quad y_l^{(c)} \quad z_l^{(c)} \quad \psi_l^{(c)} \quad \theta_l^{(c)} \quad \Delta_l^{(c)}\right]^T \qquad \text{for } l = 1,.2 \tag{3}$$

where $x_i^{(c)}, y_i^{(c)}, z_i^{(c)}, \psi_i^{(c)}, \theta_i^{(c)}$ have the same interpretation as for the booms and $\Delta_l^{(c)}$ is the elongation/shortening of the cylinder. The position of the cylinders is also described with respect to system $\{\}^-$. Changeable stiffness of the cylinder is taken into account depending on its length.

The position of load m_L, which hangs at the end of the rope going through points P_0, P_i, P_k, P_{n_L} on the jib (Fig.2) is described by three coordinates:

$$\mathbf{r}_L = [x_L \quad y_L \quad z_L]^T \tag{4}$$

and they depend on the length of the rope which is wound/unwound from the winch placed at P_0. The rotation angle of the winch drum φ_D is also one of the generalized coordinates. Both changeable stiffness and damping of the rope are considered. From Fig.2 it can be seen that the structure described is placed on a rotational column, the motion of which is defined by angle θ_P. In view of the above, and

using (2), (3) and (4), the vector of the generalized coordinates of the knuckle boom crane can be written as:

$$\mathbf{q} = \left[\mathbf{q}_0^{(s)T} \quad \mathbf{q}_n^{(s)T} \quad \mathbf{q}_1^{(c)T} \quad \mathbf{q}_2^{(c)T} \quad \theta_P \quad \mathbf{r}_L{}^T \quad \varphi_D\right]^T \tag{5}$$

The number of degrees of freedom of the whole model is $n = \sum_{s=1}^{2}(n_s + 1 + 6) + 5 = \sum_{s=1}^{2} n_s + 19$ in the case when bending and torsion of the booms and bending and elongation of the cylinders is considered. The motion of the system is caused by the motion of the base (vessel or platform) defined by harmonic functions; torque M_D causing the rotation of the winch drum; rotation of the column described either by moment M_P or function θ_P; and functions defining the length change of the cylinders.

2.2. Equations of motion

The geometry of the system and transformations between the coordinate systems are performed using homogenous transformations. The equations of motion are derived using the Lagrange equations and to this end the kinetic energy, potential energy of gravitational forces and spring deformations as well as energy dissipation have to be calculated. In the model it is assumed that the rfes between themselves, as well as the boom with the column and with cylinders are connected by means of spherical joints. Because the motion of the rfes and all subsystems of the model is described by independent generalized coordinates which are components of vectors (2), (3) and (4), the constraint equations and their reactions have to be introduced in the system. Index s (the jib number) is omitted in the considerations concerned with reactions in connections between rfes.

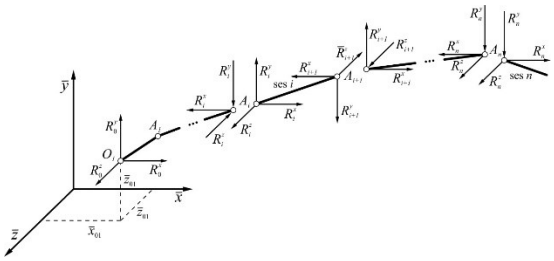

Figure 3. Constraint reactions of the boom

Fig.3 shows the way the constraints reactions are introduced between rigid elements into which the booms are discretized. All reactions as well as external forces acting on the system are introduced by means of generalized forces. Generalized force resulting from force **F** which acts at a point with coordinates defined by vector **r,** are calculated according to the following formula:

$$Q_j = \left(\frac{\partial \mathbf{r}}{\partial q_j}\right)^T \mathbf{F} \tag{6}$$

where q_j is the generalized coordinate, Q_j is the generalized force.

When rfe i $(i = 0, \ldots., n_s)$ is considered (Fig.3), the following reactions occur:

- force $\mathbf{R}_i = \begin{bmatrix} R_i^x & R_i^y & R_i^z \end{bmatrix}^T$ at point A_i– the beginning of rfe i,

- force $-\mathbf{R}_{i+1} = \begin{bmatrix} R_{i+1}^x & R_{i+1}^y & R_{i+1}^z \end{bmatrix}^T$ at point A_{i+1}– the end of rfe i.

Coordinates of points A_i and A_{i+1} can be calculated as follows:

$$\mathbf{r}(A_i) = \mathbf{A}^{(i)}\mathbf{r}'_{i,L} \tag{7.1}$$

$$\mathbf{r}(A_{i+1}) = \mathbf{A}^{(i)}\mathbf{r}'_{i,R} \tag{7.2}$$

where $\mathbf{A}^{(i)}$ is the transformation matrix from local coordinate system assigned to rfe i to system $\{\quad\}^-$, $\mathbf{r}'_{i,L}$ is the local coordinate vector of point A_i, $\mathbf{r}'_{i,R}$ is the local coordinate vector of point A_{i+1}.

In view of (6) the following generalised forces

$$Q_{Rj}^{(i)} = \left(\mathbf{A}_j^{(i)}\mathbf{r}'_{i,L}\right)^T \mathbf{R}_i - \left(\mathbf{A}_j^{(i)}\mathbf{r}'_{i,R}\right)^T \mathbf{R}_{i+1} \tag{8}$$

where $j = 1, \ldots., m$; $\mathbf{A}_j^{(i)} = \frac{\partial \mathbf{A}^{(i)}}{\partial q_{i,j}}$ have to be introduced in the equation of motion for rfe i.

In this way $3(n+1)$ additional unknowns are introduced into the equations of motions and thus additional constraints equations are formulated in the form:

$$\mathbf{r}_{A_0}(\mathbf{q}_0) = \mathbf{r}_{01} = \text{const} \equiv \mathbf{A}^{(0)}\mathbf{r}'_{0,L} = \mathbf{r}_{01} = \text{const} \tag{9.1}$$

$$\mathbf{r}_{A_i}(\mathbf{q}_i) = \mathbf{r}_{A_i}(\mathbf{q}_{i-1}) \equiv \mathbf{A}^{(i)}\mathbf{r}'_{i,L} = \mathbf{A}^{(i-1)}\mathbf{r}'_{i-1,R}, \quad i = 1, \ldots, n \tag{9.2}$$

The reactions have to be introduced for both jibs (index s).

Similarly, reactions and constraint equations have to be also introduced for cylinders as well as at points A, B, C, D (Fig.2) where the cylinders are connected with booms.

After all the necessary transformations and double differentiation of the constraint equations the equation of motion can be written in the form:

$$\mathbf{M}\ddot{\mathbf{q}} = \mathbf{D}\mathbf{R} + \mathbf{f} \tag{10.1}$$

$$\mathbf{D}^T\ddot{\mathbf{q}} = \mathbf{G} \tag{10.2}$$

where $\mathbf{M}$ is the mass matrix, $\mathbf{D}$ is the matrix with coefficients derived from the constraint equations, $\mathbf{f}$ is the vector consisting of components resulting from the kinetic energy, potential energy of gravity forces and spring deformations of booms, cylinders and rope system, $\mathbf{G}$ is the right side of constraint equations.

The equations of motion are integrated using the Runge-Kutta method of the fourth order with constant step.

3. Numerical simulations

Computer implementation of the proposed model of dynamics has been carried out in Borland Delphi 7.0 environment. It enables us to simulate dynamics of the crane during basic operations (lifting and droping the load, rotating the crane). The program is equipped with a sophisticated graphical interface enabling the constructors to define parameters of a crane in a convenient way (Fig.4). Simulation results are presented in the form of grouped charts, tables and also saved in files. The results from files can be then processed using different software.

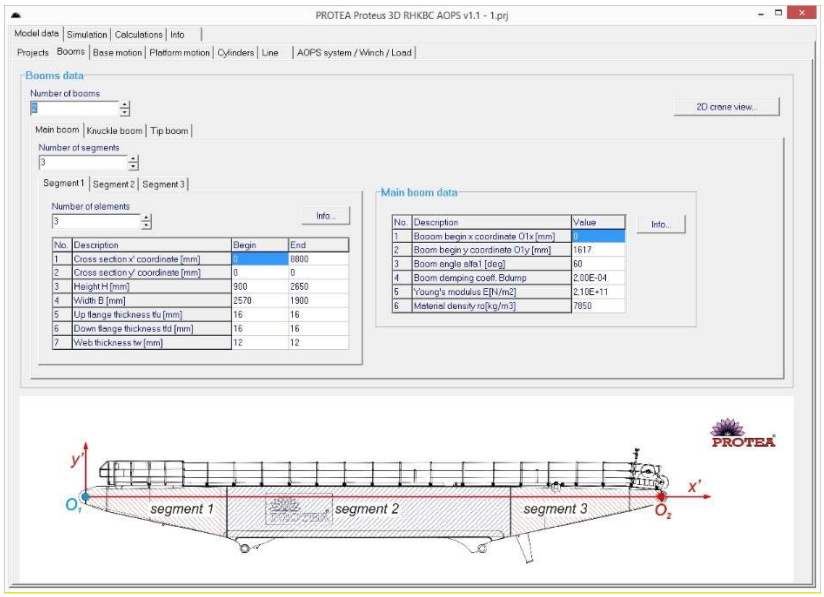

Figure 4. Screenshot of the window for definition of jib parameters

Below we present some possibilities of the software for dynamic analysis of the crane in the following problems:

– rotation of the base (P1),

– lifting the load by means of the change of the cylinders length (P2),

– testing AOPS (Active Overload Protection System) (P3).

All simulation results presented below are obtained for the crane with maximal crane radius R_{max} = 57 m and boom inclinations $\alpha_1 = 60^o$ and $\alpha_2 = 20^o$. There is mass m_L = 7000 kg attached at the end of the rope.

The rotation of the crane with respect to the undeformable column in task P1 is defined as a kinematic function. It is assumed that the rotation about 90^o is performed during 10 s. The course of function θ_P (the angle of crane rotation) and its derivative with respect to time is presented in Fig. 5. Fig. 6 shows trajectories of the end of the rope together with the attached load and the end of the second jib (point G) projected on plane xz. Jib deflections U_y, U_z and values of overload coefficient in the rope system ψ are presented in Fig. 7 and 8.

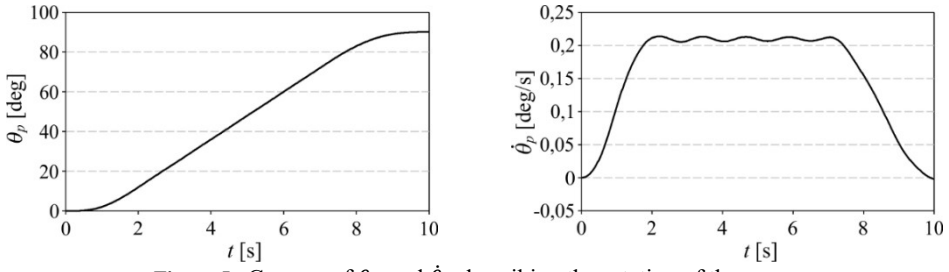

Figure 5. Courses of θ_P and $\dot{\theta}_P$ describing the rotation of the crane

Dynamic coefficient in the rope system ψ is calculated according to the formula:

$$\psi = \frac{S}{S_{WL}} \tag{11}$$

where: S – the force in the rope, $S_{WL} = \frac{m_L g}{i_L}$, m_L– mass of the load, i_L– rope system ratio.

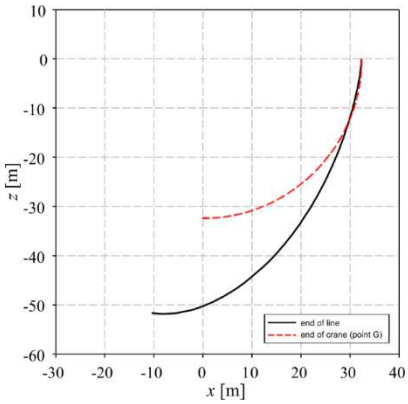

Figure 6. Trajectory of the rope end and the second jib end (point G) projected on plane xz

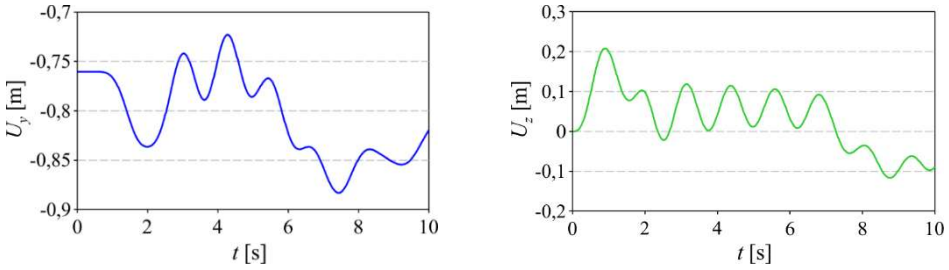

Figure 7. Jib deflections U_y, U_z – problem P1

The value of coefficient ψ during the analysed rotation of the crane does not exceed 1.2 m. Vertical U_y and horizontal U_z deflections of the crane caused by the rotary movement increased by about 0.2 m.

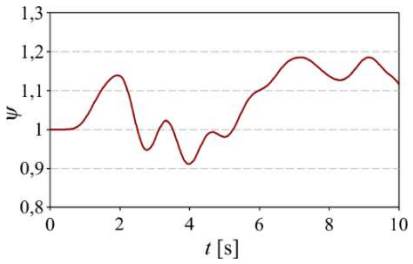

Figure 8. Dynamic coefficient in the rope system ψ - problem P1

Lifting the load caused by the change in the length of cylinders δC_1 and δC_2 is realised as presented in Fig. 9. Courses δC_1 and δC_2 are obtained by interpolation of discrete data using spline functions of the third order.

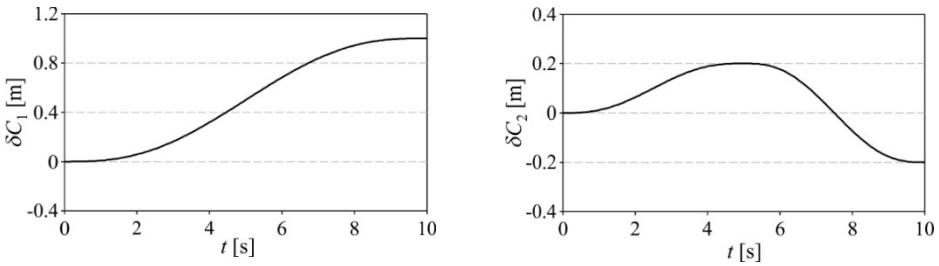

Figure 9. Courses of the elongation of cylinders δC_1 and δC_2 in problem P2 – lifting the load

While lifting the load in this way values of the dynamic coefficient of the rope ψ as well as vertical deflections U_y of the crane are analysed. Courses of both values are shown in Fig. 10.

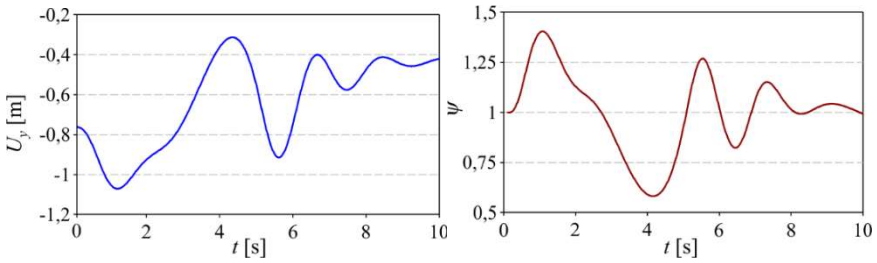

Figure 10. Vertical deflection U_y and dynamic coefficient in the rope ψ – problem P2

Analysis of changes of the values of dynamic coefficient in the rope ψ during the process of lifting the load allows us to define the moment when the largest strain on the rope system and thus the crane occur. In the task considered this situation occur at the beginning of lifting the load (at t = 1.1 s). The elongations of the two cylinders are then $\delta C_1 = 0{,}06$ m and $\delta C_1 = 0$ m respectively, while the vertical deflection of the crane equals U_y = -1.07 m.

4. Conclusions

Computer programmes developed and used during the design stage of the offshore equipment facilitate engineering work. Mathematical models and software elaborated on their basis take into account many parameters (dynamic loads) which are specific for the environment in which the device is exploited. The program presented enables offshore knuckle cranes to be tested during loading/unloading on the sea. Courses of deflections of the crane and loads in the rope system create valuable source of information for engineers for the choice of jib cross-sections, rope system and parameters of cylinders. They are also the basis for obtaining permission from independent regulatory authorities to use the crane in real conditions.

References

[1] Than, T.K., Langen , I., and Birkeland, O. Modelling and simulation of offshore crane operations on a floating production vessel. In *Proceedings of the Twelfth (2002) International Offshore and Polar Engineering Conference.* Kitakyushu, Japan. 2002.

[2] Bak, M.K., Hansen, M.R., and Nordhammer, P.A. Virtual prototyping – model of offshore knuckle boom crane. In *Proceedings of the 24th International Congress on Condition Monitoring and Diagnostic Engineering Management.* Stavanger, Norway. 2011.

[3] Henriksen, J.,Bak, M.K., and Hansen, M.R. A method for finite element based modelling of flexible components in time domain simulation of knuckle boom crane. In *Proceedings of the 24th International Congress on Condition Monitoring and Diagnostic Engineering Management.* Stavanger, Norway. 2011.

[4] Bak, M.K., and Hansen, M.R. Analysis of offshore knuckle boom crane – part one: modelling and parameter identification. *Modeling, Identification and Control* 34, 4(2013) 157-174.

[5] Connely, J.D., Huston, R.L. The dynamics of flexible multibody systems: A finite segment approach-I. Theoretical aspects. *Computer & Structures* 50, 2(1994), 252-258.

[6] Connely, J.D., Huston, R.L. The dynamics of flexible multibody systems: A finite segment approach-II. Example problems. *Computer & Structures* 50, 2(1994), 259-262.

[7] Wittbrodt, E., Adamiec–Wójcik, I., Wojciech S. *Dynamics of flexible multibody systems: rigid finite element method*, Berlin: Springer, 2006.

[8] Wittbrodt, E., Szczotka, M., Maczyński, A., Wojciech, S. *Rigid finite element method in analysis of dynamics of offshore structures.* Springer–Verlag, Berlin Heidelberg, 2013.

[9] Drąg, Ł. *Modelling ropes, risers and cranes with the rigid finite element method.* Bielsko-Biala University Press, Bielsko-Biała, 2017.

[10] Maczyński, A., Wojciech, S. Stabilization of load's position in offshore cranes. *Journal of Offshore Mechanics and Arctic Engineering* 134(2012), 1-10.

[11] Osiński, M., Wojciech, S. Application of nonlinear optimisation methods to input shaping of the hoist drive of an off-shore crane. *Nonlinear Dynamics* 17, 4 (1998), 369-386.

Iwona Adamiec-Wójcik, Professor: University of Bielsko-Biala/Faculty of Management and Transport/Department of Computer Modelling, Willowa 2, 43-309 Bielsko-Biała, Poland (i.adamiec@ath.bielsko.pl).

Łukasz Drąg, Lecturer: University of Bielsko-Biala/Faculty of Management and Transport/Department of Computer Modelling, Willowa 2, 43-309 Bielsko-Biała, Poland (ldrag@ath.bielsko.pl). The author gave a presentation of this paper during one of the conference sessions.

Kamil Nadratowski, Protea sp z o.o., Galaktyczna 30a, 80-299 Gdansk, Poland (kamil.nadratowski@protea.pl).

Stanisław Wojciech, Professor: University of Bielsko-Biala/Faculty of Management and Transport/Department of Computer Modelling, Willowa 2, 43-309 Bielsko-Biała, Poland (swojciech@ath.bielsko.pl).

Modelling Coulomb friction by extended Filippov systems

Mate Antali, Gabor Stepan

Abstract: When modelling the contact of two rigid bodies in the presence of Coulomb friction, a special system of first-order differential equation is obtained, which is discontinuous on a codimension-2 submanifold of the state space. This leads to the concept of Extended Filippov Systems, which was introduced recently by the authors. By using the developed methods, the conditions of slipping or rolling/sticking of the contacting rigid bodies can be analysed from purely the structure of the phase space of the slipping dynamics. By calculating the so-called limit directions of the points of the discontinuity set, our theory provides a deeper understanding of the transitions between rolling and slipping in mechanical problems. Moreover, the calculation of the limit directions helps us to create an effective numerical method to simulate these systems.

1. Introduction

The presence of dry friction between rigid bodies leads to discontinuous dynamical models. In case of the simple Coulomb friction model in 2D contact problems, the friction force changes sign at zero relative velocity of the surfaces. A similar but more complicated singularity occurs in the 3D case. Then, for infinitesimally small relative velocities, the Coulomb model provides continuously many directions of the friction force with a constant finite amplitude.

The direct substitution of the discontinuous friction models into the dynamical equations leads to discontinuous systems of differential equations. In the 2D case, the Coulomb friction leads to *Filippov systems* (for an overview and examples, see [6]). Considering the friction as a set-valued force law leads to *differential inclusions*, which is a completely different point of view of modelling (see [8] for an overview). A further approach can be found in [3].

The generalization of the Filippov systems to codimension-2 discontinuity sets in the phase space leads to the concept of *extended Filippov systems* (see [1] and [2]). This type of differential equation can be used for modelling and analysis of the 3D Coulomb friction, which has been demonstrated in specific mechanical examples in [2]. However, no general analysis has been presented about the contact between rigid bodies.

In this paper, we analyse the dynamics of a single rigid body in contact with a fixed rigid plane. The formal derivation of the general equations of motion is presented with the appropriate choice of the variables (Section 2). After an overview of the basic concepts of

extended Filippov systems (Section 3), the nonsmooth differential equations of the rigid body is analysed (Section 4). By determining the so-called limit directions at the discontinuity set, the occurrence and the properties of the transitions are analysed between rolling and slipping.

2. Dynamics of a rigid body on a flat surface

2.1. Kinematics

We consider a rigid body in contact with a fixed rigid plane (see Figure 1). The centre of gravity of the body is denoted by C and the instantaneous contact point is denoted by P. It is assumed that the surface of the body is smooth and there is a single contact point during the motion. The relation between the velocities $\mathbf{v}_C$ and $\mathbf{v}_P$ of C and P is given by

$$\mathbf{v}_C = \mathbf{v}_P + \boldsymbol{\omega} \times \mathbf{r}_{PC}, \tag{1}$$

where $\boldsymbol{\omega}$ is the angular velocity of the body and $\mathbf{r}_{PC}$ is the position vector of C from the contact point P. During the motion, P is related to different points of the rigid body. Therefore the time derivative of (1) can be calculated from two different viewpoints. If we follow the motion of the *material point of the body currently located at* P then the time derivative of (1) becomes the usual formula

$$\mathbf{a}_C = \mathbf{a}_P + \boldsymbol{\alpha} \times \mathbf{r}_{PC} + \boldsymbol{\omega} \times (\mathbf{v}_C - \mathbf{v}_P), \tag{2}$$

where $\mathbf{a}_C$ and $\mathbf{a}_P$ are the acceleration of the points C and P, respectively, and $\boldsymbol{\alpha}$ denotes the angular acceleration of the body. Then, the time derivative of $\mathbf{r}_{CP}$ originates from the difference between the velocities of the two points.

However, if we follow the *instantaneous geometric contact point* P then the time derivative of (1) becomes

$$\mathbf{a}_C = \dot{\mathbf{v}}_P + \boldsymbol{\alpha} \times \mathbf{r}_{PC} + \boldsymbol{\omega} \times (\mathbf{v}_C - \mathbf{w}_P). \tag{3}$$

In (3), $\dot{\mathbf{v}}_P$ denotes the time derivative of the velocity $\mathbf{v}_P$ of P. This derivative is not the same as $\mathbf{a}_P$ because the point P is related to different material points of the body along the motion. In this sense, the time derivative of $\mathbf{r}_{CP}$ is caused by the difference between the velocity $\mathbf{v}_C$ of C and the velocity $\mathbf{w}_P$ of the *translation of the contact point* along the plane. This velocity is composed from two parts,

$$\mathbf{w}_P = \mathbf{v}_P + \mathbf{w}_{P0}. \tag{4}$$

The two terms of (4) show that the translational velocity $\mathbf{w}_P$ of the contact point originates partly from the slipping velocity $\mathbf{v}_P$ of the instantaneous contact point and the translation

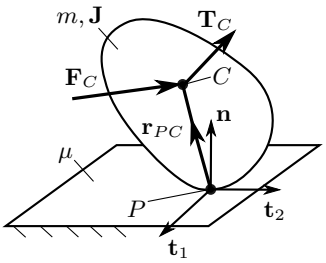

Figure 1. Sketch of the mechanical system. A rigid body is moving in contact with a fixed plane. In this paper, the transitions between slipping and rolling are investigated.

$\mathbf{w}_{P0}$ caused by the rolling of the body. It can be shown that the latter quantity is determined by

$$\mathbf{w}_{P0} = \frac{1}{\kappa} (\boldsymbol{\omega} \times \mathbf{n}) , \tag{5}$$

where $\mathbf{n}$ is the unit normal vector of the plane and κ denotes the normal curvature of the surface of the body in the plane determined by $\boldsymbol{\omega} \times \mathbf{n}$. For simple geometries, the normal curvature κ can be specified intuitively; and for general surfaces, it is determined by the second fundamental form of the surface (see [7], p. 206).

By using the expressions (1) and (3)-(5), it is possible to express all quantities on the velocity and acceleration level by $\mathbf{v}_P$, $\boldsymbol{\omega}$ and their derivatives. The Coulomb friction model is discontinuous at $\mathbf{v}_P = \mathbf{0}$, and by this choice of variables, the discontinuity set of the differential equation can be described easily.

2.2. Dynamics

Let $\mathbf{F}_P$ denote the force acting on the body at the contact point P. The effect of all other forces and torques acting on the body are substituted by a force $\mathbf{F}_C$ and a torque $\mathbf{T}_C$ acting at the centre C of gravity. Then, the Newton-Euler equations of the body become

$$\begin{aligned} m\mathbf{a}_C &= \mathbf{F}_C + \mathbf{F}_P, \\ \mathbf{J}\boldsymbol{\alpha} + \boldsymbol{\omega} \times (\mathbf{J}\boldsymbol{\omega}) &= \mathbf{T}_C - \mathbf{r}_{PC} \times \mathbf{F}_P, \end{aligned} \tag{6}$$

where m is the mass of the body and $\mathbf{J}$ is the moment of inertia tensor with respect to the centre of gravity C.

The equations (6) are supplemented by additional equations according to the rolling or slipping state of the contact. In case of rolling, the motion satisfies the rolling constraint

$$\mathbf{v}_P \equiv 0. \tag{7}$$

By assuming slipping, the force acting at P can be expressed by the Coulomb friction law

$$\mathbf{F}_P = N \cdot \left(\mathbf{n} - \mu \frac{\mathbf{v}_P}{|\mathbf{v}_P|} \right), \tag{8}$$

where μ denotes the friction coefficient and N is the normal contact force between the surfaces. The analysis is restricted to the slipping or rolling states only, and we do not consider other phenomena like separation of the surfaces, impact without collision and consistency problems between the contact modes (see [5]).

2.3. Differential equation for the slipping case

By combining (1)-(5) and (6), the time derivatives of $\mathbf{v}_P$ and $\boldsymbol{\omega}$ can be expressed,

$$\dot{\boldsymbol{\omega}} = \boldsymbol{\alpha} = -\mathbf{J}^{-1} \cdot (\boldsymbol{\omega} \times (\mathbf{J}\boldsymbol{\omega})) + \mathbf{J}^{-1} \cdot \mathbf{T}_C - \mathbf{J}^{-1} \cdot (\mathbf{r}_{PC} \times \mathbf{F}_P), \tag{9}$$

$$\dot{\mathbf{v}}_P = \frac{\mathbf{F}_C}{m} + \frac{\mathbf{F}_P}{m} - \dot{\boldsymbol{\omega}} \times \mathbf{r}_{PC} - \boldsymbol{\omega} \times \left(\boldsymbol{\omega} \times \mathbf{r}_{PC} - \frac{1}{\kappa} (\boldsymbol{\omega} \times \mathbf{n}) \right). \tag{10}$$

To get an ordinary differential equation from (9)-(10), we introduce coordinates both in the displacement and the velocity level. Assume that in the neighbourhood of a chosen initial state, the position and the orientation of the rigid body is described by five generalized coordinates in the form

$$q = (q_1, q_2, q_3, q_4, q_5). \tag{11}$$

The sixth degree of freedom of the rigid body is fixed by the constraint of the normal contact between the body and the plane.

Let us choose an orthonormal coordinate system consisting of two unit vectors $\mathbf{t}_1$ and $\mathbf{t}_2$ laying in the tangent plane of the contact and the normal unit vector $\mathbf{n}$ defined before (see Figure 1). Then, the velocity state of the body is described by the set

$$s = (u_1, u_2, \omega_1, \omega_2, \omega_3) \tag{12}$$

of quasi-velocities (see [9], p. 254), where the components of $\mathbf{v}_P$ and ω are defined by

$$\mathbf{v}_P = u_1 \mathbf{t}_1 + u_2 \mathbf{t}_2, \qquad \boldsymbol{\omega} = \omega_1 \mathbf{t}_1 + \omega_2 \mathbf{t}_2 + \omega_3 \mathbf{n}. \tag{13}$$

The generalized coordinates (11) and the quasi-velocities (12) can be used to compose a set of first-order ordinary differential equations of the body. The time derivatives of the generalised coordinates are expressed in the form

$$\dot{q} = K(q) \cdot s, \tag{14}$$

where $K(q)$ is a 5 by 5 matrix depending on the generalized coordinates q. By taking the time derivative of (13), we get

$$\dot{\mathbf{v}}_P = \dot{u}_1\mathbf{t}_1 + \dot{u}_2\mathbf{t}_2, \qquad \dot{\boldsymbol{\omega}} = \dot{\omega}_1\mathbf{t}_1 + \dot{\omega}_2\mathbf{t}_2 + \dot{\omega}_3\mathbf{n}. \tag{15}$$

That is, the left-hand sides of (9)-(10) contain the time derivatives of the five quasi-velocities (12). From the last component of (10), the unknown normal force N can be expressed algebraically, which is necessary to calculate the friction forces in the Coulomb model (8).

On the right-hand sides of (9)-(10), all quantities can be expressed by q and s. The geometric quantities $\mathbf{r}_{PC}(q)$ and $\kappa(q)$ depend on the generalised coordinates, and the moment of inertia tensor $\mathbf{J}(q)$ is affected by the orientation of the body, as well. We assume that there is no explicit time dependence in the external forces, that is, the resultant $\mathbf{F}_C(q,s)$ and $\mathbf{T}_C(q,s)$ is expressed by q and s. In case of slipping, the force $\mathbf{F}_P$ from (8) can be expressed in the form

$$\mathbf{F}_P = -\mu N \frac{u_1}{\sqrt{u_1^2+u_2^2}}\,\mathbf{t}_1 - \mu N \frac{u_2}{\sqrt{u_1^2+u_2^2}}\,\mathbf{t}_2 + N\mathbf{n}. \tag{16}$$

Finally, the equations (9)-(10) can be transformed into the form

$$\dot{s} = f(q,s), \tag{17}$$

where the function f can be derived from (9) and (10).

From equations (14) and (17), a set of first-order differential equations can be composed for the variables s and q. This differential equation is not defined at $u_1 = u_2 = 0$ because of the formula of the friction force in (16). The states with $u_1 = u_2 = 0$ correspond to *rolling*, which behaviour is described by another differential equations by including the rolling constraint (7). However, the discontinuous behaviour of the slipping equations at $u_1 = u_2 = 0$ becomes important when the system switches between rolling and slipping. An analysis of the system can be provided by the tools of the extended Filippov systems, which are presented briefly in the next section.

3. Basic concepts of extended Filippov systems

In this section, the most important concepts and definitions of extended Filippov systems are presented, which are applied for the analysis of the rigid body on the plane. For a more detailed description of these systems can be found in [1] and [2].

Suppose that the vector field is located in the domain $\mathcal{D} \in \mathbb{R}^m$. Consider an $m-2$ dimensional smooth manifold $\Sigma \subset \mathcal{D}$, where the vector field is discontinuous in the sense defined below. At a point $x_0 \in \Sigma$, let the tangent space denoted by $\mathcal{T}_{x_0}\Sigma$, and its orthogonal

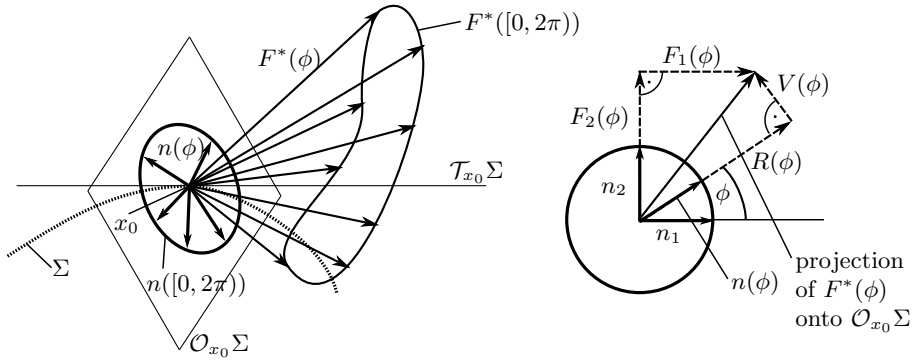

Figure 2. Basic concepts of extended Filippov systems. Left panel: the behaviour of the vector field at a point of the discontinuity manifold Σ. Right panel: the definition of the functions $R(\phi)$ and $V(\phi)$ in the orthogonal space of the discontinuity manifold.

complement is denoted by $\mathcal{O}_{x_0}\Sigma$ (see the left panel of Figure 2). In other words, $\mathcal{O}_{x_0}\Sigma$ contains the vectors $v \in \mathbb{R}^m$ for that $\langle v, w\rangle = 0$ for all $w \in \mathcal{T}_{x_0}\Sigma$, where $\langle .,. \rangle$ denotes the usual scalar product in $\mathbb{R}^m$.

At a point $x_0 \in \Sigma$, consider an orthonormal basis $(n_1, n_2)(x_0)$ of $\mathcal{O}_{x_0}\Sigma$ with $\langle n_1, n_1\rangle = \langle n_2, n_2\rangle = 1$ and $\langle n_1, n_2\rangle = 0$, where n_1 and n_2 depends smoothly on x_0. Then, let us define the function

$$n(\phi)(x_0) := \cos\phi \cdot n_1(x_0) + \sin\phi \cdot n_2(x_0). \tag{18}$$

That is, $n(\phi)$ maps the interval $[0, 2\pi)$ onto the unit vectors of $\mathcal{O}_{x_0}\Sigma$. The parameter $\phi \in [0, 2\pi)$ can be imagined as an angle corresponding to the possible directions orthogonal to Σ at x_0 (see the left panel of Figure 2).

Definition 1 *(Extended Filippov system) Consider the vector field*

$$\dot{x} = F(x), \qquad x \in \mathcal{D} \subset \mathbb{R}^m, \qquad F : \mathcal{D} \setminus \Sigma \to \mathbb{R}^m, \tag{19}$$

where Σ is an $m-2$ dimensional smooth manifold in $\mathcal{D}$. The system (19) is called an ***extended Filippov system*** *if the following properties are satisfied:*

1. *The vector field F is smooth on $\mathcal{D} \setminus \Sigma$.*

2. *The limit*

$$F^*(\phi)(x_0) := \lim_{\epsilon \to 0^+} F\left(x_0 + \epsilon n(\phi)(x_0)\right) \tag{20}$$

exists for all $x_0 \in \Sigma$ and for all $\phi \in [0, 2\pi)$.

3. For all x_0, there exist $\phi_1, \phi_2 \in [0, 2\pi)$ for that $F^*(\phi_1) \neq F^*(\phi_2)$.

The three requirements of Definition 1 prescribe that the discontinuity of the system is restricted to the manifold Σ, the limit of the vector field does not diverge from any direction, and there is indeed a discontinuity all along Σ. In the sense of Definition 1, Σ is called a ***codimension–2 discontinuity manifold of*** F.

At a chosen point $x_0 \in \Sigma$, the function $F^*(\phi)$ is called the ***limit vector field*** *of* F (see Figure 2). The projection of this limit vector field onto $\mathcal{O}_{x_0}\Sigma$ can be described by the quantities

$$R(\phi) := \langle F^*(\phi), n(\phi) \rangle \,, \qquad\qquad V(\phi) := \langle F^*(\phi), n(\phi + \pi/2) \rangle \,. \tag{21}$$

The function $R(\phi)$ describes the vector field in the radially inward or outward direction, and $V(\phi)$ gives the dynamics rotating around the discontinuity set (see the right panel of Figure 2). By using the polar coordinates r and ϕ, the system $\dot{r} = R(\phi)$, $\dot{\phi} = V(\phi)/r$ describes the dynamics of the projected vector field into the orthogonal space $\mathcal{O}_{x_0}\Sigma$.

Definition 2 *(Limit direction) Consider an extended Filippov system $\dot{x} = F(x)$ and a point $x_0 \in \Sigma$ of the discontinuity manifold. The roots of the equation $V(\phi) = 0$ are called the* ***limit directions*** *of x_0 with respect to F. A limit direction ϕ_1 with $V(\phi_1) = 0$ is called* ***attracting*** *if $R(\phi_1) < 0$ and it is called* ***repelling*** *if $R(\phi_1) > 0$.*

The limit directions have an important role because they correspond to the trajectories of F tending to x_0 in forward (attracting limit direction) or backward time (repelling limit direction). If all limit directions of x_0 are either attracting or repelling then the dynamics of F gets stuck into Σ in forward or backward time, respectively. This leads to the so-called ***sliding dynamics*** generated inside the discontinuity manifold Σ. For the exact derivations and a more detailed explanation, see [1] and [2].

The introduction of the definition of extended Filippov systems were motivated by mechanics because the slipping 3D of rigid bodies on each other with Coulomb friction leads to this type of dynamical system. Then, the rolling behaviour corresponds to the sliding dynamics of the extended Filippov system. Therefore, the analysis of the limit directions can be applied to explore the transitions between slipping and rolling between the bodies.

4. Application of the tools of extended Filippov system

4.1. Modelling by an extended Filippov system

Let us consider the problem of the rigid body on the plane, which was presented in Section 2. From (11) and (12), we can compose the state variable

$$x = (s, q) = (u_1, u_2, \omega_1, \omega_2, \omega_3, q_1, q_2, q_3, q_4, q_5) \in \mathbb{R}^{10}. \tag{22}$$

By using the vector field $F = (f(s,q), K(q) \cdot s)$, the differential equation from (14) and (17) can be written in the form

$$\dot{x} = F(x). \tag{23}$$

The discontinuity of the vector field $F(x)$ is caused by the terms $u_1/\sqrt{u_1^2 + u_2^2}$ and $u_2/\sqrt{u_1^2 + u_2^2}$ (see (16)). The structure of (9) and (10) shows that these discontinuous terms are subjected to addition and multiplication by smooth terms. Therefore, the resulting vector field $F(x)$ can be written in the form

$$F(x) = \frac{u_1}{\sqrt{u_1^2 + u_2^2}} \cdot A(x) + \frac{u_2}{\sqrt{u_1^2 + u_2^2}} \cdot B(x) + C(x), \tag{24}$$

where $A(x), B(x)$ and $C(x)$ are smooth vector fields.

Let us check whether the system (24) is indeed an extended Filippov system. The discontinuity manifold Σ of (24) is the hyperplane defined by $u_1 = u_2 = 0$. At any point $x_0 \in \Sigma$, the basis of the orthogonal complement $\mathcal{O}_{x_0}\Sigma$ can be fixed to $n_1 = (1, 0, \dots 0)$ and $n_2 = (0, 1, \dots 0)$. Then, (18), becomes

$$n(\phi) = n_1 \cdot \cos\phi + n_2 \cdot \sin\phi = (\cos\phi, \sin\phi, 0, \dots 0), \tag{25}$$

and direct calculation of (20) leads to

$$F^*(\phi)(x_0) = \cos\phi \cdot A(x_0) + \sin\phi \cdot B(x_0) + C(x_0). \tag{26}$$

It can be seen from (24) and (26) that the conditions of Definition 1 are satisfied and (24) is an extended Filippov system.

4.2. Limit directions

The discontinuity set Σ is defined by $u_1 = u_2 = 0$ in the 10 dimensional phase space, thus, its points can be given by the remaining 8 variables in the form $x_0 = (0, 0, \omega_1, \omega_2, q_1, q_2, q_3, q_4, q_5)$.

We want to categorize these points of Σ according to the number and type of the limit directions of the system (see Definition 2). At a given point $x_0 \in \Sigma$, let us calculate the functions R and V from (21). Then, we get

$$R(\phi) = \frac{A_1 + B_2}{2} + C_1 \cos\phi + C_2 \sin\phi + \frac{A_1 - B_2}{2} \cos 2\phi + \frac{B_1 + A_2}{2} \sin 2\phi, \tag{27}$$

$$V(\phi) = \frac{A_2 - B_1}{2} + C_2 \cos\phi - C_1 \sin\phi + \frac{B_1 + A_2}{2} \cos 2\phi - \frac{A_1 - B_2}{2} \sin 2\phi, \tag{28}$$

where the first two components of the vectors A, B, C are defined by $A = (A_1, A_2, \dots)$, $B = (B_1, B_2, \dots)$, $C = (C_1, C_2, \dots)$.

Determining the roots of the finite Fourier series $V(\phi)$ leads to an eigenvalue problem of a 4 by 4 complex matrix, which results in maximum 4 real roots on the interval $[0, 2\pi)$ (see [4]). Hence, the system has maximum 4 limit directions. Moreover, it can be shown by direct calculation from (9)-(10) that $A_2 = B_1$. Therefore, the constant term of (28) vanishes and the integral of $V(\phi)$ on $[0, 2\pi)$ becomes zero, which requires at least 2 roots. *Consequently, the system* (24) *has 2, 3 or 4 limit directions.*

Although the limit directions $\phi_1, \phi_2, \dots$ can be expressed analytically, the resulting general formula is too lengthy for deciding the sign of $R(\phi)$ in Definition 2. However, from Definition 2, the boundary case between an attracting and repelling limit direction is given by $R(\phi) = V(\phi) = 0$, which leads to

$$(A_1 B_2 - A_2 B_1)^2 = (A_1 C_2 - A_2 C_1)^2 + (B_1 C_2 - B_2 C_1)^2. \tag{29}$$

The quantities $A_1 \dots C_2$ depends smoothly on the phase variables $\omega_1 \dots q_5$ from (22). Therefore, (29) is an implicit formulation of a 7 dimensional smooth surface in the 8 dimensional discontinuity set Σ. This surface separate the regions in Σ with a different types of limit directions.

From the theoretically possible numbers and types of limit directions, let us find and characterise the most important and physically realistic cases. The case with 3 limit directions corresponds to the occurrence of multiple root of (28) with $V(\phi_1) = \mathrm{d}V(\phi_1)/\mathrm{d}\phi = 0$. Thus, from the possible numbers of the limit directions, the cases 2 and 4 occur in general.

Let us suppose that the behaviour of the system should be unique in forward time, in accordance with the usual mechanical expectations. Exact checking of this assumption from the structure of (9)-(10) can be a task of the further research. This uniqueness requires that there can be maximum 1 repelling direction, because otherwise, the transition from rolling to slipping would result in more different solutions.

The typical phase portraits and the limit directions can be seen in Figure 3. First panel: 2 attracting limit directions; second panel: 1 attracting and 1 repelling direction; third panel: 4 attracting directions; fourth panel: 3 attracting and 1 repelling directions.

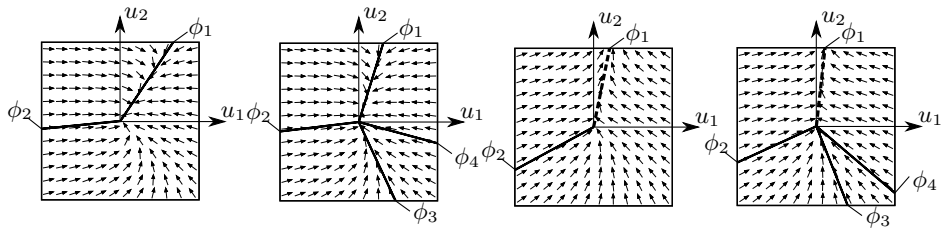

Figure 3. Sketch of the dynamics of (24) projected into the orthogonal space at some typical cases of points. The origin of the diagrams corresponds to the discontinuity of the slipping equations at the rolling limit case $u_1 = u_2 = 0$. The solid lines denote the *attracting limit directions*, the dashed lines denote the *repelling limit directions*.

4.3. Mechanical consequences

The system $F(x)$ in (23) was introduced to describe the *slipping* behaviour of the body. The discontinuity manifold Σ is the line $u_1 = u_2 = 0$, which coincides with the condition of the rolling constraint (7). That is, the *rolling* dynamics of the system is defined on Σ. The (smooth) rolling vector field can be derived either from the Newton-Euler equations (6) with the rolling constraint (7), or directly from the limit vector field (26) of the slipping case (see [1] about the *sliding dynamics*).

We want to show the consequences on the presented results on the transitions between the rolling and the slipping behaviour. In the projected phase portraits in Figure 3, the corresponding point x_0 of the discontinuity set Σ is located in the origin. In this phase portraits, the transition between rolling and slipping corresponds to the trajectories which tend to the origin in forward or backward time. It can be shown that these trajectories reach the origin in *finite time* (see [2] for the proof). The limit directions show the directions where the trajectories can reach the origin, thus, they determine the possibility and the properties of slipping-rolling transitions.

If there are only attracting limit directions (see the first and the second case in Figure 3) then *all* nearby trajectories tend to the origin of the projected phase space and they cannot be continued after a while. Then, the dynamics continues inside the discontinuity set Σ, which correspond to rolling. *Therefore, in case of attracting directions only, the rolling is realizable because the effect of small slipping perturbations are eliminated by the dynamics.*

It can be seen from the phase portraits that the behaviour of the different attracting limit directions are not the same. There are some *dominant* attracting directions (see e.g. ϕ_1 in the first panel of Figure 3), which attract the adjacent trajectories to the limit direction. However, there are some less dominant attracting directions (see e.g. ϕ_2 in the first panel

of Figure 3), which do not have this property. The different behaviour is determined by the sign of $\mathrm{d}V(\phi_i)/\mathrm{d}\phi$ at the limit directions, which becomes negative in case of a dominant direction. It can be shown that almost all trajectories reach the origin tending to the dominant attracting limit directions. *That is, the transition of the slipping into rolling is realized through these dominant attracting directions.* Note that in the second case of Figure 3, there are two dominant attracting directions (ϕ_1 and ϕ_3).

If there is a repelling limit direction (see the third and the fourth cases of Figure 3) then there is a possibility for escaping from the vicinity of the discontinuity set. *Therefore, in the presence of a repelling limit direction, the rolling is not realizable because the effect of small slipping perturbations can push the system away from the rolling state.*

Note that the dynamic behaviour in the third and the fourth cases of Figure 3 is fundamentally different. In the third panel, there is no dominant attracting direction, thus, most of the trajectories do not reach the origin but they avoid that. That is, the system gets close to the rolling behaviour, but it typically does not reach it. However, in the fourth panel, the dominant direction ϕ_3 attract all trajectories between ϕ_2 and ϕ_4 and makes them to reach the origin, and to be continued through the repelling direction ϕ_1. That is, a typical behaviour of the system is to reach the rolling behaviour for a moment but to start slipping immediately again.

5. Conclusion

The dynamical equations of a rigid body were derived which body is in contact with a rigid fixed surface. The key step of the derivation was expressing of the kinematic quantities by the velocity and acceleration of the instantaneous contact point between the body and the plane. As a result of the Coulomb friction model, the resulting dynamical system is discontinuous at the zero velocity of the contact point. By the methods of extended Filippov systems, the type and the number of the limit directions were analysed, which are strongly related to the slipping-rolling transitions of the rigid body. The important scenarios were investigated to explore the possible changes of the dynamics between rolling and slipping. The results lead to a deeper understanding of the problem, and they provide a guideline for the analysis of the specific mechanical problems. The information about the properties of the limit directions can be useful when creating an effective numerical simulation in the vicinity of this type of discontinuity in the phase space.

Acknowledgments

The research leading to these results has received funding from the European Research Council under the European Union's Seventh Framework Programme (FP/2007-2013) /

ERC Advanced Grant Agreement n. 340889.

References

[1] Antali, M. *Dynamics of Dual-Point Rolling Bodies.* PhD thesis, Budapest University of Technology and Economics, 2017.

[2] Antali, M., and Stepan, G. Sliding and crossing dynamics in extended filippov systems. *SIAM J. Applied Dynamical Systems* (2017). in publication.

[3] Batlle, J. A. The sliding velocity flow of rough collisions in multibody systems. *J. Appl. Mech. 63*, 3 (1996), 804–809.

[4] Boyd, J. P. Computing the zeros, maxima and inflection points of chebyshev, legendre and fourier series: solving transcendental equations by spectral interpolation and polynomial rootfinding. *Journal of Engineering Mathematics 56*, 3 (2006), 203–219.

[5] Champneys, A. R., and Varkonyi, P. R. The painlev paradox in contact mechanics. *IMA Journal of Applied Mathematics 81*, 3 (2016), 538–588.

[6] di Bernardo, M., Budd, C. J., Champneys, A. R., and Kowalczyk, P. *Piecewise-smooth Dynamical Systems.* Springer, 2008.

[7] Frankel, T. *The Geometry of Physics.* Cambridge University Press, 2012.

[8] Glocker, C. *Set-Valued Force Laws.* Springer, 2001.

[9] Greenwood, D. T. *Advanced Dynamics.* Cambridge University Press, 2003.

Mate Antali, Assistant professor: Budapest University of Technology and Economics, Muegyetem rkp 3, H-1111, Budapest, Hungary (*antali@mm.bme.hu*). The author gave a presentation of this paper during one of the conference sessions.

Gabor Stepan, Professor: Budapest University of Technology and Economics, Muegyetem rkp 3, H-1111, Budapest, Hungary (*stepan@mm.bme.hu*).

Nonlinear dynamics of inhomogeneous in two directions nano-beams with topologic optimal microstructure

J. Awrejcewicz, S.P. Pavlov, M.V. Zhigalov, V.A. Krysko

Abstract: In the first step of our study a microstructure is designed based on the method of topological optimization. Namely, for the specific conditions of loading and fastening of the beam a topological optimization of its microstructure is carried out by the criterion of maximum stiffness. In result, an optimized beam exhibits heterogeneity in two directions, i.e. in thickness and length. In the second step our investigations are aimed on the static and dynamic behavior of the beam using the Bernoulli–Euler model, including the size-dependent behavior on the basis of the modified couple stress theory and the geometric nonlinearity of the von Kármán type. Comparison of static and dynamic results for the optimal and homogeneous beams has been carried out taking into account the size-dependent behavior for various boundary conditions and load types. It is shown that for an uniform beam and a beam with optimal microstructure, the stress deformed state and the values of natural frequencies are significantly different, both for linear and nonlinear cases.

1. Introduction

The non-homogenous materials (NM) are composed of the multi-phase composites and their phase volumes can be changed in the required direction. The latter property allows for improvement of the material strength characteristics without occurrence of the harmful stress concentration. Owing to this feature, beams made from NM are widely used in numerous engineering fields including the gas turbines, wind turbines, rotor blades of a helicopter, wings, tethering paddles, wicket gates, ship power screws, as well as various structural elements of the cosmic and sea structures [1].

The change of the material property along an arbitrary direction can be described by the polynomials or exponential functions. In the case of beams the change of NM properties can be oriented in two directions simultaneously, i.e. in directions of the beam length and thickness. As the review of the state-of-the art of the available literature shows, a change of the elastic properties on the micro-structure level has been predicted by a constructer with a help of the methods of optimization.

Furthermore, majority of the so far carried out investigations are focused on a study of the NM beam free vibrations with an account for the change of the material properties with regard to beam thickness. The main goal of the carried out investigations was to find the frequencies of the different modes of beam vibrations using different methods [2-8].

However, analysis of the free vibrations of beam with non-homogenous transversal cross-section or with changeable material properties of a beam in its longitudinal direction is more complex in comparison to the beams of homogenous transversal cross-sections and made from the homogenous materials [9,10]. The occurred variable coefficients in the beam governing equations cause many problems and only a few analytical solutions have been found in the case of the free vibrations of beams exhibiting the change of material properties in the axial directions [11,12]. Non-linear behavior of non-homogenous beam with an account of the von Kármán geometric non-linearity using the finite element method (FEM) has been studied in reference [13]. FEM has been also employed to study free vibrations of axially and transversally non-homogenous beams made from NM and exhibiting large displacements [14]. Free vibrations of cantilever beams having both axially and transversally non-homogeneity using both FEM and the Euler-Bernoulli beam models have been analyzed in reference [15]. References [16-18] report vibrations and stability of a beam made from NM within the Euler-Bernoulli and Timoshenko models (they have been studied numerically). The Galerkin method has been employed to study geometrically non-linear beams made from NM in reference [19]. In order to investigate beams with an account for either homogenous or non-homogenous properties of the beam materials, numerous numerical models have been developed being based on the various beam theories including the Euler-Bernoulli [9,20-26] and Timoshenko [17, 27-30] models. Investigations of free vibrations and dynamic characteristics f the NM beams with changeable transversal cross-sections have been carried out in papers [31-33].

In our work, in contrary to the classical and widely used approaches based on the design engineers intuition and experience, the micro-structure of the beams has been defined with a help of the method of a topological optimization. The approach consists of two steps. In the first step, for the a priori defined loading conditions and boundary conditions for a given beam, the topological optimization of its microstructure based on getting the maximum stiffness is employed. In result of this procedure the beam with optimal microstructure exhibits non-homogeneity in two directions, i.e. along its thickness and length. In the second step, the static and dynamic beam behavior based on the Euler-Bernoulli hypothesis and taking into account the size dependent effects under employment of the modified momentous theory and the geometric von Kármán non-linearity, has been studied.

It has been shown that for the case of a homogenous beam and a beam with the optimized microstructure the stress-strain state and the fundamental frequencies are essentially different in either linear or non-linear case.

2. Mathematical background

In order to approximate the material properties in the process of optimization the RAMP (rational approximation of material properties) law is employed, where the thermo-elastic material characteristics are function of a fictitious density $r(\mathrm{x})$ [34]:

$$E(\mathrm{x}) = E_0 \frac{r(\mathrm{x})}{(1+p\cdot(1-r(\mathrm{x}))}, \quad \alpha(\mathrm{x}) = \alpha_0 \frac{r(\mathrm{x})}{(1+q\cdot(1-r(\mathrm{x}))}, \quad \rho(x) = \frac{r(\mathrm{x})}{(1+p\cdot(1-r(\mathrm{x}))}, \ \mathrm{x}\in\Omega, \tag{1}$$

where the Young modulus $E(\boldsymbol{x})$ and the coefficient of the temperaturee extension $\alpha(\boldsymbol{x})$ stand as a function of the artificially introduced density $r(\mathrm{x})$, which plays a role of the controlled variable in the optimization process for the Young modulus $E(x)$ and the coefficient $\alpha(x)$ of the reinforced material.

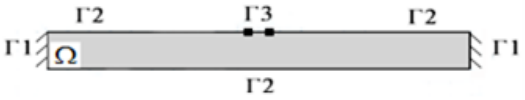

Figure 1. Computational beam model

The coefficients $p\geq 1$ and $q\geq 1$ are the penalty parameters. For $r(x)=1$ the whole space is filled be the reinforced material. The investigations are carried out for the thermos-elastic beam model 1:40, and for steel as the beam material (E_0 = 200 MPa, α_0 = 12.3E-6 1/K, $\rho_0 = 7800\,\mathrm{kg/m^3}$). The computational model and boundary conditions are shown in Fig.1. The beam is clamped along its boundary Γ1, whereas it is free from the loading on the boundary Γ2. On the boundary Γ3 the beam is under the vertical load $F=10$ MN.

Beam flexibility is measured by the functional $J(r)=\int_{\Gamma_3}\nu\cdot F ds$, where ν stands for the beam displacement in direction of the load employed on the boundary Γ_3 [2]. Therefore, we need to find $\min J(\rho)$ and the constraints $0\leq\int_{\Omega}\rho(x)\,d\Omega\leq\gamma\mathrm{A},\ 0<\delta\leq\rho(\mathrm{x})\leq 1,$ where γ measures the part of the reinforced material, and A is the surface of the optimized space Ω. In order to get a numerical solution in each beam point, the introduced density cannot vanish in entively and therefore we take $\delta=10^{-5}$. This allows to avoid singularity of the stiffness matrix while solving the problem of optimization. We also fixed the concentration coefficient of the reinforced material $\gamma=0.5$.

The optimal topology of the beam microstructure has been obtained on the basis of solution to the problem of thermoelasticity using FEM matched with the method of moving asymptotes. Examples of

optimal topology of the beam material distribution under action of the different temperatures T_{onm} are shown in Fig 2, where red color stands for reinforced material.

a) b) c)

Figure 2. Optimal beam topologies: a) $T_{opt} = 20^0 C$, b) $T_{opt} = 50^0 C$, c) $T_{opt} = -30^0 C$

In order to analyze sensitivity of the optimal beams versus temperature change, we studied the stress-strain states (Table 1) of the beams subjected to action of the exploitation temperatures $T_{\exp}$ being different from the optimization temperature T_{opt} .

Table 1. Maximum values of the Mises stresses (MPa)

$T_{\exp}$ \ T_{opt}	243	293	323
243	13.604E7	29.937E7	45.605E7
293	40.397E7	5.8906E7	17.813E7
323	61.175E7	25.714E7	8.7453E7

It follows from Table 1 that for $T_{\exp}$ different from T_{opt} the maximum stresses are essentially increased. It means that if $T_{\exp}$ are a priori not known, then it is recommended to take $T_{opt} = T_{\exp}$. Our further investigations have been carried out for the temperature T_{opt} equal to the temperature of the surrounding matter $T_{opt} = T_{\exp} = 20^0 C$.

3. Results and discussions

Based on the solution of the problem of optimization we have obtained the distribution of the Young modulus and density of the beam along the beam length (see Fig. 3, where $\tilde{E} = E \cdot 10^{-6}$, $\tilde{\rho} = \rho \cdot 10^{-2}$). The obtained values of the physical quantities have been employed to study static and dynamics problem of the non-linear Euler-Bernoulli beam model governed by the following PDEs:

$$\frac{\partial}{\partial x}\left\{k_1\left(\frac{\partial u}{\partial x}+\frac{1}{2}\left(\frac{\partial w}{\partial x}\right)^2\right)\right\} = b_1\frac{\partial^2 u}{\partial t^2},$$
$$\frac{\partial}{\partial x}\left\{\left[k_1\left(\frac{\partial u}{\partial x}+\frac{1}{2}\left(\frac{\partial w}{\partial x}\right)^2\right)\right]\frac{\partial w}{\partial x}\right\} - \frac{\partial^2 w}{\partial x^2}\left(k_3\frac{\partial^2 w}{\partial x^2}\right) + q(x,t) = b_1\frac{\partial^2 w}{\partial t^2} + \varepsilon\frac{\partial w}{\partial t}. \quad (2)$$

where: $k_1 = \int_A (\lambda + 2\mu) dA, k_3 = \int_A \left[(\lambda + 2\mu) z^2 + \frac{1}{2} \mu l^2 \right] dA, b_1 = \int_A \rho(x)\, dA$, $\lambda = \frac{E(x)\nu}{(1+\nu)(1-2\nu)}$, $\mu = \frac{E(x)}{2(1+\nu)}$.

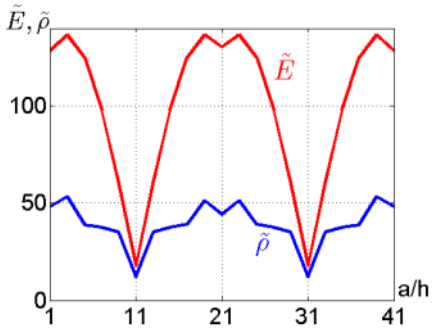

Figure 3. Young modulus $\tilde{E}$ and material density $\tilde{\rho}$ of the beam versus *a/h*.

The boundary conditions correspond to rigid clamping of two beam ends

$$w(0,t) = w(a,t) = 0;\ \partial w(0,t)/\partial x = \partial w(a,t)/\partial x = 0;\ u(0,t) = u(a,t) = 0, \tag{3}$$

and the initial conditions are as follows

$$w(x,0) = \partial w(x,0)/\partial t = 0;\ u(x,0) = \partial u(x,0)/\partial t = 0. \tag{4}$$

Numerical investigation of static and dynamics problems has been carried out for the non-dimensional PDEs and the following fixed parameters: relative beam length $\gamma_1 = a/h = 40$ and the size-dependent parameter $\gamma_2 = l/h = 0;\ 0.3$.

3.1. Methods of solution

In order to reduce PDEs (2) to a system of ODEs we have first used the FDM (finite difference method) regarding the spatial coordinates u, w. The Cauchy problem has been solved by the 4th (rk4) and 2nd (rk2) order Runge-Kutta methods, the 4th order Runge-Kutta-Fehlberg (rkf45), the 4th order Cash-Carp method (rkck), the 8th order Runge-Kutta-Dormand-Prince method (rk8pd) and the implicit 2nd (rk2imp) and 4th (rk4imp) Runge-Kutta methods. The optimal integration step has been chosen based on the Runge principle.

Solutions to the static problems have been obtained based on the analysis of the dynamic equations (2). This approach will be further called the relaxation method. If the load $[\bar{q}]$ does not depend on time, we can obtain a solution to the problem of statics based on the dynamic approach. The initial conditions play a role of excitation of the static problem, whereas the term of the first derivative consisting the dissipation coefficient plays a role of damping of the excited solution. When the solution achieves its steady state, it is interpreted as the solution to the static problem.

3.2. Solving the static problem

The so far described methods have been employed to investigate four different combinations of the parameters: 1 - without account of the size-dependent effect; 1* - without account of the size-dependent effect but with optimization; 2 - taking into account the size-depended effect; 2* - taking into account the size-dependent effect and optimization.

Figures 4 and 5 present dependencies *w(n)* and *q(w)* for the non-linear case. The carried out analysis has shown that for the employed values of the coefficients and result of optimization, the curves *q(w)* for the optimal problem without the size-dependent behavior and the homogeneous problem with an account for the size-dependent beam behavior are close to each other, in particular for the non-linear curve. The optimal beam deflections are less than the homogenous beam deflections. Differences between the values of the maximum deflection of the homogenous and optimal beam for both linear and nonlinear case with/without an account for the size-dependent coefficient $\gamma_2 = 0.3$ are shown in Table 2.

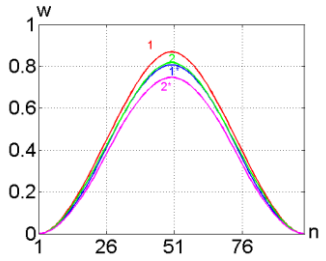

Figure 4. Dependence *w(n)* for the non-linear problem

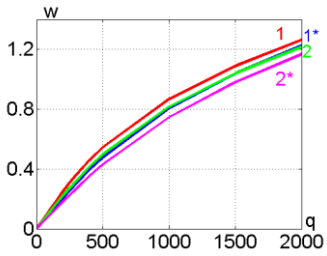

Figure 5. Dependence *q(w)* for the non-linear size dependent problems $\gamma_2 = 0$

Table 2. Differencies in the maximum beam deflection for the linear and nonlinear problem

Linear problem		Noninear problem (*q*=500)	
$\gamma_2 = 0$	$\gamma_2 = 0.3$	$\gamma_2 = 0$	$\gamma_2 = 0.3$
23,6%,	23,1%	14.13%	15.74%

Table 3. Differencies in estimating the beam fundamental frequencies for the linear and nonlinear problems

Linear problem		Nonlinear problem (*q*=320)	
$\gamma_2 = 0$	$\gamma_2 = 0.3$	$\gamma_2 = 0$	$\gamma_2 = 0.3$
6.54%	6.16%	2.56%	0.5%

Based on the results reported in Table 2 one may conclude that the developed method for optimization allows to get constructions with the optimal properties wither with or without the size-dependent beam behavior.

We have investigated an influence of the optimal beam structure on the value of eigenfrequencies of both linear and nonlinear problems (Table 3).

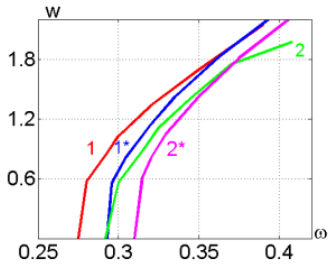

Figure 6. Beam deflection versus frequency

The optimal beam exhibits similar deflection for either existence or lack of the size-dependent problem. Besides, while constructing the dependence frequency-deflection $\omega(w)$ of the optimal (1*,2*) and non-optimal (1,2) problems (Fig. 6) increase of the load implies convergence if the results and respectively of the beam deflections.

3.3. Non-linear problem

In order to study an influence of the optimal beam topology on the beam dynamics the following characteristics are considered: the Fourier spectra, the wavelet spectra based on the basis of the mother Morlet wavelet, the Poincaré section, the phase portraits and the values of the largest Lyapunov exponents (LLEs). The results are obtained under action of the sinusoidal transversal load $q = q_0 \sin(\omega_p t)$, and the damping ciefficient $\varepsilon = 1$. In order to verify the reliability of LLEs computed via the Wolf [36] algorithm, they have been also estimated by Rosenstein [37], Kantz [38] and neural network (NW) [39] methods.

Table 4 consists of the following results: a) signal $w(0.5;t)$; b) Fourier spectrum based on the FFT (fast Fourier transform) $S(\omega)$; c) 2D wavelet spectrum; d) phase portrait $\dot{w}[w(t)]$; e) LLEs estimated by the four different methods.

In the case study 1 ($\gamma_2 = 0$, homogenous mode), the power spectrum consists of 22 fundamental frequencies covering the interval of 0.218. The spectrum exhibits period-doubling $\omega_1 = \omega_p / 2$ and period-quadrupling $\omega_2 = \omega_p / 4$ bifurcations. The maximum powerful frequency, in spite of the

excitation frequency, is $\omega_3 = 2.092$. The Morlet wavelet (1c) shows that the spectrum is not uniformly distributed, and certain frequencies are switched-on or switched-off in time

For the case 1* ($\gamma_2 = 0$, optimal beam) the Fourier spectrum consists of the fundamental frequencies $\omega_1 = 0.486$, $\omega_2 = 1.46$, $\omega_3 = 2.078$, $\omega_4 = 3.052$, $\omega_5 = 4.026$. Pairs of those frequencies exhibit the following remarkable relations: $\omega_2 - \omega_1 = \omega_4 - \omega_3 = \omega_5 - \omega_4 = \omega_p - \omega_5 = 0.974$. In other words, it means that the frequencies $\omega_3, \omega_4, \omega_5$ are dependent on the excitation frequency ω_p.

Table 4. The vibrational characteristics (see the text description)

Case study	1) Ln=0, Opt=0, ω=5, q=38000	1*) Ln=0, Opt=1, ω=5, q=38000	2) Ln=0.3, Opt=0, ω=5, q=55000	2*) Ln=0.3, Opt=1, ω=5, q=55000
a)	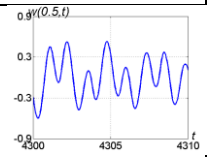	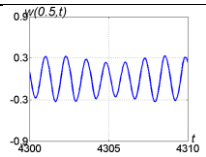	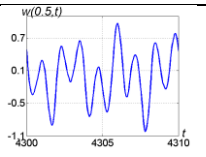	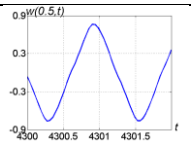
b)	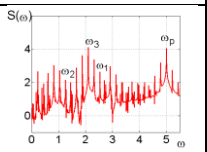	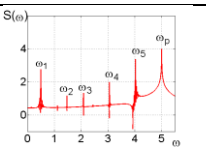	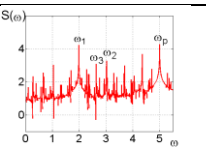	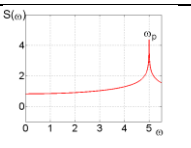
c)	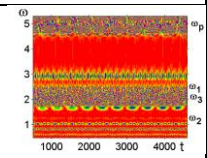	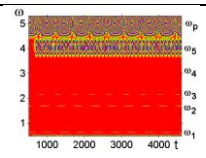	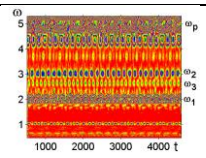	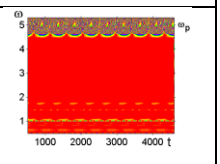
d)	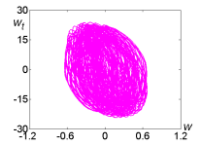	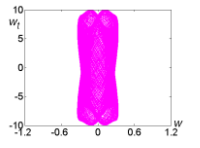	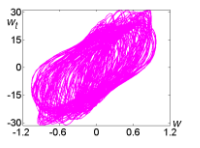	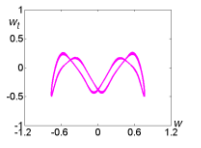
e)	Rosenstein 0.0672; Kantz 0.0246; Wolf 0.0054	Rosenstein 0.0645; Kantz 0.0216; Wolf 0.00704	Rosenstein 0.066 Kantz 0.0198 Wolf 0.061	Rosenstein -0.001 Kantz -0.00065 Wolf -0.00928

The frequency ω_2 depends on ω_1, whereas the latter one is independent. The frequency spectrum exhibits a series of frequencies of small power, which depend on the frequencies ω_p and

ω_1. The Morlet wavelet, similarly to the previous case, exhibits switching-on and switching-off of the frequencies ω_1, ω_2, ω_3 in time.

In the case study 2 ($\gamma_2 = 0.3$, homogenous beam) time histories (2a) and the Fourier spectrum (2b) imply chaotic vibrations. The frequency $\omega_1 = 1.982$ is equal to ω_p with respect to their powers. The Morlet wavelet also validates the chaotic vibrations and equality of the powers of the frequencies ω_p and ω_1. Besides, practically all remaining frequencies depend on time, and time instants of their part switching-on correspond to switching-off of the other frequencies. The phase portrait presents an attractor with two centers corresponding to ω_p and ω_1.

For the case study 2* ($\gamma_2 = 0.3$, optimal beam) the vibration character is essentially different. The Fourier spectrum validates periodic vibrations. However, the Morlet wavelet exhibits frequencies of rather small power localized in the low part of the spectrum. Those frequencies play a role of the noise, which disturb the previous sinusoidal shape of the signal (2*a), and also the phase portrait (2*e).

4. Concluding remarks

We have constructed the mathematical background aimed on getting the optimal topology of the beam for the given loads and boundary conditions. The algorithms and programs have been worked out yielding the optimal distribution of the beam material and the criterion of the minimum flexibility. In result of the carried out static dynamic investigations, we have presented examples exhibiting influence of the optimal beam structure on the change of beam deflection, beam fundamental frequencies and its dynamic characteristics. The carried out investigations show that the beams with optimal topology possess better material characteristics in comparison to the standard homogenous beams.

Acknowledgements

This work has been supported by the Grant RSF № 16-11-10138

References

[1] D.J. Goorman, *Free Vibrations of Beams and Shafts*, Wiley, New York, 1975.

[2] M. Aydogdu, V. Taksin, Free vibration analysis of functionally graded beams with simply supported edges, *Mater. Des.* 28 (2007) 1651-1656.

[3] H.-T. Thai, T.P. Vo, Bending and free vibration of functionally graded beams using various higher order shear deformation beam theories, *Int. J. Mech. Sci.* 62 (2012) 57-66.

[4] S.A. Sina, H.M. Navazi, H. Haddadpour, An analytical method for free vibration analysis of functionally graded beams, *Mater. Des.* 30(3) (2009) 741–747.

[5] M. Sëimsëek, Fundamental frequency analysis of functionally graded beams by using different higher-order beam theories, *Nucl. Eng. Des.* 240(4) (2010) 697–705.

[6] S. Kapuria, M. Bhattacharyya, A.N. Kumar, Bending and free vibration response of layered functionally graded beams: a theoretical model and its experimental validation, *Compos. Struct.* 82(3) (2008) 390–402.

[7] K.-K. Pradhan, S. Chakraverty, Free vibration of Euler and Timoshenko functionally graded beams by Rayleigh–Ritz method, *Compos. Part B: Eng.* 51(4) (2013) 175–184.

[8] M. Sëimsëek, T. KocatËurk, Së. D. Akbasë, Static bending of a functionally graded microscale Timoshenko beambased on the modified couple stress theory, *Compos. Struct.* 95 (2013) 740–747.

[9] A. Shahba, S. Rajasekaran, Free vibration and stability of tapered Euler-Bernoulli beams made of axially functionally graded materials, *Appl. Math. Model.* 36(7) (2012) 3094–3111.

[10] S. Rajasekaran, Differential transformation and differential quadrature methods for centrifugally stiffened axially functionally graded tapered beams, *Int. J. Mech. Sci.* 74(3) (2013) 15–31.

[11] I. Calio, I. Elishakoff, Closed-form solutions for axially graded beam-columns, *J. Sound Vibr.* 280(3–5) (2005) 1083–1094.

[12] I. Elishakoff, V. Johnson, Apparently the first closed-form solution of vibrating inhomogeneous beam with a tip mass, *J. Sound Vibr.* 286(4-5) (2005) 1057–1066.

[13] M. Hemmatnezhad, R. Ansari, G.H. Rahimi, Large-amplitude free vibrations of functionally graded beams by means of a finite element formulation, *Appl. Math. Model* 37 (2013) 8495-8504.

[14] N.D. Kien, Large displacement response of tapered cantilever beams made of axially functionally graded material, *Compos. Part B* 55 (2013) 298e305.

[15] A.E. Alshorbagy, M.A. Eltaher, F.F. Mahmoud, Free vibration characteristics of a functionally graded beam by finite element method, *Appl. Math. Model.* 35(1) (2011) 412–25.

[16] A. Shahba, R. Attarnejad, S. Hajilar, Free vibration and stability of axially functionally graded tapered Euler–Bernoulli beams, *Shock Vib*. 8(5) (2011) 683–96.

[17] A. Shahba, R. Attarnejad, M. Tavanaie Marvi, S. Hajilar, Free vibration and stability analysis of axially functionally graded tapered Timoshenko beams with classical and non-classical boundary conditions, *Compos. Part B: Eng*. 42(4) (2011) 801–8.

[18] A. Shahba, S. Rajasekaran, Free vibration and stability of tapered Euler–Bernoulli beams made of axially functionally graded materials, *Appl. Math. Model.* 36(7) (2012) 3094–111.

[19] L.L. Ke, J. Yang, S. Kitipornchai, An analytical study on the nonlinear vibration of functionally graded beams, *Meccanica* 45 (2010) 743-752.

[20] Y. Huang, X.-F. Li, A new approach for free vibration of axially functionally graded beams with non-uniform crosssection, *J. Sound Vibr*. 329(11) (2010) 2291–2303.

[21] X.-F. Li, Y.-A. Kang, J.-X. Wu, Exact frequency equations of free vibration of exponentially functionally graded beams, *Appl. Acoust.* 74(3) (2013) 413–420.

[22] B. AkgËoz, Ë.O. Civalek, Free vibration analysis of axially functionally graded tapered Bernoulli-Euler microbeams based on themodified couple stress theory, *Comp. Struct.* 98 (2013) 314–322.

[23] Q. Mao, S. Pietrzko, Free vibration analysis of a type of tapered beams by using Adomian decomposition method, *Appl. Math. Comput.* 219(6) (2012) 3264–3271.

[24] J.-C. Hsu, H.-Y. Lai, C.-K. Chen, Free vibration of nonuniform Euler–Bernoulli beams with general elastically end constraints using Adomian modified decomposition method, *J. Sound Vibr.* 318(4-5) (2008) 965–981.

[25] O.Ë Ozdemir, M.O. Kaya, Flapwise bending vibration analysis of a rotating tapered cantilever Bernoulli-Euler beam by differential transform method, *J. Sound Vibr.* 289(1-2) (2006) 413–420.

[26] J.R. Banerjee, H.Su, D.R. Jackson, Free vibration of rotating tapered beams using the dynamic stiffness method, *J. Sound Vibr.* 298(4-5) (2006) 1034–1054.

[27] S. Rajasekaran, Free vibration of centrifugally stiffened axially functionally graded tapered Timoshenko beams using differential transformation and quadrature methods, *Appl. Math. Model.* 37(6) (2013) 4440–4463.

[28] S. Rajasekaran, E. Norouzzadeh Tochaei, Free vibration analysis of axially functionally graded tapered Timoshenko beams using differential transformation element method and differential quadrature element method of lowest-order, *Meccanica* 49(4) (2014) 995–1009.

[29] O.-O. Ozgumus, M.O. Kaya, Flapwise bending vibration analysis of a rotating double-tapered Timoshenko beam, *Arch. Appl. Mech.* 78(5) (2008) 379–392.

[30] B. Yardimoglu, Vibration analysis of rotating tapered Timoshenko beams by a new finite element model, *Shock Vibr.* 13(2) (2006) 117–126.

[31] M. Baghani, H. Mazaheri, H. Salarieh, Analysis of large amplitude free vibrations of clamped tapered beams on a nonlinear elastic foundation, *Appl. Math. Model.* 38(3) (2013) 1176-1186.

[32] A. Shahba, R. Attarnejad, S. Hajilar, A mechanical-based solution for axially functionally graded tapered Euler-Bernoulli beams, *Mech. Adv. Mat. Struct.* 20 (2012) 696-707.

[33] Y. Huang, L.E. Yang, Q.Z. Luo, Free vibration of axially functionally graded Timoshenko beams with non-uniform cross-section, *Compos. Part B: Eng*. 45 (2013) 1493-8.

[34] M. Stolpe, K. Svanberg, An alternative interpolation scheme for minimum compliance topology optimization, Struct. Multidisc. Optim. 22(2) (2001) 116-124.

[35] Q. Li, G.P. Steven, Y.M. Xie, Displacement minimization of thermoelastic structures by evolutionary thickness design. *Comput. Meth. Appl. Mech. Engrg.* 179 (1999) 361–378.

[36] A. Wolf, J.B. Swift, H.L. Swinney, J.A. Vastano, Determining Lyapunov exponents from a time series, *Physica D* 16 (1985) 285-317.

[37] M.T. Rosenstein, J.J. Collins, C.J. De Luca, F practical method for calculating largest Lyapunov exponents from small data sets, *Physica D* 65 (1993) 117-134.

[38] H. Kantz, A robust method to estimate the maximal Lyapunov exponents of a time series, *Phys. Lett. A* 185 (1994) 77-87.

[39] V. Dobriyan, J. Awrejcewicz, V.A. Krysko, On the Lyapunov exponents computation of coupled non-linear Euler-Bernoulli beams, *Proceedings of the Fourteenth International Conference on Civil "Structural and Environmental Engineering Computing"*, Civil-Comp Press, Stirlingshire, UK, 2013, pp. 53.

Jan Awrejcewicz: Department of Automation, Biomechanics and Mechatronics, Lodz University of Technology, 1/15 Stefanowski St., 90-924 Lodz, POLAND; (*awrejcew@p.lodz.pl*). The author gave a presentation of this paper during one of the conference sessions

Sergey P. Pavlov: Department of Mathematics and Modeling, Saratov State Technical University, Politehniekhskaya 77, 410054, Saratov, Russian Federation, *(pspsar@yandex.ru)*.

Maxim V. Zhigalov: Department of Mathematics and Modeling, Saratov State Technical University, Politehniekhskaya 77, 410054, Saratov, Russian Federation, (*max.zhigalov@gmail.com*).

Vadim A. Krysko: Department of Mathematics and Modeling, Saratov State Technical University, Politehniekhskaya 77, 410054, Saratov, Russian Federation, *(tak@san.ru)*

Tracking control of a muscle-like actuated double pendulum

Carsten Behn, Konrad Siedler

Abstract: Adaptive control strategies are analyzed in numerical simulations to control a robot arm with a double pendulum structure. Powered by antagonistic, muscle-like actuators, the controller shall enable the system to track prescribed trajectories for a desired movement as quickly and precisely as possible. But, due to the natural muscle behavior, the control variables underly prescribed bounds: the limited control inputs are generated by muscle intensities. Therefore, feedback strategies are sought which have to be limited from the very beginning. For this, at first, the principles of adaptive lambda-tracking control are introduced by simulations of a system with a DoF=1. Lambda-tracking allows a simple feedback and gain adaptation structure. A preselection of the best-rated controllers is made to apply them to a system with DoF=2. After some model adjustments to the real mechanics of a prototype (for experimental verification), an intensity control is determined, to divide the controller variables to the respective muscle pairs. Then, various numerical simulations of a system with DoF=2 are performed. The previously described and analyzed control structures are then checked regarding to set-point control and tracking. For the optimization of the simulation results different approaches are introduced, for example: limitation of the muscle activity, the insertion of an error vector, adaptive determination of factors of a saturated controller.

1. Introduction

Nowadays, adaptive control strategies are used to dominate technical systems, possible inspired from biology, which underlie uncertainties from the environment. For example, technical sensor systems – inspired by the paragon mechanoreceptor cells from biology – are used for monitoring and measuring ground excitation, whereas these ground excitations play an uncertain role, wherefore adaptive control strategies are used to control a seismic point mass in such a way to get information about the environment [3].

In this paper at hand, we deal with the problem in controlling a compliant robotic system by means of actuators with muscle-like properties, which underlie prescribed bounds due to the natural muscle behavior. Hence, we need to design control strategies with input saturation because of limited resources. Due to the compliance of the system, many parameters and of course the load of the robotic system, which has to be handled, are unknown and/or uncertain. Therefore, adaptive control strategies are chosen. In order to show that the developed strategies work effectively and are powerful, we choose this typical example of a (inverted)

pendulum with $DoF \geq 2$, see [2] and [5], but contrary considering muscle-like actuators instead of conventional torque ones.

First, we present the corresponding mathematical model of the considered system in Section 2. Section 3 is devoted to the favored adaptive control strategy, which has to be limited/saturated in Section 4 and converted into intensities due to the muscle behavior. The effectiveness of the controller is tested in numerical simulations in Section 5. The experimental setup is shown in Section 6 which is used for a verification.

2. Mathematical modeling

First of all, the considered compliant system is introduced. As mentioned above, a biological inspired robot arm in form of a double pendulum (simplified SCARA-type) with two antagonistic muscle pairs is chosen to be tested under the adaptive control strategies from Section 3. The robotic structure and the mechanical quantities of the system are depicted in Fig. 1. Using this model, the efficiency of the designed control strategies should be well visible.

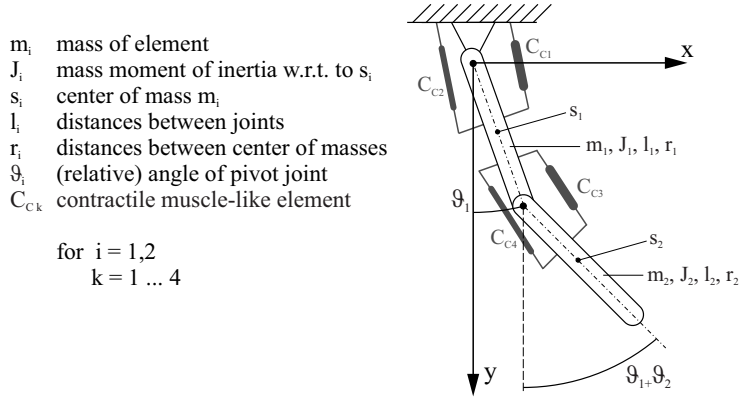

Figure 1. Considered double pendulum structure with actuator arrangement.

The governing equations of motion of the system are derived using Euler-Lagrange equations of the 2nd kind with the generalized coordinates $q_1 := \vartheta_1$ and $q_2 := \vartheta_2$. The following matrix-vector notation results [1]:

$$M(q)\ddot{q} + C(q,\dot{q})\dot{q} + G(q) = u, \tag{1}$$

with:

$$M(q) = \begin{pmatrix} m_1 r_1^2 + J_1 + m_2\left[l_1^2 + r_2^2 + 2l_1 r_2\cos(q_2)\right] + J_2 & m_2\left[r_2^2 + l_1 r_2\cos(q_2)\right] + J_2 \\ m_2\left[r_2^2 + l_1 r_2\cos(q_2)\right] + J_2 & m_2 r_2^2 + J_2 \end{pmatrix}$$

$$C(q,\dot{q})\,\dot{q} = \begin{pmatrix} -m_2\, l_1\, r_2 \sin(q_2)\,\left[\dot{q}_2^2 + 2\dot{q}_1\,\dot{q}_2\right] \\ \dot{q}_1^2\, m_2\, l_1\, r_2 \sin(q_2) \end{pmatrix}$$

$$G(q) = \begin{pmatrix} \sin(q_1)[m_1\, g\, r_1 + m_2\, g\, l_1] + m_2\, g\, r_2 \sin(q_1 + q_2) \\ m_2\, g\, r_2 \sin(q_1 + q_2) \end{pmatrix}$$

The vector of control inputs u, which formerly consists only of classical control torques, has to be developed in dependence on the muscle-like actuators and their intensities. Before doing this, we present the chosen adaptive control strategy in the new section.

3. Control strategies

Several control strategies are tested in numerical simulations in [4], [8] and [9], with the focus on simplicity of the feedback and gain adaptation laws in contrast to literature, e.g. [6]. The best working strategy is the so-called λ-tracking Eq. (2):

$$\left.\begin{aligned} e_i(t) &:= q_i(t) - q_{Ref\,i}(t) \\ u_i(t) &= -k_i(t)\, e_i(t) - \kappa_i\, k_i(t)\, \dot{e}_i(t) - \eta_i\, k_i(t) \int_0^t e_i(t)dt \\ \dot{k}_i(t) &= \begin{cases} \gamma_i\, (\|e_i(t)\| - \lambda_i)^2 & \text{for} \quad \|e_i(t)\| \geq \lambda_i \\ 0 & \text{else} \end{cases} \end{aligned}\right\} \tag{2}$$

Its improved version is the advanced λ-tracking strategy Eq. 3 [4]:

$$\left.\begin{aligned} e_i(t) &:= q_i(t) - q_{Ref\,i}(t) \\ u_i(t) &= -k_i(t)\, e_i(t) - \kappa_i\, k_i(t)\, \dot{e}_i(t) - \eta_i\, k_i(t) \int_0^t e_i(t)dt \\ \dot{k}_i(t) &= \gamma_i \begin{cases} (\|e_i(t)\| - \varepsilon_i\lambda_i)^2 & \text{for} \quad \varepsilon_i\lambda_i + 1 \leq \|e_i(t)\| \\ (\|e_i(t)\| - \varepsilon_i\lambda_i)^{\frac{1}{2}} & \text{for} \quad \varepsilon_i\lambda_i \leq \|e_i(t)\| < \varepsilon_i\lambda_i + 1 \\ 0 & \text{for} \quad \|e_i(t)\| < \varepsilon_i\lambda_i \ \wedge\ t - t_{ei} < t_{di} \\ -\delta_i(\|e_i(t)\|, \varepsilon_i\lambda_i)\, k_i(t) & \text{for} \quad \|e_i(t)\| < \varepsilon_i\lambda_i \ \wedge\ t - t_{ei} \geq t_{di} \end{cases} \\ &\text{with } \delta_i(\|e_i(t)\|, \varepsilon_i\lambda_i) := \sigma_i \cdot \left(1 - \frac{\|e_i(t)\|}{\varepsilon_i\lambda_i}\right) \end{aligned}\right\} \tag{3}$$

with some additional parameters:

Both strategies Eqs. (2) and (3) consist of a feedback law in form of a PID-structure and a gain adaptation law, because constant gains are unsuited for to control systems with uncertainties. The tuning of constant gain parameters (by trial&error-methods) of conventional

ε	-	proportional factor to force the gain factor to rise up *before* the error value leaves the tolerance area;
$\delta(\,\cdot\,)$	-	function to reduce the gain factor;
t_e	-	time stamp, when the system value enters the tolerance area;
t_d	-	time how long the system value has to stay in the tolerance area, before the gain factor will be reduced by δ.

PID-strategies will consume a lot of time. Hence, we introduce time-varying gain parameters which adjust their necessary control values on their own using these adaptation laws. Using these adaptation laws, a so-called λ-tolerance area is introduced, in which the error value of the system is tolerated. Outside this area the gain factor will rise up in dependence on the deviation from the tolerance area. The factor γ describes a proportional factor to gain the growth of the gain factor.

4. Intensities and saturation

Now, we have to introduce the muscle-structure to the input variables. Hence, we have to consider the input variables u_i as a superposition of the resulting torques of the muscle forces M_{Ck}, k=1,...,4, see Fig. 1:

$$u_1 := M_{C1} - M_{C2}\,, \quad \text{and} \quad u_2 := M_{C3} - M_{C4}\,, \tag{4}$$

In the following, we exemplarily show the dependence of M_{C1} on its intensity v_1:
To calculate the torque the mechanical properties are respected, i.e., the joint of the limb elements are positioned at the height of the muscle's joints, see Fig. 2. Then, we have

$$M_{C1} = F_{C1}\, a_1\, \cos(q_1)\,, \tag{5}$$

whereas F_{C1} is the muscle force of actuator "1". This muscle force depends

- on its intensity v_1 (with $v_1 \in [0, 1]$, whereas "0" means "no" activation of the muscle force, and "1" means full activation), and
- on the muscle characteristic curve of HILL h_1 (force-velocity-relation, representation from [7]) in dependence on the muscle contraction velocity $\dot{S}_1$.

We get:

$$F_{C1} = v_1\, h_1(\dot{S}_1)\,, \quad \text{with} \quad S_1 = a_1\, \sin(q_1)\,. \tag{6}$$

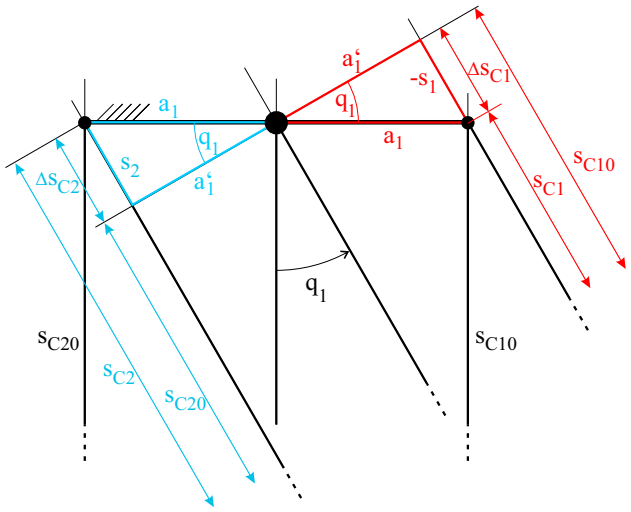

Figure 2. Sketch of the mechanical property at one joint.

The needed muscle force F_{C1} can be interpreted as a percentage of the possible maximum power – this ratio is called *intensity* v_1 [10]. The force-velocity-relation can easily be approximated [1]:

$$h_1(\dot{S}_1) = a_1^* - b_1^* \arctan(c_1^* \dot{S}_1) \qquad \text{with } a_1^*, b_1^*, c_1^* \in \mathbb{R}\,. \tag{7}$$

Finally, the muscle actuator with number "1" causes the following torque:

$$M_{C1} = F_{C1}\, a_1\, \cos(q_1) = v_1\, h_1(\dot{S}_1)\, a_1\, \cos(q_1) \quad \text{with} \quad \dot{S}_1 = a_1\, \dot{q}_1\, \cos(q_1)\,. \tag{8}$$

Substituting all these facts into Eq. (5), it yields the effective torques at each joint:

$$u_1 := M_{C1} - M_{C2} = \Big(v_1\, h_1(\dot{S}_1) - v_2\, h_2(-\dot{S}_1)\Big)\; a_1\, \cos(q_1)\,, \quad \text{and} \tag{9}$$

$$u_2 := M_{C3} - M_{C4} = \Big(v_3\, h_3(\dot{S}_2) - v_4\, h_4(-\dot{S}_2)\Big)\; a_2\, \cos(q_2) \tag{10}$$

Equations (9) and (10) allow to introduce the effective muscle force at each joint as the difference of the antagonistic muscles pairs:

$$F_{e1} := v_1\, h_1(\dot{S}_1) - v_2\, h_2(-\dot{S}_1), \quad F_{e2} := v_3\, h_3(\dot{S}_2) - v_4\, h_4(-\dot{S}_2)\,. \tag{11}$$

As a consequence now, the control input variable u_i has to be converted to the muscle torques, more precisely, to the muscle forces F_{ei}, and the joint angle velocity $\dot{q}_i$ has to be converted to the contraction velocity $\dot{S}_i$, with $i = 1, 2$:

$$F_{ei} = \frac{u_i}{a_i\, \cos(q_i)}\,. \tag{12}$$

To do this, we have to guarantee that the control variable is in the admissible area restricted by the $h(\cdot)$-functions of the muscle pairs, see Eq. (11). There are several ways in doing this

- Trial&Error-Methods in choosing the parameters a_k^*, b_k^*, c_k^* of the muscles, which is certainly not satisfactory.

- The control variable can be saturated so that no higher values of the control variable are allowed than the system can process. The Eqs. (2) and (3) need a hard "cut-off", so following saturation is included for the upcoming simulations:

$$\left.\begin{aligned} &-h_2(-\dot{S}_1)v_2 \geq F_{e1} \leq h_1(\dot{S}_1)v_1 \\ &\qquad \text{with } v_1 = 1 \text{ for } F_{e1} > h_1(\dot{S}_1) \text{ and } v_2 = 1 \text{ for } F_{e1} < -h_2(-\dot{S}_1) \\ &-h_4(-\dot{S}_2)v_4 \geq F_{e2} \leq h_3(\dot{S}_2)v_3 \\ &\qquad \text{with } v_3 = 1 \text{ for } F_{e2} > h_3(\dot{S}_2) \text{ and } v_4 = 1 \text{ for } F_{e2} < -h_4(-\dot{S}_2) \end{aligned}\right\} \tag{13}$$

  To solve Eq. (11) and get admissible muscle intensities, we introduce the following complimentary-slackness condition:

$$v_1\, v_2 = 0 \quad \text{and} \quad v_3\, v_4 = 0 \tag{14}$$

- At last, a much more specified system of rules can reflect the real model much better. The following rules are implemented to active the contra muscle for a moving to the course against the intended one. Additionally, the factor ξ allows to switch this behavior to the movement of a segment by a relaxation of the active muscle, so that the targeted position can be reached more stable. Equation (15) exemplarily presents rules for the first segment:

$$\left.\begin{aligned}
&\text{for} \quad \cos(q_1) > 0\,, \quad \dot{q}_1 > \xi_1\,, \quad F_{e1} > 0: \quad v_1 = \frac{F_{e1}}{h_1(\dot{S}_1)}\,, \quad v_2 = 0 \\
&\text{for} \quad \cos(q_1) > 0\,, \quad \dot{q}_1 > -\xi_1\,, \quad F_{e1} < 0: \quad v_1 = \frac{F_{e1}}{-h_1(-\dot{S}_1)}\,, \quad v_2 = 0 \\
&\text{for} \quad \cos(q_1) > 0\,, \quad \dot{q}_1 < \xi_1\,, \quad F_{e1} > 0: \quad v_1 = 0\,, \quad v_2 = \frac{F_{e1}}{h_2(\dot{S}_1)} \\
&\text{for} \quad \cos(q_1) > 0\,, \quad \dot{q}_1 < -\xi_1\,, \quad F_{e1} < 0: \quad v_1 = 0\,, \quad v_2 = \frac{F_{e1}}{-h_2(-\dot{S}_1)} \\
&\text{for} \quad \cos(q_1) < 0\,, \quad \dot{q}_1 > \xi_1\,, \quad F_{e1} > 0: \quad v_1 = 0\,, \quad v_2 = \frac{F_{e1}}{h_2(\dot{S}_1)} \\
&\text{for} \quad \cos(q_1) < 0\,, \quad \dot{q}_1 > -\xi_1\,, \quad F_{e1} < 0: \quad v_1 = 0\,, \quad v_2 = \frac{F_{e1}}{-h_2(-\dot{S}_1)} \\
&\text{for} \quad \cos(q_1) < 0\,, \quad \dot{q}_1 < \xi_1\,, \quad F_{e1} > 0: \quad v_1 = \frac{F_{e1}}{h_1(\dot{S}_1)}\,, \quad v_2 = 0 \\
&\text{for} \quad \cos(q_1) < 0\,, \quad \dot{q}_1 < -\xi_1\,, \quad F_{e1} < 0: \quad v_1 = \frac{F_{e1}}{-h_1(-\dot{S}_1)}\,, \quad v_2 = 0
\end{aligned}\right\} \tag{15}$$

5. Simulation

We choose the following system parameters, according to [9]:

$$m_1 = m_2 = 2 \quad r_1 = r_2 = 1 \quad l_1 = l_2 = 2 \quad J_1 = J_2 = 1$$

$$a_k^* = 1000 \qquad b_k^* = \frac{2a_k^*}{\pi} \qquad c_k^* = 10 \qquad \xi_i = 0.1 \qquad \text{with} \;\; k \in \{1,\dots,4\},\; i \in \{1,2\}.$$

The initial state is $(q_1; \dot{q}_1; q_2; \dot{q}_2) = (0; 0; 0; 0)$, the target one $(q_1; \dot{q}_1; q_2; \dot{q}_2) = (0.8; 0; 0; 0)$. This means, the first segment of the arm is moving 0.8 rad counterclockwise, the second segment shall hold its position.

The simulation results are shown in the Figs. 3 and 4, using the following control parameters:

$$\left.\begin{array}{llllllll} \lambda_1 = 0.026 & \varepsilon_1 = 0.7 & \gamma_1 = 640 & \kappa_1 = 0.5 & \eta_1 = 0.2 & \sigma_1 = 0.2 & t_{d1} = 2 \\ \lambda_2 = 0.026 & \varepsilon_2 = 0.7 & \gamma_2 = 400 & \kappa_2 = 0.5 & \eta_2 = 0.2 & \sigma_2 = 0.2 & t_{d2} = 2 \end{array}\right\} \tag{16}$$

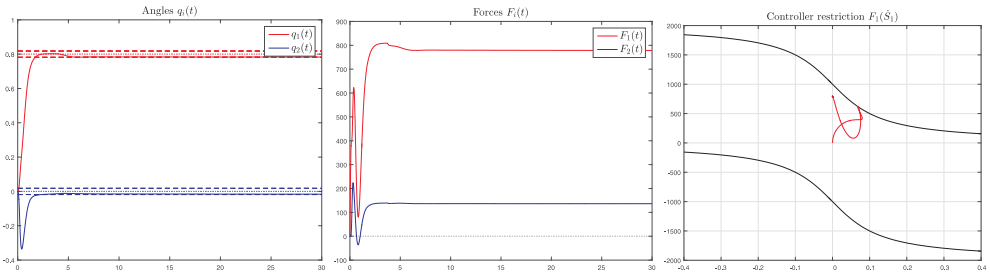

Figure 3. Joint angles (left), forces (middle), controller restriction of first joint (right).

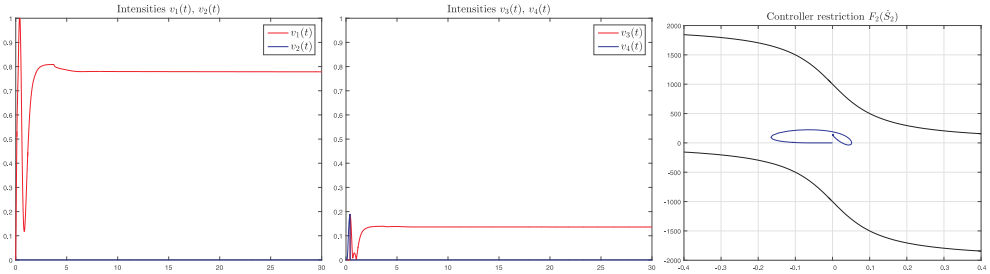

Figure 4. Intensities of muscles C_{C1}, C_{C2} (left), Intensities of muscles C_{C3}, C_{C4} (middle), controller restriction of second joint (right).

The simulation shows a very good stabilization of the target position: in a very short time the position is reached without any important overshoot. Thereby, the limits of one muscle force is touched for short time, but according to the saturation Eq. (15) not exceeded. With

this ability the controller parameters can be chosen comparatively high without opposing the danger to damage the system.

6. Prototype and verification

To verify the working principle of the control strategy, an experimental test rig (Fig. 5-left) with $DoF = 2$ consists of four fluidic muscles of the company "FESTO", according to Fig. 1. Simulations with real system parameters shall show the performance of the controller and shall indicate the magnitude of the controller parameters. For this, the parameters a_k^*, b_k^* and c_k^* of the approximation Eq. (7) have to be identified using an additional test rig (Fig. 5-right). A potentiometer connected to a wheel was rotated by the contracting fluidic muscle

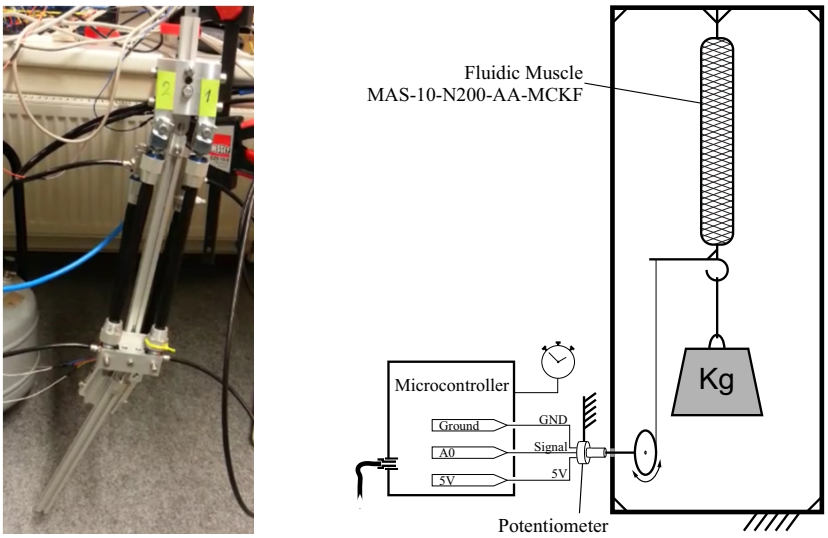

Figure 5. Prototype (left), sketch of test rig for parameter identification (right).

which was loaded with several weights between 5 kg and 30 kg. If the potentiometer moves, its positions are logged by a micro-controller together with the time stamps. Out of these measuring points the force-velocity-relation in Fig. 6 is generated.

To ensure and to realize the widest possible range of functionality of the fluidic muscles, the approximation curve has to lie left to all measured points and has to be as close as possible to all of them. A Hill approximation in form of Eq. (7) does not make a good job. An approximation with the tanh(·)-function shows much better results:

$$h_k(\cdot) = a_k^* - b_k^* \tanh(c_k^* \cdot) \qquad \text{with } a_k^*, b_k^*, c_k^* \in \mathbb{R}, k = 1, \ldots, 4\,. \tag{17}$$

In the following simulation, the controller Eq. (3) is tested with the parameters of the

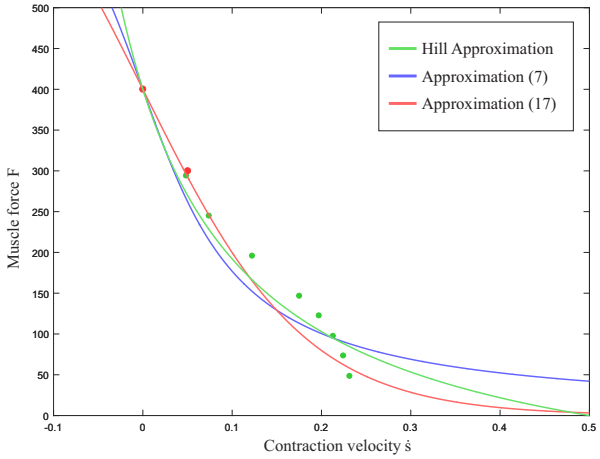

Figure 6. Measuring points (green points) with approximations to Hill (green), approximation Eq. (7) (blue) and the new one Eq. (17) (red).

prototype and its Hill approximation Eq. (17), $k \in \{1, \ldots, 4\}$ and $i \in \{1, 2\}$:

$$\left.\begin{array}{lllll} m_1 = 0.890 & r_1 = 0.180 & l_1 = 0.36 & J_1 = 0.0384 & a_1 = 0.025 \\ m_2 = 0.480 & r_2 = 0.145 & l_2 = 0.29 & J_2 = 0.0135 & a_2 = 0.025 \\ a_k^* = 400 & b_k^* = 400 & c_k^* = 5.5 & \xi_i = 0.1 & \end{array}\right\} \tag{18}$$

The initial state is $(q_1; \dot{q}_1; q_2; \dot{q}_2) = (0; 0; 0; 0)$, the target one $(q_1; \dot{q}_1; q_2; \dot{q}_2) = (0.2; 0; -0.2; 0)$. This means, the first segment of the arm is moving 0.2 rad and the second one -0.2 rad, so that the second segment will stay vertically. The following control parameters are used, similar to Eq. (16):

$$\left.\begin{array}{llllllll} \lambda_1 = 0.026 & \varepsilon_1 = 0.7 & \gamma_1 = 5 & \kappa_1 = 0.5 & \eta_1 = 0.2 & \sigma_1 = 0.5 & t_{d1} = 2 \\ \lambda_2 = 0.026 & \varepsilon_2 = 0.7 & \gamma_2 = 5 & \kappa_2 = 0.5 & \eta_2 = 0.2 & \sigma_2 = 0.5 & t_{d2} = 2 \end{array}\right\} \tag{19}$$

The quite short movement of segment 1 costs about 6 seconds before the position reaches the tolerance area. That leads to only a slight utilization of the muscle power limits.

Now, the prototype – shown in Fig. 5(left) – is used to verify the control strategy Eq. (3). Therefore, a micro-controller adjusts the position of proportional pressure valves to control the pressure in the muscles by using the intensities v_j, calculated by Eq. (15). The used control parameters are the same as above, see Eq. (19).

Because of measurements, we enlarge the following point plots for a better presentation. In doing so, we present only the the behavior of the angles in Fig. 9(left) and the time history

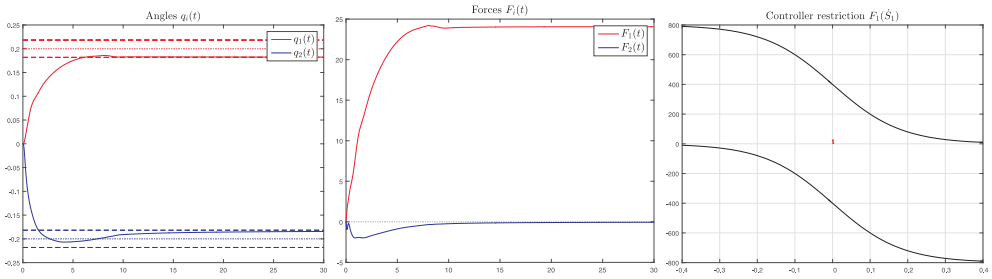

Figure 7. Joint angles (left), forces (middle), controller restriction of first joint (right).

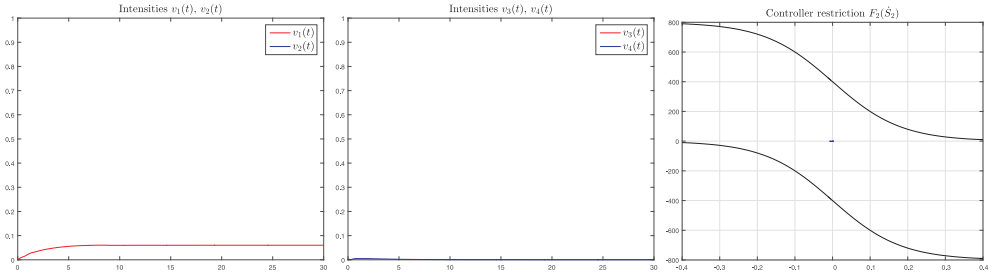

Figure 8. Intensities of muscles C_{C1}, C_{C2} (left), Intensities of muscles C_{C3}, C_{C4} (middle), controller restriction of second joint (right).

of the gain factors in Fig. 9(right). The gain factors show that the control strategy works as expected.

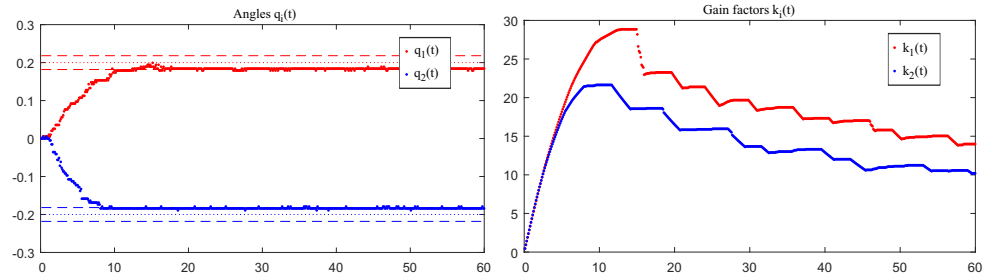

Figure 9. Experiment of the prototype: segment angles (left) and gain factors (right).

In comparison to the simulation shown in Figs. 7 and 8, the behaviors of the angles are quite similar. The experiment shows a higher settling time, but the controller can stabilize the position, too. Even the second segment is a little bit faster than the first one as visible in the simulations. The settling time can be reduced by increasing the value of γ_i. But, because of the limited range of movement to ± 0.35 rad of the prototype's segments, the limits of the

muscle power is already much more exhausted than shown in the simulation. Thus, these limits are already reached with a value of $\gamma_i > 100$.

7. Conclusions

In this paper, we presented a biologically inspired manipulation system which is actuated by muscle-like actuators. Due to the natural behavior, we had to focus on limited resources to control the system in a desired way, i.e., tracking or stabilization. With respect to literature, we set up a simple control strategy in form of a PID-feedback with a simple gain adaptation law to overcome the problem in dealing with uncertainties (e.g. not exactly known system parameters or uncertainties from the surrounding like loads). Due to former investigations we picked the best working strategy: advanced adaptive λ-stabilization. Numerical simulations showed that this adaptive control strategy was very promising in controlling compliant systems. In order to perform these simulations, we had to guarantee the boundedness of the controller variable, which can be done in some trial&error-choices of the corresponding muscle behavior or to claim an external saturation. Because of the effectiveness of the controller in simulations, a prototype was built to have a verification. After a determination of the muscle behavior of the real muscles from FESTO, we implemented this force relation to a micro-controller to calculate necessary control values. In these experiments, the theoretical functionality became visible by means of the prototype. The measurement results were similar to the simulation ones.

Because of the proven functionality, future work is addressed to the tracking problem of more complicated trajectories instead of only stabilizing reference positions. Possible trajectories – to be tracked by the adaptively controlled, muscle-actuated pendulum – can be the "house of St. Nicholas" as depicted in Fig. 10.

References

[1] Abesser, H., Behn, C., Steigenberger, J., and Zimmermann, K. Steueraufgaben für Zweiarm-roboter mit muskelähnlichen Antrieben. In *Proceedings of the 47th Ilmenau Scientific Colloquium (ISC 2002), September 23 - 27, 2002, Ilmenau, Germany.*

[2] Awrejcewicz, J., Reshmin, S., Wasilewski, G., and Kudra, G. Swing up a double pendulum by simple feedback control. In *Proceedings of the 6th EUROMECH Conference ENOC 2008, June 30 - July 4, 2008, Saint Petersburg, Russia.*

[3] Behn, C. Modeling, analysis and control of mechanoreceptors with adaptive features. In *Informatics in Control, Automation and Robotics Lecture Notes in Electrical Engineering (LNEE)*, J.-L. F. et al., Ed., vol. 325. Springer International Publishing, 2015.

[4] Behn, C., Loepelmann, P., and Steigenberger, J. Analysis and simulation of

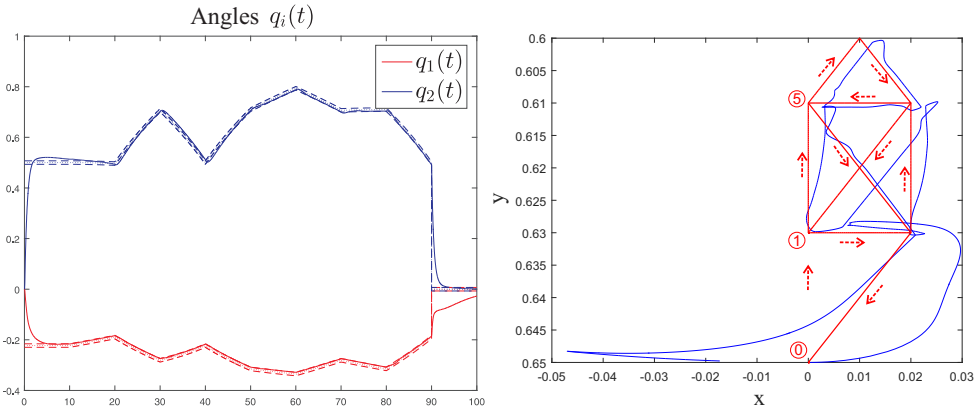

Figure 10. Simulation of the "house of St. Nicholas": segment angles within their λ-tubes (left) and house-drawing incl. directions (right).

adaptive control strategies for uncertain bio-inspired sensor systems. *Mathematics In Engineering, Science and Aerospace (MESA) 6*, 3 (2015), 567588.

[5] Gluck, T., Eder, A., and Kugi, A. Swing-up control of a triple pendulum on a cart with experimental validation. *Automatica 49*, 3 (2013), 801–808.

[6] Ortega, R., Loría, A., Nicklasson, P., and Sira-Ramírez, H. *Passivity-based Control of Euler-Lagrange Systems*. Springer, London, 1998.

[7] Schmalz, T. *Biomechanical Modeling of Human Motion*. Hofmann-Publisher, Schorndorf, 1993.

[8] Siedler, K., and Behn, C. Adaptively controlled dynamical behavior of sensory systems based on mechanoreceptors. *International Journal of Structural Stability and Dynamics 17*, 5 (2017), 14. DOI 10.1142/S0219455417400028.

[9] Siedler, K., Steigenberger, J., and Behn, C. Saturated adaptive control of muscle-like compliant manipulation systems. In *Proceedings of the 9th EUROMECH Conference ENOC 2017, June 25 - 30, 2017, Budapest, Hungary*.

[10] Wagner, H., and Blickhan, R. Stabilizing function of skeletal muscles: an analytical investigation. *Journal of Theoretical Biology 199*, 2 (1999), 163–179.

Carsten Behn, Associate Professor: Technische Universität Ilmenau / Department of Mechanical Engineering / Technical Mechanics Group, Max-Planck-Ring 12, 98693 Ilmenau, Germany (*carsten.behn@tu-ilmenau.de*). The author gave a presentation of this paper during one of the conference sessions.

Konrad Siedler, M.Sc.: Technische Universität Ilmenau / Department of Mechanical Engineering / Technical Mechanics Group, Max-Planck-Ring 12, 98693 Ilmenau, Germany (*konrad-siedler@web.de*).

Reconstruction of motor force during stick balancing

László Bencsik, Bálint Bodor, Tamás Insperger

Abstract: Understanding the control mechanism behind human balancing is a challenging task, which becomes more and more important with the aging society. The core problem is the stabilization of a body around an unstable equilibrium in the presence of a reaction time delay and sensory uncertainties. Stick balancing on the fingertip plays an important role in human balancing research since it incorporates the above features still it has a relatively simple mechanical model, namely, the inverted pendulum subjected to delayed feedback control. The goals of stick balancing measurements are to find the control forces and to identify the nature of the human controller during. An important step of this identification is the accurate estimation of the control force. In this paper, an approach is proposed to estimate the control force based on techniques used for underactuated mechanical systems.

1. Introduction

The aim of this work is to reconstruct the control force from position measurements during stick balancing on the fingertip (see in Fig. 1). In most of the identification processes the input and the output is typically known and the model of the system should be identified [4]. In case of stick balancing, the mechanical model is known (an inverted pendulum) and the input (the control force) is unknown. A straightforward idea is to use an inverse dynamical calculation for the computation of the input. The inverse calculation requires the knowledge of the position, the velocity and the acceleration of the stick. During balancing experiments, we have used a camera based motion capturing system which gives only the positions of the measured markers in time. The numerical computation of the velocity and acceleration signal via discrete differentiation amplifies the noise of the source data [7], which strongly affects the accuracy and the reliability of the computed forces. A possible solution is the application of classical filtering techniques, such as moving average, or the Kalman filter [5]. Filtering techniques have to be accommodated to the problem in hand, which is not a straightforward tasks, since the exact signals are not available for comparison. In this paper, a different approach is proposed: a method, which is based on a control technique specially devoted to underactuated mechanical systems.

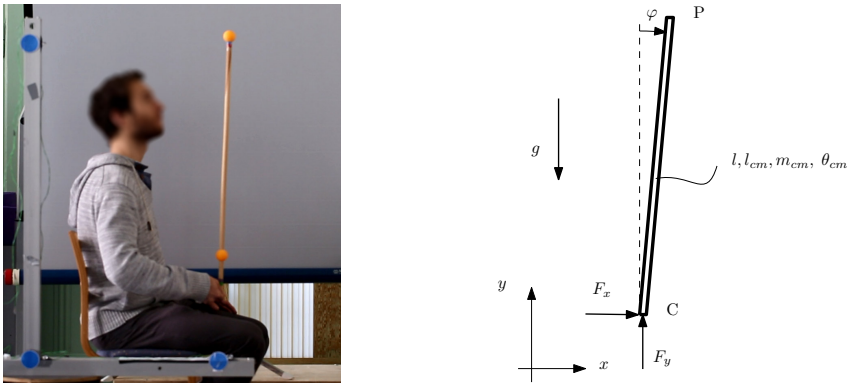

Figure 1. The measurement setup and the mechanical model.

2. Predictive force identification method

The goal of this work is to recalculate the control forces during stick balancing. This problem can be considered as a a trajectory tracking control problem. The predictive controller is applied, which was presented in [1] and [2]. The main idea of the predictive controller is based on the partition of the descriptor coordinates to actuated coordinates $\mathbf{q}_a$ that are controlled directly by the control forces and to unactuated coordinates $\mathbf{q}_u$. It is assumed that the actuated coordinates are known in time and using this assumption we approximate the unactuated coordinates with a linearized model. Then the trajectory following error $\mathbf{E}_s$ and a cost function J can be constructed, which enables us to define a minimization problem and find the optimal values for the actuated coordinates. Finally, the optimal control forces can be calculated, which can be considered as an estimation of the actual forces during balancing.

2.1. Predicting the unactuated motion of the balanced stick

We investigate stick balancing in the anterior-posterior plane only [6]. The corresponding mechanical model is shown in Fig. 1. In the estimation process first the equation of motion of the stick is generated. The vector of the generalized coordinates is $\mathbf{q}^\intercal = [x_C, y_C, \varphi]^\intercal$ (see in Fig. 1). For the sake of brevity ,the trigonometrical functions are denoted as: $c_\varphi = \cos\varphi$ and $s_\varphi = \sin\varphi$. Using Lagrange's equation the governing equation of motion can be written as:

$$\begin{bmatrix} m_{cm} & 0 & l_{cm}m_{cm}c_\varphi \\ 0 & m_{cm} & -l_{cm}m_{cm}s_\varphi \\ l_{cm}m_{cm}c_\varphi & -l_{cm}m_{cm}s_\varphi & l_{cm}^2 m_{cm} + \theta_{cm} \end{bmatrix} \begin{bmatrix} \ddot{x}_C \\ \ddot{y}_C \\ \ddot{\varphi} \end{bmatrix} + \begin{bmatrix} l_{cm}m_{cm}s_\varphi \dot{\varphi}^2 \\ m_{cm}(g - l_{cm}c_\varphi \dot{\varphi}^2) \\ -g m_{cm} l_{cm} s_\varphi \end{bmatrix} = \begin{bmatrix} 1 & 0 \\ 0 & 1 \\ 0 & 0 \end{bmatrix} \begin{bmatrix} F_x \\ F_y \end{bmatrix}. \tag{1}$$

As a first step, the coordinates are partitioned in to two groups. The vector of actuated coordinates is $\mathbf{q}_a = [x_C \; y_C]^\intercal$ (x_C and y_C are controlled directly by F_x and F_y) and the coordinate which is not actuated directly is $\mathbf{q}_u = [\varphi]$. Thus, the equation of motion (1) can be written in the following compact form:

$$\begin{bmatrix} \mathbf{M}_{aa} & \mathbf{M}_{au} \\ \mathbf{M}_{ua} & \mathbf{M}_{uu} \end{bmatrix} \begin{bmatrix} \ddot{\mathbf{q}}_a \\ \ddot{\mathbf{q}}_u \end{bmatrix} + \begin{bmatrix} \mathbf{c}_a \\ \mathbf{c}_u \end{bmatrix} = \begin{bmatrix} \mathbf{H}_a \\ \mathbf{0} \end{bmatrix} \boldsymbol{\tau}. \tag{2}$$

The relation between the unactuated accelerations $\ddot{\mathbf{q}}_u$ and the actuated accelerations $\ddot{\mathbf{q}}_a$ can be expressed from the second row of the above equation. This relation can be linearized about a given configuration $\mathbf{q}_0$, $\dot{\mathbf{q}}_0$, $\ddot{\mathbf{q}}_0$ as:

$$\boldsymbol{\alpha}_u \ddot{\mathbf{q}}_u + \boldsymbol{\beta}_u \dot{\mathbf{q}}_u + \boldsymbol{\gamma}_u \mathbf{q}_u = \boldsymbol{\alpha}_a \ddot{\mathbf{q}}_a + \boldsymbol{\beta}_a \dot{\mathbf{q}}_a + \boldsymbol{\gamma}_a \mathbf{q}_a + \boldsymbol{\delta}. \tag{3}$$

Equation (3) is a system of linear differential equations, which has the same number of equations as the number of the unactuated coordinates, therefore, it is possible to determine the values of the unactuated coordinates. For the solution it is assumed that the actuated coordinates are known in the following form:

$$\mathbf{q}_a = \mathbf{P}_a \boldsymbol{\varphi}_n = \left(\sum_{i=1}^{N_a} p_{a,i} \mathbf{P}_{a,i} \right) \boldsymbol{\varphi}_n, \tag{4}$$

where the matrix $\mathbf{P}_a$ contains the yet unknown $p_{a,i}$ coefficients. In the sum $N_a = m\,(n-1)$, where m denotes the number of the actuated coordinates and n is equal to the order of the polynomial base $\boldsymbol{\varphi}_n$. The basic goal of the whole optimization process is to determine these coefficients.

The unactuated coordinates $\mathbf{q}_u$ can be determined by solving Eq. (3). First the homogeneous part of the equation should be solved. For this, we rewrite the homogeneous part of Eq. (3) in first order form:

$$\frac{d}{dt} \underbrace{\begin{bmatrix} \mathbf{q}_{u,h} \\ \dot{\mathbf{q}}_{u,h} \end{bmatrix}}_{\mathbf{z}_h} = \underbrace{\begin{bmatrix} \dot{\mathbf{q}}_{u,h} \\ \ddot{\mathbf{q}}_{u,h} \end{bmatrix}}_{\dot{\mathbf{z}}_h} = \underbrace{\begin{bmatrix} \mathbf{0} & \mathbf{I} \\ -\boldsymbol{\alpha}_u^{-1}\boldsymbol{\gamma}_u & -\boldsymbol{\alpha}_u^{-1}\boldsymbol{\beta}_u \end{bmatrix}}_{\mathbf{A}_h} \begin{bmatrix} \mathbf{q}_{u,h} \\ \dot{\mathbf{q}}_{u,h} \end{bmatrix}. \tag{5}$$

The solution can be given in matrix exponential form [3] as:

$$\mathbf{z}_h = e^{\mathbf{A}_h t} \mathbf{C}. \tag{6}$$

Here $\mathbf{C}$ is an unknown constant coefficient, which depends on the initial values. The vector $\mathbf{q}_{u,h}$ can be expressed using a constant selector matrix, i.e, $\mathbf{q}_{u,h} = \mathbf{K}_u \mathbf{z}_h$.

The next step is to determine the particular solution of the inhomogenous equation Eq. (3). For this we search the unactuated coordinates in the following form:

$$\mathbf{q}_{u,ih} = \mathbf{P}_u \boldsymbol{\varphi}_n. \tag{7}$$

Here the notations are similar to the ones used in Eq. (4).

Substituting the coordinates and their derivatives defined in Eq. (4) and in Eq. (7) into Eq. (3) and considering that the elements of the functions $\boldsymbol{\varphi}_n$ are linearly independent we get the following expression:

$$\boldsymbol{\alpha}_u \mathbf{P}_u \mathbf{D}^2 + \boldsymbol{\beta}_u \mathbf{P}_u \mathbf{D} + \boldsymbol{\gamma}_u \mathbf{P}_u = \boldsymbol{\alpha}_a \mathbf{P}_a \mathbf{D}^2 + \boldsymbol{\beta}_a \mathbf{P}_a \mathbf{D} + \boldsymbol{\gamma}_a \mathbf{P}_a + \boldsymbol{\delta} \mathbf{K}_{1,n}, \tag{8}$$

where $\mathbf{D}$ is the matrix of the differential operator which satisfies the relation $\dot{\boldsymbol{\varphi}} = \mathbf{D}\boldsymbol{\varphi}$. Here we introduce a row vector $\mathbf{K}_{1,n}$ which gives $\mathbf{K}_{1,n}\boldsymbol{\varphi}_n = 1$. If the the number of unactuated coordinates is one then the coefficients of $\mathbf{P}_u$ are scalars, which can be collected directly. Thus $\mathbf{P}_u$ can be determined as:

$$\mathbf{P}_u = (\alpha_u \mathbf{D}^2 + \beta_u \mathbf{D} + \gamma_u \mathbf{I})^{-1} (\boldsymbol{\alpha}_a \mathbf{P}_a \mathbf{D}^2 + \boldsymbol{\beta}_a \mathbf{P}_a \mathbf{D} + \boldsymbol{\gamma}_a \mathbf{P}_a + \boldsymbol{\delta} \mathbf{K}_{1,n}). \tag{9}$$

It should be noted that in case of higher number of unactuated coordinates $\mathbf{P}_u$ can also be given using additional transformations.

Now the solution of Eq. (3) can be formalized. The unknown coefficient $\mathbf{C}$ can be determined from the initial values $\mathbf{q}_u(0)$ and $\dot{\mathbf{q}}_u(0)$ and the complete solution can be written in the form:

$$\mathbf{q}_u = \mathbf{K}_u e^{\mathbf{A}t} \underbrace{\left(\mathbf{z}|_{t=0} - \begin{bmatrix} \mathbf{P}_u \\ \mathbf{P}_u \mathbf{D} \end{bmatrix} \boldsymbol{\varphi}|_{t=0} \right)}_{\mathbf{C}} + \mathbf{P}_u \boldsymbol{\varphi}. \tag{10}$$

After this the general coordinates $\mathbf{q}$ can be computed.

2.2. Constraint with the measurement results

During the measurement the lower and the upper endpoints of the stick can be measured. The motion of the stick can be characterized with the motion of the lower endpoint (point C) and with the inclination of the stick. The corresponding generalized coordinates are:

$$\mathbf{r} = \begin{bmatrix} x_C & y_C & x_P - x_C \end{bmatrix}^\intercal = \begin{bmatrix} x_C & y_C & l \sin\varphi \end{bmatrix}^\intercal. \tag{11}$$

These coordinates can be also computed from the measured values as:

$$\mathbf{r}_m = \begin{bmatrix} x_{C,m} & y_{C,m} & x_{P,m} - x_{C,m} \end{bmatrix}^\intercal. \tag{12}$$

The idea behind the identification process is that we are looking for an input, which induces a motion, which is the closest to the measured motion. Therefore, we define an error vector as:

$$\mathbf{E}_s = \begin{bmatrix} s_0\mathbf{I} & \mathbf{0} & \mathbf{0} \\ \mathbf{0} & s_1\mathbf{I} & \mathbf{0} \\ \mathbf{0} & \mathbf{0} & s_2\mathbf{I} \end{bmatrix} \left(\begin{bmatrix} \mathbf{r} \\ \dot{\mathbf{r}} \\ \ddot{\mathbf{r}} \end{bmatrix} - \begin{bmatrix} \mathbf{r}_m \\ \dot{\mathbf{r}}_m \\ \ddot{\mathbf{r}}_m \end{bmatrix} \right). \tag{13}$$

This vector contains the errors at position, at velocity and at acceleration level. These components are weighted by the constants $s_0,\ s_1,\ s_2$. The quadratic error for the whole motion can be defined as:

$$J = \int_{t_1}^{t_2} \mathbf{E}_s^{\intercal}\mathbf{E}_s \, dt = \langle \mathbf{E}_s,\ \mathbf{E}_s \rangle = \|\mathbf{E}_s\|^2. \tag{14}$$

This integral have to be minimized and the motion of the system which is closest to the measured one can be selected. For this we substitute the solution of the unactuated coordinates $\mathbf{q}_u$ (see Eq. (10)) and the supposed form of the actuated coordinates $\mathbf{q}_a$ (see Eq. (4)) into Eq. (14). Therefore we get:

$$J = \left\| \boldsymbol{\Psi} - \sum_{i=1}^{N_a} p_{a,\,i}\boldsymbol{\psi}_i \right\|^2 \tag{15}$$

where $\boldsymbol{\psi}_i$ contains the coefficients of $p_{a,\,i}$, which are the coefficients in the assumed solution form Eq.(4) of the actuated coordinates and $\boldsymbol{\Psi}$ contains the remaining terms. In the optimization the following initial conditions have to be satisfied:

$$\begin{aligned} -\underbrace{\mathbf{q}_a|_{t=0} + \sum_{i=1}^{N_a} p_{a,i}\mathbf{P}_{a,i}\boldsymbol{\varphi}|_{t=0}}_{\mathbf{q}_a(0)} = \mathbf{0},\ -\underbrace{\dot{\mathbf{q}}_a|_{t=0} + \sum_{i=1}^{N_a} p_{a,i}\mathbf{P}_{a,i}\mathbf{D}\boldsymbol{\varphi}|_{t=0}}_{\dot{\mathbf{q}}_a(0)} = \mathbf{0}, \\ -\underbrace{\ddot{\mathbf{q}}_a|_{t=0} + \sum_{i=1}^{N_a} p_{a,i}\mathbf{P}_{a,i}\mathbf{D}^2\boldsymbol{\varphi}|_{t=0}}_{\ddot{\mathbf{q}}_a(0)} = \mathbf{0}. \end{aligned} \tag{16}$$

In order to determine the unknown constants $p_{a,\,i}$, we use the method of Lagrange multipliers, which results in the modified cost function as:

$$J_L = \left\| \boldsymbol{\Psi} - \sum_{i=1}^{N_a} p_{a,\,i}\boldsymbol{\psi}_i \right\|^2 + (\mathbf{a}_0 + \sum_{i=1}^{N_a} c_i\mathbf{a}_i)^{\intercal}\boldsymbol{\lambda}. \tag{17}$$

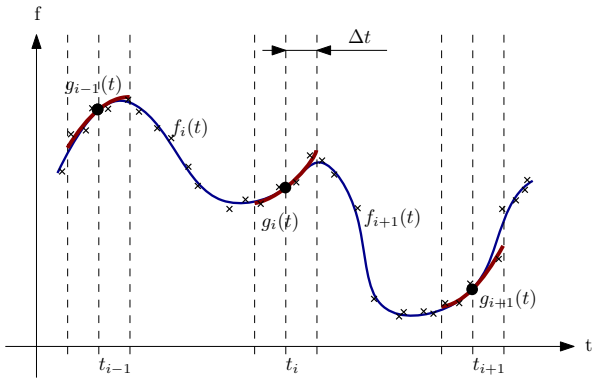

Figure 2. The idea behind the fitting of the polynomials.

Here $\mathbf{a}_0$ and $\mathbf{a}_i$ can be calculated from the initial values shown in Eq. (16). Then the coefficients $p_{a,i}$ and the optimal actuated coordinates $\mathbf{q}_a$ can be calculated, which are needed to determine the applied balancing forces from Eq. (2) as:

$$\boldsymbol{\tau} = \mathbf{H}_a^{-1}(\mathbf{M}_{aa}\ddot{\mathbf{q}}_a - \mathbf{M}_{au}\mathbf{M}_{uu}^{-1}(\mathbf{M}_{ua}\ddot{\mathbf{q}}_a + \mathbf{c}_u) + \mathbf{c}_a). \tag{18}$$

With this computed torque the measured motion can be re-simulated based on the equation of motion (1).

3. Numerical study

The measured data usually contains high frequency noisy vibrations. If we fit a polynomial, which approximates the signal with the required precision, then we have to use a polynomial of high order, which is numerically expensive and due to the higher order terms could lead to numerical instability. Therefore, we do the fitting with lower-order polynomials on shorter intervals. In this approach the measured signal is divided into $N_{int} = 35$ segments of length of 1 s, namely, over the intervals $[t_i, t_i + 1]$, $i = 0, 1, \cdots, N_{int} - 1$, and the polynomials are fitted over these intervals. This enables us to use fairly low degree polynomials, where the consecutive polynomials have to be C^2 continuous in the connection points. For the sake of better numerical results, we fit the second order polynomials $g_i(t)$ around every division points t_i in the intervals $[t_i - \Delta t, t_i + \Delta t]$, $i = 0, 1, \cdots, N_{int}]$ (see the red curves in Fig. 2). In Fig. 2, the black crosses denote the measured data. These polynomials will determine the conditions to obtain the above mentioned continuity. Then the polynomials $f_i(t)$ have to be fitted (see the blue curves in Fig. 2).

Using the proposed technique the balancing force is recalculated during stick balancing experiments. Here the results of one particular measurement is presented and the control

force in the anterior-posterior plane is plotted in Fig. 3. Using this force, the equation of motion is integrated with the same initial conditions. The results of the numerical simulations are shown in Fig. 4, where the results are compared with the measured results. Based on Fig. 4, it can be concluded that the agreement between the measured and the recalculated signal is good. The quadratic error of the estimation process was $RMS = 0.0056[m]$.

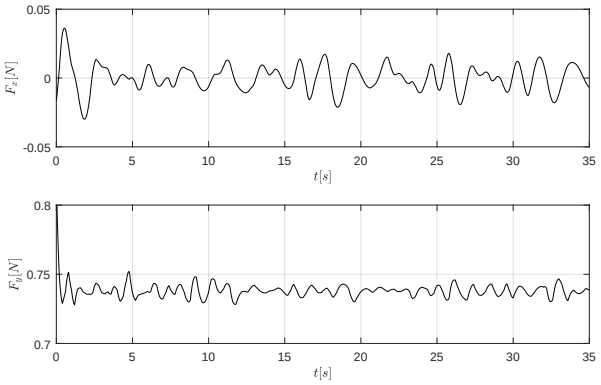

Figure 3. The reconstructed contact forces.

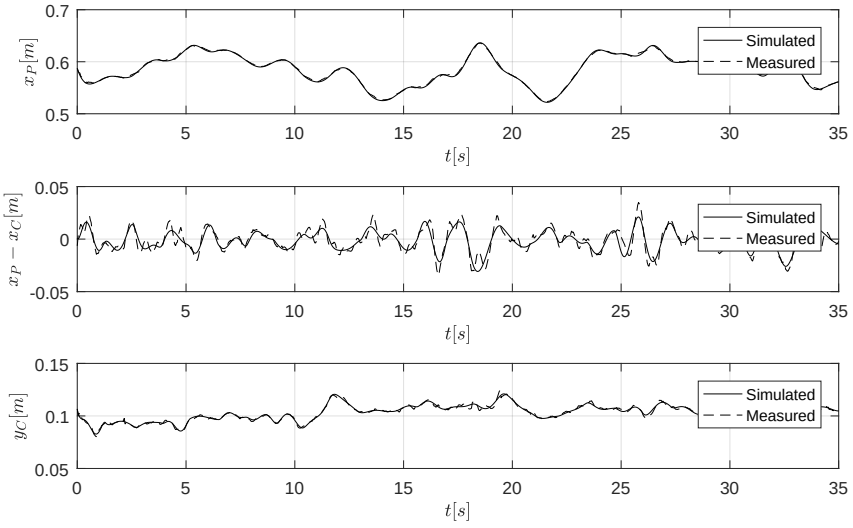

Figure 4. The measured and the simulated coordinates.

4. Conclusions

In this study for the investigation of a special human balancing task, namely, stick balancing on the fingertip was analyzed. In order to understand the mechanism of balancing, first, the control forces have to be estimated. In this paper, a novel approach was presented. We have extended a predictive control technique where the goal was to find a control force which results a motion which is appropriately close the captured motion. We applied the technique to the balancing a stick on the fingertip in the anterior-posterior plane. Since the proposed technique is general in a future work we apply it in the investigation of spatial balancing problems. This research has been supported by the ÚNKP-2017 New National Excellence Program of the Ministry of Human Capacities.

References

[1] Bencsik, L., Kovács, L., and Zelei, A. Predictive trajectory tracking of underactuated systems. *In proceedings of The 4th Joint International Conference on Multibody System Dynamics* (2016).

[2] Bodor, B., and Bencsik, L. Predictive control of robot manipulators with flexible joints. *In proceedings of the 9th European Nonlinear Dynamics Conference* (2017).

[3] DeCarlo, R. *A State Variable Approach with Numerical Implementation.* Prentice Hall, 1989.

[4] Goodwin, G. C., and Payne, R. *Dynamic System Identification: Experiment Design and Data Analysis.* Academic Press, 1977.

[5] Kalman, R. A new approach to linear filtering and prediction problems. *Journal of Basic Engineering 1*, 82 (1960).

[6] Nordin, M., and Frankel, V. H. *Basic biomechanics of the musculoskeletal system.* Lea & Febiger, 1989.

[7] Whitaker, S., and Pigford, R. L. An approach to numerical differentiation of experimental data. *Industrial & Engineering Chemistry 52*, 2 (1960), 185–187.

László Bencsik, Ph.D.: MTA-BME Lendület Human Balancing Research Group, H-1111, Budapest Muegyetem rkp 5., Hungary (*bencsik@mm.bme.hu*). The author gave a presentation of this paper during one of the conference sessions.

Bálint Bodor, B.Sc.(M.Sc. student): Department of Applied Mechanics, Budapest University of Technology and Economics and MTA-BME Lendület Human Balancing Research Group, H-1111, Budapest Muegyetem rkp 5., Hungary (*bodor.balus@gmail.com*).

Tamás Insperger, D.Sc.: Department of Applied Mechanics, Budapest University of Technology and Economics and MTA-BME Lendület Human Balancing Research Group, H-1111, Budapest Muegyetem rkp 5., Hungary (*insperger@mm.bme.hu*).

A novel human "broomstick" forward fall model and its application in the strength analysis of the human upper extremity

Paweł Biesiacki, Dariusz Grzelczyk, Jerzy Mrozowski, Jan Awrejcewicz

Abstract: In this paper we consider a human forward fall model simulating the process of "falling like a broomstick" to the ground on the outstretched arms as the worst scenario of a forward fall. The biomechanical relationships between the hands and the ground are modelled by a non-linear impact law and the parameters of the model are estimated based on the scanned computer model of the human body as well as the experimental investigations performed with the help of the Optitrack motion capture system. The applied fall model allows to estimate time histories of ground reaction force in various scenarios of fall, and the obtained numerical simulations fit qualitatively and quantitatively other results presented in the literature. The obtained ground reaction force is used as a time-varying load condition in the finite element model of the human upper extremity created in Mimics software from computed tomography data. Finally, strength analysis of radius with two different fracture risk criteria is carried out, and the performed numerical analysis indicates that the strain criterion seems to be more useful for estimating the radius fracture site in comparison to the stress criterion.

1. Introduction

Falls belong to the common accidents in human daily life. The most upper extremity injuries occur as a result of a forward fall with direct impact on the extended arms [1]. Practically, all population groups are exposed to these risk factors, including children playing in the playground, teenagers practicing sports with high risk of injuries, adults performing activities related to their employment in an occupational environment, and the elderly during normal walking. As a result of fall, the risk to hands, torso, head, and/or other body parts of the human is possible. However, fractures of radial bone are the most common in eldery women with osteoporosis due to their compromised bone density/quality, and, probably, due to the increased risk of falling in this population group. The most common type of fracture of the radial bone is the so-called Colles' fracture as an injury of distal radius of a forearm [2]. The aforementioned Colles' fracture, as an injury of the radius, is a direct result of exceeding the maximum value of force allowable for this bone. For instance, Kim and Ashton-Miller used the value equal to 2400 N as a distal radius fracture threshold [3]. In other recent paper by Burkhart et al. [4], the estimated values of force causing fracture of the studied bones derived from cadavers were approximately equal to 2150 N. In this paper we considered a novel human

"broomstick" forward fall model. Next, the obtained vertical ground reaction force (GRF) has been applied in the strength analysis of the human radial bone as an impact force.

2. Forward fall models – a brief literature review

Recent few decades have brought several models related to the impact of the human upper extremities to the ground as a result of a fall in forward or backward direction. The simplest model of the human falling motion is a single-degree-of-freedom (DoF) linear mass-spring-damper mechanical system subjected to sudden velocity input or impulse force input. This model can be extended to systems with many DoFs. A fall model proposed by Chiu and Robinovitch [5] applies to the human forward fall from a low height on the outstretched and fully extended upper extremity as the worst-case scenario of such a fall. This model is constructed based on a 2-DoFs lumped-parameter mechanical system containing elastic and damping elements. DeGoede and Ashton-Miller [6] used Adams software to develop a half-body, symmetric model of the human forward fall consisting of five segments (i.e. legs, torso with head and neck, upper arm, forearm and hand). The main goal of the authors of that paper was to study the possibility of injury of upper extremities among older women. Kim and Ashton-Miller [3] proposed another flat forward fall model as a two DoFs system constructed based on a mechanical double pendulum rotating freely around the pivot corresponding to the ankles of lower human extremities. The mechanical system was reduced to a system of linear translational movement with 2-DoFs with spring-damper elements responsible for attenuation action of the human muscles.

To conclude, it can be stated that the considered falling process was usually modelled based on flat and linear mechanical systems consisting of two rigid bodies with masses moved by transverse motion connected by linear spring-damper elements. These models were usually presented as a second-order ordinary differential equations of motion [5], or the equations written in the state space [3]. In the case of the more complex mechanical model, numerical simulations were performed only using commercial software [6]. In this paper we consider mathematical model of the human forward fall on the outstretched arms previously introduced in our previous paper [7]. On the contrary to the aforementioned reference, in this paper we applied more adequate a nonlinear model of impact at the wrist-ground interface, and kinematics of the faller during fall process were estimated using an Optitrack motion analysis system. Moreover, the obtained ground reaction forces have been applied as load conditions in the developed finite element model of the human radius analysed in Ansys.

3. The considered "broomstick" forward fall model

The human "like a broomstick" forward fall on the outstretched arms and human body parameters required for numerical simulation are presented in reference [7]. On the contrary to the previous

paper, in this paper a non-linear model of impact at the wrist-ground interface has been applied to predict the vertical ground reaction force (GRF) $F_y(t)$. The applied model has the following form

$$F_y(t) = k_y \left| y(t) \right|^3 (1 - b_y \dot{y}(t)) \cdot \mathbf{1}(-y(t)), \tag{1}$$

where parameters k_y, b_y denote ground stiffness and damping coefficients in the vertical direction, respectively, and function $\mathbf{1}(-y(t))$ is the step function defined as

$$\mathbf{1}(-y(t)) = \begin{cases} 1 & \text{if} \quad y(t) < 0, \\ 0 & \text{if} \quad y(t) \geq 0. \end{cases} \tag{2}$$

This formulation of GRF had been used previously to model the heel strike in running [8] as well as to model GRF at the hand-ground interface in human fall model [6]. In our calculations we did not include the horizontal force component $F_x(t)$ which is required to prevent the hand from sliding.

The kinematic analysis of the faller during the fall process were observed using an Optitrack optoelectronic motion analysis system. The location of the individual markers on the faller's human body required to carry out the experimental observations are shown in Fig. 1. The selected frames from the recorded fall process in regular time intervals are depicted in Fig. 2.

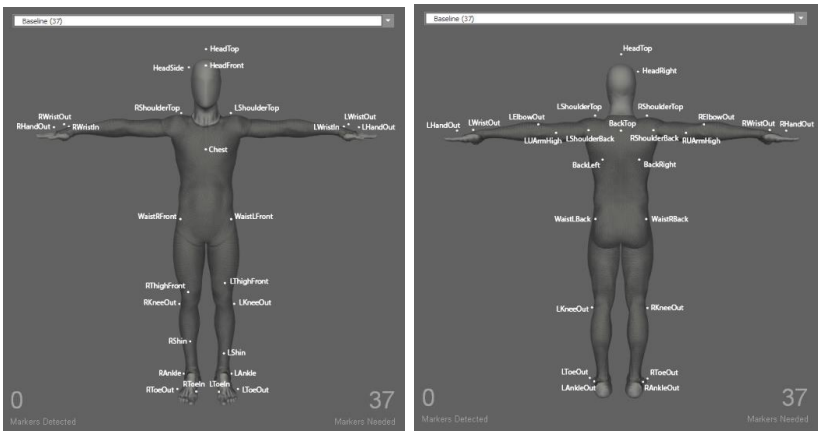

Figure 1. The location of the 37 passive reflective markers distributed on the faller's body: front view (on the left) and back view (on the right).

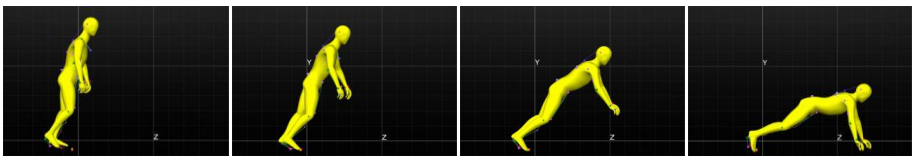

Figure 2. Forward fall from a standing position to the soft mattress observed by the Optitrack system using 37 passive reflective markers distributed on the faller's body.

The averaged time history of angle $\theta_2(t)$ (the angle measured between torso and arms) obtained from experiment for human walking speed v_0 =1.5 m/s and its approximation are presented in Fig. 3.

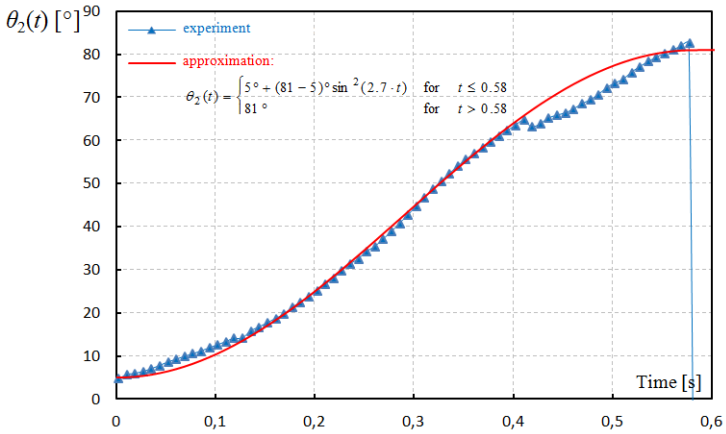

Figure 3. Time history of angle $\theta_2(t)$ obtained from the experiment (points) and its analytical approximation (curve) by analytical smooth function.

During numerical experiments we tested different values of the parameters k_y and b_y in order to obtain GRF which corresponds to the GRFs presented by DeGoede and Ashton-Miller [6]. In that paper, the authors tested five healthy young male volunteers aged between 22 and 28 years with the average body mass of 72±7 kg and the overall height of 173±3 cm [9]. Finally, the best degree of fit we obtained for k_y = 50 000 N/m^3 and b_y = 0.6 s/m.

4. Numerical simulation of the considered fall model

The results presented in Fig. 4 show the influence of different values of velocity v_0 on time histories of the force $F_y(t)$ acting on a single hand for ϕ_{Arm} = 15° (the angle between the arm and the vertical axis of the Cartesian coordinate system at the moment of the impact to the ground). For larger values of the parameter v_0, duration of the fall is smaller while the maximum value of GRF is greater. The value of GRF increases from 2246 N for $v_0 = 0.5$ m/s to 2534 N for $v_0 = 2.0$ m/s. It means that for smaller speed v_0 (i.e. v_0 < 1.5 m/s), the GRF is less than the distal radius fracture threshold [3], whereas for larger values of v_0 (i.e. v_0 > 1.5 m/s) this threshold is exceeded.

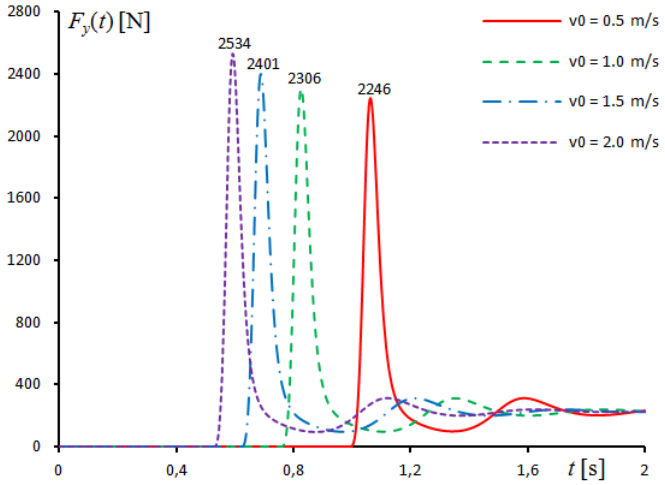

Figure 4. Time histories of GRFs $F_y(t)$ for $\phi_{\text{Arm}} = 15°$ and different values of velocity v_0.

5. Finite element analysis of the radius

The DICOM data used in this paper come from cadaver of 35-years-old man with a height of 1.73 m and a weight of 75 kg. These data have been obtained using a Siemens 64 Slice computed tomography (CT) Scanner in the Department of Forensic Medicine, Jagiellonian University Medical College, Krakov, Poland. The DICOM file of the radial bone was imported to Mimics and the computer model of this bone was obtained and finally verified using *Fix Wizard* function (Fig. 5, on the left). As a result, a realistic 3D FE model of the radius consisting of 15751 FEs was obtained (Fig. 5, on the right). We used the SOLID185 FE-shaped tetrahedron element and isotropic material of the bone. Material inhomogeneity of the radius was also modelled in Mimics based on the CT images. As a result, mechanical properties of the considered radial bone were calculated using on the density-elasticity relationships proposed by Rho et al. [10]:

$$\rho = 1.067\text{HU} + 131, \tag{3}$$

$$E = 0.004\rho^{2.01}, \tag{4}$$

where ρ [kg/m^3] represents density of bone, HU is the nondimensional Hounsfield Unit, E [MPa] denotes Young's modulus, while ν is Poisson's ratio. The obtained range of Young's modulus of the radial bone vary in the range 0.6-12 GPa, whereas Poisson's ratio equals 0.3 for all FEs.

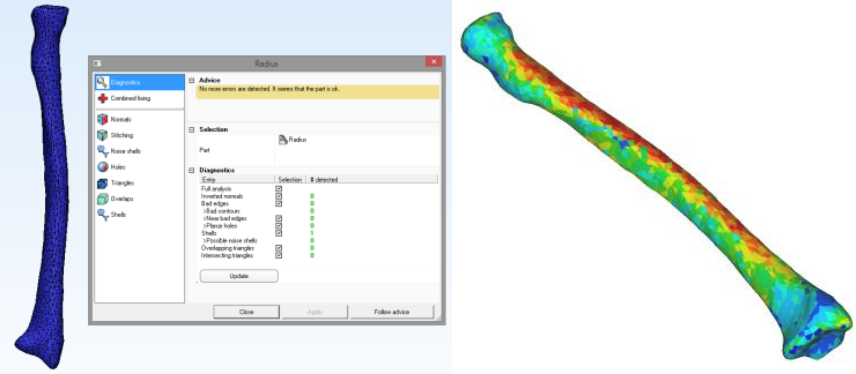

Figure 5. Meshed radial bone verified by *Fix Wizard* function in Mimics (on the left) and spatial distribution of inhomogeneous material properties (on the right).

Numerical results presented in Fig. 4, which correspond to the GRF for a straight position and the walking speed v_0 = 1.5 m/s, were used as load conditions of the developed FE model of the radius. In terms of boundary conditions applied in the analysed model of the radius, all six spatial DoFs in the proximal radius (region of the elbow joint) were fixed. The angle between the longitudinal axis of the radius and gravity direction was equal ϕ_{Arm}, while the GRF was applied in the region of the radial neck in the vertical direction (i.e. gravity direction).

In order to predict bone fracture sites, first the maximum von Mises stress, as a main criterion, has been used. Also the maximal strains of the bones, as another criterion, were calculated, for a better assessment of the radius fracture location and failure load value. The obtained results are presented in Fig. 6 as a both von Mises stress and strain distributions.

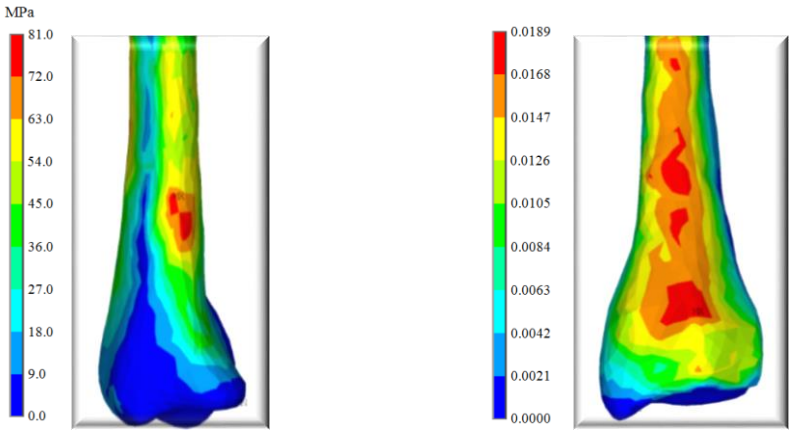

Figure 6. Finite element analysis of the radius bone: von Mises stress distribution (on the left) and strain distribution (on the right).

As can be seen, the maximum stress occur on the medial side (diaphysis) of the radius bone while the maximum strains occur in the distal region of this bone. Colles' fracture is the most common type of injury related to the forward fall on the outstretched arms. Therefore, the presented results indicate that the strain criterion can be more useful for estimating the radius fracture site, since the maximum strains are concentrated in the distal radius.

6. Conclusions

The fall model considered in this paper enables to estimate the vertical ground reaction force acting on the hands in different scenarios of the human fall, and the obtained numerical results agree with other results met in the literature [3]. The parameters describing the human body and modelling biomechanical properties between the palmar cartilages and the ground have a great impact on the obtained results. However, it should be noted that the developed model has also some limitations. Namely, the movement of the shoulder with respect of the torso and stiffness/damping properties of the shoulder joint have not been considered in this fall model. Nevertheless, the mentioned limitations may be of interest for our future study.

The obtained simulations showed that maximum values of the GRF that occur during a fall in forward direction on the outstretched upper extremities are sufficient to determine fracture sites and these results agree with numerical and experimental studies met in the literature [11]. Moreover, it has also been shown that the maximal strain criterion can be more useful for estimation of the fracture site than the von Mises stress criterion.

Acknowledgments

The work has been partially supported by the National Science Centre of Poland under the grant OPUS 9 no. 2015/17/B/ST8/01700 for years 2016-2018. This article does not contain any studies performed on animals. The presented experimental studies have been performed using one of the author of this paper (Paweł Biesiacki), without any other human participants.

References

[1] Palvanen, M., Kannus, P., Parkkari, J., Pitkajarvi, T., Pasanen, M., Vuori, I., Jarvinen, M. The injury mechanisms of osteoporotic upper extremity fractures among older adults: a controlled study of 287 consecutive patients and their 108 controls. *Osteoporosis International* 11, (2000), 822-831.

[2] Johnell, O., Kannis, J.A. An estimate of the worldwide prevalence and disability associated with osteoporotic fractures. *Osteoporosis International* 17, (2006), 1726-1733.

[3] Kim, K.-J., Ashton-Miller, J.A. Segmental dynamics of forward fall arrests: A system identification approach. *Clinical Biomechanics* 24, (2009), 348-354.

[4] Burkhart, T.A., Andrews, D.M., Dunning, C.E. Multivariate injury risk criteria and injury probability scores for fractures to the distal radius. *Journal of Biomechanics* 46, (2013), 973-978.

[5] Chiu, J., Robinovitch, S.N. Prediction of upper extremity impact forces during falls on the outstretched hand. *Journal of Biomechanics* 31, (1998), 1169-1176.

[6] DeGoede, K.M., Ashton-Miller, J.A. Biomechanical simulations of forward fall arrests: effects of upper extremity arrest strategy, gender and aging-related declines in muscle strength. *Journal of Biomechanics* 36, (2003), 413-420.

[7] Biesiacki, P., Mrozowski, J., Grzelczyk, D., Awrejcewicz, J. Modelling of forward fall on outstretched hands and a system with ground contact. *Springer Proceedings in Mathematics and Statics - Dynamical Systems: Modelling*. Ed. J. Awrejcewicz, Springer, 2016, 61-72.

[8] Gerritsen, K.G.M., van den Bogert, A.J., Nigg, B.M. Direct dynamics simulation of the impact phase in heel–toe running. *Journal of Biomechanics* 28, (1995), 661-668.

[9] DeGoede, K.M., Ashton-Miller, J.A. Fall arrest strategy affects peak hand impact force in a forward fall. *Journal of Biomechanics* 35, (2002), 843-848.

[10] Rho, J.Y., Hobatho, M.C., Ashman, R.B. Relations of mechanical properties to density and CT number in human bone. *Medical Engineering & Physics* 17, (1995), 347-355.

[11] Edwards, W.B., Troy, K.L. Finite element prediction of surface strain and fracture strength at the distal radius. *Medical Engineering & Physics* 34, (2012), 290-298.

Paweł Biesiacki, M.Sc. (Ph.D. Student): Lodz University of Technology, Department of Automation, Biomechanics and Mechatronics, 1/15 Stefanowski Str., 90-924 Lodz, Poland (*pawel.biesiacki@dokt.p.lodz.pl*). The author gave a presentation of this paper during one of the conference sessions.

Dariusz Grzelczyk, Ph.D.: Lodz University of Technology, Department of Automation, Biomechanics and Mechatronics, 1/15 Stefanowski Str., 90-924 Lodz, Poland (*dariusz.grzelczyk@p.lodz.pl*).

Jerzy Mrozowski, Ass. Professor: Lodz University of Technology, Department of Automation, Biomechanics and Mechatronics, 1/15 Stefanowski Str., 90-924 Lodz, Poland (*jerzy.mrozowski@p.lodz.pl*).

Jan Awrejcewicz, Professor: Lodz University of Technology, Department of Automation, Biomechanics and Mechatronics, 1/15 Stefanowski Str., 90-924 Lodz, Poland (*jan.awrejcewicz@p.lodz.pl*).

Tympanoplasty of the middle ear with a retraction pocket: recommendations based on the modal finite element analysis

Sergei Bosiakov, Gennadi Mikhasev, Kirill Yurkevich,
Alina Dutina, Lyudmila Petrova, Marina Maisyuk, Feliks Stachowicz

Abstract: The aim of this study is to formulate recommendations for surgery of a retraction pocket of the tympanic membrane and improving of hearing. The FEM analysis of the natural frequencies of the oscillatory systems for the normal, diseased and reconstructed middle ear subjected to tympanoplasty is carried out. In the FEM simulation, the diseased eardrum with a retraction pocket is treated as a nonhomogeneous shell with elastic properties varying in the region of the retraction pocket. The geometric dimensions of the cartilage graft of the tympanic membrane are assessed to generate the acoustic conditions corresponding to the hearing functions of the normal middle ear. The outcomes of this paper may be employed to estimate the optimal thickness of the cartilage graft assigned for reconstruction of a diseased eardrum with a retraction pocket.

1. Introduction

Retraction pocket (RP) of the tympanic membrane (TM) is a clinical manifestation of otitis media [15, 16]. Its formation can lead to imbalance of pressure in the cavities of the middle ear, as well as changes in the structure of the TM itself (thinning and changing its physical properties) [4]. The feature of the RP is its latent nature caused by primarily not evident symptoms and by pathological dynamics. The RP may progress into heavier forms or complications (infections, polyps, perforation) and in some cases turn into cholesteatoma [8, 17] and lead to the hearing loss [5].

One of the preventive measures for the development of the middle ear cholesteatoma is surgical treatment of the RP at an early stage of its formation. Surgery means mounting a cartilage graft in the area of the post-superior quadrant (PSQ) of the TM in order to increase the rigidity of this part of the TM and preserve its auditory function which corresponds to a healthy (normal) middle ear [2, 14]. Therefore, a cartilage tissue is widely used in tympanoplastic in order to provide mechanical stability of TM [16,19]. At the same time, the quantitative influence of a cartilage graft on the middle ear acoustical conductivity was not considered yet. Only a few FEM studies consider acoustic properties of TMs with cartilage graft. In particular, a FEM model was used in [9, 10, 18] to study the technique of graft

application during miringoplasty. In [5] on the basis of biomechanical analysis, the optimal thickness of a cartilage graft from 0.1 to 0.2 mm was established for medium and large TM perforations. However, there are no objective recommendations for choosing the thickness of the cartilage needed to restore the function of the middle ear through the reconstruction of a TM, when removing retraction pockets in the PSQ region. The aim of this study is to formulate recommendations for determining the geometric dimensions of a cartilage graft for various pathologies of a TM to create acoustic conditions corresponding to the functions of a healthy TM, as well as recommendations for operations to eliminate a RP in an eardrum and improve hearing.

2. Finite-element simulation

The finite-element (FE) model of the middle ear is elaborated on the basis of tomography data and consists of malleus, incus, stapes and tympanic membrane. In detail, the solid and FE models of the middle ear are described in [12]. In accordance with [3, 6, 11] the TM contour is rigidly fixed, which corresponds to the ossification of the contact area of the TM and tympanal ring. Elastic modulus of malleus, incus, stapes is about 13.7 GPa, Poisson's ratio is 0.3 [1,5]. The elastic moduli of *pars tensa* (PT) and *pars flaccida* (PF) are approximately 33.4 and 11.1 MPa respectively (with the exception of PSQ). The Poisson's ratio for these two regions is 0.4 [7]. The elastic modulus of the PSQ for the middle ear without pathologies is 33.4 MPa. For the middle ear with pathological changes in elastic properties of the TM the modulus of elasticity of PSQ was assumed to be 22.0, 11.0, 9.0, 3.0, 0.1 MPa and 34.0 kPa. Negative pressure in the tympanic cavity, leading to TM retraction and RP formation was modeled by the application of a static uniformly distributed normal load on the outside of the TM. In our case, the negative pressure is 20 Pa. The cartilage graft was superimposed on the PSQ from the inside of the TM of the middle ear with pathological changes in elastic properties. The graft thickness had discrete values equal to 250 μm, 500 μm, 750 μm, 1000 μm and 1500 μm. The elastic modulus of the cartilage tissue is 3.4 MPa, Poisson's ratio is 0.3 [13]. When calculating the frequency of free oscillations of the middle ear with pathological changes in elastic properties with cartilage graft, the TM contour was rigidly fixed. A part of the graft contour located along the TM contour was also rigidly fixed.

2.1. Middle ear in normal state and with PSQ pathology

The natural frequencies of the normal middle ear and the middle ear with pathological changes (with the RP formation) for the first 30 mode shapes are shown in Figure 1.

Figure 1 depicts that the PSQ elastic modulus decrease leads to the decrease of eigen-

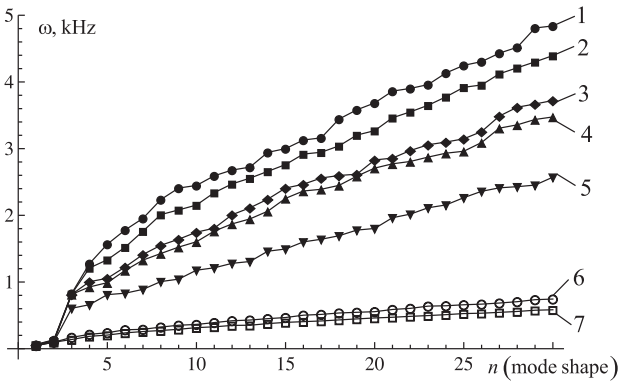

Figure 1. Eigenfrequencies for the first 30 modes: 1 - normal middle ear; curves from 2 to 7 - diseased middle ear with the PSQ elastic moduli equal to 22, 11, 9, 3, 0.1, 0.034 MPa, respectively.

frequencies for related mode shapes. With increasing a number of the mode, the difference between the values of the natural frequencies increases. At the same time, for the first two modes the values of frequencies coincide, independently of the elastic modulus of the PSQ.

2.2. Estimation of cartilage graft thickness

The estimation of the thickness of the cartilage graft applied to PSQ was carried out from the condition of an approximate equality of eigenfrequencies for certain modes of the normal middle ear and the middle ear under various pathological changes in the elastic properties of the PSQ. The cartilage graft thickness was used as an argument of the regression function for each mode. The values of the function were frequencies of free vibrations of the middle ear with a cartilage graft of the corresponding thickness. The regression was carried out on the basis of the exponential and power functions. The mean square error did not exceed 8%. An approximate thickness of the cartilage graft for the corresponding mode was determined as a result of the numerical solution of a transcendental equation in the form of the regression function equality to the natural frequency of the middle ear without pathologies. Figure 2 shows diagrams coupling the frequency of free oscillations of the normal ear with the thickness of the cartilage graft which should be superimposed on the PSQ with pathological changes in order to achieve a coincidence of the natural frequencies for the normal and diseased middle ear. The diagrams were obtained as the results of numerical solutions of nonlinear equations obtained on the basis of the regression functions.

It can be seen from Figure 2 that the thickness of the cartilage graft for the PSQ with a modulus of elasticity of 22 MPa varies in a wide range for both low and high natural

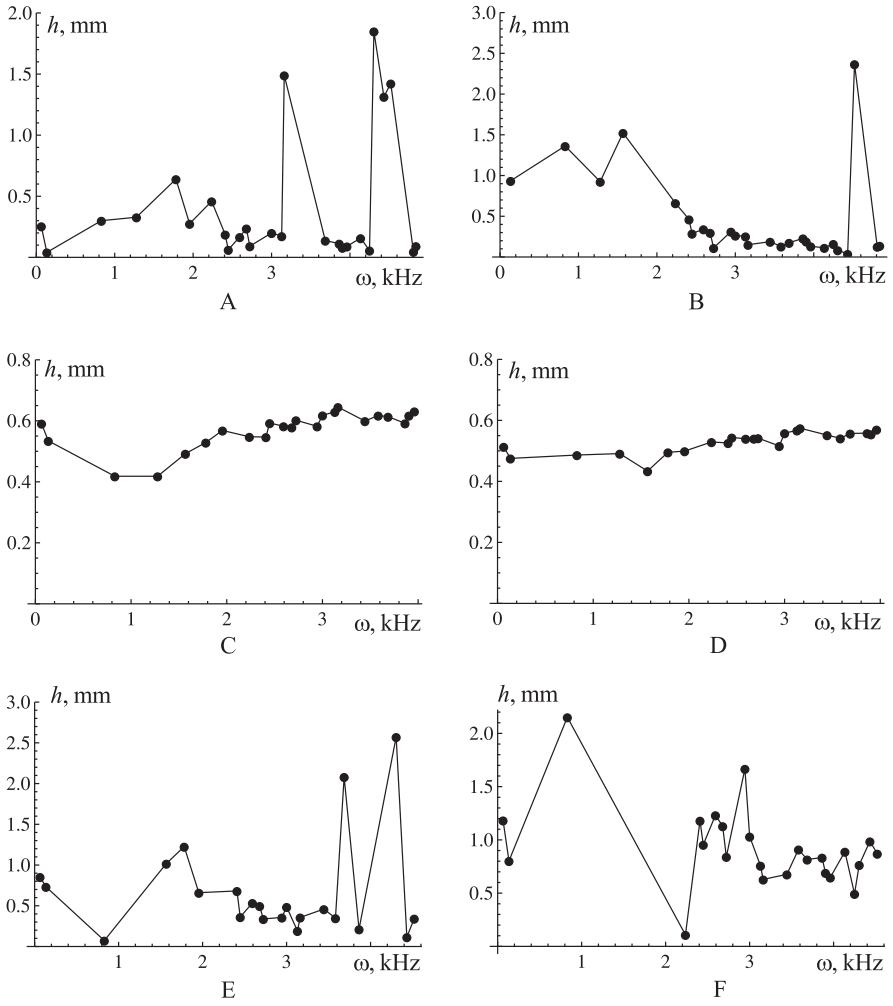

Figure 2. The required thickness of cartilage graft versus eigenfrequency of the normal middle ear for different values of the Young's modulus of the diseased PSQ: (A) - 22.0 MPa, (B)- 11.0 MPa, (C) - 9.0 MPa, (D) - 3.0 MPa; (E) - 0.1 MPa; (F) - 0.034 MPa

frequencies. In particular, for low eigenfrequencies the graft thickness varies from 200 to 890 μm (Figure 2, A), and for frequencies from the auditory range, it may vary from 40 to 1800 μm. The average values of the graft thickness for eigenfrequencies from the auditory range are about 160 – 180 μm. For the diseased middle ear with the PSQ elastic modulus of about 11 MPa, in order to compensate the reduction of elastic properties at eigenfrequencies from the hearing range, the average graft thickness should be approximately 360 μm (Figure 2,

Table 1. The thickness of cartilage graft for the retraction pocket with various elastic moduli of PSQ and the range of eigenfrequencies on which it is possible to compensate for hearing loss after tympanoplasty.

Elastic modulus of the PSQ, MPa	Diapason of cartilage graft thickness estimation, μm	Diapason of eigenfrequencies compensation of hearing loss
22.0	40 – 650	from 2.0 kHz to 5.0 kHz
11.0	360 – 450	from 2.3 kHz to 5.0 kHz
9.0	400 – 650	all eigenfrequencies
3.0	450 – 580	all eigenfrequencies
0.1	1800 – 2200	from 2.5 kHz to 4.0 kHz
0.034	2000 – 2200	from 2.5 kHz to 3.5 kHz

B). For the middle ear with Young's modulus equal to 9 or 3 MPa, imposing a cartilage graft with a certain thickness on the PSQ may result in closeness of almost all natural frequencies of the reconstructed middle ear to the corresponding frequencies of the normal middle ear. Nevertheless, if the PSQ elasticity modulus is equal to 9 MPa, the the required cartilage graft thickness is still in a wide range (400 – 600 μm) at low frequencies and is in a narrower (550 – 650 μm) range for high frequencies (Figure 2, C). For the middle ear with the PSQ elasticity modulus equal to 3 MPa, the thickness of the cartilage graft is about 450 – 580 μm for the considered frequency range (Figure 2, D). In this regard it could be concluded that the surgical treatment of the RP is most effective when the PSQ modulus of elasticity is reduced by 11 times when compared with the normal middle ear. The effectiveness of the surgical treatment is provided by both the possibility of improving auditory conductivity at all natural frequencies and a fairly accurate value of the thickness of the transplant itself. With further reduction of the PSQ elasticity modulus (below 3 MPa), the required thickness of the cartilage graft varies widely and does not allow to reach the simultaneous coincidence of natural frequencies in different ranges (see Figure 2, E and F).

The Table 1 systemizes the ranges of varying of thicknesses of the cartilage graft placed on the RP for the various PSQ elastic moduli. In addition, it lists the eigenfrequencies of the middle ear with pathological changes in the elastic properties of the PSQ after the installation of the cartilage graft, which approximately coincide with the corresponding natural frequencies of the normal middle ear.

For the practical application of the data from Table 1, the ratio between the RP deflection under negative sound pressure for the normal ear and the diseased ear with pathological changes of the PSQ elastic properties can be used. The static FEM analysis of the TM

deflection shows that the cartilage graft should be used when the PSQ deflection increases more than three times corresponding to a decrease in the PSQ elastic modulus to 9.0 MPa, but less than ten times corresponding to a decrease in the PSQ elastic modulus to 3 MPa under the influence of negative pressure on the TM. In the first case, the average thickness of the cartilage graft is approximately 525 μm, while for the second case, it is 515 μm. In the both cases, the implementation of tympanoplasty allows almost completely approximating the auditory conductivity of the middle ear with RP to the auditory that of the normal middle ear.

3. Conclusions

The natural frequencies of the middle ear with the pathological changing elastic properties of the PSQ, which are described by means of a reduced modulus of elasticity, decrease in comparison with the eigenfrequencies of the normal middle ear. The difference between the frequencies increases together with the mode number. For the first two modes, the natural frequencies of the middle ear almost coincide for different PSQ elastic moduli. The thickness of the cartilage graft utilized for the surgical treatment of the RP in the early stages of its formation depends on the RP modulus of elasticity. To save the auditory conductivity and functional indicators, as well as to reduce the risk of recurrence of the disease, it is necessary to use a cartilage graft of a certain thickness. The performed calculations have shown that the most appropriate case for superimposing a cartilage graft on the diseased PSQ is the case when elastic moduli of the PSQ vary in the range from 3.0 to 9.0 MPa. In this case, the installation of a cartilage graft allows for the auditory functions of the diseased middle ear to be approached to those of the normal middle ear. The average thickness of the cartilage graft corresponding to the PSQ modulus of elasticity equal to 3.0 or 9.0 MPa is about 515 and 525 μm, respectively. The grafts with specified aforementioned thicknesses are advised to be used if the maximum deflection of the RP at a negative sound pressure exceeds the maximum deflection of the PSQ of the normal middle ear approximately 3 and 10 times, respectively.

It should be however noticed that the installation of a cartilage graft does not permit to achieve the complete compensation of the auditory conductivity at all frequencies. If the PSQ elastic modulus goes down to 9.0 MPa, the compensation of the hearing function is possible in the range from 2.3 kHz to 5.0 kHz, the average thickness of the cartilage graft being approximately 375 μm. If the PSQ elastic modulus decreases by less than 11 times, the cartilage graft usage does not really make sense because of the compensated auditory frequencies are significantly reduced (up to 2.5 kHz). In this case, the optimal thickness of the cartilage graft is about 2.0 mm.

Acknowledgments

The research leading to these results has received funding from the People Programme (Marie Curie Actions) of the European Union's Seventh Framework Programme FP7/2007-2013/under REA grant agreement IRSES-GA-2013-610547-TAMER.

References

[1] Beer, H.-J., Bornitz, M., Hardke, H.-J., Schmidt, R., Hofman, G., Vogel, U., Zahnert, T., and Hüttenbrink, K.-B. Modeling of components of the human middle ear and simulation of their dynamic behavior. *Audiology and Neurotology 4* (1999), 156–162.

[2] Cassano, M., and Cassano, P. Retraction pockets of pars tensa in pediatric patients: Clinical evolution and treatment. *International Journal of Pediatric Otorhinolaryngology 74* (2010), 178–182.

[3] Elkhouri, N., Liu, H., and Funnell, W. Low-frequency finite-element modeling of the gerbil middle ear. *JARO-Journal of the Association for Research in Otolaryngology 7* (2006), 399–413.

[4] Esteve, D., Dubreuil, C., Delia Vedova, C., Normand, B., Lavieille, J., and Ch., M. Physiologic et physiopathologie de la fonctiond'ouverture de la trompe auditive - apports de la tubomanometrie. *Journal françaisd'oto-rhino-laryngologie 50*, 5 (2001), 233–241.

[5] Fung, Y. *Biomechanics: Mechanical Properties of Living Tissues*. Springer, New York, 1993.

[6] Funnell, W., and Laszlo, C. Modelling of the cat eardrum as a thin shell using the finite-element method. *Journal of the Acoustical Society of America 63*, 5 (1978), 1461–1467.

[7] Kirikae, J. *The middle ear*. The University of Tokyo Press, Tokyo, 1960.

[8] Larsen, P., and Tos, M. Ear polyps in posterior superior retraction pockets, herodion. histopathological and pathogenetic aspects. *ORL Journal For Oto-Rhino-Laryngology and its Related Specialties 54*, 6 (1992), 328–330.

[9] Lee, C., Chen, J., Chou, Y., Hsu, L., Chen, P., and Liu, T. Optimal graft thickness for different sizes of tympanic membrane perforation in cartilage myringoplasty: a finite element analysis. *Laryngoscope 117*, 4 (2007), 725–730.

[10] Lee, C., Hsu, L., Chen, P., Chou, Y.F. abd Chen, J., and Liu, T. Biomechanical modeling and design optimization of cartilage myringoplasty using finite element analysis. *Audiology and Neurotology 11*, 6 (2006), 380–388.

[11] Lesser, T., and Williams, K. The tympanic membrane in cross section: a finite element analysis. *Journal of Laryngology and Otology 102* (1988), 209–214.

[12] Mikhasev, G., Bosiakov, S., Petrova, L., Maisyuk, M., and Yurkevich, K. *Assessment of eigenfrequencies of the middle ear oscillating system: effect of the cartilage transplant.* In: Awrejcewicz J. (Ed.), Dynamical systems: modelling, Springer Proceedings in Mathematics and Statistics, 2016.–Vol. 181.–P. 243–255.

[13] Mikhasev, G., Ermochenko, S., and Bornitz, M. On the strain-stress state of the reconstructed middle ear after inserting a malleus-incus prosthesis. *Mathematical Medicine and Biology 27* (2010), 289–312.

[14] Neumann, A., and Jahnke, K. Die trommelfellrkonstruktionmit knorpel: Indikationeatechniken und ergebnisse. *HNO 53* (2005), 573–586.

[15] Ohnishi, T., Shirahata, Y., Fukami, M., and S., H. The atelectatic ear and its classification. *Auris-Nasus-Larynx 12*, 1 (1985), 211–213.

[16] Tos, M., Stangerup, S., and P., L. Dynamics of eardrum changes following secretory otitis. a prospective study. *Archives of Otolaryngology 113*, 4 (1987), 380–385.

[17] Wells, M., and Micheals, L. Role of retraction pockets in cholesteatoma formation. *Clinical Otolaryngology 8* (1983), 39–45.

[18] Wen, Y., Hsu, L., Chen, P., and Lee, C. Design optimization of cartilage myringoplasty using finite. *Tzu Chi Medical Journal 18* (2006), 370–377.

[19] Yung, M. Cartilage tympanoplasty: literature review. *Journal of Laryngology and Otology 122* (2008), 663–672.

Sergei Bosiakov, Ph.D.: Belarusian State University, Department of Theoretical and Applied Mechanics, 4 Nezavisimosti Avenue, Minsk 220030 Belarus (*bosiakov@bsu.by*).

Gennadi Mikhasev, D.Sc.: Belarusian State University, Department of Bio- and Nanomechanics, 4 Nezavisimosti Avenue, Minsk 220030 Belarus (*mikhasev@bsu.by*).

Kirill Yurkevich, Ph.D.: Belarusian State University, Department of Theoretical and Applied Mechanics, 4 Nezavisimosti Avenue, Minsk 220030 Belarus (*YurkevichKS@bsu.by*).

Alina Dutina, M.Sc. (Ph.D. student): Belarusian State University, Department of Theoretical and Applied Mechanics, Nezavisimosti Avenue, Minsk 220030 Belarus (*alinammf@gmail.com*). The author gave a presentation of this paper during one of the conference sessions.

Lyudmila Petrova, D.Sc.: Belarusian Medical Academy of Post-Graduate Education, 3, Brovki str., build 3, Minsk 220013 Belarus (*bsm21@mail.ru*).

Marina Maisyuk, M.Sc. (Ph.D. student): National Centre of Otorhinolaryngology, 8, Suhaya str., Minsk 220004 Belarus (*merylmmm@mail.ru*).

Feliks Stachowicz, D.Sc. (hab.): Rzeszow University of Technology, Department of Plastic Processing, al. Powstańców Warszawy 12, 35-959 Rzeszów PL (*stafel@prz.edu.pl*).

Preliminary research and analysis on the possibility of using an acoustic wave as an information carrier on an approaching train

Rafał Burdzik, Ireneusz Celiński

Abstract: The concept of using sound as a source of information about approaching of people, animals, vehicles, etc., has been known for centuries and is due to the natural properties of the sense of hearing. There are many engineering attempts on the use of this phenomenon, which can be collectively referred to as the "ear of the Indian". Constant develop of measurement capabilities are causing more and more interesting applications of this phenomenon in the large scope of detection. This article presents the preliminary results of the sound pressure measurement in the immediate proximity of the rail to analyze and evaluate the use of acoustic wave as an information carrier on the approaching train. A number of in-situ experiments were conducted and case studies were compared. These studies are part of a larger research agenda in the field of vibroacoustic energy propagation in a solid structure as rail.

1. Introduction

The researches on railway noise are mostly focused on the environmental and human impact. However an important scope of the research on railway noise is the quantification of aeroacoustic and rolling noise sources emitted by trains externally. The paper [1] presents comprise source localisation using two-dimensional acoustic array measurements and assessment of the wayside noise increase as a function of the speed. The paper [2] describes the aerodynamic noise radiation from a vestibule side door on a high-speed train surface calculated by the combination of unsteady incompressible fluid flow analysis and acoustic analysis. Other group of research are focused on the noise impact. Sleep disturbance by train and road noises was studied through in situ physiological recordings on two groups of people submitted to both types of exposure in paper [3]. The train noise in a station is identified by a series of train noises occurring while a train arrives, stops and leaves a station. The paper [4] presents study on determine the acoustical characteristics of train noise in stations, according to the architectural elements such as location and differing platform styles. Although some studies compared the train noise propagated by various types of trains on largely free sound propagation [5,6].

Mechanisms associated with the interaction of the wheel and the rail dominate the noise production of railway operations at conventional speeds and remain significant (but not dominant) even for high-speed trains. This wheel/rail noise may be divided into three main categories. Rolling

noise occurs on straight track and is predominantly caused by undulations of the wheel and rail surfaces which induce a vertical relative vibration. Impact noise can be considered as an extreme form of rolling noise occurring at discontinuities of the wheel or rail surface. Squeal noise, occurring on sharp radius curves, is usually induced by a lateral excitation mechanism [7].

A solid, which is a rail and substructure and railway embankment, can be considered as elastic centre. A moving rail vehicle causes the external force to be directed to the track which causes stresses in the structure and consequently deformation. The stresses generated in the rail and substructure create an opposite force to the force generated by the passing rail vehicle. This force returns the elastic structure (rail) to the original geometric parameters. The effect of the generation of forces on the elastic structure is the formation of a wave as a disturbance spreading within certain limits [8-13]. The acoustic wave is generated by the rails, whose parameters depend on such factors as: mass of moving rail vehicle, its velocity, technical condition (especially suspension), substructure condition, air temperature, soil temperature, humidity and other parameters. This wave disappears with increasing distance from the track in which it is generated by the moving rail vehicle.

2. Research methodology

Due to the research aim as analysis on the possibility of using an acoustic wave as an information carrier on an approaching train the research methodology was developed. Figure 1 presents the idea of experiment and concept of noise measurement and determination of rail vehicle localization in railway network. The sound level metres (4) are measuring sound level function (3) generate by the aeroacoustic (6) and rolling noise (soil and substructure-5, rail vehicle-1 and rail track-2 interaction).

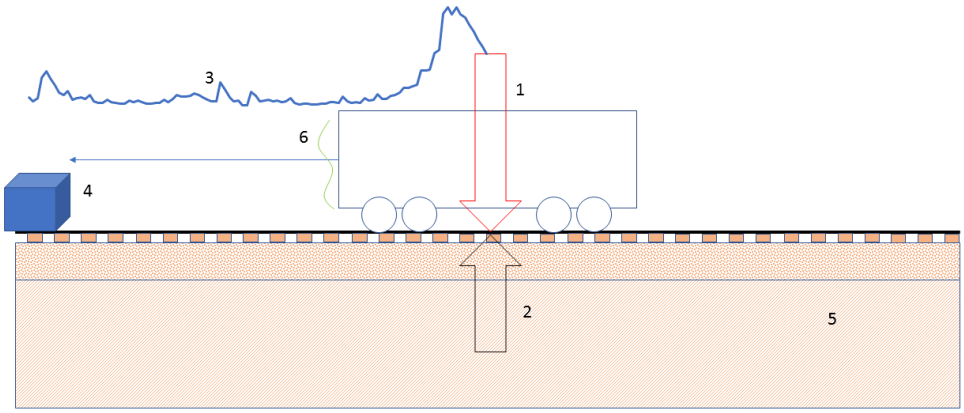

Figure 1. The idea of the experiment.

The idea of the proposed methodology (the so-called „ear of the Indian") is to measure the acoustic waveform at a certain distance from the moving rail vehicle. The purpose of the measurement is to test the possibility of identifying the position of the rail vehicle in the railway network and to assess the functionality of the presented methodology. Two sound level meters were used: Voltcraft SL-451 and Benetech GM 1356. The sound level was measured at selected characteristic points of the railway network using a filter with characteristic A.

The passage of the passenger train EN 57 running on a regular passenger line was examined. Two sound level meters were placed in distance 12 [m] from each other and 0.6 [m] from the head of rail and 1.4 [m] from central axis of the track and 0.2 [m] above the head of rail level. The Benetech GM 1356 was placed next to rails connection and the Voltcraft SL-451 was placed in the half the length of the rail.

3. Research results

As far as constant distance between sound level meters is 12 [m] and rail vehicle at the same time is in the distances X from GM 1356 and Y from SL-451 and it is moving at constant velocity, both sound level meters will show real time sound level as follow:

$$L_{p1}=f(X(t),V(t),M) \quad [dB]$$

and (1)

$$L_{p2}=f(Y(t),V(t),M) \quad [dB]$$

,where:

V - rail vehicle velocity [km/h]

M- mass of the rail vehicle (constant at the measuring section) [t].

Equation (1) does not include such factors as substructure stiffness, air temperature and subsoil, and many others. The mass of train EN 57 is about 125 t, the speed of travel over the microphone is in range 10 km/h to 20 km/h. The distribution of sound level measured on both sound level meters have been depicted in Figures 2 and 3.

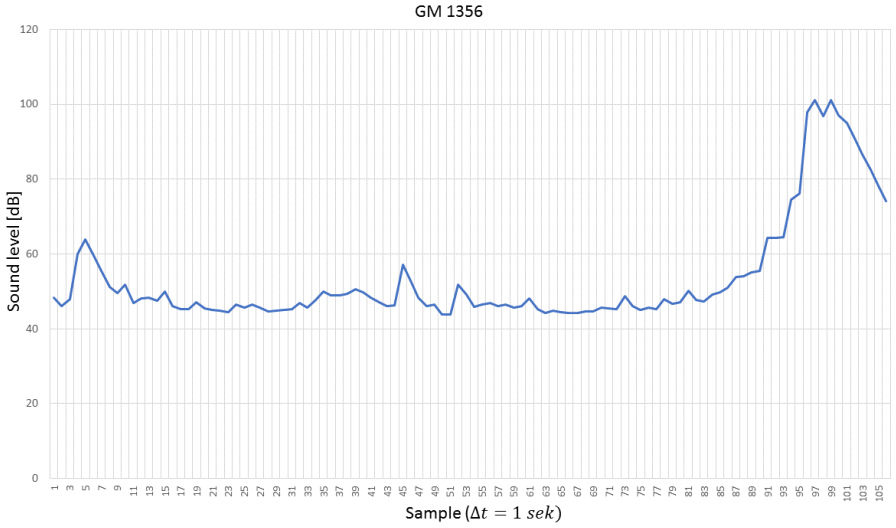

Figure 2. Distribution of sound level, sound level meter GM 1356.

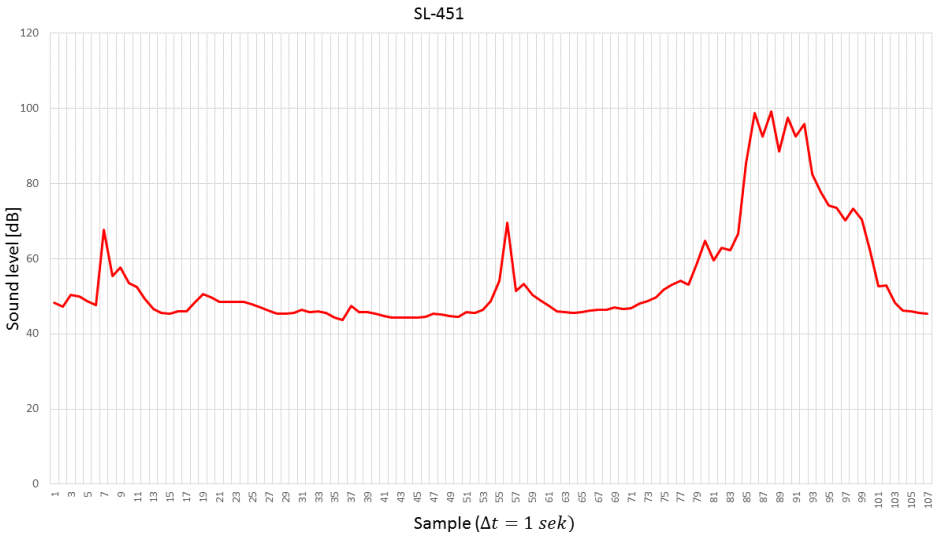

Figure 3. Distribution of sound level, sound level meter SL-415.

It can be observed on Figures 2 and 3 that the sound level is increasing due to rail vehicle approaching. The magnitude of the increase in around 50 [dB] on the measuring section 1100 [m]. At the same time some local increasing section, with local maximum values, are observed.

The comparison of the sound level distribution with the correction due to different distance from first and second sound level meters and rail vehicle have been depisted in Figure 4. The time shift was 5 [s].

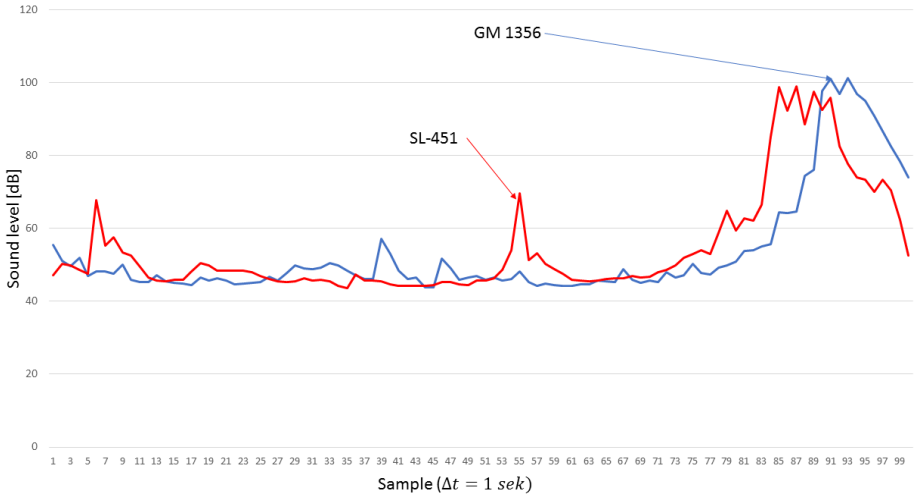

Figure 4. Comparison of the sound level distribution with the time shift correction.

The measurement of both microphones compared with their displacement in the rail network (only at a distance of 12 meters) shows that the results can not be interpreted only within the range of variables included in equation (1). The acoustic wave generated by the rail vehicle changes dynamically depending on the position of the rail vehicle. Susceptible elements, especially in rail connection area, generate local changes in the signal. Thus probably better recommendation is to locate the sound level meter at the half the length of the rail. Hence it can be hypothesized that both of the analysed microphones locations have different functionalities for detecting the position of a rail vehicle.

The rail vehicle approaching the microphone, from the moment the signal is detected until the sensor passes, generates a sound pressure level similar to the exponential distribution (red line in Figure 5). At the same time train is approaching and the distance to sensor decrease (green line in Figure 5). Of course the decrease distance function is depended on velocity (constant or not).

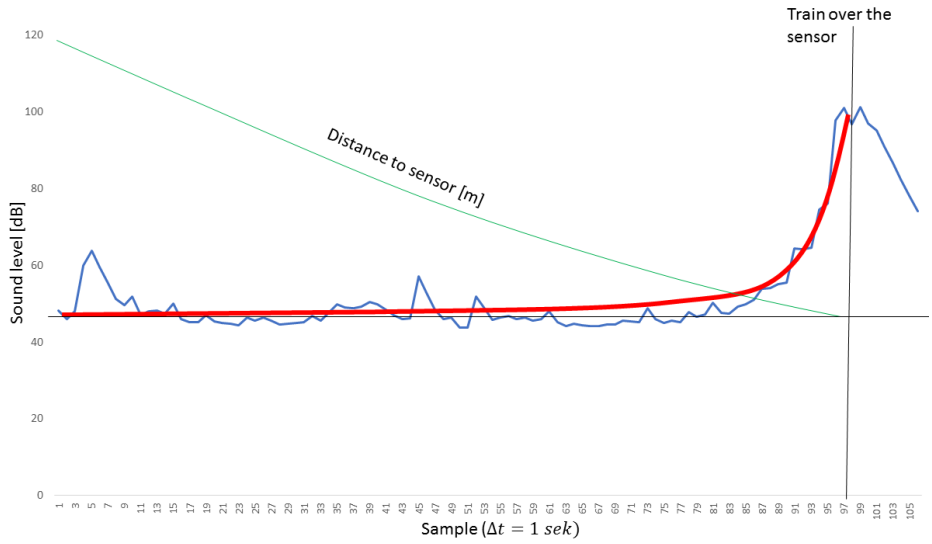

Figure 5. Characteristic of sound pressure as a function of distance to the sensor (microphone).

The characteristics shown in Figures 2÷5 are a combination of the sounds generated by the rail head and the rail vehicle itself (aeroacoustic and rolling noise). At a distance of over one kilometre, the sounds of the rail head dominate. As the proximity to the sensors location approaches, the signal sounds coming directly from the moving rail vehicle (aeroacoustic noise) become dominant. The Figure 6 illustrates this phenomena.

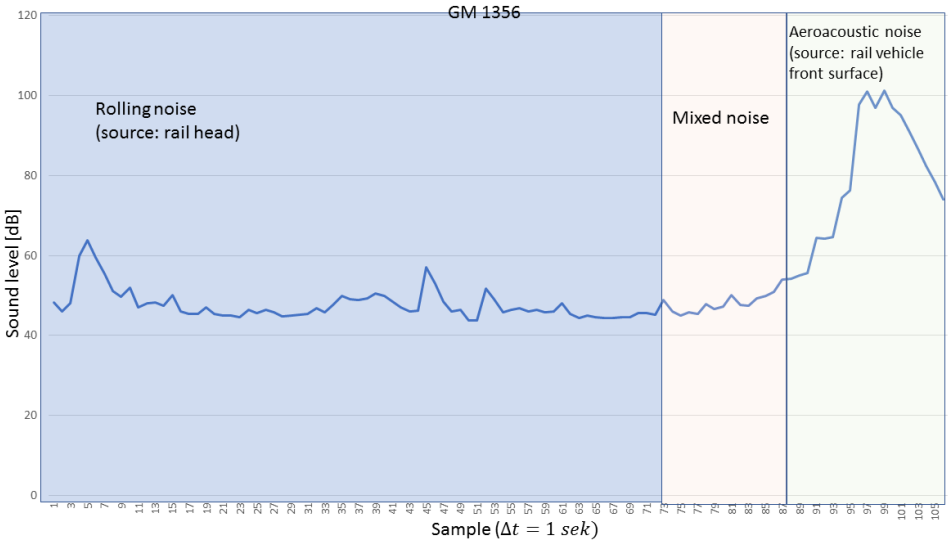

Figure 6. Compartments of dominant sources of rail vehicle noise.

4. Conclusions

Due to the results of the pilot studies presented in this article, it can be stated that the test of the position of a rail vehicle with an acoustic sensor in the acoustic band is technically feasible and it has been verified. Studies have shown that the noise level characteristics associated with trains are likely to affect the area of the entire embankment in the cross-section in which the sound level meter is installed, while the location of the microphone heads slightly changes the observed characteristics.

Also the result confirm that the emitted noise is increased with higher speeds too, but while the rolling noise rises with a speed exponent of about 3, the sound emitted by aerodynamic sources rises with a speed exponent of about 6 [14].

Note that with respect to the measurement conditions shown in this article, the sound level meter can be extended even further to the rail head (<< 60 cm). The authors have set up such a different sound level meter configuration relative to the rail head due to the possible snowfall of the railway track and the exposure to pollution of the measuring system. Moreover it is possible to isolate the microphones from external other noise.

In addition, further testing may be used to narrow the width of the audio band to be tested. This requires testing various rail vehicles within the range of their sound level. It may be possible to increase the distance in which rail vehicles can be detected using this test methodology.

The pilot studies show the possibility of using an acoustic wave as an information carrier on an approaching train. Thus it can be considered as potential applications, for example as support for the railway safety system or monitoring system [15-18].

References

[1] Mellet, C., et al. High speed train noise emission: Latest investigation of the aerodynamic/rolling noise contribution. *Journal of sound and vibration*, 293.3 (2006), 535-546.

[2] Sassa, T., T. Sato, and S. Yatsui. Numerical analysis of aerodynamic noise radiation from a high-speed train surface. *Journal of Sound and Vibration*, 247.3 (2001), 407-416.

[3] Vernet, M. Comparison between train noise and road noise annoyance during sleep. *Journal of Sound and Vibration*, 87.2 (1983), 331-335.

[4] Shimokura, R., Yoshiharu S. Characteristics of train noise in above-ground and underground stations with side and island platforms. *Journal of Sound and Vibration*, 330.8 (2011), 1621-1633.

[5] Stuber, C. Air- and structure-borne noise of railway. *Journal of Sound and Vibration*, 43 (1975), 281–289.

[6] Kurze, U.J., Diehl, R.J., Weibenberger, W. Sound emission limits for rail vehicles. *Journal of Sound and Vibration*, 231 (2000), 497–504.

[7] Thompson, D. J., and Jones. C. J. C. A review of the modelling of wheel/rail noise generation. *Journal of sound and vibration*, 231.3 (2000), 519-536.

[8] Lei, X., Noda, N-A. Analyses of dynamic response of vehicle and track coupling system with random irregularity of track vertical profile. *Journal of sound and vibration* 258.1 (2002), 147-165.

[9] Ling, L., et al. *A 3D model for coupling dynamics analysis of high-speed train/track system*. *Journal of Zhejiang University SCIENCE* A 15.12 (2014), 964-983.

[10] Auersch, L. Theoretical and experimental excitation force spectra for railway induced ground vibration: vehicle-track-soil interaction, irregularities and soil measurements. *Vehicle System Dynamics*, 48, 235–261.

[11] Krylov, V. Spectra of low frequency ground vibrations generated by high speed trains on layered ground. *J Low Freq Noise Vib Active Control*,16(4), (1997), 257–70.

[12] Burdzik, R., Nowak, B. Identification of the Vibration Environment of Railway Infrastructure. *Procedia Engineering* 187 (2017), 556-561.

[13] Dabrowski, Z. and Zawisza, M. Investigations of the Vibroacoustic Signals Sensitivity to Mechanical Defects not Recognised by the OBD System in Diesel Engines. *Solid State Phenomena*, 180 (2012) 194-199.

[14] Martens, A., et al. High speed train noise-sound source localization at fast passing trains. Deutsche Bahn AG, Sociedad Espanola de Acoustica, *SEA* (2009).

[15] Siergiejczyk, M., Paś, J., Rosiński, A. Issue of reliability–exploitation evaluation of electronic transport systems used in the railway environment with consideration of electromagnetic interference. *IET Intelligent Transport Systems*, 10 (1) (2016), 587–593.

[16] Siergiejczyk, M., Rosiński, A. The concept of monitoring a teletransmission track of the highway emergency response system. *Diagnostyka*, 16(4) (2015), 49-54.

[17] Burdzik, R., Nowak, B., Młyńczak, J., & Deuszkiewicz, P. Analysis of the detection and crossing signaling system in safety terms. *Diagnostyka*, 17(4), (2016), 65-72.

[18] Młyńczak, J., Burdzik, R., Celiński, I. Research on Dynamics of Shunting Locomotive During Movement on Marshalling Yard by Using Prototype of Remote Control Unit. *Dynamical Systems: Theoretical and Experimental Analysis*, Springer International Publishing, (2016), 279-292.

1) Rafał Burdzik, Professor: Silesian University of Technology, Faculty of Transport, Department of Automotive Vehicle Construction, Krasinskiego Street 8, 40-019 Katowice, Poland (*rafal.burdzik@polsl.pl)*, the author presented this work at the conference.

2) Ireneusz Celiński, M. Sc. : Silesian University of Technology, Faculty of Transport, Department of Transport Systems and Traffic Engineering, Krasinskiego Street 8, 40-019 Katowice, Poland (*ireneusz.celiński@polsl.pl).*

Nonlinear dynamics of external cavity semiconductor laser system with elements of a chaos

Vasily V. Buyadzhi, Alexander S. Belodonov, Dmitry Mironenko, Alexander A. Mashkantsev, Sergey V. Kir'yanov, Anna A. Buyadzhi and Alexander Glushkov

Abstract: A general, uniform chaos-geometric computational approach to analysis, modelling and prediction of the non-linear dynamics of quantum and laser systems (laser and quantum generators system etc) with elements of the deterministic chaos is briefly presented. The approach is based on using the advanced generalized techniques such as the wavelet analysis, multi-fractal formalism, mutual information approach, correlation integral analysis, false nearest neighbour algorithm, the Lyapunov's exponents analysis, and surrogate data method, prediction models etc There are firstly presented the numerical data on the topological and dynamical invariants (in particular, the correlation, embedding, Kaplan-York dimensions, the Lyapunov's exponents, Kolmogorov's entropy and other parameters) for laser system (the semiconductor GaAs/GaAlAs laser with a retarded feedback) dynamics in a chaotic and hyperchaotic regimes

1. Introduction

In a modern computational quantum and laser physics, electronics and others there are studied various systems and devices (such as atomic and molecular systems in an electromagnetic field, multi-element semiconductors and gas lasers etc), dynamics of which can exhibit a chaotic behaviour. These systems can be considered in the first approximation as a grid of autogenerators (quantum generators), coupled by different way [1-4]. It is easily to understand that a quantitative studying of the chaos phenomenon features is of a great interest and importance for many scientific and technical applications. At the present time it became one of the most actual and important problems of computational physics of the complex non-linear systems.

In this work we firstly applied a general, uniform chaos-geometric formalism to analysis and modelling of non-linear dynamics of the laser systems with elements of a chaos. The formalism is based on using the advanced generalized techniques such as the wavelet analysis, multi-fractal formalism, mutual information approach, correlation integral analysis, false nearest neighbour algorithm, the Lyapunov's exponents analysis, and surrogate data method, prediction models etc (see details in Refs. [5-31]). There are firstly presented the numerical data on topological and dynamical invariants of chaotic systems, in particular, the correlation, embedding, Kaplan-York dimensions, the

Lyapunov's exponents, Kolmogorov's entropy etc for laser (the semiconductor GaAs/GaAlAs laser with retarded feedback) systems dynamics in chaotic and hyperchaotic regimes.

2. Universal chaos-dynamical approach in analysis of dynamics of the complex geosystems

As many blocks of the used approach have been developed earlier and need only to be reformulated regarding the problem studied in this paper, here we are limited only by the key moments following to Refs. [1-32]. The important step of the quantitative studying chaotic dynamics of different dynamical systems is an numerical analysis of the characteristic time series, i.e. the time series of the key dynamical characteristics. Let us formally consider scalar measurements $s(n) = s(t_0 + n\Delta t) = s(n)$, where t_0 is the start time, Δt is the time step, and is n the number of the measurements. In a general case, $s(n)$ is any time series, particularly the amplitude level. Packard et al. [22] introduced the method of using time-delay coordinates to reconstruct the phase space of an observed dynamical system. The direct use of the lagged variables $s(n + \tau)$, where τ is some integer to be determined, results in a coordinate system in which the structure of orbits in phase space can be captured. Then using a collection of time lags to create a vector in d dimensions,

$$\mathbf{y}(n) = [s(n), s(n + \tau), s(n + 2\tau), \ldots, s(n + (d-1)\tau)], \quad (1)$$

the required coordinates are provided. In a nonlinear system, the $s(n + j\tau)$ are some unknown nonlinear combination of the actual physical variables that comprise the source of the measurements. The dimension d is called the embedding dimension, d_E. Any time lag will be acceptable is not terribly useful for extracting physics from data. If τ is chosen too small, then the coordinates $s(n + j\tau)$ and $s(n + (j + 1)\tau)$ are so close to each other in numerical value that they cannot be distinguished from each other. Similarly, if τ is too large, then $s(n + j\tau)$ and $s(n + (j + 1)\tau)$ are completely independent of each other in a statistical sense. Also, if τ is too small or too large, then the correlation dimension of attractor can be under- or overestimated respectively. It is therefore necessary to choose some intermediate (and more appropriate) position between above cases. First approach is based on computing the linear autocorrelation function. Another approach is based on using the average mutual information.

The next principal step is to determine an embedding dimension determination and to reconstruct a Euclidean space R^d large enough so that the set of points d_A can be unfolded without ambiguity. In accordance with the embedding theorem, the embedding dimension, d_E, must be greater, or at least equal, than a dimension of attractor, d_A, i.e. $d_E > d_A$. In other words, we can choose a fortiori large dimension d_E, e.g. 10 or 15, since the previous analysis provides us prospects that the

dynamics of our system is probably chaotic. However, two problems arise with working in dimensions larger than really required by the data and time-delay embedding [24]. Firstly, many of computations for extracting interesting properties from the data require search and other operations in R^d whose computational cost rises exponentially with d. Secondly, but more significant from the physical viewpoint, in the presence of noise or other high dimensional contamination of the observations, the extra dimensions are not populated by dynamics, already captured by a smaller dimension, but entirely by the contaminating signal. In too large an embedding space one is unnecessarily spending time working around aspects of a bad representation of the observations which are solely filled with noise. Further it is necessary to determine the dimension d_A. There are a few standard approaches to reconstruct an attractor dimension (see, e.g., [1-8]), but usually there are applied only two methods. The first correlation integral analysis uses the correlation integral, $C(r)$, to distinguish between chaotic and stochastic systems. To compute the correlation integral, the algorithm of Grassberger and Procaccia [26] is the most commonly used approach, where the correlation integral is

$$C(r) = \lim_{N\to\infty} \frac{2}{N(n-1)} \sum_{\substack{i,j \\ (1\le i<j\le N)}} H\left(r - \| \mathbf{y}_i - \mathbf{y}_j \|\right) \tag{2}$$

where H is the Heaviside step function with $H(u) = 1$ for $u > 0$ and $H(u) = 0$ for $u \le 0$, r is the radius of sphere centered on $\mathbf{y}_i$ or $\mathbf{y}_j$, and N is the number of data measurements. The correlation exponent d t can be determined as the slop of line in the coordinates log $C(r)$ versus log r by a least-squares fit of a straight line over a certain range of r, called the scaling region. To verify the results obtained by the correlation integral analysis, one can use surrogate data method. This method (look for example, [3,4]) is an approach that makes use of the substitute data generated in accordance to the probabilistic structure underlying the original data.

The next important step is computing the Lyapunov's exponents, which are the dynamical invariants of a nonlinear system. In a general case, the orbits of chaotic attractors are unpredictable, but there is the limited predictability of chaotic physical system, which is defined by the global and local Lyapunov's exponents. In a chaos theory, the spectrum of the Lyapunov's exponents is considered a measure of the effect of perturbing the initial conditions of a dynamical system. Note that both positive and negative Lyapunov's exponents can coexist in a dissipative system, which is then chaotic. In fact, if one manages to derive the whole spectrum of the Lyapunov's exponents, other invariants of the system, i.e. Kolmogorov entropy and attractor's dimension can be found. The Kolmogorov entropy, K, measures the average rate at which information about the state is lost with time. An estimate of this measure is the sum of the positive Lyapunov's exponents. The inverse of the

Kolmogorov entropy is equal to the average predictability. The estimate of the dimension of the attractor is provided by the Kaplan and Yorke conjecture:

$$d_L = j + \frac{\sum_{\alpha=1}^{j} \lambda_\alpha}{|\lambda_{j+1}|}, \tag{4}$$

where j is such that $\sum_{\alpha=1}^{j} \lambda_\alpha > 0$ and $\sum_{\alpha=1}^{j+1} \lambda_\alpha < 0$, and the Lyapunov's exponents λ_α are taken in descending order. There are a few approaches to computing the Lyapunov's exponents. One of them is based on the Jacobi matrix of system. In the case where only observations are given and the system function is unknown, the matrix has to be estimated from the data. In this case, all the suggested methods approximate the matrix by fitting a local map to a sufficient number of nearby points. In our work we use the method with the linear fitted map proposed by Sano and Sawada, although the maps with higher order polynomials can be also used. To calculate the spectrum of the Lyapunov's exponents from the amplitude level data, one could determine the time delay τ and embed the data in the four-dimensional space. In this point it is very important to determine the Kaplan-York dimension and compare it with the correlation dimension, determined by the Grassberger-Procaccia algorithm. It is worth to remind that results of state-space reconstruction are highly sensitive to the length of data set (i.e. it must be sufficiently large) as well as to the time lag and embedding dimension determined. Indeed, there are limitations on the applicability of chaos theory for observed (finite) time series arising from the basic assumptions that the time series must be infinite.

3. Analysis of the SMEAR station atmospheric radon concentration time series (2003) and conclusion

As illustration, below we present the results of computational studying the low- and high dimensional dynamics of a chaos generation in the semiconductor GaAs/GaAlAs laser with the retarded feedback. Fischer et al [32] have carried out the excellent experimental studying dynamics of a chaos generation in the semiconductor GaAs / GaAlAs Hitachi HLP1400 laser; an instability is generated by means of the retarded feedback during changing the control parameter such as the feedback strength μ (or in fact an injection current). Of course, depending on the system μ there is appeared a multi-stability of different states with the modulation period: $T_n=2\tau/(2n+1)$, n=0, 1,2,… The state of n = 0 is called as a ground one. With respect to the frequency modulation, other states are called as the third harmonic, fifth harmonic and so on. In the figure 1 we list the measured data on the time-dependent intensities for a semiconductor laser device with feedback: a) the time series, which illustrates a chaotic wandering between the ground state and the state of the third harmonic; b) the time series for a system

in a state of the global chaotic attractor. In Table 1 we present our original data on the correlation dimension d_2, the embedding dimension, computed on the basis of the false nearest neighboring points algorithm (d_N) with percentage of false neighbors (%) which are calculated for different lag times τ.

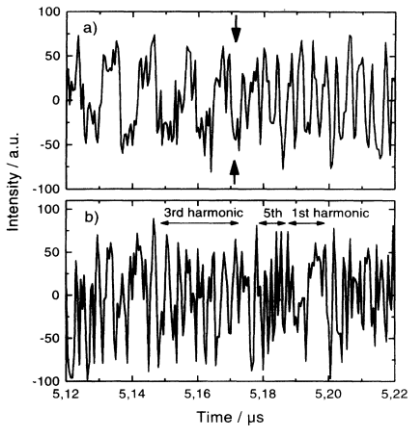

Figure 1. The time series of intensity in the GaAs/GaAlAs Hitachi HLP1400 laser (the measured data, from Ref. [32]).

Table 1. The correlation dimension d_2, the embedding dimension, computed on the basis of the false nearest neighboring points algorithm (d_N) with percentage of false neighbors (%) which are calculated for different lag times τ

Chaos regime (I)			Hyperchaos regime (II)		
τ	d_2	(d_N)	τ	d_2	(d_N)
58	3.4	5 (8.1)	67	8.4	11 (15)
6	2.2	4 (1.05)	10	7.4	8 (3.4)
8	2.2	4 (1.05)	12	7.4	8 (3.4)

The data are presented for two interesting regimes: I. chaos and II. hyperchaos. In Table 2 our computational data on the Lyapunov's exponents, Kaplan-York attractor dimensions, the Kolmogorov entropy K_{entr} are listed. One can see that there are the Lyapunov's exponents positive and negative values. A scenario of chaos generation is in converting initially periodic states into individual chaotic states with increasing the parameter μ through a sequence of the period doubling bifurcations. Further there is appeared a global chaotic attractor after merging an individual chaotic attractors according to a few complicated scenario (see details in Refs. [1,4,32]).

Table 2. The Lyapunov's exponents: λ_1–λ_4, the Kaplan-York attractor dimension d_L and the Kolmogorov entropy K_{entr}

Regime	λ_1	λ_2	λ_3	d_L	K_{entr}
Chaos (I)	0.151	0.00001	-0.188	1.8	0.15
Hyperchaos (II)	0.517	0.192	-0.139	7.1	0.71

To conclude, in this paper we have presented the pre,iminary results of computing nonlinear chaotic dynamics characteristics for the semiconductor GaAs/GaAlAs laser with retarded feedback system. The corresponding data have been obtained on the basis of using the advanced non-linear-analysis techniques such as a wavelet analysis, multi-fractal formalism, mutual information approach, correlation integral analysis and other methods. The correlation dimension method provided a low (or high-) fractal-dimensional attractor thus suggesting a possibility of an existence of the chaotic behaviour. The method of surrogate data, for detecting nonlinearity, provided significant differences in the correlation exponents between the original data series and the surrogate data sets. It has been finally confirmed that the studied laser system dynamics exhibit a nonlinear behaviour with elements of the low-and high-dimensional chaos.

References

[1] Glushkov, A.V. *Methods of a chaos theory.* Astroprint, Odessa, 2012.

[2] Glushkov, A.V., Buyadzhi, V.V., Kvasikova, A.S., Ignatenko, A.V., Kuznetsova, A.A., Prepelitsa, G.P., and Ternovsky, V.B. Nonlinear chaotic dynamics of Quantum systems: Molecules in an electromagnetic field and laser systems. *Quantum Systems in Physics, Chemistry, and Biology. Series: Progress in Theoretical Chemistry and Physics,* ed. A.Tadjer, R.Pavlov, J.Maruani, E.Brändas, G.Delgado-Barrio (Springer). 30 (2016), 71-84.

[3] Khetselius, O.Yu., Brusentseva, S.V., and Tkach, T.B. Studying interaction dynamics of chaotic systems within non-linear prediction method: Application to neurophysiology. *Dynamical Systems Applications*, ed. J. Awrejcewicz, M. Kazmierczak, P. Olejnik, J, Mrozowski. Wydawn. Politechniki Łódzkiej, Łódz. T2 (2013), 251-259.

[4] Glushkov, A.V., Kuzakon, V.M., and Zaichko, P.A. Geometry of Chaos: Advanced approach to forecasting evolution of low-attractor chaotic systems. *Proc. International Geometry Center*. 7, 3 (2014), 67-72.

[5] Glushkov, A.V., Kuzakon', V.M., Khetselius, O.Yu., Bunyakova, Yu.Ya., and Zaichko P.A. Geometry of Chaos: Consistent combined approach to treating chaotic dynamics atmospheric pollutants and its forecasting. *Proc. International Geometry Center*. 6, 3 (2013), 6-13.

[6] Buyadzhi, V.V., Glushkov, A.V., Mansarliysky, V.F., Ignatenko, A.V., and Svinarenko A.A. Spectroscopy of atoms in a strong laser field: New method to sensing AC Stark effect, multiphoton resonances parameters and ionization cross-sections. *Sensor Electr. and Microsyst. Techn*. 12, 4 (2015), 27-36.

[7] Prepelitsa, G.P., Glushkov, A.V., Lepikh, Ya.I., Buyadzhi, V.V., Ternovsky,V.B., and Zaichko P.A. Chaotic dynamics of non-linear processes in atomic and molecular systems in electromagnetic

field and semiconductor and fiber laser devices: new approaches, uniformity and charm of chaos. *Sensor Electr. and Microsyst.Techn*.11, 4 (2014), 43-57.

[8] Glushkov, A.V., Khetselius, O.Yu., Bunuakova, Yu.Ya., Buyadzhi, V.V, Brusentseva, S.V., and Zaichko P.A. Sensing interaction dynamics of chaotic systems within a chaos theory and microsystem technology Geomath with application to neurophysiological systems. *Sensor Electr. and Microsyst.Techn*. 11, 3 (2014), 62-69.

[9] Glushkov, A.V., Mansarliysky, V.F., Khetselius, O.Yu., Ignatenko, A.V., Smirnov, A., and Prepelitsa, G.P. Collisional shift of hyperfine line for thallium in an atmosphere of the buffer inert gas. J. Phys.: Conf. Ser. 810 (2017), 012034.

[10] Svinarenko, A.A., Glushkov, A.V., Khetselius, O.Yu., Ternovsky, V.B., Dubrovskaya, Yu.V., Kuznetsova, A.A., and Buyadzhi, V.V. Theoretical Spectroscopy of Rare-Earth Elements: Spectra and Autoionization Resonances. *Rare Earth Element*, ed. Jose E. A. Orjuela, InTech. (2017), 83-104.

[11] Glushkov, A.V. *Relativistic Quantum theory. Quantum Mechanics of Atomic Systems.* Astroprint, Odessa, 2008.

[12] Khetselius, O.Yu. *Hyperfine structure of atomic spectra.* Astroprint, Odessa, 2008.

[13] Glushkov, A.V., Khokhlov, V.N., and Tsenenko, I.A. Atmospheric teleconnection patterns: Wavelet analysis. *Nonlinear Processes in Geophysics*. 11, 3 (2004), 285-293.

[14] Khetselius, O.Yu. Hyperfine structure of radium. *Photoelectronics*. 14 (2005), 83-85.

[15] Glushkov, A.V., Safranov, T.A., Khetselius, O.Yu., Ignatenko, A.V., Buyadzhi, V.V., and Svinarenko A.A. Analysis and forecast of the environmental radioactivity dynamics based on methods of chaos theory: General conceptions. *Environmental Problems*. 1, 2 (2016), 115-120.

[16] Glushkov, A.V., Khetselius, O.Y., Brusentseva, S.V., Zaichko, P.A., and Ternovsky, V.B. Studying interaction dynamics of chaotic systems within a non-linear prediction method: application to neurophysiology. *Advances in Neural Networks, Fuzzy Systems and Artificial Intelligence, Series: Recent Advances in Computer Engineering*, Ed. J.Balicki. WSEAS Pub., Gdansk. 21 (2014), 69-75.

[17] Glushkov, A.V., Svinarenko, A.A., Buyadzhi, V.V., Zaichko, P.A., and Ternovsky, V.B. Chaos-geometric attractor and quantum neural networks approach to simulation chaotic evolutionary dynamics during perception process. *Advances in Neural Networks, Fuzzy Systems and Artificial Intelligence, Series: Recent Advances in Computer Engineering*, Ed. J.Balicki. WSEAS Pub., Gdansk. 21 (2014), 143-150.

[18] Glushkov, A.V., Prepelitsa, G.P., Svinarenko, A.A., and Zaichko, P.A. Studying interaction dynamics of the non-linear vibrational systems within non-linear prediction method (application to quantum autogenerators). *Dynamical Systems Theory*, ed. J. Awrejcewicz, M. Kazmierczak, P. Olejnik, J, Mrozowski. Wydawn. Politechniki Łódzkiej, Łódz. T1 (2013), 467-477.

[19] Glushkov, A.V., Kuzakon, V.M., Ternovsky, V.B., and Buyadzhi, V.V. Dynamics of laser systems with absorbing cell and backward-wave tubes with elements of a chaos. *Dynamical Systems Theory*, ed. J. Awrejcewicz, M. Kazmierczak, P. Olejnik, J, Mrozowski. Wydawn. Politechniki Łódzkiej, Łódz. T1 (2013), 461-466.

[20] Khetselius, O.Yu. Forecasting evolutionary dynamics of chaotic systems using advanced non-linear prediction method. *Dynamical Systems Applications*, ed. J. Awrejcewicz, M. Kazmierczak, P. Olejnik, J, Mrozowski. Wydawn. Politechniki Łódzkiej, Łódz. T2 (2013), 145-152.

[21] Gottwald, G.A., and Melbourne, I., Testing for chaos in deterministic systems with noise. *Physica D*. 212 (2005), 100–110.

[22] Packard, N.H., Crutchfield, J.P., Farmer, J.D., and Shaw, R.S. Geometry from a time series. *Phys. Rev. Lett.* 45 (1980), 712–716.

[23] Kennel, M.B., Brown, R., and Abarbanel, H. Determining embedding dimension for phase-space reconstruction using a geometrical construction. *Phys. Rev.* A 45 (1992) 3403-3411.

[24] Abarbanel, H.D.I., Brown, R., Sidorowich, J.J., and Tsimring, L.Sh. The analysis of observed chaotic data in physical systems. *Rev. Mod. Phys.* 65 (1993), 1331–1392.

[25] Schreiber, T. Interdisciplinary application of nonlinear time series methods. Phys. Rep. 308 (1999), 1–64.

[26] Grassberger, P., and Procaccia, I. Measuring the strangeness of strange attractors. *Physica D*.9 (1983), 189–208.

[27] Fraser, A.M., and Swinney, H.L. Independent coordinates for strange attractors from mutual information. *Phys. Rev. A.* 33 (1986), 1134–1140.

[28] Gallager, R.G. *Information theory and reliable communication*. Wiley, N-Y., 1986.

[29] Bunyakova, Yu.Ya., and Glushkov, A.V. *Analysis and forecast of the impact of anthropogenic factors on air basein of an industrial city*. Ecology, Odessa, 2010.

[30] Bunyakova, Yu.Ya., and Khetselius, O.Yu. Non-linear prediction statistical method in forecast of atmospheric pollutants. *Proc. of 8th International Carbon Dioxide Conference*. T2-098 (2009).

[31] Glushkov, A.V., Vaschenko, V.N., Gerasimenko, G., and Bunyakova, Yu.Ya. Atmospheric pollutants concentrations temporal dynamics for the industrials ukrainian cities: Low-dimensional chaos. *Dynamical Systems Applications*, ed. J. Awrejcewicz, M. Kazmierczak, P. Olejnik, J, Mrozowski. Wydawn. Politechniki Łódzkiej, Łódz. T2 (2013), 241-250.

[32] Fischer, I., Hess, O., Elsaber, W., and Gobel, E. High-dimensional chaotic dynamics of an external cavity semiconductor laser. *Phys. Rev. Lett.* 73 (1994) 2188-2191.

[*]Vasily V. Buyadzhi, Ph.D.: Odessa State Environmental University, Pure and Applied Mathematics Department, L'vovskaya str. 15, 65009 Odessa, Ukraine (*vbuyad@mail.ru*) The author gave a presentation of this paper during one of the conference sessions

[*]Alexander S. Belodonov, Stud.: Odessa State Environmental University, Pure and Applied Mathematics Department, L'vovskaya str. 15, 65009 Odessa, Ukraine (*belodonovas17@gmail.com*)

[*]Dmitry Mironenko, Ph.D. stud.: Odessa State Environmental University, Pure and Applied Mathematics Department, L'vovskaya str. 15, 65009 Odessa, Ukraine (*dmitrymironenko777@gmail.com*)

[*]Alexander A. Mashkantsev, Ph.D. stud.: Odessa State Environmental University, Pure and Applied Mathematics Department, L'vovskaya str. 15, 65009 Odessa, Ukraine (*mashkantsevaa17@gmail.com*)

[*]Sergey V. Kir'yanov, Ph.D. stud.: Odessa State Environmental University, Pure and Applied Mathematics Department, L'vovskaya str. 15, 65009 Odessa, Ukraine (*kiryanovsv17@gmail.com*)

[*]Anna A. Buyadzhi, Ph.D. stud.: Odessa State Environmental University, Pure and Applied Mathematics Department, L'vovskaya str. 15, 65009 Odessa, Ukraine (*buyadzhiaa@gmail.com*)

[*]Alexander V. Glushkov, Professor: Odessa State Environmental University, Pure and Applied Mathematics Department, L'vovskaya str. 15, 65009 Odessa, Ukraine (*dirac13@mail.ru*).

Multi layer composite coating technology for high damping mechanical structural applications

Giuseppe Catania, Stefano Amadori

Abstract: Multi layer coating technology can be an effective tool to design composite materials with specifically designed damping behavior and some applications are recently known in the aerospace and in the automotive industry. Dynamic mechanical measurements were made on thin-walled components, in the form of multi layered beam specimen, to investigate the composite dissipative properties. Conventional beam theories, can be unsuitable to accurately describe the complex damping behavior of multi layered beams and cannot take into account of contributions such as the frictional actions and slipping at the interface between layers. In this work, multi layered composite beams are modelled, by means of a modified, third order, zig zag model where the contribution of the stiffness of the coating layer materials and of the hysteretic actions at the layer interfaces is taken into account. Third order polynomial functions are adopted to describe the longitudinal displacement of the beam and the continuity of the shear stress across the multi layered beam depth is enforced. The number of kinematic variables used to define the beam motion may depend on the number of layers of the beam, and on the imposed kinematic and dynamic continuity conditions. Such a model is used to get optimal coating solutions with specific dissipative properties at the modelling stage. Some applications are presented and results are discussed.

1. Introduction

Composite materials, designed to exhibit high damping properties without sacrificing the stiffness and the resistance properties, are of great interest for the aerospace and automotive industry. Coating technology proved to be effective for obtaining such improved damping behaviour [1-3]. Component dissipative behaviour can be augmented by the application of single or multi layered coatings made of high damping materials or maximizing frictional actions at the interface between layers [4-7].

Damping behaviour of the coating application have been experimentally investigated by many researchers [8-11], in particular by means of dynamic mechanical experiments made on coated beam and plates in forced excitation [12-14]. Together with the experimental activity, Some models of composite beams and plates have been developed in the past by many researchers [15-19], but no effort was dedicated on modeling the system internal dissipative actions and validating it by experimental tests. The classic Bernoulli-Euler and Timoshenko beam theories can be modified to deal with multi-layered composite beams where the layer mechanical and geometrical characteristics

vary significantly. High-order beam theories taking into account of different stress strain relationship related to the different layers, e.g. layer-wise theories [20-21], have also been considered. Nevertheless, by adopting some layer-wise beam theories, the number of kinematic variables increase with the number of layers and the computational load tend to increase as well. Other layer-wise theories, such as the zig-zag beam and shell theories [22-25], are associated to a fixed number of state space variables, not dependent on the number of layers. An extended multi-layer beam model is presented in this work, taking into account of the dissipative actions exhibited at the interface between the different layers. It must be observed that an effective multi-layered beam model must be able to take into account the many different factors that contributes to the damping behaviour, i.e. the coating architecture, the substrate and coating layers materials and the local friction at the interface between the layers. In this work a multi-layered beam model that takes into account of the different layer's thickness and material constitutive relationships, and also modeling friction actions at the interfaces by means of a hysteretic contribution is presented.

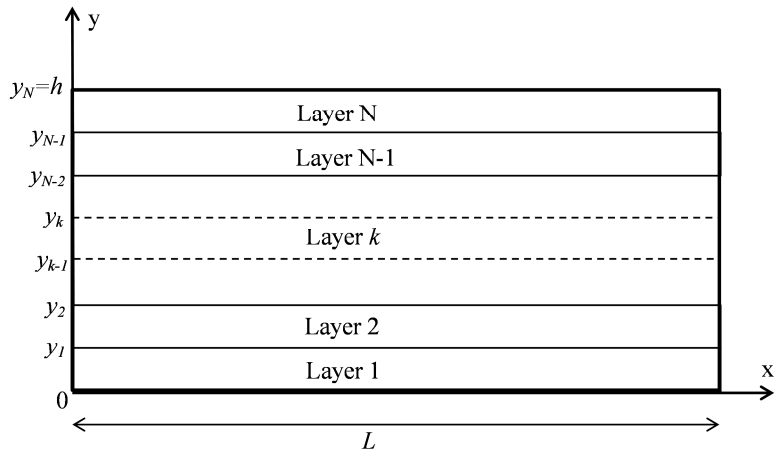

Figure 1. Schematic representation of the multi-layered beam

2. Multi-layer beam model

Fig. 1 shows a schematic representation of a multi-layered beam modeled, uniform rectangular section $S=b\times h$. The multi-layered beam is made up of N layers. L refers to the beam length, b to the width, h to the thickness, ρ_k to the k-th layer density. It is assumed that, for each k-th layer, the relationships between stress ($\sigma=\sigma_{xx}$) and strain($\varepsilon=\varepsilon_{xx}$), shear stress($\tau=\tau_{xy}$) and shear strain($\gamma=\gamma_{xy}$), are:

$$\sigma = E_k \cdot \varepsilon \quad , \quad \tau = G_k \cdot \gamma \quad , \quad k = 1,\ldots,N \tag{1}$$

E_k and G_k are the longitudinal and shear elastic moduli of the *k*-th layer. The beam transverse displacement (*w*) is assumed to be stationary with respect to *y*. The transverse displacement (*w*) and longitudinal displacement (*u*) kinematical variables can be defined as a function of coordinates *x*, y and time *t*, being $\xi=x/L$ and $\eta=y/h$, $\eta_k=y_k/h$:

$$\begin{aligned} & w = w(\xi,t) \\ & u(\xi,t) = u_0 + \alpha\cdot\eta + \left(\eta^3 + \beta\cdot\eta^2\right)\cdot\varphi \quad , \quad 0 \le \eta \le \eta_1 \\ & u(\xi,\eta,t) = u_0 + \alpha\cdot\eta + \left(\eta^3 + \beta\cdot\eta^2 + c_2^k\cdot\eta + c_1^k\right)\cdot\varphi \quad , \quad \eta_{k-1} \le \eta \le \eta_k, \;\; k = 2\ldots N \end{aligned} \tag{2}$$

where:

$$\begin{aligned} & u_0 = u_0(x,t) \quad , \quad \alpha = \alpha(x,t) \quad , \quad \beta = \beta(x,t) \quad , \quad \varphi = \varphi(x,t) \\ & c_2^k = c_2^k(x,t) \quad , \quad c_1^k = c_1^k(x,t) \;\; ; \;\; k=2,\ldots,\mathrm{N} \end{aligned}$$

The strain (ε) and shear strain (γ) kinematical assumptions are:

$$\begin{aligned} & \varepsilon = \frac{u'}{L} \\ & \gamma = \frac{\partial u}{\partial y} + \frac{w'}{L} = \frac{1}{h}\frac{\partial u}{\partial \eta} + \frac{w'}{L} = \frac{w'}{L} + \frac{\alpha}{h} + \left(3\cdot\eta^2 + 2\cdot\beta\cdot\eta + c_2^k\right)\cdot\frac{\varphi}{h} \quad , \quad \eta_{k-1} \le \eta \le \eta_k, \;\; k>1 \\ & \gamma = \frac{w'}{L} + \frac{\alpha}{h} + \left(3\cdot\eta^2 + 2\cdot\beta\cdot\eta\right)\cdot\frac{\varphi}{h} \quad , \quad 0 \le \eta \le \eta_1 \end{aligned} \tag{3}$$

where $(\,)' = \partial(\,)/\partial\xi = L\cdot\partial(\,)/\partial x$. The τ stress continuity at the beam layer interfaces is imposed, and it is assumed that τ vanishes at the upper (η=1) and lower (η=0) faces of the beam:

$$\begin{aligned} & \tau(0) = G_1\cdot\gamma(0) = 0 \;\; \Rightarrow \;\; \gamma(0) = 0 \quad , \quad \tau(1) = G_N\cdot\gamma(1) = 0 \;\; \Rightarrow \;\; \gamma(1) = 0 \,, \\ & \tau(\eta_k)^- = G_k\cdot\gamma(\eta_k)^- = G_{k+1}\cdot\gamma(\eta_k)^+ = \tau(\eta_k)^+ \end{aligned} \tag{4}$$

From Eqs. 3,4:

$$\begin{aligned} & \alpha = -h\cdot w' \\ & c_2^N = -2\cdot\beta - 3 \\ & G_1\cdot\left(3\cdot\eta_1^2 + 2\cdot\beta\cdot\eta_1\right) = G_2\cdot\left(3\cdot\eta_1^2 + 2\cdot\beta\cdot\eta_1 + c_2^2\right) \\ & G_k\cdot\left(3\cdot\eta_k^2 + 2\cdot\beta\cdot\eta_k + c_2^k\right) = G_{k+1}\cdot\left(3\cdot\eta_k^2 + 2\cdot\beta\cdot\eta_k + c_2^{k+1}\right), \;\; k = 2\ldots N-1 \end{aligned} \tag{5}$$

From Eq. 5, a system of *N-1* equations result, and can be arranged as:

$$\begin{cases} G_2 \cdot c_2^2 = 3 \cdot \eta_1^2 \cdot (G_2 - G_1) + 2 \cdot \beta \cdot \eta_1 \cdot (G_2 - G_1) \\ \dots \\ G_{k+1} \cdot c_2^{k+1} - G_k \cdot c_2^k = 3 \cdot \eta_k^2 \cdot (G_{k+1} - G_k) + 2 \cdot \beta \cdot \eta_k \cdot (G_{k+1} - G_k) \\ \dots \\ G_N \cdot c_2^N - G_{N-1} \cdot c_2^{N-1} = 3 \cdot \eta_{N-1}^2 \cdot (G_N - G_{N-1}) + 2 \cdot \beta \cdot \eta_{N-1} \cdot (G_N - G_{N-1}) \end{cases} \tag{6}$$

By equating the sum of Eq. 6 right side to the sum of its left side, and from Eq. 5:

$$\beta = -\frac{3 \cdot \left(\sum_{k=1}^{N-1} \eta_k^2 \cdot (G_{k+1} - G_k) + G_N \right)}{2 \cdot \left(\sum_{k=1}^{N-1} \eta_k \cdot (G_{k+1} - G_k) + G_N \right)} \tag{7}$$

It can be seen from Eq. 7 that β is stationary and its value is determined by the thickness and the shear modulus of the beam layers. From Eq. 6, c_2^k values result from the following iterative procedure:

$$\begin{cases} c_2^2 = 3 \cdot \eta_1^2 \cdot \dfrac{(G_2 - G_1)}{G_2} + 2 \cdot \beta \cdot \eta_1 \cdot \dfrac{(G_2 - G_1)}{G_2} \\ c_2^{k+1} = \dfrac{G_k}{G_{k+1}} \cdot c_2^k + \dfrac{G_k - G_{k+1}}{G_{k+1}} \cdot \left(3\eta_k{}^2 + 2 \cdot \beta \cdot \eta_k \right), \qquad k = 2 \dots N-1 \end{cases} \tag{8}$$

It is assumed that *u(x,η,t)* can show slip discontinuity at the interfaces η_k between different layers:

$$\begin{aligned} & u(\eta_1)^+ - u(\eta_1)^- = \left(c_2^2 \cdot \eta_1 + c_1^2 \right) \cdot \varphi \\ & u(\eta_k)^+ - u(\eta_k)^- = \left(\left(c_2^{k+1} - c_2^k \right) \cdot \eta_k + c_1^{k+1} - c_1^k \right) \cdot \varphi \quad , \quad k = 2, \dots, N\text{-}1 \end{aligned} \tag{9}$$

The following elastic-hysteretic constitutive relationship, is assumed at the beam layer interfaces :

$$\tau(\eta_k) = G_k \cdot \gamma(\eta_k) = \Gamma_k \cdot \left(u(\eta_k)^+ - u(\eta_k)^- \right), \qquad \Gamma_k = K_k + j \cdot \mu_k, \; k = 1 \dots N-1 \tag{10}$$

where $j = \sqrt{-1}$ is the imaginary unit. From Eqs. 9-10, c_1^k values result from the following iterative procedure:

$$\begin{aligned} & c_1^2 = -c_2^2 \cdot \eta_1 + \frac{\Lambda_1 \cdot G_1}{h} \cdot \left(3 \cdot \eta_1^2 + 2 \cdot \beta \cdot \eta_1 \right) \\ & c_1^{k+1} = c_1^k - \left(c_2^{k+1} - c_2^k \right) \cdot \eta_k + \frac{\Lambda_k \cdot G_k}{h} \cdot \left(3 \cdot \eta_k^2 + 2 \cdot \beta \cdot \eta_k + c_2^k \right), \quad k = 2 \dots N-1 \end{aligned} \tag{11}$$

where $\Lambda_k = (K_k + j \cdot \mu_k)^{-1} = (K_k - j \cdot \mu_k) / |\Gamma_k|^2$.

It can be seen from Eqs. 7,8,11 that β, c_1^k, c_2^k are stationary values, only depending by the thickness, the shear modulus and the mechanical complex impedance of the beam layers.
The three independent system state variables can be collected as follows:

$$\mathbf{Z} = \begin{Bmatrix} u_0 \\ w \\ \varphi \end{Bmatrix} = \mathbf{Z}(x,t) \tag{12}$$

3. Equation of motion

The equation of motion can be obtained by minimizing the system total potential energy:

$$\Pi = U + W_{in} + W_{ex} + \Delta\Pi \tag{13}$$

U is the contribution of the internal elastic-hysteretic energy, W_{in} is the contribution of the inertial actions, W_{ex} is the contribution of the external forces, $\Delta\Pi$ is the contribution of the work of the distributed viscous-elastic constraints.

$$U = \frac{1}{2}\cdot\int_{\Omega}(\sigma\cdot\varepsilon\cdot d\Omega + \tau\cdot\gamma\cdot d\Omega) = \frac{\Omega}{2}\cdot\int_0^1\left[\int_0^1(\sigma\cdot\varepsilon\cdot d\eta + \tau\cdot\gamma\cdot d\eta)\right]\cdot d\xi \tag{14}$$

$$W_{in} = \int_{\Omega}(\rho\cdot u\cdot\ddot{u}\cdot d\Omega + \rho\cdot w\cdot\ddot{w}\cdot d\Omega) = \Omega\cdot\int_0^1\left[\int_0^1(\rho\cdot u\cdot\ddot{u}\cdot d\eta + \rho\cdot w\cdot\ddot{w}\cdot d\eta)\right]\cdot d\xi \tag{15}$$

$$W_{ex} = -F\cdot w(\bar{\xi}) - L\int_{\xi_1}^{\xi_2} f(\xi)\cdot w\cdot d\xi \tag{16}$$

$$\Delta\Pi = \frac{\Omega}{2}\cdot\left(\int_0^1 k_t\cdot w\cdot w\cdot d\xi + \int_0^1\int_o^1 k_a\cdot u\cdot u\cdot d\eta\cdot d\xi\right) + \Omega\cdot\left(\int_0^1 c_t\cdot w\cdot\dot{w}\cdot d\xi + \int_0^1\int_o^1 c_a\cdot u\cdot\dot{u}\cdot d\eta\cdot d\xi\right) \tag{17}$$

where $\Omega=Lbh$ is the beam volume, ρ the beam density, $\dot{(\,)} = \partial(\,)/\partial t$, $\ddot{(\,)} = \partial^2(\,)/\partial t^2$, F is a lumped transverse force applied at $\xi = \bar{\xi}$ and $f(\xi)$ is a distribuited force applied at $\xi_1 \le \xi \le \xi_2$, $k_t(\xi)$ and $k_a(\xi,\eta)$ are the constraint elastic stiffness parameters and $c_t(\xi)$ and $c_a(\xi,\eta)$ the constraint viscosity parameters. The Eq.12 system state unknown solution variables are assumed satisfy $Z_i(\xi,t)=f_i(x)\times p_i(t)$, i=1,2,3, and unknown functions $f_i(x)$ are restricted to a set of known Fourier functions:

$$\mathbf{Z}(\xi,t) = \begin{Bmatrix} u_0 \\ w \\ \varphi \end{Bmatrix} = \mathbf{N}(\xi)\cdot\boldsymbol{\delta}(t) = \begin{bmatrix} \mathbf{N}_0(\xi) & \mathbf{0} & \mathbf{0} \\ \mathbf{0} & \mathbf{N}_w(\xi) & \mathbf{0} \\ \mathbf{0} & \mathbf{0} & \mathbf{N}_\varphi(\xi) \end{bmatrix}\cdot\boldsymbol{\delta}(t) \tag{18}$$

Z is defined by means of the three normal mode functions vectors and of a coefficient vector:

$$\begin{aligned}
&\mathbf{N}_0 = \sqrt{2}\cdot\left[1/\sqrt{2} \quad \sin(\pi\cdot\xi) \quad \cos(\pi\cdot\xi) \quad \ldots \quad \sin(n_0\cdot\pi\cdot\xi) \quad \cos(n_0\cdot\pi\cdot\xi)\right]\\
&\mathbf{N}_w = \sqrt{2}\cdot\left[1/\sqrt{2} \quad \sqrt{12}\cdot(\xi-0.5) \quad \sin(\pi\cdot\xi) \quad \cos(\pi\cdot\xi) \quad \ldots \quad \sin(n_w\cdot\pi\cdot\xi) \quad \cos(n_w\cdot\pi\cdot\xi)\right]\\
&\mathbf{N}_\varphi = \sqrt{2}\cdot\left[\sin(\pi\cdot\xi) \quad \cos(\pi\cdot\xi) \quad \ldots \quad \sin(n_\varphi\cdot\pi\cdot\xi) \quad \cos(n_\varphi\cdot\pi\cdot\xi)\right]\\
&\boldsymbol{\delta} = \left[\delta_1 \quad \ldots \quad \delta_n\right]^T,\ n = n_0 + n_w + n_\varphi + 3
\end{aligned} \tag{19}$$

From Eqs. 2,3,18:

$$\begin{aligned}
&w = \begin{bmatrix}0 & 1 & 0\end{bmatrix}\cdot\mathbf{Z} = \begin{bmatrix}0 & \mathbf{N}_w & 0\end{bmatrix}\cdot\boldsymbol{\delta} \ ,\ u = \left[1 \quad -\frac{h\cdot\eta}{L}\cdot\frac{\partial}{\partial\xi} \quad \psi(\eta)\right]\cdot\mathbf{Z} = \mathbf{A}^T(\eta)\cdot\mathbf{L_1}\cdot\mathbf{N}\cdot\boldsymbol{\delta}\\
&\varepsilon = \frac{1}{L}\cdot\mathbf{A}^T(\eta)\cdot\mathbf{L_2}\cdot\mathbf{N}\cdot\boldsymbol{\delta} \ ,\ \gamma = \left[0 \quad 0 \quad \frac{1}{h}\cdot\frac{\partial\psi(\eta)}{\partial\eta}\right]\cdot\mathbf{N}\cdot\boldsymbol{\delta} = \mathbf{B}^T(\eta)\cdot\mathbf{N}\cdot\boldsymbol{\delta}
\end{aligned} \tag{20}$$

where

$$\begin{aligned}
&\psi(\eta) = \eta^3 + \beta\cdot\eta^2 \quad ,\quad 0 \le \eta \le \eta_1\\
&\psi(\eta) = \eta^3 + \beta\cdot\eta^2 + c_2^k\cdot\eta + c_1^k \quad ,\quad \eta_{k-1} \le \eta \le \eta_k,\quad k = 2\ldots N
\end{aligned} \tag{21}$$

$$\mathbf{A}(y) = \begin{bmatrix}1\\ -\frac{h\cdot\eta}{L}\\ \psi(\eta)\end{bmatrix},\ \mathbf{L_1} = \begin{bmatrix}1 & 0 & 0\\ 0 & \frac{\partial}{\partial\xi} & 0\\ 0 & 0 & 1\end{bmatrix},\ \mathbf{L_2} = \begin{bmatrix}\frac{\partial}{\partial\xi} & 0 & 0\\ 0 & \frac{\partial^2}{\partial\xi^2} & 0\\ 0 & 0 & \frac{\partial}{\partial\xi}\end{bmatrix},\ \mathbf{B}(\eta) = \begin{bmatrix}0\\ 0\\ \frac{1}{h}\cdot\frac{\partial\psi(\eta)}{\partial\eta}\end{bmatrix}$$

From Eqs. 14-17:

$$\begin{aligned}
&U = \frac{1}{2}\cdot\boldsymbol{\delta}^T\cdot\mathbf{K}\cdot\boldsymbol{\delta} \quad ,\quad \mathbf{K} = \Omega\cdot\left(\frac{1}{L^2}\cdot\int_0^1(\mathbf{L_2}\cdot\mathbf{N})^T\cdot\mathbf{AE}\cdot(\mathbf{L_2}\cdot\mathbf{N})\cdot d\xi + \int_0^1\mathbf{N}^T\cdot\mathbf{GB}\cdot\mathbf{N}\cdot d\xi\right)\\
&\mathbf{AE} = \left[\sum_{k=1}^{N}E_k\cdot\int_{\eta_{k-1}}^{\eta_k}\mathbf{A}(\eta)\cdot\mathbf{A}^T(\eta)\cdot d\eta\right] \quad ,\quad \mathbf{GB} = \left[\sum_{k=1}^{N}G_k\cdot\int_{\eta_{k-1}}^{\eta_k}\mathbf{B}(\eta)\cdot\mathbf{B}^T(\eta)\cdot d\eta\right]
\end{aligned} \tag{22}$$

$$\begin{aligned}
&W_{in} = \boldsymbol{\delta}^T\cdot\mathbf{M}\cdot\ddot{\boldsymbol{\delta}} \quad ,\quad \mathbf{M} = \Omega\cdot\left(\int_0^1(\mathbf{L_1}\cdot\mathbf{N})^T\cdot\boldsymbol{\rho}\mathbf{A}\cdot(\mathbf{L_1}\cdot\mathbf{N})\cdot d\xi + \widetilde{\rho}\cdot\int_0^1\begin{bmatrix}0 & 0 & 0\\ 0 & \mathbf{N}_w^T\cdot\mathbf{N}_w & 0\\ 0 & 0 & 0\end{bmatrix}\cdot d\xi\right)\\
&\boldsymbol{\rho}\mathbf{A} = \sum_{k=1}^{N}\rho_k\cdot\int_{\eta_{k-1}}^{\eta_k}\mathbf{A}(\eta)\cdot\mathbf{A}^T(\eta)\cdot d\eta \quad ,\quad \widetilde{\rho} = \sum_{k=1}^{N}\frac{\rho_k\cdot h_k}{h}
\end{aligned} \tag{23}$$

$$W_{ex} = -\boldsymbol{\delta}^T \cdot \mathbf{F} \quad , \quad \mathbf{F} = F \cdot \begin{Bmatrix} 0 \\ \mathbf{N}_w^T\left(\overline{\xi}\right) \\ 0 \end{Bmatrix} + L \cdot \int_{\xi_1}^{\xi_2} f\left(\xi\right) \cdot \begin{Bmatrix} 0 \\ \mathbf{N}_w^T\left(\xi\right) \\ 0 \end{Bmatrix} \cdot d\xi \tag{24}$$

$$\begin{aligned}
&\Delta\Pi = \frac{1}{2} \cdot \boldsymbol{\delta}^T \cdot \boldsymbol{\Delta K} \cdot \boldsymbol{\delta} + \boldsymbol{\delta}^T \cdot \Delta C \cdot \dot{\boldsymbol{\delta}} \quad , \\
&\boldsymbol{\Delta K} = \Omega \cdot \left(\int_0^1 \begin{bmatrix} 0 & 0 & 0 \\ 0 & k_t \cdot \mathbf{N}_w^T \cdot \mathbf{N}_w & 0 \\ 0 & 0 & 0 \end{bmatrix} \cdot d\xi + \int_0^1 \boldsymbol{\delta}^T \cdot \left(\mathbf{L_1} \cdot \mathbf{N}\right)^T \cdot \mathbf{kA} \cdot \left(\mathbf{L_1} \cdot \mathbf{N}\right) \cdot d\xi \right) \\
&\boldsymbol{\Delta C} = \Omega \cdot \left(\int_0^1 \begin{bmatrix} 0 & 0 & 0 \\ 0 & c_t \cdot \mathbf{N}_w^T \cdot \mathbf{N}_w & 0 \\ 0 & 0 & 0 \end{bmatrix} \cdot d\xi + \int_0^1 \left(\mathbf{L_1} \cdot \mathbf{N}\right)^T \cdot \mathbf{cA} \cdot \mathbf{L_1} \cdot \mathbf{N} \cdot d\xi \right) \\
&\mathbf{kA}\left(\xi\right) = \sum_{k=1}^{N} \int_{\eta_{k-1}}^{\eta_k} k_a\left(\xi\right) \cdot \mathbf{A}\left(\eta\right) \cdot \mathbf{A}^T\left(\eta\right) \cdot d\eta, \quad \mathbf{cA}\left(\xi\right) = \sum_{k=1}^{N} \int_{\eta_{k-1}}^{\eta_k} c_a\left(\xi\right) \cdot \mathbf{A}\left(\eta\right) \cdot \mathbf{A}^T\left(\eta\right) \cdot d\eta
\end{aligned} \tag{25}$$

By minimizing the total potential, the equation of motion results:

$$\mathbf{M} \cdot \ddot{\boldsymbol{\delta}} + \boldsymbol{\Delta C} \cdot \dot{\boldsymbol{\delta}} + \left[\mathbf{K} + \boldsymbol{\Delta K}\right] \cdot \boldsymbol{\delta} = \mathbf{F} \tag{26}$$

It must be outlined that resulting **M**, **K**, **ΔK, ΔC** are complex matrices because of the hysteretic model assumption. The beam frequency response function $\widetilde{H}(\xi_i, \xi_s)$, related to transverse lumped excitation at abscissa ξ_s and transverse response $w(\xi=\xi_i)$, can be found as follows. By applying to both sides of Eq. 26 the Fourier transform operator $\mathcal{F}(\,) = (\,\widehat{}\,)$:

$$\left(\mathbf{K} + \boldsymbol{\Delta K} + j \cdot \omega \cdot \boldsymbol{\Delta C} - \omega^2 \cdot \mathbf{M}\right) \cdot \hat{\boldsymbol{\delta}} = \hat{\mathbf{F}} \tag{27}$$

The discrete system frequency response function **H** matrix is:

$$\mathbf{H}\left(j\omega\right) = \left(\mathbf{K} + \boldsymbol{\Delta K} + j \cdot \omega \cdot \boldsymbol{\Delta C} - \omega^2 \cdot \mathbf{M}\right)^{-1} = \left(\mathbf{Q}_0\left(j\omega\right) + \Delta\mathbf{Q}\left(j\omega\right)\right)^{-1} \tag{28}$$

where:

$$\begin{aligned}
&\mathbf{Q}_0\left(j\omega\right) = \mathrm{Re}\left(\mathbf{K} + \boldsymbol{\Delta K}\right) + j \cdot \omega \cdot \mathrm{Re}\left(\boldsymbol{\Delta C}\right) - \omega^2 \cdot \mathrm{Re}\left(\mathbf{M}\right) \\
&\Delta\mathbf{Q}\left(j\omega\right) = j \cdot \left(\mathrm{Im}\left(\mathbf{K} + \boldsymbol{\Delta K}\right) + j \cdot \omega \cdot \mathrm{Im}\left(\boldsymbol{\Delta C}\right) - \omega^2 \cdot \mathrm{Im}\left(\mathbf{M}\right)\right)
\end{aligned}$$

From Eq. 28:

$$\begin{aligned}
&\mathbf{H}_0 = \mathbf{Q}_0^{-1} = \left(\mathrm{Re}\left(\mathbf{K} + \boldsymbol{\Delta K}\right) + j \cdot \omega \cdot \mathrm{Re}\left(\boldsymbol{\Delta C}\right) - \omega^2 \cdot \mathrm{Re}\left(\mathbf{M}\right)\right)^{-1}, \\
&\mathbf{H}_0 \cdot \left(\mathbf{Q}_0 + \Delta\mathbf{Q}\right) \cdot \mathbf{H} = \mathbf{H}_0 \quad , \quad \Rightarrow \mathbf{H} = \left(\mathbf{I} + \mathbf{Q}_0^{-1} \cdot \boldsymbol{\Delta Q}\right)^{-1} \cdot \mathbf{Q}_0^{-1} = \left(\mathbf{I} + \mathbf{H}_0 \cdot \boldsymbol{\Delta Q}\right)^{-1} \cdot \mathbf{H}_0
\end{aligned} \tag{29}$$

where closed form $\mathbf{H}_0(j\omega)$ expression can be easily expressed by means of modal decomposition [26]. Beam $\tilde{H}(\xi_i,\xi_s)$ frequency response function then results:

$$\tilde{H}(\xi_i,\xi_s)=\begin{bmatrix}0 & \mathbf{N}_w(\xi_i) & 0\end{bmatrix}\cdot\mathbf{H}(j\omega)\cdot\begin{Bmatrix}0\\ \mathbf{N}_w^T(\xi_s)\\ 0\end{Bmatrix} \tag{30}$$

Table 1: beam layer data

	h_k [mm]	E_k [GPa]	G_k [GPa]	ρ_k (10^3 kg/m^3)
A	{30, 60}	{8, 210}	{3.3 , 80}	{2.7, 7.85}
B	{20, 60, 20}	{70, 210, 70}	{27, 80, 27}	{2.7, 7.85, 2.7}
C	{5, 20, 50, 20, 5}	{300, 7, 210, 7, 300}	{120, 2.8, 80, 2.8, 120}	{5.8, 2.7, 7.85, 2.7, 5.8}

Table 2: beam constraint parameters

	k'_a	k'_t	c'_a	c'_t	c''_a	c''_t
	[10^{15} N/m^4]		[10^5 N·s/m^4]			
A	10	1	1	10	2	5
B	10	1	3	5	1	3
C	10	1	2	8	0.1	5

Table 3: beam interface parameters

	K_k [GPa/m]	μ_k [GPa/m]
A	{0.8}	{70}
B	{0.8, 0.8}	{100, 100}
C	{1, 0.4, 0.4,1}	{300, 20, 20, 300}

4. Applications and results

Three different system configurations are presented, namely A, B, C. All of the beams share the same length L=1.1 m and width b=0.1 m. Beam layer data, e.g. layer thickness and material properties are reported in Tab. 1. Tab.2 reports the beam constraint parameters, and Tab.3 reports the values of the different constants K_k and μ_k at k-th interface.

Table 4: Natural frequencies and damping ratios

	Natural frequency (Hz)			Damping ratio (%)		
	1	2	3	1	2	3
A_0	62.86	393.49	1496.51	6.52	1.19	0.313
A_f	62.69	397.12	1592.55	6.65	0.973	8.07
B_0	83.06	523.69	1965.3	3.15	0.568	0.152
B_f	47.75	275.89	1663.38	19.2	2.36	2.76
C_0	87.37	516.7	1821.74	5.21	0.983	0.289
C_f	51.67	233.78	1146.1	19.6	8.46	4.31

Distributed ($0 \leq \xi \leq 0.09$) viscoelastic clamped-free boundary conditions are taken into account, whose constant parameters are k_a', k_t', c_a', c_t'. Uniformly distributed ($0 \leq \xi \leq 1$) viscous actions, by means of parameters c_a'', c_t'', are also considered to model system inherent damping. The effect of hysteretic dissipation (system configurations A_f, B_f, C_f) at the layer interfaces is evaluated by comparing results in Figs. 2-4, where interface slipping, parameters K_k, μ_k, is taken into account with the corresponding results (system configurations A_0, B_0, C_0) where no slipping occurs. Tab.4 reports the natural frequencies and damping ratios associated to the first three vibration modes in the [0-2000] Hz frequency range, for each system configuration. In the general complex case where slipping is considered, the damping ratio is estimated by means of the SDOF (Single Degree Of Freedom) circle fit method [26], while, when no slipping occurs, the damping ratio simply results from the solution of a generalized eigenvalue problem [26].

Beam inertance FRF frequency response function ($-\omega^2 \cdot \tilde{H}(\xi_i, \xi_s)$) is evaluated and real, imaginary part and the ratio of the imaginary part to the modulus ($\mathrm{Im}(\tilde{H})/|\tilde{H}|$) are plotted in the 0-2000 Hz frequency range, Figs. 2-4. $\mathrm{Im}\left(\tilde{H}\right)/\left|\tilde{H}\right| \in [0,1]$ can be used as a system damping estimate. Inertance $\mathrm{Im}(\tilde{H})/|\tilde{H}|$ damping estimate plotted in Figs. 2-4 show that the proposed slipping elastic-hysteretic model proposed in this work can effectively be used to model the damping behaviour exhibited by multi-coated beam components. Since $2 \cdot (N\text{-}1)$ interface parameters are required by this approach, an effective experimental identification technique can be used to obtain this unknown data. A procedure to obtain the model damping-related constants, K_k, μ_k starting from forced excitation dynamic mechanical measurements of simple dual layer and multi-layer beam systems, is currently under development in our research team.

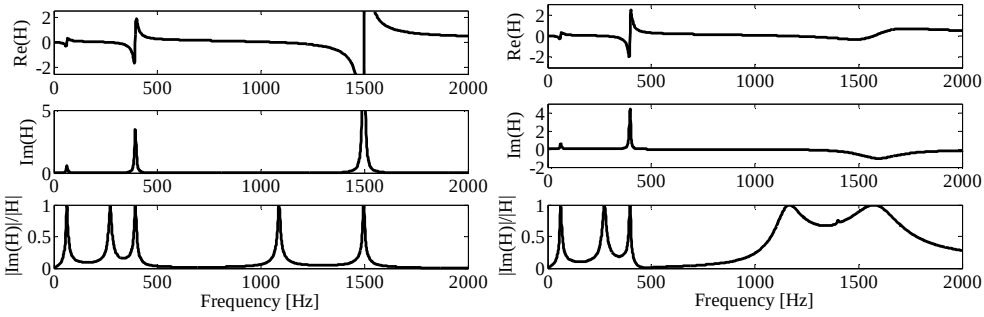

(a) (b)

Figure 2. $-\omega^2 \cdot \widetilde{H}(\xi_i = 1\,, \xi_s = 1)$ inertance FRF: (a) A_0, (b) A_f .

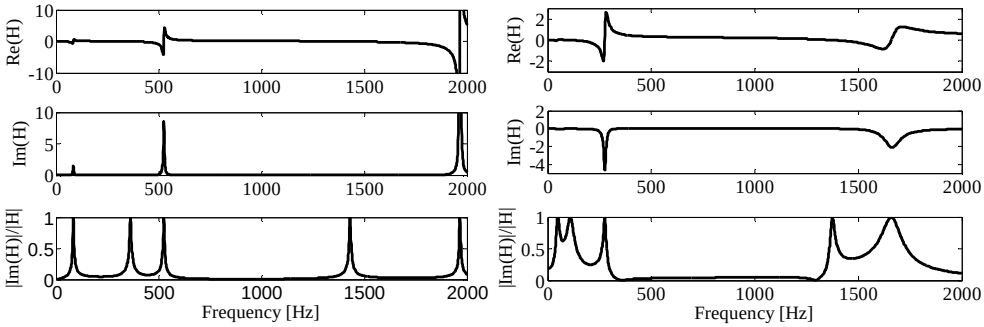

(a) (b)

Figure 3. $-\omega^2 \cdot \widetilde{H}(\xi_i = 1\,, \xi_s = 1)$ inertance FRF: (a) B_0, (b) B_f .

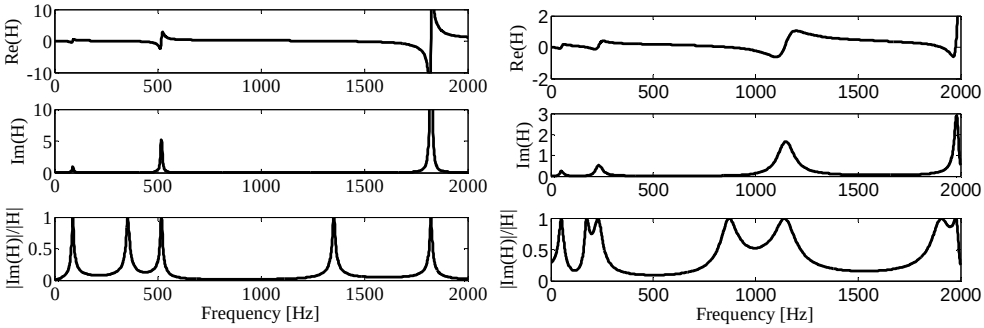

(a) (b)

Figure 4. $-\omega^2 \cdot \widetilde{H}(\xi_i = 1\,, \xi_s = 1)$ inertance FRF: (a) C_0, (b) C_f .

5. Conclusions

A discrete, *n*-dofs model for multi-layered beams, based on a extended high order zig-zag beam theory taking into account of layer interface slipping dissipative actions, is proposed. The model employs a limited number of kinematic variables to increase the computational efficiency. The continuous beam frequency response function is obtained and formulated in the general case where system discrete model matrices are complex. A damping estimator, based on the ratio between the imaginary part and the modulus of the beam continuous frequency response function is proposed. Numerical examples for beams with different multi-layered structures and different dissipative properties are presented and discussed.

Acknowledgments

This study was developed within the CIRI-MAM with the contribution of the Regione Emilia Romagna, progetto POR-Fesr- Tecnopoli. Support from Mr. Andrea Zucchini and Marzocchi pompe S.p.A., Casalecchio di Reno, Italy, is also kindly acknowledged.

References

[1] Tassini, N., Pastias, S., Lambrinou, K. Ceramic coatings: A phenomenological modeling for damping behavior related to microstructural features *Material Science and Engineering A* 442 (2006), 509-513.

[2] Yu, L., Ma, Y., Zhou, C., Xu, H. Damping efficiency of the coating structure *International Journal of Solids and Structures* 42 (2005), 3045-3058.

[3] Ustinov, A.I., Movchan, B.A. A study of damping ability of tin-and yttrium-coated flat specimens of Ti-6%Al-4%V titanium alloy *Strength of Materials* 33, 4 (2001), 339-343.

[4] Rongong, J.A., Goruppa, A.A., Buravalla, V.R., Tomlinson, G.R., Jones, F.R. Plasma deposition of constrained layer damping coating *Proc. Instn Mech. Engrs* Vol. 218 Part C*: J. Mechanical Engineering Science* 218 (2004) 669-680.

[5] Guangyu, D., Zhen, T., Dechum, B., Kun, L., Qingkai, H. Damping properties of a novel porous Mg-Al alloy coating prepared by arc ion plating *Surface&Coatings Technology* 238 (2014) 139-142.

[6] Casadei, F., Bertoldi, K., Clarke, D.R. Vibration damping of thermal barrier coatings containing ductile metallic layers ASME *Journal of Applied Mechanics* 81, (2014), 101001_1-101001_10.

[7] Colorado, H.A., Velez, J., Salva, H.R., Ghilarducci, A.A. Damping behavior of physical vapor-deposited TiN coatings on AISI 304 stainless steel and adhesion determination *Material Science and Engineering A* 442 (2006), 514-418.

[8] Fu, Q., Lundin, D., Nicolescu, C.M. Anti-vibration Engineering in Internal Turning Using a Carbon Nanocomposite Damping Coating Produced by PECVD Process *Journal of Materials Engineering and Performance* 23, 2 (2014), 506-5017.

[9] Blackwell, C., Palazzotto, A., George, T.J., Cross, C.J. The evaluation of the damping characteristics of hard coating on titanium *Shock and Vibrations* 14 (2007), 37-51.

[10] Wang, X., Pei, Y., Ma, Y. The effect of microstructure at interface between coating and substrate on damping capacity of coating systems *Applied Surface Science* 282 (2013), 60-66.

[11] Khor, K.A., Chia, C.T., Gu, Y.W., Boey, F.Y.C. High temperature damping behavior of plasma sprayed NiCoCrAlY coatings *Journal of Thermal Spray Technology* 11, 3 (2002), 359-364.

[12] Reed, S.A., Palazzotto, A.N., Baker, W.P. An experimental technique for the evaluation of strain dependent material properties of hard coatings *Shock and Vibration* 15 (2008), 697-712.

[13] Torvik, P.J. Determination of mechanical properties of non-linear coatings from measurements with coated beams *International Journal of Solids and Structures* 46 (2009), 1066-1077.

[14] Berthelot, J.M. Damping Analysis of laminated beams and plates using the Ritz method *Composite Structures* 74 (2006) 186-201

[15] Sun, W. Liu, Y., Guangyu, D. Analytical Modeling of Hard-Coating Cantilever Composite Plate considering the Material Nonlinearity of Hard Coating *Mathematical Problems in Engineering* Volume 21015, Article ID 978392

[16] Ganapathi, M., Patel, B.P., Boisse, P., Polit, O. Flexural loss factor of sandwich and laminated composites beam using linear and nonlinear dynamic analysis *Composites: Part B* 30 (1999), 245-256

[17] Librescu, L. Schmidt, R. A general linear theory of laminated composite shells featuring interlaminar bonding imperfections *International Journal of Solid Structures* 38 (2001), 3355-3375

[18] Sun, C.T., Whitney, J.M., Theory for the Dynamic Response of Laminated Plates *AIAA Journal* 11, 2 (1973), 178-183

[19] Reddy, J.N. On refined theories of composite laminates *Meccanica* 25 (1990), 230-238

[20] Liu, D., Li X. An overall view of laminate theories based on the diplacement hypothesis *Journal of Composite Materials* 30, 14 (1996), 1539-1561.

[21] Wang, G., Unal, A., Zuo, Q.H. Modelling and Analyssis of Multilayered Elastic Beam Using Spectral Finite Element Method *Journal of Vibrations and Acoustics* 138 (2016), 041013_1-041013_12.

[22] Di Sciuva, M., , Gherlone, M., Librescu, L. Implications of damaged interfaces and of other non-calssical effevts on the load carrying capacity of multilayered composite shallow shells *International Journal of Non-Linear Mechanics* 37 (2002), 851-867.

[23] Di Sciuva, M, Multilayered anisotropic plate models with continuous interlaminar stresses *Composite Structures* 22 (1992), 149-167

[24] Averill, R.C., Yip, Y.C. Development of simple robust finite elements based on refined theories for thick laminated beams *Computer & Structures* 59, 2 (1996), 529-546

[25] Iurlaro, L., Gherlone, M, Di Sciuva, M., Tessler, A. Refined Zigzag Theory for laminated composite and sandwich plated derived from Reissner's Mixed Variational Theorem *Composites Structures* 133 (2015) 809-817

[26] Ewins, D. J. *Modal Testing: Theory, Practice and Applications*, 2nd edition. Research Studies Press, University of Michigan, 2000

Giuseppe Catania, Professor: Din, Ciri Mam, University of Bologna, viale Risorgimento 2 40136 Bologna Italy (g*iuseppe.catania@unibo.it*).

Stefano Amadori, Researcher: Din, Ciri Mam, University of Bologna, viale Risorgimento 2 40136 Bologna Italy (stefano.amadori@unibo.it).

Model based research on electrochemical battery connected with 3 diodes model of PV module – selected properties

Adrian Chmielewski, Robert Gumiński, Krzysztof Bogdziński, Przemysław Szulim, Jędrzej Mączak, Jakub Możaryn, Piotr Piórkowski

*Abstract:*In the article, a model of an electrochemical battery connected with three diode model of a photovoltaic module is presented. To calculate selected parameters of the electrochemical battery model an iteration-approximation method have been employed. In herein work, while applying specific load cycle to the battery-PV module with a control unit, the power distribution of system was analyzed. Then there are presented chosen curves of $LiFePO_4$ batteries obtained from the experimental research and simulation model. Moreover, by using a simulation model the heat generation of the battery has been calculated.

1. Introduction

An adequate energy storage techniques is an essential element of the energy efficiency improvement e.g. in microcogeneration / polygeneration systems. Many different methods of the energy storage are developed in the industry, R&D centers and academia[1-3]. The methods depend on the form of the stored energy e.g. Battery Energy Stores - BES (electrochemical energy) [4-13], Flywheel Energy Stores - FES (mechanical energy) [1], SuperCapacitors - SC (electrical energy) [3], Superconductive Magnetic Coils - SMC (electrical energy) [2], Pumped Hydroelectric Storage - PHS (mechanical energy) [1-3], Compressed Air Energy storage (mechanical energy stored in underground rock caverns), heat accumulators (thermal energy) and many others [3]. Chosen energy storage techniques have been presented in detail in [1,3].

Many studies demonstrate increasing interest in the development of simulation models of hybrid stationary systems [14-21] and Electric Vehicles (EV) based on PV modules with battery [22, 23].

To improve the relevant algorithms for control in the battery management systems (BMS) it is essential to know the operating characteristics of typical batteries for mobile or stationary use which can be supported by simulation models, especially in hybrid systems [17-21].Research of the static and dynamic operation of an electrochemical battery in a specific load cycle supported by a simulation model connected with 3 diode PV module can give the answers to numerous questions regarding the operation of batteries in technical facilities [24-28].

In herein work, in Chapter 2 the test stand of electrochemical energy storage systems ($LiFePO_4$) has been employed. Chapter 3 presents analytical relations of electrochemical battery and PV module.

Based on presented relations, the simulation model, which was subsequently validated against experimental research results, has been described in Chapter 4. Finally, concluding remarks are given in Chapter 5.

2. Experimental test stand

To conduct the research, the test stand has been prepared, complete with data acquisition, load control unit and software application for long duration tests. The measurement circuit of the test stand (Fig.1) consists of: PC class computer, modular data acquisition chassis (National Instruments hardware), TTi CPX400DP programmable laboratory power supply, loading control unit (load circuit connects the battery to a controllable load power unit – individual controllable current source which was prepared by the authors) and control application which has been written in LabVIEW 2016. The application allows for measurement of the following parameters of the battery: voltage measured at the terminals of the battery, the value and direction of current flow while charging / discharging, temperatures at battery terminals, battery body and ambient temperature which were acquired with type K thermocouples. During research all measured values were sampled at the rate of 100 Hz. A detailed description of the test stand is presented in [29].

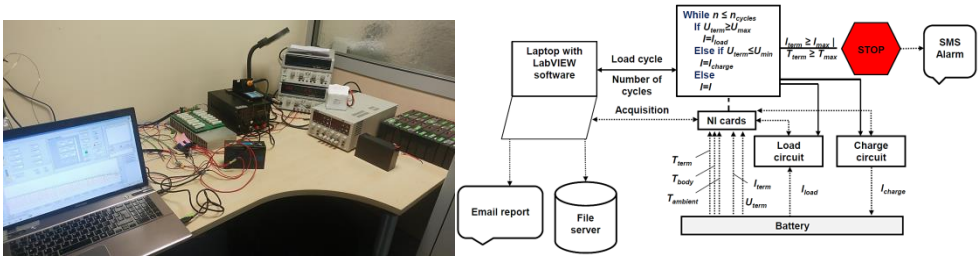

Figure 1. The test stand.

3. The models – analytical description

3.1. The model of electrochemical battery

In order to analyze the performance of batteries two different models were used (Fig.2). The first one is a known thermal resistance model (Fig. 2a) that allows a detailed assessment of the heat losses occurring in the battery (e.g. Li-ion, LiFePO4) [24-28].

The second one (Fig. 2b) is based on the physical model of the battery and takes into account experimental research where the iteration-approximation method can be employed [4, 5, 7, 9].

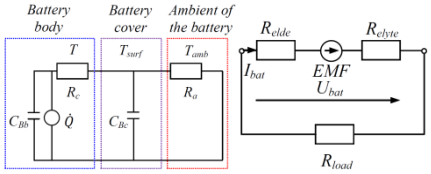

Figure 2. Models of electrochemical battery: a) The thermal resistance model – radial direction, b) the physical model.

The thermal model has been employed, to calculate and analyze the heat generation process of $LiFePO_4$ battery. Based on [24, 27] following equations describe reversible heat generation rate $\dot{Q}_{rev}$, irreversible heat generation rate $\dot{Q}_{irrev}$ and the total heat generation rate $\dot{Q}$:

$$\dot{Q} = P_Q = \dot{Q}_{rev} + \dot{Q}_{irrev} = I(t)\left(\eta_{conv}(t) + \eta_{activ}(t) + \eta_{ohmic}(t) - T(t)\frac{dU_{OCV}}{dT}\right) = I(t)\left(\eta_{conv}(t)(t) + \eta_{activ}(t) + \eta_{ohmic}(t) - T(t)\overbrace{\left\{\frac{dU_{OCV}(t)}{dT}\bigg|_{pos} - \frac{dU_{OCV}(t)}{dT}\bigg|_{neg}\right\}}^{\frac{dU_{ocv}}{dT}}\right) \quad (1)$$

The ohmic polarization overpotential can be expressed as:

$$\eta_{ohmic}(t) = R_{ohmic} I(t) = \overbrace{\exp\left[\lambda_{ohmic}\left(\frac{1}{T_r} - \frac{1}{T_{\text{int}}}\right)\right]}^{R^r_{ohmic}} I(t) \quad (2)$$

where:R_{ohmic} – ohmic resistance [Ω], R^r_{ohmic}– the ohmic resistance at reference temperature [K], T_r – reference temperature [K], T_{int} – the internal temperature of the battery [K], λ_{hmic} - the proportional coefficient of activation energy [K].

The concentration of polarization over-potential can be written as follows:

$$\eta_{conv}(t) = \frac{2RT(t)}{F}(1 - t_+)\ln\left(\frac{\Delta c^i_{init} + \Delta c^i(t)}{\Delta c^i_{init} - \Delta c^i(t)}\right) \quad (3)$$

where: $\Delta c^i(t_i) = \Delta c^i(t_i) + \frac{1}{\tau_{con\,e}}\left(P_{conv} I(t_i) - \Delta c^i(t_i)\right)\left(t_{i+1} - t_i\right)$ - discrete form of concentration deviation between two current collectors [mol·m^{-3}], $P_{conv} = P^r_{conv} \exp\left(\lambda_{conv}\left(1/T_r - 1/T_{\text{int}}\right)\right)$ - the proportional coefficient of the liquid phase diffusion [mol·m^{-3}·A^{-1}], λ_{conv} - the proportional coefficient of activation energy [K], τ_{conve} -time constant of liquid phase diffusion [s].

The reaction of polarization of overpotential can be written as follows:

$$\eta_{activ}(t) = \frac{2RT(t)}{F}\left(\ln\left(\sqrt{m_{neg}^2(t)+1}+m_{neg}(t)\right)+\ln\left(\sqrt{m_{pos}^2(t)+1}+m_{pos}(t)\right)\right) \quad (4)$$

where: R- ideal gas constant [J·mol^{-1}·K^{-1}], F – Faraday's constant [C·mol^{-1}],

$m_{pos} = P_{activ} I(t) \frac{1}{6Q_{pos}\Delta c_{init}^{i\ 0.5}} \frac{1}{(1-y_{surf})^{0.5}(y_{surf})^{0.5}}$, $P_{activ} = P_{activ}^{r} \exp\left(\lambda_{activ}\left(1/T_{init} - 1/T\right)\right)$- the coefficient of the anode reaction polarization, P_{activ}^{r} - the coefficient of the anode reaction polarization at the reference temperature, $T(t_i) = T(t_{i-1}) + (t_i - t_{i-1})\left(Q(t_{i-1}) - \frac{(T(t_{i-1}) - T_{surf}(t_{i-1})}{R_{cond}}\right)\frac{1}{m_{roll}c_p}$ - the battery internal temperature [K], $T_{surf}(t_i) = \frac{T_{surf}(t_{i-1})m_{can}c_{can}R_{cond} + (t_i - t_{i-1})(T(t_i) + R_{cond}A_0 hT_{amb}}{m_{can}c_{can}R_{cond} + (t_i - t_{i-1}) + (t_i - t_{i-1})R_{cond}A_0 h}$ - the discrete formations of the surface temperature [K],m_{can} - the mass of the battery cover [kg], c_{can} – the heat capacity ratio of the battery cover (J·kg^{-1}·K^{-1}), R_{cond} – the thermal resistance [K·W^{-1}], A_0 – the effective heat dissipation area [m^2], h – the heat transfer coefficient (W·m^{-2}·K^{-1}),T_{amb} – the ambient temperature [K] $y_{surf}(t) = y_{aver}(t) + \Delta y'(t) = \overbrace{y_0 + It/Q_{pos}}^{y_{aver}} + \Delta y'(t)$ - solid phase of the surface stoichiometric number of positive electrode [-], $\Delta y'(t_{i+1}) = \Delta y'(t_i) + \frac{1}{\tau_{pos}^2}\left(\frac{12}{7}\frac{\tau_{pos}^2}{Q_{pos}} I(t_i) - \Delta y'(t_i)\right)(t_{i+1} - t_i)$ - the discrete formations of deviations between solid phase surface y_{surf} and average stoichiometric numbers of electrodes y_{avger} [-], Q_{pos}, Q_{neg} - capacities of effective active material in the positive and negative electrodes respectively (A·s), $m_{neg} = P_{activ} I(t) \frac{1}{6Q_{neg}\Delta c_{init}^{i\ 0.5}} \frac{1}{(1-x_{surf})^{0.5}(x_{surf})^{0.5}}$,

$x_{surf}(t) = x_{aver}(t) + \Delta x'(t) = \overbrace{(1 - y_{offset} - y_{aver})Q_{pos}/Q_{neg}}^{x_{aver}} + \Delta x'(t)$ - the solid phase surface stoichiometric number of negative electrode [-], $\Delta x'(t_{i+1}) = \Delta x'(t_i) + \frac{1}{\tau_{neg}^2}\left(\frac{12}{7}\frac{\tau_{neg}^2}{Q_{neg}} I(t_i) - \Delta x'(t_i)\right)(t_{i+1} - t_i)$ - the discrete formations of the deviations between x_{surf} and x_{aver} [-], x_{surf} - the solid phase surface of stoichiometric number of the negative electrode [-], the solid phase average stoichiometric number of the negative electrode [-], τ_{pos} - solid phase diffusion time constants of the negative electrode [-],

$\Delta y'(t_{i+1}) = \Delta y'(t_i) + \frac{1}{\tau_{pos}^2}\left(\frac{12}{7}\frac{\tau_{pos}^2}{Q_{pos}} I(t_i) - \Delta y'(t_i)\right)(t_{i+1} - t_i)$ -the discrete formation of deviations between y_{surf} and y_{aver} [-].

The terminal voltage of the battery can be described as:

$$U_{term}(t) = E_{OCV}(t) - \eta_{conv}(t) - \eta_{activ}(t) - \eta_{ohmic}(t) = \overbrace{E^{r}_{OCV}(t) + (T(t) - T_r)\frac{dE_{OCV}}{dT}}^{E_{OCV}(t)} - \eta_{conv}(t) +$$
$$- \eta_{activ}(t) - \eta_{ohmic}(t) = \underbrace{U_{pos}(y_{surf}) - U_{neg}(x_{surf})}_{E^{r}_{OCV}} + (T(t) - T_r)\frac{dE_{OCV}}{dT} - \eta_{conv}(t) - \eta_{activ}(t) - \eta_{ohmic}(t) \quad (5)$$

Based on the analysis of the figure 2b the internal resistance R_i of the battery can be calculated as:

$$R_i(i_{bat}, T, Q) = R_{elde}(T, Q) + R_{elyte} + aEMF(i_{bat}, T, Q)I_n^{-1} \quad (6)$$

Where:

$aEMF(i_{bat},T,Q)I_n^{-1}$ – the ratio which defines the relative change of the electromotive force of polarization during flow of nominal current I_n versus *EMF* for the nominal capacity of Q_n.R_{elde}, R_{eleyte} – electrodes and electrolyte resistance, respectively.

In this article the experimental data has been employed to determine R_i:

$$R_i = (U_m - U_{m+1})/(I_{m+1} - I_m) \quad (7)$$

where: $U_m > U_{m+1}$ and $I_{m+1} > I_m$.

The family of U_m, U_{m+1} characteristics was determined during experimental research, described in [4, 6, 13, 29]. Once R_i was determined, while transforming the below equation (8), it became possible to calculate the *EMF*, respectively for charging (+) and discharging(-):

$$U_{term} = EMF \pm i_{bat}R_i \Rightarrow EMF = U_{term} \mp i_{bat}R_i \quad (8)$$

The internal resistance of the battery R_i was determined using the iteration-and-approximation method [**4**] and subsequently it was used in the simulation model in order to account for the change of the battery's resistance depending on the change of its state of charge. The properties of the electrochemical battery were defined by using the Peukert's equation: $K_p = i_{bat}^{k(T)}t$. This relationship defines the battery's discharge capacity. It combines discharge current of the battery (i_{bat}) with time t while taking into account the external conditions $\kappa(T)$ (the Peukert's constant)[**5, 7, 9**]. Normally battery manufacturers indicate the rated capacity of a cell for standard conditions (T = 298K = 25°C, then $T=T_{nom}$). However,the Peukert's constant value depends on battery type.

$$Q_{Bu}(i_{bat}, t, T) = c_T(T)\eta(i_{bat}, T)Q_n \pm \int_0^t i_{bat}(t)dt \quad (9)$$

Knowing that the battery's state of charge (SOC) is the ratio of its effective capacity to nominal capacity, one can write:

$$SOC = \frac{Q_{Bu}}{Q_n} = \frac{w_T(T)\eta(i_{bat}, T)Q_{nom} - \int_0^t i_{bat}(t)dt}{Q_n} = \overbrace{w_T(T)\eta(i_{bat}, T)\big|_{\substack{i_{bat}\cong I_n \\ T\cong Tn}}}^{\cong 1} - \frac{1}{Q_{nom}}\int_0^t i_{bat}(t)dt = 1 - \frac{1}{Q_{nom}}\int_0^t i_{bat}(t)dt \quad (10)$$

The EMF electromotive force, which depends on the SOC, can be expressed in the following form [4,7,9]:

$$EMF(SOC) = EMF_{\min} + \Delta U_{term} \cdot SOC = EMF_{\min} + (EMF_{\max} - EMF_{\min}) \cdot SOC \tag{11}$$

The EMF_{min} and EMF_{max} values have been determined on the basis of experiments [4, 6, 13, 29]. The power supplied/ took from the battery can be expressed as follows:

$$P_{bat} = U_{term} i_{bat} \eta(i_{bat}, T) = U_{term} i_{bat} \left(\frac{i_{bat}(t)}{I_n} \right)^{-B(\tau)} \tag{12}$$

3.2. The model 3 diode PV module with losses

In this subsection, the 3 diode model of the photovoltaic cell with losses [20, 21] has been presented. Figure 3 illustrates an equivalent scheme of the 3 diode photovoltaic cell.

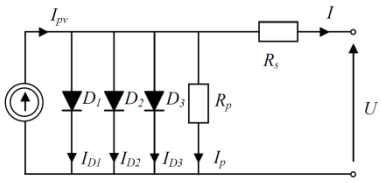

Figure 3. 3 diodes model of PV module.

Based on the analysis of the circuit given in Fig. 3, the current I obtained from conversion of the solar energy to electric energy can be written as [20-22]:

$$I_{ph} = \frac{G}{G_0} \left[I_z + J_0 (T - T_a) \right] \tag{13}$$

where: I_{sc} - the stalling current in G_0 conditions (Standard Testing Conditions, STC: T=298K and G_0=1000W/m^2) [A], T_a – ambient temperature in STC [K], G – solar radiation power density [W/m^2], J_0 – temperature coefficient [A/K].

General equation for the current I_{Dn} flowing through the diode D_n can be expressed as:

$$I_{Dn} = I_{0n} \left(\exp\left\{ \frac{q(U + R_s I)}{N_s \alpha_n k_b T} \right\} - 1 \right) \tag{14}$$

where:

$$I_{0n} = I_{D0n} \left(\frac{T}{T_{amb}} \right)^3 \exp\left(\frac{qE_q m}{\alpha_n k_B} \left(\frac{1}{T_a} - \frac{1}{T} \right) \right) \tag{15}$$

Where:E_q- the energy gap [eV], q - elementary charge [C].

Generally, the dark current of the diode D_n can be written:

$$I_{D0n} = \frac{I_{SC}}{\exp\left(\frac{qU_0}{N_s \alpha_n k_B T}\right) - 1} \tag{16}$$

For n=1, the current I_{D1} flowing through the diode D_1 (Fig. 3) can be expressed as follows:

$$I_{D1} = I_{01}\left(\exp\left\{\frac{q(U + R_s I)}{N_s \alpha_1 k_b T}\right\} - 1\right) \tag{17}$$

Moreover:

$$I_{01} = I_{D01}\left(\frac{T}{T_{amb}}\right)^3 \exp\left(\frac{qE_q m}{\alpha_1 k_B}\left(\frac{1}{T_a} - \frac{1}{T}\right)\right) \tag{18}$$

The dark currentI_{D01} of the diode D_1 can be writtenas follows:

$$I_{D01} = \frac{I_{SC}}{\exp\left(\frac{qU_0}{N_s \alpha_1 k_B T}\right) - 1} \tag{19}$$

The current I_p flowing via R_p shunt resistance can be expressedas follows:

$$I_p = U + R_s I / R_p \tag{20}$$

Based on 1st Kirchoff's law (Fig. 3), the value of the current I flowing through a series resistance R_s can be written as:

$$I = I_{pv} - I_{D1} - I_{D2} - I_{D3} - I_p = I_{pv} - \sum_{n=1}^{n=3} I_{Di} - I_p \tag{21}$$

The electrical power of the PV modules can be determined as:

$$P_{pv} = U_{pv} I \tag{22}$$

The electrical power supplied to / taken from the battery, by the inverter, can be described as:

$$P_{bat} = \eta_{inv}(i)\left(P_{pv} - P_{load}\right) \tag{23}$$

where: $\eta_{inv}(i)$ - the inverter efficiency [30], P_{load} – external power load(e.g. daily household cycle of the energy consumption).

4. The simulation model, simulation results and research results

Based on the relationships (1-23), which are presented in chapter 3, the simulation model has been prepared. The model describes selected properties of PV module which has been connected with electrochemical battery by DC/DC inverter.

Figure 4 shows chosen parameters influence of PV polycrystalline module on power generated (P_{pv}). It presents the results of the simulations for the following main parameters - PV module: R_p=300Ω, R_s=0.2Ω, T=295K – summer, T=273K – winter, $G_{December}$=220W/m^2 – winter, G_{July}=740W/m^2 – summer, J_0=0.0013A/K, I_{sc}=3.11A, $\alpha_n=\alpha_1=\alpha_2=\alpha_3$=1.3, U_{ocv}=21.7V, N_s=36, N_p=50, q=1.6021·10^{-19}C,k_b=1.3805·10^{-23}J/K, E_q=1.12eV.

Based on analysis of the Figure 4 it can be stated that increase of the value of the series R_s (Fig.4a-d),the shunt resistance (Fig.4e-h) and the temperature (Fig.4k-l) of PV module have negative influence on power and photo current generation value. Increasing the value of irradiation affects (Fig. g-j) growth of the power and photo current generation values both in winter and in summer, respectively.

The main parameters of electrochemical battery model chosen for simulation were : Q_{nom}=325Ah, U_{nom}=26.4V, the number of cells connected in series -8, number of cells connected in parallel – 130, nominal capacity of single cell – Q_1=2.5Ah, nominal voltage of single cell – U=3.3V, I_{nom}=130A, $B(\tau)$=1.05.

Figure 5a presents the curve of internal resistance of the LiFePO4 battery. The change of internal resistance was described by 9 degree polynomial. The approximated general equation has been implemented to simulation model. Figure 5b illustrates the voltage at the terminals of LiFePO4 battery from: experimental research, from approximation and from simulation model for discharge current i_{load}=6A. The relative error between experimental research and simulation model for a single LiFePO4 cell is smaller than 2% (the error is acceptable for practical use this method). Figure 5c presents the total heat generated by the battery based on experimental research.

Figure 6a illustrates the curves of daily power generated of PV module gathered from simulation model (the average value of daily irradiation for July, located at Warsaw city was assumed; the mean daily temperature T=295K). The maximum value of daily power generated by PV was equal to 637.36W for G_{July}=978W/m^2 (at 11:52 AM) and inclination of plane of PV module was equal to 35deg.

Figure 6b shows the external load cycle similar to daily energy consumption in several person household [8]. During simulations there was assumed, that designated household appiliances and other devices worked all the time (stand-by mode, eg: TV set, digital decoder, wireless router and others). Also, the external daily load cycle has been implemented in the simulation model.

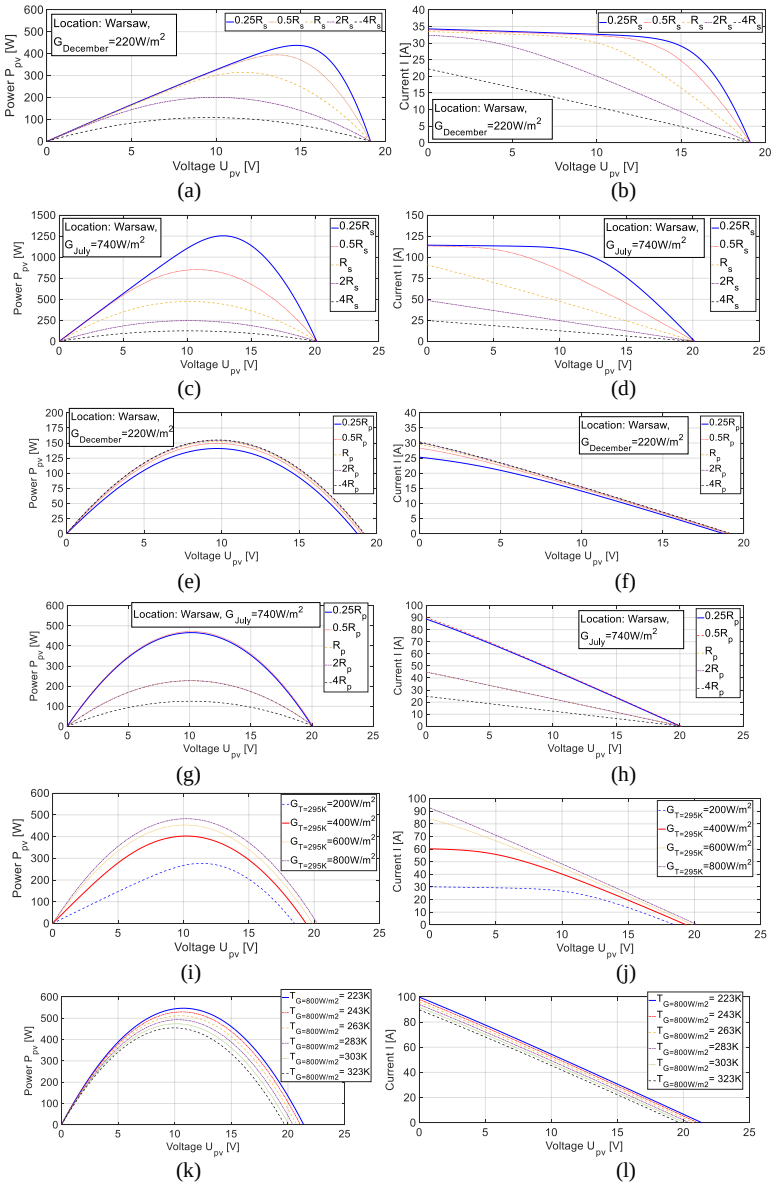

Figure 4. The curve of: a) R_s influence on P_{pv} value in winter, b) R_s value influence on I value in winter, c) R_s influence on P_{pv} value in summer, d) R_s influence on I value in summer, e) R_p influence on P_{pv} value in winter, f) R_p influence on I value in winter, g) R_p influence on P_{pv} value in summer, h) R_s influence on I value in summer, i) G influence on P_{pv} value in summer, j) G influence on I value in summer, k) T influence on P_{pv} value for G=800W/m^2, l) T influence on I value for G=800W/m^2.

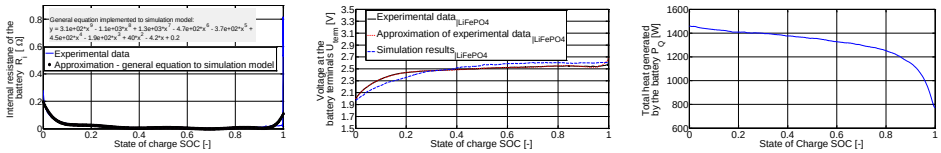

(a) (b) (c)

Figure 5. The curve of: a) internal resistance of the battery – general equation, b) the voltage at the terminal of the battery from model and experimental research, c) total heat generated by the battery - experiment.

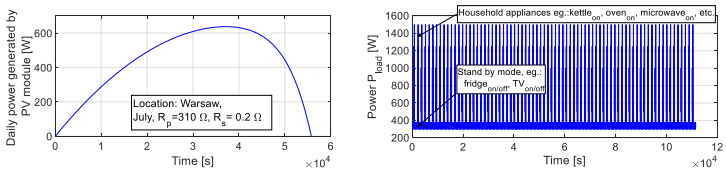

(a) (b)

Figure 6. a) Daily power generated by PV module, b) daily energy consumption – external load cycle to simulation model.

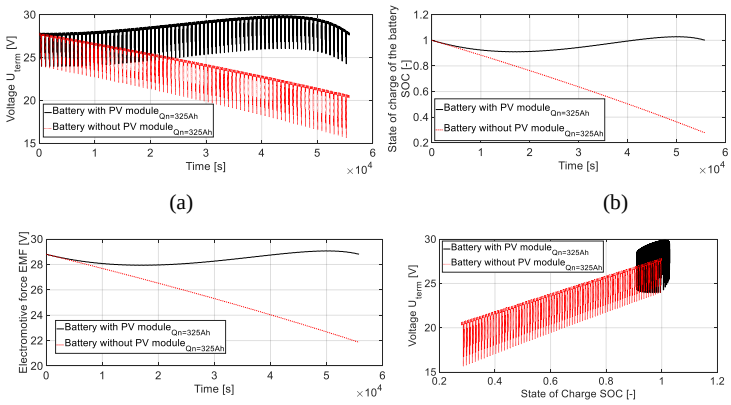

(a) (b)

(c) (d)

Figure 7. a) Voltage at the terminals of battery, b) State of Charge, c) Electromotive Force, d) Voltage at the terminals of battery as SOC function from the model with and without of PV module in specific daily cycle.

Figure 7 presents the curves of: voltage at the terminals (Fig. 7a), State of charge (Fig. 7b), Electromotive Force (Fig. 7c), voltage at the terminals of battery as SOC function (Fig 7d) from the model with and without of PV module in specific daily cycle. It was assumed that the cell state of charge would amount to *SOC*=1 (Fig.7b) during the next iteration (the cell fully charged) with PV module case. Figure 7d presents closed loop diagram ofU_{term}(SOC) with PV module. The closed loop diagram is very similar to the ellipse for sinusoidal functions - such behavior is very popular in rotary machines.

5. Conclusions

In this article, selected properties of 3 diode PV module with losses connected $LiFePO_4$ battery in specific daily load cycle for typical household has been discussed. Based on experimental research and simulation model the total heat generated by the battery has been calculated.

In presented work, there was analyzed and discussed the influence of chosen parameters of the PV module (eg.: irradiance, temperature, series resistance R_s, shunt resistance R_p) on generated power.

The relative error between experimental research and simulation model for a single LiFePO4 cell is smaller than 2% (the error is acceptable for practical use this method). Presented results have also practical dimension - knowing the battery type, the work of such a battery can be simulated before the actual purchase the PV module. From such analyses, research and simulations, the degree of the most economical management of the limited-power energy source, can be estimated.

References

[1] Kularatna N., Energy storage devices - a general overview. Energy Storage Devices for Electronic Systems, Elsevier, pp.1-28, 2015.

[2] Chmielewski A., Lubikowski K., Radkowski S., Energy storage technologies: Review, Zeszyty Naukowe Instytutu Pojazdów - Proceedings of the Institute of Vehicles Vol. 102, pp. 13-21, 2015.

[3] Luo X., Wang J., Dooner M., Clarke J., Overview of current development in electrical energy storage technologies and the application potential in power system operation. Applied Energy, Vol. 137, pp. 511-536, 2015.

[4] Chmielewski A., Mączak J., Szulim P. Experimental research and simulation model of electrochemical energy stores, Automation 2017, 15-17 march Warsaw, Advances in Intelligent Systems and Computing, Vol. 550, pp. 236-246, 2017.

[5] Szumanowski A., Chang Y., Piórkowski P., Method of Battery Adjustment for Hybrid Drive by modeling and simulation, IEEE, pp. 681-687, 2005.

[6] Chmielewski A., Mączak J., Szulim P. Experimental research of electrochemical energy storage, Automation 2017, 15-17 march Warsaw, Advances in Intelligent Systems and Computing, Vol. 550, pp. 227-235, 2017.

[7] Szumanowski A., Piorkowski P., Chang Y., Batteries and ultracapacitors set in hybrid propulsion system,Power Engineering, Energy and Electrical Drives, 2007. POWERENG 2007, IEEE, pp. 122-127, 2007.

[8] Chmielewski A., Lubikowski K., Radkowski S. Simulation of energy storage work and analysis of cooperation between micro combined heat and power (μchp) systems and energy storage. RynekEnergiiNr 2(117) - pp. 126-133, 2015.

[9] Szumanowski A., Chang Y., Battery Management System Based on Battery Nonlinear Dynamics Modeling," IEEE Transactions on Vehicular Technology, Vol. 57, No. 3, pp. 1425-1432, May 2008.

[10] Chmielewski A., Gontarz S., Gumiński R., Mączak J., Szulim P. Badania elektrochemicznych magazynów energii (Research on electrochemicalenergy stores), Przegląd Elektrotechniczny, No. 10, pp. 231-234, 2016.

[11] Czerwiński A., Akumulatory, baterie, ogniwa. WKŁ, 2012.

[12] Chmielewski A., Radkowski S., Modelowanie procesu ładowania akumulatora elektrochemicznego pracującego w układzie kogeneracyjnym. ZeszytyNaukoweInstytutuPojazdów 2(98) pp. 83-89, 2014.

[13] Chmielewski A., Gontarz S., Szulim P., Modelowo-wsparte badania elektrochemicznych magazynów energii. Rynek Energii No. 5, Vol. 126, pp. 37-45, 2016.

[14] Chmielewski A., Możaryn J., Krzemiński M., Theoretical and Experimental Background for Artificial Neural Network Modeling of Alpha Type Stirling Engine, 22nd International Conference on Methods and Models in Automation & Robotics, Międzyzdroje, DOI: 10.1109/MMAR.2017.8046891, IEEE pp. 570-575, 2017.

[15] Chmielewski A., Gumiński R., Mączak J., Radkowski S., Szulim P., Aspects of balanced development of RES and distributed micro cogeneration use in Poland: case study of a μCHP with Stirling engine, Renewable & Sustainable Energy Reviews, Vol. 60, pp. 930-952, 2016.

[16] Chmielewski A., Szurgott P., Modelling and simulation of repeated charging/discharging cycles for selected Nickel-Cadmium batteries. Journal of Kones, 22 (1), pp. 55-62, 2015.
[17] Micallef A., Apap M., Spiteri-Staines C., Guerrero J.M., Mitigation of harmonics in grid-connected and islanded microgrids via virtual admittances and impedances, IEEE Tran. on Smart Grid, Vol.8, Iss. 2, pp. 651-661, 2015.
[18] Chia Y. Y. et al., A load predictive energymanagement system for supercapacitor-battery hybrid energy storage system in solar application using the Support Vector Machine, Appl.Energ., Vol. 137, pp. 588–602, 2015.
[19] Kalogirou S.A., Mellit A., Artificial intelligence techniques for photovoltaic applications: A review, Progress in Energy and Combustion Science, Vol. 34, pp. 574-632, 2008.
[20] Koohi-Kamali S., Rahim N.A., Mokhlis H., Tyagi V.V., Photovoltaic electricity generator dynamic modeling methods for smart grid applications: A review, Renew. and Sust. Energ. Rev., Vol. 57, pp. 131–172, 2016.
[21] Illanes R., Francisco A. D., Núñez F., Blas M. D., García A., Torres J. L., Dynamic simulation and modelling of stand-alone PV systems by using state equations and numerical integration methods, Appl. Energ. Vol. 135 pp. 440–449, 2014.
[22] Chmielewski A., Szulim P., Gregorczyk M., Gumiński R., Mydłowski T., Mączak J., Model of an electric vehicle powered by a PV cell – a case study, 22nd International Conference on Methods and Models in Automation & Robotics, Międzyzdroje, DOI: 10.1109/MMAR.2017.8046968, IEEE, pp. 1009-1014, 2017.
[23] Szumanowski A., Chang Y., Piórkowski P., Analysis of different control strategies and operating modes of compact hybrid planetary transmission drive, IEEE Vehicle Power and Propulsion Conference, Chicago, pp. 673-680, 2005.
[24] Lai Y. et. al., Insight into heat generation of lithium ion batteries based on the electrochemical-thermal model at high discharge rates. International Journal of Hydrogen Energy, Vol. 40, pp. 13039-13049, 2015.
[25] Li J., Cheng Y., Jia M., Tang Y., Lin Y., Zhian Z., Y. Liu., An electrochemical-thermal model based on dynamic responses for lithium iron phosphate battery. Journal of Power Sources, Vol. 255, 130-143, 2014.
[26] Saito Y., Shikano M., Kobayashi H.. Heat generation behavior during charging and discharging of lithium-ion batteries after long-time storage. Journal of Power Sources, Vol. 244, pp. 294-299, 2013.
[27] Li J., Wang L., Lyu C., Wang H., Liu X., New method for parameter estimation of an electrochemical-thermal coupling model for LiCoO2 battery, Journal of Power Sources, Vol. 307, pp. 220-230, 2016.
[28] Gu W.B., Wang C.Y., Thermal-electrochemical modeling of battery systems, Journal of Electrochemical Society, Vol. 147, pp. 2910-2922, 2000.
[29] Chmielewski A., Bogdziński K., Szulim P., Mydłowski T., Test stand for operational research of Energy storage: description and preliminary research, Zeszyty Naukowe Instytutu Pojazdów, 2017 [In print].
[30] Dileep. G, Singh S.N., Selection of non-isolated DC-DC converters for solar photovoltaic system, Renewable and Sustainable Energy Reviews, Vol. 76, 1230-1247, 2017.

Adrian Chmielewski, M.Sc. (Ph.D. Candidate):Warsaw University of Technology, Faculty of Automotive and Construction Machinery Engineering, Institute of Vehicles, Narbutta 84, 02–524 Warsaw, Poland (*a.chmielewski@mechatronika.net.pl*). The author gave a presentation of this paper during one of the conference sessions.

Robert Gumiński, Ph.D. (Assistant Professor): Warsaw University of Technology, Faculty of Automotive and Construction Machinery Engineering, Institute of Vehicles, Narbutta 84, 02–524 Warsaw, Poland (*rgumin@simr.pw.edu.pl*).

Krzysztof Bogdziński, M.Sc. (Ph.D. student): Warsaw University of Technology, Faculty of Automotive and Construction Machinery Engineering, Institute of Vehicles, Narbutta 84, 02–524 Warsaw, Poland (*k.bogdzinski@mechatronika.net.pl*).

Przemysław Szulim, Ph.D. (Assistant Professor): Warsaw University of Technology, Faculty of Automotive and Construction Machinery Engineering, Institute of Vehicles, Narbutta 84, 02–524 Warsaw, Poland (*p.szulim@mechatronika.net.pl*).

Jędrzej Mączak, Ph.D. D.Sc. (Associate professor): Warsaw University of Technology, Faculty of Automotive and Construction Machinery Engineering, Institute of Vehicles, Narbutta 84, 02–524 Warsaw, Poland (*jma@mechatronika.net.pl*).

Jakub Możaryn, Ph.D. (Assistant Professor): Warsaw University of Technology, Faculty of Mechatronics, Institute of Automatic Control and Robotics, Sw. A. Boboli 8, 02-525 Warsaw, POLAND (*j.mozaryn@mchtr.pw.edu.pl*).

Piotr Piórkowski, Ph.D. (Assistant Professor): Warsaw University of Technology, Faculty of Automotive and Construction Machinery Engineering, Institute of Construction Machinery Engineering, Narbutta 84, 02–524 Warsaw, POLAND (*piotr.piorkowski@simr.pw.edu.pl*).

Wheel-surface model parameters estimation for all-terrain vehicle - experimental basis

Tomasz Czapla, Marcin Fice, Roman Niestrój

Abstract: The aim of the paper is to present the experimental basis for model parameters estimation for all-terrain vehicle dynamics simulation. Traction and side forces assessment methods and tire with the ground models for on-road vehicles are widely described. In case of off-road vehicles, there is variety of terrain characteristics and tire-surface interaction forms, including soil or sand deformation that are not adequately described by theoretical models. Experiment methodology includes test in various ground condition and different driving direction. Test data were acquired for sand, for various tire tilt angle. Traction and side forces were acquired and used to identify black-box model parameters of the wheel-ground interaction.

1. Introduction

Although the on-road vehicles traction characteristics and wheel-road interaction models and description are well described and various models are introduced for dynamics calculation, there is a need of the off-road vehicles behavior based on wheel-surface definition. The off-road vehicles have significantly higher fuel consumption due to higher than in railway and on-road cases traction resistance. Furthermore, rolling resistance and grip strongly depend on terrain characteristics. Another parameter that increase the rolling resistance is lower than in case of on-road vehicles tire pressure. For off-road conditions, surface cannot be considered as a rigid body and, in consequence, the interaction model should contain the tool for ground plastic deformation assessment.

Modern drive systems, especially hybrid electric and electric drives performance and control system optimization should be provided with the accurate data including traction effort energy consumption. Since on-road vehicles driving cycles and road characteristics are known and well-described, load cycle of the power station can be estimated. In case of off-road vehicles, maximum traction effort has to be taken into account, what could lead to overestimate the power consumption and lead to overpower the power station and energy management system for Ackerman steering systems. In case of skid-steered vehicles the power consumption strongly depend on number of maneuvers during its operation, so that it is vital to assess the turning characteristics and perform simulation for various terrain conditions and maneuver intensity. For straight path, the power consumption is similar to classical solutions, for turns the power consumption rises.

The state of art analysis shows, that most authors focus on the wheel soil interaction during the ride on a straight path that limits measurements and simulations to longitudinal wheel and vehicle dynamics. In case of skid-steered vehicles, transverse during the turn has to be calculated.

2. State-of-art analysis

The wheel – rigid surface interaction for road conditions include tire deformation under vertical load in a steady-state condition, deformation under the longitudinal and lateral (transverse) force why applying the torque and cornering condition respectively. Stress pattern in fingerprint changes according to load conditions. Wheel deformation under the side-load significantly increases the rolling resistance [8] although in most cases is neglected in analytical wheel – surface interaction models and numerical calculation methods. For more adequate calculations several methods are used: empirical models, spring-damper wheel models and numerical calculation methods [7].

The early stage of tire-ground interaction development was based on experimental tests including cone testing for soil shear, tension and extension strength [3,4]. Modern Cone Penetrometer Testing methods use electromechanical sensors to achieve ground characteristic along the measurement line. For vehicle performance, vital information can be provided with test performed on the ground surface. Surface testing technology was introduced by Bekker [1]. Methodology was based on two tests: plate sinkage test and shear test. A number of plates with certain dimensions were used to measure the sinkage and shear rings or plates simulated the shear. Test results achieved with various methods are used to calculate relationship between pressure and ground deformation indicated by sinkage.

$$\sigma = \left(\frac{k_c}{B} + k_\varphi\right) \cdot z^n, \tag{1}$$

$$\tau = (k_{cohesion} + \sigma \cdot \sin\varphi) \cdot \left(1 - e^{j/K}\right), \tag{2}$$

where:

σ – normal pressure,

k_c, k_ϕ, n – soil properties parameters,

z – soil sinkage,

B – tire width,

ϕ – free angle of shearing soil resistance,

τ – shear stress,

$k_{cohesion}$ – soil cohesion,

j – shear displacement.

Bekker [2] model based was the first significant approach to stress calculation in the tire – soil contact area and beneath. Bekker equation is used to calculate the normal pressure as a function of the

sinkage (Eq. 1), modified Coulomb equation (Eq. 2) allows to calculate the shear stress with taking into account shear displacement, cohesion and soil shear deformation parameters [6].

The Bekker model and other approaches based on rigid wheel neglect the tire deformation influence on wheel – surface dynamics. Models developed later by Schmid [5] allow to take into account the tire deformation. Further research methods and interaction models in most of cases are based on Finite Element Analysis.

3. Methodology description

The method, described in the paper is a part of the project focused on providing an accurate model of traction effort for skid-steered vehicle case. Longitudinal and lateral forces were measured during laboratory and field testing. Analytical model and FE Model are formed with using preliminary ground and tire properties. Model validation is performed then to achieve the most accurate simulation results. Since the field test cannot provide all possible terrain conditions, FE model is used to predict the final black-box model parameters (Fig. 1).

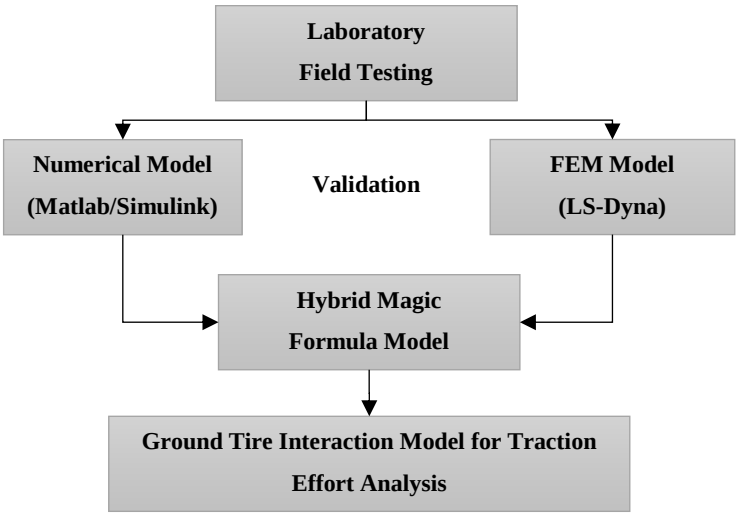

Figure 1. Ground Tire Interaction Model .

Based on experiment results, skid-steered vehicle rolling resistance can be calculated. In case of skid-steered vehicle, different velocities on both sides of machines technique is used to achieve turn. The greatest advantage over classical solutions is higher maneuverability and simplified design. Additional feature for advanced transmission systems is zero-turn availability.

On the Fig. 2 the basic and simplified geometrical model of the skid-steering vehicle is shown. Simplified because this is a symmetrical skid-steering model, wherein the mass center is in real

geometrical center of vehicle and is running on ideal surface. In this case it can be neglected, because presented research is aimed at determining the resistance of the wheel-surface.

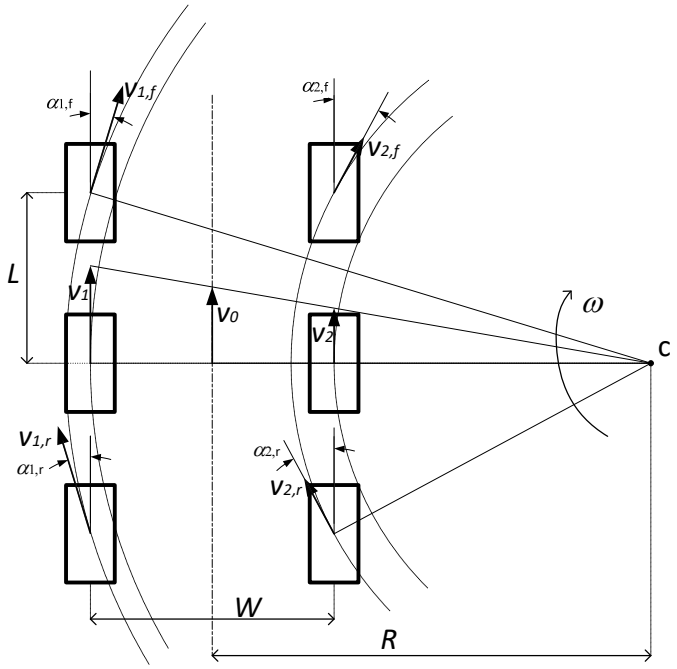

Figure 2. Simplified geometric skid-steering model, where: R – turning radius of the center of vehicle, W – width between the wheels center, c – turn center, ω – angular velocity, L – wheelbase, vn,x - direction and movement speed of wheels, αn,x – slip angle of wheels.

$$|\alpha_{1,f}| = |\alpha_{1,r}| = |\alpha_1| = \operatorname{atan}\frac{L}{R+\frac{1}{2}W}, \tag{3}$$

$$|\alpha_{2,f}| = |\alpha_{2,r}| = |\alpha_2| = \operatorname{atan}\frac{L}{R-\frac{1}{2}W}. \tag{4}$$

Table. 1. Values of slip angle in depending on a turn radius.

R	$\lvert\alpha_1\rvert$, degrees	$\lvert\alpha_2\rvert$, degrees
0	45	45
W/2	26.5	90
W	18.4	45
2W	11.3	18.4
3W	8.1	11.3

The wheel during the tests was propelled by pulling it with external excitation system. The wheel had no drive for presented tests. Propulsion system is based on a rail with a cart propelled by an electric motor. Rail is responsible for keeping the direction of motion of the cart and allows the system to rotate in the rail axis. A frame containing the wheel suspension is placed on a moving cart. Wheel is attached to the frame via rotating fork, that allows to change the attack angle. The fork has two degrees of freedom constrained by rods equipped with force transducers, thus the lateral and longitudinal forces are isolated and measured (Fig. 3).

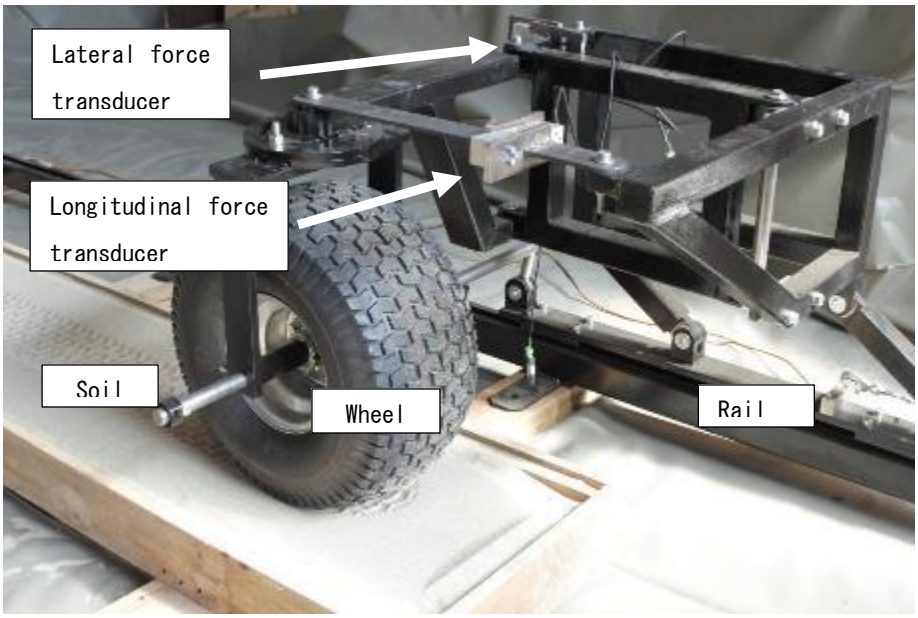

Figure 3. Experimental stand.

Experimental stand was intended to perform various wheel behavior tests in specific surface conditions. Laboratory stand allows to change a wide range of parameters including: wheel angle of attack (difference between wheel vertical symmetry plane and direction of motion), wheel pressure, wheel vertical load, ground structure. Unique design of the stand allows to isolate and measure longitudinal and lateral force in the coordinate system related to moving cart. The tests were carried out with using an 20x10.00-8" all-terrain wheel. On the Fig. 4 wheel geometry during the skid-steering maneuver and measured forces are shown.

Based on obtained results of forces produces an effect on the wheel - longitudinal and lateral to the movement direction, it is possible to calculate forces related to the geometry of the wheel. Flog and Flat forces are the projection of resultant force F on the coordinate system related to the wheel geometry. Mentioned above forces can be derived with using Park transform assuming that x-axis defines lateral forces in coordinate system attached to the frame.

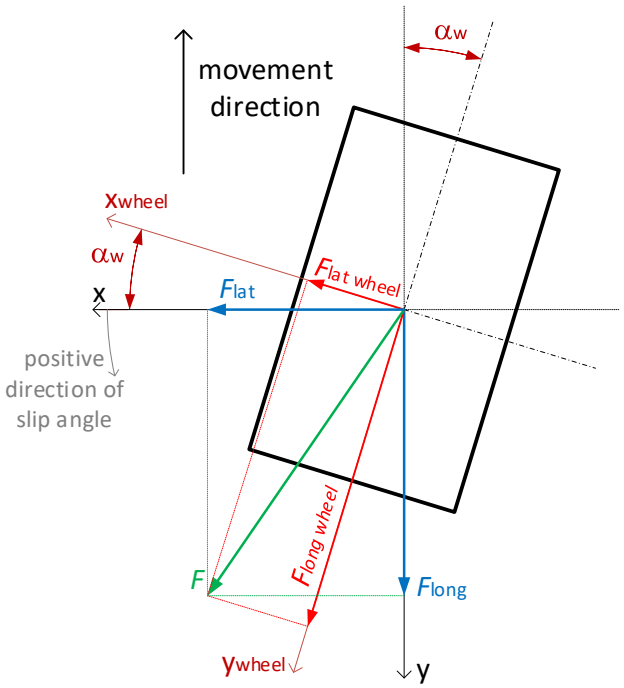

Figure 4. Geometrical model of the wheel, top view. x-y – coordinate axes relate to the movement direction, x_{wheel}-y_{wheel} – coordinate axes related to the wheel geometry, F_{long} – measured longitudinal force related to the movement direction, F_{lat} – measured lateral force related to the movement direction, F – the resultant force related to coordinate axes of movement direction, $F_{long\ wheel}$ – longitudinal component of the force related to geometrical wheel axes, Flat wheel – lateral component of the force related to geometrical wheel axes, α_w – slip angle (between movement direction and wheel coordinate system).

Related to the figure 4 total longitudinal and transverse forces related to geometrical axes of the wheel can be expressed as below:

$$F_{\text{long wheel}} = F_{\text{long}} \cdot \cos(-\alpha_{\text{w}}) - F_{\text{lat}} \cdot \sin(-\alpha_{\text{w}}), \tag{5}$$

$$F_{\text{lat wheel}} = F_{\text{long}} \cdot \sin(-\alpha_{\text{w}}) + F_{\text{lat}} \cdot \cos(-\alpha_{\text{w}}). \tag{6}$$

For the case shown in the Fig. 4 for chosen coordinate system Flat wheel has negative value. In case of maximum wheel turn angle, $\alpha_w = 90°$, xwheel axis is parallel to y axis and ywheel axis will be consequently parallel to x-axis, so:

$$F_{\text{long wheel}} = -F_{\text{long}}, \tag{7}$$

$$F_{\text{latwheel}} = F_{\text{lat}}. \tag{8}$$

Resultant longitudinal force Flong wheel, is responsible for traction torque generation. It can be assumed to be traction effort force. Each wheel generates the resistant force caused by slip necessary for turn performance in case of skid-steered vehicle.

4. Results analysis

Tests were carried out for 4 slip angles α_w = 0°, 30°, 60° and 90°. The pressure in the tire was 0,15 MPa, and wheel axis load was 80 kg. The wheel was propelled on the sand surface with the speed of 0,5 m/s. Results for steady-state conditions are shown in graphs and photos below.

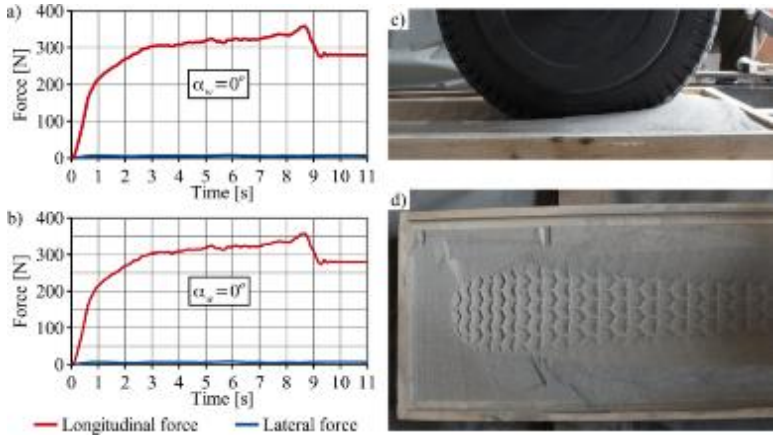

Figure 5. Waveforms of measured longitudinal and lateral forces related to movement direction (a) and calculated longitudinal and lateral forces related to the wheel geometry (b) for αw = 0°. The wheel on the experimental stand, after test (c) and tire track (d).

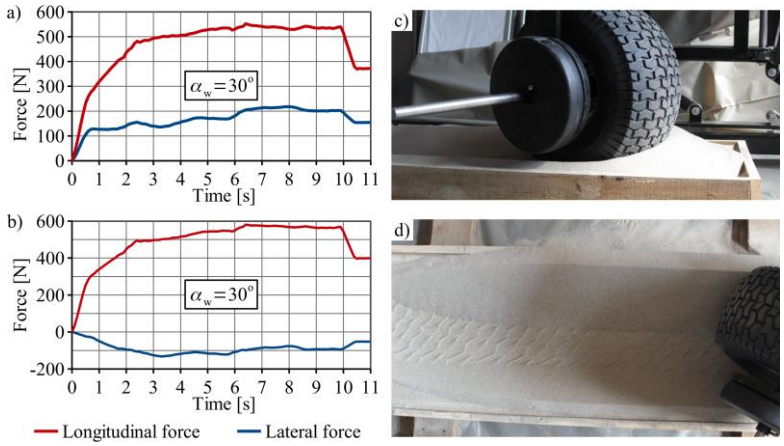

Figure 6. Waveforms of measured longitudinal and lateral forces related to movement direction (a) and calculated longitudinal and lateral forces related to the wheel geometry (b) for α_w = 30°. The wheel on the experimental stand, after test (c) and tire track (d).

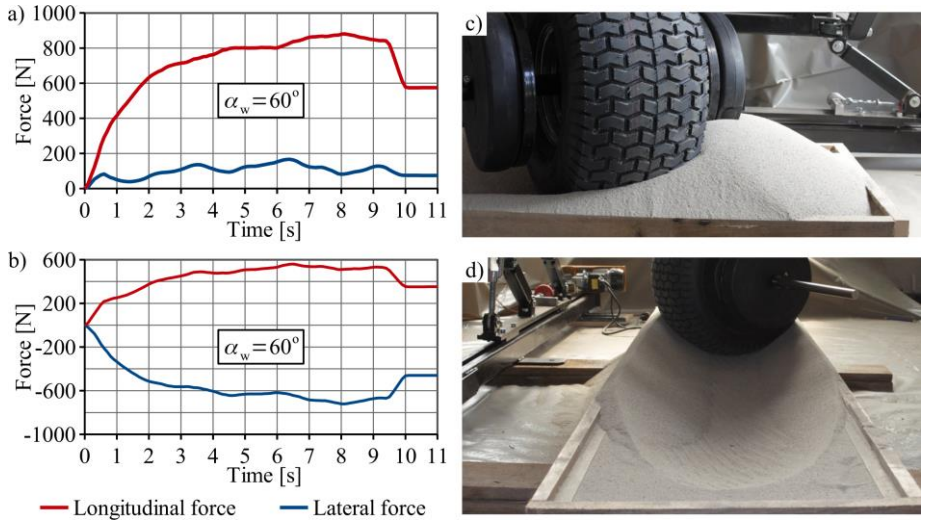

Figure 7. Waveforms of measured longitudinal and lateral forces related to movement direction (a) and calculated longitudinal and lateral forces related to the wheel geometry (b) for αw = 60°. The wheel on the experimental stand, after test (c) and tire track (d).

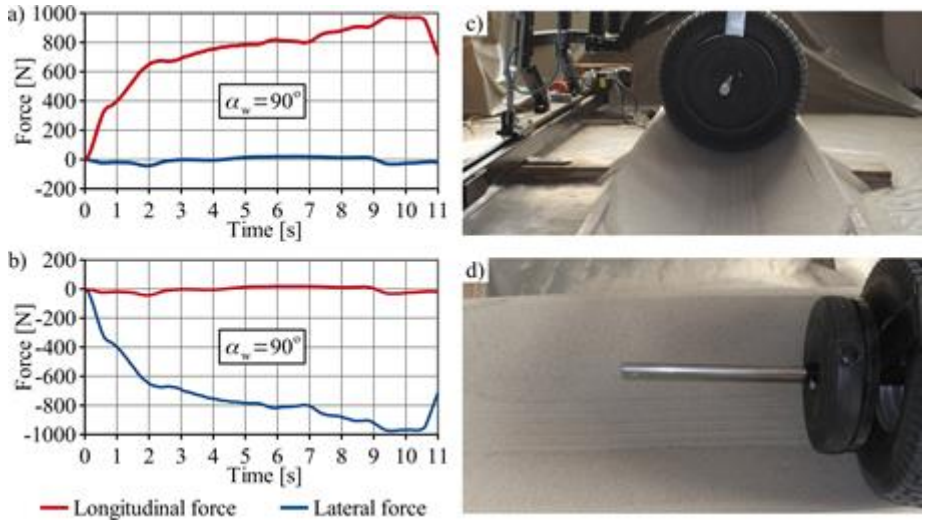

Figure 8. Waveforms of measured longitudinal and lateral forces related to movement direction (a) and calculated longitudinal and lateral forces related to the wheel geometry (b) for αw = 90°. The wheel on the experimental stand, after test (c) and tire track (d).

On the figures 5-8 there could be observed that forces values vary during the measurement period. The experiment starts when the wheel is placed on flat sand surface, not in the tire track. Before the wheel was reaching the edge of sand container, it generated the sand pile in the front that caused the

force increase (Fig. 9 and 10). Figures 9 and 10 show detailed view of test results for αw = 0° and wheel on tested surface for ground behavior pattern. For further analysis, averaged forces values were taken into account from the range from approximately 3 to 7 seconds.

Longitudinal force increased in the function of slip angle αw and for 60° and 90° was similar. For 60° angle the wheel turn decayed what could be observed on the photos showing the tire track. The wheel pattern track cannot be indicated. Lateral force for angles 0° i 90° was equal approx. 0 N what can be explained by the symmetry of kinematical structure.

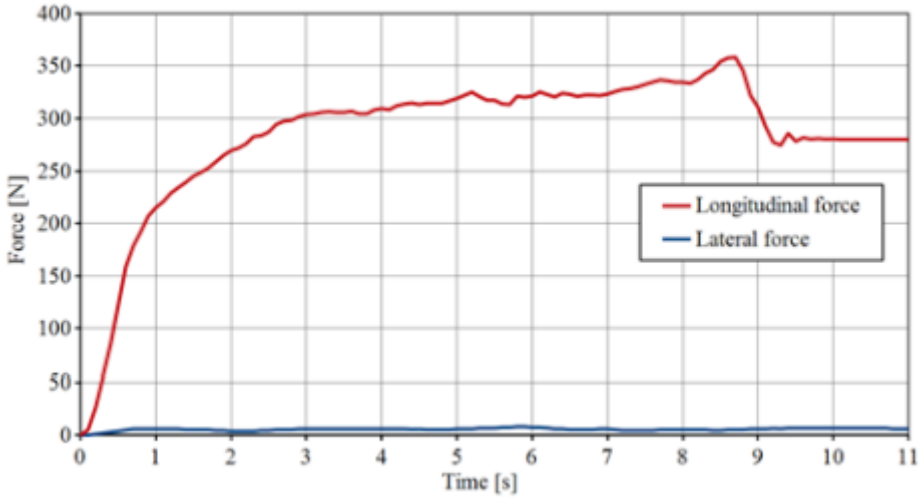

Figure 9. Waveforms of measured longitudinal and lateral forces for αw = 00.

Figure 10. The wheel on the experimental stand, after test with $\alpha_w = 0°$.

5. Wheel-surface model formulation

Proposed approach leads to empirical traction effort calculation model development for skid-steered vehicle. The effect of the model application is accurate calculation of yaw moment value for skid-steered wheeled vehicle in various terrain conditions. The first step was resistance forces calculation function that allows to obtain torque for each wheel.

- Input parameters for the model are:
- Slip angle,
- Normal force (wheel vertical load),
- Wheel pressure,
- Ground pattern.

Output parameters of the model:

- Longitudinal force – contribution to the traction resistance of the vehicle,
- Lateral force – contribution to the traction resistance of the vehicle,
- Longitudinal wheel force – generates traction resistance for each wheel,
- Lateral wheel force – generates bending moment for the wheel and loads for the suspension system.

Magic formula model is based on experimentally derived load patterns for loads acting on each vehicle wheel. Figure 11 shows an averaged test results in the function of slip angle for performed test conditions.

Resultant traction resistance could be derived as it is shown in Eq. 9

$$F_t = g_m \cdot p_t \cdot f_t(\alpha_w), \tag{9}$$

where:
f_t = traction resistance coefficient,
p_t – tire pressure coefficient,
g_m – wheel load.

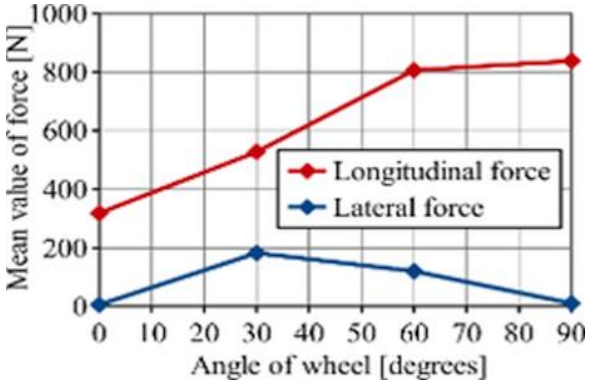

Figure 11. Values of longitudinal and lateral forces depending of the slip (attack) angle.

In order to generalize results, two coefficients are introduced: longitudinal and lateral resistance coefficient (Eq.10,11).

$$f_{long} = \frac{F_{long}}{G} \text{ - longitudinal wheel resistance coefficient,} \quad (10)$$

$$f_{lat} = \frac{F_{lat}}{G} \text{ – lateral wheel resistance coefficient,} \quad (11)$$

where:
G – vehicle weight (m·g)

Fig. 12 shows the range of mentioned above coefficients in the function of slip angle for dry sand case. In addition, approximation of coefficient values for all wheel slip range with using 3rd rank polynomial.

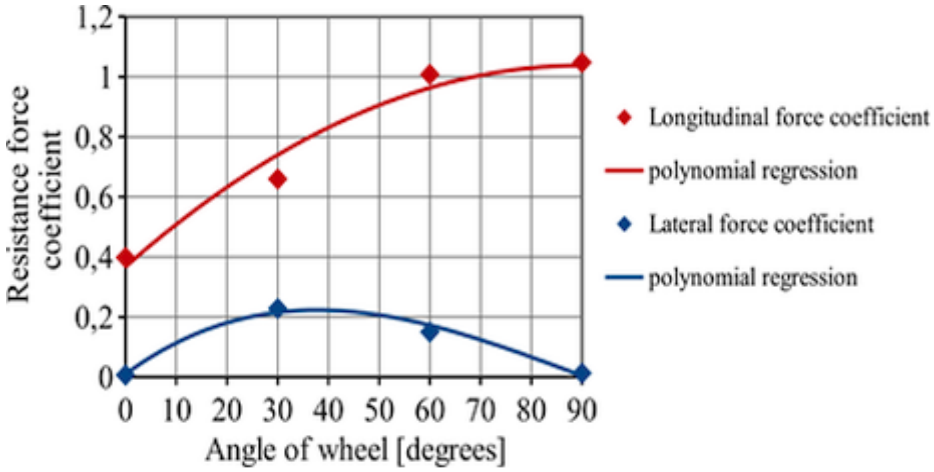

Figure 12. Values of longitudinal and lateral force coefficients depending of the slip (attack) angle.

6. Conclusions

The methodology presented in the article is based on test facility designed by authors and has unique abilities for direct traction loads measurement for various wheel-surface configurations.

Since the tests were performed with using preliminary setup and were intended to verify the methodology correctness, the track was relatively short and narrow. Laboratory facility development plans include the test track modification. Increasing track length will allow to achieve longer periods of force stable values. Test track modification will also allow to avoid possible collisions between the tire and the track walls.

Presented tests were performed for technical conditions assessment for laboratory facility development and future work will be focused on methodology mastering, evaluation of complementary,

FEM model and measurement automation and widening the parameters range (speed measurement, tire track investigation methods).

Presented methodology is not intended to develop the wheel-surface interaction models, so that considerations of mentioned phenomena will be limited to the range that is necessary for turning moment of skid-steered vehicle assessment.

Since, the wheel was propelled by external device (dragging rod), the difference between dragged and driven wheel has to be investigated. Laboratory equipment will be developed in order to enable driven wheel tests performance for various terrain conditions.

References

[1] Bekker, M. G.: Off-the-road locomotion. Ann Arbor, Michigan: The University of Michigan Press, 1960

[2] Bekker, M. G.: Theory of land locomotion. Ann Arbor, Michigan: The University of Michigan Press, 1956

[3] Collins, J. G.: Forecasting trafficability of soil. Technical Memo 3-331, Vicksburg, Miss: USA Corps of Engineers Waterways Experiment Station, 1971

[4] Herrick E. J., Jones T. L.: A dynamic cone penetrometer for measuring soil penetration resistance Article July 2002

[5] I.C. Schmid.: Interaction of vehicle and terrain results for 10 years research at ikk. Journal of Terramechanics, 32(1):3–26, 1995

[6] Janamoto and B. Hanamoto.: An analysis of the drawbar pull vs slip relationship for track laying vehicles. Technical report, U.S. Army Ordnance Tank-Automotive Command, 1961

[7] Sharma A. K., Pandey K. P.: A review on area measurement of pneumatic tyre on rigid and deformable surfaces. Journal of Terramechanics, Vol. 33. No. 5, pp. 253-264, Elsevier Science Ltd. 1997

[8] Wong, J. Y,: Theory of Ground Vehicles , John Wiley & Sons, New York. , 2001

1) Tomasz Czapla, Ph.D.: Silesian University of Technology, Akademicka 2A, 44-100, Gliwice, POLAND (Tomasz.Czapla@polsl.pl), the author presented this contribution at the conference.

2) Marcin Fice, Ph.D.: Silesian University of Technology, Akademicka 2A, 44-100, Gliwice, POLAND (Marcin.Fice@polsl.pl).

3) Roman Niestrój, Ph.D.: Silesian University of Technology, Akademicka 2A, 44-100, Gliwice, POLAND (Roman.Niestroj@polsl.pl).

Inverse dynamics simulation of the snatch in weightlifting

Adam Czaplicki, Krzysztof Dziewiecki, Zenon Mazur, Wojciech Blajer

Abstract: The purpose of this paper is to present the results of an inverse dynamics analysis of the snatch modelled as a sagittal plane movement. A planar model of a weightlifter composed of 16 rigid segments (the lower trunk, thighs, lower legs, and feet) connected by 15 hinge joints was used in the computations. The equations of motion of the model were obtained using a projective technique. Kinematic data were recorded with a Vicon system with a sampling frequency of 200 Hz. The ground reaction forces were measured separately for the left and right limb on two force platforms. The inverse dynamics formulation then made it possible to assess the internal loads (the muscle forces and joint reactions), limited here to the lower limbs. The obtained results reveal that the snatch, a motor activity which tends to be geometrically symmetrical in the sagittal plane, is not necessarily characterised by symmetry of internal loads. The relatively high differences in the reactions in the joints and muscle forces in the left and right side of the body were identified. We are convinced that if coaches were to have information concerning the asymmetry of internal loads, this could have implications for adjusting the training, assessing whether or not the motor activity has been performed correctly, and helping the lifter eliminate habits that may cause injury.

1. Introduction

The snatch is one of the two lifts performed in Olympic weightlifting. It consists in lifting the barbell from the floor to above the head in one continuous motion, performing a squat, locking the barbell overhead, and adopting an erect position. Despite the fact that the lift lasts a relatively short time, the movement is complex, since as many as six distinct phases have been identified [1-3], including one in which the feet lose contact with the ground. Another important feature of the snatch lift is that the upper limbs and the barbell form a closed biokinematic chain. It restricts the use of standard biomechanical models provided by motion capture system manufacturers (e.g. Vicon Plug-in-Gait model). Taking into account these aspects, it may be stated that the dynamics of the snatch lift has not been fully explained to date. The aim of this paper is to demonstrate that the snatch, a motor activity which tends to be geometrically symmetrical in the sagittal plane, is not necessarily characterised by symmetry of internal loads.

2. Material and methods

We recorded 30 lifts done by 5 athletes who used barbells with different loads (Tab. 1). Kinematic data

were gathered with a Vicon system (Oxford Metrics Ltd., UK) with a sampling frequency of 200 Hz. The ground reaction forces were measured separately for the left and right limb on two AMTI (Advanced Medical Technology Inc., USA) force platforms.

Prior to the research, the subjects were informed about the purpose of the study and gave their written consent. The research program was approved by the Senate Committee of Scientific Research Ethics at the Józef Piłsudski University of Physical Education in Warsaw.

Table 1. Body mass of the subjects and barbell weight changes during the trials.

Trial	**Subject 1** (103 kg)	**Subject 2** (76 kg)	**Subject 3** (65 kg)	**Subject 4** (77 kg)	**Subject 5** (69 kg)
	Barbell weight kg				
1	90	80	80	80	60
2	90	90	80	80	60
3	90	90	85	80	70
4	70	90	80	80	70
5	80	90	80	80	70
6	85	90	80	80	70

A planar model of a weightlifter composed of 16 rigid segments (the lower trunk, thighs, lower legs, and feet) connected by 15 hinge joints was used in the computations. A similar model and formulation for an inverse dynamics simulation has been described in detail in our previous publications [4, 5]. The equations of motion of the model were obtained using a projective technique [6, 7], which allowed for effective solution of the inverse dynamics problem and assessment of the joint reactions and muscle forces, limited here to the lower limbs (Fig. 1).

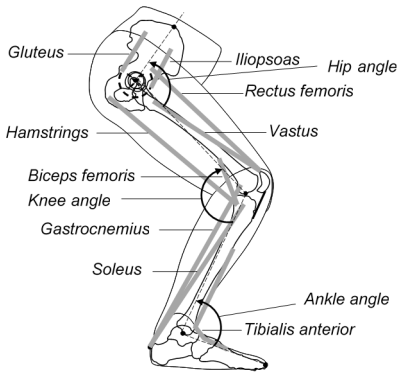

Figure 1. Muscle model of the lower limbs and joint angles definition.

3. Results

Figure 2 shows time characteristics of the joint angles computed for three selected trials. The black solid lines (right lower limbs) and the grey ones (left lower limbs) have similar shapes. This indicates the symmetry of movement between the lower extremities during the snatch. The closest matching of the curves has been identified for the first subject (Fig. 2, left).

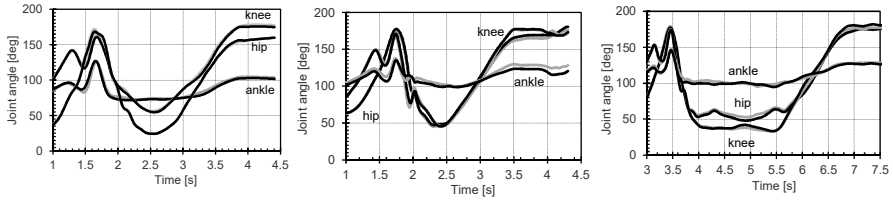

Figure 2. Time characteristics of the joint angles (subject 1, trial 3 (left); subject 4, trial 5 (middle); subject 2, trial 5 (right)).

The horizontal ground reaction forces of the subjects are depicted in Figure 3. The curves have been smoothed by 4th order low-pass Butterworth filter with cut-off frequency of 10 Hz. The opposite sign and similar magnitudes of the reaction forces acting on the feet are clearly visible. This means that the reactions form a force couple pointing indirectly to the rotation of the barbell with respect to the vertical axis.

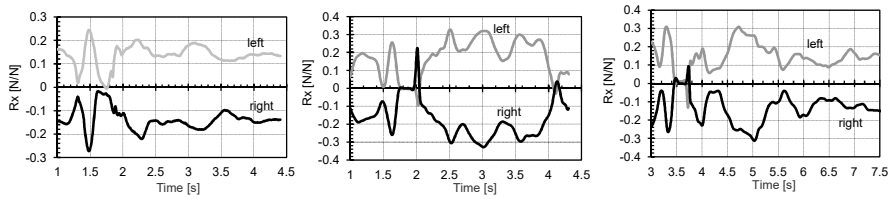

Figure 3. Time curves of the horizontal ground reaction force of the subjects.

Figure 4 shows the smoothed time courses of the vertical ground reaction force during the snatch. One can recognize the low variability of the courses within the subjects (except of the 3rd case) and large variability between them.

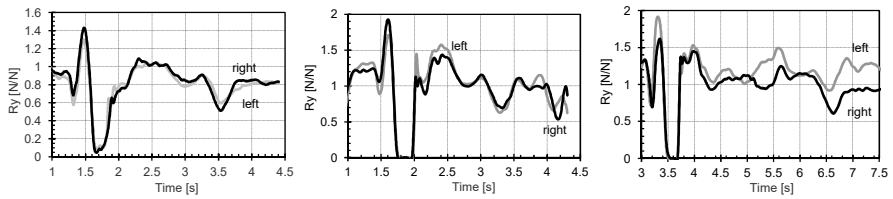

Figure 4. Time characteristics of the vertical ground reaction force of the subjects.

The tension curves of glutei muscles for the first subject are presented in Figure 5. We have deliberately chosen that athlete for the analysis because his time characteristics of the joint angles are very similar for both lower limbs (Fig. 2, left). There is a remarkable difference in the tension level between the right and left gluteus during the snatch. The largest percentage differences at the level of 88% and 40% can be observed during the second pull phase (at about 1.5 s) and in the middle of the catch phase (at about 2.5 s), respectively.

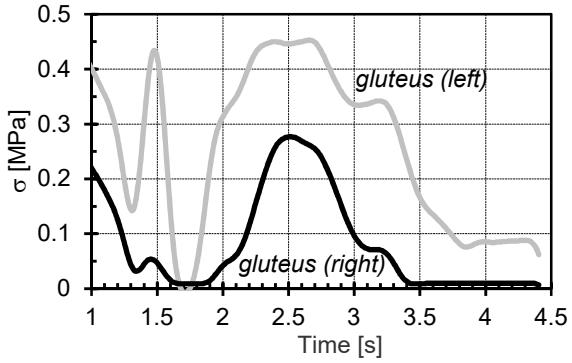

Figure 5. Tension curves of glutei muscles during the snatch.

The tension curves of vasti muscles for the selected subject are presented in Figure 6. A notable difference has also been found in the tension level between both muscles during the snatch. However, in contrast to glutei muscles, the right muscle is much more activated than the left one. The largest percentage difference at the level of 88% can be observed in the middle of the catch phase (at about 2.3 s).

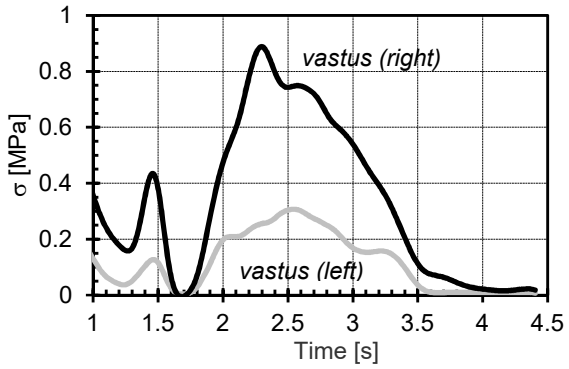

Figure 6. Tension curves of vasti muscles during the snatch.

Figure 7 shows the tension curves of the left and right soleus. Contrary to the previously presented characteristics, a similarity between the tension curves may be observed during the snatch. Two local

maxima at the beginning of the second pull and in the middle of the catch phase are again discernible in the curves. The largest percentage differences at the level of 76% and 48% appear during the transition phase (at about 1.3 s) and at the beginning of the catch phase (at about 2 s), respectively. As for the left gluteus, one can notice the highest tension in the left soleus as well.

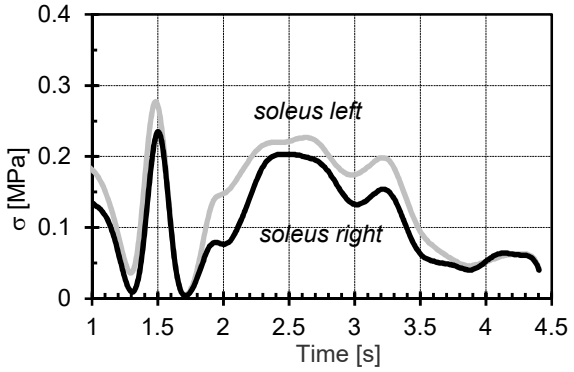

Figure 7. Tension curves of soleus muscles during the snatch.

The succeeding Figures 8-10 show the time characteristics of internal reactions in the joints of the lower extremities. Thick black lines mark the reactions in the joints of the right lower limb whereas grey lines are attributed to the left side of the body. The characteristics has been normalised with respect to the body weight of the subject. One can observe significant differences between the corresponding pairs of these reactions in all the joints. The highest level of the vertical reaction has been identified in the right knee joint during the catch phase, and in the left ankle joint at the beginning of the second pull. The largest horizontal reactions have been obtained for the left hip joint, right knee and left ankle joint during the catch phase.

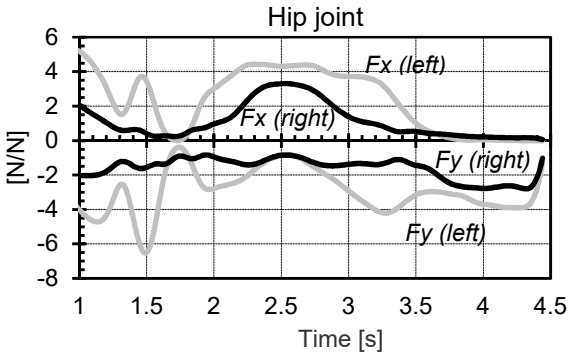

Figure 8. Normalised time characteristics of internal reactions in the hip joint.

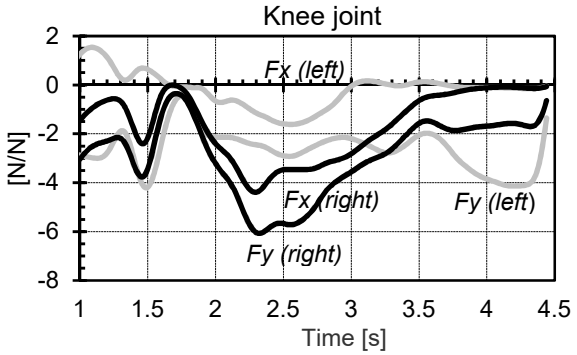

Figure 9. Normalised time characteristics of internal reactions in the knee joint.

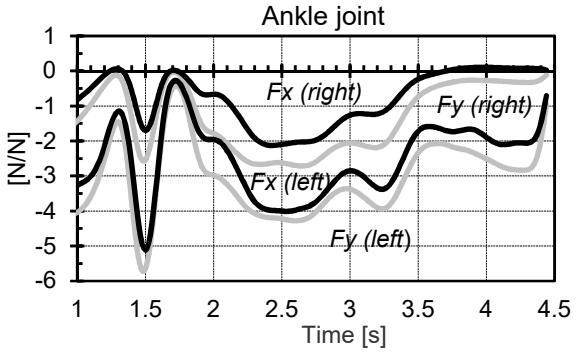

Figure 10. Normalised time characteristics of internal reactions in the ankle joint.

4. Discussion

The inverse dynamic problem for the snatch in weightlifting has been solved in this work in order to answer the question whether the symmetry of the movement of a weightlifter matches the symmetry of the internal loads in the joints of the lower limbs.

The necessary kinematic and kinetic data were first gathered for solving the problem. The obtained time characteristics of the joint angles for both lower extremities turned out to be similar to each other. The shapes of these characteristics are also in accordance to those reported by others [8, 9]. The analysis of the kinetic data, however, revealed that the horizontal ground reaction forces acting on the feet have the opposite sign and similar magnitudes. They do not interlace each other and keep the same sign during a trial. The horizontal ground reactions form thus a force couple hampering the rotation of the barbell with respect to the vertical axis. This unexpected feature of the snatch has been determined for all the trials and was independent of the athlete's and barbell weight.

The results of the inverse dynamic solution have been presented in the second part of the study. They were computed for the subject with the highest symmetry of movement of the lower limbs. The obtained results confirmed asymmetrical distribution of internal loads in the joints during the snatch. This can be noticed by clear differences between peak tension values of both glutei and vasti muscles as well as by the opposite sign of tension difference between a corresponding pair of muscles: gluteus right – gluteus left and vastus right – vastus left. The asymmetry of internal loads has also been found in the time courses of the internal reactions in the joints.

We assume that the rotation of the barbell is due to unequal involvement of lower and upper extremities of the subject during the snatch. It is possible that the dominant extremities exerted more pressure on the barbell when executing this lift. The rotation may also be caused by the preserved movements originating from the clean and jerk technique, as during the jerk the lifter raises the barbell above the head after splitting the legs into a lunge position. Finally, it should be emphasized that such rotations are small because of the large moment of inertia of the barbell with respect to the vertical axis and can be hardly observed by coaches.

5. Conclusions

Although geometrical symmetry was achieved, asymmetry was found in the internal loads acting on the musculoskeletal system in all of the lifts. The relatively high differences in the reactions in the joints and muscle forces in the left and right side of the body may be due to, among others, the horizontal components of the ground reaction force which are comparatively low but usually act in the opposite direction.

While weightlifting coaches are able to assess the correctness of the geometry of movement, reaction forces, particularly internal ones, are hardly ever assessed. If coaches were to have information concerning the asymmetry of internal loads, this could have implications for adjusting the training, assessing whether or not the motor activity has been performed correctly, and helping the lifter eliminate habits that may cause injury.

Acknowledgments

The work has been supported by the Ministry of Science and Higher Education of Poland under the grant No. 0045/RS3/2015/53 for years 2015-2018.

The experimental data were obtained in the Laboratory of Biomechanics and Kinesiology in the Regional Centre of Research and Development in Biała Podlaska. The Centre was co-financed under the European Regional Development Fund, Operational Programme Development of Eastern Poland 2007-2013.

References

[1] Baumann, W., Gross, V., Quade, K., Galbierz, P., Schwirtz, A. The snatch technique of world class weightlifters at the 1985 World Championships. *International Journal of Sport Biomechanics* 4, 1988, 68–89.

[2] Gourgoulis, V., Aggelousis, N., Mavromatis, G., Garas, A. Three dimensional kinematic analysis of the snatch of elite Greek weightlifters. *Journal of Sports Sciences* 18, (8) 2000, 643–652.

[3] Häkkinen, K., Kauhanen, H., Komi, P. Biomechanical changes in the Olympic weightlifting technique of the snatch and clean and jerk from submaximal to maximal loads. *Scandinavian Journal of Sports Sciences* 6, 2 (1984), 57-66.

[4] Dziewiecki, K., Blajer, W., Mazur, Z., Czaplicki, A. Contact modelling and inverse dynamics identification of the handspring front somersault in pike position. *Proceedings of the Institution of Mechanical Engineers, Part K: Journal of Multi-body Dynamics* 227, 42 (2013), 330-343.

[5] Dziewiecki, K., Blajer, W., Mazur, Z., Czaplicki, A. Modelling and computational issues in the inverse dynamics simulation of triple jump. *Multibody System Dynamics* 32, 3 (2014), 299-316.

[6] Blajer, W. *Methods of multibody dynamics*. Wydawnictwo Politechniki Radomskiej, Radom, 1998. [in Polish]

[7] Czaplicki, A. *Modelling in natural coordinates in biomechanics*. Akademia Wychowania Fizycznego, Biała Podlaska, 2009. [in Polish]

[8] Akkus, A., Harbili, E. Three-dimensional kinematic analysis of the snatch technique for lifting different barbell weights. *Journal of Strength and Conditioning Research* 26, 6 (2012), 1568-1576.

[9] Gourgoulis, V., Aggeloussis, N., Garas, A., Mavromatis, G. Unsuccessful vs. successful performance in snatch lifts. *Journal of Strength and Conditioning Research* 23, 2 (2009), 486-494.

Adam Czaplicki, Associate Professor: Józef Piłsudski University of Physical Education in Warsaw, Faculty of Physical Education and Sport, Akademicka 2, 21-500 Biała Podlaska, Poland (*adam.czaplicki@awf-bp.edu.pl*). The author presented this contribution at the conference.

Krzysztof Dziewiecki, Ph.D.: Kazimierz Pułaski University of Technology and Humanities, Faculty of Mechanical Engineering, Institute of Applied Mechanics and Energetics, Krasickiego 54, 26-600 Radom, Poland (*krzysztof.dziewiecki@uthrad.pl*).

Zenon Mazur, M.Sc.: Kazimierz Pułaski University of Technology and Humanities, Faculty of Mechanical Engineering, Institute of Applied Mechanics and Energetics, Krasickiego 54, 26-600 Radom, Poland (*z.mazur@uthrad.pl*).

Wojciech Blajer, Professor: Kazimierz Pułaski University of Technology and Humanities, Faculty of Mechanical Engineering, Institute of Applied Mechanics and Energetics, Krasickiego 54, 26-600 Radom, Poland (*w.blajer@uthrad.pl*).

Comparative analysis of tire models for simulation of longitudinal motion of lightweight wheeled mobile robots

Przemyslaw Dabek, Maciej Trojnacki

Abstract: The paper is concerned with analysis of tire models from the point of view of their use in studies of dynamics of the lightweight wheeled mobile robots. The focus of the work is on longitudinal motion of a mobile robot on rigid ground. Emphasis is put on discussion of results yielded by the robot dynamics model depending on used tire model. The modeled robot is a four-wheeled lightweight skid-steered robot developed for the purpose of investigations of robot kinematics and dynamics. Models of robot kinematics and dynamics used during studies are only briefly described, because detailed treatment was provided in other works of the authors. Analysed tire models are presented in details. Models are implemented and solved using Matlab/Simulink software. Results of numerical analyses are compared with results of experiments. Models fidelity is described with quality indexes to better guide the assessment. In-depth discussion of the obtained results concludes the paper.

1. Introduction

Modern methods of computer aided engineering analysis (CAE) increasingly become more important in the process of design of wheeled mobile robots. The approach to design involving CAE is promoted in the 2014-2020 Strategic Research Agenda for Robotics in Europe [8].

The virtual prototypes of mobile robots are based on mathematical models of dynamics, in which the key element is the model describing the effector interaction with environment. The purpose of this model is determination of effector forces and moments of force, which besides the gravity force, virtually alone determine motion of a robot. In case of the wheeled mobile robots, the role of effectors is usually played by wheels, most often equipped with rubber tires which interact with grounds of various properties.

The objective of the work is to evaluate two commonly used tire models from the point of view of their use in conditions typical for the wheeled mobile robots. The analysis focus is on modeling the tire-ground contact patch and the case of tire interaction with rigid grounds. In this paper longitudinal motion of the robot is analyzed.

The work extends current knowledge about capabilities of the existing tire models in application to wheeled robot dynamics studies.

2. Mathematical model

2.1. Main modeling assumptions

In the present work full mathematical model of the vehicle (full-vehicle model) comprises vehicle body model and the tire model, which is a separate component of the full-vehicle model. The vehicle model is identical to the one described in the previous work of the authors [3], so it will be only briefly described in the present work.

Full vehicle model. Scope of the study is limited to longitudinal motion, therefore plane model of vehicle is assumed. The object of modeling is a lightweight robot with four non-steered wheels.

Tire model. In the present work, two models are subject to analysis, namely Pacejka model in accordance with MF-Tire/MF-Swift 6.1.2 Equation Manual [6] and Dugoff model in a modified form proposed by Lo Bianco and Gerelli [1]. Both tire models are widely used by the vehicle dynamics researchers community.

2.2. Robot kinematics

The following coordinate systems are relevant to the present study: the fixed coordinate system O; the moving coordinate systems with axes parallel to the fixed coordinate system: CM origin at the robot center of mass, A_i origins at centers of wheels, C_i origins at the intersections of A_{iz} axes with tire tread surfaces; the moving coordinate systems with axes fixed to the robot body 0 (rotating with body 0): CM' origin at the robot centre of mass, A_i' origins at centers of wheels; the moving coordinate systems with axes spinning with robot wheels: A_i'' origins at centers of wheels. Throughout the paper the index i may be substituted by $i = f, b$, where f denotes pair of front wheels (that is, $f = 1$ or $f = 2$), and b, pair of rear wheels (Fig. 1a).

The following notation of a vector: ${}^{i}\mathbf{vector}_j = [{}^{i}x_j, {}^{i}y_j, {}^{i}z_j]^T$ means that coordinates of a point j are given in the coordinate system of origin i. Angle of rotation Θ (θ_i) is measured from ${}^{CM}x$ (${}^{Ai'}x$) axis to ${}^{CM'}x$ (${}^{Ai''}x$) axis, with positive sense of the angle according to right-hand rule. The linear velocities (angular velocities) and displacements (angular displacements) are obtained from acceleration (angular acceleration) of the center of mass ${}^{O}\mathbf{a}_{CM}$ ($\ddot{\Theta}$) by successive integrations.

It is assumed that point CM is in rectilinear motion, and therefore total acceleration of the point CM is assumed to be identical with the tangential acceleration of the point CM (normal acceleration neglected).

For modeling convenience, an engineering point R is considered on the robot which is a midpoint between front and rear axle along the line segment connecting points A_f and A_r. Positions of certain points on the robot body are defined using this point.

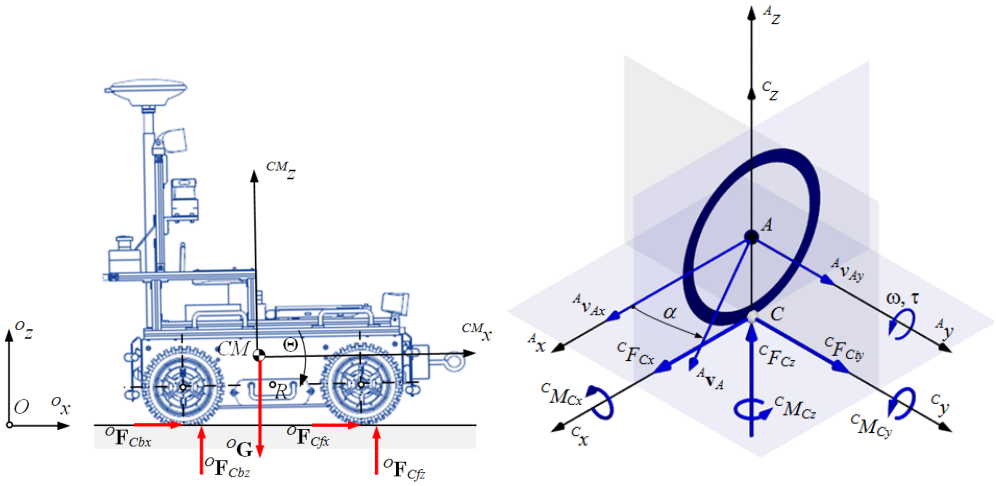

Figure 1. Forces and moments of force: a acting on the mobile robot, b acting on the tire (according to ISO convention)

2.3. Points of contact of tires with the ground

The points of contact of tires with the ground C_i have their positions in the fixed coordinate system O given by:

$$^{O}\mathbf{r}_{Ci} = ^{O}\mathbf{r}_{Ai} + ^{Ai}\mathbf{r}_{Ci} \tag{1}$$

where $^{Ai}\mathbf{r}_{Ci}$ is the vector of position of point C_i in the moving coordinate system $\{A_i\}$. It is assumed that the point C_i lies on the A_{iz} axis, thus $^{Ai}\mathbf{r}_{Ci} = [0, 0, ^{Ai}z_{Ci}]^T$. The value of $^{Ai}z_{Ci}$ coordinate depends on position of wheel center A_i with respect to ground, where ground is assumed to be Oxy plane, that is on $^{O}z_{Ai}$, and can be calculated from the following relationship:

$$^{Ai}z_{Ci} = \begin{cases} -r_{0i} & \text{for} \quad ^{O}z_{Ai} > r_{0i} \\ -^{O}z_{Ai} & \text{for} \quad r_{0i} \geq ^{O}z_{Ai} \geq 0, \\ 0 & \text{for} \quad ^{O}z_{Ai} < 0. \end{cases} \tag{2}$$

The actual (or deformed) radius of the tire is equal to $r_i = |^{Ai}z_{Ci}|$, and the radial deformation of the i-th tire Δr_i is given by:

$$\Delta r_i = r_{0i} - r_i \tag{3}$$

2.4. Wheel slip definition

The longitudinal and lateral wheel slip velocities are respectively given by:

$$ {}^{O}v_{Six} = {}^{O}v_{Aix} - \dot{\theta}_i r_{si}, \tag{4} $$

$$ {}^{O}v_{Siy} = {}^{O}v_{Aiy}, \tag{5} $$

where $\dot{\theta}_i$ is angular velocity of wheel spin and r_{si} is called the slip radius [6].

Then, the longitudinal κ_i and lateral $\tan\alpha_i$ slip ratios are defined by (ISO convention [6]):

$$ \kappa_i = \begin{cases} 0 \quad : \quad \max(|v_{pi}|, |{}^{O}v_{Aix}|) = 0 \\ -{}^{O}v_{Six} / \max(|v_{pi}|, |{}^{O}v_{Aix}|) : \max(|v_{pi}|, |{}^{O}v_{Aix}|) \neq 0 \end{cases} \tag{6} $$

$$ \tan\alpha_i = \begin{cases} 0 \quad : \quad \max(|v_{pi}|, |{}^{O}v_{Aix}|) = 0 \\ -{}^{O}v_{Siy} / \max(|v_{pi}|, |{}^{O}v_{Aix}|) : \max(|v_{pi}|, |{}^{O}v_{Aix}|) \neq 0 \end{cases} \tag{7} $$

2.5. Tire-ground interaction models

The components of reaction forces and moments of force generated by a rubber tire in the tire-ground contact patch and studied in the vehicle dynamics, are listed below and shown in Fig. 1b: ${}^{O}F_{Cix}$ – longitudinal force, ${}^{O}F_{Ciy}$ – lateral force, ${}^{O}F_{Ciz}$ – normal force, ${}^{O}M_{Cix}$ – overturning moment, ${}^{O}M_{Ciy}$ – rolling resistance moment, ${}^{O}M_{Ciz}$ – (self-)aligning moment.

Pacejka model. The Pacejka model is given by the following equation for longitudinal tire-ground contact force:

$$ {}^{O}F_{Cix} = D_{ix} \sin[C_{ix} \arctan(B_{ix}\kappa_i - E_{ix}(B_{ix}\kappa_i - \arctan(B_{ix}\kappa_i)))] \tag{8} $$

where: B_{ix} is the stiffness factor, C_{ix} the shape factor, D_{ix} the peak value and E_{ix} the curvature factor, and in general all coefficients are given individually for each i-th tire. The B_{ix} through E_{ix} coefficients can be expressed in terms of tire structural and operational parameters, for example according to equations given below, which have the simplest physically sensible form (for full set of equations refer to work [6]):

$$ B_{ix} = {}^{O}F_{Ciz} p_{Kx1} / (C_{ix} D_{ix} + \epsilon_{ix}) \tag{9} $$

$$ C_{ix} = p_{Cx1} \tag{10} $$

$$ D_{ix} = \mu_i {}^{O}F_{Ciz} \tag{11} $$

$$ E_{ix} = p_{Ex1} \tag{12} $$

where: μ_i is the tire-ground friction coefficient, ϵ_{ix} is a certain small value to handle division by zero problem, and p_{Cx1}, p_{Ex1}, p_{Kx1} are model parameters. One may also note that the tire longitudinal slip stiffness $k_{i\kappa}$ can be expressed as:

$$k_{i\kappa} = B_{ix} C_{ix} D_{ix}. \tag{13}$$

Dugoff model (modified by Lo Bianco and Gerelli). For longitudinal tire-ground contact force, the modified Dugoff model is given by:

$$^{O}F_{Cix} = -(k_{i\kappa}/k_i)\|\mathbf{F}_i\| \cos\psi_i \tag{14}$$

where the norm of the tire total shear force $\|\mathbf{F}_i\|$ is given by:

$$\|\mathbf{F}_i\| = \mu_i {}^{O}F_{Ciz} \begin{cases} p_i & \text{for} \quad p_i \leq 0.5 \\ 1 - 1/(4p_i) & \text{for} \quad p_i > 0.5 \end{cases} \tag{15}$$

where

$$p_i = \frac{\lambda_i k_i}{2\mu_i {}^{O}F_{Ciz}} \tag{16}$$

and

$$\lambda_i = \begin{cases} 0 & \text{for} \quad \max(|v_{pi}|, |{}^{O}v_{Aix}|) = 0 \\ \sqrt{\kappa_i^2 + \tan^2\alpha_i} & \text{for} \quad \max(|v_{pi}|, |{}^{O}v_{Aix}|) \neq 0 \end{cases} \tag{17}$$

$$k_i = \sqrt{(k_{i\kappa}\cos\psi_i)^2 + (k_{i\alpha}\sin\psi_i)^2} \tag{18}$$

and in equation (18) $k_{i\alpha}$ is the tire lateral slip stiffness. The angle ψ_i between slip speed vector and the ${}^{Ai}x$ axis of the wheel reference frame is given by:

$$\psi_i = \begin{cases} 0 & \text{for} \quad {}^{O}v_{Six} = 0 \\ \arctan2({}^{O}v_{Siy}, {}^{O}v_{Six}) & \text{for} \quad {}^{O}v_{Six} \neq 0 \end{cases} \tag{19}$$

where $\psi_i \in \langle -\pi, +\pi \rangle$ thanks to using Matlab four-quadrant inverse tangent function.

Tire-ground friction coefficient. Both models include tire-ground friction coefficient μ_i. Value of this coefficient depends on several factors, one of which is wheel slip velocity ${}^{O}v_{Six}$. In the present work this dependency will be expressed following [1] as:

$$\mu_i = \mu_s/(1 + A_s|{}^{O}v_{Six}|) \tag{20}$$

where A_s is a constant and μ_s is tire-ground static friction coefficient.

2.5.1. Normal ground reaction

Normal ground reaction on the tire ${}^{O}F_{Ciz}$ is a function of kinematics of tire deformation, and in the present model, the following formula will be used:

$$ {}^{O}F_{Ciz} = k_{ti}\Delta r_i + c_{ti}\Delta\dot{r}_i \mathrm{sgn}(\Delta r_i) \tag{21} $$

where: k_{ti} (c_{ti}) is tire radial stiffness (damping) and sgn() is the signum function.

2.6. Robot dynamics model

It is assumed that the robot as an isolated body is under action of the external forces (Fig. 1a): ground reaction forces ${}^{O}\mathbf{F}_{Ci} = [{}^{O}F_{Cix}, {}^{O}F_{Ciy}, {}^{O}F_{Ciz}]^T$ acting on each wheel calculated from tire-ground interaction models and gravity force ${}^{O}\mathbf{G}_{CM} = m_R {}^{O}g_z$ where: m_R robot total mass, ${}^{O}g_z$ gravitational acceleration vector component ${}^{O}\mathbf{g} = [0, 0, {}^{O}g_z]^T$.

Due to rolling resistance, points of application of normal ground reaction forces are shifted by the so-called coefficient of rolling resistance with dimension of length:

$$ e_i = f_{ir}\mathrm{sgn}(\dot{\theta}_i) r_i \tag{22} $$

where f_{ir} is the dimensionless coefficient of rolling resistance.

Dynamic equations of motion of the robot and of spin of individual wheels in ${}^{O}x{}^{O}z$ plane have the form:

$$ m_R {}^{O}a_{CMx} = \sum_{i=1}^{4} {}^{O}\mathbf{F}_{Cix} \tag{23} $$

$$ m_R {}^{O}a_{CMz} = \sum_{i=1}^{4} {}^{O}\mathbf{F}_{Ciz} - m_R {}^{O}g_z \tag{24} $$

$$ I_{CM'y}\ddot{\Theta} = {}^{CM}z_{Ci} \sum_{i=1}^{4} {}^{O}F_{Cix} - 2({}^{CM}x_{Cf} + e_f) {}^{O}F_{Cfz} - 2({}^{CM}x_{Cb} - e_b) {}^{O}F_{Cbz} \tag{25} $$

$$ I_{Ai''y}\ddot{\theta}_i = \tau_i - {}^{O}F_{Cix} r_i - {}^{O}F_{Ciz} e_i, \tag{26} $$

where: ${}^{CM}z_{Ci}, {}^{CM}x_{Ci}$ are coordinates of the vector ${}^{CM}\mathbf{r}_{Ci} = {}^{CM}\mathbf{r}_{Ai} + {}^{Ai}\mathbf{r}_{Ci}$, $I_{CM'y}$ mass moment of inertia of robot about the axis ${}^{CM'}y$, $I_{Ai''y}$ mass moment of inertia of the wheel about its spin axis ${}^{Ai''}y$, and τ_i is driving/braking torque applied to wheel axle.

2.7. Drive model and controller

It is assumed that each of the robot drive units consists of identical DC motor, encoder, and transmission system. The DC motor model of the i-th drive unit is described by:

$$ \frac{\mathrm{d}i_i}{\mathrm{d}t} = (u_i - k_e n_d \dot{\theta}_i - R_d i_i)/L_d, \quad \tau_i = \eta_d n_d k_m i_i \tag{27} $$

where: u_i, i_i, L_d, R_d rotor winding voltage, current, inductance, resistance, k_e electromotive force constant, k_m motor torque coefficient, n_d, η_d transmission gear ratio and efficiency.

Based on the desired and actual angles and angular velocities of wheel spin $\boldsymbol{\theta}_d = [\theta_{fd}, \theta_{bd}]^T$ and $\dot{\boldsymbol{\theta}}_d = [\dot{\theta}_{fd}, \dot{\theta}_{bd}]^T$ as well as $\boldsymbol{\theta} = [\theta_f, \theta_b]^T$ and $\dot{\boldsymbol{\theta}} = [\dot{\theta}_f, \dot{\theta}_b]^T$, and the respective errors $\mathbf{e}_\omega = \boldsymbol{\theta}_d - \boldsymbol{\theta}$ and $\mathbf{e}_\theta = \dot{\boldsymbol{\theta}}_d - \dot{\boldsymbol{\theta}}$ the controller determines the control signal for motors of driven wheels $\mathbf{u}_c = [u_{c1}, u_{c2}, u_{c3}, u_{c4}]^T$ in (V) based on the control law:

$$\mathbf{u}_c = k_P \mathbf{e}_\theta + k_D \mathbf{e}_\omega, \tag{28}$$

where: k_P, k_D controller gains.

The current $\mathbf{i} = [i_1, i_2, i_3, i_4]^T$ flowing through the rotor windings is limited using the saturation function and a limited power of electric drives is taken into account.

3. Results

Robot desired motion has three phases: accelerating with maximum acceleration a_{CMmax} on the distance of l_r, steady motion with constant velocity ${}^O v_{CMd} = v_{CMu}$ and braking with maximum deceleration $-a_{CMmax}$ on the distance of l_h. Length of desired straight-line path is L_p. The maximum acceleration of desired motion was assumed to reflect a ramp at which desired discrete control signals at 0.01 s are fed into drive controller by robot controller.

Simulation studies were carried out in Matlab/Simulink R2010 environment. The full vehicle model described in section 2 was implemented. The Runge-Kutta fixed-step solver (ode4) was chosen with step size Δt.

The object of the study is a lightweight four-wheeled mobile robot called PIAP GRANITE (Ground Robot for ANalyzes of wheels Interaction with various TErrain). This robot has been developed for the purpose of vehicle dynamics research, so its designed parameters are known with good accuracy. Ground-truth data were obtained in experiment described in [3]. The values of parameters of tire models and of the PIAP GRANITE robot are assumed identical as given in the work [3].

To better guide the comparison of results of simulation and experiment, the following quality indexes were introduced:

- $e_{rms} = \sqrt{\frac{1}{N}\Sigma_{n\in\{1,N\}} e_n^2}$ – root mean square of the errors over a certain interval of the time history of discrete quantity,
- $e_{max} = \max_{n\in\{1,N\}} (e_n)$ – maximum (minimum) value of the error in a certain interval of the time history of discrete quantity,
- $\Sigma e_+ = \Sigma_{n\in\{1,N\}} (e_n)$ iff $(e_n) > 0$ – sum of the errors greater (smaller) than zero over a certain interval of the time history of discrete quantity,

where $e_n = q_{E,n} - q_{S,n}$ and $q_{E,n}(q_{S,n})$ are discrete values of a given quantity obtained from experiment (simulation).

The results are presented in Fig. 3 and Tab. 1. In case of indexes e_{max} (e_{min}) the corresponding time instants when the extremum occured are given as well. The quality indexes were calculated for time histories of the following quantities: actual angular velocities of spin of wheels, longitudinal wheel slip ratios, longitudinal velocity of robot mass center, net longitudinal force acting on robot mass center. To treat separately the transient conditions during acceleration and braking maneuvers, the quality indexes were calculated for three distinct intervals of motion: acceleration phase ($t \in \langle 0\text{s}, 0.50\text{s}\rangle$), steady motion phase ($t \in (0.50\text{s}, 2.52\text{s}\rangle$), braking phase ($t \in (2.53\text{s}, 3.02\text{s}\rangle$). The boundaries of intervals are also marked with vertical dashed lines in Fig. 3. Time histories of reference parameters from empirical experiment are shown using blue lines, of Pacejka model using red lines, and of Dugoff model using green lines.

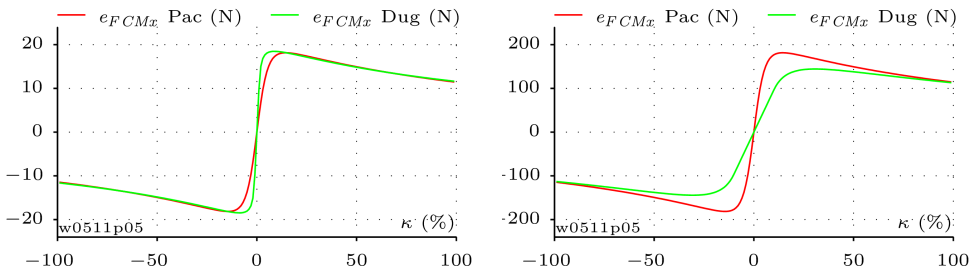

Figure 2. Comparison of forces produced by two models for different normal loads on wheel axle equal to 20 N – a) and 200 N – b).

Fig. 3a shows time histories of errors of wheel spin velocities obtained from simulation for two tire models with respect to experimental values. For each tire model (Pacejka and Dugoff), time histories of right front and right rear wheels are presented. In Fig. 3b the time plot of signal obtained by averaging signals for all four wheels from simulations based on either tire model is shown. The quality indexes in Tab. 1 pertain to Fig. 3b, that is, to the averaged signals. From both figures it is evident that the most significant discrepancies between simulation and experiment occur during acceleration and braking. One can notice, that while the plots of errors during acceleration phase are almost identical for simulations based on two investigated models, there is a marked difference in the braking phase. The difference between behaviour of front wheels (subscript 2) and rear wheels (4) can be noticed - it looks like the front wheels do spin much faster during simulation, than it happens in experiment with the real robot.

Table 1. Quality indexes for time histories of errors of particular quantities

		e_{rms}	e_{max}	t_{max}	e_{min}	t_{min}	Σ_{e+}	Σ_{e-}
		Actual angular velocity of wheel spin – all wheel average [rad/s]						
acceleration	Pac	2.93	0.92	0.30 s	-6.73	0.04 s	11.7	-84.8
	Dug	3.01	0.80	0.30 s	-6.86	0.04 s	10.7	-88.2
steady motion	Pac	0.07	0.16	0.79 s	-0.12	0.63 s	12.3	-0.4
	Dug	0.08	0.17	0.79 s	-0.11	0.63 s	13.0	-0.4
braking	Pac	3.59	8.19	2.56 s	-0.30	2.93 s	114.9	-3.1
	Dug	5.28	12.83	2.58 s	-0.34	2.93 s	160.5	-3.8
		Longitudinal wheel slip ratio – all wheel average [%]						
acceleration	Pac	15.45	47.46	0.05 s	-5.65	0.14 s	303.5	-100.3
	Dug	14.01	42.34	0.05 s	-8.86	0.14 s	257.4	-168.4
steady motion	Pac	2.19	5.70	2.43 s	-3.30	0.78 s	310.4	-62.3
	Dug	2.05	5.43	2.43 s	-3.62	0.78 s	262.3	-75.3
braking	Pac	92.19	192.49	2.80 s	-121.91	2.99 s	3140.2	-438.3
	Dug	92.54	170.54	2.80 s	-142.58	2.99 s	3531.0	-570.9
		Actual longitudinal velocity of robot mass center [m/s]						
acceleration	Pac	0.15	0.08	0.38 s	-0.33	0.09 s	1.5	-4.6
	Dug	0.15	0.09	0.31 s	-0.32	0.09 s	1.8	-4.3
steady motion	Pac	0.04	0.05	0.78 s	-0.09	2.43 s	0.7	-6.2
	Dug	0.04	0.05	0.78 s	-0.08	2.43 s	0.9	-5.4
braking	Pac	0.33	0.64	2.66 s	-0.20	2.83 s	9.8	-2.7
	Dug	0.23	0.42	2.65 s	-0.20	2.84 s	6.7	-2.6
		Net longitudinal force at robot mass center [N]						
acceleration	Pac	98.38	137.45	0.29 s	-256.50	0.02 s	1913.7	-1647.0
	Dug	98.69	139.45	0.29 s	-255.46	0.02 s	1918.3	-1631.6
steady motion	Pac	20.79	55.87	0.75 s	-55.94	1.50 s	1477.8	-1865.8
	Dug	20.79	55.85	0.75 s	-55.97	1.50 s	1475.6	-1868.2
braking	Pac	224.87	415.53	2.54 s	-478.29	2.74 s	3655.0	-4421.1
	Dug	166.52	347.89	2.54 s	-420.78	2.77 s	3197.1	-2917.2

Figs. 3c,d follow similar presentation logic as described for the Figs. 3a,b. The errors of longitudinal slip ratios for individual wheels are much greater during braking phase than during acceleration phase. It is evident that during braking the wheel slip pattern is significantly different in simulation and in experiment. The differences in time plots of wheel slip ratio directly affect the values of calculated longitudinal wheel contact forces.

Fig. 3e presents longitudinal velocity of robot mass center obtained from simulation involving Pacejka tire model and from experiment. Apart from longitudinal velocity of mass centre, the lateral component of velocity of this point is shown as well, but it is of little significance because the motion takes place along a straight line on even horizontal ground. In Fig. 3f the errors of simulation of the longitudinal velocity against experimental velocity

are shown. In contrast to the previously discussed quantities, this time, significant errors are noticeable during the steady motion phase also. The time history of error resembles oscillations of relatively constant period, but variable amplitude. They may be related to the tire tread blocks which are not explicitly modeled by the investigated tire models.

Fig. 3g shows time histories of net longitudinal force acting on the robot mass center, which originates from the longitudinal components of contact forces that develop between tires and the ground. From the error plot (Fig. 3h) it is evident that the situation is similar in case of both tire models. The significant errors during braking phase are related to: (1) slight shift in phase of the simulated and experimental signals, (2) different rates (slopes) at which the longitudinal force builds up and releases. In case of experiment the slopes are slightly less steep. This effect may be related to rotational (circumferential) flexibility of a real tire, which is not included in the investigated tire models.

The differences of simulation results obtained when the two different tire models were used (despite their parametrisation for identical conditions and tire properties), can be related among other factors to different sensitivity of the models to the normal load (the load present on wheel axle) (Fig. 2).

4. Conclusion

The most important conclusions from the study are as follows:

- Significant discrepancies between experiment and simulations involving the investigated tire models are found during acceleration and braking phases of motion. Tire models should probably include elasticity in the wheel circumferential direction to account for the less steep slopes of building-up and releasing force as shown by experimental evidence.

- During the steady motion the time history of error seems to have periodic character of irregular amplitude. The inclusion of tire tread in a tire model should be investigated as a way to explain this phenomenon and take it into account when more realistic simulation is required by the application.

- Although the parametrization of the tire models was equivalent, there are significant differences between results, most pronounced during the braking phase of motion.

Acknowledgments

This work was partly supported by Industrial Research Institute for Automation and Measurements (PIAP) under statutory funds and partly by Ministry of Higher Education of the Republic of Poland under funds for young researchers.

References

[1] Bianco, C. G. L., and Gerelli, O. An alternative model for the evaluation of tyre shear forces under steady-state conditions. In *Intelligent Robots and Systems, 2008. IROS 2008. IEEE/RSJ International Conference on* (2008), IEEE, pp. 1983–1989. 00000.

[2] Dabek, P., and Trojnacki, M. Requirements for Tire Models of the Lightweight Wheeled Mobile Robots. In *Mechatronics: Ideas, Challenges, Solutions and Applications*, J. Awrejcewicz, K. J. Kaliński, R. Szewczyk, and M. Kaliczyńska, Eds., no. 414 in Advances in Intelligent Systems and Computing. Springer International Publishing, 2016, pp. 33–51. DOI: 10.1007/978-3-319-26886-6_3.

[3] Dabek, P., and Trojnacki, M. Tire Models for Studies of Wheeled Mobile Robot Dynamics on Rigid Grounds – A Quantitative Analysis for Longitudinal Motion. In *Recent Advances in Systems, Control and Information Technology* (May 2016), R. Szewczyk and M. Kaliczyńska, Eds., Advances in Intelligent Systems and Computing, Springer International Publishing, pp. 409–424. DOI: 10.1007/978-3-319-48923-0_44.

[4] Heverly, M., Matthews, J., Lin, J., Fuller, D., Maimone, M., Biesiadecki, J., and Leichty, J. Traverse performance characterization for the mars science laboratory rover. *Journal of Field Robotics 30*, 6 (2013), 835–846.

[5] Kobayashi, T., Fujiwara, Y., Yamakawa, J., Yasufuku, N., and Omine, K. Mobility performance of a rigid wheel in low gravity environments. *Journal of Terramechanics 47*, 4 (2010), 261–274.

[6] Pacejka, H. B. *Tire and Vehicle Dynamics*, 3rd ed. ed. Elsevier, 2012.

[7] Ray, L. R., Brande, D. C., and Lever, J. H. Estimation of net traction for differential-steered wheeled robots. *Journal of Terramechanics 46*, 3 (June 2009), 75–87.

[8] SPARC. Strategic Research Agenda For Robotics in Europe. 2014-2020.

Przemyslaw Dabek, M.Sc.: Industrial Research Institute for Automation and Measurements (PIAP), Al. Jerozolimskie 202, 02-486 Warsaw, Poland (*pdabek@piap.pl*). The author gave a presentation of this paper during one of the conference sessions.

Maciej Trojnacki, Ph.D., D.Sc.: Institute of Vehicles, Warsaw University of Technology, Narbutta 84 St., 02-524 Warsaw, Poland (*mtrojnacki@simr.pw.edu.pl*).

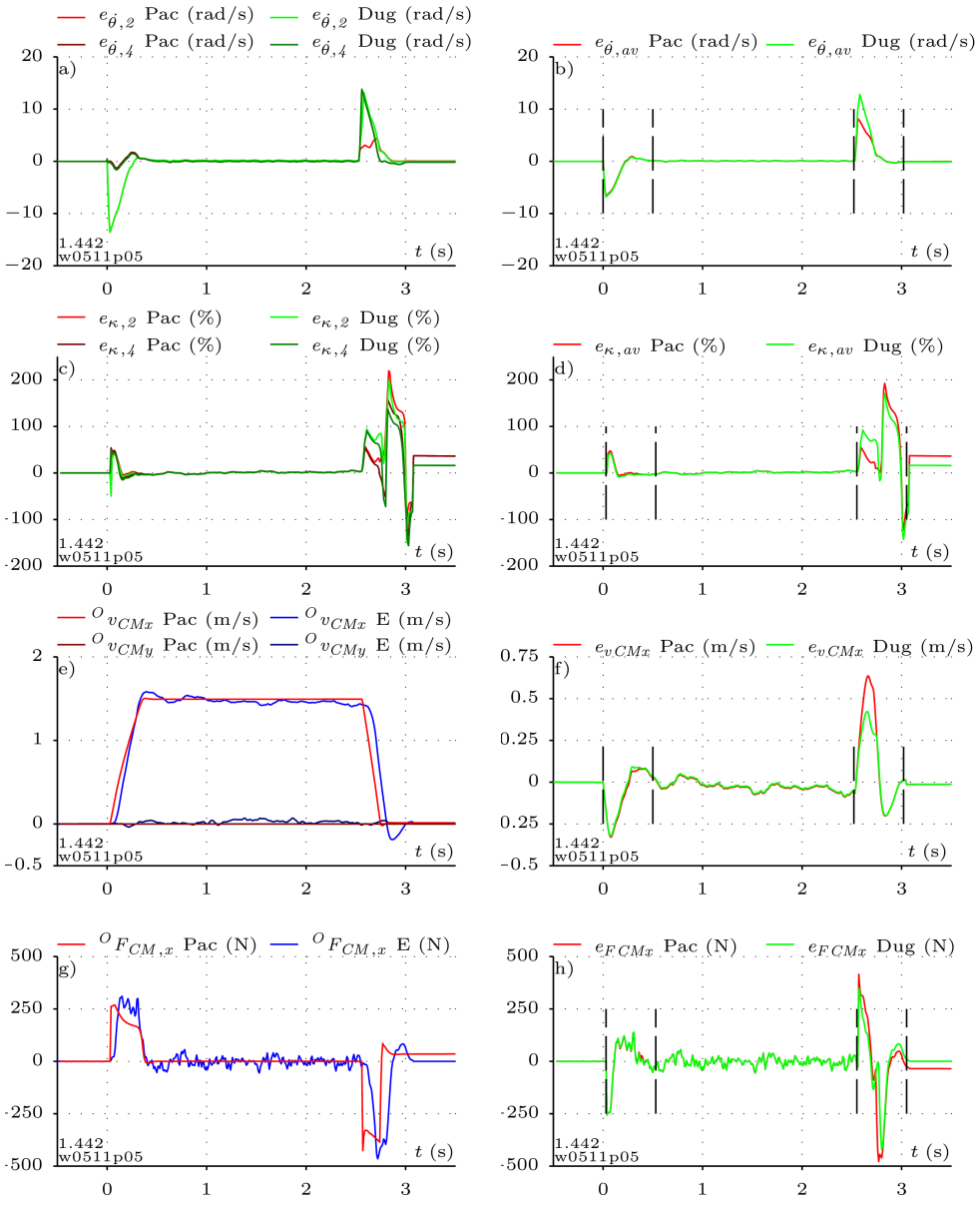

Figure 3. Simulation results obtained using Pacejka and Dugoff tire models: a, b - actual wheel angular velocities (errors of individual wheels and averaged), c, d - longitudinal wheel slip ratios (errors of individual wheels and averaged), e, f - linear velocities of robot mass center (actual quantity and its averaged error), g, h - net longitudinal force applied at robot mass center (actual quantity and its averaged error)

Rotation of vane with viscous filling

Marat Dosaev

Abstract: The motion of a four-blade axisymmetric vane with fixed point is considered in the constant flow of medium. The quasi-steady approach is used for modeling an aerodynamic load. Nonlinear approximation of the aerodynamic fineness function is used. This is a mechanical system with variable dissipation. A case for blades with low fineness is considered. Corresponding dynamic system is simulated for different set of parameters. Two types of body (oblate and oblong) as well as two types of cavity are considered.

1. Introduction

The problem of motion of complex-shape bodies interacting with medium has a lot of applications and attracts scientists all around a world.

Problems of motion of finned bodies in media are investigated analytically, experimentally, and using contemporary methods of integrating differential equations of motion, including finite elements methods that getting be more and more popular. Advanced computer techniques allow obtaining trajectories of body motion under a wide range of initial conditions. Nevertheless, such methods are still time-consuming and need huge computer resources. So, mathematical modeling is very useful for such mechanical problems that allows performing a qualitative analysis of corresponding dynamical systems.

General features of the motion of a finned body in a medium were distinguished in [1-3] using a quasi-steady approach for description of aerodynamic forces. Quasi-steady approach is very useful for studying problems of body motion in a flow. There are many examples when this technique gives results agreeing with experimental data (for example [4]).

A motion of bodies containing cavities with liquid filling is a classical mechanical problem. Problems of stability of motion of bodies with viscous filling began to be investigated in XX century. Sufficient stability and instability conditions for motion of rigid body containing a cavity filled by viscous liquid were obtained by Rumyantsev [5]. The phenomenological model for moment of interaction between walls of vessel and viscous filling was proposed by Samsonov [6] as a linear function between an angular speed of vessel and a vortex of filling. A method of introduction of this model into dynamical system describing a motion of body with filling was presented in [7, 8].

This approach was applied for solving the problem of stability of autorotation of a dynamically symmetric finned body (vane) around a fixed point [9, 10]. The vane has an axisymmetric cavity filled with uniform incompressible viscous liquid. The internal friction was introduced as a moment, which depends linearly on the difference between the vortex of the filling and angular velocity of the body. Aerodynamic load acting on the mechanical system is an external force that interacts with internal moment of friction. Aerodynamic forces were considered applying to rotor blades only, and aerodynamic load was modeled by means of the quasi-steady approach. A dynamic system describing motion of body with viscous filling in a flow is presented and the stability conditions for autorotation along the axis of symmetry were obtained.

In this paper the dynamic system is numerically calculated for range of a coefficient of interior friction. A type of blade shapes with low aerodynamic fineness is considered. Results of calculations are obtained for different combinations of oblate and oblong vessels and cavities.

2. Problem statement

A motion around the fixed point O of a dynamically symmetric finned body (vane) with mass M_1 in a constant flow of resisting medium (Fig. 1) is considered. **V** is the flow speed.

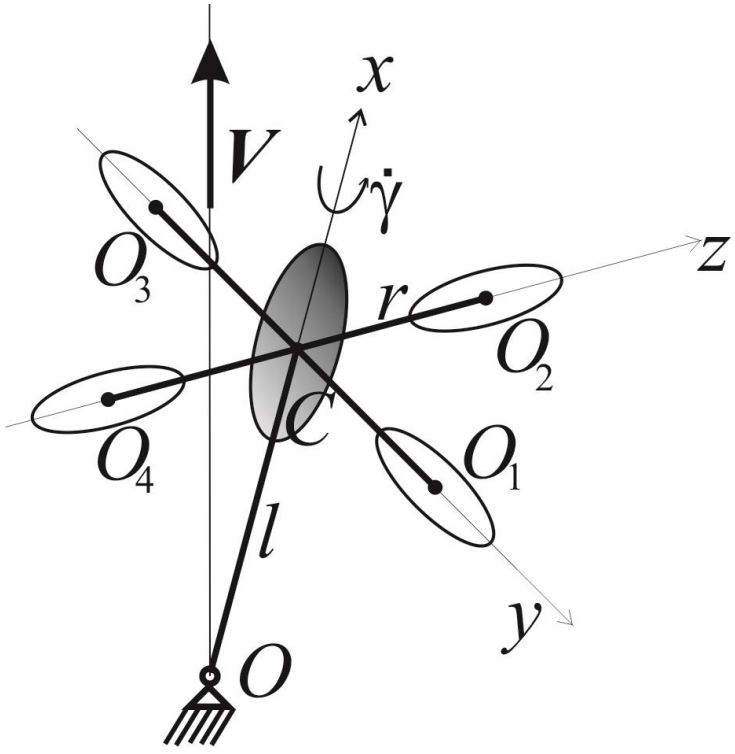

Figure 1. The four-blade axisymmetric vane with cavity.

The fin assembly consists of four identical blades fixed symmetrically. The vane has an axisymmetric cavity filled with uniform uncompressible liquid with mass M_2. For sake of simplicity the cavity center coincides with the center of mass C of the body. We defined the body orientation by Krylov angles: $\varphi, \vartheta,$ and γ. The angles φ and ϑ describe the orientation of the symmetry axis, angle γ specifies the body rotation around the symmetry axis Ox.

The gravity is neglected and aerodynamic forces are supposed acting upon blades only. We represent the aerodynamic impact using quasi-steady approach as a sum of drag and lifting forces. Under these conditions the body can perform autorotation with some angular velocity around the dynamic symmetry axis.

We assumed that liquid can perform the uniform vortex motion. Thus the state of the filling can be described by the vortex components satisfying the Helmholtz equations. The dynamic system describing the mechanical system motion looks as follows in the principal axes of inertia $Cxyz$ ([8, 9]):

$$\begin{cases} \left(A_O^1 + A_O^*\right)\dot{\omega}_1 + A_O^{'}\dot{\Omega}_1 + B_O^{'}(\omega_2\Omega_3 - \omega_3\Omega_2) = M_x \\ \left(B_O^1 + B_O^*\right)\dot{\omega}_2 + B_O^{'}\dot{\Omega}_2 + (A_O^1 + A_O^* - B_O^1 - B_O^*)\omega_1\omega_3 + A_O^{'}\omega_3\Omega_1 - B_O^{'}\omega_1\Omega_3) = M_y \\ \left(B_O^1 + B_O^*\right)\dot{\omega}_3 + B_O^{'}\dot{\Omega}_3 + (B_O^1 + B_O^* - A_O^1 - A_O^*)\omega_1\omega_2 + B_O^{'}\omega_1\Omega_2 - A_O^{'}\omega_2\Omega_1) = M_z \end{cases} \quad (1)$$

$$\begin{cases} \dot{\Omega}_1 = (1+e)(\omega_3\Omega_2 - \omega_2\Omega_3) - \sigma_1\left(A_O^1 + A_O^*\right)(\Omega_1 - \omega_1) / \left(A_O^1 A_O^{'}\right) \\ \dot{\Omega}_2 = \omega_1\Omega_3 - (1-e)\omega_3\Omega_1 - e\Omega_1\Omega_3 - \sigma_2\left(B_O^1 + B_O^*\right)(\Omega_2 - \omega_2) / \left(B_O^1 B_O^{'}\right) \\ \dot{\Omega}_3 = -\omega_1\Omega_2 + (1-e)\omega_2\Omega_1 + e\Omega_1\Omega_2 - \sigma_2\left(B_O^1 + B_O^*\right)(\Omega_3 - \omega_3) / \left(B_O^1 B_O^{'}\right) \end{cases} \quad (2)$$

where ω_i and Ω_i are components of the angular speed of the vane and vortex of filling in axes $Cxyz$ correspondingly; σ_1, σ_2 are coefficients of internal friction; e is the parameter characterizing the cavity geometry; M_x, M_y, M_z are components of the external moment $\mathbf{M}$; $\mathbf{M}$ is the moment of aerodynamic forces around the fixed point; A_O^1, B_O^1, A_O^*, B_O^*, and $A_O^{'}, B_O^{'}$ are diagonal elements of tensor of inertia of body, of tensor of inertia of so called equivalent body, and of difference between tensor of inertia of filling and tensor of inertia of equivalent body in the axes $Cxyz$ correspondingly.

So, we have the nonlinear dynamic system (1-2) consisting from 3 first-order and 3 second-order equations for 9 variables: $\gamma, \varphi, \vartheta, \dot{\gamma}, \dot{\varphi}, \dot{\vartheta}, \Omega_1, \Omega_2, \Omega_3$. The variable γ is the cyclic one.

The dynamic system (1-2) has the steady solution:

$$\varphi = \vartheta = 0, \dot{\varphi} = \dot{\vartheta} = 0, \Omega_2 = \Omega_3 = 0, \dot{\gamma} = \Omega_1 = \dot{\gamma}_0 \quad (3)$$

The steady solution (3) corresponds to vane autorotation around the symmetry axis with constant angular speed $\dot{\gamma}_0$. It can be shown that in established autorotation mode angles of attack α_i (i = 1,2,3,4) of each blade are equal to each other and equal α_0. The steady value of angle of attack α_0 for this mode can be obtained from the following equation: $-k(\alpha_0)+tg(\alpha_0-\beta)=0$, where $k(\alpha_0)$ is aerodynamic fineness for steady angle of attack; β is the blade's pitch angle. The constant value of angular speed for steady rotation one can obtain from following relation: $\dot{\gamma}_0 = -Vtg(\alpha_0-\beta)/r$.

3. Calculation Parameters

We select parameters for calculations. The solid body inertia can be described by two parameters: A_O^1, B_O^1. There are also 5 parameters describing liquid filling: $A_O^*, B_O^*, A_O^{'}, B_O^{'}$, and e in the system (1, 2). Due to the fact that filling fills the cavity entirely, linear dimensions of cavity specify inertia parameters of filling. We assume that it is enough 3 dimensional parameters: M_2, a_1, a_2, for describing inertia characteristics of liquid filling in an axisymmetric cavity . M_2 is mass of the filling; a_1, a_2 are linear dimensions of the cavity.

We consider two types of solid body:

1. $A_O^1 = 0.0688\ kgm^2, B_O^1 = 0.0698\ kgm^2$; (oblong body)
2. $A_O^1 = 0.0688\ kgm, B_O^1 = 0.0658\ kgm$; (oblate body)

And two types of cavity:

1. $a_1 = 0.07m, a_2 = 0.04m$ (oblate cavity)
   $A_O^* = 0, B_O^* = 0.000157\ kgm^2$, $A_O^{'} = 0.00092\ kgm^2, B_O^{'} = 0.00045\ kgm^2$
2. $a_1 = 0.03m, a_2 = 0.04m$ (oblong cavity)
   $A_O^* = 0, B_O^* = 0.000018\ kgm^2$,

These parameters are taken from a problem of rotation a cylinder with viscous filling on a rough plane. A difference in cylinder behavior was uncovered in experiments for different values of viscosity of filling and same features were described by mathematical model [8] for different range of coefficient of interior friction.

We use lift and drag coefficients approximation for a thin disc with low aerodynamic fineness from [9] extended for negative values of angles of attack.

In this paper we consider that interior friction is anisotropic, then we assume the following: $\sigma_1 = \sigma_2 = \sigma$.

Other parameters were taken for sake of simplicity: the density of the media $\rho = 1$; the blade area $S = 1$; the distance from the center of mass C to fixed point O $l = 1$; the distance from each blade center of pressure A_i (i = 1,2,3,4) to the axis of symmetry OC $r = 1$; the flow speed $V = 1$; the blade pitch angle $\beta = 0.174$.

4. Results of calculations

Dynamic system (1-2) contains variables, characteristic times of which are significantly different. As a result numerical calculating the system (1-2) is rather time-consuming process. Results of calculations are shown in Fig. 2-4. In these pictures a solid curve is time-dependence of angle ϑ, a dashed curve is time-dependence of angular speed $\dot{\vartheta}$, dotted one is time-dependence of angular speed of autorotation $\dot{\gamma}$. Initial conditions of trajectories presented in these pictures are chosen equal to make it easier to compare

Calculations show that if coefficient of interior friction σ is not equal to zero, then influence of initial conditions of filling state can be neglected.

We consider 4 different combinations of oblate and oblong vessel and cavity:

Case 1: oblong body + oblate cavity Case 2: oblong body + oblong cavity

Case 3: oblate body + oblate cavity Case 4: oblate body + oblong cavity

For case 1 (oblong body + oblate cavity) for all range of initial conditions the steady rotation around the axis of symmetry (3) is stable. The calculated angular speed of autorotation differs from $\dot{\gamma}_0$ in fourth digit after decimal point. Trajectories tend to this steady motion aperiodically (Fig.2).

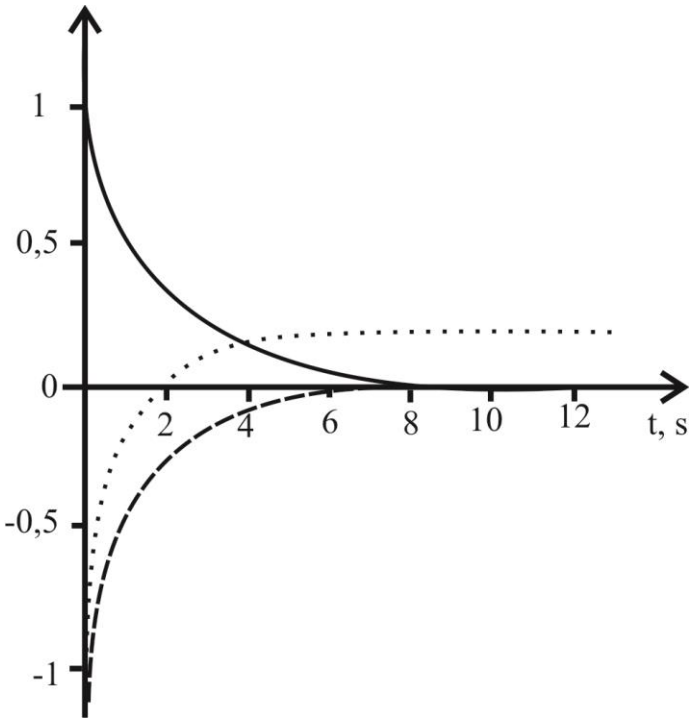

Figure 2. Time-dependencies for case “oblong body + oblate cavity”.

For case 2, oblong body + oblong cavity, for small values of σ ($\sigma \ll 1$) the steady rotation around the axis of symmetry (3) is stable and trajectory behavior is similar to case 1. For $\sigma \sim 1$ steady motion (3) is also stable but angle ϑ may change its sign (Fig.3). For $\sigma \sim 10$ and greater trajectory tends to steady motion (3) by damped oscillations.

For cases oblate body + oblong cavity and oblate body + oblate cavity for small values of σ the steady rotation around the axis of symmetry (3) is also stable. For $\sigma > 10$ axis of symmetry performs precession (Fig.4) around direction of flow. A frequency of oscillations grows with increasing of parameter σ.

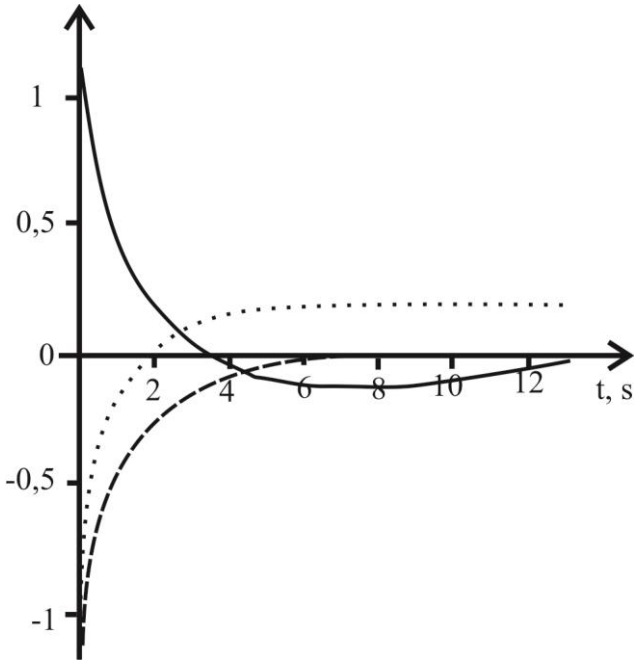

Figure 3. Time-dependencies for case "oblong body + oblong cavity" ($\sigma \sim 1$).

5. Conclusions

The motion of a four-blade axisymmetric vane with fixed point is considered in the constant flow of medium. The quasi-steady approach is used for modeling an aerodynamic load. Nonlinear approximation of the aerodynamic fineness function for blades with low fineness is used. Corresponding dynamic system is numerically integrated for chosen set of parameters and wide range of values of coefficient of interior friction. Two types of body (oblate and oblong) as well as two types of cavity are considered. Calculations show that the mechanical system in consideration has

several different modes of motion: steady rotation, damped oscillations, precessions, and so on. The system is interesting for further study.

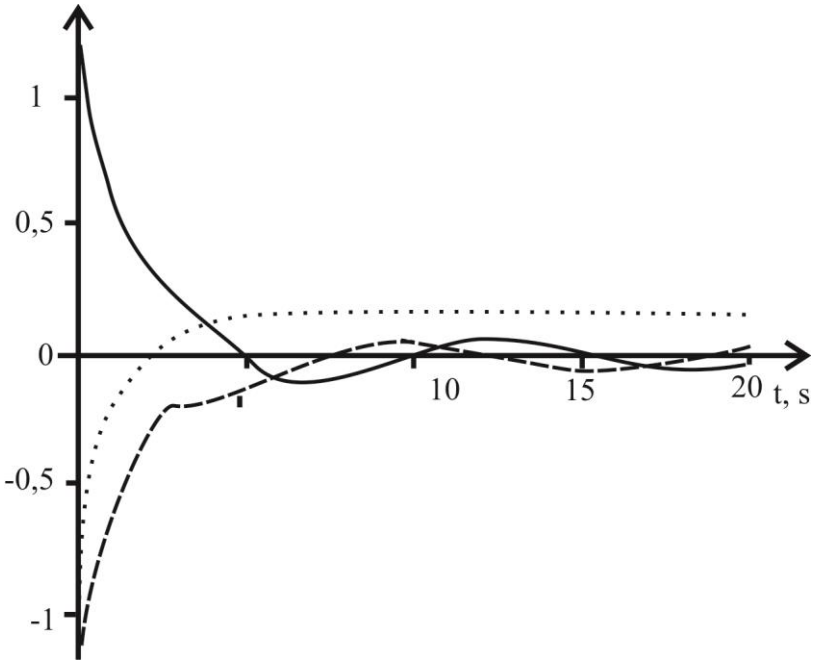

Figure 4. Precession of oblate body for great enough values of σ .

Acknowledgments

This work was partially supported by the Russian Foundation for Basic Research, projects NN 15-01-06970 and 17-08-01366.

References

[1] Privalov V.A., Samsonov V.A.: On stability of motion for autorotating body in a stream of medium. *Izv. Acad. Nauk USSR, Mechanics of solids* 2 (1990), 32-38.

[2] Privalova O.G., Okunev Yu.M., and Samsonov V.A.: On the Stability of Axis-Symmetric Motion of a Finned Body in a Resisting Medium. *Vestnik NGU* 4, 2 (2011), 287-289.

[3] Okunev, Yu., Privalova O., and Samsonov V. On the Motion of a Finned Body in a Resisting Medium. *Automation and Remote Control* 74, 8 (2013), 1326-1333.

[4] Selyutskiy Yu D., Klimina L.A. Effect of nonlinear electromechanical interaction upon wind power generator behavior. *AIP Conference Proceedings*, 1628 (2014), 982-987

[5] Vladimirov V.A., and Rumyantsev V.V.: Inversion of Lagrange's theorem for a rigid body with a cavity containing a viscous liquid. *Journal of Applied Mathematics and Mechanics* 54, 2 (1990), 190-200.

[6] Savchenko A., Samsonov V., and Sudakov S. *Phenomenological model of action of filling upon walls of precessing vessel.* Rep. of Inst. of Mech. 3617 LMSU, Moscow, 1988.

[7] Dosaev M.Z., Samsonov V.A. On stability of rotation of solid body with viscous filling. *Journal of Applied Mathematics and Mechanics* 66, 3 (2002), 427-433.

[8] Dosaev M.Z.: Phenomenological model of motion of rigid body with viscous filling. Ph.D. thesis, Lomonosov Moscow State University, 2002, Samsonov V.A.

[9] Dosaev M. Stability of autorotation of vane containing viscous filling. *12 International Conference "Dynamical systems: theory and applications"*, Lodz, Poland. (2013) 277-282.

[10] Dosaev M. Stability domains for vane with viscous filling. *AIP Conference Proceedings*, 1798, 1 (2017), 020048-1-020048-7

Marat Zakirdzhanovich Dosaev, Associate Professor: Lomonosov Moscow State University, Institute of Mechanics, Michurinsky prosp.,1, 119192, Moscow, Russia, (*dosayev@imec.msu.ru*).

Simulation of contact equilibrium between two deformable axisymmetric bodies

Marat Dosaev, Vladislav Bekmemetev, Vitaly Samsonov

Abstract: A portable pneumatic video-tactile sensor for determining the local stiffness of soft tissue and the methodology for its application are considered. The device is designed to determine the characteristics of tissues that are close in mechanical properties to the skin with subcutis and muscles. The expected rate of local elastic modulus that can be estimated by the sensor is 100 kPa - 10 MPa. A numerical simulation of the contact between the sensor head and the soft tissue was performed using the finite element method. Results of experiments with device prototype are used for approval of adequacy of mathematical modelling in case of large deformations. For small loads and deformations, the results of the calculation correlate with estimates obtained from the Hertz theory. Simulation results can be used to create soft tissue databases, which will be required to determine the local hardness of soft tissues by the sensor.

1. Introduction

Progress in the field of computer technology made a significant contribution to the development of medicine. For example, the invention of a miniature video camera in 1982 gave a powerful impetus to the development of minimally-invasive surgical operations. Laparoscopic operations are performed, in which the surgical intervention in the internal organs of the human abdominal cavity is made through small holes of diameter up to 1.5 cm. During the operation, an important objective of the surgeon is to recognize various operated tissues and conduct their diagnosis. During cavitary operations, the surgeon has the opportunity not only to examine, but also to feel the patient's organs. During laparoscopic operations, direct tactile contact with the internal tissues of the patient's body is impossible. Therefore, the development of an instrument that would give the surgeon quantitative information about the state of these tissues is an important and urgent task of modern biomechanics.

Thus, a number of devices that allow one to determine certain elastic characteristics of soft tissues have been developed in medical technology. For example, medical ultrasound [9], magnetic resonance elastography [8], contact pressure sensors [5]. The paper [1] presents a polyvinylidene fluoride micromechanical tactile sensor integrated into the endoscope grip to provide tactile feedback. The experimental results showed that the position and magnitude

of the applied force can be determined from the signal measured by a polyvinylidene fluoride film. In [3], a PVDF film was used at the catheter's surface to determine the pressure between the catheter and the vessel in order to increase the safety of the operation.

Paper [12] proposed the use of a multifunctional integrated film for the development of the three tactile sensors and their installation at the tip of the catheter for operations approaching cerebral vessels. Due to the fact that the film needs to be replaced in each individual case, these methods proved too costly. Paper [14], however, presents a method of optical tactile sensing with a sensor made of off-the-shelf materials, which is easier to manufacture. A silicon-based tactile sensor is proposed in [7], which is able to determine the three-dimensional forces that result from contact with the object.

The main purpose of these devices is to find malignant inclusions and determine their size. There is a device [10], which allows to determine tissue density during the laparoscopic operation, which is transmitted to the tactile display of the measuring device. A close analog of this device is a sensor that measures the pressure and deformation of the tissue surface [6].

In recent years, a joint Russian-Taiwan scientific group has developed a video-tactile sensor [2] to determine the local stiffness of soft tissue and suggested a technique for its use. Preliminary tests of the sensor on the pig liver demonstrated the ability of the device to indentate samples with a modulus of elasticity in the range of 1-10 kPa (characteristics close to those of a healthy pig liver).

A miniature version of a video-tactile sensor was considered in [4]. Identification of elastic modulus of soft material (gelatin jelly) was carried out, an analysis of the dependence of the contact characteristics on the magnitude of the load and hydrostatic pressure inside the shell of the sensor, as well as on the coefficient of friction. It is shown that the mechanical behavior of jelly during the contact interaction with the sensor is well described by the model of an incompressible linear elastic body. The error in the evaluation of the modulus of elasticity of the test sample does not exceed 10 % in the range 10-25 kPa.

In this paper we consider a portable device that differs from the previously proposed by the sensor shell configuration: it has a relatively high stiffness, larger size, and is intended to determine the characteristics of tissues which properties are close to the skin, fat layer, muscles. Without using additional pressure supply the sensor is efficient for estimating local elastic moduli from the range of 100-200 kPa. There are different approaches for mathematical modeling biological tissues, particularly muscles. An advanced mathematical model of pennate muscle is established in [13]. Our objective is to design an adequate model of contact between the sensor head and a soft tissue that allows us to estimate local stiffness of tissue in consideration. For simplicity sake we model biological tissue by linear elastic material supposing particularly that a speed of indentation is small enough.

Our objective is to design an adequate model of contact between the sensor head and a soft tissue.

2. Indentor

To determine the elastic characteristics of soft biological material, an experimental video-tactile pneumatic sensor was developed. Schematic diagram of the device is shown in Fig.1.

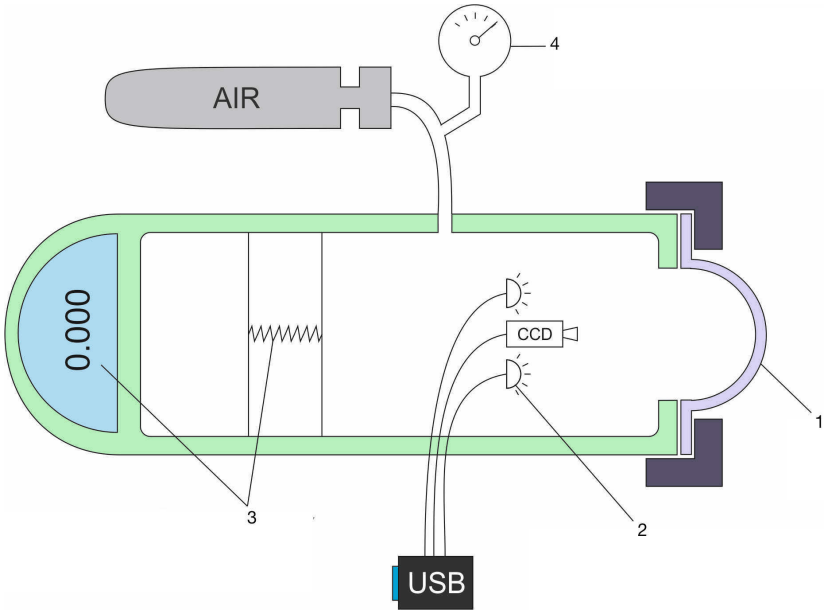

Figure 1. 1 - sensor shell (head), 2 - light source, 3 - load sensor, 4 - air supply hose to the sensor head

The video tactile pneumatic sensor consists of a sealed cylinder fixed at one of its ends to the load sensor. A soft silicone shell is mounted at the other end of the cylinder. A video camera and two LEDs are positioned inside the cylinder. LEDs that perform the function of a light source provide the possibility to adjust the illumination inside the silicone shell in order to visualize the optical image obtained by the video camera.

During the experiments and calculations, it was found that when indenting soft tissue, the central part of the head flexes inwards. In this case, the contact area takes the form of a ring. To avoid this and obtain a convex contact area, the cylinder can be provided with an excess air pressure by means of a hose and a compressed air reservoir.

Under the assumptions made, the following geometric model of the deformed shell is formed, the meridional cross section of which is shown in Fig.2.

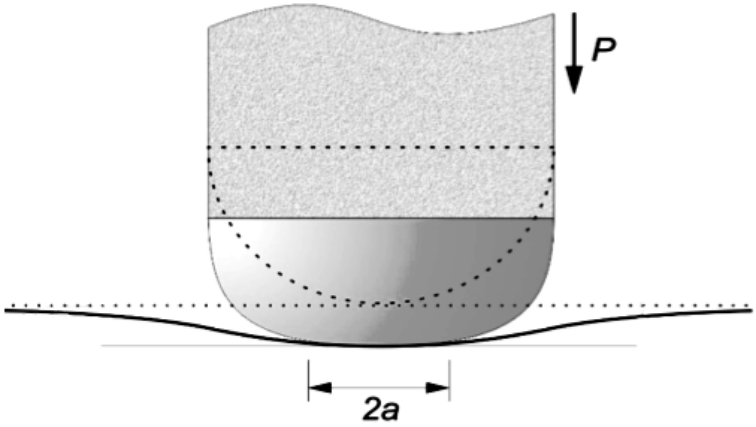

Figure 2. Scheme of contact of the sensor shell with the base, where the dashed lines indicate the undeformed state at the initial moment of contact. a is the radius of the contact area.

3. Statement of the problem

The objective is to determine the modulus of elasticity of soft materials (according to the method proposed in [4]) using the developed video-tactile pneumatic sensor. When indenting the load sensor readings are recorded, the radius of the contact area is determined using the camera. Taking into account the elastic characteristics of the shell, the characteristics of the investigated body are determined.

4. Model

4.1. Material properties

The sensor element is made of a transparent polydimethylsiloxane-based silicone. For the chosen level of load, this material demonstrates elastic behavior. The modulus of elasticity of the material used is $E_1 = 2100$ kPa. The Poisson's ratio is $\nu_1 = 0.4$. To model the indenter, we will use a linear elastic isotropic material with the following parameters:

$E_1 = 2100$ kPa, $\nu_1 = 0.4$

As was shown in [11], a linear elastic incompressible material with Poisson's ratio $\nu_2 = 0.499$ is suitable for modeling soft biological tissues.

To model the body, we will use several different configurations of elastic parameters:

$$E_2^1 = 1\text{kPa},\ E_2^2 = 10\text{kPa},\ E_2^3 = 100\text{kPa}$$

$$\nu_2^1 = 0.499\ \nu_2^2 = 0.499\ \nu_2^3 = 0.499$$

And 10% larger to check the accuracy of the method:

$$E_2^1 = 1.1\text{kPa},\ E_2^2 = 11\text{kPa},\ E_2^3 = 110\text{kPa}$$
$$\nu_2^1 = 0.499\ \nu_2^2 = 0.499\ \nu_2^3 = 0.499$$

4.2. Contact

We propose an axisymmetric formulation of the problem, since the indenter and the silicone cylinder are coaxial, and the sample is sufficiently large in comparison with the contact region. Hence, the initial contact of the shell and the response sample occurs at a point located on the axis of symmetry.

An important characteristic in solving contact problems for each contact pair is the coefficient of friction. According to the relevant literature, the coefficient of friction between silicone and soft tissues varies from 0.1 to 6. In this paper, $\mu = 0.2$ is chosen. The value was selected taking into account the results of previous studies. Calculations with this coefficient had shown good results in [4]. We choose contiguous edges as contacting surfaces.

4.3. Mesh

To determine the modulus of elasticity of the studied tissue, the contact problem is solved, and the results of the solution are compared with the experimental data. Due to the fact that in the process of indentation the objects experience significant deformations, the problem is nonlinear, so the solution is carried out numerically, using the finite element method. For this, the ANSYS package is used.

The calculational scheme for solving the problem in the contact region is presented by a regular finite element mesh. We use axisymmetric eight-node planar finite elements. The calculations are carried out under the assumption of large deformations of the objects, which allows to take into account the influence of the changing shapes of the bodies in the process of deformation.

To construct a mesh of both bodies, we will use the Face Meshing algorithm with quadrangular elements and dividing each edge by a given number of elements. The model contains 1950 quadrangular elements.

To verify the quality of calculations, we constructed another model composed of a similar type of elements of a smaller size. The total number of elements is 4694. A denser mesh provides more detailed calculations. Fig.3 shows the different meshing of the main and the reference models.

Due to the fact that the problem is axisymmetric, we impose symmetry conditions on the edges **A** and **B**. Since the sample is immobile, we impose the condition of the absence of horizontal and vertical displacements on the edge **C**. The force acts downwards on the edge

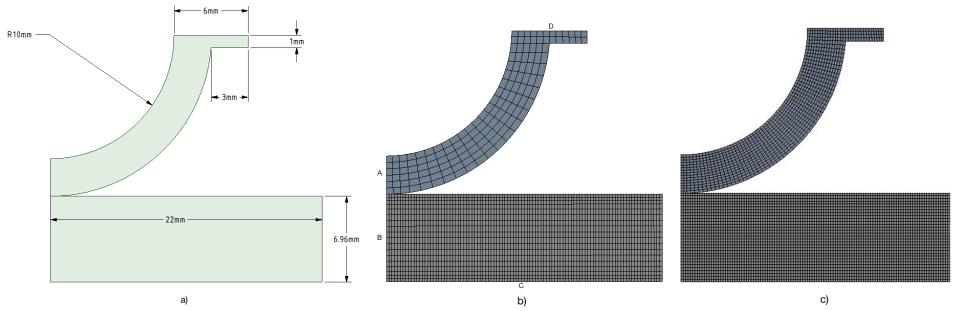

Figure 3. a) depicts the model's geometry. b), c) are the main and the reference models respectively.

D. Since the shell is fixed inside the indenter, we impose the condition of no displacements along the horizontal axis on the edge **D**.

5. Finite element analysis

Fig.4 shows model's diagram of deformations along the horizontal axis.

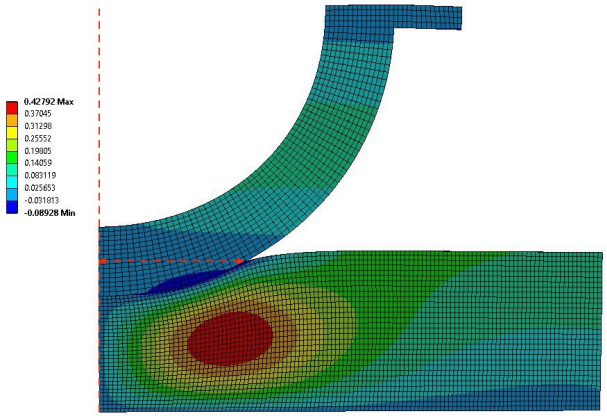

Figure 4. Diagram of deformations along the horizontal axis. We determine the radius of the contact area as the distance from the vertical axis to the last contacting node.

Let us vary the force for each elastic modulus of the body and calculate the radius of the contact area as the distance from the axis to the last contacting node. Then construct a graph of the dependence of the radius on the force.

Calculations were carried out in different ranges of elastic modulus of the studied tissue:

1 kPa, 10 kPa, 100 kPa. The results of the calculations are shown in Fig.6, Fig.7, Fig.8. Each graph shows the calculation points. Approximated curves are constructed using the power function whose coefficients were selected by the expert method.

The results are also shown in Table 1 below.

Table 1

$E = 1$ kPa		$E = 10$ kPa		$E = 100$ kPa	
F, gram-force	a, mm	F, gram-force	a, mm	F, gram-force	a, mm
10	1,87	100	2,09	100	0,99
25	3,63	400	3,85	1200	1,32
50	4,654	800	5,5	400	1,87
100	4,658	1500	7,59	1500	5,83
400	7,04	–	–	2200	7,74
–	–	–	–	3000	8,95
$E = 1.1$ kPa		$E = 11$ kPa		$E = 110$ kPa	
F, gram-force	a, mm	F, gram-force	a, mm	F, gram-force	a, mm
10	1,84	100	1,91	100	0,95
25	3,52	400	3,71	1200	1,3
50	3,63	800	5,25	400	1,85
100	4,51	1500	7,37	1500	5,5
400	6,9	–	–	2200	7,55
–	–	–	–	3000	8,9

5.1. Influence of the number of mesh elements on the results of calculations

The sample $E_2 = 10$ kPa was calculated for the main and reference models. The results are shown in Table 2.

Table 2

$E = 10$ kPa		
F, gram-force	a, mm, main model	a, mm, reference model
100	1,87	1,85
400	3,31	3,33
800	4,4	4,422
1200	5,15	5,15
2000	5,15	6,03

Differences in the determination of the contact area radius turned out to be insignificant (on average, analyzing the calculated points, 1.74%), which means that there is little

dependence on the number of mesh elements. Taking into account that the calculations for a more detailed model take, on average, 2 times as long, it is preferable to use the less detailed model as the main one.

5.2. Influence of measurement error on calculation results

Let us estimate the effect of the error in radius measuring on the determination of the elastic characteristics of the body.

We construct approximation curves from the calculated data. A dependence of the radius of the contact area a (mm) on the force F (gram-force) is shown in Fig.7, Fig.8, Fig.9. The solid lines correspond to the samples with elastic moduli $E_2 = \{1.10, 100\}$, the dashed lines correspond to the samples with elastic moduli $E_2 = \{1.1, 11, 110\}$

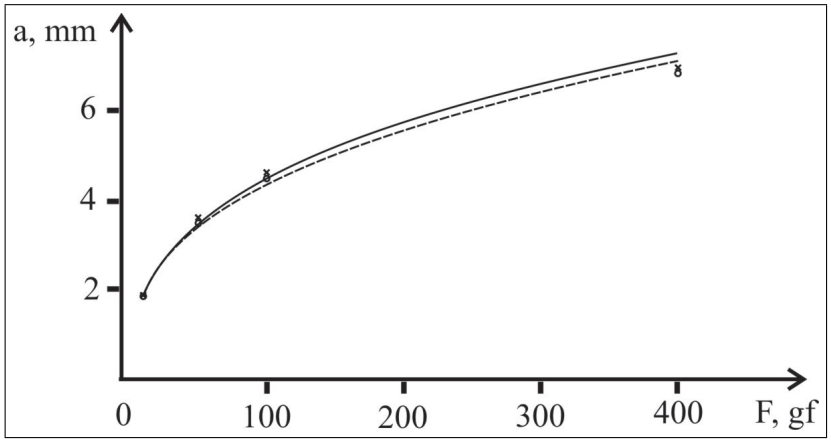

Figure 5. Radius of a contact area as a function of force in case of 1 kPa, 1.1 kPa. 1kPa – solid line, 1.1kPa – dashed line

Let us cross the constructed curves with 3 vertical lines (we select the abscissa values depending on the position of the calculated points on each of the graphs), then find the intersection points of these lines with the two graphs. In each pair of points, we calculate the percentage $\Delta^i = (a_2^i - a_1^i)/a_2^i \cdot 100\%$, showing the difference between the ordinates of the curves. Where a_2^i is the radius corresponding to the intersection point of the curve with the lower elasticity coefficient. a_1^i corresponds to the one with a larger elasticity coefficient. I is the index denoting the pair of points under consideration. The arithmetic average of the obtained quantities equals $\Delta_0 = \sum_{i=1}^{3} \Delta_i/3$. Results are shown in Table 3.

When calculating 100 kPa, a sharp decrease in accuracy is observed. It happens due to the fact that with a given stiffness of the sample, occurs a bending of the central part

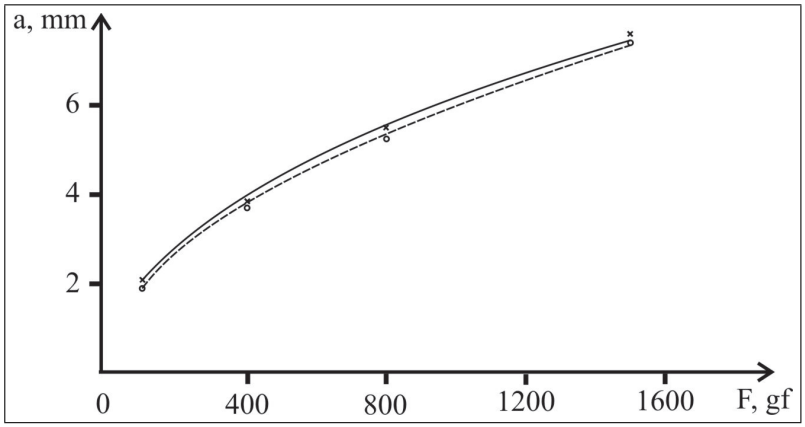

Figure 6. Radius of a contact area as a function of force in the case of 10kPa, 11kPa. 10kPa – solid line, 11kPa – dashed line

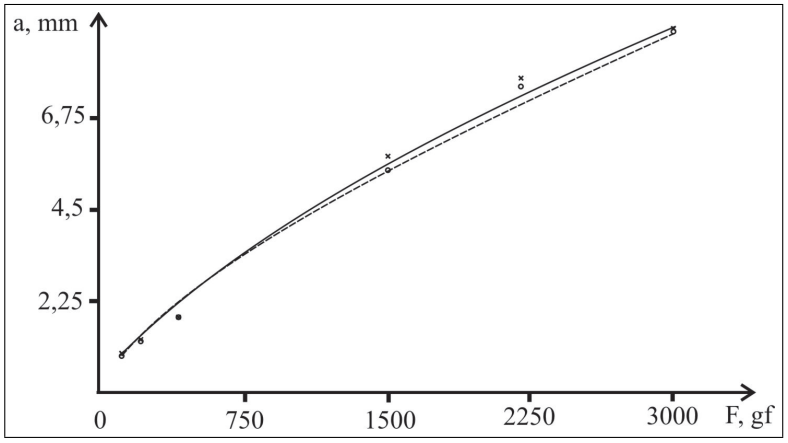

Figure 7. Radius of a contact area as a function of force in the case of 100kPa, 110kPa. 100kPa – solid line, 110kPa – dashed line

of the head. To solve this problem by providing additional pressure in the cylinder, air is fed through a special hose. However, in this paper we consider a simplified model, omitting the possibility of supplying air pressure. Therefore, we leave the range of 100-500 kPa for further research.

Table 3

$E_2 = \{1, 1.1\}$ kPa				
F, gram-force	a_1, mm	a_2, mm	$\Delta^i, \%$	$\Delta_0, \%$
100	4,35383	4,46526	2,5	2,57
200	5,58549	5,73362	2,58	
300	6,46173	6,63659	2,63	
$E_2 = \{10, 11\}$ kPa				
400	3,76363	3,97281	5,27	4,05
800	5,30895	5,52227	3,86	
1200	66,49236	6,69543	3,03	
$E_2 = \{100, 110\}$ kPa				
1500	5,44796	5,5778	2,33	2,28
2250	7,20846	7,37618	2,27	
3000	8,79276	8,99372	2,23	

6. Experiment

In order to measure linear dimensions of the objects obtained from the video camera, we calibrate it. The soft head was indentated into a rigid base, on which concentric circles of a known radius were drawn. Comparing the actual diameter of the circle with the diameter of the circle shown on the screen, the following relation was established: 1 cm on the image from the camera $\approx 0,5$ mm in reality. Table 4 includes experimental and calculated data.

Table 4

F, gram-force	a, mm, experiment	a, mm, calculation	$\Delta^i, \%$
50	1,75	1,65	6,06
120	2,5	2,53	1,19
150	3	3,08	2,6
250	3,4	3,52	3,41
400	3,75	3,95	5,06
$\Delta_0 = 3,66\%$			

7. Results and discussion

The results obtained in Section 5.2 are interpreted as follows: let us consider the range of tissues with a local modulus of elasticity of 10 kPa. For example, if we obtain the contact radius with the 2 % measurement error, the results of the calculations show that in this case the error in the evaluation of the modulus of elasticity does not exceed 10 %.

Using the developed model for determining the characteristics of the contact, the dependence of the contact area radius on the force of pressing was obtained for samples with different stiffness.

The developed model is consistent with the experimental data obtained.

The error in determining the modulus of elasticity of the material will depend on its absolute value. Thus, in modeling materials comparable in modulus with the material of the sensor head, the error in the determined module can be more than 10 % when the calculated curve deviates from the experimental data by less than 1 %. Therefore, at this stage, the developed device allows to more accurately determine the Young's modulus of elastic materials at a value of less than 100 kPa. When calculating more rigid materials, additional air pressure is necessary.

8. Conclusion

In this paper, the design of a vision-based tactile sensor system was presented. Mathematical model of the contact was constructed, it's adequacy validated. The accuracy of this research methodology was assessed. The error in the evaluation of the modulus of elasticity of an absolutely rigid sample does not exceed 3%.

The range of approach of the device is limited from above, since the fact that for the large values of the indentation force, a transition to the ring-shaped contact region is possible. An additional parameter for controlling the stiffness of the sensor is the air pressure created inside the shell of the sensor element. Increasing the air pressure in the chamber provides a wider range of approach for the indenter. The results obtained are promising for the application in medicine with the purpose of determining the elastic characteristics of soft tissues.

Acknowledgments

The paper is supported by Russian Foundation for Basic Research (project #16-58-52033)

References

[1] Dargahi, J., Parameswaran, M., and Payandeh, A. Micromachined piezo- electric tactile sensor for an endoscopic grasper-theory, fabrication and experiments. *Microelectromechanical Systems*, 9(3) (2000), 329–335.

[2] Dosaev, M., Goryacheva, I., et al. Application of video-assisted tactile sensor and nite element simulation for estimating youngs modulus of porcine liver. *Journal of Medical and Biological Engineering* (2015), 510–516, doi.org/10.1007/s40846–015–0064–1.

[3] Feng, W.-X., Huan-Ran, W., Guo, S.-X., Wang, K.-J., and Ye, X.-F. Design and experiments of a catheter side wall tactile sensor for minimum invasive surgery. *Mechatronics and Automation* (2007), 1073–1078.

[4] Gubenko, M., Morozov, A., Lyubicheva, A., et al. Video-tactile pneumatic sensor for soft tissue elastic modulus estimation. *BioMedical Engineering OnLine* (2017), https://doi.org/10.1186/s12938–017–0390–3.

[5] Imran, A. Apparatus and method for detecting contact pressure. *United States Patent 5396887* (1995).

[6] Kaspar, A., Dinusha, Z., Pinyo, P., and Lakmal, S. Air cushion sensor for tactile sensing during minimally invasive surgery. *US Patent No. 20110071436* (2011).

[7] Katragadda, R. B., Wang, Z., and Xu, Y. A high-sensitivity 3-d tactile sensor for minimally invasive surgery. *Sensors*, 9(3) (2007), 808–810.

[8] Manduca, A., Oliphant, T., Dresner, M., and others. Magnetic resonance elastography: A review. *Med Image Anal.*, 5(4) (2001), 237–54.

[9] Mariappan, Y., Glaser, K., and Ehman, R. Magnetic resonance elastography: A review. *Clinical Anatomy*, 23 (2010).

[10] Sadovnichy, V., et al. The device of the tactile display for research of density of a fabric. *The patent of the Russian Federation 2488343* (2013).

[11] Skovoroda, A. *Problems of the theory of elasticity in the diagnosis of pathologies of soft biological tissues*. Fizmatgiz, Moscow, 2005.

[12] Takizawa, H., Tosaka, H., Ohta, R., Kaneko, S., and Ueda, Y. Development of a microfine active bending catheter equipped with mif tactile sensors. *Micro Electro Mechanical Systems* (1999), 412–417.

[13] Wojnicz, W., Zagrodny, B., Ludwicki, M., Awrejcewicz, J., and Wittbrodt, E. Mathematical model of pennate muscle. *Dynamical Systems - Mechatronics and Life Sciences* (2015), 595–608.

[14] Yamaguchi, A., and Atkeson, C. G. Combining finger vision and optical tactile sensing: Reducing and handling errors while cutting vegetables. *Humanoid Robots (Humanoids)* (2016).

Marat Dosaev, Ph.D.: LMSU Institute of Mechanics, Michurinskiy pr., 1, Moskva, Russia, 119192 (*dosayev@imec.msu.ru*). The author gave a presentation of this paper during one of the conference sessions.

Vladislav Bekmemetev, M.Sc. (student): LMSU Institute of Mechanics, Michurinskiy pr., 1, Moskva, Russia, 119192 (*winter.in.head@gmail.com*).

Vitaly Samsonov, Prof.: LMSU Institute of Mechanics, Michurinskiy pr., 1, Moskva, Russia, 119192 (*samsonov@imec.msu.ru*).

An approach to the mechanical modeling of contact problems in the application to friction stir welding

Nataliia Dubovikova, Erik Gerlach, Igor Zeidis, Klaus Zimmermann

Abstract: The joining process Friction Stir Welding (FSW) is an established solid state welding technique. We investigate a pre-immersion period of FSW process from the mechanical point of view using analytical considerations. This is a part of the real technological process, when the instrument reaches the touchdown point, preheats the contact zone, but does not penetrate the material itself. It brings insight into the process on a level, where the system parameters are known and an experimental evaluation of theoretical results is possible. Out of these considerations we analytically estimate power input of dry friction during rotation and translation in parallel. The stir process below the melting temperature of the material leads, as a consequence, to other forms of friction. FSW experiments have been done to validate the calculated results.

1. Introduction

The joining process Friction Stir Welding (FSW) is an established solid state welding technique [2], [7]. The process involves connection of two clamped metal species by mechanical mixing of their edging zone with a rotating tool. The applied stirring induces external and internal friction within the workpieces, which generates sufficient amount of heat energy to change metals' state from solid to plastic and supports the mixing. By FSW no consumable materials are needed unlike the standard welding methods [6].

A rotating cylindrical tool is moving along the workpieces edges and mechanically connects them (Fig. 1). The rotating instrument consists of two parts: a pin and a shoulder; both of them are playing important role within the process [5].

Since its invention [9] in 1991, a lot of papers are devoted to the understanding and improvement of FSW process. Most of them goes into details and consider special questions like the temperature-deformation distribution and the heat transfer process by applying numerical methods like finite element and finite difference methods [1], [4].

At the start of the FSW process the instrument is preheating a contact surface of workpiece by Coulomb friction [8]. We investigate the role of Coulomb friction in the pre-immersion stage of FSW process. This stage has significant role within the welding process and creates necessary conditions for further instrument penetration.

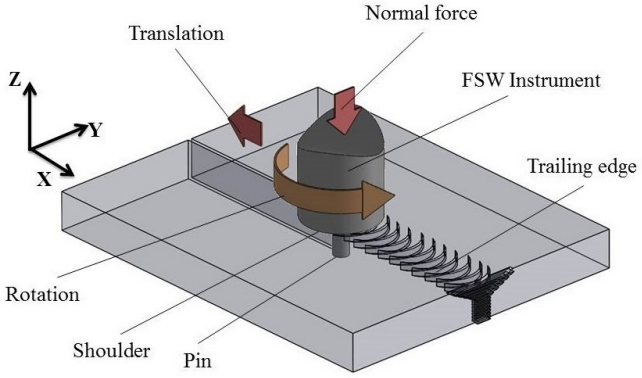

Figure 1. Model of the FSW problem.

2. Theoretical model

2.1. Forces and power analysis

Consider the following mechanical model for FSW. We assume that a body that has a vertical axis of symmetry is moving at a velocity of v on a fixed rough plane along the axis $\mathbf{O}_1\mathbf{X}_1$ of the fixed coordinate frame $\mathbf{O}_1\mathbf{X}_1\mathbf{Y}_1\mathbf{Z}_1$. At the same time, the body is rotating around its axis of symmetry at an angular velocity ω (see Fig. 2a). We assume that the contact area at each time instant is a circle of radius a centered at the point $\mathbf{O}$ on the axis of rotation (see Fig. 2b).

To calculate the friction resultant force and torque $\overline{F}_{\mathrm{R}}$ and $\overline{M}_{\mathrm{R}}$ we use classical Coulomb's law in the local form. Let $\mathbf{A}$ be an arbitrary point of the contact area D. Then, in accordance with Coulomb's law, the force of friction $\overline{F}_{\mathrm{R}}(\mathbf{A})$ at the point $\mathbf{A}$ is defined by:

$$\overline{F}_{\mathrm{R}}(\mathbf{A}) = -kp(\mathbf{A})\frac{\overline{v}(\mathbf{A})}{|\overline{v}(\mathbf{A})|}, \mathbf{A} \in D, |\overline{v}(\mathbf{A})| \neq 0, \tag{1}$$

Here k is the coefficient of friction, p($\mathbf{A}$) is the normal stress (pressure) at the point $\mathbf{A}$, and $\overline{v}(\mathbf{A})$ is the slip velocity at the point $\mathbf{A}$.

The local torque of the force of friction $\overline{M}_{\mathrm{R}}(\mathbf{A})$ is defined by:

$$\overline{M}_{\mathrm{R}}(\mathbf{A}) = \overline{\mathbf{OA}} \times \overline{F}_{\mathrm{R}}(\mathbf{A}). \tag{2}$$

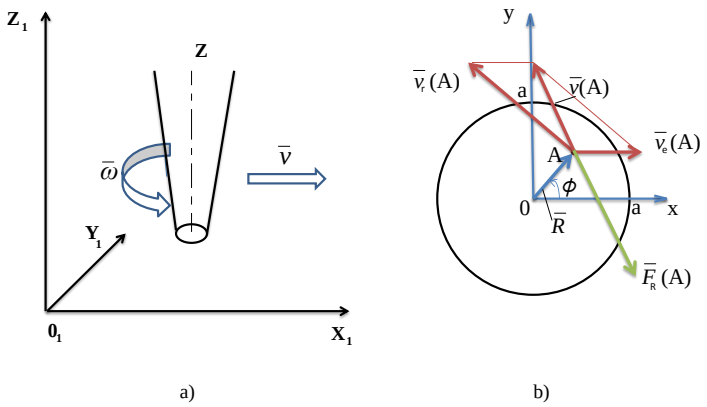

Figure 2. a) Model of the FSW problem; b) velocity and force vectors.

Then in accordance with relation (1) we obtain:

$$\overline{M}_{\mathrm{R}}(\mathbf{A}) = -kp(\mathbf{A})\frac{\overline{\mathbf{OA}} \times \overline{v}(\mathbf{A})}{|\overline{v}(\mathbf{A})|}, |\overline{v}(\mathbf{A})| \neq 0. \tag{3}$$

We calculated the velocity $\overline{v}(\mathbf{A})$ of the point $\mathbf{A}$ (Fig. 2b). To this end we introduce a coordinate system $\mathbf{OXYZ}$ with the origin located at the point $\mathbf{O}$, the axis $\mathbf{OX}$ pointing along the axis $\mathbf{O_1X_1}$, and the axis $\mathbf{OZ}$ coinciding with the symmetry axis of the body. Use the addition rule for velocities to obtain:

$$\overline{v}(\mathbf{A}) = \overline{v}_r(\mathbf{A}) + \overline{v}_e(\mathbf{A}), \tag{4}$$

where $\overline{v}_r(\mathbf{A})$ and $\overline{v}_e(\mathbf{A}$ are the relative velocity of the point $\mathbf{A})$ and its velocity due to the motion of the reference frame.

The relative velocity $\overline{v}_r(\mathbf{A})$ of the point $\mathbf{A}$ is orthogonal to the position vector $\overline{\mathbf{OA}}$ and points in the direction of the rotation of the body; $|\overline{v}_r(\mathbf{A})| = \omega r$, $|\overline{\mathbf{OA}}| = r = \sqrt{x^2 + y^2}$. the velocity $\overline{v}_e(\mathbf{A})$ due to the motion of the rotation frame for the point $\mathbf{A}$ is parallel to the axis $\mathbf{O_1X_1}$. As a result we obtain:

$$\overline{v}(\mathbf{A}) = (v - \omega r \sin\phi)\overline{\mathrm{e}}_{\mathrm{x}_1} + \omega r \cos\phi \overline{\mathrm{e}}_{\mathrm{y}_1}, \tag{5}$$

where ϕ is the angle between the vector $\overline{\mathbf{OA}}$ and the axis $\mathbf{OX}$,

$$|\overline{v}(\mathbf{A})| = \sqrt{v^2 - 2\omega r \sin\phi + \omega^2 \mathrm{r}^2}. \tag{6}$$

The resultant force $\overline{F}_{\mathrm{R}}$ and the resultant torque $\overline{M}_{\mathrm{R}}$ of friction about the symmetry axis $\mathbf{OZ}$ of the body are defined by:

$$\overline{F}_{\mathrm{R}} = -k \iint\limits_D p(\mathbf{A}) \frac{\overline{v}(\mathbf{A})}{|\overline{v}(\mathbf{A})|} dD, \tag{7}$$

$$\overline{M}_{\mathrm{R}} = -k \iint\limits_D p(\mathbf{A}) \frac{\overline{\mathbf{OA}} \times \overline{v}(\mathbf{A})}{|\overline{v}(\mathbf{A})|} dD. \tag{8}$$

The relation (6) implies that for $\omega \neq 0$, the quantity $|\overline{v}(\mathbf{A})|$ may vanish at each time instant at one point at most ($\cos\phi = 0$, $|\overline{v}| = \omega r$). Ignoring such points does not influence the result of the integration. For $\omega = 0$, the relation $|\overline{v}(\mathbf{A})| = 0$ holds only if $v = 0$, which implies that the body is not moving.

The local power $P_{\mathrm{R}}(\mathbf{A})$ of the forces of friction is given by:

$$P_{\mathrm{R}}(\mathbf{A}) = \overline{F}_{\mathrm{R}}(\mathbf{A}) \cdot \overline{v}(\mathbf{A}) = -kp(\mathbf{A})|\overline{v}(\mathbf{A})|, \tag{9}$$

and the total power P_{R} is expressed by:

$$P_{\mathrm{R}} = -k \iint\limits_D p(\mathbf{A})|\overline{v}(\mathbf{A})| dxdy. \tag{10}$$

Using polar coordinates for the infinitesimal surface element $dD = rdrd\phi$, the expressions (7), (8) and (10) become:

$$\overline{F}_{\mathrm{R}} = F_{\mathrm{Rx_1}} \overline{e}_{\mathrm{x_1}} + F_{\mathrm{Ry_1}} \overline{e}_{\mathrm{y_1}}, \tag{11}$$

$$F_{\mathrm{Rx_1}} = -k \int_0^a \int_0^{2\pi} \frac{p(r)(v - \omega r \sin\phi)}{\sqrt{v^2 - 2\omega r v \sin\phi + \omega^2 r^2}} r dr d\phi, \tag{12}$$

$$F_{\mathrm{Ry_1}} = -k \int_0^a \int_0^{2\pi} \frac{p(r)\omega r \cos\phi}{\sqrt{v^2 - 2\omega r v \sin\phi + \omega^2 r^2}} r dr d\phi, \tag{13}$$

$$\overline{M}_{\mathrm{R}} = -k \int_0^a \int_0^{2\pi} \frac{p(r)}{\sqrt{v^2 - 2\omega r v \sin\phi + \omega^2 r^2}} r dr d\phi \overline{e}_z, \tag{14}$$

$$P_{\mathrm{R}} = -k \int_0^a \int_0^{2\pi} \sqrt{v^2 - 2\omega r v \sin\phi + \omega^2 r^2} r dr d\phi. \tag{15}$$

Expression (13) for $F_{\mathrm{Ry_1}}$ can be represented as follows:

$$F_{\mathrm{Ry_1}} = -k \int_0^a p(r) \Big(\int_0^{2\pi} \frac{\omega r \cos\phi}{\sqrt{v^2 - 2\omega r v \sin\phi + \omega^2 r^2}} d\phi \Big) r dr. \tag{16}$$

Then after integration we receive:

$$\int_0^{2\pi} \frac{wr\cos\phi}{\sqrt{v^2 - 2wrv\sin + w^2r^2}} d\phi = -k\sqrt{v^2 - 2wrv\sin + w^2r^2}|_0^{2\pi} = 0. \tag{17}$$

$$\overline{F}_{\mathrm{R}} = -k \int_0^a \int_0^{2\pi} \frac{p(r)(v - wr\sin\phi)}{\sqrt{v^2 - 2wrv\sin\phi + w^2r^2}} r dr d\phi \overline{e}_{x_1}, \tag{18}$$

The identification of the function $p(r)$ is a separate problem. Let the velocity of propagation of the elastic waves on the material of the body be much greater than the velocities of the points of the body. In that case, we may use static distribution laws $p(r)$ for the normal pressure. Consider three distribution laws: 1) uniform distribution, 2) Hertz point contact for the case where the contacting surfaces are locally spherical, and 3) contact between a rigid cylindrical body and an elastic half-space. All three distribution laws can be represented as follows:

$$p(r) = p_0(n)(1 - (r/a)^2)^n. \tag{19}$$

Let N_0 be the normal pressure force. Then:

1) For the uniform friction force distribution:

$$n = 0, p_0 = \frac{N_0}{\pi a^2}, p(r) = \frac{N_0}{\pi a^2}. \tag{20}$$

2) For Hertz function (point contact):

$$n = 1/2, p_0 = \frac{3N_0}{2\pi a^2}, p(r) = \frac{3N_0}{2\pi a^2}\sqrt{1 - (r/a)^2}. \tag{21}$$

3) For contact of a rigid cylindrical body with an elastic half-space surface:

$$n = -1/2, p_0 = \frac{N_0}{2\pi a^2}, p(r) = \frac{3N_0}{2\pi a^2\sqrt{1 - (r/a)^2}}. \tag{22}$$

Introduce the notation $\lambda = v/(wa)$ and $\xi = r/a$ to represent relations (14), (15) and (18) as follows:

$$\overline{F}_{\mathrm{R}} = -ka^2 p_0(n) \int_0^a \int_0^{2\pi} \frac{(1 - \xi^2)^n \xi(\lambda - \xi\sin\phi)}{\sqrt{\lambda^2 - 2\lambda\xi\sin\phi + \xi^2}} d\xi d\phi \overline{e}_{x_1}, \tag{23}$$

$$\overline{M}_{\mathrm{R}} = -ka^3 p_0(n) \int_0^a \int_0^{2\pi} \frac{(1 - \xi^2)^n \xi^2(\xi - \lambda\sin\phi)}{\sqrt{\lambda^2 - 2\lambda\xi\sin\phi + \xi^2}} d\xi d\phi \overline{e}_z, \tag{24}$$

$$P_{\mathrm{R}} = -ka^3 \omega p_0(n) \int_0^a \int_0^{2\pi} (1 - \xi^2)^n \xi\sqrt{\lambda^2 - 2\lambda\xi\sin\phi + \xi^2} d\xi d\phi. \tag{25}$$

Let $f_0(n) = a^2 p_0(n)$, where $f_0(n)$ be independent of a. If the contact area D degenerates into a point (a tend to 0), we obtain:

$$\lim_{a\to 0} F_{\mathrm{R}} = -2\pi k f_0(n) \int_0^a (1-\xi^2)^n \xi d\xi = -\frac{\pi k f_0(n)}{n+1} = -kN_0, \tag{26}$$

$$\lim_{a\to 0} M_{\mathrm{R}} = -ka f_0(n) \int_0^a \int_0^{2\pi} (1-\xi^2)^n \xi^2 (-\sin\phi) \mathrm{d}\xi \mathrm{d}\phi = 0, \tag{27}$$

$$\lim_{a\to 0} P_{\mathrm{R}} = -2\pi k v f_0(n) \int_0^a (1-\xi^2)^n \xi d\xi = -\frac{\pi k v f_0(n)}{n+1} = -kvN_0. \tag{28}$$

The obtained values correspond to point contact between an instrument and a workpiece.

2.2. Thermal analysis

For an analytical solution of the thermal problem we assume that a workpiece is a semi infinite solid (a solid, which extends to infinity in all but one direction). If a sudden change of conditions is imposed at this surface, transient, one-dimensional conduction will occur within the solid [3].

With no internal heat generation in the workpiece and the assumption of its constant thermal conductivity, general heat diffusion equation can be written as:

$$\frac{\partial^2 \mathrm{T}}{\partial \mathrm{x}^2} = \frac{1}{\alpha} \frac{\partial \mathrm{T}}{\partial \mathrm{t}}, \tag{29}$$

Where x is a deepness of the workpiece, T - its temperature, α is a thermal diffusivity and t is the time passed since the initial contact with an instrument. The contact area of a pin is small relatively to the area of workpiece itself and can be assumed as a point.

An initial condition implies uniform temperature distribution at time $t = 0$ and interior boundary condition:

$$T(\mathrm{x}, 0) = \mathrm{T}_0, \tag{30}$$

$$T(\mathrm{x} \to \infty, \mathrm{t}) = \mathrm{T}_0. \tag{31}$$

We calculate the power of friction force by (25) and assume it completely proceed to a workpiece due to its higher thermal conductivity relative to an instrument. Then temperature increase of the workpiece due to Coulomb friction can be evaluated as solution of ((29)) and dependence on the power:

$$\left.\frac{\partial T}{\partial \mathrm{x}}\right|_{\mathrm{x}=0} = \frac{P_{\mathrm{R}}}{Bl}. \tag{32}$$

With a value of contact area it gives us a value of heat flux ingoing to the workpiece. Hereafter we determine the temperature value at defined depth of workpiece and at defined time after process start as:

$$T(\mathrm{x},\mathrm{t}) - \mathrm{T}_0 = \frac{2\mathrm{P}_\mathrm{R}\sqrt{\alpha \mathrm{t}/\pi}}{\mathrm{Bl}}\exp(-\frac{\mathrm{x}^2}{4\alpha \mathrm{t}}) - \frac{\mathrm{xP}_\mathrm{R}}{\mathrm{Bl}}\mathrm{erfc}(\frac{\mathrm{x}}{2\sqrt{\alpha \mathrm{t}}}), \tag{33}$$

where l is thermal conductivity of a workpiece, B is the area of instrument surface, the function erfc is the complementary error function:

$$\mathrm{erfc}(\mathrm{z}) = \frac{2}{\sqrt{\pi}}\int_\mathrm{z}^\infty \mathrm{e}^{-\tau^2}\mathrm{d}\tau. \tag{34}$$

The (33) allow to determine temperature at the contact point of instrument and workpiece reached at each period of FSW process pre-heating stage.

3. Experimental results

For full problem examination additional experiments were performed. For these tests we used robotic FSW system based on an articulated armrobot (KUKA system). Such machines are flexible and their process automation allows sufficiently good repeatability. The experiments were repeated three times to ensure reproducibility of the obtained data and we used mean values for further calculations.

The conditions of the tests correspond to the described analytical model: a rotating tool moved along an aluminum plate without immersion providing Coulomb friction arrangements between the tool and workpiece. Characteristics of applied instruments and the process parameters are presented in Table 1.

Process force:	$2000N$	Workpiece material:	EN-AW 6060 T66
Instrument diameter:	$13mm$	Rotation speed:	$1000r.p.m.$
Translation speed:	$0.1m/min$	Measured temperature:	$458^\circ C$

Table 1. Parameters of the Coulomb friction experiment

4. Results

We plug the obtained experimental data into our theoretical model and use temperature as a control parameter. For this we applied equations (23), (24), (25) under conditions (20), (21), (22). The calculation results of friction forces, torques and power values for uniform force distribution, Hertz point contact $n = 1/2$, uniform force distribution $n = 0$ and cylinder-to

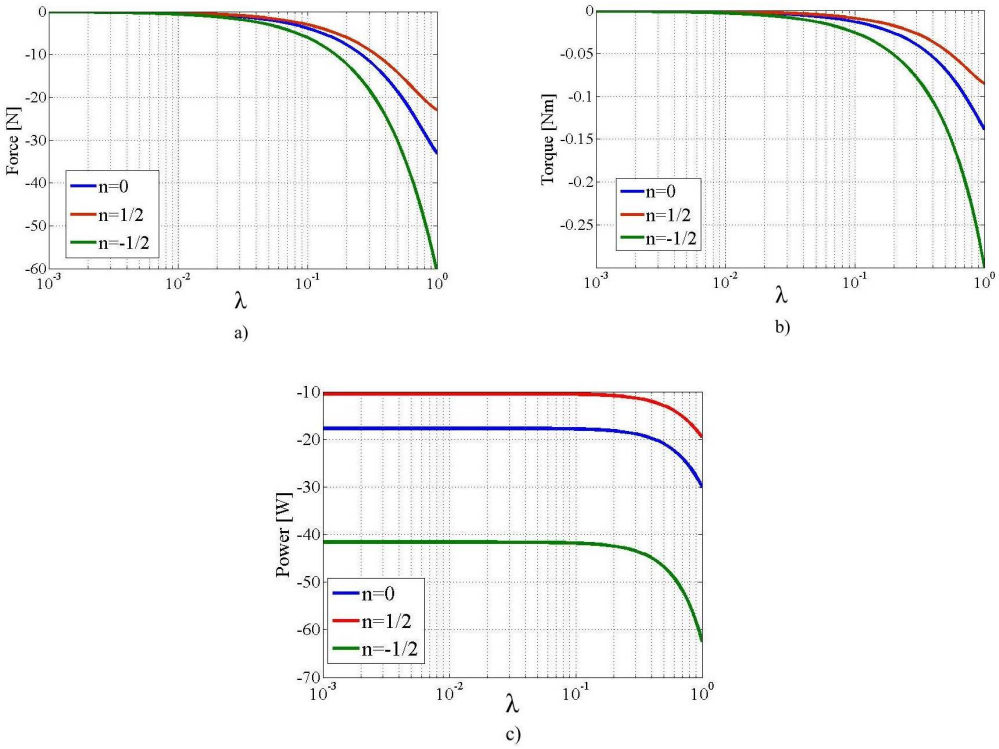

Figure 3. Force (a), torque (b) and power (c) generated by Coulomb friction process in the pre-immersion period of FSW

ellipse contact $n = -1/2$ are presented on Fig. 3. The presented curves depend on the parameter $\lambda = v/(\omega a)$ in the range from 10^{-3} to 10^{0}. In the experiment the value λ is equal to 2.5x10^{-3}, so it lays within the investigated range.

Maximal values of Coulomb friction force, torque and, respectively, power can be reached under maximal λ when rotation and translation velocities are equal. For FSW process the values are naturally laying within the lower limit of the range. Hence Coulomb friction should not have significant influence to workpiece heating process, what we checked with workpiece temperature calculation by thermal analysis. For this purpose we consider the depth value $x = 0.5$ mm (the distance from instrument tip) and imply it together with other experimental values from Table 1 to (33). The results are presented in 3D form (Fig. 4) depending on process time and λ. We can observe the same tendency as at the previous Fig. 3 – temperature here rises with λ increase. But even the highest analytically obtained temperature value does not exceed $80°C$ which is significantly less than the measured temperature (Table 1).

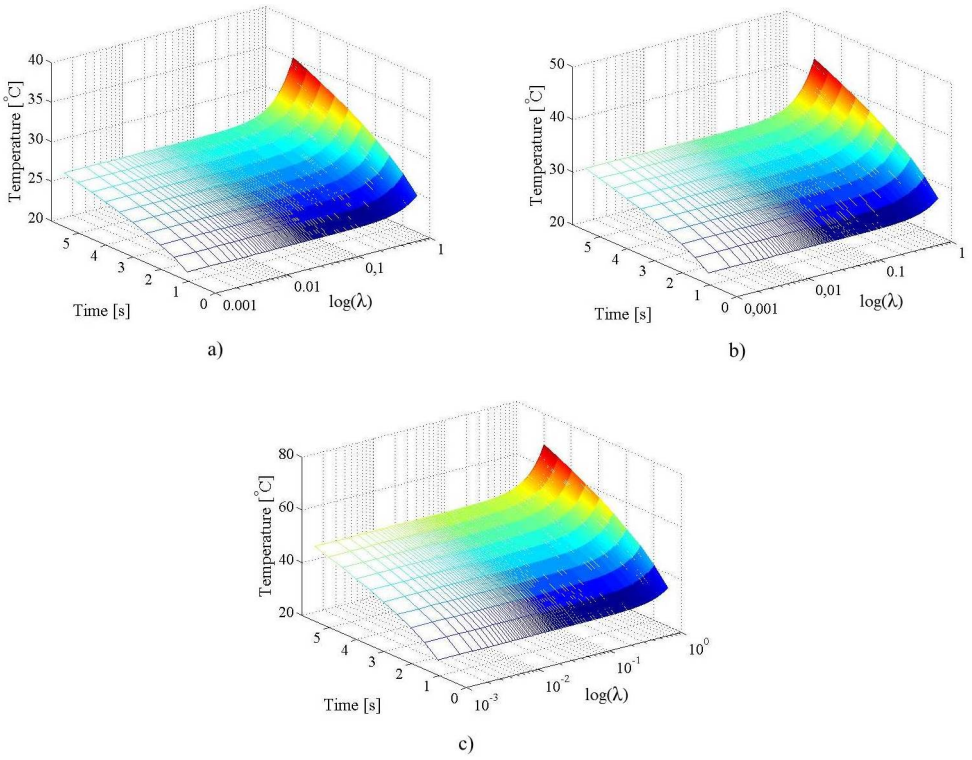

Figure 4. Temperature reached under influence of Coulomb friction in the pre-immersion period of FSW for $n = 1/2$ (a), $n = 0$ (b) and $n = -1/2$ (c)

The difference can be explained in the following way: the tip of instrument with predefined normal force 2000 N contacts the workpiece top plane and causes fractional deformation of the surface, which leads to additional heat generation due to material straining.

5. Conclusions

An analytical model approach has been described for analysis of a pre-immersion period of FSW process. The model concerns mechanical and thermal effects of Coulomb friction on power and temperature characteristics of the process. As the result we proved that the Coulomb friction plays significant role in preheat of the workpiece in front of the tool pin. But the Coulomb friction heat only provides not enough energy to make material plastic, hence further investigation of the topic is required.

Acknowledgments

This work was supported by Europäische Sozialfonds Europa für Thüringen and Europäische Union within the project Emissionsarme Maschinen und Prozesse (EMiMasch).

References

[1] Awang, M., M. V. F. Z., and David, S. Thermo-mechanical modeling of friction stir spot welding (fssw) process: use of an explicit adaptive meshing scheme. *SAE Technical Paper*, 01-1251 (2005).

[2] Bergmann, J.P.; Regensburg, A. F. K. Prozessentwicklung zur quantitativen Bewertung der Materialverteilung mit friction stir processing-hergestellten surface composites. *DVS Congress, DVS Berichtsband*, 215 (2015).

[3] Incropera, F., D. D. B. T., and Lawine, A. *Fundamentals of heat and mass transfer, 6th ed.* John Wiley and Sons, Hoboken, 2006.

[4] Iordache, M., B. C. I. D., and Nitu, E. Numerical simulation of the friction stir welding process using coupled eulerian lagrangian method. *IOP Conf. Series: Materials Science and Engineering*, 145 (2016).

[5] Mishra, R. S., M. M. W. *Friction stir welding and processing.* Springer, New York, 2007.

[6] Narrish, J. *Advanced welding processes.* Woodhead Publishing, Cambridge, 2006.

[7] Simar, A., A.-F. M.-N. State of the art about dissimilar metal friction stir welding. *Science and technology of welding and joining 22*, 5 (2017), 389–403.

[8] Song M., K. R. Thermal modeling of friction stir welding in a moving coordinate system and its validation. *Machine tools and manufacture*, 43 (2003), 605615.

[9] Thomas, M.W.; Nicholas, J. N.-J. M. M. T.-S. P. D. C. *Friction stir butt welding.* Great Britain Patent No. 9125978.8, Great Britain, 1991.

Nataliia Dubovikova, Ph.D.: Ilmenau Technical University, Max-Planck-Ring 12, 98693 Ilmenau (*nataliia.dubovikova@tu-ilmenau.de*). The author gave a presentation of this paper during one of the conference sessions.

Erik Gerlach, Ph.D.: Ilmenau Technical University, Max-Planck-Ring 12, 98693 Ilmenau (*erik.gerlach@tu-ilmenau.de*).

Igor Zeidis, Ph.D.: Ilmenau Technical University, Max-Planck-Ring 12, 98693 Ilmenau (*igor.zeidis@tu-ilmenau.de*).

Klaus Zimmermann, Prof.: Ilmenau Technical University, Max-Planck-Ring 12, 98693 Ilmenau (*klaus.zimmermann@tu-ilmenau.de*).

Design study and development of mechatronic treadmill for gait reeducation

Slawomir Duda, Grzegorz Gembalczyk, Eugeniusz Switonski

Abstract: The purpose of this article is to present a novel mechatronic system for gait reeducation which consists of two main components: body weight support system (BWS) and training treadmill. In addition, the device is equipped with sensors for measuring the rope tension, rope inclination angle and foot pressure on the ground. The transmission of control and measurement signals between the reeducation device and the computer with the control system is realized by means of three real time boards. This publication covers issues related to the process of device design, integration of all developed components and implementation of the treadmill speed control system. The treadmill is controlled by a feedback loop with a rope angle measurement but it requires a proper conversion of the continuous signal to a digital square wave signal of variable period. Due to the connection of the treadmill control signals to the buttons in the treadmill control panel and related limitations, developing an optimal treadmill speed control system was an interesting engineering problem.

1. Introduction

Reeducation of walking is one of the key stages of the rehabilitation program for paralyzed persons – most often as a result of strokes, spinal cord injuries or neurological disorders. In traditional gait reeducation methods, physiotherapists, often in the course of rehabilitation, support patients during gait reeducation. In order to facilitate and improve the locomotive function recovery process, researchers have developed new therapeutic strategies and therapies in recent years. Today, the therapist's work is greatly enhanced by mechatronic devices.

Since the 1980s, the studies on locomotive training are conducted with the use of the partial body weight support (BWS). This strategy assumes that the weight of the patient is reduced by the winch, and the training itself is performed using the treadmill. In addition, therapists manually assist the patient in obtaining correct leg movements [1,2].

The effectiveness of this method has been confirmed by numerous studies performed on persons with various diseases [3-7]. The main advantage of exercises with the treadmill and relief is the high repetition of exercises, much greater than in case of traditional methods.

Despite favorable statistics, the training using the treadmill and stationary winch limits the patient's freedom of movement, which contributes to the maintenance of an unnatural gait pattern.

This disadvantage has been minimized in the ZeroG device [8], as well as in the mechatronic device for reeducation of gait, developed at the Institute of Theoretical and Applied Mechanics (IMTS) at the Silesian University of Technology [9] (see Fig.1). In these devices, the patient moves on the floor and the relief system follows them.

a)  b) 

Figure 1. Devices for gait rehabilitation: a) zeroG, b) mechatronic device for lokomotor training developed at Silesian University of Technology

The device developed at the IMTS worked on the principle of the crane following the patient. The movement of the trainer and the winch was therefore possible in all directions, and it was limited only by the supporting frame structure. According to the experimental studies, when using the winch following movement behind the patient's lateral movements, the recorded kinetic parameters of the patient's gait corresponded better to the parameters of the natural gait (especially displacement in the lateral axis), unlike using the stationary relief system [10,11]. This advantage has a good effect on improving the stability of the human body in the frontal (medial-lateral) axis [12]. The implementation of the device of such a large size in the rehabilitation center is often a big problem due to local conditions, and the frame structure itself (made of aluminum structural profiles) significantly raises the cost of the device. For these reasons, a simplified version of the device was developed, which aimed at minimizing the dimensions and prices. From the designer point of view in the process of designing an optimal system the key is to create solutions with greater autonomy, which is associated with re-configuring of existing objects [13]. In order to obtain the possibility of the following movement of the winch behind the patient's lateral movements, the structure of the winch, winch trolley and their drive systems are left unchanged, while the winch movement in the patient's sagittal plane takes place using the commercial treadmill. The desirability of such systems is the automatic adjustment of the speed of the treadmill which can be generally interpreted as an active system for minimizing the angle of rope inclination [14,15]. This type of system should autonomously

adjust the speed of the walking belt of the treadmill to the patient's gait speed, and this change must be made in a smooth and safe manner, without the physiotherapist's interference [16]. This article outlines the issue concerning the development of the treadmill speed control system with minimum interference in electronic and mechanical systems of the commercial treadmill. This is done by simulating the press of buttons on the treadmill control panel. Due to the type of connection between the control unit and the buttons in the treadmill control panel as well as related limitations, developing an optimal treadmill speed control system was an interesting engineering problem.

2. Mechatronic system for gait reeducation

The main components constituting the electromechanical part of the discussed rehabilitation system are shown in the next illustration (see Fig.2).

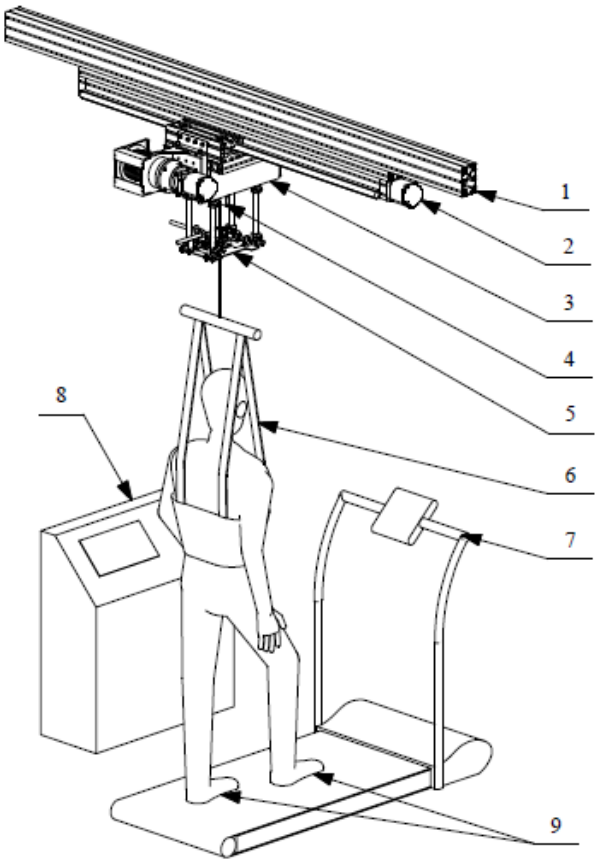

Figure 2. Mechatronic treadmill for gait reeducation

Unlike other devices of this type, currently available on the market, the unloading system (3) can move – it performs the linear movement along the girder (1). This beam is attached to the ceiling,

which is not shown in the illustration. The winch movement is done by the propeller that is coupled with the servo motor (2). It is important that the direction of movement of the trolley is perpendicular to the direction of the patient's walk on the treadmill (7). The trainee is fastened to the end of the winch rope by means of the orthopedic harness (6). The illustration also shows the control unit (8) in which servo amplifiers are mounted. Additional elements used to control the operation of the device are systems for measuring the rope tension (4), angle of rope inclination (5) and shoe inserts with pressure sensors (9). These inserts are used to identify the foot pressure on the ground and determine the patient's gait phase, as well as predictions of potentially dangerous situations, such as falls. If the foot pressure configuration meets the relevant safety criterion, then the device operates in the working mode. Otherwise, the device is stopped. In the research conducted in this study, the signals from the inserts were not used.

The described gait reeducation device works in real-time mode and is controlled by the MATLAB/Simulink software, installed on a PC computer. The coupling between the unloading system and the PC is realized by means of two RT-DAC4/PCI Real time boards. Measurement signals are conditioned via a specially designed interface. The signals generated by the computer are sent to the control unit in which the servo inverters of the drive motors are located. The developed version of the device uses the commercially available treadmill designed for walking along with the 0.8 kW synchronous motor. The communication between the treadmill and the computer is done via the real time RT-DAC/USB2 card and the additionally developed electronic system. The idea of components cooperation in this device for gait reeducation is shown in the picture below (see Fig.3).

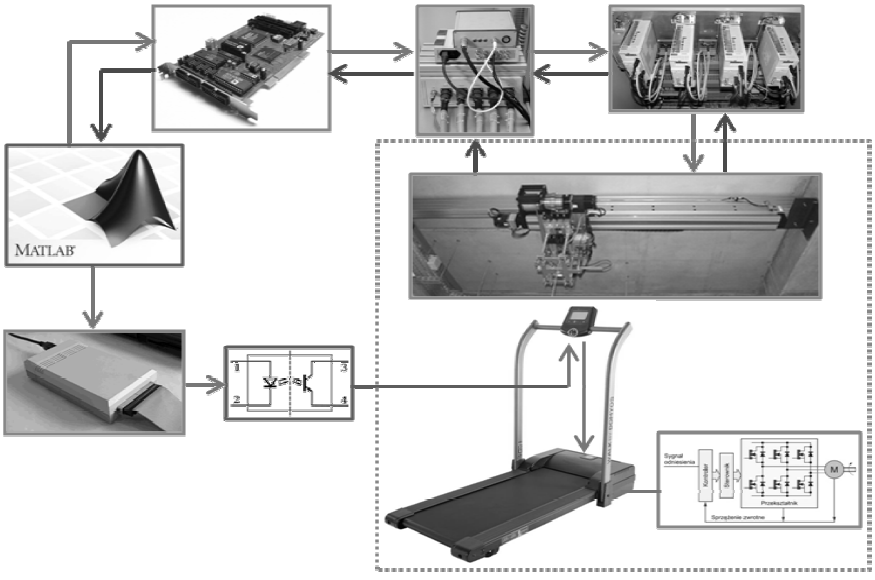

Figure 3. Components cooperation in mechatronic treadmill for gait reeducation

In order to minimize the interference with the treadmill drive system, only the control panel was modified. This was accomplished by the parallel connection of an additional controller, designed to simulate the operation of the buttons located in the treadmill control panel. The developed electronic system was built using opto-couplers controlled by digital signals, generated by the control system in the PC. The change of the digital signal from high to low (and return to high status after a minimum of 0.2 seconds) was equivalent to the press of the button on the treadmill control panel, which results in a speed change of 0.1 km/h.

3. Treadmill speed control system

This paper presents the adjustment algorithm, in which the speed of the treadmill is adjusted to the walking speed of the patient. The adaptation of the treadmill speed in the developed solution is based on the measurement of the rope inclination angle. If the rope inclination angle φ is within the range of the adopted reference value, the speed of the treadmill remains unchanged. If the trainee moves forward, and the rope inclinations above the reference value, the treadmill is started and accelerates until the angle value is within the reference value range. Likewise, if the rope inclination angle is smaller than the reference value, the speed of the treadmill is reduced
(see Fig. 4).

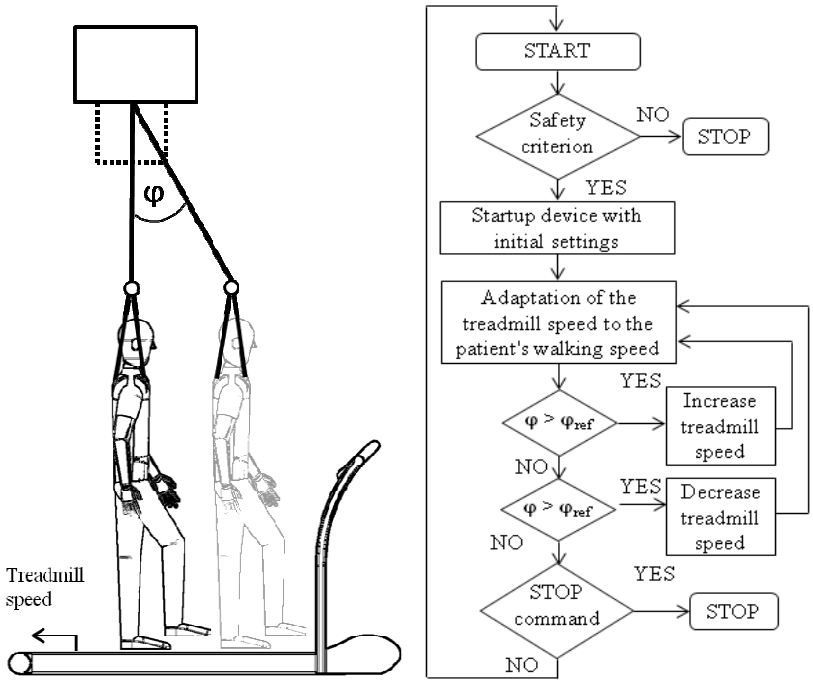

Figure 4. Scheme of algorithm for treadmill speed adaptation

Due to the technical solution for the treadmill speed control system, which assumes the simulation of the press of buttons on the treadmill control panel by changing the digital signal value at the output of the real-time card, the output signal should be a periodically variable rectangular signal. This condition was achieved by developing the speed change generator, in which the forcing frequency is increased along with the change in the rope inclination angle. When the permissible range of the rope inclination ($-\varphi_{ref}$; φ_{ref}) is exceeded, the digital signal change at the outputs that control the opto-coupler system, connected to the treadmill control panel, is generated. The speed control change algorithm uses the sine function of the global variable T_i, which is calculated at each interaction and depends on the value of the rope inclination angle and the calculation step T0. In turn, the rectangular signal was obtained by using the signum function. The output value of the signal is given by:

$$y = \frac{1}{2}(sign(\sin(T_i)) + 1)). \quad (1)$$

In the case, where the rope inclination angle φ is between 1° and 2.5°, the parameter T_i is defined as:

$$T_i = 2\pi\left(T_{i-1} + T_0 + T_0(\varphi - \varphi_{ref})par\_\varphi\right), \quad (2)$$

however, when the angle φ is greater than 2.5°:

$$T_i = 2\pi(T_{i-1} + 5T_0). \quad (3)$$

The frequency of the sinusoidal signal also depends on the additional variable par_φ that determines the linear relationship between the rope inclination angle and the sinus function frequency. The experiments showed that the maximum frequency of the change of the forcing signal that is recorded by the treadmill driver is about 3 Hz. At a higher frequency signal, not all pulses were recorded. It was also assumed that the permissible rope inclination angle (angle at which the speed is unchanged) is 1° and the maximum forcing frequency is achieved at the inclination angle of 2.5°. Based on this data, the value of the parameter par_φ was 1.33.

The next diagram (see Fig. 5) shows how the sinusoidal signal frequency changes in the function of the rope inclination angle and what value is added in each iteration to the variable T_i.

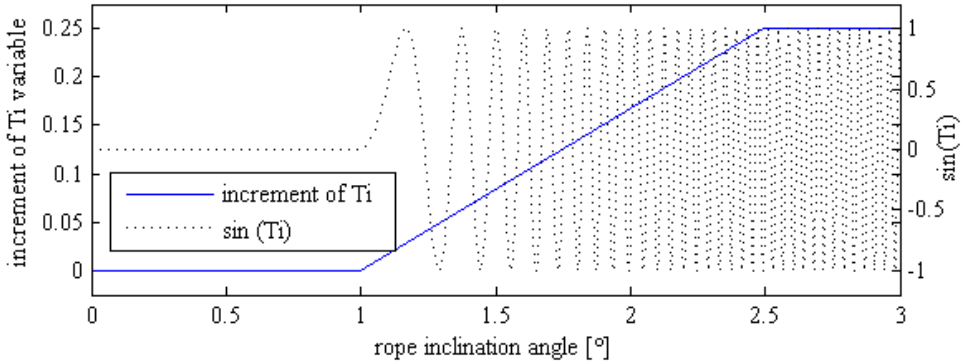

Figure 5. Increment of variable T_i and the sine function of the global variable T_i as a function of the rope inclination angle

In addition, to avoid delays in the control signal that result from adding the variable T_i, the additional reset module of this variable was added when decreasing/increasing the rope inclination angle to the accepted value. The developed control signal generator was implemented in the Matlab Simulink environment. The analogous algorithm was implemented to generate the digital signal responsible for speed reduction, with negative angles being multiplied by -1.

4. Experimental studies

The developed algorithm was tested on a real object. The study was performed for two variants. In the first one (see Fig. 6 and Fig. 7), the testing person was moving at a different speed of walking on the treadmill running at a constant speed of 2 km/h (the treadmill speed control system was inactive).

Another diagrams presented the recorded change in the rope inclination angle value and digital signals that control the buttons responsible for increasing and decreasing the speed of the treadmill.

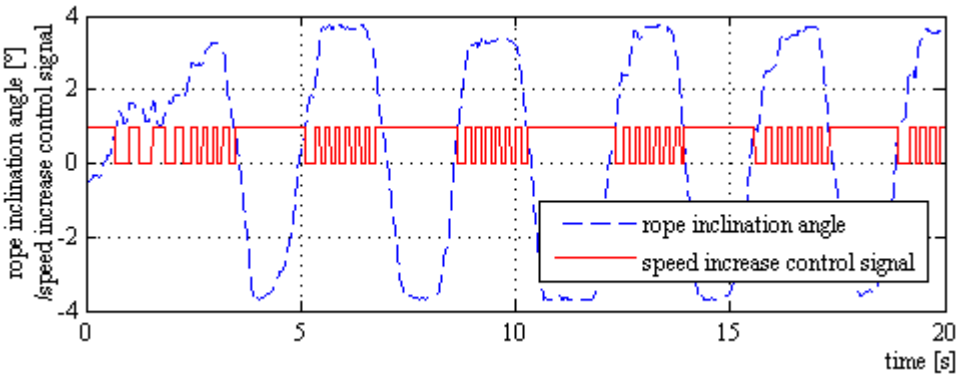

Figure 6. Rope inclination angle and signal for increasing the treadmill speed as a function of time

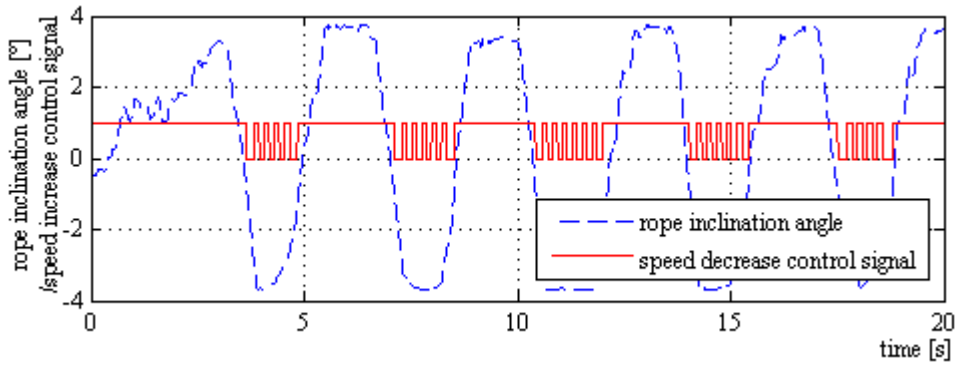

Figure 7. Rope inclination angle and signal for decreasing the treadmill speed as a function of time

In the second test, the testing person was moving at different walking speeds with the active treadmill speed control system (the speed of the treadmill movement is adapted to the walking speed). Two more graphs (see Fig. 8 and Fig. 9) show the results of experimental studies performed with the active treadmill speed control system.

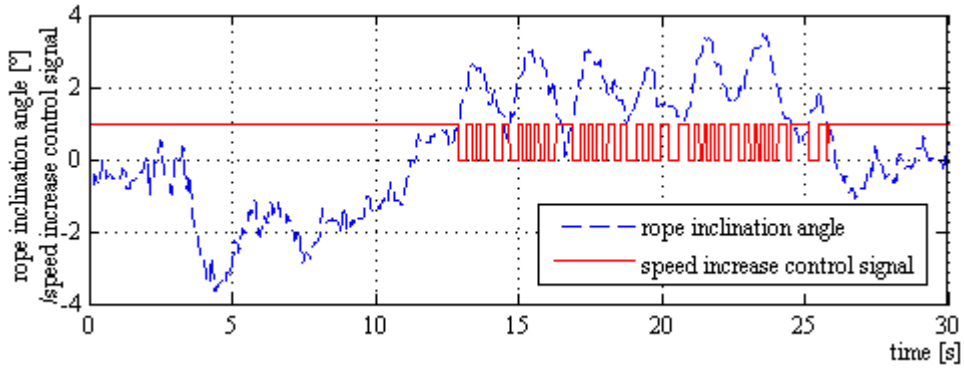

Figure 8. Rope inclination angle and signal for increasing the treadmill speed as a function of time

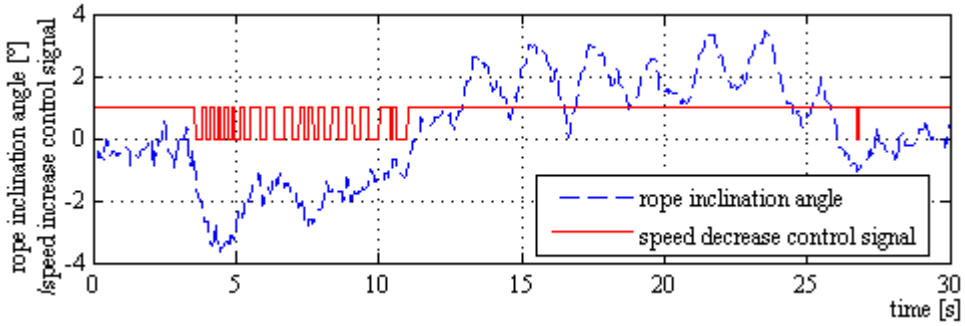

Figure 9. Rope inclination angle and signal for decreasing the treadmill speed as a function of time

5. Conclusions

The article presents the mechatronic device for locomotive training with the controlled treadmill speed, using the commercial treadmill. The treadmill speed control method, implemented by the treadmill motion coupling with the inclination angle of the relief system utilizes an additional control system that simulates the press of buttons on the treadmill speed control manual panel. The presented solution was reported for patent.

The basic problem solved in this paper is the development of the treadmill speed control system with the least possible interference in its design, treadmill system coupling with the relief system, development of treadmill speed control algorithms.

The experimental studies showed that the developed algorithm works correctly – the treadmill speed varies depending on the rope inclination angle. Compared to the tests performed for the treadmill operating at a constant belt speed, the rope inclination angle is reduced. However, the dynamics of changes is unsatisfactory. This problem is caused by a small acceleration of the treadmill, which results from the factory settings of the drive motor controller.

As presented in this article, there are several couplings between the subsystems in the system under consideration. The treadmill speed control is performed without direct feedback loop with its speed measurement. The coupling is the result of the rope inclination, being the consequence of a faster or slower walk with respect to the moving treadmill. Despite the correct operation of the control system, the results of studies indicate the need to modify the device. Further works will concern the modernization of the treadmill drive system, in order to increase the dynamics of the drive system's response to forcing signals.

References

[1] Lovely, R.G., Gregor, R.J., Roy, R.R. and Edgerton, V.R. Effects of training on the recovery of full-weight-bearing stepping in the adult spinal cat. *Experimental neurology* 92, 2 (1986), 421-435.

[2] Tefertiller, C., Pharo, B., Evans, N. and Winchester, P. Efficacy of rehabilitation robotics for walking training in neurological disorders: A review. *Journal of Rehabilitation Research & Development* 48, 4 (2011), 387-416.

[3] Protas, E.J., Holmes, S.A., Qureshy, H., Johnson, A., Lee, D. and Sherwood, A.M. Supported treadmill ambulation training after spinal cord injury: a pilot study. *Archives of physical medicine and rehabilitation* 82, 6 (2001), 825-831.

[4] Hesse, S., Werner, C., Bardeleben, A. and Barbeau, H. Body weight-supported treadmill training after stroke. *Current atherosclerosis reports* 3, 4 (2001), 287-294.

[5] Barbeau, H. and Visintin, M. Optimal outcomes obtained with body-weight support combined with treadmill training in stroke subjects. *Archives of physical medicine and rehabilitation* 84, 10 (2003), 1458-1465.

[6] Giesser, B., Beres-Jones, J., Budovitch, A., Herlihy, E. and Harkema, S. Locomotor training using body weight support on a treadmill improves mobility in persons with multiple sclerosis: a pilot study. *Multiple Sclerosis Journal* 13, 2 (2007), 224-231.

[7] Scherer, M. Gait rehabilitation with body weight-supported treadmill training for a blast injury survivor with traumatic brain injury. *Brain injury* 21, 1 (2007), 93-100.

[8] Hidler, J., Brennan, D., Black, I., Nichols, D., Brady, K. and Nef, T. ZeroG : Overground gait and balance training system. *Journal of Rehabilitation Research & Development* 48, 4 (2011), 287-298.

[9] Duda, S., Gąsiorek, D., Gembalczyk, G., Kciuk, S. and Mężyk, A. Mechatronic device for locomotor training. *Acta mechanica et automatica* 10, 4 (2016), 310-315.

[10] Duda, S., Gembalczyk, G., Jurkojć, J., Kciuk, S. and Michnik, R. Mechatronic solution of components cooperation in the device for gait reeducation. *Multibody dynamics.* Barcelona, 2015.

[11] Mrozowski, J. and Awrejcewicz, J. Changes in the gait characteristics caused by external load, ground slope and velocity variation. *Communications in Nonlinear Science and Numerical Simulation* 16, 5 (2011), 2313-2318.

[12] Mrozowski, J., Awrejcewicz, J. and Bamberski, P. Analysis of stability of the human gait. *Journal of theoretical and applied mechanics* 45, 1 (2007), 91-98.

[13] Sękala, A., Banaś, W., Gwiazda, A., Monica, Z., Kost, G. and Hryniewicz, P.: Modelling of robotic work cells using agent based-approach. *IOP Conference Series: Materials Science and Engineering* 145, 5 (2016), 751-756.

[14] Sibielak, M., Raczka, W., Konieczny, J. and Kowal, J.: Optimal control based on a modified quadratic performance index for systems disturbed by sinusoidal signals. *Mechanical Systems and Signal Processing* 64-65 (2015), 498-519.

[15] Świtoński, E. Modelowanie mechatronicznych układów napędowych [Modelling of mechatronic drive systems]. Wydawnictwo Politechniki Śląskiej, Gliwice, 2004. [In Polish]

[16] Mężyk, A., Czapla, T., Klein, W. and Mura, G. Numerical simulation of active track tensioning system for autonomous hybrid vehicle. *Mechanical Systems and Signal Processing* 89 (2017), 108-118.

Slawomir Duda, Associate Professor: Silesian University of Technology, Institute of Theoretical and Applied Mechanics, Akademicka 2A, 44-100 Gliwice, Poland (S*lawomir.Duda@polsl.pl*).

Grzegorz Gembalczyk, M.Sc. (Ph.D. student): Silesian University of Technology, Institute of Theoretical and Applied Mechanics, Akademicka 2A, 44-100 Gliwice, Poland (Grzegorz. Gembalczyk@*polsl.pl*). The author gave a presentation of this paper during one of the conference sessions.

Eugeniusz Switonski, Professor: Silesian University of Technology, Institute of Theoretical and Applied Mechanics, Akademicka 2A, 44-100 Gliwice, Poland (Eugeniusz.Switonski@*polsl.pl*).

Macro- and micro-scanners for laser applications: Non-linear characteristics and their impact on biomedical imaging

Virgil-Florin Duma

Abstract: We present some of our main results in the field of optomechatronic laser scanners, built both as macro- and micro-devices. Several types of scanners are considered, from those that are the most utilized nowadays: with oscillatory mirrors (galvanometer scanners (GSs) or Micro-Electro-Mechanical Systems (MEMS)), with rotational polygonal mirrors (PMs) with different configurations, and with rotational refractive elements (also named Risley prisms). The advantages and drawbacks of each solution are pointed out, in a comparative look. The optimization of oscillatory scanners with strongly non-linear scanning functions is briefly presented from the point of view of their duty cycle and of their capability to provide distortion-free images in biomedical applications, for example for Optical Coherence Tomography (OCT). The exact characteristics of rotational PMs are discussed, with regard to their actual non-linearity with regard to approximate, linear functions. Risley prisms are presented, with their exact scan patterns that we have determined using mechanical design programs, in order to capture and model their non-linearity (while experimental works have validated these results). Conclusions are drawn regarding the application of such devices, especially for high-end fields like OCT.

1. Introduction

Laser scanners are one of the most used optomechatronic devices nowadays. They are employed in a large area of applications, from low cost, commercial ones such as barcode scanning to industrial ones (e.g., for laser manufacturing or optical metrology) and finally, to high-end ones, especially in biomedical imaging. The challenges of the latter has imposed since the early 1990s a strong development of laser scanners in order to allow for real time *in vivo* imaging, with techniques like Optical Coherence Tomography (OCT) [1,2] or Confocal Microscopy (CM) [3].

Numerous scanning systems have been developed [4, 5], but there are five types that are most used nowadays: polygon mirrors (PMs), galvanometer scanners (GSs), refractive, acousto-, or electro-optical scanners. The present paper discusses the first three types of such devices (i.e., the most common ones), with a stress on our contributions in their analysis and optimization, especially for high-end applications like OCT [6]. This brief overview is focused on the non-linear aspects of their characteristics, i.e., of the one-dimension (1D) scanning functions of PMs or GSs, as well as of the scan patterns of two-dimensional (2D) scanners with refractive rotational Risley prisms.

2. Polygon mirror (PM) scanning heads: characteristics and applications

PMs have different configurations: normal and inverted, simple or double, prismatic or pyramidal [4]; they have high rotational speeds and a certain number of facets (from 5 to 72, typically, but also up to 128), therefore high scan frequencies, but they are also large, with mechanical issues like vibrations and wear, as well as with higher costs per scan axis – with regard to other scanners [7].

PMs have, with regard to GSs, another major issue: their facets are placed at a certain distance (R, the apothem of the PM) from its pivot O – Fig. 1(a) [8]. This produces a non-linearity of the scanning function, i.e., of the current position $h(\theta)$ of the laser beam that is refracted by the objective lens L_1 of the scanner parallel to its optical axis (O.A.) – Fig. 1(b).

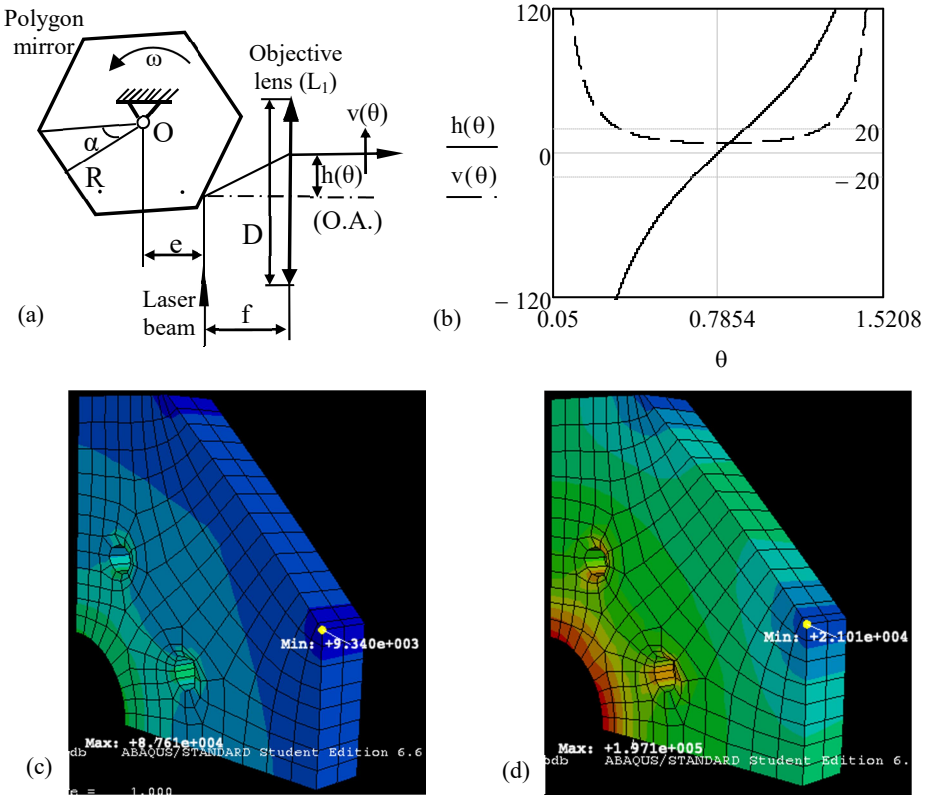

Figure 1. (a) Polygon mirror (PM) scanning head with constructive parameters (R, e, $L=f$, $\alpha=\pi/n$, D) and characteristic functions (h and v); (b. c) values of the mechanical stress for n=8, with R=25 mm, for (b) ω=80 krpm and (c) ω=120 krpm – Finite Element Analysis with ABAQUS aluminium alloy 5052 (tensile strength equals 268 MPa) shown for a quarter of the PM.

In numerous studies this non-linearity is neglected – especially when small fields-of-view (FOV) of the PM are considered. For example in swept sources (SS)/broadband laser sources swept in frequency in SS-OCT (i.e., for PMs with numerous width facets [9, 10]). Other studies have approached this issue, in order to optimize the off-axis position of the PM for a minimum non-linearity of $h(\theta)$. In contrast to more complicated vectorial approaches or to approximate ones, we developed a rigorous, but easy-to-use theory for the analysis of PMs, deducing novel, simple equations for: $h(\theta)$, the scanning speed $v(\theta)$ – Fig. 1(b), the characteristic angles, and the duty cycle η of the device (the latter defined for PMs as the ratio of the useful scan angle (considered for scanning the L1 lens) and the total scan angle of a PM facet) [11]:

$$h(\theta) = R\sqrt{2} - e - \frac{R}{\cos\theta} + e \cdot \tan\theta - \frac{L}{\tan 2\theta} \tag{1}$$

$$v(t) = \frac{dh}{d\theta} \cdot \frac{d\theta}{dt} = \frac{\omega}{\cos^2\theta}\left[e - R\sin\theta + \frac{L}{2\sin^2\theta}\right] \tag{2}$$

$$\eta = n\frac{\theta_2 - \theta_1}{2\pi} \tag{3}$$

where the following notations were used: e, eccentricity of the incident beam with regard to the pivot O; n, number of facets => angle of half of PM facet $\alpha=\pi/n$; $L=f$, distance from the fixed beam to the lens L_1 (to its principal object plane), equal to the focal length of L_1; D, diameter of the lens L_1, equal to the maximum scanning domain; θ_1 and θ_2, rotational angles of the PM for which the margins of the useful scanned space (i.e., of the objective lens) are reached.

This theory also allows for considering the finite width of the laser beam, although it has been developed in a simple way, using a single ray approach (i.e., the axis of the laser beam, as shown in Fig. 1(a)) [11].

3. Galvanometer-based scanners: analysis and optimization

Oscillatory mirror scanners – resonant or galvanometer-based, the latter with an adjustable oscillatory/scan frequency, have numerous advantages: they are light weight, with good scan amplitudes and reasonable costs, while their technology is mature [12]; they also have a major drawback, i.e., lower scan frequencies than PMs, because of their oscillatory movement. Thus, their necessary deceleration and acceleration periods (the so-called “stop-and-turn” portions) limit severely the time efficiency/duty cycle of GSs, defined in this case as the ratio of the useful/”active” time interval t_a (considered for scanning with constant speed) and the total period T of the oscillation of the galvomirror of the device (Fig. 1):

$$\eta = t_a / T\,. \tag{4}$$

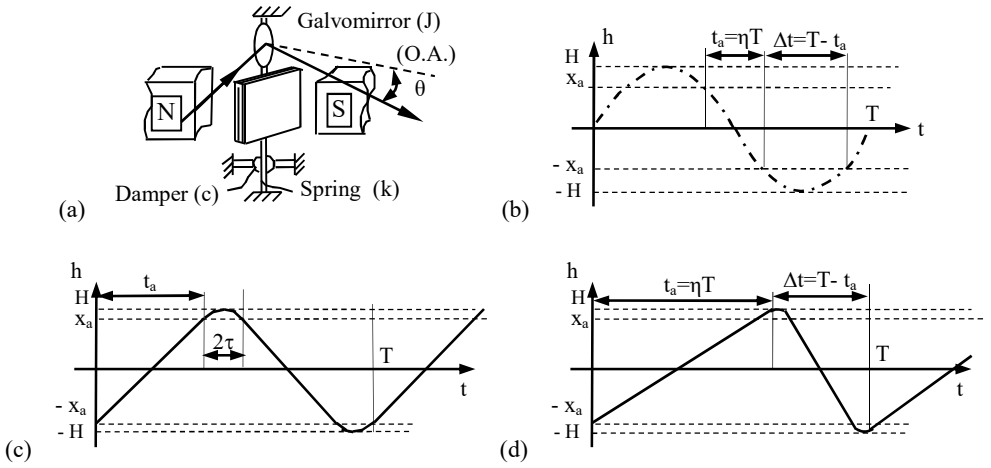

Figure 2. (a) Galvanometer-based scanner (GS), with characteristic parameters; (b-d) Scanning functions (output signals) of the GS: (b) sinusoidal; (c) triangular; (d) sawtooth.

We have investigated GSs, especially with regard to high-end applications like OCT. Thus, as most GS users usually assume that they are working just the same regardless of their working parameters such as theoretical duty cycle (i.e., of the input signal of the device), scan frequency and scan amplitude, a first experimental study has been focused on the real behavior of GSs for tough mechanical regimes [13]. Thus, we demonstrated that as the scan frequency and scan amplitude increase, there is an *effective duty cycle* (a parameter that, to our knowledge, we have introduced), which characterizes the output signal of the GS (i.e., the current position of the galvomirror), which is lower than the theoretical one. This is due to the fact that, as the scan frequency and amplitude increase, the device needs more time to decelerate, stop, and accelerate. The stop-and-turn portions, therefore the time interval of the non-linear portions of the scanning functions – see Figs. 2(c) and (d) – increase, thus η decreases. For imaging techniques like OCT, we demonstrated in [13] that triangular scanning is the most convenient from this point of view, of obtaining as high as possible duty cycles. Sinusoidal scanning – Fig. 2(b) - is convenient from a mechanical point of view, as it is the smoothest oscillatory regime, but the pixels in a generated image are not equally spaced, therefore the image is distorted, and the duty cycle is the smallest one. Limits of the scan amplitude that can be used as a function of the scan frequency have also been deduced [13].

Using the above study, another group has applied sawtooth scanning [14], but discarding the distorted portions, calculated based on [13]; collated images of the retina (for Doppler OCT) has thus been obtained [14]. Inspired by this study, we have deepened the investigations on GSs, in order to offer the community a useful tool to obtain collated images. The necessity for such images is given by

the fact that OCT images for example are obtained on small areas of the investigated samples (even 0.5 x 0.5 mm^2) in order to have high lateral resolutions. Samples, however, are usually larger (e.g., for retina, teeth, skin, or endoscopy), therefore individual OCT images have to be put together to get the whole picture. If distorted areas appear at the margins of individual images, than the whole image will be affected by a sort of grid of blurred lines that could limit investigations or even generate false responses.

To solve this issue, in [15] we have performed a detailed study of this topic, obtaining first the effective duty cycle as a function of the theoretical duty cycle, with regard to different levels of the scan frequency and of the scan amplitude. To our knowledge, an interesting phenomenon has been observed for the first time regarding this aspect, i.e., a saturation of the GS: if the theoretical duty cycle is increased too much, the effective one does not increase any more - not even a little; it actually starts to decrease. Its maximum value is thus not reached towards 90% in terms of theoretical duty cycle, but at the level of 75%. As expected, this phenomenon is more obvious as the scan frequency is higher and as the scan amplitude is larger.

With this evaluation, relationships of the effective duty cycle have been obtained for both triangular and sawtooth scanning signals, and also for different regimes of the above parameters. Using the high resolution Gabor Domain Optical Coherence Microscopy (GD-OCM) developed in Rochester [16], we validated these relationships by measuring directly the distortions in the OCT images. For triangular scan for example – Fig. 2(c), the expression of this effective duty cycle is [15]:

$$\eta = \frac{1}{2} - \frac{2\tau}{T} . \tag{5}$$

Algorithms to discard these distorted portions and thus to obtain collated images without artifacts have also been obtained [15].

The solution in order to obtain the maximum possible effective duty cycle of GSs has been indicated in the literature [12]: to introduce in the input signal of the GS a controlled non-linearity. While this non-linear portion has been indicated to be ideally sinusoidal [12], we have approached this problem and demonstrated theoretically that [17], for a maximum duty cycle, not a sinusoidal, but a parabolic stop-and-turn portion should be introduced between the useful, linear portions of the scanning function. In this optimal case, the duty cycle has the expression [17]:

$$\eta_p = \frac{T_i - 1}{T_i + 1}, \tag{6}$$

where

$$T_i = \frac{4HL[1 + (H/L)^2]T_{\max}}{Jv^2}, \tag{7}$$

with the following notations: J is the moment of inertia of the mobile element, L is the distance from the pivot of the galvomirror to the scanned plane, H is the scan amplitude (Fig. 2), T_{max} is the maximum torque, and v is the scanning speed (constant, of the linear portion of the scanning function/output signal of the GS).

An important aspect that has to be highlighted is related to the fact that in all the studies above the GS system has been considered as a black box. However, the control structure of the scanner also has to be optimized, and this problem has been approached in numerous studies [18, 19]. In [20] we have offered alternative, low-cost solutions for the GS control that provide speed and/or stability to disturbances – in the meanwhile using existing structures of off-the-shelf GSs.

4. Handheld scanning probes for OCT

Dual axis 2D scanners (usually with two GSs with perpendicular axis) are necessary for all OCT setups which have lateral scanning of samples. For experimental OCT systems, placed on the optical table, such scanners are fixed. In a clinical environment, however, the scanning system has to be included in a handheld probe that can be placed in front of the area of interest of the patient (i.e., eye, teeth or gums, different portions of the skin, ear, or throat. For existing systems applied in the clinic, such handheld probes are well-designed and with good functionality, but heavy, around 2 kg – therefore difficult to handle by the medical personnel throughout the day.

Efforts have been thus made by different groups to develop alternative, improved probes. The seminal work in [21] has thus achieved a handheld probe with a 2D double GS. To achieve an even lower weight, in [22] Micro-Electro-Mechanical Systems (MEMS)-based handheld probes have been developed, and they reached a weight as low as 0.5 kg.

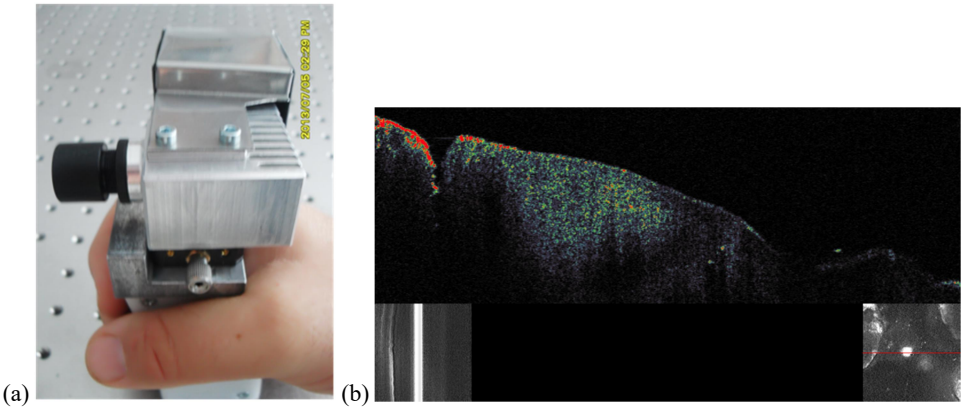

Figure 3. (a) Handheld scanning probe with a 1D GS for OCT [24, 25]; (b) cross-section obtained with an in-house developed OCT system and a handheld scanning probe of the type (a) – for the interface between the ceramic inlay and the tooth in the treatment of dental cavities [28].

Our approach in this respect has been to develop an as simple as possible, low cost, and low weight handheld probe – with minimum, but still with a satisfactory functionality. The solution has been to develop a range of 1D GS-based probes, which only provide B-scans/cross-sections of the investigated sample [23-25]. In numerous applications, for example in dentistry [26], this is satisfactory, as the dentist scans anyway the tooth or the gingiva in the area of interest, thus providing the third scan axis on the sample [27, 28]. A convenient mass of 0.25 kg has been obtained for these handheld probes, and their functionality has been demonstrated for ENT (ear-nose-throat) [23], dental prostheses [24], or tissue [25]. Another major direction of investigation is also related to the Non-Destructive Testing (NDT) for industrial applications, for which we have demonstrated that OCT can replace the more costly, labor consuming and lab-based technique, i.e. Scanning Electron Microscopy (SEM) – for the assessment of fractures of metallic materials [29].

5. Scanners with Micro-Electro-Mechanical Systems (MEMS)

While 2D MEMS-based probes have been explored [22], and they are more light weight with regard to GS-based probes, they have been employing the sinusoidal scanning, that is specific to resonant scanners. As discussed above, we demonstrated in this respect that such sinusoidal scanning produces the largest distortions in OCT images, while triangular scanning is capable to produce the most distortion-free OCT image at the highest duty cycle, with regard to the other two common scanning regimes, i.e., sawtooth and sinusoidal [13]. The latter, used by Fujimoto *et al.* at MIT [22], required extensive post-processing of images, which makes real-time (thus, *in vivo*) imaging impossible and adds significant costs; one must also carefully account for how noise in the original images may affect image quality after post-processing. In this context, we achieved the first distortion-free OCT imaging (without post-processing) [30], with a prototype MEMS-based probe - for a particular technique, Gabor Domain Optical Coherence Microscopy (GD-OCM) [16].

6. Scanners with rotational Risley prisms

While analytical approaches of such scanners prove to be quite complicated [4, 5], our proposed modeling method has obtained scan patterns of this device in a simple, fast, and exact manner – the latter aspect in contrast to approximate approaches [31]. Our analysis was carried out with regard to each characteristic of the scanner, and considering the parameters introduced by Marshall: k, the ratio of the prisms angles (θ_1 and θ_2) and M, the ratio of the rotational speeds (ω_1 and ω_2) [31]:

$$k = \theta_2 / \theta_1 \quad \text{and} \quad M = \omega_2 / \omega_1 . \tag{8}$$

Risley prisms scanners have been used in only one study so far for imaging, and not for OCT, but for CM [32]. Our approach in [33, 34] aims to employ these scanners in OCT, as well.

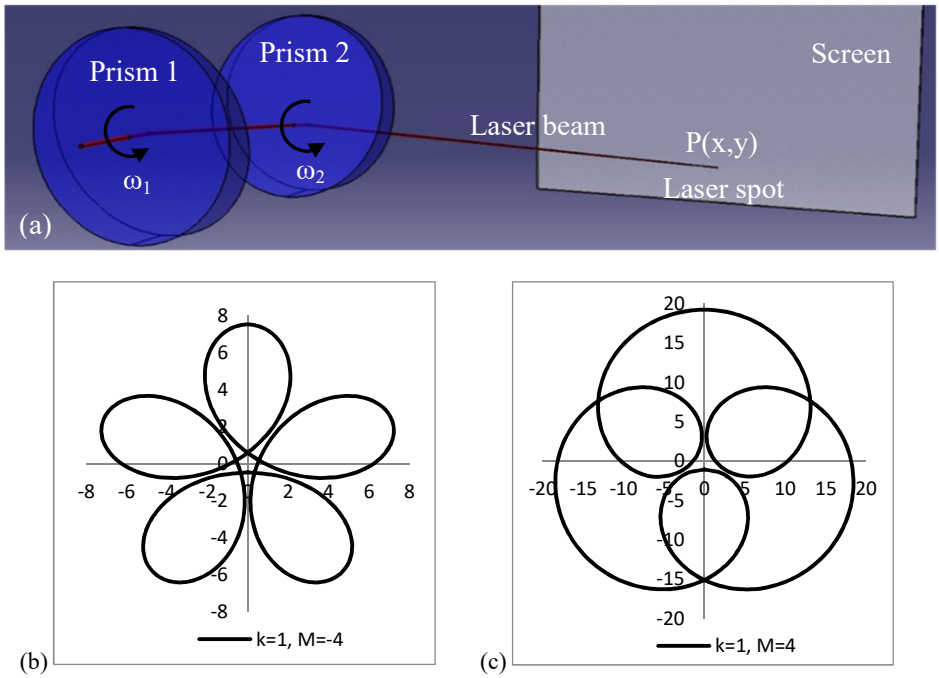

Figure 4. (a) Simulation of the refraction of a laser beam through a scanner with rotational Risley prisms – using a commercial mechanical design program, CATIA V5R20 (Dassault Systèmes, Paris, France); (b, c) scan patterns for two identical prisms and a ratio of M=-4 (b) and M=4 (c) of the rotational velocities of the prisms [33, 34].

7. Conclusions

A presentation of the main contributions and directions of research of our group in the field of optomechatronic laser scanners has been made, for the most used such devices and for high-end applications, i.e., biomedical imaging using Optical Coherence Tomography (OCT).

Polygon mirror, galvanometer scanners, Micro-Electro-Mechanical Systems (MEMS), and rotational Risley prisms have thus been discussed. Future works in these directions have also been pointed out, in our current projects focused mainly on the development of handheld scanning probes for OCT, as well as in a gamut of applications, both in biomedical imaging – especially for dentistry - and in industrial applications – especially for NDT.

Acknowledgments

This work is currently supported by the Romanian National Authority for Scientific Research, CNDI–UEFISCDI project PN-III-P2-2.1-PTE-2016-0181 (http://3om-group-optomechatronics.ro/).

References

[1] Huang, D., Swanson, E. A., Lin, C. P., Schuman, J. S., Stinson, W. G., Chang, W., Hee, M. R., Flotte, T., Gregory, K., Puliafito, C. A., Fujimoto, J. G. Optical coherence tomography. *Science* 254, 5035 (1991), 1178-1181.

[2] Drexler, W., Liu, M., Kumar, A., Kamali, T., Unterhuber, A., et al. Optical coherence tomography today: speed, contrast, and multimodality. *J. Biomed. Opt.* 19, 7 (2014), 071412.

[3] Podoleanu, A. Gh., and Rosen, R. B. Combinations of techniques in imaging the retina with high resolution. *Progress in Retinal and Eye Research* 27 (2008), 464– 499.

[4] Marshall, G. F. *Handbook of Optical and Laser Scanning.* CRC Press – Taylor & Francis, New York, 2011.

[5] Bass, M. *Handbook of optics.* 3rd Edition, Mc. Graw-Hill Inc., New York, 30.1-30.68, 2009.

[6] Duma, V.-F., Rolland, J. P., Podoleanu, A. Gh. Perspectives of optical scanning in OCT. *Proc. SPIE* 7556 (2010), 7556-10.

[7] Duma, V.-F., and Podoleanu, A. Gh. Polygon mirror scanners in biomedical imaging: a review. *Proc. SPIE* 8621 (2013), 8621V.

[8] Sweeney, M. N. Polygon scanners revisited. *Proc. SPIE* 3131 (1997), 65-76.

[9] Yun, S. H., Boudoux, C., Tearney, G. J., Bouma, B. E., "High-speed wavelength-swept semiconductor laser with a polygon-scanner-based wavelength filter," *Opt. Letters* 28, (2003) 1981-1983.

[10] Oh, W. Y., Yun, S. H., Tearney, G. J., Bouma, B. E., "115 kHz tuning repetition rate ultrahigh-speed wavelength-swept semiconductor laser," *Opt. Letters* 30, (2005) 3159-3161.

[11] Duma, V.-F. Polygonal mirror laser scanning heads: Characteristic functions. *Proc. of the Romanian Academy Series A* 18, 1 (2017)25-33.

[12] Montagu, J. Scanners - galvanometric and resonant, in *Encyclopedia of Optical Engineering*, Driggers, R. G., Hoffman, C., Driggers, R., Eds., 2465-2487, Taylor & Francis, N.Y., 2003.

[13] Duma, V.-F., Lee, K.-S., Meemon, P., Rolland, J. P. Experimental investigations of the scanning functions of galvanometer-based scanners with applications in OCT. *Appl. Opt.* 50, 29 (2011), 5735-5749.

[14] Braaf, B., Vermeer, K. A., Vienola, K. V., de Boer, J. F. Angiography of the retina and the choroid with phase-resolved OCT using interval-optimized backstitched B-scans. *Opt. Express* 20 (2012), 20516-20534.

[15] Duma, V.-F., Tankam, P., Huang, J., Won, J. J., Rolland, J. P. Optimization of galvanometer scanning for Optical Coherence Tomography. *Appl. Opt.* 54, 17 (2015), 5495-5507.

[16] Tankam, P., Santhanan, A. P., Lee, K., Won, J., Canavesi, C., Rolland, J. P. Parallelized Multi-Graphics Processing Unit Framework for High-Speed Gabor-Domain Optical Coherence Microscopy. *J. Biomed. Opt.* 19, 7 (2014), 071410.

[17] Duma, V.-F. Optimal scanning function of a galvanometer scanner for an increased duty cycle. *Opt. Eng.* 49, 10 (2010), 103001.

[18] Hayakawa, T., Watanabe, T., Senoo, T., Ishikawa, M. Gain-compensated sinusoidal scanning of a galvanometer mirror in proportional-integral-differential control using the pre-emphasis technique for motion-blur compensation. *Appl. Opt.* 55, 21 (2016) 5640-5646.

[19] Yoo, H. W., Ito, S., Schitter, G. High speed laser scanning microscopy by iterative learning control of a galvanometer scanner. *Control Engineering Practice* 50, (2016) 12-21.

[20] Mnerie, C., Preitl, S., Duma, V.-F. Galvanometer-based scanners: Mathematical model and alternative control structures for improved dynamics and immunity to disturbances. *Intl J of Structural Stability and Dynamics* 17, (2017) 1740006.

[21] Jung, W., Kim, J., Jeon, M., Chaney, E. J., Stewart, C. N., Boppart, S. A**.** Handheld optical coherence tomography scanner for primary care diagnostics. *IEEE Transactions on Biomedical Engineering* 58 (2011), 741-744.

[22] Lu, C. D., Kraus, M. F., Potsaid, B., et al., Fujimoto, J. Handheld ultrahigh speed swept source optical coherence tomography instrument using a MEMS scanning mirror. *Biomed. Opt. Express* 5 (2014), 293-311.

[23] Cernat, R., Tatla, T. S., Pang, J., et al. Dual instrument for *in vivo* and *ex vivo* OCT imaging in an ENT department. *Biomed. Opt. Express* 3 (2012), 346-3356.

[24] Demian, D., Duma, V.-F., et al., Podoleanu, A. Gh. Design and testing of prototype handheld scanning probes for optical coherence tomography. *J. of Eng. in Medicine* 228, 8 (2014), 743-753.

[25] Duma, V.-F., Dobre, G., Demian, D., Cernat, R., Sinescu, C., Topala, F. I., Negrutiu, M. L., Hutiu, Gh., Bradu, A., Podoleanu, A. Gh. Handheld scanning probes for optical coherence tomography. *Romanian Reports in Physics* 67, 4 (2015).

[26] Fried, D., Xie, J., Shafi, S., Featherstone, J. D. B., Breunig, T. M., Le, C. Imaging caries lesions and lesion progression with polarization sensitive optical coherence tomography. *J. Biomed. Opt.* **7,** 4 (2002), 618-627.

[27] Sinescu, C., Negrutiu, M. L., Bradu, A., Duma, V.-F., Podoleanu, A. Gh. Noninvasive quantitative evaluation of the dentin layer during dental procedures using Optical Coherence Tomography. *Computational and Mathematical Methods in Medicine*, Paper ID 709076 (2015).

[28] Oancea, R., Bradu, A., et al., Duma, V.-F., Podoleanu, A. Gh. Assessment of the sealant/tooth interface using optical coherence tomography. *J. of Adhesion Sc. and Technology* 29, 1 (2015), 49-58.

[29] Hutiu, Gh., Duma, V.-F., Demian, D., Bradu, A., Podoleanu, A. Gh. Surface imaging of metallic material fractures using optical coherence tomography. *Appl. Opt.* 53, 26 (2014), 5912-5916.

[30] Cogliati, A., Canavesi, C., Hayes, A., Tankam, P., Duma, V.-F., Santhanam, A., Thompson, K. P., Rolland, J. P., MEMS-based handheld scanning probe for distortion-free images in Gabor-Domain Optical Coherence Microscopy, *Opt. Express* 24(12), 13365-13374 (2016).

[31] Marshall, G. F. Risley prisms scan patterns, *Proc. SPIE* 3787 (1999), 74-86.

[32] Warger II, W. C. and DiMarzio, Ch. A. Dual-wedge scanning confocal reflectance microscope. *Opt. Lett.* 32 (2007), 2140-2142.

[33] Schitea, A., Tuef, M., Duma, V.-F. Modeling of Risley prisms devices for exact scan patterns. *Proc. SPIE* 8789 (2013), 8789-40.

[34] Duma V.-F., Schitea A., Laser scanners with rotational Risley prisms: Exact scan patterns, *Proceedings of the Romanian Academy Series A* 19 (2018) – accepted for publication.

Virgil-Florin Duma, Professor and Head of the 3OM Optomechatronics Group (http://3om-group-optomechatronics.ro/), "Aurel Vlaicu" University of Arad, 77 Revolutiei Ave., Arad 310130, Romania; Doctoral School, Polytechnic University of Timisoara, 1 Mihai Viteazu Ave., Timisoara 300222, Romania (duma.virgil@osamember.org).
The author gave a presentation of this paper during one of the conference sessions.

Tumor growth and decay predictability based on chaotic attractors in the phase spaces

Larysa Dzyubak, Oleksandr Dzyubak, Jan Awrejcewicz

Abstract: In Radiation Oncology and Radiobiology the modeling of tumor growth and decay depending on set of system parameters is very important to improve the control of cancer treatment. In a simple approach, the multi-scale diffusion cancer-invasion model describes the interactions of the tumor cells, matrix-metalloproteinases, matrix-degradative enzymes and oxygen. This model demonstrates chaotic attractors. In this work we studied the control parameter planes 'number of tumor cells vs diffusion saturation level' depending on glucose level. The regions where interaction of the basic system indicators is predictable and unpredictable were found. Time histories of the regular damped/un-damped motion, chaotic attractors in the phase spaces of basic indicators of the system are presented. Qualitative analysis of the results can be used by professionals who deals with the tumor growth and decay simulation and who is involved in the treatment planning process.

1. Introduction

Cancer Care and, in particular, Radiation Therapy, as one of the most efficient way of treating cancer, has significantly improved as a result of new approaches and techniques developed over the last years [1-2]. Despite the success in treating cancer, the different cancer cell resistance against treatments expressed in patient populations initiated multiple research studies related to prediction of outcomes [3-6]. To predict cell response to Radiation Therapy, statistical approaches based on quantities “Tumor Control Probability” (TCP) and “Normal Tissue Complication Probability” (NTCP) are widely used [7-8]. These quantities were summarized by the QUANTEC group for variety of organs [9] and currently the TCP an NTCP models are actively used in clinic [10].

Another way of prediction tumor behavior is the mathematical modeling of cancerous systems [11-15] where the modeling is considered from the point of view of having stochastic regimes [16-17]. A chaotic time history of concentrations of basic components of the metabolic process in a biological cancerous cell system was associated with carcinogenesis and a generic concept of carcinogenesis and metastasis was formulated on the basis of existence of a chaotic cancer attractors which are sensitive to the initial conditions [14-15].

The purpose of the simulations in this study was to define conditions resulting in carcinogenesis in a biological system as well as to study influence of glucose level on carcinogenesis. The results of this study could be used to improve the treatment planning process and predictability of the outcomes.

2. Mathematical model

Cancer is generally defined as a malignant tissue growth resulting from an uncontrolled division of cells [18]. The approach based on the wandering trajectories analysis [19-20] was applied to investigate the control parameter planes 'number of tumor cells vs diffusion saturation level'. In the model studied in this work, the tumor development is governed by the inhomogeneous dissipative set of differential equations [14,15]:

$$\dot{n} = 0, \tag{1}$$

$$\dot{f} = \alpha\eta(m - f), \tag{2}$$

$$\dot{m} = \beta\kappa n + f(\gamma - c) - m, \tag{3}$$

$$\dot{c} = \upsilon f m - \omega n - \delta f c. \tag{4}$$

where n denotes the tumor cell density, f is the matrix–metalloproteinases (MM) concentration, m corresponds to the matrix-degradative enzymes (MDE) concentration, and c denotes the oxygen concentration. Parameters α is a tumor cell volume, β – glucose level, γ – number of tumor cells, δ – diffusion saturation level; η and κ are coefficient that characterise the growth and decay of MM and MDE concentration respectively; υ , ω, φ are parameters that govern growth and decay of the oxygen concentration.

The model (1)-(4) possesses three chemical equilibria

$$m^e_{1,2,3} = f^e_{1,2,3} = A + B, -\frac{A+B}{2} \pm \frac{A-B}{2}\sqrt{-3}, \tag{5}$$

$$c^e_{1,2,3} = \frac{1}{\delta\phi}(\upsilon(f^e_{1,2,3})^2 - \omega n), \tag{6}$$

$$A = \sqrt[3]{-\frac{q}{2} + \sqrt{\frac{q^2}{4} + \frac{p^3}{27}}}, B = \sqrt[3]{-\frac{q}{2} - \sqrt{\frac{q^2}{4} + \frac{p^3}{27}}}, \tag{7}$$

$$p = \frac{\delta\phi}{\upsilon}(1 - \gamma - \omega n), q = \frac{\delta\phi}{\upsilon}\beta\kappa n. \tag{8}$$

As mentioned in [21] pertaining to the self-organizing chemical systems: as soon as the product is also a part of the same chemical reaction, the system can express unstable behaviour which can be controlled by the reaction parameters. Depending on control parameter values and initial conditions, the considered biological cancerous cell system can also approach different states: a) stationary equilibrium state where any changes are damped; b) stable periodic chemical process or so called

'chemical clock' (a limit cycle); c) state of chemical instability with chaotic behaviour of MM, MDE and oxygen concentrations.

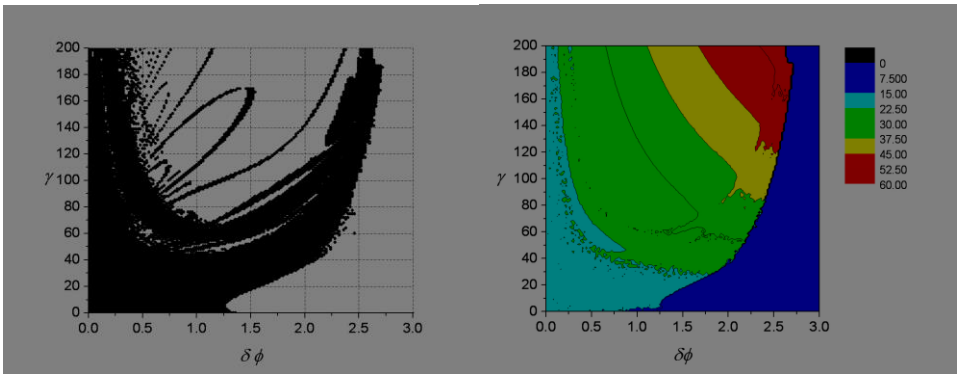

(a) (b)

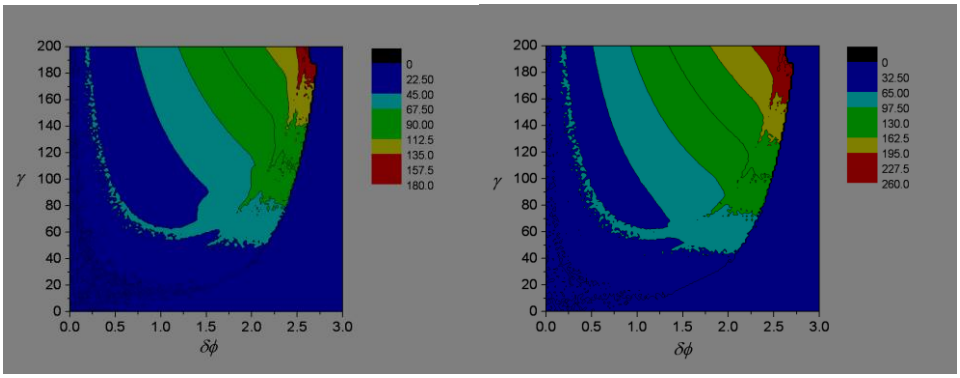

(c) (d)

Figure 1. Simulations at the glucose level β=0.05: (a) Region of chaotic behaviour (in Green) for model (1)-(4) in the control parameter plane ($\delta\varphi$, γ); (b) Amplitude level contours of matrix-metalloproteinases, (c) Amplitude level contours of matrix-degradative enzymes, (d)Amplitude level contours of oxygen concentration in the model.

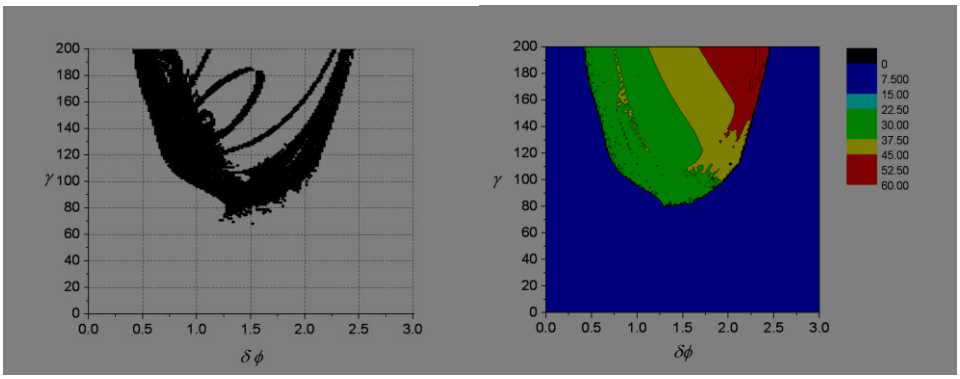

(a) (b)

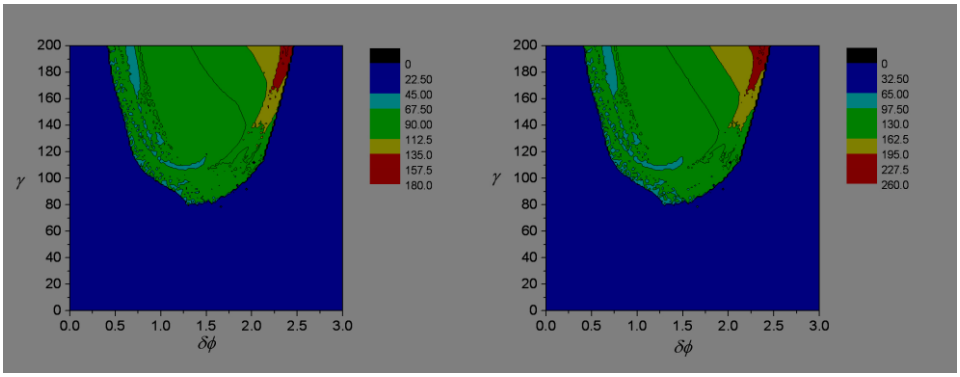

(c) (d)

Figure 2. Simulations at the glucose level β=5.0: (a) Region of chaotic behaviour (in Green) for model (1)-(4) in the control parameter plane ($\delta\varphi$, γ); (b) Amplitude level contours of matrix-metalloproteinases, (c) Amplitude level contours of matrix-degradative enzymes, (d)Amplitude level contours of oxygen concentration in the model.

3. Numerical results

Chaotic cancer attractors exist within certain parameter ranges of studied mathematical model (1)-(4) describing the tumor development in a biological system. The set of all pairs of values of these parameters defines the chaotic regions in a control parameter planes 'number of tumor cells vs diffusion saturation level'. The part of this plane ($0\leq\delta\varphi\leq3$, $0\leq\gamma\leq200$) was sampled as a uniform rectangular grid using two families of straight lines drawn through the dividing points of the axes:

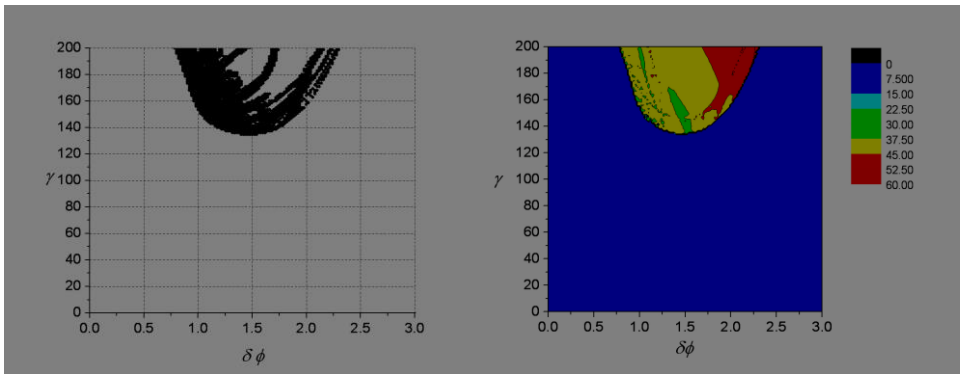

(a) (b)

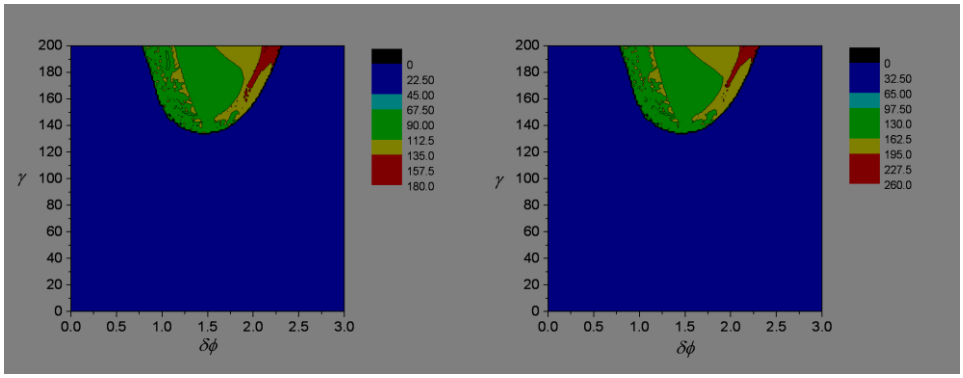

(c) (d)

Figure 3. Simulations at the glucose level β=10.0: (a) Region of chaotic behaviour (in Green) for model (1)-(4) in the control parameter plane ($\delta\varphi$, γ); (b) Amplitude level contours of matrix-metalloproteinases, (c) Amplitude level contours of matrix-degradative enzymes,(d)Amplitude level contours of oxygen concentration in the model.

$$\delta\varphi = \delta\varphi^i = i\Delta\delta\varphi \quad (i=0, 1,\ldots, L), \tag{9}$$

$$\gamma = \gamma^j = j\Delta\gamma \ (j=0, 1,\ldots, M). \tag{10}$$

Here $\Delta\delta\varphi=3\times10^{-2}$, $\Delta\gamma=2$, L=100, M=100. Then in the nodal points ($\delta\varphi^i$, γ^j) of the constructed grid the governing equations (1)-(4) are twice solved numerically with two nearby initial conditions. Initial conditions of the nearby trajectories are distinguished by 0.5 percent with ratio to the characteristic vibration amplitudes A_f, A_m, A_c

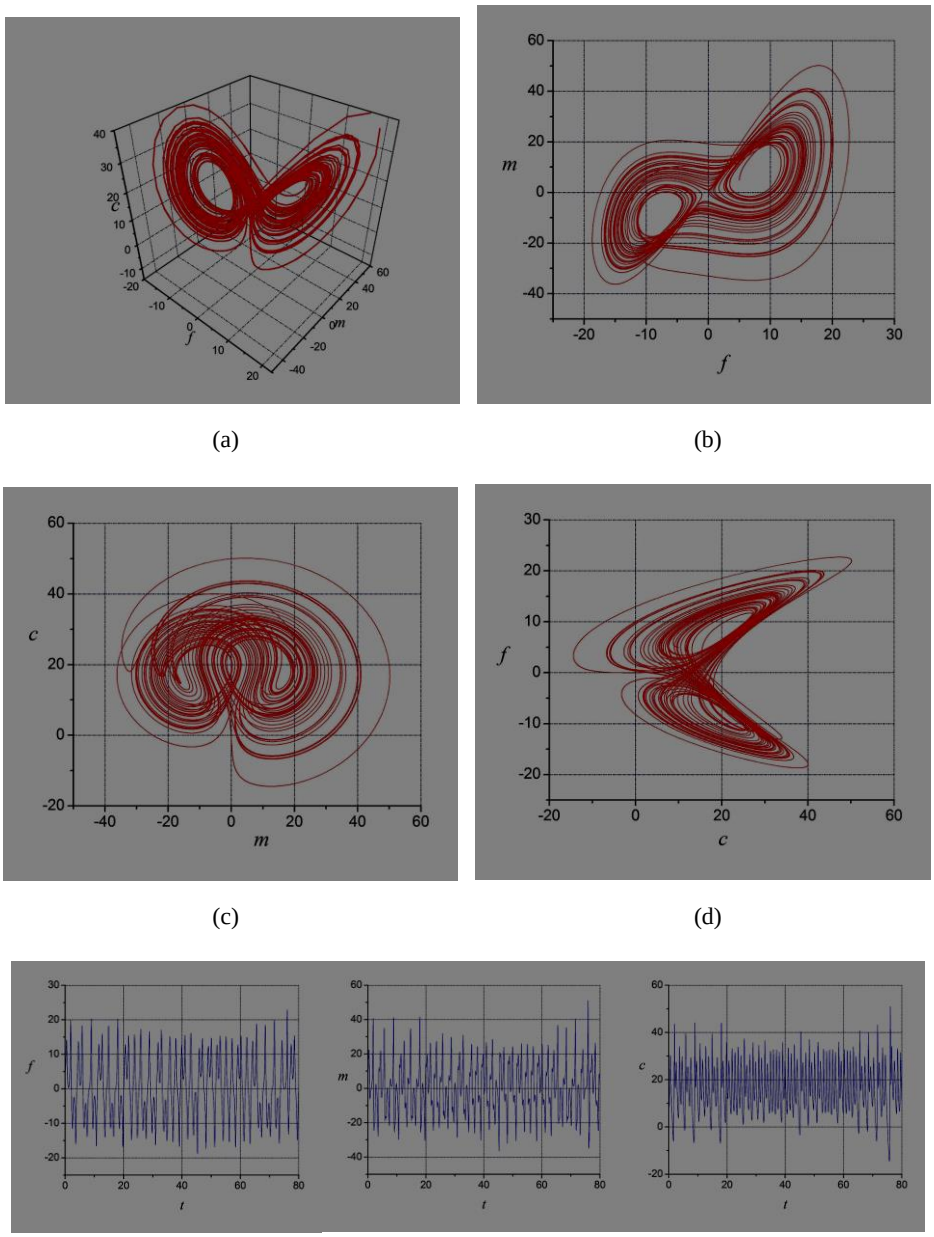

Figure 4. Behaviour of the model (1)-(4) corresponding to the chaotic regions: (a) Chaotic attractor in the phase space (*f*, *m*, *c*); (b), (c), (d) Phase planes (*f*, *m*), (*m*, *c*) and (*c*, *f*) respectively; (e) Chaotic trajectories *f*, *m*, *c*.

$$A_f = \frac{1}{2}|\max_{t_1 \leqslant t \leqslant T} f(t) - \min_{t_1 \leqslant t \leqslant T} f(t)|, \quad (11)$$

$$A_m = \frac{1}{2}|\max_{t_1 \leqslant t \leqslant T} m(t) - \min_{t_1 \leqslant t \leqslant T} m(t)|, \quad (12)$$

$$A_c = \frac{1}{2}|\max_{t_1 \leqslant t \leqslant T} c(t) - \min_{t_1 \leqslant t \leqslant T} c(t)|, \quad (13)$$

e.g. the starting points of these trajectories are in the three-dimensional parallelepiped

$$|f(t_0) - \tilde{f}(t_0)| < 0.005A_f, \quad (14)$$

$$|m(t_0) - \tilde{m}(t_0)| < 0.005A_m, \quad (15)$$

$$|c(t_0) - \tilde{c}(t_0)| < 0.005A_c. \quad (16)$$

Characteristic vibration amplitudes A_f, A_m, A_c are calculated for all nodal points ($\delta\varphi^i$, γ^j) of the constructed grid simultaneously with the integration of the governing equations. The time period for the simulation T is of 50 non-dimensional time units. During computations, 2/3 of the time period T corresponds to the time interval $[t_0, t_1]$, where transient processes are damped. The integration step size is 5/300. After the integration of the governing equations (1)-(4), the condition

$\exists t^* \in [t_1, T]$:

$$\{(|f(t^*) - \tilde{f}(t^*)| > \alpha A_f) \vee (|m(t^*) - \tilde{m}(t^*)| > \alpha A_m) \vee (|c(t^*) - \tilde{c}(t^*)| > \alpha A_c)\} \quad (17)$$

was verified. The parameter α is chosen to be equal 1/3. In that way the manifold of the nodal points ($\delta\varphi^i$, γ^j), for which the inequality (17) is satisfied, sets up regions of chaos.

In Figs 1-3 (a) we can observe the evolution of the chaotic regions for the model (1)-(4) in the control parameter plane 'number of tumor cells vs diffusion saturation level' ($\delta\varphi$, γ), ($0 \leq \delta\varphi \leq 3$, $0 \leq \gamma \leq 200$) depending on glucose level β=0.05, β=5.0, β=10.0 with fixed other parameters n=50, α=0.06, η=50, κ=1, υ=0.5, ω=0.57 and the initial conditions $f(0)$=5.0; $m(0)$=5.0; $c(0)$=10.0. Under conditions considered, the increase in glucose level has a suppress effect (restraining effect) to carcinogenesis. Figs 1-3 (b), (c), (d) for the same conditions as Figs 1-3 (a) represent the evolution of amplitude level contours of matrix–metalloproteinases, matrix–degradative enzymes and oxygen concentrations respectively. In all cases the carcinogenesis is accompanied by a significant increase in chemical oscillations amplitudes of MM, MDE and oxygen concentrations.

In Fig. 4 chaotic behaviour ((a), (b), (c), (d) chaotic cancer attractors; (e) chaotic time histories of MM, MDE and oxygen concentrations) of the biological system (1)-(4) is depicted at $\delta\varphi$=0.5, γ=20.0 and n=50, α=0.06, β=0.05, η=50, κ=1, υ=0.5, ω=0.57. Initial conditions are $f(0)$=5.0; $m(0)$=5.0; $c(0)$=10.0. These parameters characterize chaotic regions presented in Fig. 1 (a).

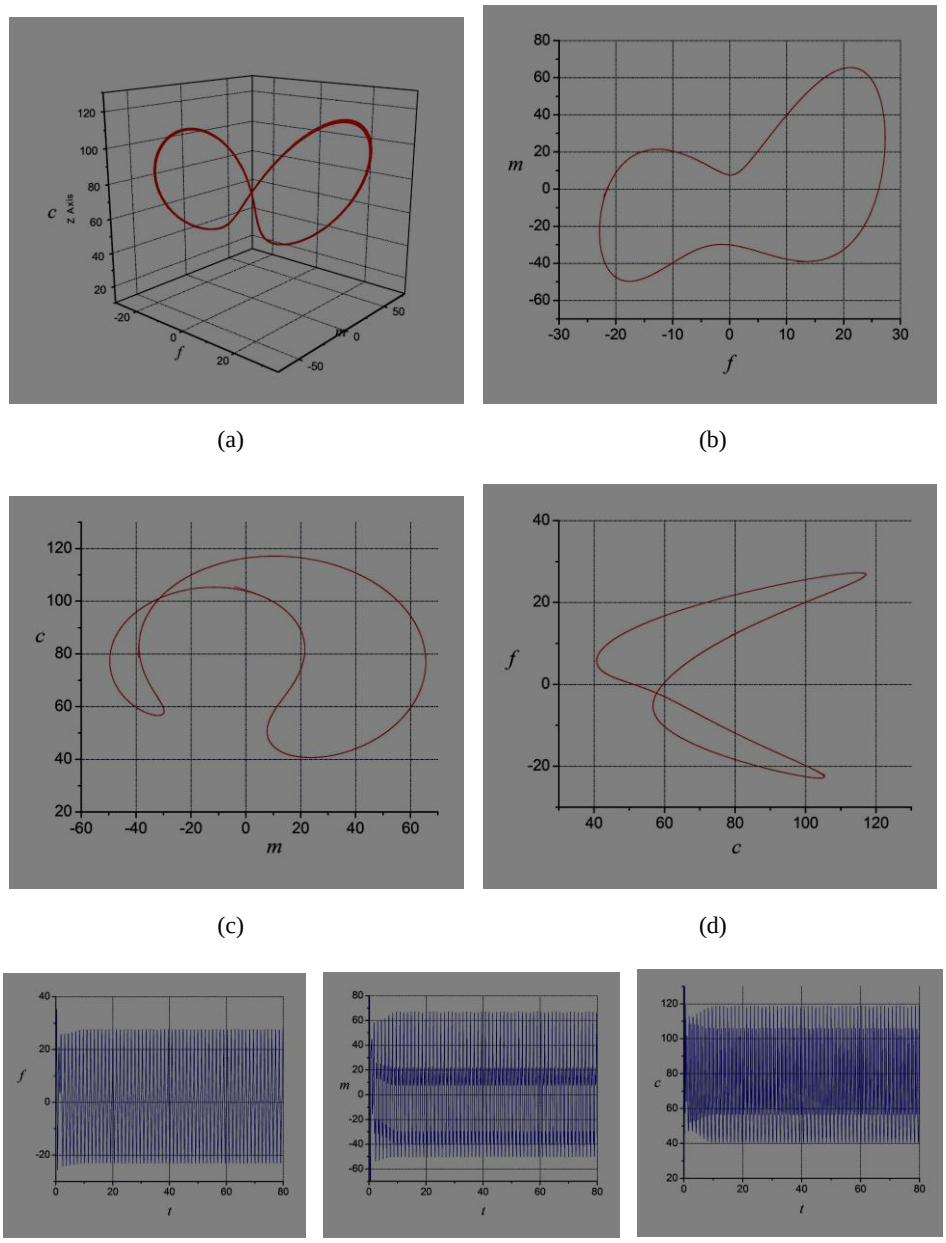

Figure 5. Behaviour of the model (1)-(4) corresponding to the regular regions: (a) Limit cycle in the phase space (*f, m, c*); (b), (c), (d) Phase planes (*f, m*), (*m, c*) and (*c, f*) respectively; (e) Periodic time histories *f, m, c*.

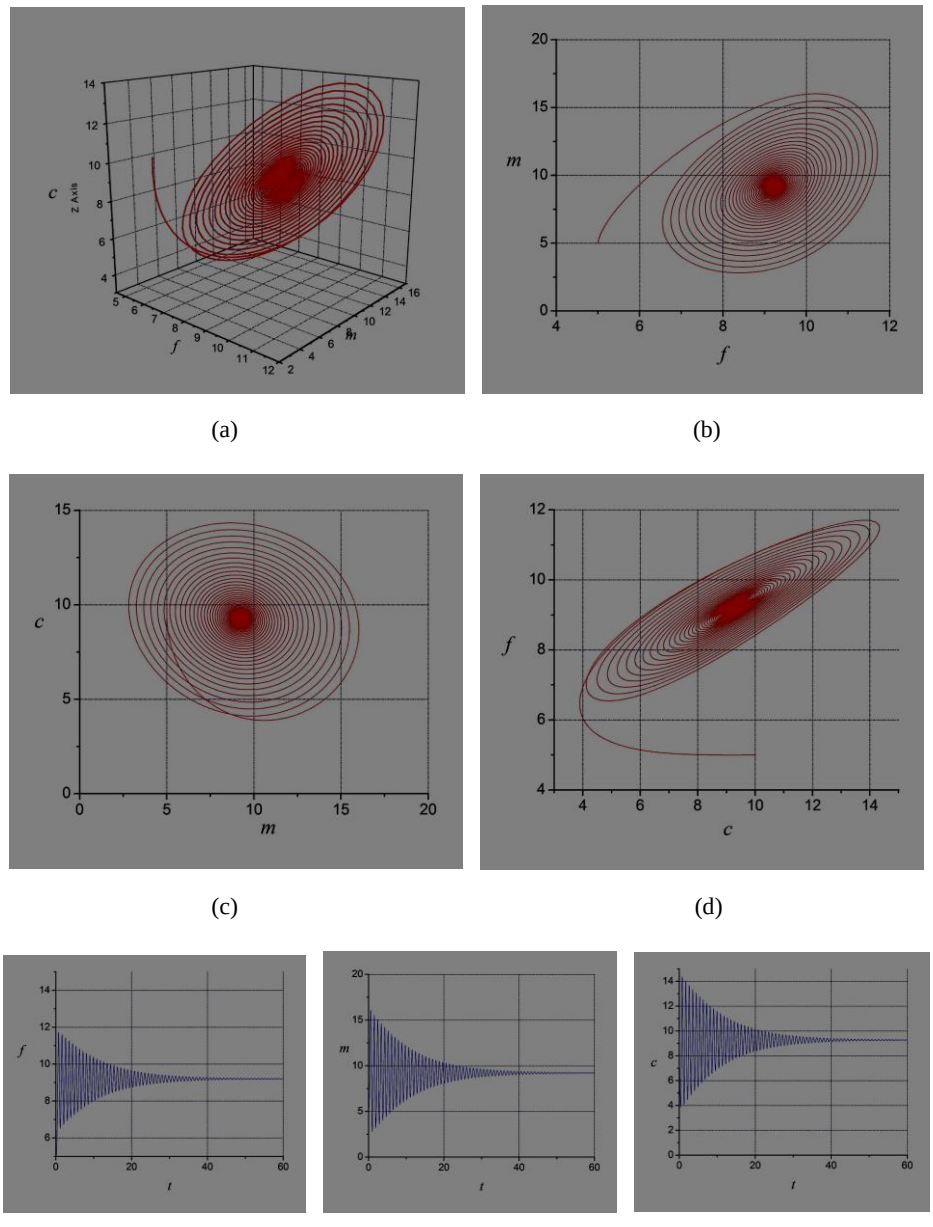

Figure 6. Behaviour of the model (1)-(4) corresponding to the regular regions: (a) Stable focus in the phase space (*f*, *m*, *c*); (b), (c), (d) Stable focuses in the phase planes (*f*, *m*), (*m*, *c*) and (*c*, *f*) respectively; (e) Periodic damped trajectories *f*, *m*, *c*.

In Fig. 5 we can observe the chemical clock or the periodic/regular un-dumped oscillations ((a), (b), (c), (d) the limit cycles; (e) periodic time histories of MM, MDE and oxygen concentrations) of the biological system (1)-(4) at $\delta\varphi$=1.0, γ=80.8 and n=50, α=0.06, β=0.05, η=50, κ=1, υ=0.5, ω=0.57.Initial conditions are $f(0)$=5.0; $m(0)$=5.0; $c(0)$=10.0. Parameters $\delta\varphi$=1.0, γ=80.8 correspond to regular region presented in Fig. 1 (a), *e. g*. they don't belong to chaotic regions.

In Fig. 6 we can observe the regular dumped oscillations near one of the chemical equilibrium ((a), (b), (c), (d) the stable focuses in the phase space and in the phase planes, (e) dumped oscillations time histories of MM, MDE and oxygen concentrations) of the biological system (1)-(4) at $\delta\varphi$=1.5, γ=10.0 and n=50, α=0.06, β=0.05, η=50, κ=1, υ=0.5, ω=0.57. Initial conditions are $f(0)$=5.0; $m(0)$=5.0; $c(0)$=10.0. Parameters $\delta\varphi$=1.5, γ=10.0 correspond to regular region presented in Fig. 1 (a).

All presented Figs. 4-6 are in good accordance with the chaotic/regular regions obtained (Figs 1-3).

4. Conclusions

Based on the performed analysis of the mathematical model describing the tumor development in a biological system, the parameter sets resulting in occurring chaotic cancer attractors or carcinogenesis were found. All chaotic regions were juxtaposed with amplitude level contours of matrix–metalloproteinases, matrix–degradative enzymes and oxygen concentrations with the same fixed parameters. In all cases the carcinogenesis is accompanied by a significant increase in chemical oscillations amplitudes of matrix–metalloproteinases, matrix–degradative enzymes and oxygen concentrations.

Time histories and phase spaces of the regular un-damped oscillations (the chemical clock), regular damped motion near one of the chemical equilibrium as well as chaotic attractors of basic indicators of the biological system with parameters that correspond to the chaotic/regular regions obtained were presented.

The analysis of parameter influence on the biological system demonstrates that the glucose level defines the evolution of chaotic attractors of cancer regions in the control parameter planes 'number of tumor cells vs diffusion saturation level' and under conditions considered, the increase in glucose level has a suppress effect to carcinogenesis. Thus, this allows controlling and stabilizing unpredictable behaviour of metabolic reactions and carcinogenesis.

References

[1] Vogelzang, N.J., Benovitz, S.I., et al. Clinical cancer advances 2011: annual report on progress against cancer from the American Society of Clinical Oncology. *Journal of Clinical Oncology* 30, 2012, 88–109.

[2] Fraass, B.A., Moran, J.M. Quality, technology and outcomes: evolution and evaluation of new treatments and/or new technology. *Seminars in Radiation Oncology* 22, 2012, 3–10.

[3] Liu, D., Ajlouni, M., Jin, J.-Y., et al. Analysis of outcomes in radiation oncology: An integrated computational platform. *Medical Physics Journal* 36(5), 2009, 1680–1689.

[4] Lambin, P., Stiphout, R.G.P.M., Starmans, M.H.W., et al. Predicting outcomes in radiation oncology multifactorial decision support systems. *Nature Reviews Clinical Oncology* 10(1), 2013, 27–40.

[5] Oh, J.H., Kerns, S., Ostrer, H., et al. Computational methods using genome-wide association studies to predict radiotherapy complications and to identify correlative molecular processes. *Scientific Reports* 7, 2017, 1–10.

[6] Incoronato, M., Aiello, M., Infante, T., et al. Radiogenomic analysis of oncological data: a technical survey. *International Journal of Molecular Sciences* 18(4), 2017, 805, 1–28.

[7] Baumann, M., Petersen, C. TCP and NTCP: a basic introduction. *Rays* 30(2), 2005, 99–104.

[8] Baumann, M., Petersen, C., Krause, M. TCP and NTCP in preclinical and clinical research in Europe. *Rays* 30(2), 2005, 121–126.

[9] Bentzen, S.M., Constine, L.S., Deasy, J.O., et al. Quantitative Analyses of Normal Tissue Effects in the Clinic (QUANTEC): an introduction to the scientific issues. *International Journal of Radiation Oncology, Biology, Physics* 76(3), 2010, S3–S9.

[10] Marks, L.B., Yorke, E.D., Jackson, A., et al. Use of normal tissue complication probability models in the clinic. *International Journal of Radiation Oncology, Biology, Physics* 76(3), 2010, S10–S19.

[11] Anderson, A.R.A., Chaplain, M.A.J., Newman E.L., Steele, R.J.C., Thompson, A.M. Mathematical modelling of tumor invasion and metastasis. *Journal of Theoretical Medicine* 2, 2000, 129–154.

[12] Anderson, A.R.A. A hybrid mathematical model of solid tumour invasion. *Mathematical Medicine and Biology* 22, 2005, 163–186.

[13] Komarova, N.L. Building Stochastic Models for Cancer Growth and Treatment. In: Deisboeck, T., Stamatakos, G.S. ed. *Multiscale Cancer Modeling*. CRC Press, London, New York, 339–358.

[14] Ivancevic, T.T., Bottema, M.J., Jain, L.C. A theoretical model of chaotic attractor in tumor growth and metastasis. arXiv: 0807.4272 in Cornell University Library's arXiv.org, 2008, 1–17.

[15] Harney, M., Yim, W. Chaotic Attractors in Tumor Growth and Decay: A Differential Equation Model. In: Vlamos P., Alexiou A. (eds) *GeNeDis* 2014. *Advances in Experimental Medicine and Biology* 820. Springer, Cham, 2014, 193–206.

[16] Berezovoj, V.P., Bolotin, Y.L., Dzyubak, A.P., et al. Nuclear Stochastic Resonance. *Journal of Experimental and Theoretical Physics Letters* 74, 2001, 411-414.

[17] Berezovoj, V.P., Bolotin, Y.L., Dzyubak, O.P., et al. Stochastic resonance in a periodically modulated dissipative nuclear dynamics, *Fermilab Report*, Jan 2001 FERMILAB-CONF-01-009-T, http://lss.fnal.gov/archive/2001/conf/Conf-01-009-T.pdf, 8 pages.

[18] Watson, J.D., Baker, T.A., Bell, S.P., Gann, A., Levine, M., Losick, R. *Molecular Biology of the Gene.* Pearson, New York, 2014.

[19] Awrejcewicz, J., Dzyubak, L.P. Chaos caused by hysteresis and saturation phenomenon in 2-dof vibrations of the rotor supported by the magneto-hydrodynamic bearing. *International Journal of Bifurcation and Chaos* 15(6), 2011, 2041–2055.

[20] Awrejcewicz, J., Dzyubak, L.P. Modelling, chaotic behavior and control of dissipation properties of hysteretic systems. In: *Models and Applications of Chaos Theory in Modern Sciences*, Z. Elhadj, (Ed.), CRC Press Taylor & Francis Group, 2011, 645-667.

[21] Prigogine I., Stengers, I. *Order Out of Chaos*. Heinemann, London, 1984.

Larysa Dzyubak, Associate Professor: Department of Applied Mathematics, National Technical University, 2 Kyrpychova Str., 61002 Kharkiv, Ukraine (*dzyubak.larissa@interdiscipline.org*).The author gave a presentation of this paper during one of the conference sessions.

Oleksandr Dzyubak, Ph.D.: Ascension All Saint Cancer Center, 3809 Spring Street, Racine, WI 53405, USA (*Dzyubak.Oleksandr@gmail.com*).

Jan Awrejcewicz, Professor: Department of Automation, Biomechanics and Mechatronics, the Lodz University of Technology, 1/15 Stefanowski Str., 90-924 Lodz, Poland (*jan.awrejcewicz@p.lodz.pl*).

The process of energy dissipation during a front-to-side collision of passenger cars

Mirosław Gidlewski, Leon Prochowski, Leszek Jemioł, Dariusz Żardecki

Abstract: For the analysis of road accidents, a balance of the energy dissipated during the collision of the vehicles involved is often taken as a basis. To determine some important items of such a balance, crash tests with a front-to-side collision of passenger cars of the same make and model (i.e. with an impact at a right angle against a side, close to pillar B, of a moving car) were carried out. The experiment results were used to build a model of the dynamics of motor car collision, in order to take the model as a basis for determining the force, displacement, and velocity in the zone of vehicle contact during the collision. This made it possible to determine a combined vehicle deformation curve and then the important components of the energy lost during the contact phase of vehicle collision.
During the analysis of the energy dissipation process, the processes of deformation of the vehicle bodies and the post-impact motion of the vehicles involved were taken into account. Based on results of the model and experimental tests, conclusions were formulated which can provide important support for the reconstruction of a right-angle collision of motor cars and for the calculation of the pre-impact speed of the impacting vehicle.

1. Introduction

Right-angle collisions of motor vehicles amount to more than 25 % of road accidents in Poland. Their analysis may be based on results of calculations of the balance of energy dissipated during the collision. The energy dissipation process takes place when the colliding vehicles are in contact and when they move separately after the impact. The following energy components may be discerned in the contact phase of vehicle collision:

- initial kinetic energy of the vehicles, determined by their pre-impact translational motion;
- work of deformation of vehicle bodies in their contact zone;
- friction work done when the vehicle bodies slide over each other in their contact zone;
- work related to vehicles' displacement in their post-impact translational and rotational motion;
- energy dissipated in vehicles' suspension systems and tyres;
- thermal and vibrational energy released in result of deformations and processes of destruction of vehicle components.

The vehicle energy dissipation process during a frontal collision is usually analysed from the point of view of the reconstruction of complex (complicated) accidents. In [7], the energy dissipated for vehicle deformation during a collision was determined for a case where the vehicles involved significantly differed from each other in their mass. Sometimes, the energy dissipated during a side collision is only roughly determined, with using the coefficient of restitution [1]. In works [8, 9], results of an analysis of a few crash tests carried out on cars of the years 1983-1989 were used to estimate the relation between the frontal deformation of a car body and the energy expressed by means of the value of $\sqrt{2E/w}$ (where E and w are the energy and average deformation, respectively) as well as the drop in the velocity of the impacting vehicle (delta V). Such a relation facilitates the calculation of the impact velocity at the reconstruction of road accidents. Similar results obtained by analysing vehicle deformation at a front-to-side collision of motor vehicles and at a motor vehicle impact against a deformable barrier have been presented in [3] and [2], respectively.

The energy dissipated during a vehicle collision depends to a significant degree on the properties of the vehicle body side structure and on the method used for its previous repair, if any [11]. In [6], an extension of the range of analysing the car collision processes is considered, with taking as a basis a planar model of vehicle dynamics during a side collision, in order to obtain exact values of vehicle motion parameters.

At the present stage, the previous approach to the analysis of front-to-side collision of motor vehicles has been extended. To acquire knowledge of the course of accidents of this kind, experimental tests were prepared and performed and the results of these tests will be used for improving the methods of modelling and reconstruction of road accidents. Several initial stages of such an analysis have been presented by the authors in publications [4, 5].

Within this paper, important items of the balance of the energy dissipated in result of a collision of motor cars will be identified. In the studies dedicated to the reconstruction of road accidents, an assumption is usually made (e.g. in [10]) that the main part of the kinetic energy lost at vehicle collisions is consumed by permanent deformation of the vehicle components that come into direct contact with each other and that other parts of the energy dissipated may be ignored due to their insignificant value. In this paper, this assumption will be verified for the front-to-side collision of passenger cars, based on results of crash tests and computer modelling.

2. Experimental tests

At the Automotive Industry Institute (PIMOT) in Warsaw, experimental tests were carried out where the front of car A crashed into the left side of car B (Fig. 1). The pre-impact speed of car A was about 50 km/h and it was twice as high as that of car B. The location of the point of impact on the side of car B was defined by the distance L_{AB} between the longitudinal plane of symmetry of car A and

the front wheel axis of car B. The values of the characteristic parameters of the crash tests have been specified in Table 1.

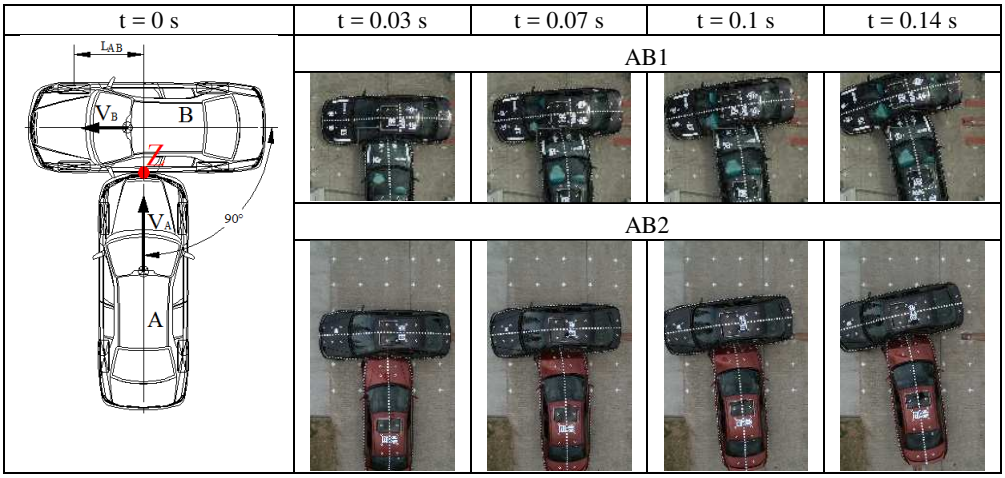

Figure. 1. Relative position of cars A and B during the collision

Table 1. Velocity of car A at the instant of the collision

Test symbol	AB1	AB2
L_{AB} [m]	1.25	1.34
Velocity V_A [m/s]	15.1	12.7

The crash tests were carried out on a PIMOT test yard with dry concrete surface. During the tests, the steering wheels of both cars were left free and their road wheels were not braked. The tests were performed on Honda Accord cars. At the centre of mass of each car, there was a three-axial acceleration sensor, installed together with sensors measuring the angular velocities of the car body in relation to the three coordinate axes. High-speed cameras were installed above the crash test place to record consecutive car positions with a frequency of 1 000 frames per second.

3. Modelling of the collision and the energy dissipation process

To analyse the processes that took place during the motor car collision, the following coordinate systems were adopted:

- Local coordinate systems, fixed to the bodies of cars „i". The local coordinate system $O_ix_iy_iz_i$ has its origin O_i situated at the centre of mass of car „i" and its O_ix_i axis is parallel to the longitudinal car centreline (index „i" corresponds to car A and B as appropriate). The quantities whose values were recorded during the crash tests in the local coordinate systems were components of the vectors of acceleration of the centre of car mass (a_{xi}, a_{yi}, a_{zi}) and of the angular velocity (P_i, Q_i, R_i) of cars A and B.

- Local levelled coordinate systems, attached to the centres of mass of cars „i". The local coordinate system $O_iX_{Pi}Y_{Pi}Z_{Pi}$ has its origin O_i situated at the centre of mass of car „i", the $O_iX_{Pi}Y_{Pi}$ plane is parallel to the road surface plane, and the O_iX_{Pi} axis is parallel to the longitudinal car symmetry plane. The local levelled coordinate systems were used for the formulation of the equations of motion of the planar model of the collision.
- Global coordinate system $O_GX_GY_GZ_G$, attached to the road. The $O_GX_GY_G$ plane of this system is situated at the road surface level and the O_GZ_G axis is pointing vertically upwards. The O_GX_G axis is parallel to the vector of pre-impact velocity of car A and the O_GY_G axis is parallel to the vector of pre-impact velocity of car B. In the global coordinate system, the translational and rotational velocities and the trajectories of the cars involved were expressed.

The measurement results expressed in the local coordinate system fixed to a car body may be transformed to other coordinate systems. The rotation of the local systems in relation to the global coordinate system is defined by angles Φ_i - vehicle roll angle, Θ_i - vehicle pitch angle and Ψ_i -vehicle yaw angle.

The angular velocities of a car body in the global coordinate system are described as follows:

$$\begin{bmatrix} \dot{\Phi}_i \\ \dot{\Theta}_i \\ \dot{\Psi}_i \end{bmatrix} = \begin{bmatrix} 1 & \sin\Phi_i \, tg\Theta_i & \cos\Phi_i \, tg\Theta_i \\ 0 & \cos\Phi_i & -\sin\Phi_i \\ 0 & \dfrac{\sin\Phi_i}{\cos\Theta_i} & \dfrac{\cos\Phi_i}{\cos\Theta_i} \end{bmatrix} \cdot \begin{bmatrix} P_i \\ Q_i \\ R_i \end{bmatrix} \tag{1}$$

The acceleration of the centre of car mass in the levelled coordinate system is expressed by a formula:

$$\begin{bmatrix} a_{xPi} \\ a_{yPi} \\ a_{zPi} \end{bmatrix} = \begin{bmatrix} \cos\Theta_i & \sin\Theta_i \sin\Phi_i & \sin\Theta_i \cos\Phi_i \\ 0 & \cos\Phi_i & -\sin\Phi_i \\ -\sin\Theta_i & \cos\Theta_i \sin\Phi_i & \cos\Theta_i \cos\Phi_i \end{bmatrix} \begin{bmatrix} a_{xi} \\ a_{yi} \\ a_{zi} \end{bmatrix} \tag{2}$$

The accelerations of the centres of mass of individual cars in the global coordinate system are described by formulas:

$$\begin{bmatrix} \ddot{X}_{GA} \\ \ddot{Y}_{GA} \\ \ddot{Z}_{GA} \end{bmatrix} = \begin{bmatrix} \cos\Psi_A & -\sin\Psi_A & 0 \\ \sin\Psi_A & \cos+\Psi_A & 0 \\ 0 & 0 & 1 \end{bmatrix} \begin{bmatrix} a_{xPA} \\ a_{yPA} \\ a_{zPA} \end{bmatrix} \tag{3}$$

$$\begin{bmatrix} \ddot{X}_{GB} \\ \ddot{Y}_{GB} \\ \ddot{Z}_{GB} \end{bmatrix} = \begin{bmatrix} \cos(90^0+\Psi_B) & -\sin(90^0+\Psi_B) & 0 \\ \sin(90^0+\Psi_B) & \cos(90^0+\Psi_B) & 0 \\ 0 & 0 & 1 \end{bmatrix} \begin{bmatrix} a_{xPB} \\ a_{yPB} \\ a_{zPB} \end{bmatrix} \tag{4}$$

The impact energy dissipation process was analysed with the use of a planar model of the dynamics of a motor vehicle collision, where the forces and moments acting on the cars during the collision were expressed in the local levelled coordinate systems (Fig. 2). The derivation of the equations of motion (5) of cars A and B was based on the equilibrium of forces and moments that act on cars A and B in the corresponding levelled coordinate systems.

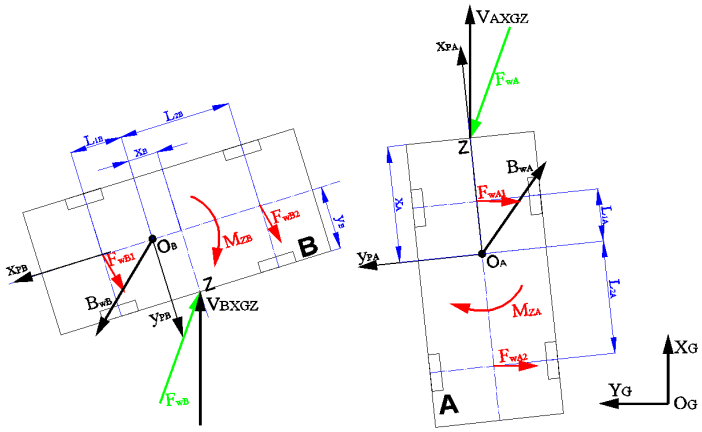

Figure 2. Coordinate systems, basic dimensions, and position of the impact force vector.

$$\begin{cases} m_A \cdot a_{xPA} = F_{nA} + F_{xA1} + F_{xA2} \\ m_A \cdot a_{yPA} = F_{sA} + F_{yA1} + F_{yA2} \\ I_A \cdot \ddot{\Psi}_A = F_{sA} \cdot x_A - F_{nA} \cdot y_A + F_{yA1} \cdot L_{1A} + F_{yA2} \cdot L_{2A} \\ m_B \cdot a_{xPB} = F_{sB} + F_{xB1} + F_{xB2} \\ m_B \cdot a_{yPB} = F_{nB} + F_{yB1} + F_{yB2} \\ I_B \cdot \ddot{\Psi}_B = F_{nB} \cdot x_B - F_{sB} \cdot y_B + F_{yB1} \cdot L_{1B} + F_{yB2} \cdot L_{2B} \\ F_{nB} = F_{nA} \cdot \cos\gamma_{AB} - F_{sA} \cdot \sin\gamma_{AB} \\ F_{sB} = F_{nA} \cdot \sin\gamma_{AB} + F_{sA} \cdot \cos\gamma_{AB} \end{cases} \tag{5}$$

where:

B_i (B_{ix}, B_{iy}) – inertial force acting on the i^{th} car;

M_{zi} – moment of the resistance put up by the inertial force acting on the car to the car rotation around the vertical axis Oz;

m_i, I_i – vehicle mass and mass moment of inertia of the car relative to the vertical axis;

a_{xPi}, a_{yPi} – longitudinal and lateral components of the vector of acceleration of the centre of car mass, calculated from (2);

F_{i1}(F_{xi1}, F_{yi1}) – tangent road reaction acting on the wheels of the front car axle and components of this reaction force;

$F_{i2}(F_{xi2}, F_{yi2})$ – tangent road reaction acting on the wheels of the rear car axle and components of this reaction force;

$F_{wi}(F_{ni}, F_{si})$ – impact force acting on the vehicle and the normal and tangent components of this force;

x_i, y_i – coordinates of point Z, i.e. the point of application of the impact force, in the levelled coordinate system (Fig. 2);

γ_{AB} – angle of rotation of vehicle B relative to vehicle A around the vertical axis ($\gamma_{AB} = \Psi_A - \Psi_B$).

In consequence, a system of six differential equations with respect to the coordinates defining the positions of the centres of mass and rotation of cars A and B plus two algebraic equations was obtained (5); further on, this system will be treated as a system of exclusively algebraic equations, because time histories of components of the vector of translational acceleration of the centre of mass and of the vector of angular acceleration of the cars are known. The said time histories were calculated from the experiment results (with a time step of $\Delta t = 0.001$ s), by transposing the measurement results to the levelled coordinate systems with using relation (2). In this connection, the unknowns in equations (5) are the normal and tangent components F_{nA}, F_{sA}, F_{nB}, F_{sB} of the impact force and lateral reaction forces F_{yA1}, F_{yA2}, F_{yB1}, F_{yB2} acting on car wheels.

4. Experimental test and modelling results

An analysis was carried out for the time histories of individual quantities measured during the period from the instant when car A just came into contact with car B, i.e. from $t = 0$ s, to the instant of $t = 0.2$ s. During this period, the following phases of the experiment were observed (Fig. 1):

- collision of the cars and temporary contact between them (compression and restitution phase);
- separation of the cars;
- separate post-impact movements of the cars.

Fig. 3 shows the course of changes in the normal component F_{nA} of the impact force acting on car A. It was calculated by solving the system of equations (5). The said normal component F_{nA} will be used for determining the work of deformation of the front of car A and the side of car B. An analysis of the curves presented in Fig. 3 made it possible to identify the instant at which cars A and B came out of contact with each other. In tests AB1 and AB2, the contact was broken at $t_k = 0.12$ s and $t_k = 0.09$ s, respectively. The vehicle separation was assumed to take place when the normal force component F_{nA} reached a zero value. The time instants thus identified are necessary to calculate the values of translational and rotational velocities of the cars and to determine the position of the cars in relation to each other and to the road when they became separated.

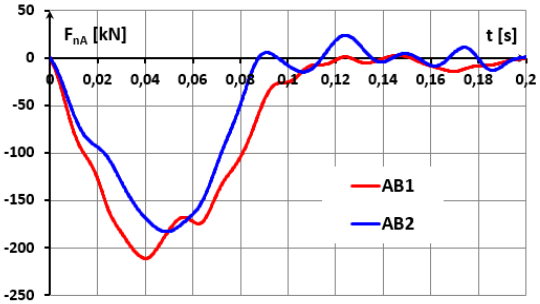

Figure 3. Changes in the normal component F_{nA} of the vector of the impact force acting on car A.

Fig. 4 shows experimental test and calculation results after transformation of the measurement results to the global coordinate system. The curves represent time histories of translational velocities V_{wA} and V_{wB} of the centres of mass of cars A and B and angular velocities $\dot{\Psi}_A$ and $\dot{\Psi}_B$ of these cars around the vertical axis. The angular velocities were calculated according to (1) and the translational velocities were determined from (6), with the velocity vector components having been previously calculated by numerical integration with respect to time (by the trapezoidal rule) of the longitudinal and lateral components of the vectors of acceleration of the centres of car mass according to (3)

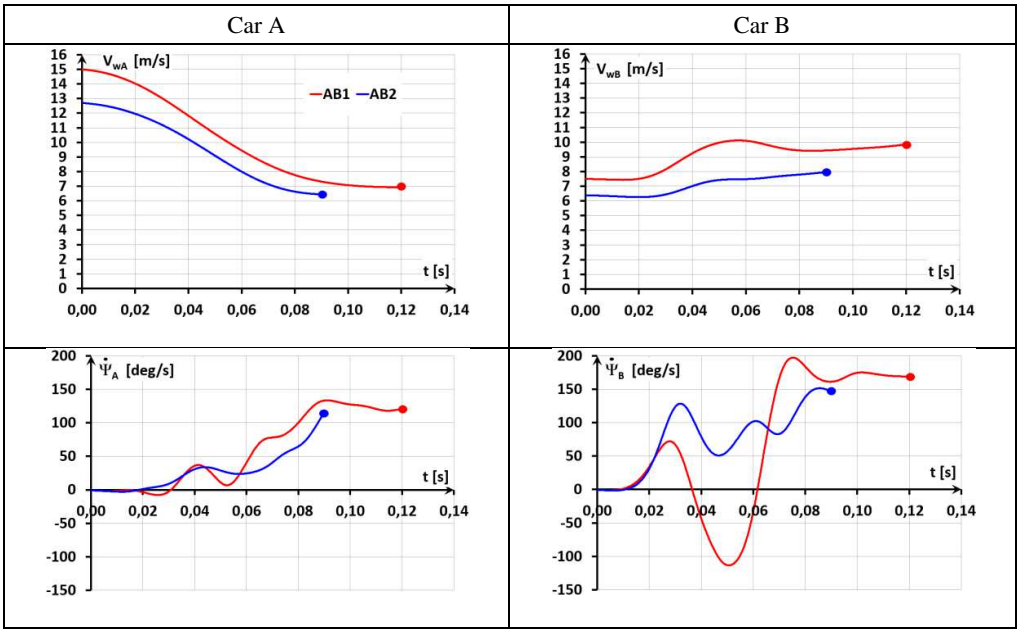

Figure 4. Time histories of translational velocities V_{wA} and V_{wB} of the centres of mass of cars A and B and angular velocities $\dot{\Psi}_A$ and $\dot{\Psi}_B$ of car bodies during.

and (4). The curves above show important elements needed to calculate the energy dissipated. The car velocity values thus determined were used to calculate the kinetic energy of the cars just at the end of the vehicle contact phase, i.e. at the instant of start of the post-impact vehicle motion.

$$V_{wi} = \sqrt{\dot{X}_{Gi}^2 + \dot{Y}_{Gi}^2} \tag{6}$$

Changes in the positions of cars A and B (Fig. 5) were described with the use of three quantities, i.e. longitudinal and lateral displacements of the centres of car mass (X_{Gi} and Y_{Gi}) and vehicle body yaw angles Ψ_i. The axes of the coordinate systems $O_{Gi}X_{Gi}Y_{Gi}Z_{Gi}$ are parallel to those of the global coordinate system and their origins (points O_{Gi}) coincide with the positions of the centres of mass of the respective cars at the instant of the first contact between the vehicles. Noteworthy is also the fact that during the collision, the longitudinal centrelines of cars A and B only slightly deviated from their pre-impact positions. At the instant of t_k, the yaw angle Ψ_A of car A did not exceed 5 ° and the yaw angle Ψ_B of car B was less than 7°. So, the angle between the cars remained almost unchanged during the vehicle contact phase in relation to that observed at the initial instant (i.e. at t = 0 s). This finding was utilized for determining the combined deformation of both cars, with an assumption made

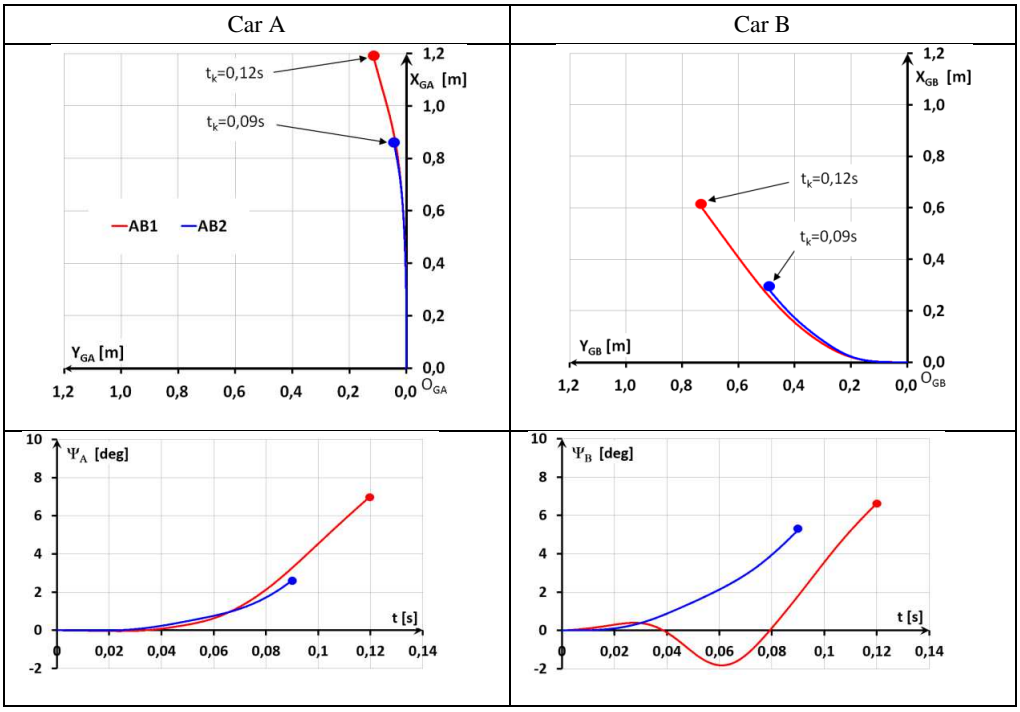

Figure 5. Displacements of the centres of mass of cars A and B in the coordinate system $O_iX_{Gi}Y_{Gi}Z_{Gi}$ and yaw angles Ψ_i (angles of rotation around the vertical axis) of both cars

that the deformation proceeded in the direction defined by the longitudinal centreline of car A. All this means that the calculations described above are essential for the analysis presented.

Changes in the positions of the centres of mass of car „i" $O_i(X_{Gi}, Y_{Gi})$ in the global coordinate system $O_GX_GY_GZ_G$ are defined by the values of corresponding coordinates expressed as functions of time, i.e. $O_A(X_{GA}, Y_{GA})$ for car A and $O_B(X_{GB}, Y_{GB})$ for car B; similarly, changes in the yaw angles of individual cars are also represented by functions of time Ψ_i. Based on the knowledge of all these functions of time, equations of straight lines going through points O_A and O_B and coinciding with the longitudinal car centrelines at any instant during the contact phase of vehicle collision may be determined (Fig. 6).

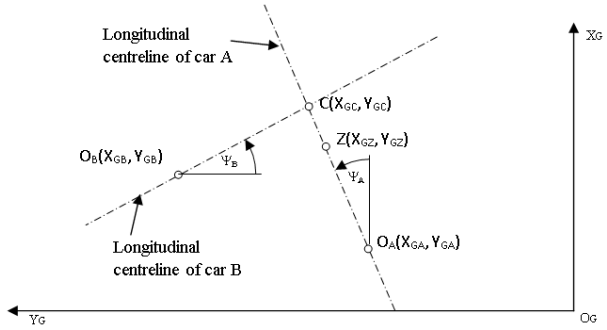

Figure 6. Method of determining the coordinates of point C and line segment O_AC.

Point $C(X_{GC}, Y_{GC})$ is defined by the intersection of the straight lines coinciding with the longitudinal centrelines of cars A and B and its coordinates may be determined by solving the system of equations created by simple equations.

The centre of mass O_A of car A and point C define the line segment O_AC (Fig. 6), the length of which is:

$$|O_AC| = \sqrt{(X_{GC} - X_{GA})^2 + (Y_{GC} - Y_{GA})^2} \tag{7}$$

The change in the length of the line segment $O_AC($ during the contact phase of vehicle collision makes it possible to determine the combined deformation c_A of the front of car A and the side of car B:

$$c_A(t) = \left||O_AC(t)| - O_AC^0\right| \tag{8}$$

where:

O_AC^0 – length of the line segment O_AC at the instant of t = 0 s.

The combined deformation of the front of car A and the side of car B during the contact phase of vehicle collision has been shown in Fig. 7. The combined deformation of both cars c_A is increasing during the compression phase until the maximum deformation value c_{Amax} is attained and then it is decreasing (the restitution phase) to reach a value of c_R at the instant of vehicle separation ($t = t_k$).

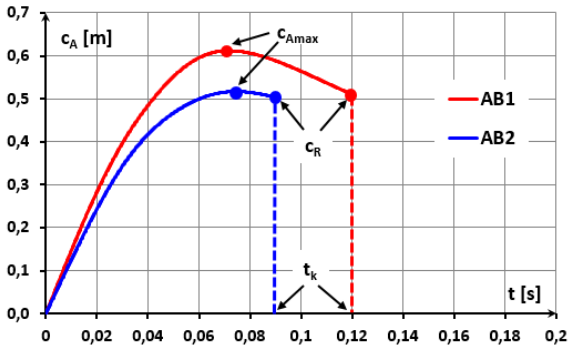

Figure 7. Combined deformation of the front of car A and the side of car B.

Based on the results of calculations of $F_{nA}(t)$ and $c_A(t)$, a force vs deformation curve was plotted for the combined deformation of the front of car A and the side of car B that occurred during the contact phase of vehicle collision; the curve has been presented in Fig. 8. The area between the deformation curve and the c_A axis represents the energy lost for the deformation of the front of car A and the side of car B.

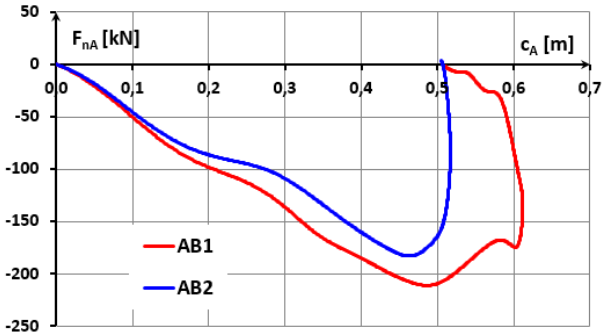

Figure 8. Force vs deformation curve for the combined deformation of the front of car A and the side of car B.

5. Basic energy components involved in the energy dissipation process

The following energy components were discerned as being involved in the contact phase of vehicle collision and in the post-impact vehicle motion:

– initial energy of both cars

$$E_1 = \frac{m_A \cdot V_A^2}{2} + \frac{m_B \cdot V_B^2}{2} \tag{9}$$

– the part of the initial energy that was maintained by the vehicles until the instant of their separation

$$E_2(t_k) = \frac{m_A \cdot V_{wA}^2(t_k)}{2} + \frac{I_A \cdot \dot{\Psi}_A^2(t_k)}{2} + \frac{m_B \cdot V_{wB}^2(t_k)}{2} + \frac{I_B \cdot \dot{\Psi}_B^2(t_k)}{2} \tag{10}$$

– work of deformation of the front of car A and the side of car B during the contact phase of vehicle collision, representing the energy lost

$$E_3 = \int_{c_A=0}^{c_{A\max}} F_{nA} \cdot dc_A - \int_{c_{A\max}}^{c_R} F_{nA} \cdot dc_A \tag{11}$$

The remaining energy lost during the collision phase was determined as follows:

$$E_p = E_1 - E_2 - E_3 \tag{12}$$

The energy balance items calculated as described above have been brought together in Table 2.

Table 2. Main items of the energy balance

	Test AB1	Test AB2		Test AB1	Test AB2
E_1 [kNm]	220.6	156.0	E_1 [%]	100	100
E_2 [kNm]	126.4	92.3	E_2 [%]	57.3	61.2
E_3 [kNm]	75.3	51.4	E_3 [%]	34.2	32.9
E_p [kNm]	18.9	12.3	E_p [%]	8.5	7.9

Table 2 shows that during the contact phase of the collision under consideration, the motor cars involved lost 40.8-42.7 % of their initial energy. Most of the energy lost (80-81 %) was consumed by the car deformation work. This finding shows an important difference between the front-to-side collisions and the head-on collisions of passenger cars, as practically all the initial energy is consumed by vehicle deformation during the contact phase in the latter case. The research work carried out has shown that in the case of the front-to-side collisions, the energy dissipated (i.e. the E_p component) is also consumed by such phenomena as e.g. friction between the vehicles involved and friction between the tyres and the road during their lateral displacement. This part of the energy lost should not be ignored in the calculations carried out at the reconstruction of front-to-side collisions of motor vehicles. To verify the influence of this item of the energy balance on the result of calculations of the pre-impact speed of car A, calculations based on the following equation were made [10]:

$$\Delta E = 0{,}5 \cdot \left(1 - k^2\right) \frac{m_A m_B}{m_A + m_B} \left(V_A - V_B\right)^2 \tag{13}$$

where:

ΔE – energy lost during the collision;

k – coefficient of restitution;

m_A, m_B – masses of the cars;

V_A, V_B – pre-impact speeds of the cars.

Equation (13) is used for the analysis of head-on car collisions, for which it has been derived. With some assumptions having been adopted, however, an attempt was made to utilize this formula for analysing the front-to-side (right-angle) collisions. In the latter case, it was assumed that only the values of the longitudinal component of the vector of the pre-impact velocity of car A (which struck the other one with its front) and of the lateral component of the vector of velocity of car B (which was struck on its side) changed in result of the collision. Any possible changes in the other components of the velocity vectors of cars A and B were ignored. For the assumptions as described above, equation (13) may be written in the following form:

$$V_A = \sqrt{\frac{2 \cdot \Delta E \cdot (m_A + m_B)}{(1 - k^2) \cdot m_A m_B}} \tag{14}$$

Now, the pre-impact speed V_A of car A in tests AB1 and AB2 was calculated from formula (14), with the $E_3 + E_p$ and E_3 energy values being substituted in turn for ΔE. The value of the coefficient of restitution, necessary for the calculations, was determined from experiment results.

The results of calculation of the pre-impact speed of car A have been given in Table 3.

Table 3. Pre-impact speed of car A, obtained from the experiment and by calculations

	AB1	AB2
V_A [m/s] (obtained from the experiment)	15.1	12.7
V_A [m/s] (calculated for $\Delta E = E_3 + E_p$)	15.6	12.8
V_A [m/s] (calculated for $\Delta E = E_3$)	13.9	11.5

The calculation results presented in Table 3 are an example of using the balance of energy of the front-to-side motor car collision. They have shown that the values of the car body deformation work done during collisions of this type, often used for accident reconstruction purposes, result in underestimating the speed of the impacting car by 8-10 %.

A few important conclusions may be drawn from the calculation example set forth above:

- The consistency of the calculated pre-impact speed of car A with the experiment results has confirmed that the method of combined analysis of experiment and modelling results when determining individual items of the energy balance during the contact phase of vehicle collision is correct and does not result in calculation errors; moreover, it enables significant improvement in the accuracy of the process of reconstruction of complex road accidents.
- Thanks to this, the values thus determined of the energy consumed by deformation of both vehicles may be used by forensic experts to verify the methods employed at calculations of the vehicle deformation work from permanent vehicle distortions.

– The calculation results have shown that equation (13) may also be applicable to right-angle car collisions. In such a case, the energy value determined from permanent vehicle distortions must be raised by about 20 %, i.e. by the value of the energy generally covered by E_p.

6. Recapitulation and conclusions

The course of the energy dissipation process was analysed on the grounds of results of:

– measurements carried out during motor car crash tests;
– identification of car positions, based on a frame-by-frame analysis of video records of the experiments;
– calculations of the forces, velocities, and displacements in the car contact zone, based on a model of the dynamics of motor car collision.

An analysis of the results obtained from experimental and model tests has led to conclusions developing the previous approach to the reconstruction of the front-to-side collision of passenger cars (an impact at a right angle against a side, close to pillar B, of a moving car). In particular:

1. The applicability of equation (13) to the calculation of the impacting car's speed in the front-to-side collisions of passenger cars has been more precisely defined by specifying the initial assumptions that must be adopted and the need of raising the value of the energy lost ΔE by about 20 % relative to the energy value calculated from the post-impact vehicle deformation.
2. It has been pointed out that the work of deformation of the front and side parts of the cars involved in a right-angle collision makes about 80 % of the total energy lost by the vehicles during the contact phase of the collision (Table 2) and that this percentage is definitely lower than that observed at the head-on car collisions.
3. During a right-angle collision, the vehicles involved remain in practically unchanged position in relation to each other for the whole time of duration of the contact phase of the collision (until t_k = 0.090-0.12 s, Fig. 1), in spite of their translational and rotational motion during that period. This fact considerably facilitates the interpretation of the measurement results obtained from the experiments.

The calculation results presented in Table 3 have shown that the method of combined analysis of experiment and modelling results, as used here to determine individual items of the energy balance during the contact phase of vehicle collision, provides a possibility of significant improvement in the accuracy of the process of reconstruction of complex road accidents.

References

[1] Bailey M. N., Lawrence J. M., Fowler S. J., Williamson P. B., Cliff W. E., Nickel J. S.: *Data from Five Staged Car to Car Collisions and Comparison with Simulations.* SAE Paper No 2000-01-0849, USA 2000.

[2] Carpenter N., Welcher J.: *Stiffness and Crush Energy Analysis for Vehicle Collision and Its Relationship to Barrier Equivalent Velocity (BEV).* SAE Paper No 01-0500, USA 2001.

[3] Germane G. J., Munson T. S., Henry K. C.: *Side Impact Motor Vehicle Structural Characteristics from Crash Tests.* SAE Paper No 02-0495, USA 2003.

[4] Gidlewski M., Prochowski L.: *Analysis of motion of the body of a motor car hit on its side by another passenger car.* IOP Conference Series: Materials Science and Engineering. Vol. 148/2016, Paper No 012039.

[5] Gidlewski M., Prochowski L., Zielonka K.: *Analysis of the Influence of Motor Cars' Relative Positions During a Right-Angle Crash on the Dynamic Loads Acting on Car Occupants and the Resulting Injuries.* Paper No 15-0107, 24th ESV International Technical. Gothenburg, Sweden, 2015. Available on the Internet www.nhtsa.gov/ESV.

[6] Johnson N., Gabler H. C.: *Evaluation of WinSmash Accuracy in NHTSA Side Crash Test Reconstructions.* Paper No 000389, 22nd ESV International Technical Conference.

[7] Kitagawa Y., Makita M., Pal C.: *Evaluation and Research of Vehicle Body Stiffness and Strength for Car to Car Compatibility.* SAE Paper No 2003-01-0908, USA 2003.

[8] Prasad A. K.: *Energy Absorbed by Vehicle Structures in Side-Impacts.* SAE Paper No 910599, USA 1991.

[9] Prasad, A. K.: *Energy Dissipated in Vehicle Crush – A Study Using the Repeated Test Technique.* SAE Paper No 900412, USA 1990.

[10] Prochowski L., Unarski J., Wach W., Wicher J.: *Podstawy rekonstrukcji wypadków drogowych (Fundamentals of the reconstruction of road accidents).* WKiŁ, Warszawa, 2014.

[11] Schmortte U.: *Crash-Test Results to Analyse the Impact of Non-Professional Repair on the Performance of Side Structure of a Car.* Paper No 000310, 22nd ESV International Technical Conference.

Mirosław Gidlewski, PhD. Eng.: University of Technology and Humanities in Radom, Malczewski Street 29, 26-600 Radom, Automotive Industry Institute (PIMOT), Jagiellonska Street 55, 03-301 Warsaw, Poland (*miroslaw.gidlewski@uthrad.pl*, *m.gidlewski@pimot.eu*).

Leon Prochowski, Prof.: Military University of Technology (WAT), Kaliski Street 2, 00-908 Warsaw, Automotive Industry Institute (PIMOT), Jagiellonska Street 55, 03-301 Warsaw, Poland (*leon.prochowski@wat.edu.pl*).

Leszek Jemioł, MSc. Eng.: University of Technology and Humanities in Radom, Malczewski Street 29, 26-600 Radom, Poland (*leszek.jemiol@uthrad.pl*).

Dariusz Żardecki, Prof.: Automotive Industry Institute (PIMOT), Jagiellonska Street 55, 03-301 Warsaw, Military University of Technology (WAT), Kaliski Street 2, 00-908 Warsaw, Poland (*d.zardecki4@upcpoczta.pl*, *dariusz.zardecki@wat.edu.pl*).

Simulation of the octopod robot controlled by different Central Patterns Generators

Dariusz Grzelczyk, Bartosz Stańczyk, Olga Szymanowska, Jan Awrejcewicz

Abstract: In this paper we focus on kinematic simulation of the octopod robot during its walking on a flat and hard surface. The robot legs are kinematically excited by different well-known mechanical non-linear oscillators as well as new (proposed) ones, working as Central Pattern Generators (CPGs). Time histories of kinematic parameters of the octopod locomotion process are obtained. In particular, we considered displacement and velocity fluctuations of the robot gravity centre in different directions. Eventually, some advantages of the proposed CPGs are outlined, i.e. the lack of the acceleration and deceleration of the robot gravity centre, minimisation of the ground reaction forces between the robot and the ground as well as low energy consumption of the robot during walking.

1. Introduction

Investigations of walking machines were initiated in 1960s by McGhee and Frank who constructed the first four-legged robot called "Phoney Pony" [1]. Since that time, a wide spectrum of quadruped (four-legged) robots have been built. At the same time, six-legged robots have been also constructed and investigated. For instance, interesting state-of-the-art in this area can be found in references [2, 3], where a summary related to biological paragon from nature, methods of studies of animals locomotion and the constructed walking robots are discussed. Recently, also eight-legged robots have become very popular, for instance: a biomimetic eight-legged robot SCORPION [4], eight-foot robot named OctoRoACH [5], and searching and rescuing robot Halluc II [6].

In one of our recent papers [3], we introduced the prototype of the hexapod robot designed based on the biomechanics of insects for inspection and operation applications. In that paper a detailed discussion on the mechanical construction, electronic control system, devices installed on the robot body and the control problem of the robot legs are presented. Finally, we proposed other model of CPG based on the oscillator describing stick-slip induced vibrations. Both numerical and experimental results showed some analogies between the characteristics of the simulated walking robot and animals met in nature. Furthermore, the benefits of the proposed stick-slip vibrations as a CPG are outlined. In our other paper [7] we focused on the kinematic, dynamic and power consumption analysis of the second version of the hexapod robot. The same stick-slip oscillator working as a CPG was investigated from the viewpoint of fluctuations of the robot gravity centre both

in vertical and movement direction, ground reaction forces between the robot legs and the ground as well as energy demand of the whole robot during walking. Time histories of the key kinematic and dynamic quantities describing locomotion of the robot were studied numerically and verified experimentally. Also, we showed the benefits of the proposed stick-slip oscillator working as a CPG. On the contrary to the previous references [3, 7], in the present paper we investigate kinematics of the walking octopod robot controlled by different CPGs. For this purpose, we use previously developed methods and models for robot leg control and models describing kinematic parameters of the robot. However, we propose another CPG model based on sine function which makes it possible to control the movement of the robot legs in simple way, and is easy to generate by both computer software and electronic circuits. In addition, numerical results were also obtained for other CPGs (Toda-Rayleigh lattice and the proposed CPG model) and other values of parameters describing the analyzed robot and parameters of the single robot stride. Finally, we showed that the proposed CPG model based on the sine function can be most efficient with respect to kinematic (and dynamic) parameters of the robot and its energy demand during walking.

2. The prototype of the octopod robot

The CAD project of the considered octopod robot is presented in Fig. 1. To develop the presented model, we used CAD three-joint leg mechanism of the hexapod robot leg and definitions of its links and joints, which can be found in references [3, 7]. The developed virtual model can be useful for design optimization and virtual experiments of the robot motion. The mechanical design of the robot focuses on two main components, i.e. the body and the legs. The full size of the CAD model of the robot is about 590 mm × 370 mm × 150 mm (length × width × height).

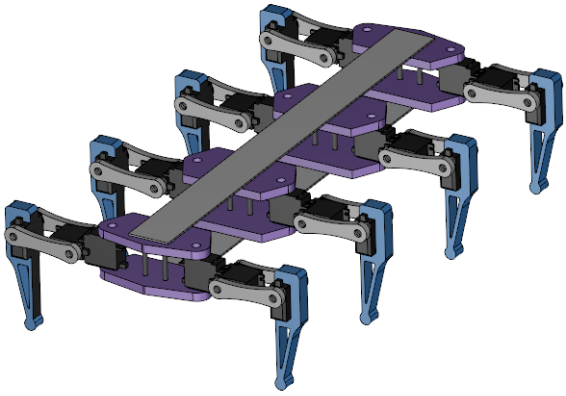

Figure 1. CAD model of the investigated octopod robot created in Inventor.

3. Kinematics of the octopod robot

A kinematic model of the analyzed robot supported by different legs is presented in Fig. 2. In order to obtain this model, we used a method similar to the one presented in our previous papers [3, 7]. The octopod robot is embedded in the Cartesian coordinate system xyz, in the gravity field of the Earth, and it is supported by four legs which form the support polygon (quadrangle) of the robot. Eight identical legs of the robot are denoted as L1, L2, L3, L4 (on the left side of the robot) and R1, R2, R3, R4 (on the right side of the robot). Distances between the ground and the robot gravity centre are denoted by $h_a(t)$, $h_b(t)$. Due to symmetry of the considered robot, it can be assumed that the contact forces $R(t)$ are the same in each robot legs (see Fig. 2). Moreover, we assumed relatively large friction between the robot legs and the ground, which is required to prevent the legs from sliding during walking.

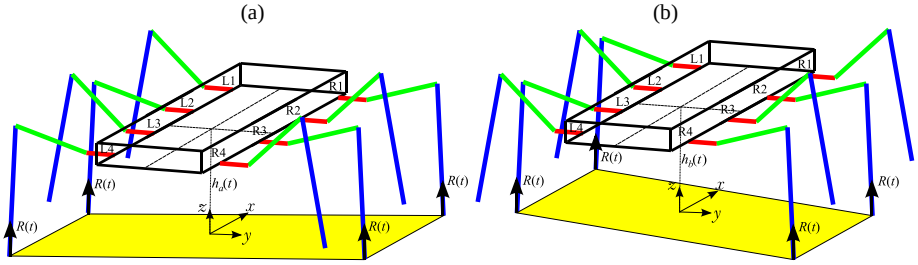

Figure 2. Model of the octopod robot in two different gait configuration: (a) the robot supported by the legs R1, R3, L2 and L4; (b) the robot supported by the legs L1, L3, R2 and R4.

As can be seen, in this model the robot legs are divided into two groups, i.e. the group *a* (legs R1, R3, L2 and L4) and group *b* (legs L1, L3, R2 and R4). The movements of all robot legs are controlled by the same CPG, however, the signals applied to the group *b* of the legs are in anti-phase with respect to signals applied to the group *a*. As a result, the robot is supported by the legs from the group *a* (Fig. 2a) in one phase and by the legs from the group *b* (Fig. 2b) in the other one. Each of the robot legs contains three links of the lengths $l_1 = 40\,\text{mm}$, $l_2 = 70\,\text{mm}$ and $l_3 = 120\,\text{mm}$, which correspond to the Coxa, Femur and Tibia, respectively.

4. Control of the robot leg movements by CPGs

The first CPG model was proposed in 1980s by Cohen et al. through the study on the dissection of a lamprey spinal cord [8]. Since then, numerous investigators have been applying the CPG algorithms to control different bio-inspired walking multi-legged robots. A brief literature review devoted to the implementation of CPG algorithms to control hexapod motion can be found, for instance, in references [3, 9, 10].

Below we consider the first three popular non-linear mechanical oscillators described by non-dimensional ordinary differential equations (ODEs) and working as a CPGs, namely: Hopf oscillator, van der Pol oscillator and Toda-Rayleigh lattice. A simple Hopf oscillator is governed by the first-order ODEs

$$\begin{cases} \dot{X} = (\mu - X^2 - Z^2)X + \omega Z, \\ \dot{Z} = (\mu - X^2 - Z^2)Z - \omega X, \end{cases} \tag{1}$$

van der Pol oscillator is described by the first-order ODEs

$$\begin{cases} \dot{X} = Z, \\ \dot{Z} = \mu(1 - X^2)Z - \omega^2 X, \end{cases} \tag{2}$$

whereas the Toda-Rayleigh lattice is governed by the first-order ODEs

$$\begin{cases} \dot{X}_1 = Z_1, \\ \dot{Z}_1 = \omega^2(e^{X_2 - X_1} - e^{X_1 - X_2}) + \mu(1 - Z_1^2)Z_1, \\ \dot{X}_2 = Z_2, \\ \dot{Z}_2 = \omega^2(e^{X_1 - X_2} - e^{X_2 - X_1}) + \mu(1 - Z_2^2)Z_2. \end{cases} \tag{3}$$

Stable orbits of these oscillators obtained for fixed values $\omega = 2$, $\mu = 6$ and different initial conditions (marked with squares) are presented in Fig. 3. The obtained trajectories oscillate stably, and therefore they were often used to generate the trajectory of a leg tip of robot legs. By changing the values of parameters μ and ω, we can change the shape of the stable orbit and its period. As a result, we can control the parameters of the single robot stride. However, the obtained trajectories cannot be directly used to control the robot leg. They must be converted to the workspace of the leg mechanism first, and then to the joints space of the leg using inverse kinematics relationships.

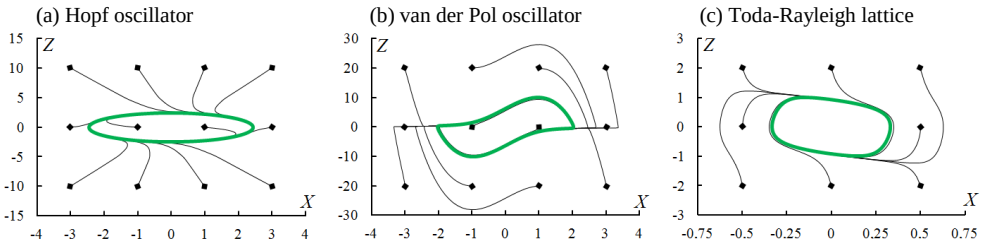

Figure 3. Phase trajectories of three different typical non-linear oscillators for $\omega = 2$, $\mu = 6$ and various initial conditions.

Motivated by investigations of a trajectory of a leg tip of real insects and different biologically inspired robots, we propose other generator based on the sine function, further referred to as a SINE generator. The proposed model is described by the relations

$$X_2(t)=\begin{cases}\dfrac{2}{\pi}\,\mathrm{modulo}(\omega t,\pi) & \text{if} \quad 0<\mathrm{modulo}(\omega t,2\pi)\le\dfrac{\pi}{2},\\ 1-\dfrac{2}{\pi}\,\mathrm{modulo}\left(\omega t-\dfrac{\pi}{2},\pi\right) & \text{if} \quad \dfrac{\pi}{2}<\mathrm{modulo}(\omega t,2\pi)\le\dfrac{3}{2}\pi,\\ -1+\dfrac{2}{\pi}\,\mathrm{modulo}\left(\omega t-\dfrac{3}{2}\pi,\pi\right) & \text{if} \quad \dfrac{3}{2}\pi<\mathrm{modulo}(\omega t,2\pi)\le 2\pi,\end{cases} \tag{4}$$

$$Z_2(t)=\left|\sin^2\left(\omega t+\frac{\pi}{2}\right)\right|\cdot\mathbf{1}\left(-\sin\left(\omega t+\frac{\pi}{2}\right)\right), \tag{5}$$

$$X_1(t)=-X_2(t), \tag{6}$$

$$Z_1(t)=-Z_2(t), \tag{7}$$

where $\mathbf{1}\left(-\sin\left(\omega t+\frac{\pi}{2}\right)\right)$ is the classical step function. The stable orbit for the proposed SINE generator is presented in Fig. 4, and it resembles the shape of the trajectory of a leg tip of a real stick insect presented in references [11, 12].

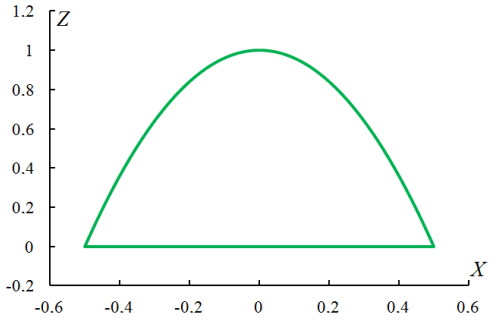

Figure 4. Phase trajectories of the proposed SINE generator.

The presented phase trajectories of the considered oscillators can be applied to control the leg tip of the robot. The size and shape of these trajectories have a great impact on the length and height of a single robot stride, while the orbit period corresponds to the period of the single robot stride. As a result, it is possible to change the gait parameters by changing parameters of the used CPG model, or converting the trajectory of CPG into the workspace of the robot leg [3, 7]. The patterns of the stable orbits of four considered CPG models are depicted in Fig. 5a. By multiplying the variables X and Z of an oscillator working as a CPG, we are able to change directly both the length and height of

the single robot stride. The examples of the trajectories of CPG scaled to the workspace of the robot leg mechanism are presented in Fig. 5b.

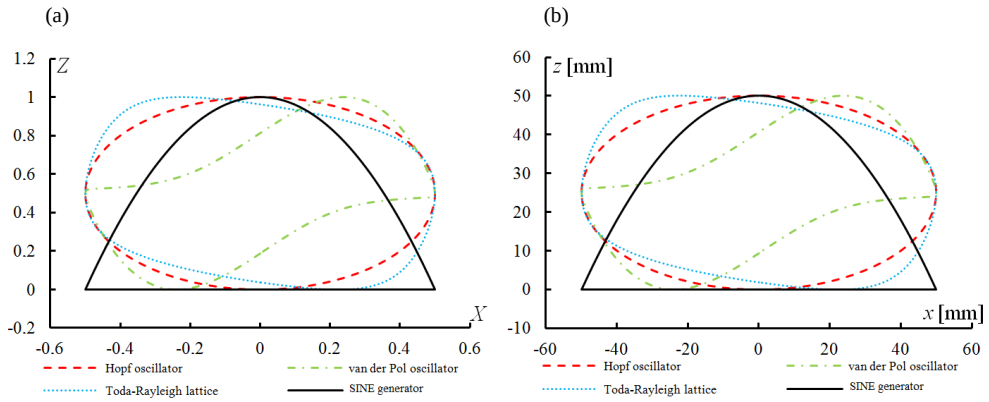

Figure 5. The stable orbits of the investigated CPGs: (a) normalized periodic orbits; (b) the same orbits converted into workspace of the leg mechanism (the stride length $l = 100\,\text{mm}$, the stride height $h = 50\,\text{mm}$).

In further numerical simulations we used variable X of CPG to control the leg tip in x-direction, variable $\dot{X} = Z$ to control the leg tip in the z-direction, whereas the coordinate y of the leg tip is fixed (in this case we used $y = 110\,\text{mm}$).

5. Numerical simulations

In numerical simulations, we applied the standard fourth-order Runge–Kutta method implemented in Scilab. Initial parameters of the considered robot gait are: the stride length $l = 100\,\text{mm}$, the stride height $h = 50\,\text{mm}$ and the stride period $T = 3\,\text{s}$. As a result, the average speed of the robot movement in the forward direction is equal to 0.0667 m/s.

Fig. 6 presents the trajectories plotted by the robot gravity centre $z_C(t)$ in the vertical direction and trajectories plotted by the robot leg tips (group *a* – solid curves, and group *b* – dashed curves). When the three first oscillators controlling the robot legs are applied (see Figs. 6a-c), on the contrary to the results presented in Fig. 6d, considerable fluctuations of the robot gravity centre are clearly observed. For Hopf oscillator, van der Pol oscillator and Toda-Rayleigh lattice, the gravity centre is periodically moved up and down and varies in the range of about a half of the stride height, whereas no fluctuations are observed if the proposed SINE generator is used. As can be seen, the proposed CPG model does not have the mentioned disadvantages, because the robot gravity centre is at a constant level in each phase of its motion.

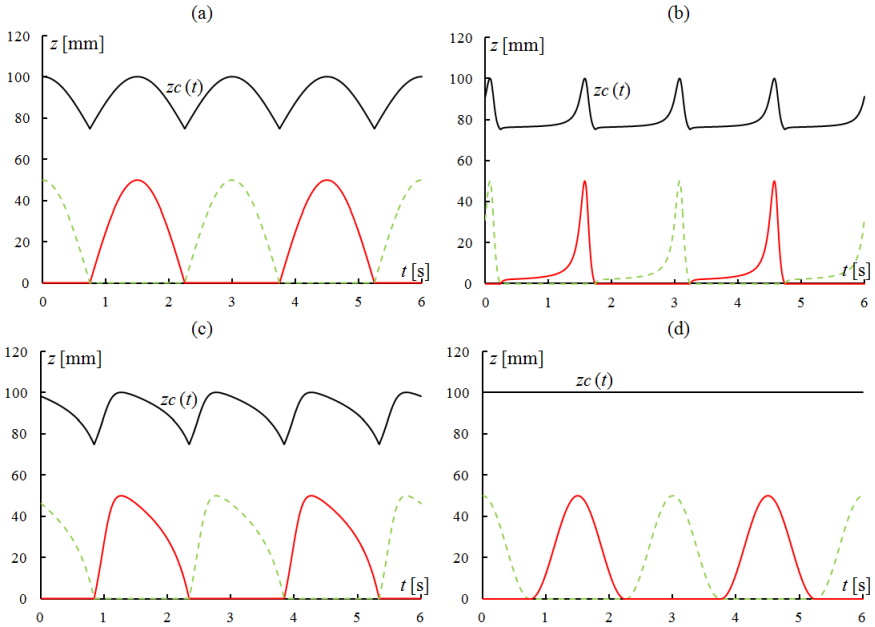

Figure 6. Fluctuation curves of the robot gravity centre $z_C(t)$ and trajectories plotted by the robot legs for different CPGs (solid curves denote group *a* of the robot legs, whereas dashed curves denote group *b* of the robot legs): (a) Hopf oscillator; (b) van der Pol oscillator; (c) Toda-Rayleigh lattice; (d) SINE generator.

Displacement curves of the robot gravity centre in both z and x direction, obtained for different CPGs, are presented in Fig 7. The adequate results regarding the velocity curves (obtained by numerical differentiation of the displacement curves) are presented in Fig. 8. Analysis of the results presented in Figs. 6-8 indicates that in the cases of Hopf oscillator, van der Pol oscillator and Toda-Rayleigh lattice, there exist such phases of the robot motion in which the distance between the centre of the coordinate system and the leg tips touching the ground changes significantly. Moreover, for the van der Pol oscillator some periods of the robot motion are realized faster, while others slower, and therefore the presented fluctuations of the robot gravity centre are the largest for this CPG model. In this case, we can observe the greatest unnecessary accelerations and decelerations of the robot gravity centre in both forward and vertical directions. In the case of the proposed SINE generator working as a CPG, fluctuations of the gravity centre of the robot in any phase of its movement are not observed. It should be noted that the velocities of the robot gravity centre have been obtained by simple numerical differentiation of the displacement variations, and therefore can be slightly different from reality. However, the presented results show characteristic fluctuation of the robot velocity (twice per one robot stride), which are not detected for the proposed CPG model.

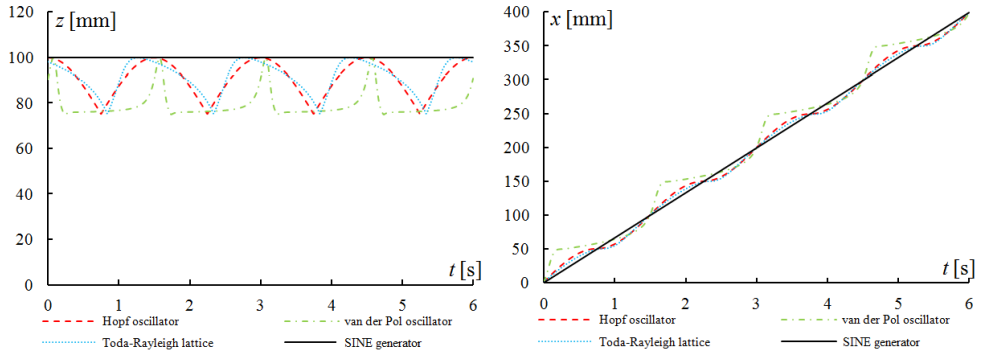

Figure 7. Fluctuations of the displacement curves of the robot gravity centre obtained numerically for different CPGs: (a) in z direction; (b) in x direction.

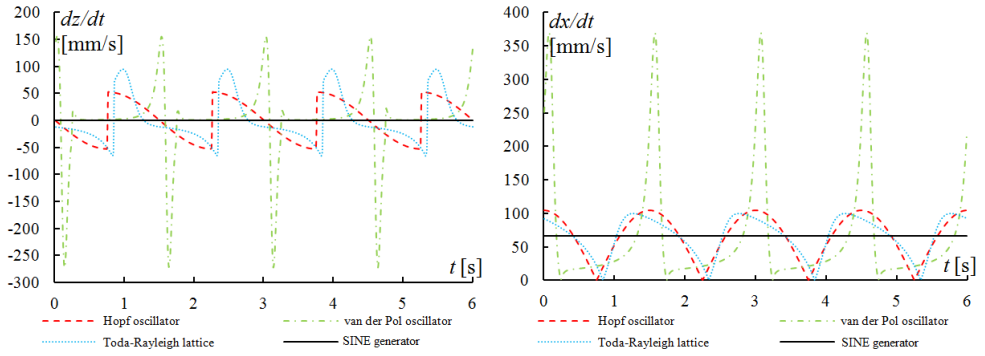

Figure 8. Fluctuations of the velocity curves of the robot gravity centre obtained numerically for different CPGs: (a) in z direction; (b) in x direction.

It should be noted that the fluctuations of the robot gravity centre presented in Figs. 6-8, due to its acceleration/deceleration in the vertical direction, have a great impact on the contact forces acting on the robot legs. Due to the mentioned fluctuation of the robot, the values of reaction forces oscillate (increase and decrease) around the reaction force resulting from the weight of the robot. Therefore, the most frequent and the largest oscillations of contact forces occur in the case of the van der Pol oscillator, while the lowest fluctuations of contact forces exist when the proposed SINE generator is applied.

It should be also noted that power consumption belongs to one of the main operational restrictions on autonomous walking machines. During the last three to four decades, numerous researchers have been also exploring power consumption optimization techniques for these walking robots [13-15]. Fluctuations of the gravity centre and unnecessary changes of speed and acceleration in the moving direction of the robot can have a great impact on energy costs during walking process of the robot.

For this reason, the variation curves of the gravity centre and acceleration of the robot in moving direction should be relatively small during typical walking process of the robot. Therefore, the proposed SINE generator working as a CPG allows for relatively low energy consumption during walking of the robot.

6. Conclusions

A biologically-inspired CAD model of the octopod robot is presented and modelled to study kinematic parameters describing the robot locomotion. The walking process of the considered robot on a flat and hard ground is realized by four different CPG models. A choice of a relatively hard ground has its justification, since this kind of surface generates greater contact forces when the robot legs touch the ground.

The proposed SINE generator based on the sine function is relatively simple in comparison with other control methods presented in the literature and it is useful especially in cases when robot walks on the flat, regular surfaces. We showed that the choice of the applied CPG has a great impact on the kinematical (and dynamical) parameters of the robot gait. The model of CPG constructed based on the van der Pol oscillator appears to be the worst, because the largest unnecessary accelerations and decelerations, both in the vertical and horizontal (movement) directions of the robot, have been detected. As a result, the mentioned fluctuations have a great impact on the energy consumption during walking. That is why during normal walking both the variation curves of the gravity centre and acceleration of the robot in the movement direction should be possibly close to zero. The robot controlled by the proposed CPG does not have unnecessary fluctuations of the gravity centre and low acceleration/deceleration in moving direction. As a result, this generator can be more efficient from the viewpoint of energy cost in comparison to other CPGs. The obtained information can be useful for further analysis of the strength and structural stability of the whole robot and its legs, trouble-free use as well as extension of life and operating time of the robot.

Acknowledgments

The work has been partially supported by the National Science Centre of Poland under the grant OPUS 9 no. 2015/17/B/ST8/01700 for years 2016-2018.

References

[1] McGhee, R., Frank, A. On the stability properties of quadruped creeping gaits. *Mathematical Biosciences* 3, (1968), 331-351.

[2] Chen, X., Wang, L., Ye, X., Wang, G., Wang, H. Prototype development and gait planning of biologically inspired multi-legged crablike robot. *Mechatronics* 23, (2013), 429-444.

[3] Grzelczyk, D., Stańczyk, B., Awrejcewicz, J. Prototype, control system architecture and controlling of the hexapod legs with nonlinear stick-slip vibrations. *Mechatronics* 37, (2016), 63-78.

[4] Klaassen, B., Linnemann, R., Spenneberg, D., Kirchner, F. Biomimetic walking robot SCORPION: control and modeling. *Robotics and Autonomous Systems* 41, (2002), 69-76.

[5] Pulliny, A.O., Kohuty, N.J., Zarrouk, D., Fearing, R.S. Dynamic turning of 13 cm robot comparing tail and differential drive. *Proceeding of 2012 IEEE International Conference on Robotics and Automation*, Minnesota, USA, May 14-18, 2012, 5086-5093.

[6] http://www.pinktentacle.com/2007/07/halluc-ii-8-legged-robot-vehicle/

[7] Grzelczyk, D., Stańczyk, B., Awrejcewicz, J. Kinematics, dynamics and power consumption analysis of the hexapod robot during walking with tripod gait. *International Journal of Structural Stability and Dynamics* 17, (2017), 17 pages.

[8] Cohen, A., Holmes, P., Rand, R. The nature of the coupling between segmental oscillators of the lamprey spinal generator or locomotion: a mathematic model. *Journal of Mathematical Biology* 13, (1982), 345-369.

[9] Chen, W., Ren, G., Zhang, J., Wang, J. Smooth transition between different gaits of a hexapod robot via a central pattern generators algorithm. *Journal of Intelligent & Robotic Systems* 67, (2012), 255-270.

[10] Ijspeert, A. Central pattern generators for locomotion control in animals and robots: a review. *Neural Network* 21, (2008), 642-653.

[11] Durr, V., Schmitz, J., Cruse, H. Behaviour-based modelling of hexapod locomotion: linking biology and technical application. *Arthropod Structure & Development* 33, (2004), 237-250.

[12] Schilling, M., Hoinville, T., Schmitz, J., Cruse, H. Walknet, a bio-inspired controller for hexapod walking. *Biological Cybernetics* 107, (2013), 397-419.

[13] Jin, B., Chen, C., Li, W. Power consumption optimization for a hexapod walking robot. *Journal of Intelligent & Robotic Systems* 71, (2013), 195-209.

[14] Nishii, J. Legged insects select the optimal locomotor pattern based on the energetic cost. *Biological Cybernetics* 83, (2000), 435-442.

[15] Nishii, J. An analytical estimation of the energy cost for legged locomotion. *Journal of Theoretical Biology* 238, (2006), 636-645.

Dariusz Grzelczyk, Ph.D.: Lodz University of Technology, Department of Automation, Biomechanics and Mechatronics, 1/15 Stefanowski Str., 90-924 Lodz, Poland (*dariusz.grzelczyk@p.lodz.pl*).

Bartosz Stańczyk, Ph.D.: Lodz University of Technology, Department of Automation, Biomechanics and Mechatronics, 1/15 Stefanowski Str., 90-924 Lodz, Poland (*bartosz.stanczyk@p.lodz.pl*). The author gave a presentation of this paper during one of the conference sessions.

Olga Szymanowska, Ph.D. Student: Lodz University of Technology, Department of Automation, Biomechanics and Mechatronics, 1/15 Stefanowski Str., 90-924 Lodz, Poland (*olga.szymanowska@dokt.p.lodz.pl*).

Jan Awrejcewicz, Professor: Lodz University of Technology, Department of Automation, Biomechanics and Mechatronics, 1/15 Stefanowski Str., 90-924 Lodz, Poland (*jan.awrejcewicz@p.lodz.pl*).

Optimal and resonant start of free-piston engines

Tom Kigezi, Julian Dunne

Abstract: Combustion-driven free-piston engines (FPEs) are currently being considered for various applications such as vehicle range extenders, power sources in the field, and domestic combined heat and power systems. FPEs can offer higher efficiency, better power-weight ratio, and simpler construction owing to absence of the slider-crank mechanism that is found in conventional engines. Starting an FPE however requires using low power to drive the piston to overcome large opposing forces. The concept of the engine starting by mechanical resonance has been proposed in the literature but lacks analytical treatment. This paper addresses mechanical resonance starting for an FPE whose rebound device is a mechanical spring and proposes a boundary value problem for an FPE whose rebound device is a bounce chamber. The paper further considers the idea of optimally starting FPEs with a minimized, i.e. optimal, starting force. For the case of a mechanical spring rebound device, a starting procedure is proposed that allows development of a closed-form optimal starting force. For the case of a bounce chamber rebound device, a numerical approach is considered. Simulation results and comparative discussions are presented throughout the paper.

1. Introduction

Free-piston engines (FPEs) are increasingly being considered as compact power generators [4] and as combined heat and power systems [3]. Unlike conventional internal combustion (IC) engines, piston motion in FPEs is not constrained by a slider-crank mechanism. This feature not only allows for variable stroke, but also for great compactness and extremely low friction losses. Power output of FPEs is realized by converting the piston thrust energy directly into another useful form, commonly electrical energy.

As with conventional engines, FPEs have a brief starting period in which the engine gets thermodynamically ready for the first combustion event. The goal of engine start is to drive the piston from its rest state to a required piston amplitude which corresponds to a required compression ratio. There is no power generation during engine start. Rather, the FPE's generator is operated as a motor to drive the piston; a process known as *motoring*.

In FPE starting, it would appear that the motoring force must overcome large opposing forces due to gas or spring compression. Yet, arbitrarily large motoring forces are not possible, as the motoring force is greatly limited by the peak current rating of the motor

coils [10]. To overcome this problem, a mechanical resonance inducing strategy has been proposed [5, 10], where a motoring force always acts in the direction of the piston motion such that growing oscillation amplitudes are realized. Despite the strategy's apparent success in practice [5, 6], it has not been the subject of analytical consideration in the literature.

This paper has two objectives. The first is to propose an analytical approach to starting FPEs by mechanical resonance, and by so-doing fill a gap in the literature. The second is to consider a previously unexplored strategy of starting FPEs, i.e. optimally. In optimally starting an FPE, one seeks to minimize the motoring force during the starting process. In turn, the current drawn from an external battery is minimized, and consequently so are the resistive losses in the motor circuit. Indeed, an optimal starting strategy with minimal battery discharge current is especially useful in field or remote FPE deployment where access to an alternative power supply is limited.

The paper considers two FPEs of different rebound device types: one with a mechanical spring [1, 3] and the other with an air bounce chamber [9, 11]. Development of explicit motoring force functions is elaborated and tested by simulation.

2. FPE modelling

An idealized schematic of a single piston two-stroke FPE is shown in Fig. 1. The engine comprises three major parts, namely: a piston-translator assembly (the moving mass), a rebound device (for returning the piston), and an integrated generator (for power generation or motoring). It is noted that various FPE configurations are possible [11], although their analysis can be simplified with the single piston model [12].

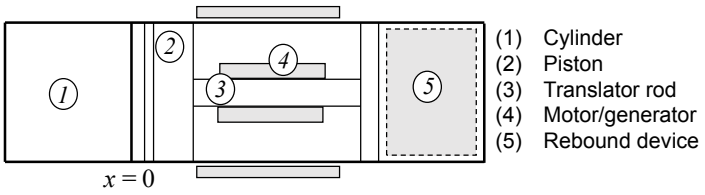

Figure 1. Idealized FPE Schematic.

Considering the compression stroke as the positive direction for piston displacement, piston motion is described by Newtons second law as:

$$-m\ddot{x} = F_c + F_{rd} + F_f + F_m \tag{1}$$

where m is the piston-translator mass (also known as the moving, or active mass), F_c is the cylinder gas force in the combustion chamber, F_{rd} is the rebound device force, F_f is the

friction, and F_m is the generating/motoring force depending on the engine operation mode. For a piston of crown area A, forces F_c and F_{rd} are modelled as:

$$F_c = AP_c \tag{2a}$$

$$F_{rd} = \begin{cases} kx & \text{if rebound device is a mechanical spring} \\ -AP_{rd} & \text{if rebound device is a bounce chamber} \end{cases} \tag{2b}$$

Here, P_c is the in-cylinder pressure, P_{rd} is the bounce chamber pressure, and k is a spring stiffness. The pressures P_c and P_{rd} are respectively related to their associated volumes $V_c(x)$ and $V_{rd}(x)$ through a polytropic process:

$$P_i(x) = \frac{C_i}{V_i(x)^{\underline{n}_i}}, \qquad i = c, rd \tag{3}$$

Here C is a constant and $\underline{n}$ is a polytropic index. Assuming a sufficiently fast starting process for which heat exchange with the surrounding is negligible, $\underline{n}$ can be taken as the ratio of specific heats of the contents of the volume V. Friction force F_f in (1) is typically modelled with a static and viscous component as [10]:

$$F_f = a_f \operatorname{sgn}(\dot{x}) + b_f \dot{x} \tag{4}$$

where a_f and b_f are constants that are determined empirically. It is assumed that the piston does no scavenging work. The implication is that the scavenging process, which replaces exhaust gas with fresh charge, is done by an externally powered pump.

3. Starting using mechanical resonance

Starting by mechanical resonance requires a small motoring force be supplied to produce large piston oscillation amplitudes. The idea is to supply a motoring force that constantly acts in the direction of piston motion. Such a force always does positive work on the piston, yielding continued growth of piston oscillations until limited by some form of system damping. The starting process ends when the piston oscillations reach the required amplitude i.e. a required compression ratio. In the following subsections, resonance is exploited to derive a small motoring force that yields a required piston oscillation amplitude. An analytical solution is successfully developed for an FPE whose rebound device is a mechanical spring. A boundary value problem is constructed for an FPE whose rebound device is a bounce chamber.

3.1. Spring as the rebound device

It is proposed that the combustion chamber remains vented, or open, during the starting process i.e. $F_c = 0$ in (1). To safely limit growth of piston oscillations, rather than rely

on friction, a viscous damper of coefficient b is proposed to be active during the starting process. Accordingly, the force

$$F_d = b\dot{x} \tag{5}$$

is introduced on the right-hand side of (1). With these considerations, equations (1)–(5) reveal the dynamics of a linear oscillator if the rebound device is a mechanical spring. A sinusoidal motoring force of amplitude $\bar{F}_m$ and frequency ω is then proposed as:

$$F_m(t) = -\bar{F}_m \cos \omega t \tag{6}$$

where the minus sign on the right-hand side of (6) is introduced to mean motoring (as opposed to generation). Neglecting friction and incorporating (6) into (1), and introducing damping force (5) on the right-hand side of (1) yields:

$$\ddot{x} + \gamma\dot{x} + \omega_0^2 x = \bar{F} \cos \omega t \tag{7}$$

where

$$\gamma = \frac{b}{m}, \qquad \omega_0 = \sqrt{\frac{k}{m}}, \qquad \bar{F} = \frac{\bar{F}_m}{m} \tag{8}$$

The task is to find $\bar{F}_m$ that produces a required oscillation amplitude. To this end, equation (7) has the general solution:

$$x(t) = A_p \cos(\omega t + \phi) + e^{-\frac{\gamma}{2}t}\left(A_{h1} \cos \omega_h t + A_{h2} \sin \omega_h t\right) \tag{9}$$

where A_{h1} and A_{h2} are arbitrary constants and

$$A_p = \frac{\bar{F}}{\sqrt{(\omega_0^2 - \omega^2) + \gamma^2\omega^2}}, \qquad \tan\phi = \frac{-\gamma\omega}{\omega_0^2 - \omega^2}, \qquad \omega_h = \omega_0\sqrt{1 - \left(\frac{\gamma}{2\omega_0}\right)^2}. \tag{10}$$

As time increases, the second term in (9) diminishes, allowing the first term which represents a constant amplitude sinusoid to dominate. Also observe from (10) that A_p is a function of the motoring force frequency ω. The maximum of $A_p(\omega)$ occurs when the derivative of its denominator in (10) is maximum, i.e. at:

$$\omega = \sqrt{\omega_0^2 - \frac{\gamma^2}{2}} \tag{11}$$

The stiffness of an FPE rebound spring tends to be very high, usually greater than 100kN/m [1,12]. So, it is expected therefore that $\gamma << \omega_0$. Consequently it can be said that the maximum of $A_p(\omega)$, and hence that of $x(t)$, occurs with $\omega \approx \omega_0$. Taking $\omega = \omega_0$ gives:

$$A_p(\omega_0) = \frac{\bar{F}}{\gamma\omega_0} = \frac{\bar{F}_m}{b\omega_0} \qquad \text{and} \qquad \phi(\omega_0) = -\frac{\pi}{2} \tag{12}$$

For a *target* oscillation amplitude s, $\bar{F}_m$ is found from (12) as:

$$\bar{F}_m = sb\omega_0 \tag{13}$$

thereby completing the design of $F_m(t)$ in (6). Note that in general $s << 1$ (in metres), and so $\bar{F}_m$ and hence $F_m(t)$ are by no means large. It also goes without saying that at phase $\phi(\omega_0)$ in (12), $F_m(t)$ always acts in the same direction (i.e. in phase) with the piston speed $\dot{x}$.

Linear system resonance analysis decribed by equations (7)–(12) is well-known, however the formal application of equation (13) to starting an FPEs is new, as demonstrated by simualtion of an FPE with the parameters in Table 1.

Table 1. FPE Simulation Parameters

Parameter	**Value**
Piston-translator mass	0.5 kg
Distance from zero position to cylinder end	0.0168 m
Top dead centre position (nominal)	0.0136 m
Bottom dead centre position (nominal)	-0.0152 m

The spring was of stiffness $k = 170$ kN/m and the damping coefficient was set at $b = 10$. The piston was required to achieve an amplitude $s = 0.0152$ m (the absolute value of the bottom dead centre position). Figure 2 shows the piston response when motored with force (6) at $\omega = \omega_0$ and $\bar{F}_m$ designed as in (13). It is evident that the target amplitude s is achieved in 0.4 seconds without exceeding the cylinder end (solid horizontal line) although nominal top dead centre is exceeded (upper dotted line). The root-mean-square (RMS) of the motoring force is computed to be 62.7 N.

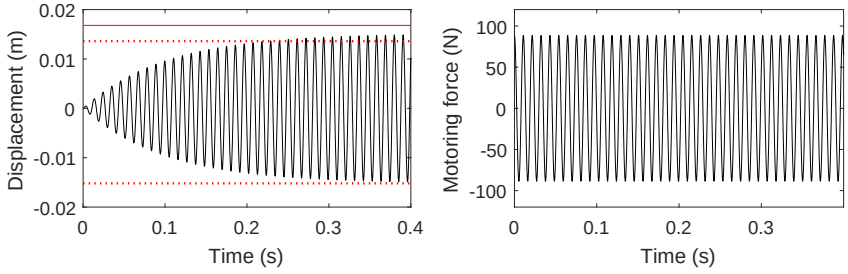

Figure 2. FPE start by mechanical resonance with spring as rebound device.

3.2. Air bounce chamber as the rebound device

Where a bounce chamber is the rebound device, it is proposed that the combustion chamber remain closed throughout the start period. This is so to allow for alternate energy storage and release between the combustion chamber and bounce chamber (a bounce chamber may itself constitute a combustion chamber, as in the dual-piston FPE configuration [11]).

The gas compression and expansion processes as modelled by (3) make the dynamics (1) highly nonlinear, yet it is non-trivial to compute characteristics of nonlinear resonances or to even predict their very appearance [7]. To overcome analytical difficulty, one may supply a *feedback* motoring force that is designed to always act in phase with piston velocity, i.e.:

$$F_m(\dot{x}) = -\bar{F}_m \operatorname{sgn}(\dot{x}), \tag{14}$$

where the minus sign once again denotes motoring and $\bar{F}_m$ is for simplicity considered constant. The question for starting an FPE becomes: what value of $\bar{F}_m$ is required to achieve a target oscillation amplitude when (14) is applied to the dynamics (1)?

An attempt can be made to solve (1) with a solution-approximation method that could relate $\bar{F}_m$ to oscillation amplitude. However, accurately approximating the polytropic process nonlinearities (3) over the entire amplitude in question may require a Taylor polynomial of unamenable high degree. Moreover, presence of the discontinuous sgn term in (14) can further complicate the analysis. A numeric approach to estimating $\bar{F}_m$ is hence proposed. Namely, to solve for $\bar{F}_m$ as a parameter for which the dynamics (1) have a solution that satisfies the four boundary conditions:

$$x(0) = \delta, \qquad \dot{x}(0) = 0, \qquad x(t_f) = x_B, \qquad \dot{x}(t_f) = 0, \tag{15}$$

where δ is a small perturbation to start the oscillations, x_B is the nominal bottom dead centre position and t_f is an unknown terminal time. Such a problem can be solved using commercially available boundary value problem solvers. To ensure finding $\bar{F}_m$ for which response $x(t)$ is oscillatory (as opposed to a single-stroke response), $\bar{F}_m$ cannot be arbitrarily large.

In testing (14), the FPE of parameters in Table 1 were considered for simulation. Note that the sgn term in (14) is a perfect switch that may be difficult to implement in practice. It was approximated to a continuous function as:

$$\operatorname{sgn}(\dot{x}) \approx \frac{\dot{x}}{|\dot{x}| + \varepsilon} \tag{16}$$

where ε is a small positive scalar that:

$$\lim_{\varepsilon \to 0} \frac{\dot{x}}{|\dot{x}| + \varepsilon} = \operatorname{sgn}(\dot{x}) \quad \text{for} \quad \varepsilon \neq 0 \tag{17}$$

A bounce chamber of compression ratio 12 was considered, and the motoring force amplitude $\bar{F}_m$ was set as 4 N. Figure 3 shows a growing, sufficiently self-limited piston response amplitude achieved in 0.8 seconds (frictionless system with no dampers employed). The amplitude stops growing at the point where the supplied motoring force cannot overcome the opposing compression forces in both combustion and bounce chambers. Although the piston exceeds the nominal top dead centre position (upper dotted line), it does not exceed the cylinder end (solid horizontal line) or the nominal bottom dead centre position (lower dotted line).

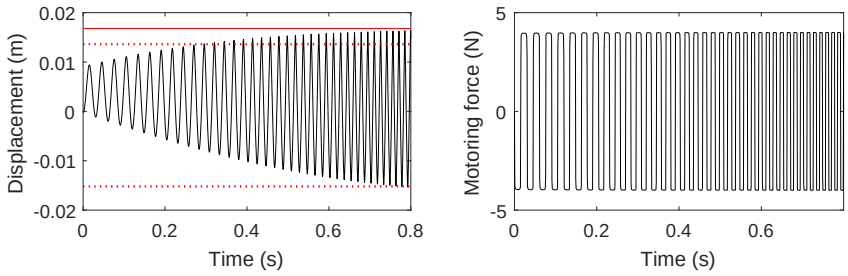

Figure 3. FPE start by mechanical resonance with bounce chamber as rebound device.

4. Optimal start

This section considers the design of *minimal* motoring force for a predetermined FPE start duration. This is to be contrasted to the previous section where a small motoring force was sought that yields large piston oscillation amplitudes. To emphasize why a minimal motoring force is desirable, consider the power equivalence between an FPE's mechanical and electrical systems given by:

$$F_m \dot{x} = \eta i_m e_m \tag{18}$$

Here i_m is the motor armature current, e_m is the armature voltage and η is the energy conversion efficiency of the FPE. From (18) it is noted that:

$$F_m \propto i_m \tag{19}$$

Thus, by minimizing the motoring force, the armature current is minimized. In turn, for a motor circuit resistance R_m, power losses attributed to $i_m^2 R_m$ are also minimized. And, if i_m is a battery discharge current, then minimizing it also prevents fast battery capacity decline, and hence longer battery usage cycles.

4.1. Spring as rebound device

With a spring as the rebound device, the proposed starting procedure involves first driving the piston from its rest state to the nominal bottom dead centre position (where the spring will be fully compressed). When the driving/motoring force is removed, the combustion chamber closed and generation mode activated, the spring then goes into tension, pushing the piston to the nominal top dead centre position within a compression stroke (assuming the spring is of correctly designed stiffness [12]). Piston transition from nominal bottom dead centre to nominal top dead centre ensures that a nominal compression ratio has been achieved, allowing combustion to start.

Assuming the combustion chamber remains open during motoring, then $F_c = 0$. And as before, neglect friction but consider a damper with force (5) introduced to limit the piston oscillations within the cylinder ends. Defining x_1 as piston position and x_2 as piston speed, the state equations for (1) are in fact linear, i.e.:

$$\begin{aligned} \dot{x}_1 &= x_2 \\ \dot{x}_2 &= -\frac{k}{m}x_1 - \frac{b}{m}x_2 - \frac{1}{m}F_m \end{aligned} \tag{20}$$

The task is to find motoring force $F_m(t)$ that drives the state $(x_1(t), x_2(t))$ from the rest state $(0, 0)$ at time $t = 0$ to a final state $(x_B, 0)$ at time $t = t_f$; where x_B is the nominal bottom dead centre position, while minimizing the performance index:

$$J(F_m) = \int_0^{t_f} r\{F_m(t)\}^2 dt \tag{21}$$

where $r > 0$ is a constant. The choice of (21) is motivated by the discussion provided for the relations (18) and (19).

Let it be the case that only smooth functions for $F_m(t)$ are admissible. Following the variational approach to optimal control [8], by defining a Hamiltonian function:

$$H = r\{F_m(t)\}^2 + p_1(t)x_2(t) + p_2(t)\left(-\frac{k}{m}x_1 - \frac{b}{m}x_2 - \frac{1}{m}F_m\right) \tag{22}$$

where $p_1(t)$ and $p_2(t)$ are costate variables: Necessary conditions for an optimal solution comprising the optimal control, state, and costate variables respectively denoted $F_m^*(t)$,$(x_1^*(t), x_1^*(t))$,

and $(p_1^*(t), p_2^*(t))$ are found as:

$$\begin{aligned}
\dot{x}_1^*(t) &= \left.\frac{\partial H}{\partial p_1}\right|_* &&= x_2^*(t) \\
\dot{x}_2^*(t) &= \left.\frac{\partial H}{\partial p_2}\right|_* &&= -\frac{k}{m}x_1^*(t) - \frac{b}{m}x_2^*(t) - \frac{1}{m}F_m^*(t) \\
\dot{p}_1^*(t) &= -\left.\frac{\partial H}{\partial x_1}\right|_* &&= \frac{k}{m}p_2^*(t) \\
\dot{p}_2^*(t) &= -\left.\frac{\partial H}{\partial x_2}\right|_* &&= -p_1^*(t) + \frac{b}{m}p_2^*(t) \\
0 &= \left.\frac{\partial H}{\partial F_m}\right|_* &&= 2rF_m^*(t) - \frac{p_2^*(t)}{m}
\end{aligned} \tag{23}$$

where $t \in [0, t_f]$. The solutions for the necessary conditions (23) are found as [2]:

$$\begin{aligned}
F_m^*(t) &= \frac{1}{2rk}\left(c_1\theta_1 e^{\theta_1 t} + c_2\theta_2 e^{\theta_2 t}\right) \\
x_1^*(t) &= \frac{c_1\theta_1 e^{\theta_1 t}}{2rk\left(\theta_1^2 m + \theta_1 b + k\right)} + \frac{c_2\theta_2 e^{\theta_2 t}}{2rk\left(\theta_2^2 m + \theta_2 b + k\right)} + c_3 e^{\theta_3 t} + c_4 e^{\theta_4 t} \\
x_2^*(t) &= \frac{c_1\theta_1^2 e^{\theta_1 t}}{2rk\left(\theta_1^2 m + \theta_1 b + k\right)} + \frac{c_2\theta_2^2 e^{\theta_2 t}}{2rk\left(\theta_2^2 m + \theta_2 b + k\right)} + c_3\theta_3 e^{\theta_3 t} + c_4\theta_4 e^{\theta_4 t}
\end{aligned} \tag{24}$$

where

$$\theta_{1,2} = \frac{1}{2}\left(\frac{b}{m} \pm \sqrt{\left(\frac{b}{m}\right)^2 - 4\frac{k}{m}}\right), \qquad \theta_{3,4} = \frac{1}{2}\left(\frac{-b}{m} \pm \sqrt{\left(\frac{b}{m}\right)^2 - 4\frac{k}{m}}\right) \tag{25}$$

and where c_1, c_2, c_3 and c_4 are integration constants. Applying the boundary conditions at $t = 0$ and $t = t_f$ to (24) yields the system of algebraic equations:

$$\begin{bmatrix} 0 \\ 0 \\ x_B \\ 0 \end{bmatrix} = \begin{bmatrix} \frac{\theta_1}{2rk\left(\theta_1^2 m+\theta_1 b+k\right)} & \frac{\theta_2}{2rk\left(\theta_2^2 m+\theta_2 b+k\right)} & 1 & 1 \\ \frac{\theta_1^2}{2rk\left(\theta_1^2 m+\theta_1 b+k\right)} & \frac{\theta_2^2}{2rk\left(\theta_2^2 m+\theta_2 b+k\right)} & \theta_3 & \theta_4 \\ \frac{\theta_1 e^{\theta_1 t_f}}{2rk\left(\theta_1^2 m+\theta_1 b+k\right)} & \frac{\theta_2 e^{\theta_2 t_f}}{2rk\left(\theta_2^2 m+\theta_2 b+k\right)} & e^{\theta_3 t_f} & e^{\theta_4 t_f} \\ \frac{\theta_1^2 e^{\theta_1 t_f}}{2rk\left(\theta_1^2 m+\theta_1 b+k\right)} & \frac{\theta_2^2 e^{\theta_2 t_f}}{2rk\left(\theta_2^2 m+\theta_2 b+k\right)} & \theta_3 e^{\theta_3 t_f} & \theta_4 e^{\theta_4 t_f} \end{bmatrix} \begin{bmatrix} c_1 \\ c_2 \\ c_3 \\ c_4 \end{bmatrix} \tag{26}$$

from which c_1, c_2, c_3 and c_4 can be obtained. The optimal control $F_m^*(t)$ in the first equation of (24) has been derived from necessary conditions of optimality (23). It can however be verified that $F_m^*(t)$ is unique and that it does indeed minimize the performance index (21).

The optimal control response was simulated for an FPE again with the parameters listed in Table 1. The spring was of stiffness $k = 170$ kN/m, the damping coefficient was set at

$b = 10$, $r = 2$ in (21) and $t_f = 0.4$ seconds (i.e. same start time as in the case of mechanical resonance in Fig 2). Figure 4 shows the piston response which, as expected, satisfies the boundary conditions in the required start time. The piston does not exceed the cylinder end (solid line), although it does exceed the nominal top dead centre position (upper dotted line). Table 2 shows the clear superiority of optimal control compared to mechancal resonance: the optimal RMS force is lower by 29 % while the optimal performance index J is less by a factor of 10.

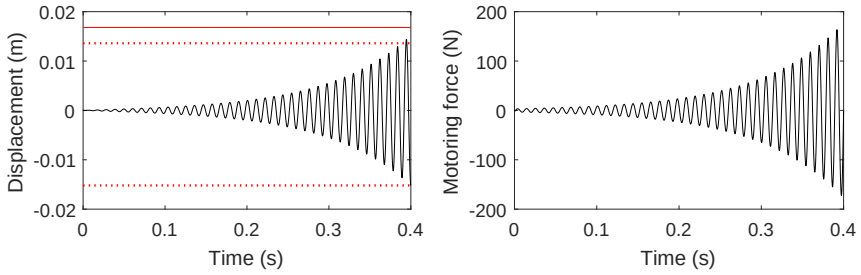

Figure 4. Optimal FPE start with spring as rebound device.

Table 2. Comparison of FPE starting strategies (spring as rebound device).

	RMS force (N)	**Performance index**
Optimal strategy	44.3	1.57×10^3
Resonance strategy	62.7	1.26×10^4

4.2. Air bounce chamber as rebound device

Finally with a bounce chamber as rebound device, first consider both combustion and bounce chambers kept closed during start. Owing to alternate compression and expansion in the chambers, a driven piston (from a perturbed rest position) can be expected to oscillate about its rest position to new amplitudes. The task therefore is to optimally drive the piston until it acquires a large enough amplitude for combustion to begin.

However, as the dynamics are highly nonlinear, one cannot expect a closed-form solution for the optimal start problem and must instead rely on numerical approaches. To improve numerical tractability, a simplification is made where at least one of the gas chambers is open during start. This avoids the complication of having two polytropic process nonlinearities (3) in the dynamics. The following starting procedure then applies:

Step 1. From the piston rest state; with an open bounce chamber (i.e. $F_{rd} = 0$) and open combustion chamber (i.e. $F_c = 0$), drive the piston to nominal top dead centre.

Step 2. Pressurize the bounce chamber i.e. fill it with air ($F_{rd} \neq 0$) and drive the piston to nominal bottom dead centre while keeping the combustion chamber open ($F_c = 0$).

At the nominal bottom dead centre position; when the motoring force is removed, the combustion chamber closed, and generation mode activated, the expanding air in the bounce chamber propels the piston to the nominal top dead centre position (assuming the bounce chamber is correctly pressurized) in a compression stroke towards the end of which combustion can start. The proposed starting procedure is relatively straight forward, but a price is paid with Step 2, where the motoring force must do work to compress the bounce chamber air *in a single stroke*. Consequently one can expect large motoring force amplitudes even with an optimal approach.

Numerical simulation was undertaken using software package GPOPS-II to generate the response in Fig. 5. The chosen FPE parameters were again those in Table 1 for a bounce chamber of compression ratio 12 and performance index (21) with $r = 2$. The piston was constrained not to exceed the nominal bottom and top dead centre positions, and the motoring force magnitude constrained at 500 N. Compared with the meager 4N required for starting the FPE by mechanical resonance in 0.8 seconds, starting by mechanical resonance is clearly the more practical approach for the case of a bounce chamber as rebound device.

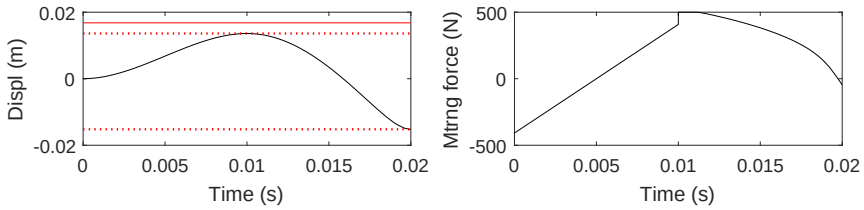

Figure 5. Optimal FPE start with bounce chamber as rebound device.

5. Conclusions

Two strategies for starting FPEs have been studied i.e. with mechanical resonance and by optimal start. Readily implementable, closed-form motoring force functions have been developed and tested where none had been previously advanced. For an FPE whose rebound device is a mechanical spring, the optimal strategy has been verified as superior with a significantly less root-mean-square motoring force and performance index than the resonance strategy. For an FPE whose rebound device is a bounce chamber, the optimal strategy should be better in principle, but can face numerical tractability hurdles. Here, a designed mechanical resonance strategy has been found adequate.

References

[1] Annen, K. D., Woodroffe, J., Agnese, M., and Stickler, D. B. Power generating system. *US Patent* (2009).

[2] Cuspinera, L. A. P. *Optimal control of a flywheel-based automotive kinetic energy recovery system*. PhD thesis, University of Sussex, 2013.

[3] Dunne, J. F. Dynamic modelling and control of semifree-piston motion in a rotary diesel generator concept. *Journal of Dynamic Systems, Measurement, and Control 132*, 5 (2010), 051003/1–051003/12.

[4] Hanipah, M. R., Mikalsen, R., and Roskilly, A. Recent commercial free piston engine developments for automotive applications. *Applied Thermal Engineering 75* (2015), 493–503.

[5] Jia, B., Zuo, Z., Feng, H., Tian, G., and Roskilly, A. P. Development approach of a spark-ignited free-piston engine generator. *SAE Technical Paper 2014-01-2894* (2014).

[6] Jia, B., Zuo, Z., Feng, H., Tian, G., and Roskilly, A. P. An experimental investigation into the starting process of free-piston engine generator. *Applied Energy 157* (2015), 798–804.

[7] Kartashova, E. *Nonlinear Resonance: Analysis, Theory, Computation, Applications*. Cambridge University Press, New York, 2010.

[8] Kirk, D. *Optimal Control Theory: An Introduction*. Dover Publications, 1998.

[9] Kosaka, H., Akita, T., Moriya, K., Goto, S., Hotta, Y., Umeno, T., and Nakakita, K. Development of free piston engine linear generator system part 1 - Investigation of fundamental characteristics. *SAE Technical Paper 2014-01-1203* (2014).

[10] Mao, J., Zuo, Z., and Feng, H. Parameters coupling designation of diesel free-piston linear alternator. *Applied Energy 88* (2011), 4577–4589.

[11] Mikalsen, R., and Roskilly, A. A review of free-piston engine history and applications. *Applied Thermal Engineering 27* (2007), 2339–2352.

[12] Nsabwa Kigezi, T., and Dunne, J. F. A model-based control design approach for linear free-piston engines. *Journal of Dynamic Systems, Measurement, and Control* (2017).

Tom Kigezi, M.Sc. (Ph.D. student): University of Sussex, School of Engineering and Informatics, Falmer, Brighton BN1 9QT U.K. (*tn212@sussex.ac.uk*).

Julian Dunne, Ph.D.: University of Sussex, School of Engineering and Informatics, Falmer, Brighton BN1 9QT U.K. (*j.f.dunne@sussex.ac.uk*).

Amplitude dependent damping of hybrid composites - experimental determination and energetic interpretation

Matthias Klaerner, Mario Wuehrl, Lothar Kroll, Steffen Marburg

Abstract: Composites with either fibre reinforcement or metal layers offer a wide range of adjusting the material behaviour by manipulating parameters such as material selection, layup and fibre orientation. These material combinations require additional modelling efforts in numerical simulations and show a non-linear dynamic behaviour. For applications of high acoustic sensitivity, hybrid composites with metal faces sheets and very thin shear-sensitive plastic cores have been developed. These materials offer significant damping properties but react non-linear depending on frequency, temperature and vibration amplitude. In this study, the amplitude dependency of the vibration damping of metal-plastic composites has been proven experimentally using free vibrations of cantilever beams. The derived decay curves have been analysed due to appropriate mathematical formulations of the amplitude dependency. Moreover, an energy based damping model is used to interpret the damping behaviour classified by material and stress state. Thus, the amplitude dependency of composites can be retraced to the dominant strain energy components with the help of numerical simulations. This results in a more precise modelling of composite dynamics and a better forecast of vibration and sound radiation of complex hybrid parts.

1. Introduction

Damping is understood as dissipation in materials and structures under cyclic loading. It is a complex micro mechanical process of irreversibly converting mechanical energy to heat [19].

An amplitude dependency of the damping has been not investigated as detailed as frequency and temperature dependency. But is is already known for several applications such as buildings with wind excitation [24] and numerous different metals: e.g. Beryllium [1], Niob [13] as well as shape memory alloys [18].

Damping is seen to be non-linearly increasing with strains $\varepsilon > 10^{-4}$ for Mg-Cu-alloys [23] using the Granato-Lcke-model as an explanation [9] and further for Mg-Al-alloys, too [11].

Due to numerous damping effects, there are manifold numerical models. A comparison of micro-mechanical damping models is given in [7] and including interface modelling in [20]. Damping can be further modelled depending on non-linear restoring forces [21] or in a combination of viscous and Coulomb damping [10]. An analytical description of a

homogenisation technique of fibre reinforced composites has been developed by [12] using a viscous damping approach. Further strain energy based models include anisotropic effects of unidirectional reinforced composites. Similar models of Adams, Bacon, Ni and Maheri are well known [2,3,14–16] and further extended e.g. by Berthelot [5] and summarised by Billups [6].

The state of the art leaks precise models for very soft plastics as well as metal-plastic-composites with such shear sensitive cores. Thus, experimental studies show the significance of considering the amplitude dependency for these high damped composites. Moreover, a strain energy based damping model is used to justify the origin of this effect.

2. Free damped vibrations

Assuming free damped vibrations of beams with the bending stiffness EI, the length L, the density ϱ, the natural frequencies are given by

$$\omega_i = \lambda_i^2 \sqrt{\frac{EH^2}{12\varrho L^4}} = 2\pi f_i \ . \tag{1}$$

The solutions λ_i of the frequency equation of cantilever beams give $\lambda_1^2 \approx 3.52$ for the first mode [8]. Rectangular cross sections of height H lead to an independence from the specimen width .

For viscous damping and only one single mode the decay of the displacement is described by an exponential envelope function $\pm Ce^{-\delta t}$ starting at the initial elongation u_0 (figure 1)

$$u(t) = u_0 \cdot e^{-\delta t} \cdot \cos(\omega t). \tag{2}$$

Moreover, the decay of the velocity follows similarly

$$v(t) = -v_0 \cdot e^{-\delta t} \cdot \sin(\omega t) = -u_0 \cdot \omega \cdot e^{-\delta t} \cdot \sin(\omega t). \tag{3}$$

Considering the whole decay period, the damping ratio is given by

$$D = \frac{\delta}{\omega_1}. \tag{4}$$

As an other dimensionless damping parameter the logarithmic decrement is the ratio of two following local maxima:

$$\Lambda = \ln\left(\frac{\hat{x}_n}{\hat{x}_{n+1}}\right) = \frac{1}{m}\ln\left(\frac{\hat{x}_n}{\hat{x}_{n+m}}\right) \tag{5}$$

Thus, Λ can be determined directly from the logarithmic representation (see figure 1) in time domain. Damping ratio and logarithmic decrement are appropriate formulations of a *constant* viscous damping.

$$D = \frac{\Lambda}{\sqrt{4\pi^2 + \Lambda^2}} \qquad \Lambda = \frac{2\pi\theta}{\sqrt{1-\theta^2}} \tag{6}$$

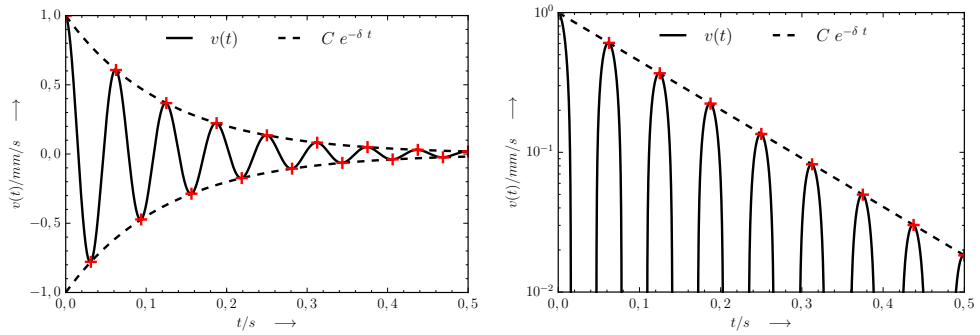

Figure 1. Decay curve: velocity over time, local maxima and exponential envelope function – in linear (left) and logarithmic (right) scale

3. Experimental damping determination

The measuring setup for the damping of the metal-plastic composites is based on bending loads to benefit from the dominant shear damping within the soft cores. A cantilever beam has been chosen as a combination of fixed end without shear deformations and a free end with lateral displacement between the outer metal layers.

In detail, a laser-Doppler-vibrometer is precisely and contactless measuring the velocity of the beam specimen at the free end (figure 2). The beams are of outer dimensions $200\times19\times1.5\ mm^3$ including a core of $0.074\ mm$ thickness. Opposite to the measuring surface, the beam is excited inductively and thus again contactless by an electromagnetic coil. The vibration behaviour is forced to the first bending mode by exciting in the resonance frequency.

Reaching a steady vibration state, the excitation is interrupted and the decay monitored. In addition, a digital low-pass filter at $3\pi f_1$ is applied suppressing the improbable contributions of the second mode at $6\pi f_1$ and all modes above. Thus, a pure harmonic decay is further evaluated in time domain.

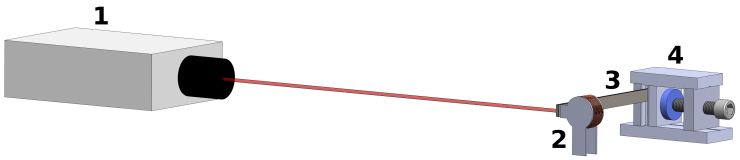

Figure 2. Experimental setup for free damped vibrations of cantilever beams: 1) laser-Doppler-vibrometer measuring the normal velocity; 2) electromagnetic coil for contact less inductive excitation; 3) beam specimen; 4) clamping with pressure force control

4. Identification of amplitude dependent damping

4.1. Global identification of viscous damping

As a first approach in detecting non-linear damping behaviour, bending tests with increasing initial elongations in a range from 0.01 to 0.50 mm have been performed. Assuming perfect viscous damping, the whole decay period has been used to examine the exponential envelope. Figure 3 summarises the envelopes of the decay curves of all different elongations with 10 specimens within each experiment. One curve is highlighted for every setup and compared to its specific exponential fit.

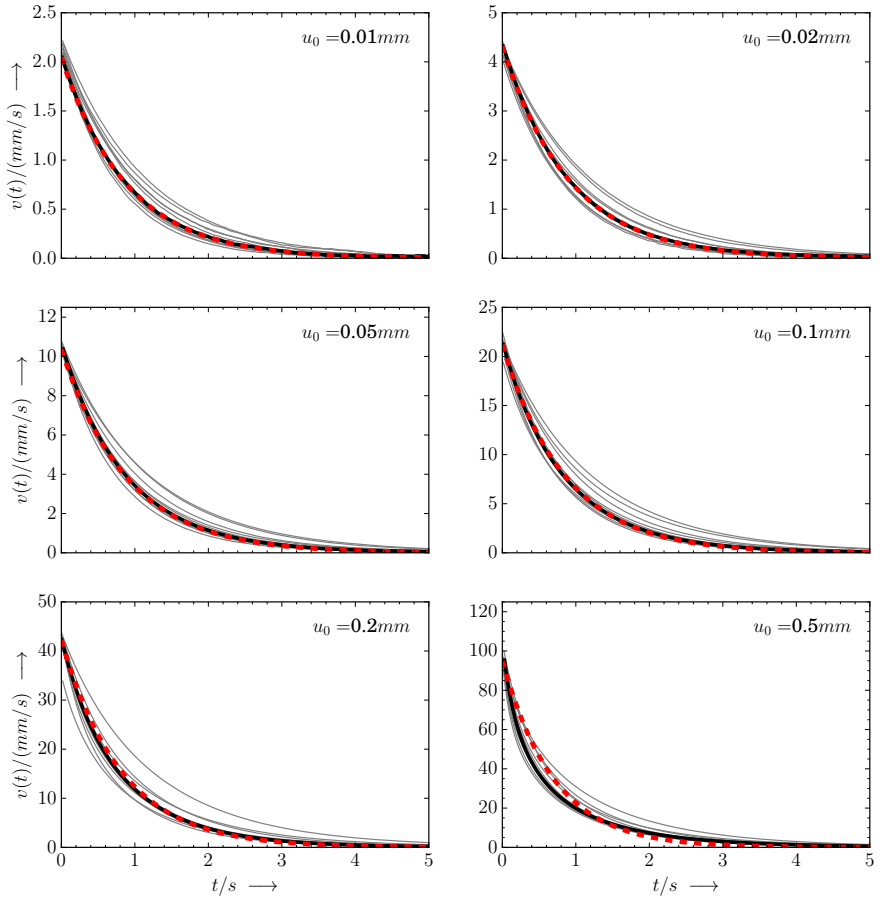

Figure 3. Envelopes of the velocity measurements of free vibrations of cantilever beams (grey) with increasing initial elongations; exemplary exponential curve fit (red) using the viscous damping approach for one single measurement (black)

In addition, the eigenfrequency has been determined and leads to the damping ratio using (4). This *global approach* already gives a good impression of the non-linear behaviour (figure 4). There, the damping is slightly decreasing up to 0.05 mm and constantly increasing further on and could be determined with similar deviation over all specimens for each elongation. In addition, the relative deviation of the minimum damping at 0.05 mm elongation and maximum damping at 0.50 mm elongation is about 25% already and thus cannot be neglected. In detail, the increase of elongation and damping is clearly disproportional.

To compare the different fits objectively, a coefficient of determination R^2 based on the measured velocity peaks $\boldsymbol{v}_m$ and derived decay curves $\boldsymbol{v}_d$ is introduced

$$R^2 = 1 - \frac{\sum\limits_i (v_{m_i} - v_{d_i})^2}{\sum\limits_i (v_{m_i} - \bar{v}_m)^2} \ . \tag{7}$$

This coefficient includes the relation of the sum of squares of the residuals to the total sum of squares of the measured values. It equals the square of the PEARSON correlation coefficient [17, 22] for linear regression and is very similar to standard MAC-analysis in vibro-acoustics [4]. As the correlation of the exponential envelopes is subjectively good (figure 3), we further compare the fraction of variance unexplained $FVU = 1 - R^2$describing the fraction of variance which is not correctly predicted. This deviation measure is shown in figure 4 for increasing elongations averaged over the number of specimens. It is clearly to be seen, that the FVU is significantly increasing for higher elongations. Thus, the validity of a pure viscous damping model is critical.

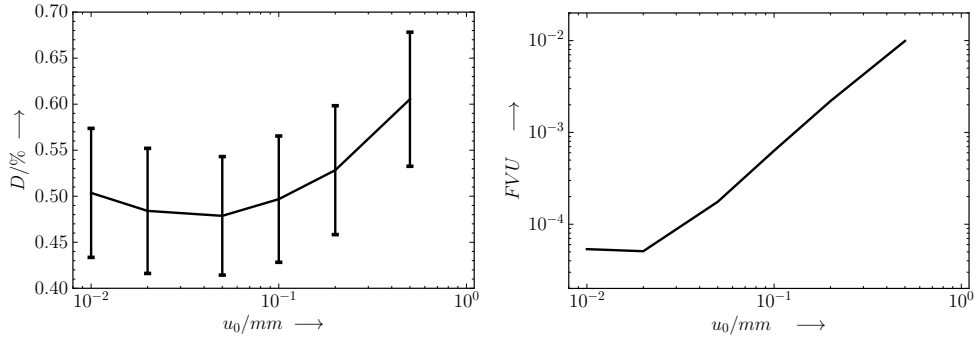

Figure 4. Damping ratio for increasing initial elongations, determined using the viscous damping approach of free vibrations of cantilever beams: damping ratio (left) and fraction of variance unexplained (right)

4.2. Local identification of viscous damping

A more detailed approach of determining the damping is the estimation of the logarithmic decrement in time domain (5). Here, a stepsize of 5 has been used to avoid too much noise for small vibrations but assure a high precision for fast decays. Furthermore, the damping ratio is calculated by (6). Integrating the measured velocities, the local damping has been plotted against the corresponding elongations in figure 5.

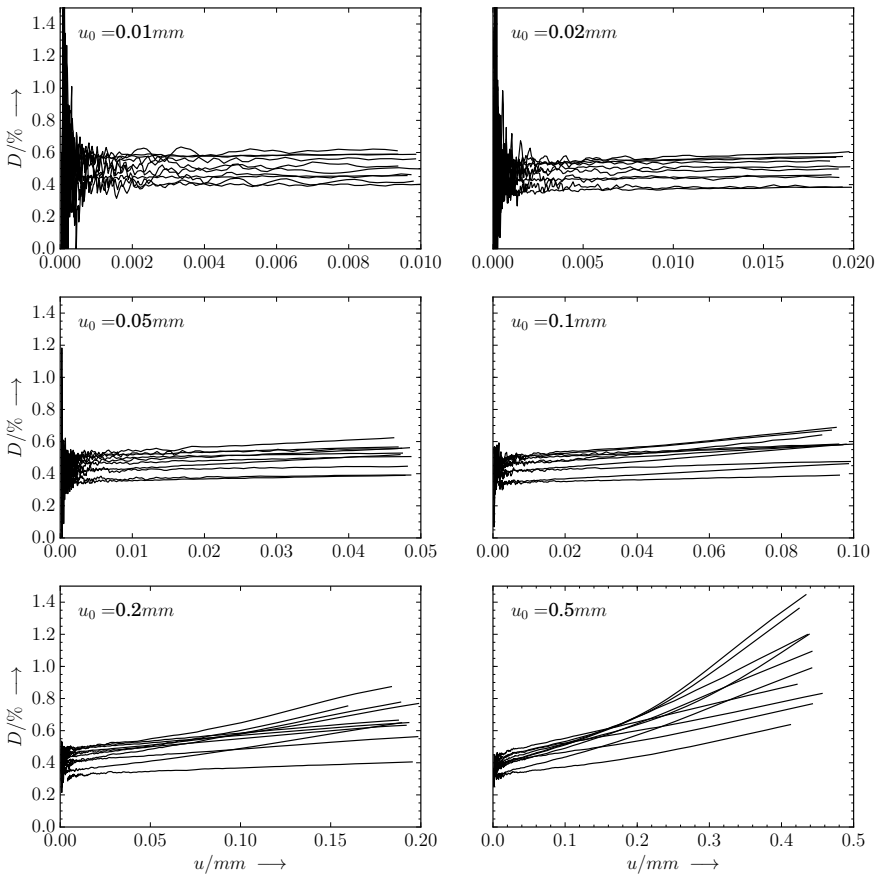

Figure 5. Local damping determination: viscous damping derived from the logarithmic decrement over the decaying elongation, ten specimens tested with increasing initial elongations

Here, the vibrations decay from right (high elongations) to left (zero). For small vibrations, a constant damping can be observed for each specimen but significant deviations between the specimens occur. Comparing the standard deviations from figure 4, the speci-

mens again differ by approximately ±12% for all elongations. In addition, the noise of this local approach is obvious, especially for very small vibrations.

With increasing amplitudes above 0.05 mm, the curves tend to slope. Starting with almost linear dependencies, the values are wide spread and show a bent behaviour for the highest amplitudes.

5. Strain energy based quantification

5.1. Strain energy and strain energy density

The general ail is finding the physical reason of derived non-linear damping of this hybrid metal-plastic-composites. Due to the soft and thus shear sensitive core, the bending behaviour is dominated by tension and compression of the metal face sheets in combination with the shear dominated core deformations.

Previous investigations of amplitude dependent damping were focussed on monolithic materials and often related to the maximum stress by strength. For bending of cantilever beams, the maximum stress is a local maxima at the outer edge on the clamping whereas the free end of the beam as well as the neutral fibres of monolithic beams remain free of stresses at all.

Moreover, the combination of different materials within different types of composites leads to locally distributed strains and material specific strengths.

Thus, either geometric or stress related amplitudes are inadequate references for an amplitude depended damping determination. As damping generally is defined as dissipated energy over the maximum potential energy within a vibration cycle

$$\psi = \frac{E_{diss}}{E_{pot}} \tag{8}$$

the strain energy has been further chosen as an appropriate amplitude measure. Generally, the strain energy is a volume integral over stress and strain

$$E_{pot} = \frac{1}{2} \int_V \sigma \varepsilon \mathrm{d}V \ . \tag{9}$$

Considering the different stresses of all N_E discretised elements with volumes V_e within an FEA-model, the energy is estimated by

$$\begin{aligned} E_{pot} &= \frac{1}{2} \sum_e^{N_e} V_e \cdot [\sigma_{11_E} \varepsilon_{11_e} + \sigma_{22_e} \varepsilon_{22_e} + \sigma_{33_e} \varepsilon_{33_e} + \sigma_{12_e} \varepsilon_{12_e} + \sigma_{13_e} \varepsilon_{13_e} + \sigma_{23_e} \varepsilon_{23_e}] \\ &= \sum_e^{N_e} [E_{11_e} + E_{22_e} + E_{33_e} + E_{12_e} + E_{13_e} + E_{23_e}] \\ &= E_{11} + E_{22} + E_{33} + E_{12} + E_{13} + E_{23} \ . \end{aligned} \tag{10}$$

In addition, the strain energy density is defined by

$$
\begin{aligned}
U &= \frac{1}{2}\sum_{e}^{N_e}[\sigma_{11_e}\varepsilon_{11_e} + \sigma_{22_e}\varepsilon_{22_e} + \sigma_{33_e}\varepsilon_{33_e} + \sigma_{12_e}\varepsilon_{12_e} + \sigma_{13_e}\varepsilon_{13_e} + \sigma_{23_e}\varepsilon_{23_e}] \\
&= \sum_{e}^{N_e}[U_{11_e} + U_{22_e} + U_{33_e} + U_{12_e} + U_{13_e} + U_{23_e}] \\
&= U_{11} + U_{22} + U_{33} + U_{12} + U_{13} + U_{23} \ . \qquad (11)
\end{aligned}
$$

We further use the mean strain energy density

$$
\overline{U} = \frac{E_{pot}}{V} = \overline{U}_{11} + \overline{U}_{22} + \overline{U}_{33} + \overline{U}_{12} + \overline{U}_{13} + \overline{U}_{23} \qquad (12)
$$

with its components U_{ij} as a measure of the vibration amplitude, too.

5.2. Numerical strain energy determination for the cantilever beams

For a strain energy based quantification of the derived damping results, the cantilever beam specimens within the given experimental setup (section 3) have been investigated numerically by static FEA. Therein, the beam specimen has been elongated by 1 mm exemplary to illustrate the energy distributions (figure 6).

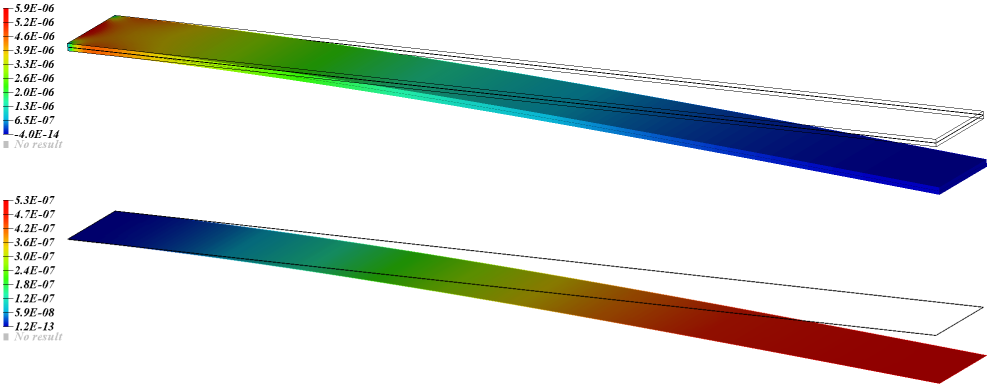

Figure 6. Cantilever beam at 1 mm elongation: strain energy distribution in mJ: steel face sheets dominated by E_{11} (top) and shear sensitive polymer core with mainly E_{12} (bottom)

The steel face sheets basically show normal strains and stresses along the beam length. Thus, the total strain energy is dominated by this component but locally distributed as follows. The energy increases from the free and elongated end to the clamping with a local maximum of $5.9 \cdot 10^{-9} J$.

In contrast, the core deformations are mainly in-plane shear and are distributed vice versa. The relative deformation of the face sheets is bonded at the clamping whereas these

shear deformations within the core peak at the free end of the beam. With a maximum of $5.3 \cdot 10^{-10} J$ the strain energy in the core is one order of magnitude smaller compared to the face sheets.

In summary, table 1 shows the components of the total strain energy as well as of the strain energy density within the composite materials. About 70% of the total energy E are stored in the stiff face sheets and related to the stresses and strains along the beam. The shear deformations within the soft core lead to 30% of the total strain energy. All other components are negligible. In contrast, considering the mean energy density $\hat{U}$ of the whole model, the core covers more than 86% due to the small thickness, whereas the tension/compression of the face sheets covers only 14%.

Table 1. Total strain energy components and mean strain energy density components for the cantilever beam at maximum elongation

	steel face sheets	polymer core
$E_{11}/10^{-6} J$	340.58	0.00
$E_{22}/10^{-6} J$	0.09	0.00
$E_{33}/10^{-6} J$	0.00	0.00
$E_{12}/10^{-6} J$	0.00	144.23
$E_{23}/10^{-6} J$	0.00	0.02
$E_{13}/10^{-6} J$	1.00	0.00
$\bar{U}_{11}/10^{-6} MPa$	60.81	0.00
$\bar{U}_{22}/10^{-6} MPa$	0.00	0.00
$\bar{U}_{33}/10^{-6} MPa$	0.00	0.00
$\bar{U}_{12}/10^{-6} MPa$	0.02	512.90
$\bar{U}_{23}/10^{-6} MPa$	0.00	0.07
$\bar{U}_{13}/10^{-6} MPa$	0.18	0.00

6. Conclusions and outlook

Within this study, a hybrid metal plastic composite has been investigated concerning amplitude dependent damping behaviour. Therefore, a methodology is presented starting from an experimental setup for free damped vibrations of cantilever beams. The derived data is further analysed in time domain by either a global or local damping determination showing a significant amplitude dependency.

Justifying the physical reasons, a strain energy based damping model is introduced. It relates the effects mainly to the shear sensitive cores due to their magnificent damping and

very high compliance.

Further studies address the analytical description $D(E), D(\bar{U})$ of the amplitude dependency of the damping of the composite as well as, if separable by experiments, layer-wise its strain energy related components. An FEA-based design of experiment will be further implied using the mean strain energy per component as a criterion rating the amplitudes.

Acknowledgments

The paper arose in the context of the project DFG-KR 1713/18-1 *Schallabstrahlung bei nichtlinearem und lokal variierendem Dämpfungsverhalten von Mehrlagenverbunden* as well as the Federal Cluster of Excellence EXC 1075 *MERGE Technologies for Multifunctional Lightweight Structures* supported by the Deutsche Forschungsgemeinschaft (DFG). Financial support is gratefully acknowledged.

References

[1] Abrams, E., Kamber, K., and Ang, C. Strain amplitude dependent internal friction in beryllium. *Acta Metallurgica 14*, 6 (1966), 729 – 740.

[2] Adams, R. D., and Bacon, D. G. C. Effect of fibre orientation and laminate geometry on the dynamic properties of cfrp. *Journal of Composite Materials 7* (1973), 402–428.

[3] Adams, R. D., and Maheri, M. R. Dynamic flexural properties of anisotropic fibrous composite beams. *Composites Science and Technology 50*, 4 (1994), 497–514.

[4] Allemang, R. The modal assurance criterion - twenty years of use and abuse. *Sound and Vibration 37*, 8 (2003), 14–21.

[5] Berthelot, J.-M. Damping analysis of laminated beams and plates using the ritz method. *Composite Structures 74*, 2 (2006), 186–201.

[6] Billups, E., and Cavalli, M. 2d damping predictions of fiber composite plates: Layup effects. *Composites Science and Technology 68*, 3-4 (2008), 727–733.

[7] Chandra, R., Singh, S., and Gupta, K. Micromechanical damping models for fiber-reinforced composites: a comparative study. *Composites Part A: Applied Science and Manufacturing 33*, 6 (2002), 787–796.

[8] Dresig, H., and Holzweissig, F. *Dynamics of Machinery: Theory and Applications*. Springer Berlin Heidelberg, Berlin, Heidelberg, 2010.

[9] Granato, A., and Lcke, K. 6 - the vibrating string model of dislocation damping. In *Applications to Quantum and Solid State Physics, Part A*, W. P. MASON, Ed., vol. 4, Part A of *Physical Acoustics*. Academic Press, 1966, pp. 225 – 276.

[10] Hartog, J. D. Forced vibrations with combined coulomb and viscous friction. *Transactions of the American Society of Mechanical Engineers - APM 53*, 9 (1931), 107–115.

[11] Hu, X.-s., He, X.-d., Zheng, M.-y., and Wu, K. Effect of small tensile deformation on damping capacities of mg-1%al alloy. *Transactions of Nonferrous Metals Society of China 20, Supplement 2*, 0 (2010), s444–s447.

[12] Kaliske, M., and Rothert, H. Damping characterization of unidirectional fibre reinforced polymer composites. *Composites Engineering 5*, 5 (1995), 551–567.

[13] Klam, R., Schultz, H., and Schaefer, H. Amplitude dependent dislocation damping in niobium. *Acta Metallurgica 28*, 3 (1980), 259 – 264.

[14] Maheri, M. R. The effect of layup and boundary conditions on the modal damping of frp composite panels. *Journal of Composite Materials 45*, 13 (2011), 1411–1422.

[15] Maheri, M. R., and Adams, R. D. Modal vibration damping of anisotropic frp laminates using the rayleigh-ritz energy mininization sceme. *Journal of Sound and Vibration 259*, 1 (2003), 17–29.

[16] Ni, R., and Adams, R. The damping and dynamic moduli of symmetric laminated composite beams-theoretical and experimental results. *Journal of Composite Materials 18*, 2 (1984), 104–121.

[17] Pearson, K. Note on regression and inheritance in the case of two parents. *Proceedings of the Royal Society of London 58*, 347-352 (1895), 240–242.

[18] Piedboeuf, M., Gauvin, R., and Thomas, M. Damping behaviour of shape memory alloys: Strain amplitude, frequency and temperature effects. *Journal of Sound and Vibration 214*, 5 (1998), 885–901.

[19] Piersol, A. G., and Paez, T. L., Eds. *Harris shock and vibration handbuch*, 6 ed. McGrawHill, 2010.

[20] Rakesh Chandra, S.P. Singh, K. G. A study of damping in fiber-reinforced composites. *Journal of Sound and Vibration 262* (2003), 475–496.

[21] Rasmussen, M. L. On the damping decrement for non-linear oscillations. *International Journal of Non-Linear Mechanics 12*, 2 (1977), 81–90.

[22] Schumacker, R., and Tomek, S. *Understanding Statistics Using R*. Springer New York, New York, NY, 2013, ch. Correlation, pp. 209–218.

[23] WAN, D.-q., HE, B.-l., XIONG, G.-y., CHEN, Z.-x., WANG, J.-c., and YANG, G.-c. High damping capacities of mg-cu based alloys. *Transactions of Nonferrous Metals Society of China 20, Supplement 2*, 0 (2010), s448–s452.

[24] Wu, J., Liu, P., and Li, Q. Effects of amplitude-dependent damping and time constant on wind-induced responses of super tall building. *Computers & Structures 85*, 15–16 (2007), 1165–1176.

Matthias Klaerner, Dipl.-Ing.: Chemnitz University of Technology, Institute of Lightweight Structures, 09107 Chemnitz, Germany (*matthias.klaerner@mb.tu-chemnitz.de*). The author gave a presentation of this paper during one of the conference sessions.

Mario Wuehrl, B.Sc.: Chemnitz University of Technology, Institute of Lightweight Structures, 09107 Chemnitz, Germany (*matthias.klaerner@mb.tu-chemnitz.de*).

Lothar Kroll, Univ.-Prof. Dr.-Ing. habil. Prof. E. h. Prof.: Chemnitz University of Technology, Institute of Lightweight Structures, 09107 Chemnitz, Germany (*matthias.klaerner@mb.tu-chemnitz.de*).

Steffen Marburg, Univ.-Prof. Dr.-Ing.: Technische Universität München, Gerhard Zeidler Endowed Professorship for Vibroacoustics of Vehicles and Machines, 85748 Garching, Germany (*steffen.marburg@tum.de*).

Modeling of dynamics of a counter-rotating horizontal axis wind turbine

Liubov Klimina, Boris Lokshin, Vitaly Samsonov, Yury Selyutskiy,
Ekaterina Shalimova, Alois Steindl

Abstract: The closed dynamical model of a counter-rotating HAWT is constructed. It is supposed that one propeller carries a rotor of an electric generator, and the other one carries a stator of the generator. The generator is connected into a local electric circuit by means of running contacts. The electromechanical interaction between the rotor and the stator is described with a linear function on a relative angular speed of the rotor. Aerodynamic torques acting upon the propellers are described using a quasi-steady approach. Flow speed in the wake of the front propeller is estimated with the use of the Betz theory. Stationary modes are studied. A trapped power coefficient is estimated depending on such parameters of the model as the external resistance in the electric circuit of the generator and the wind speed. In particular, it is shown that in the case of two similar propellers, rather high trapped power coefficient is achieved when the rear propeller is "leading" i.e. produces more power than the front one. Such an operation mode is preferable if the electric load is sufficiently high.

1. Introduction

The general scheme of a counter-rotating horizontal axis wind turbine (HAWT) was suggested at the end of the XX century [1]. Since that time, experimental tests and results of numerical simulation confirmed effectiveness of counter-rotating horizontal axis wind turbines [2–8]. Their advantages to classical single-propeller HAWTs are an increase in a trapped power coefficient; a decrease in gyroscopic loads upon the mechanism; an increase in a relative angular speed of a rotor of the generator with respect to a stator without using a gear; an auto-centering on the wind for a wide range of initial states.

Due to relatively novelty of counter-rotating HAWTs, the influence of changeable electric load upon their dynamics is still described only in several special cases [9, 10]. In particular, it is proved that such an influence produces a sufficient impact upon the behavior of so-called small-scale turbines, namely, turbines connected into a local electric circuit (e.g., circuits of individual households). In such circuits, connection/disconnection of additional consumers influences an operation of a turbine greatly. To describe such an influence, a closed few-parametric mathematical model that takes into account changeable electric load in the local circuit of a generator is constructed. This model allows performing detailed parametric analysis of operation modes of the

turbine. In particular, it is shown that nonlinearity of an aerodynamic torque (which is a function of the angular speed of the turbine) leads to the hysteresis of the operation angular speeds of propellers depending on decrease/increase in the external load. This may lead to the hysteresis effect of the power produced by the counter-rotating HAWT with respect to increasing/decreasing the external resistance in the local circuit [10]. Similar effect holds for single propeller HAWTs [11, 12].

Unlike [9,10], in this paper the influence of the front propeller upon the aerodynamics of the rear propeller is taken into account. For this purpose an axial induction factor in the wake is estimated using the approach [13–15]. A bifurcation diagram of the trapped power coefficient depending on the changeable external load coefficient is constructed. Several principle types of operation modes are revealed.

2. Description of the mechanical system

The double-propeller HAWT that is located in a steady horizontal wind flow of the speed **V** is studied (Fig. 1). The corresponding mechanical system consists of two rigid bodies: a front propeller and a rear propeller. Both propellers have similar aerodynamic properties, but are intended to rotate in the opposite directions. The shaft of one of the propellers carries a rotor of an electric generator; the shaft of the other propeller is joined to a stator of the same generator. The generator is connected to a local electric circuit by means of the running contacts. The external resistance in the circuit is a varied parameter of the model.

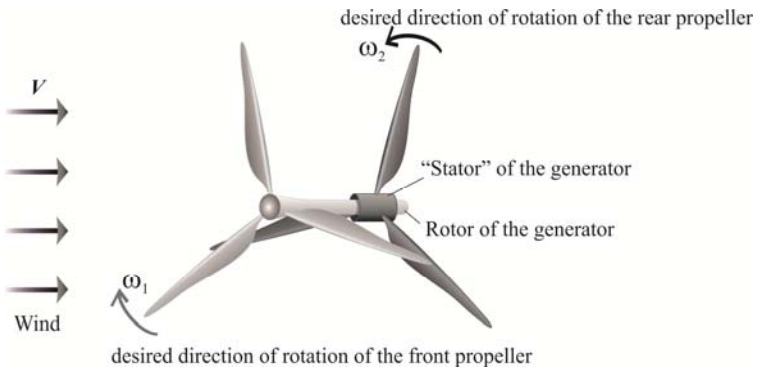

Figure 1. The scheme of the mechanism.

2.1. Geometry and mass properties of the system

Each propeller has the radius r, the swept area S of the rotor, the moment J of inertia with respect to the axis of rotation. Tip speed ratios (TSR) ω_1 and ω_2 of the front and the rear propellers, respectively, are counted in the opposite directions. In particular, when both TSR are positive it

means that propellers rotate in the opposite directions. Such counter-rotation is desired for program operation modes of the setup.

2.2. Model of active forces

The electromagnetic torque T_0 is responsible for the interaction between the rotor and the stator. This torque is supposed to be a linear function of the angular speed of the rotor with respect to the stator [11]. Thus, it is proportional to the sum of absolute angular speeds of counter-rotating propellers. The corresponding proportionality factor depends on properties of the generator itself (the coefficient Λ of electromechanical interaction, the value σ of the inner resistance of the generator) and on the value R of the external resistance in the local electric circuit of the generator:

$$T_0 = \frac{\Lambda}{(\sigma + R)} \frac{V}{r} (\omega_1 + \omega_2). \tag{1}$$

Aerodynamic action is described using a quasi-steady approach [11, 12]: it is supposed that aerodynamic torques acting on the front and the rear propellers are given by the following expressions:

$$T_1 = 0.5\rho S V^2 r f(\omega_1), \qquad T_2 = 0.5\rho S U^2 r f\left(\frac{V}{U}\omega_2\right), \tag{2}$$

where ρ is the density of the air, V is the wind speed, U is the flow speed in the wake of the front propeller. The function $f(\omega)$ is a nonlinear function of the TSR. A typical example of the function $f(\omega)$ (that is used further) is shown in the Fig. 2. Principal features of such function that are typical for a wide range of propellers are listed in [16]. This function was identified via experimental tests performed in the LMSU Institute of Mechanics. Experimental points shown in the Fig. 2 correspond to different values of the wind speed (from 4 m/s up to 6.5 m/s). These experiments were carried out in the wind tunnel with an open test chamber, minimal linear size of the test chamber was 2.5 m, the diameter of the experimental propeller was approximately 1 m.

Due to (2), values P_1 and P_2 of the trapped power of front and rear propellers and corresponding values of trapped power coefficients c_{p1} and c_{p2}, respectively, are given by the following relations:

$$\begin{aligned} &P_1 = 0.5\rho S V^3 f(\omega_1)\omega_1, \qquad c_{p1} = f(\omega_1)\omega_1; \\ &P_2 = 0.5\rho S U^2 V f\left(\frac{V}{U}\omega_2\right)\omega_2, \qquad c_{p2} = \frac{U^2}{V^2} f\left(\frac{V}{U}\omega_2\right)\omega_2. \end{aligned} \tag{3}$$

General relations of the Betz theory are used to estimate the flow speed U in the wake of the front propeller [13–15]. This speed U is the speed of the flow acting upon the rear propeller. Due to the Betz approach, an axial induction factor a is introduced:

$$\frac{U}{V} = 1 - 2a. \tag{4}$$

The following relations are supposed to be hold for the value P_1 of the power trapped by the front propeller and the corresponding trapped power coefficient c_{p1}:

$$P_1 = 2\rho V^3 a(1-a)^2 S, \qquad c_{p1} = 4a(1-a)^2. \tag{5}$$

Formulas (5) agree with experiments rather good for $a < 0.4$ [14]. The value $a = 1/3$ corresponds to the Betz limit. Further is it assumed that $a \le 1/3$.

Comparison of (5) and (3) provides the following relation:

$$4a(1-a)^2 = \omega_1 f(\omega_1). \tag{6}$$

For each ω_1, there is a unique root of the Eq. (6) in the region $a \le 1/3$. This root determines the function $a(\omega_1)$, the axial induction factor a as the function of the TSR ω_1 of the front propeller. Hence, the following relation holds for the aerodynamic torque acting on the rear propeller:

$$T_2 = 0.5\rho S V^2 r u^2(\omega_1) f\left(\omega_2 / u(\omega_1)\right), \qquad \text{where } u(\omega_1) = \frac{U}{V} = (1-2a). \tag{7}$$

For the function $f(\omega)$, the corresponding function $u(\omega_1)$ is shown in the Fig. 2. In particular, the minimal value of the function $u(\omega_1)$ corresponds to the minimal flow speed in the wake, and thus to the maximal value of the trapped power coefficient c_{p1} of the front propeller. The function $c_{p1}(\omega_1)$ is shown in the graph by the dashed curve (same scale).

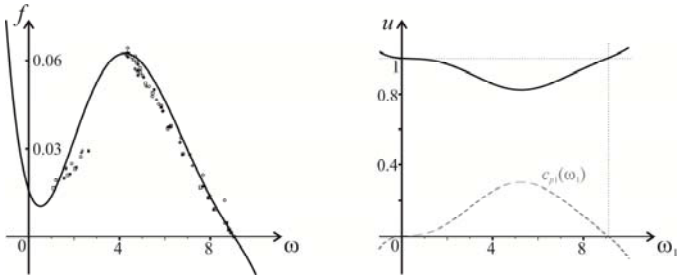

Figure 2. The function $f(\omega)$ of a dimensionless aerodynamic torque depending on the TSR. The function $u(\omega_1)$ of the relative flow speed in the wake (with respect to the wind speed).

3. Equations of motion and steady solutions

Taking into account (1), (2), (7), the dimensionless equations of motion of the system have the following form (a dot denotes the dimensionless time derivative):

$$\begin{cases} \dot{\omega}_1 = b\big(f(\omega_1) - c(\omega_1 + \omega_2)\big), \\ \dot{\omega}_2 = b\Big(u^2(\omega_1) f\big(\omega_2 / u(\omega_1)\big) - c(\omega_1 + \omega_2)\Big), \end{cases} \quad \text{where } b = \frac{\rho S r^3}{2J}, \quad c = \frac{2\Lambda}{V \rho S r^2 (\sigma + R)}. \tag{8}$$

The external load coefficient c is responsible for changeable conditions of operation of the HAWT, namely, the wind speed and the external resistance. The more consumers are in the circuit, the smaller R is and the large c is.

A steady solution $\omega_1 \equiv \Omega_1 = \text{const}, \omega_2 \equiv \Omega_2 = \text{const}$ of (8) corresponds to a steady motion of the mechanical system. A stable steady solution corresponds to an operation mode of the HAWT. For the steady solutions the following conditions hold:

$$f\left(\frac{\Omega_2}{u(\Omega_1)}\right) = \frac{f(\Omega_1)}{u^2(\Omega_1)}, \qquad \frac{f(\Omega_1)}{\Omega_1 + \Omega_2} = c. \tag{9}$$

For the function $f(\omega)$ given in Fig. 2, there can be from 1 to 5 solutions of (9) depending on the value of the parameter c.

When (9) holds, the conditions of the asymptotic stability of the steady solution are the following (the prime denotes differentiation with respect to ω):

$$\begin{cases} G_1 = -u(\Omega_1) f_2' - f_1' + 2c > 0, \\ G_2 = u(\Omega_1) f_1' f_2' + c\big(2u(\Omega_1)u'\big|_{\omega=\Omega_1} f(\Omega_2 / u(\Omega_1)) - \Omega_2 u'\big|_{\omega=\Omega_1} f_2' - f_1' - u(\Omega_1) f_2'\big) > 0, \end{cases} \tag{10}$$

where $f_1' = f'\big|_{\omega=\Omega_1}$, $f_2' = f'\big|_{\omega=\Omega_2/u(\Omega_1)}$.

The characteristic polynomial corresponding to the solution of (9) is $\lambda^2 + bG_1\lambda + b^2 G_2 = 0$.

If $G_1 < 0$ or $G_2 < 0$, then the corresponding steady solution is unstable. Using the numerical calculations, it can be shown that the case $G_1 < 0, G_2 > 0$ doesn't happen for solutions (9). Thus, it is enough to know the sign of the G_2 to check the stability of a steady point. Moreover, for the system (8), each bifurcation of merging of an unstable and a stable steady points is the saddle-node bifurcation.

The Fig. 3 represents the result of numerical calculation of the set of solutions (Ω_1, Ω_2) of (9) for varied parameter c: bold curves correspond to the set of stable steady points, thin curves correspond to the set of unstable steady points. Dotted line corresponds to $\Omega_1 = \Omega_2$ (referring line). The set (Ω_1, Ω_2) contains two continues curves: on the first one $\Omega_1 > \Omega_2$, on the second one

$\Omega_1 < \Omega_2$. The only steady point with equal values of TSR is the point O ($\Omega_1 = \Omega_2 \approx 9.1$). This point corresponds to the free rotation (no external load). The continuous curve, which begins at the point O (where $c = 0$), tends to the point $(0,0)$ with $c \to \infty$. The other continuous curve goes through the points *K, L, M, N*. For this curve, parameter c varies from approximately 0.001 (point *K*) to approximately 0.024 (point *L*).

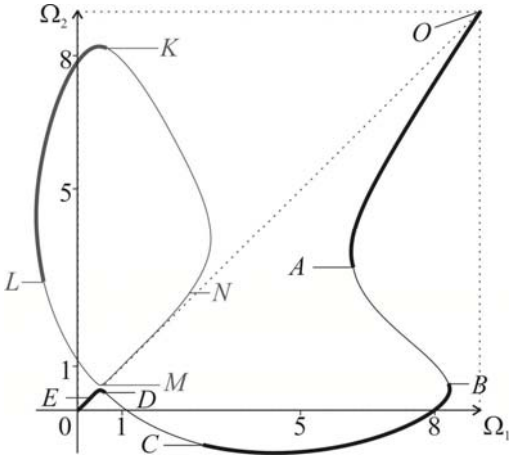

Figure 3. The set of steady points in the space (Ω_1, Ω_2) for $c \in [0, \infty)$.

The curves $\Gamma_1 = \{\dot{\omega}_1 = 0\}$, $\Gamma_2 = \{\dot{\omega}_2 = 0\}$ in the phase plane $\{\omega_1, \omega_2\}$ are represented in Fig. 4 by the dashed and dotted-dashed curves, respectively. The pictures are given for two different values of the parameter c: for $c = 0.004$ (5 steady points exist, 3 of them are stable) and for $c = 0.008$ (5 steady points exist, 2 of them are stable). Stable steady points are marked by black dots, unstable steady points are marked by white dots. Arrows in the Fig. 4 represent qualitative directions of the vector $\{\dot{\omega}_1, \dot{\omega}_2\}$ in different domains of a phase plane. Solid curves qualitatively shows separatrices of saddles.

In the case of $c = 0.004$, the colored area corresponds to the domain of attraction of the high speed counter-rotation mode. In the case of $c = 0.008$, the colored area corresponds to the domain of attraction of the co-directional rotation mode with a high speed of the front propeller.

In particular, the point $(0, 0)$ (zero initial TSR of each propeller) belongs to the domain of attraction of the high speed counter-rotation in the case of $c = 0.004$. To compare with, this point belongs to the domain of attraction of the co-directional rotation mode with a high speed of the front propeller in the case of $c = 0.008$.

The value $c = 0.004$ is close to the value of the external load coefficient *c,* for which the maximal trapped power is achieved (as it is shown further).

Notice, that in these cases, there are no limit cycles in a phase plane $\{\omega_1, \omega_2\}$ (due to the directions of the vector $\{\dot{\omega}_1, \dot{\omega}_2\}$ and numerical construction of separatrices). Stable steady points are the only attracting limit states of the system (8).

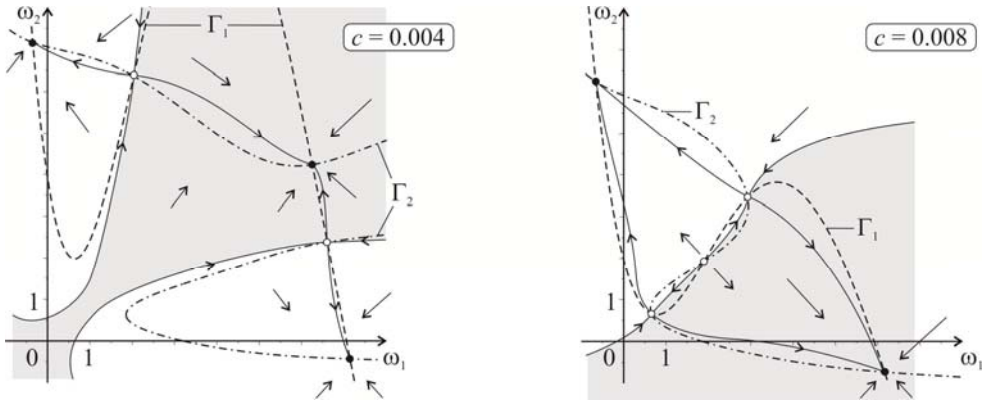

Figure 4. Steady points and the directions of phase speeds in the phase plane.

For every value of *c*, at least one stable steady motion exists. Numerical simulation has not revealed any non-steady periodic solution of the system (8). Analytical proof of existence or absence of a non-steady periodic solution and discussion of possible modification of the model that may lead to appearance of periodic cycles remains for the future research. Such an analysis can be based on the fundamental results [17]. The possibility of non-steady periodic operation modes (for the constant wind speed and the constant external resistance in the local circuit) is a topical open question in the theory of counter-rotating HAWTs.

It is reasonable to compare the behavior of the counter-rotating HAWT with the operation of a single-propeller HAWT. If, for instance, the rear propeller is stopped by the brake, dynamics of the single moving propeller is described by the first equation of the system (8) assuming $\omega_2 \equiv 0$. In this case, for a steady solution $\omega_1 \equiv \Omega = \text{const}$, the condition of stability is $f'\big|_{\omega=\Omega} < c$. A comparison of trapped power coefficient for the counter-rotating and the single HAWT is provided further.

4. Trapped power at steady motions

From (3) and (9), it follows that at a steady motion $c_{p2} = f(\Omega_1)\Omega_2$.

The value of the trapped power coefficient at steady motions of the counter-rotating HAWT is given by the formula:

$$c_p = c_{p1} + c_{p2} = f(\Omega_1)(\Omega_1 + \Omega_2). \tag{11}$$

Fig. 5 represents the bifurcation diagram $c_p(c)$ of the trapped power coefficient at steady motions depending on the external load coefficient *c*. The diagram is constructed using the same approach as in [18]. The diagram contains 4 "petals" (marked by solid lines) that are constructed numerically using (9) and (11). The diagram for a single-propeller HAWT with the same properties of the propeller is shown in the same figure by the dashed line for comparison.

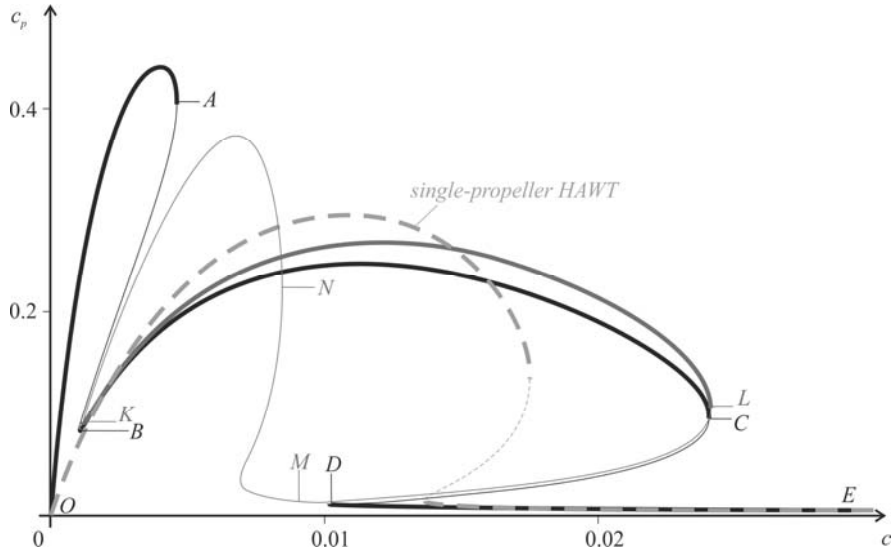

Figure 5. The bifurcation diagram of steady motions: the trapped power coefficient depending on the external load coefficient.

In the Fig. 5, bold branches correspond to stable steady motions, thin branches – to unstable steady motions. Points *A, B, C, D, K, L* are the bifurcation points where stability is lost (similar points are marked with the same letters in the Fig. 4). The point *D* belongs to the branch $\widehat{CD}$ and to the branch $\widehat{DE}$. The branch $\widehat{DE}$ prolongs further to the right from the point *E* and tends to the abscissa axis while *c* tends to infinity.

Stability conditions (10) are checked numerically for corresponding solutions of (9). Some results about stability can be confirmed analytically: in particular, it can be shown that the derivative dc/dc_p along the bifurcation curve is proportional to the value G_2, which determines the second condition of (10). Thus, the function G_2 changes its sign at the points of the bifurcation curve $c_p(c)$, where the tangent is vertical. So a stable branch of a bifurcation curve cannot go beyond a point with

a vertical tangent. The loss of stability at the bifurcation points *A, B, C, D, K, L* of the diagram is caused by the change of the sign of G_2 (as it was mentioned before, it is a saddle-node bifurcation).

4.1. Discussion

The "stable branch" $\widehat{OA}$ corresponds to the case of both propellers rotating in opposite directions with rather high values of steady TSR Ω_1 and Ω_2 (values of TSR corresponding to different steady points are shown in the Fig. 4). For such operation modes, $\Omega_1 > \Omega_2$. Thus, the front propeller collects more power than the rear propeller ($c_{p1} > c_{p2}$). The maximum value of the trapped power coefficient c_p at this branch exceeds the maximum value of the trapped power coefficient for a single-propeller HAWT for approximately 50%. The result of 50% increase in the trapped power was predicted by numerical simulation (namely, Computational Fluid Dynamics) in [6]. Increasing up to 43% was shown in [2].

The "stable branch" $\widehat{BC}$ corresponds to the case of the front propeller rotating with a high value of TSR and the rear propeller rotating with a very low TSR ($\Omega_2 \in [0, 0.55)$) or even in the same direction as the front propeller ($\Omega_2 < 0$). In the last case the rear propeller is in fact dragged by the front propeller, and the aerodynamic torque acting upon the rear propeller appears not enough to prevent the undesirable direction of rotation. For such operation modes $\Omega_1 > \Omega_2$. Thus, the front propeller traps more power than the rear propeller ($c_{p1} > c_{p2}$).

In case of a co-directional rotation, for a certain range of a load coefficient *c*, the total power coefficient c_p is higher than the power coefficient for a single-propeller HAWT (compare $\widehat{BC}$ with the diagram for a single-propeller HAWT). This nominal increase in power takes place despite the fact that the front propeller spends power not only for consumers, but also for rotation of the rear propeller. Such an unexpected fact can be explained as follows: when the rear propeller is dragged by the front one, it decreases the relative speed $(\omega_1 + \omega_2)$ of the rotor of the generator with respect to the "stator", and thus, the dissipative electromechanical torque decreases. For a certain range of *c* (when the external electric load is rather high), this decreasing of electromechanical load is more significant that losses for overcoming the aerodynamic torque acting upon the rear propeller. So for the front propeller, it is much "easier" to drag the rear propeller decreasing the effective value of electric load than to work with the nominal value of the electric load. Thus, one more degree of freedom, comparing to a single-propeller HAWT, provides new self-regulation properties of the electro-mechanical system. The aerodynamic torque acting on the rear propeller acts as a viscous damper. If

there were no such torque, the "stator" of the generator would just rotate together with the rotor, and no power would be produced.

The "stable branch" $\widehat{KL}$ corresponds to the case of the front propeller rotating with a very low TSR or even in the undesirable direction, and the rear propeller rotating with a high value of TSR. This case is rather similar to the case of the branch $\widehat{BC}$. But for such operation modes, $\Omega_2 > \Omega_1$. Thus, the rear propeller traps more power than the front propeller ($c_{p2} > c_{p1}$). Here the negative TSR of the front propeller leads to the fact that the speed in the wake is higher than the upcoming wind speed. In this case the front propeller accelerates the flow in the wake (rather similar to a ventilator rotor). It is the rear propeller that makes the front propeller rotate. For a certain range of *c,* this tricky "cooperation" allows producing more power than a single-propeller HAWT (similar as $\widehat{BC}$). Moreover, it allows $\widehat{KL}$ to be "better" than $\widehat{BC}$. It appears that if it is reasonable to decrease the relative speed $(\Omega_1 + \Omega_2)$, it is better to decrease Ω_1, because in this case the energy spent on increasing the wake speed works for capacity of the rear propeller, while in the case of $\widehat{BC}$ the increased speed in the wake of the rear propeller is not used for profit of the system.

The "stable branch" $\widehat{DE}$ corresponds to the case of counter-rotation with very low speeds of both propellers. This branch is qualitatively similar to the corresponding branch of the diagram for the single-propeller HAWT.

Roughly speaking, "unstable branches" correspond to the case of at least one propeller rotating with a medium speed. The range of medium speeds approximately coincides with the range of speeds, for which the aerodynamic torque increases with increasing the TSR. Values of the trapped power corresponding to "unstable branches" can be rather high (e.g., for branches $\widehat{AB}$, $\widehat{KN}$). Hence, stabilization of such unstable modes can be useful for applications.

5. Conclusions

The closed dynamical model of a counter-rotating HAWT is constructed. The generator is supposed to be connected into the local electric circuit with the changeable external resistance. The flow speed in the wake of the front propeller is estimated using the Betz theory. The external load coefficient is introduced. The bifurcation diagram of steady motions representing the dependence of the trapped power coefficient on the external load coefficient is constructed. Questions of stability are discussed.

Four types of steady operation modes are revealed: high-speed counter-rotation (maximal advantage in trapped power), low speed counter-rotation (almost no advantage comparing with a single-propeller HAWT), and two "collateral" types.

Notice, that the increase in the trapped power at a high-speed counter-rotating mode (compared to a single-propeller HAWT) is a qualitative result that was obtained before using experiments and numerical simulation.

The first collateral mode is characterized by a high-speed rotation of the front propeller combined with a low-speed counter-rotation or a co-directional rotation of the rear propeller. The second collateral mode implies a high-speed rotation of the rear propeller combined with a low-speed counter-rotation or a co-directional rotation of the front propeller. These modes and, specifically, their co-directional variants provide an advantage (comparing to a single-rotor HAWT) for the range of the external load coefficient, for which trapped power is significantly high. The widening of the range of the external load, for which high trapped power can be achieved, is a qualitatively new feature that was not revealed before. It draws up one extra advantage of a double-propeller HAWT.

Acknowledgments

This work was partially supported by the Russian Foundation for Basic Research, projects NN 15-01-06970, 16-31-00374, and 17-08-01366.

References

[1] Stobart, A. *Wind turbine.* International Patent WO1992012343, 1992.

[2] Shen, W.Z., Zakkam, V.A.K., Sorensen, J.N., Appa, K., Analysis of counter-rotating wind turbines. *Journal of Physics: Conference Series* 75, 1 (2007), 012003.

[3] Farthing, S.P. Robustly Optimal Contra-Rotating HAWT. *Wind engineering* 34, 6 (2010), 733–742.

[4] Lee, S., Kim, H., Son, E., Lee, S., Effects of design parameters on aerodynamic performance of a counter-rotating wind turbine. *Renewable Energy* 42 (2012), 140–144.

[5] Lee, S., Son, E., Lee, S. Velocity interference in the rear rotor of a counter-rotating wind turbine. *Renewable energy* 54 (2013), 235-240.

[6] Huang, B., Zhu, G.J., Kanemoto, T. Design and performance enhancement of a bi-directional counter-rotating type horizontal axis tidal turbine. *Ocean Engineering* 128, 1 (2016), 116–123.

[7] Ozbay, A., Tian, W., Hu, H., Experimental investigation on the wake characteristics and aeromechanics of dual-rotor wind turbines. *Journal of Engineering for Gas Turbines and Power* 138, 4 (2016), 042602.

[8] Cho, W., Lee, K., Choy, I., Back, J. Development and experimental verification of counter-rotating dual rotor/dual generator wind turbine: Generating, yawing and furling. *Renewable Energy* 114 (2017), 644–654.

[9] Shalimova, E.S., Klimina, L.A., Lin, K.-H. Torsional dynamics of a double rotor HAWT with a differential planet gear. *12th International Conference on Vibrations in rotating machines. Graz, February 15th to 17th, 2017. Proceedings. TU Graz, Austria* (2017), 390–395.

[10] Klimina, L. A., Shalimova, E. S., Dosaev, M., Garziera, R. Closed dynamical model of a double propeller HAWT. *Procedia Engineering* 00 (2017), 000–000 (in print).

[11] Dosaev, M.Z., Samsonov, V.A., Seliutski, Y.D. On the dynamics of a small-scale wind power generator. *Doklady Physics* 52, 9 (2007), 493–495.

[12] Dosaev, M.Z., Lin, Ch.-H., Lu, W.-L., Samsonov, V.A., Selyutskii, Yu.D. A qualitative analysis of the steady modes of operation of small wind power generator. *Journal of Applied Mathematics and Mechanics* 73, 3 (2009), 259–263.

[13] Betz A. Der Maximum der theoretisch möglichen Ausnützung des Windes durch Windmotoren. *Zeitschrift für das Gesamte Turbinenwesen* 26 (1920), 307–309.

[14] Hansen, M. O. L. *Aerodynamics of Wind Turbines*. Routledge, London and New York, 2015.

[15] Frandsen, S., Barthelmie, R., Pryor, S., Rathmann, O., Larsen, S., Højstrup, J., Thøgersen, M. Analytical modelling of wind speed deficit in large offshore wind farms. *Wind energy* 9, 12 (2006), 39–53.

[16] Dosaev, M., Holub, A., Klimina, L., Selyutskiy, Yu., Gritsenko, D., Tsai, M.-Ch., Yang, H.-Tz. Power output estimation of steady regimes of a HAWT with differential gearbox. *Dynamical systems. Applications. Technical University of Lodz Publishing. Poland* (2013), 647-656.

[17] Awrejcewicz, J. (Ed.). *Bifurcation and chaos: theory and applications*. Springer Science & Business Media, Berlin, Heidelberg, New York, 2012.

[18] Klimina, L., Dosaev, M., Selyutskiy, Yu. Asymptotic analysis of the mathematical model of a wind-powered vehicle. *Applied Mathematical Modelling* 46 (2017), 691-697.

Liubov Klimina, Ph.D.: Lomonosov Moscow State University, Institute of Mechanics, Michurinsky prosp.,1, 119192, Moscow, Russia (klimina@imec.msu.ru). The author gave a presentation of this paper during one of the conference sessions.

Boris Lokshin, Associate Professor: Lomonosov Moscow State University, Institute of Mechanics, Michurinsky prosp.,1, 119192, Moscow, Russia (blokshin@imec.msu.ru).

Vitaly Samsonov, Professor: Lomonosov Moscow State University, Institute of Mechanics, Michurinsky prosp.,1, 119192, Moscow, Russia (samson@imec.msu.ru).

Yury Selyutskiy, Associate Professor: Lomonosov Moscow State University, Institute of Mechanics, Michurinsky prosp.,1, 119192, Moscow, Russia (seliutski@imec.msu.ru).

Ekaterina Shalimova, Ph.D.: Lomonosov Moscow State University, Institute of Mechanics, Michurinsky prosp.,1, 119192, Moscow, Russia (ekateryna-shalimova@yandex.ru).

Alois Steindl, Professor: TU Wien, Institute of Mechanics and Mechatronics, Getreidemarkt 9/E325/A1, 1060, Vienna, Austria (alois.steindl@tuwien.ac.at).

On dynamics of a Savonius rotor-based wind power generator

Liubov Klimina, Anna Masterova, Yury Selyutskiy,
Shyh-Shin Hwang, Ching-Huei Lin

Abstract: A stand-alone wind power generator based on the Savonius rotor is considered. An empirical approach is proposed for describing the aerodynamic torque basing on available data from physical and computational experiments. Existence and attraction properties of equilibrium positions and steady motions in the system are studied. Numerical simulation of behavior of a one-stage and a three-stage Savonius wind turbine is performed for different values of parameters (including external load). Domain of attraction of a stable equilibrium position of the single-stage rotor in the space of initial conditions is constructed for different system parameters. Dynamics of a Savonius rotor-driven wheeled cart is studied.

1. Introduction

Savonius rotor is a vertical axis wind turbine. In its traditional variant proposed by the Finnish architect and inventor S.J. Savonius, this turbine consists of two similar blades of semi-cylindrical shape fixed to the common axis (this axis is parallel to the generatrix of the cylinder). When put into the wind flow, this system starts rotating under the action of aerodynamic forces, which allows using it for generation of electric power or as a power drive.

The advantage of the Savonius rotor as compared with another wide-spread type of vertical axis wind turbines, that is, Darrieus wind turbines, is the fact that it self-starts even if the wind speed is very low. Besides, contrarily to the horizontal-axis wind turbines, it does not require any additional control system to ensure its appropriate orientation with respect to the wind. The drawback of the Savonius rotor is its low rotation speed (the speed of its points which are the most distant from the rotation axis exceeds the wind speed at most by half), hence, the power generated by this device is not high.

However, the torque produced by this rotor is relatively large, which allows efficient use of this system as a power drive. Besides it can serve as an auxiliary facility ensuring the self-start of high-speed vertical axis wind turbines. This explains sustainable interest to development and study of such systems and a large number of papers dedicated to these questions.

In particular, [1-4] describe experiments with Savonius rotors with different blade shapes and different relative position of blades. In [5-6], hydrodynamic simulation of behavior of the rotor under

different loads is carried out, and data on aerodynamic forces and torques acting on the rotor, pressure and velocity fields in flow about the rotor, etc.

It should be noted that the hydrodynamic simulation requires relatively large computational resources and is time consuming. Analysis of dynamics of the system, especially in cases when the Savonius rotor is just a part of some larger mechanical system, becomes rather cumbersome. Therefore, it seems reasonable to develop a simplified approach to description of the aerodynamic load upon this object, that would not provide detailed and precise picture of the flow, but would ensure a good enough integral description of forces and torques acting upon the rotor.

Besides, in literature there are no closed models of small-scale wind power generators based on Savonius rotor comprising both mechanical and electrical parts of the system. In this work, we propose such a model for a Savonius rotor-based small-scale wind generator. Besides, a vehicle is considered which is driven by Savonius rotor.

2. Savonius wind generator

Consider a Savonius rotor located in flow (Fig. 1). Suppose that the turbine shaft is connected with the rotor of an permanent magnet DC electric generator. This electric generator is connected to the external circuit that comprises some consumers (external resistance).

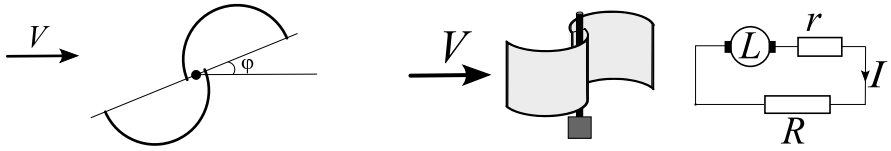

Figure 1. Savonius rotor-based wind generator.

The system state is described by the angle φ of rotation of the Savonius rotor and current I in the external circuit of the generator (in such systems, current can be considered as a generalized velocity). Then equations of motion of the system, similarly to [7], can be represented in the following form:

$$\begin{aligned} J\ddot{\varphi} &= M_a - \kappa I, \\ L\dot{I} &= \kappa\dot{\varphi} - \left(R_e + R_i\right) I \end{aligned}, \tag{1}$$

Here J is the moment of inertia of rotating elements of the system; L is the electric generator inductance; M_a is the aerodynamic torque acting upon the Savonius rotor; κ is the coefficient of electromechanical interaction; R_i is the integral internal resistance of the generator; R_e is the resistance in the external circuit.

Traditionally, the aerodynamic torque is represented in the following form:

$$M_a = \frac{\rho S}{2} V^2 b C_m . \tag{2}$$

Here ρ is the medium density; S is the cross-section area of the Savonius rotor; b is the rotor radius; V is the flow speed; C_m is the dimensionless torque coefficient. The latter needs additional discussion.

When describing C_m, we use principles adopted in the framework of the conventional quasi-steady approach, according to which the aerodynamic load is determined by the current positions and velocities of the system. Contrarily to the aerodynamic torque acting upon the horizontal-axis wind turbine, C_m depends not only upon the instantaneous angular speed, but also on the instantaneous angle that the rotor makes with the flow. Evidently, C_m is periodic in φ, and, if the rotor contains n blades, the period is $2\pi/n$.

Assume that C_m can be represented in the following form:

$$C_m = A_0(\Omega) + \sum_{k=1}^{N} A_i(\Omega)\sin kn\varphi + B_i(\Omega)\cos kn\varphi = A_0(\Omega) + \Phi(\Omega,\varphi) . \tag{3}$$

Here $\Omega = b\omega/V$ is the tip speed ratio or dimensionless angular speed.

Coefficients $A_i(\Omega)$ and $B_i(\Omega)$, as well as the estimation for the number of harmonics *N*, should be determined from experiments and/or hydrodynamic simulations.

Experiments (both physical and numerical) that are usually performed with Savonius rotors can be divided into two main types.

In experiments of the first type, the rotor is fixed so that it makes a certain constant angle with the flow, and the value of the static aerodynamic torque C_m^{st} acting on the rotor is measured (calculated). Repeating this procedure yields the dependence of C_m^{st} upon the angle φ.

In experiments of the second type, an external torque is applied to the Savonius rotor, which makes the turbine to rotate. In some studies, the external torque is constant, in other studies it is adjusted in such a way as to provide a constant angular speed. The period average aerodynamic torque $\bar{C}_m$ is calculated depending on the average tip speed ratio $\bar{\Omega}$.

Of course, this information is not sufficient to determine dependencies $A_i(\Omega)$ and $B_i(\Omega)$. This task requires additional investigations. So, in what follows, we assume that these coefficients are constant: $\Phi = \Phi(\varphi)$.

Typical dependencies $\bar{C}_m(\Omega)$ and $C_m^{st}(\varphi)$ registered in wind tunnel tests are shown in Fig. 2 for a Savonius rotor with two blades and with six blades (arranged in three stages). The data are from [2]. For $\bar{C}_m(\Omega)$, we propose the following approximation formula:

$$\bar{C}_m(\Omega) = a_0 + a_1\Omega - a_2\Omega^2, \quad \Omega \geq 0 . \tag{4}$$

It should be noted that the approximation (4) is only valid for positive angular speeds. Really, it is clear from mechanical considerations that, when Ω large (no matter, positive or negative) then the aerodynamic torque is aimed in such a way as to slow down the rotation, and hence, its sign is opposite to the sign of Ω, which is not the case for (4). However, experimental data for negative Ω are absent, and the problem of construction of torque approximation formula for the whole range of angular speed values still remains open.

The least squares method yields the following formulae for two rotors described in [2]: $\bar{C}_m(\Omega) = 0.225 + 0.194\Omega - 0.254\Omega^2$ for the 1-stage rotor, $\bar{C}_m(\Omega) = 0.259 + 0.038\Omega - 0.193\Omega^2$ for the 3-stage rotor. Approximation curves are shown in Fig. 2 with solid lines. The agreement with experimental points is quite good in the range of positive angular speeds.

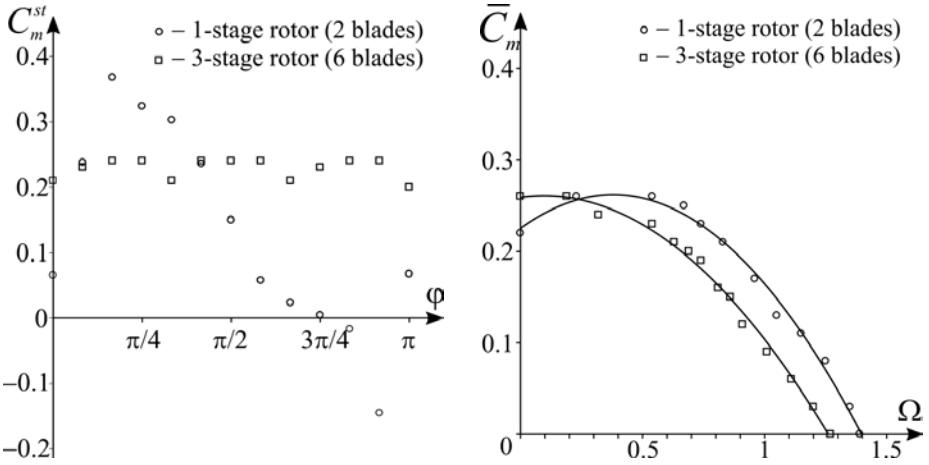

Figure 2. Dependence of C_m^{st} on φ and $\bar{C}_m$ on Ω (with approximation curves).

The quality of approximations is quite acceptable, which allows using them for numerical simulation of the system dynamics.

3. Equilibrium positions and periodic motions

Fixed points of (1) correspond to rotor positions where the aerodynamic torque equals to zero, i.e.:

$$\sum_{k=1}^{N} B_i(0)\cos kn\varphi_0 = -A(0). \tag{5}$$

Note that there exist rotors, for which the aerodynamic torque is positive in all positions (provided that the angular speed is zero). The 3-stage rotor with 6 blades, characteristics of which are shown in Fig. 2, provides an example of such situation. But if (5) has solutions, then necessary and sufficient conditions of asymptotic stability of them are as follows:

$$\begin{gathered}\Phi'_\varphi < 0, \quad J\left(R_e + R_i\right) > \frac{\rho S}{2} b^2 V L A'_{0\Omega}, \\ \left(J\left(R_e + R_i\right) - \frac{\rho S}{2} b^2 V L A'_{0\Omega}\right)\left(\kappa^2 - \frac{\rho S}{2} b^2 V L A'_{0\Omega}\left(R_e + R_i\right)\right) + \frac{\rho^2 S^2}{4} b^3 V^3 L^2 \Phi'_\varphi A'_{0\Omega} > 0\end{gathered} . \tag{6}$$

Here $A'_{0\Omega} = dA_0/d\Omega\big|_{\Omega=0}$, $\Phi'_\varphi = d\Phi/d\varphi\big|_{\varphi=\varphi_0}$, where φ_0 is solution of (5).

Note that if $A'_{0\Omega} \le 0$ and $B'_\varphi < 0$ for an equilibrium position then inequalities (6) are satisfied for all physically meaningful values of other parameters of the system. In this case, due to periodicity of $\Phi(\varphi)$, there exists another equilibrium where $\Phi'_\varphi > 0$ and which is unstable.

If $\Phi'_\varphi > 0$ then, even if for low flow speeds the equilibrium is stable, it becomes unstable for high enough values of *V*.

Strictly speaking, equilibria are “non-desired” solutions, because the rotor should perform a periodic motion in order to be able to produce power or driving torque.

In order to estimate domains of attraction of stable equilibria, numerical simulation was performed. The following values of parameters were adopted: J = 0.01 kgm^2, b = 0.2 m, S = 0.04 m^2, k = 0.3 Nm·A^{-1}, R_i = 1 Ohm.

In Fig. 3, projections of domains of attraction in the space of initial conditions onto the plane (j_i, w_i) are shown for different values of the external resistance and different flow speeds.

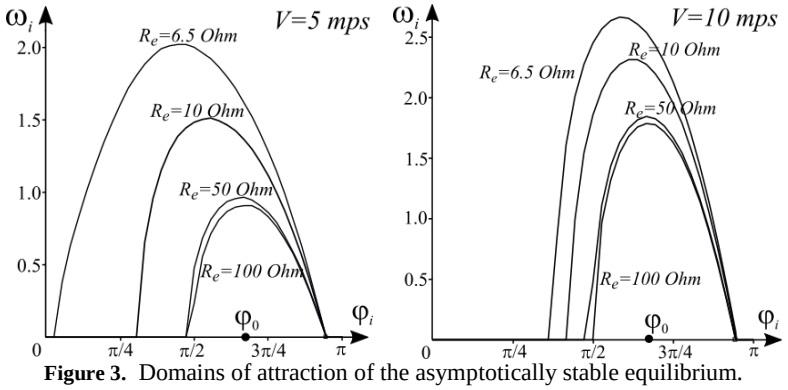

Figure 3. Domains of attraction of the asymptotically stable equilibrium.

From Fig. 3 one can see that the domain of attraction of the stable equilibrium decreases as R_e increases (that is, external load gets smaller), which is quite expectable. However, it does not retract to a point as R_e tends to infinity. It is interesting that increase in *V* results in "shrinking" of the range of initial angles covered by the domain, but, in the same time, increase in initial values of the angular speed.

If the number of blades of the Savonius rotor is large enough then $\Phi(\varphi) \ll \mathrm{A}_0$ in a certain range of Ω (like for the 3-stage rotor, characteristics of which are shown in Fig. 2). In this case it is possible to use the Poincare method for analysis of periodic motions, and the generating system looks as follows ($\omega = \dot{\varphi}$):

$$J\frac{d\omega}{dt} = -\kappa I + \frac{\rho S b}{2} V^2 A_0\left(\frac{\omega b}{V}\right)$$

$$L\frac{dI}{dt} = -\left(R_e + R_i\right) I + \kappa\omega$$

Fixed points of this dynamic system correspond to periodic motions of the initial one. The average angular speed and current on the periodic motion are given by the following relations:

$$\frac{\rho S b}{2} V^2 A_0\left(\frac{\omega_* b}{V}\right) = \frac{\kappa^2 \omega_*}{R_e + R_i}, \quad I_* = \frac{\kappa\omega_*}{R_e + R_i}. \tag{7}$$

The first equation in (7) has unique solution.

One can readily show that if $dA_0/d\omega\big|_{\omega=\omega_*} \le 0$ then the corresponding fixed point is asymptotically stable. Note that this is always the case for the discussed 3-stage rotor.

In order to investigate the structure of the phase plane, consider the following expression (Bendixson criterion):

$$\frac{\rho S b}{2J} V^2 \frac{dA_0}{d\omega} - \frac{R_e + R_i}{L}. \tag{8}$$

If (8) is negative then there exist no limit cycles, and the fixed point is globally attracting. This is the case when $dA_0/d\omega \le 0$ for all ω, or when *L* is small enough, or *J* is large enough.

For real generators, the inductance *L* is small, which means that electric processes run much quicker than mechanical ones. Then the equation of slow motions is as follows (taking into account the approximation (4):

$$J\frac{d\omega}{dt} = \frac{\rho S b}{2}\left(a_0 V^2 + a_1 \omega b V - a_2 \omega^2 b^2\right) - C\omega. \tag{9}$$

Here $C = \kappa^2 \left(R_e + R_i \right)^{-1}$. The instantaneous values of the current are given by the following relation: $I = \kappa\omega \left(R_e + R_i \right)^{-1}$.

Equation (9) can be solved analytically:

$$\omega(t) = -\frac{1}{2\rho Sb^3 a_2}\left(2C - \rho Sb^2 V a_1 - Z \tanh\left(t\frac{Z}{4J} + Q \right)\right),$$

$$Z = \sqrt{4a_0 a_2 \left(\rho Sb^2 V\right)^2 + \left(\rho Sb^2 V a_1 - 2C\right)^2}, \quad Q = \operatorname{arctanh}\left(\omega_0 \frac{2\rho Sb^3 a_2 + 2C - \rho Sb^2 V a_1}{Z} \right).$$

Here ω_0 is the initial value of the rotor angular speed.

4. Savonius rotor-driven vehicle

As was mentioned above, Savonius wind turbines can be used also as torque producing devices (power drives). One of examples is using such rotors as motors for vehicles. Systems of this kind are described, for instance, in [8].

Consider a wheeled cart, on which a Savonius rotor is installed (top and side views are represented in Fig. 4). The rotor is connected with driving wheels of the cart in such a way that when it rotates counterclockwise, the wheels also rotate counterclockwise. We neglect losses in the reduction gear.

Suppose that the cart can move along a fixed axis *OX* and is installed in airflow with the speed *V* directed along this axis. Then, if the rotor would rotate counterclockwise, the cart would move in the direction opposite to *OX* (leftwards if Fig. 4), if its wheels would not slide.

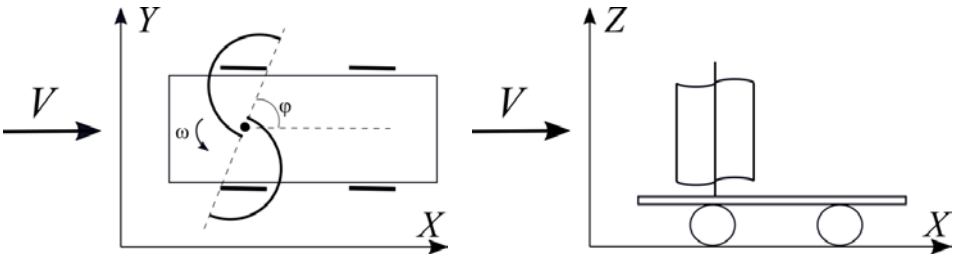

Figure 4. Cart driven by a Savonius rotor.

Equations of motion of the cart with the rotor are as follows:

$$\begin{aligned} J\dot{\omega} &= M_a - nrF_f, \\ m\dot{v} &= -F_f + F_a \end{aligned} \quad . \tag{10}$$

Here v is the cart speed, m is the mass of the vehicle together with the rotor; F_f is the friction between wheels and the supporting surface ($|F_f| \le fmg$, where f is the dry friction coefficient); n is the reduction rate of the gearbox that transmits rotation from the rotor shaft to the wheels; r the radius of wheels; $F_a =$ is the drag force acting upon the system (both rotor and cart); M_a is the aerodynamic torque acting upon Savonius blades.

As usually, represent the drag force and aerodynamic torque in the following form:

$$F_a = 0.5\rho S U^2 C_d\ ,\ M_a = 0.5\rho S R U^2 C_m\ . \tag{11}$$

Here C_d is the dimensionless drag coefficient, $U = V - v$ is the speed of the cart with respect to the flow.

Assume that the number of blades is large enough. Then, as was mentioned before, it is possible to neglect the dependence of the torque and drag coefficients upon the rotation angle. In what follows, we assume that C_d is constant.

From (10) and (11) it immediately follows that the angular speed of the rotor on the steady regime is given by the following equation:

$$RC_m(\Omega_0) = nrC_d\ . \tag{12}$$

Taking into account (4), one can readily conclude that (12) has 0, 1, or 2 solutions in the range $\Omega_0 > 0$. In particular, if the inequality $C_m^{\max} < C_d\, nr/R$ holds (here $C_m^{\max}$ is the maximum value of the aerodynamic torque coefficient in the range $\Omega > 0$) then there are no solutions with positive angular speed. If $dC_m/d\Omega \le 0$ for all $\Omega > 0$ (as is the case for the 3-stage rotor) then there exists only one solution.

Condition of asymptotic stability of the steady motion is $dC_m/d\Omega\big|_{\Omega=\Omega_0} < 0$.

It is worth noting that Ω_0 found from (12) does not depend on the wind speed or friction coefficient.

If wheels roll without slipping, the cart speed on the steady regime is given by the following formula:

$$v_0 = -\frac{\Omega_0 nrV}{R - nr\Omega_0}$$

If slipping is present then this speed is determined by the following relation:

$$v_0 = V - \sqrt{\frac{2fmg}{\rho S C_d}}$$

Comparing these formulae, one can readily obtain the critical value of the wind speed V_* such that the motion without slipping of wheels is impossible for larger V:

$$V_* = \left(1 - \frac{nr}{R}\Omega_0\right)\sqrt{\frac{2fmg}{\rho SC_d}}$$

Thus, at low wind speeds $v_0 < 0$, that is, the cart moves against the wind. The maximum speed of such motion is attained at $V = V_*$ and equals to $nrR^{-1}\Omega_0\sqrt{2fmg\left(\rho SC_d\right)^{-1}}$. If the wind speed exceeds the value $V_{**} = \sqrt{2fmg\left(\rho SC_d\right)^{-1}}$, the cart moves downwind.

Thus, appropriate choice of system parameters allows the cart to move upwind in a certain range of wind speeds.

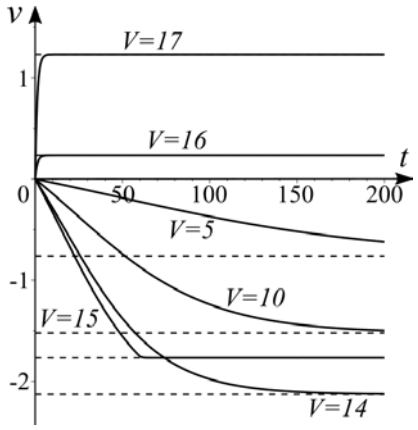

Figure 5. Cart velocity at different wind speeds.

Dynamics of the cart at different wind speeds is illustrated in Fig. 5. The following values of parameters were used for numerical simulation: $m = 0.5$, $J = 0.01$, $R = 0.1$, $n = 1$, $r = 0.02$, $f = 0.7$, $C_d = 1$ (so that $V_* \approx 14.6$ mps, $V_{**} \approx 16.8$). For relatively low wind speeds ($V < V_*$) the cart moves upwind without slipping; for $V_* < V < V_{**}$ it moves upwind, but the wheels slip; and for larger V the cart is entrained by the wind.

5. Conclusions

Mechanical system describing the behavior of a small-scale Savonius rotor-based wind power generator is considered. Conditions of asymptotic stability of equilibrium positions and steady periodic motions are obtained. Dynamics of a Savonius rotor-driven wheeled cart is analyzed. It is shown that for certain values of parameters the cart can move both in upwind and downwind directions.

Acknowledgments

The work is supported by RFBR (grants No. 15-01-06970, 16-31-00374).

References

[1] Sheldahl, R. E., Blackwell, B. F., Feltzt, L V. Wind Tunnel Performance Data for Two- and Three-Bucket Savonius Rotors. *J. Energy*, 2 (3) (1978), pages 160-164.

[2] Kamoji, M. A., Kedare, S. B., Prabhu, S. V. Experimental investigations on single stage, two stage and three stage conventional Savonius rotor. *Int. J. Energy Res.*, 32 (2008), pages.

[3] Roy, S., Saha, U. K. Wind tunnel experiments of a newly developed two-bladed Savonius-style wind turbine. *Applied Energy*,137 (2015), pages 117–125.

[4] Fujisawa, N. On the torque mechanism of Savonius rotors. *J. of Wind Engineering & Industrial Aerodynamics*, 40 (1992), pages 277-292.

[5] D'Alessandro, V., Montelpare, S., Ricci, R., Secchiaroli, A. Unsteady Aerodynamics of a Savonius wind rotor: a new computational approach for the simulation of energy performance. *Energy*, 35 (2010), pages 3349-3363.

[6] Jaohindy, P., Ennamiri, H., Garde, F., Bastide, A. Numerical investigation of airflow through a Savonius rotor. *Wind Energ.*, 17 (2014), pages 853–868.

[7] Dosaev, M.Z., Lin, C.-H., Lu, W.-N., Samsonov, V.A., Selyutskii, Yu. D. A qualitative analysis of the steady modes of operation of small wind power generators. *J. Applied Mathematics & Mechanics*, 73 (2009), pages 259-259.

[8] Kassem, Y., Hüseyin, Ç. Wind Turbine Powered Car Uses 3 Single Big C-Section Blades. Int. Conf. on Aeronautical & Manufacturing Engineering (ICAAME'2015), 2015, pages 42-45.

Liubov A. Klimina, Ph.D.: Lomonosov Moscow State University, Institute of Mechanics, Michurinsky prosp., 1, 119192 Moscow, Russia (*klimina@imec.msu.ru*).

Anna A. Masterova, Ph.D. student: Lomonosov Moscow State University, Institute of Mechanics, Michurinsky prosp. 1, 119192 Moscow, Russia (*masterovaanya@yandex.ru*). The author gave a presentation of this paper during one of the conference sessions.

Yury D. Selyutskiy, Associate Professor: Lomonosov Moscow State University, Institute of Mechanics, Michurinsky prosp., 1, 119192 Moscow, Russia (*seliutski@imec.msu.ru*).

Shyh-Shin Hwang, Associate Professor: Chien-Hsin University of Science and Technology, Department of Mechanical Engineering, 229 Jianxing Road, Zhongli District, 32097 Taoyuan City, Taiwan (*stanhwang@uch.edu.tw*).

Ching-Huei Lin, Associate Professor: Chien-Hsin University of Science and Technology, Department of Electrical Engineering, 229 Jianxing Road, Zhongli District, 32097 Taoyuan City, Taiwan (*chlin@gapps.uch.edu.tw*).

Exoskeleton – control by pressure sensors – practical solution

Mateusz Krain, Bartłomiej Zagrodny, Jan Awrejcewicz

Abstract: This work is connected with practical solution of exoskeleton control. Authors propose an approach to exoskeleton design, and its control namely creating a simple, portable control program which does not use problematic input signals such as electromyography. Instead the system utilizes solely specially designed pressure sensors, which are more resistant to failure and distortion. The research was performed initially on a LabView model, and next experimentally on a 1-DOF elbow joint test exoskeleton. The paper presents results of the research, practical implementation of the system to a simplified exoskeleton and comparison between theoretical and experimental results. Finally, conclusion on research and obtained conclusions are shown with its advantages and disadvantages.

1. Introduction

Scaling the augmentation exoskeleton technology to a commercial level, to make it accessible to the broad society requires more affordable and flexible constructions. Not only the employed mechanical construction should be optimized for large scale production but also the control algorithms have to be robust and lightweight. Usually exoskeleton control systems exhibit construction complexity ex. [1, 2, 3], therefore it is hard to implement them on low cost, low power units, such as microcontrollers and microcomputers. Furthermore, the systems usually rely partially or fully on electromyographic signals, which work well in a laboratory, but are highly susceptible to failures when put in demanding, real-world conditions. The reasons are skin-electrode contact issues, EMC distortions, problematic tracking of specific muscle activity when the body is moving, and so on. This paper proposes a different approach to exoskeleton design, namely creating a simple, portable control program which does not use "problematic" solutions such as electromyography. Instead, the system utilizes solely specially designed pressure sensors, which are resistant to failure and distortion. The research has been performed initially on a LabView model, and validated experimentally on a 1-DOF elbow joint test exoskeleton. Our research includes a comparison between theoretical and experimental results.

2. Regulation systems: state of the art

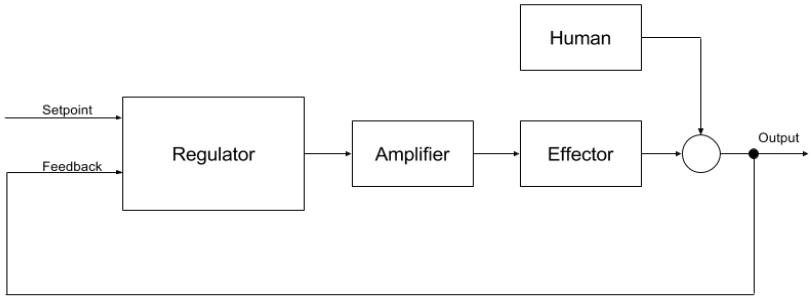

Figure 1. General block scheme of an exoskeleton system.

The architecture of choice depends on the machine's exact application, but there is also a degree of uncertainty, since the whole exoskeleton technology is not yet well investigated. Already existing exoskeleton controllers, which can be found on the market or in research papers, are usually built as one or as a mixture of the following architectures:

I. Classic error-based regulator architecture [3].

Regulators including proportional, integral, derivative and all of their combinations, which compute the output based on the current value of error, understood as difference between the aimed and the current state of the system.

II. Finite state machines [4].

Systems without memory, with a fixed and predefined number of states. The state of inputs determines the system output (used mainly for simple and limited hold/release prosthesis or exoskeletons).

III. Signal threshold system [5,6].

This is a system with only two states, which resemble the ON and OFF state of the effector. The output is depending on the current state of the input (usually myoelectric signal), and changes its value when crossing a threshold value. They are used similarly like the FSM only for simple exoskeleton designs as they usually have very limited abilities.

IV. Bilateral mirror-image system [7, 8].

A set of sensors monitors the movement of a healthy body part on one side of the body, while the regulator drives the adequate rehabilitated body part on the other side of the body with the same trajectories. Effectively, the movement of a healthy limb is copied to the augmented limb. The system is widely used for curing post-stroke motor cortex defects, due to the phenomenon of brain plasticity.

V. Neuro-Fuzzy system [1,2].

They are based on artificial neural networks. Usually the networks are implemented with the use of fuzzy logic. They require a learning procedure, and are hard to analyze, whereas they do not require deep insight into the complex kinematics of the body and offer good outcome, even for sophisticated exoskeletons, having many inputs and many possible system states.

VI. Systems based on a classic mechanical kinematic model of human movement [9].

The exoskeleton, as well as body are being approximated to standard kinematic models. The system's aim is to execute analytically formulated trajectories of human body movement, by means of translating them into exoskeleton trajectories, since the exoskeleton is a parallel mechanism relative to the human musculoskeletal system. The system requires a precise kinematic analysis, but when implemented properly, allows to control complex exoskeletons. Unfortunately, the resulting movement is often unnatural.

VII. Systems based on an intercepted real kinematic model of human movement [10, 11, 12].

An improved version of the classic mechanical kinematic model system. In this case, instead of an analytic model, the system is using a real model of human movement trajectories, which has been obtained experimentally. The solution yields a natural movement result and behaves well with complex exoskeletons.

3. Guidelines and application

We are aimed on the control system for a force amplifier type exoskeleton in which the human body is required to only create an input to the control system via a set of pressure sensors, and the exoskeleton exhibits influence on the outer matter. This kind of operation allows the exoskeleton to be implemented as a wearable supportive mechanical structure, and hence a user may work with bigger forces as well as with greater endurance (see Fig. 2.)

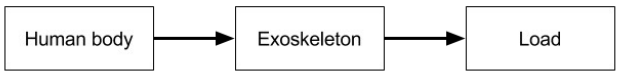

Figure 2. An exoskeleton as a force amplifier.

Examples of such applications include the support exoskeletons for soldiers, firefighters, nurses, etc., but as well patients with muscular dystrophy. An important point to note is that the user must not be totally paralyzed, he/she has to have at least minimal strength in order to create input signals for the pressure sensors. The general technical guidelines for the process of controller design include:

(i) robust and dependent operation in different circumstances, taking in account slight misplacements of the body with respect to the exoskeleton frame, sweat, varying load and electrical-environmental noise;
(ii) easy and fast installation of the exoskeleton on the body;
(iii) noticeable support of the body and rise of endurance.

4. LabView model

In order to test the initial design assumptions, a block diagram of the control system was created. See Fig. 3.

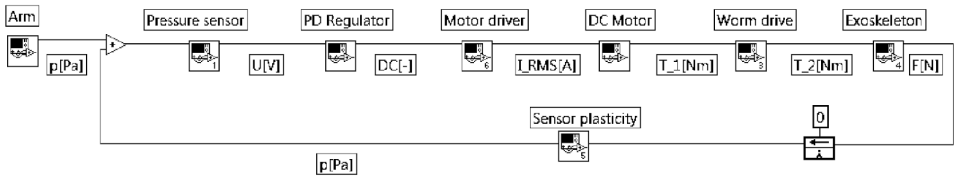

Figure 3. Time domain block simulation model (see text for more information).

The goal of the regulator is to keep pressure sensor signals at zero at all time instants. The magnitude of the signal can be interpreted as the amount of force with which the exoskeleton is acting on the human arm and vice versa. Keeping the signal level at zero effectively implies that the exoskeleton behaves regarding the user like “it is not there”. It follows every movement of the human and does not create any resistance for him. However, all the forces coming from the outside (weight of carried loads, hits, etc.) should be taken over by the exoskeleton mechanical construction and they should not influence the human body (the control system cares only about keeping the pressure sensor signals at zero).

5. Practical implementation

The finished prototype is presented in Figures 4-6. In what follows we describe briefly the kinematics, drive, chain transmission and the pressure sensors.

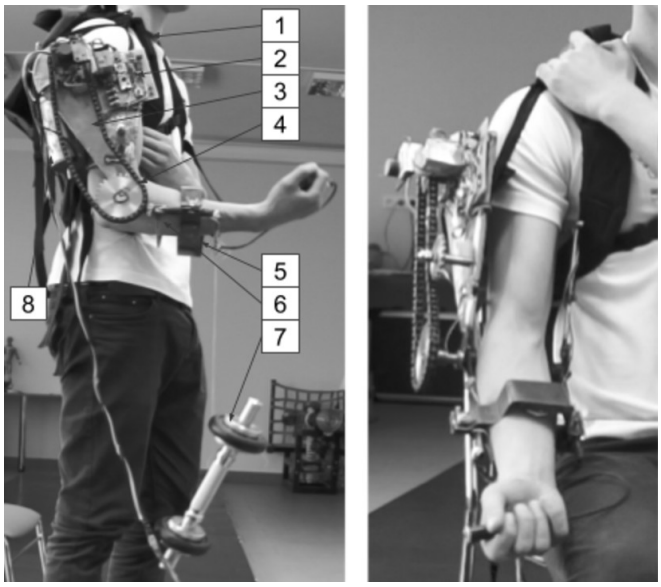

Figure 4. The arm exoskeleton prototype: 1 - straps, 2 - controller, 3 - arm part of the exoskeleton, 4 - chain transmission, 5 - braces with pressure sensors, 6 - forearm part of the exoskeleton, 7 – weight, 8 - motor with reducer.

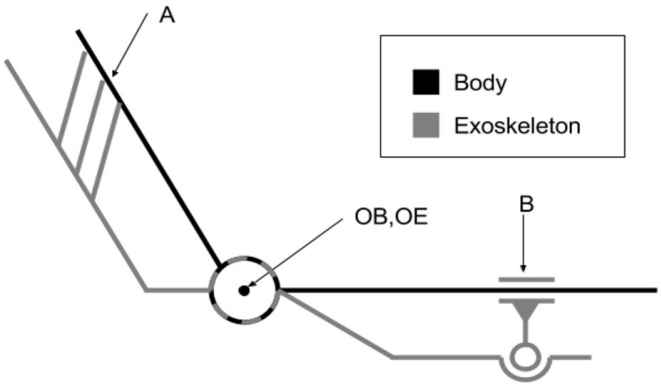

Figure 5. Kinematic model of the arm exoskeleton.

The exoskeleton has two points - A and B, in which it is connected to the body, (Fig 6). The arm connection point A is treated as a fixed connection, although it is important to note that it is not ideally solid, because human tissue is soft and flexible. This means that it allows the exoskeleton arm segments to move (slightly) relatively to the human arm. The second place where the mechanism connects to the body is point B, where a slider joint and a hinge joint secure the operation of the mechanism in case the center of rotation of the arm OB is not in the same axis as the center of rotation of the exoskeleton OE, what is true for most of the time.

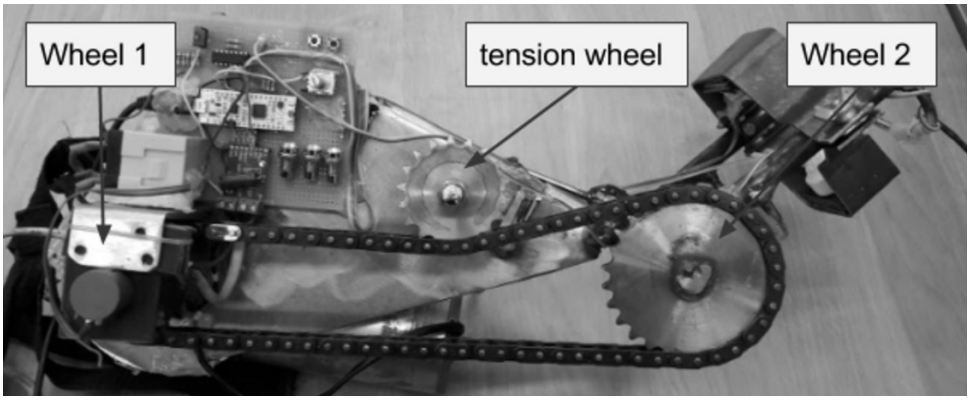

Figure 6. The chain transmission.

The physical test exoskeleton is shown in Fig. 6. A chain transmission has been implemented into the exoskeleton arm to transfer torque from the reductor output to the arm.

6. Pressure sensor construction

Figure 7. The sensor bracelet.

In order to create the exoskeleton-body connection point B, which also allows to measure the relative body-exoskeleton pressure, a special bracelet has been designed. Construction of the bracelet is shown on Figure 7. The space between two tops of the silicon rubber half-spheres is slightly smaller than the thickness of the patient's arm in this point. This ensures a secure connection with the arm, but as well, as the silicon half-spheres are normally lubricated, allows some sliding movement, what creates a slider joint effect (see Fig. 5).

ANSYS APDL 17.2 has been employed for carrying out the internal pressure distribution analysis of the silicon rubber element.

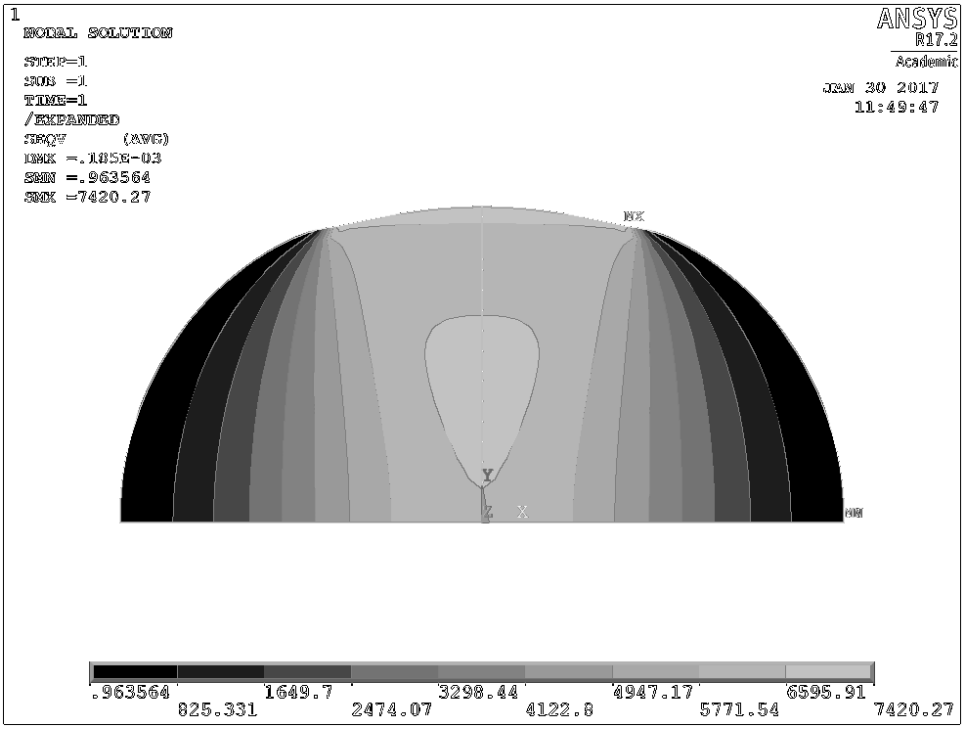

Figure 8. Cross-sectional pressure distribution for an evenly distributed pressure on the central part of the top surface of the sensor.

The analysis has validated that the silicon rubber element is successfully transferring pressure from the top to the bottom surfaces, and at the same time it is changing the pressure layout to more homogeneous (see fig. 8). The half-sphere is effectively blurring the pressure distribution inside the element.

7. Software architecture

A block diagram of the software functional architecture is presented on Fig. 9. Two different input handlers are responsible for sampling data from pressure sensors, as well as interpret user input signals. The PD regulator is the main control unit of the program. It is responsible for calculating the output based on the value of the relative exoskeleton-body pressure.

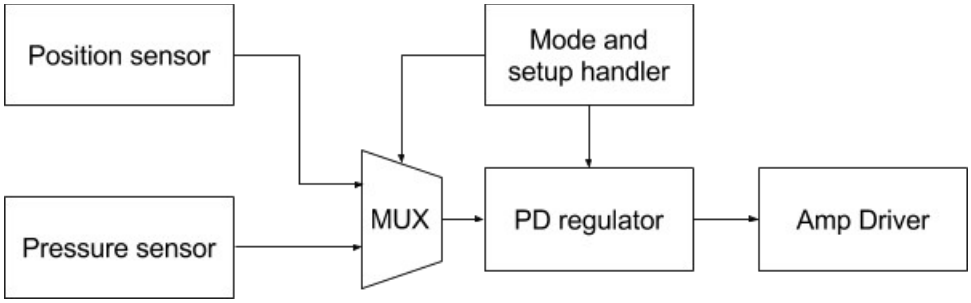

Figure 9. Software architecture.

Its setup parameters (P and D coefficients, setpoint) are given by the Mode and setup handler part of the program, which can be also described as the GUI backend. It storages PD setup parameters, and allows the user to change them via the HMI input handlers. The influence of P and D coefficients is described in the section 9. The change of setpoint value, however, allows the exoskeleton to act constantly against the human body, similarly as a gym training device. This function has been incorporated for test reasons only, and is not described in this paper.

8. Results

Both the LabView model and physical exoskeleton have been tested under different regulator setup conditions. The derivative coefficient of the PD regulator has been studied with special care, as it is the key element of a PD based exoskeleton regulation system. Figure 10 and Figure 11 present the operation of a simulational model and real exoskeleton with no derivative gain. Contrary, Figures 12 and Figure 13 present the effect of adding a derivative part to the exoskeleton regulator. Figures 12, 13 report that the derivative coefficient is responsible for a positive phase shift of the output signal relative to the input signal of the PD regulator. Furthermore, it is creating an overshoot, when the pressure sensor signal value is returning to zero, which overall contributes to a more dynamic and responsive user experience. It is important to note that an overshoot in this application is actually having a positive effect on system performance.

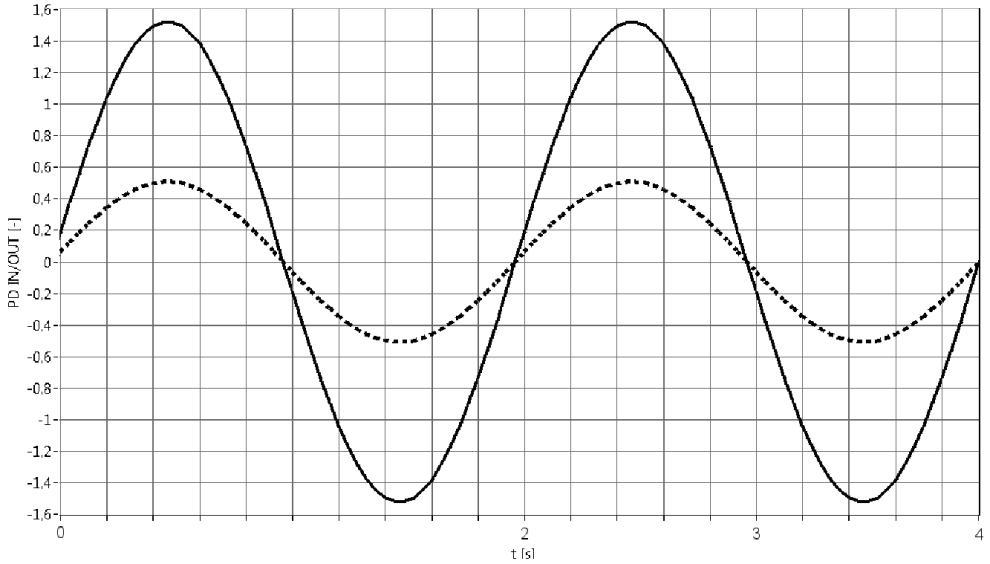

Figure 10. Simulation results (no derivative gain); dashed curve – input; continuous curve – output.

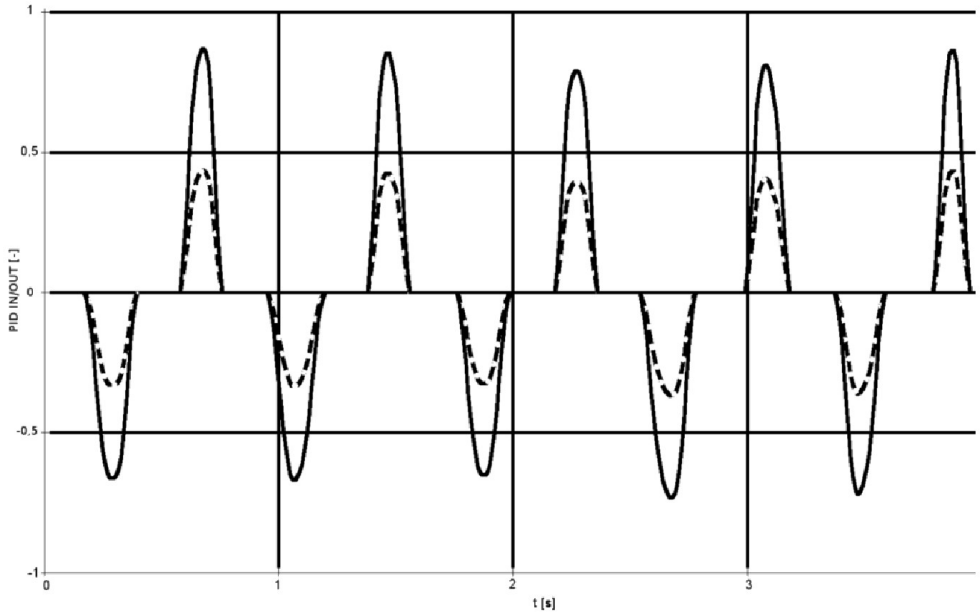

Figure 11. Experimental results (no derivative gain); dashed curve - input, continuous curve - output

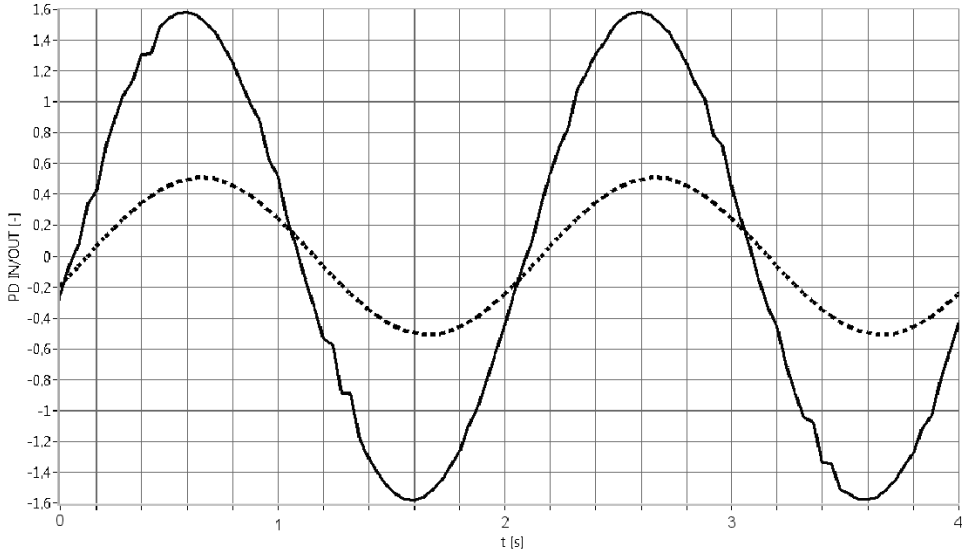

Figure 12. Simulation results (with derivative gain); dashed curve - input, continuous curve - output

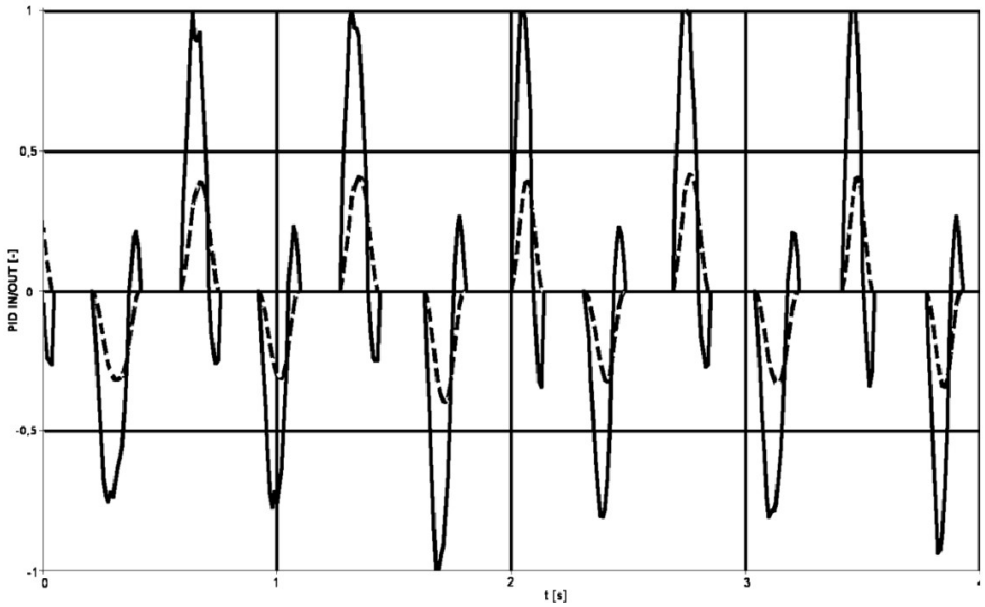

Figure 13. Experimental results (with derivative gain); dashed curve - input, continuous curve - output

9. Concluding remarks

The LabView model has produced a result (see fig. 12) which matches two phenomena, i.e. influence of both proportional and derivative terms of the PD regulator on the exoskeleton behavior. The proportional gain represents the rate of human force amplification. Increasing the value of proportional gain yields an increase of the amplitude of the output signal, and a decrease of the value of the error, and vice versa. However, this is true for a static case, in which the error value is not changing or changes slowly. The derivative gain is on the other hand responsible for the positive phase shift of the output signal, that is the advance of output signal relative to the input signal, which has far reaching effect on the overall exoskeleton behavior. If derivative gain would be set to zero (no phase shift), the user would have to act constantly against the exoskeleton frame in order to achieve exoskeleton reaction. This result in the user impression of dragging the exoskeleton instead of having his force amplified. In opposition, if the output signal is shifted to the left in time, the exoskeleton is in a certain degree predicting the human movement.

Experimental test results from the physical exoskeleton confirm the assumptions, as the exoskeleton behaves similar to the model (see Fig. 13). The results are distorted by the effect of backlash in mechanisms, and the presence of an overshoot, but the core function of proportional and derivative terms is preserved. Similarly as in the simulation the proportional gain is responsible for the output amplitude, and the derivative gain is causing an advance of output signal regarding the input signal. This results in a considerably better user experience, as the user no longer needs to act against it constantly. This is true both for increasing and decreasing the exoskeleton output force.

Finally, it should be emphasised that the initially introduced assumptions have been validated by a real, physical prototype, which gave more insight into the nature of exoskeleton control systems. Important things to note are remarkable simplicity of this solution, easiness of implementation, scalability to other body parts and extremely small computational requirements. The algorithm of operation could be successfully used for creating a number of commercial, cost effective exoskeleton devices, running on mass available low cost microcontrollers, and giving access to the exoskeleton technology to a broad group of people.

Acknowledgments

The work has been supported by the Polish National Science Centre under the grant OPUS 9 No. 2015/17/B/ST8/01700 for years 2016 – 2018

References

[1] K. Kong; D. Jeon: Design and Control of an Exoskeleton for the Elderly and Patients, IEEE/ASME Transactions on Mechatronics, Vol. 11, No. 4, 2006, pages 428-432.

[2] K. Kiguchi; T. Tanaka; T. Fukuda: Neuro-Fuzzy Control of a Robotic Exoskeleton With EMG Signals, IEEE Transactions On Fuzzy Systems, Vol. 12, No. 4, 2004, pages 481-490.

[3] Yu W., and Rosen J. Novel Linear PID Controller for an Upper Limb Exoskeleton Vito, 2010, 3548-3553.

[4] Walsh C.J., Pasch K., Herr H. An autonomous, underactuated exoskeleton for load-carrying augmentation, 2006 IEEE/RSJ International Conference on Intelligent Robots and Systems, 2007, pages 1410-1415.

[5] Mulas M., Folgheraiter M., Gini G. An EMG-controlled Exoskeleton for Hand Rehabilitation, Proceedings of the 2005 IEEE 9th International Conference on Rehabilitation Robotics, 2005, pages 371-374.

[6] Lucas L., DiCicco M., Matsuoka Y. An EMG-Controlled Hand Exoskeleton for Natural Pinching, Journal of Robotics and Mechatronics 16(5), 2004, pages 1-7.

[7] Mertz L. The Next Generation of Exoskeletons, IEEE Pulse, 2012, pages 56-61.

[8] Simkins M., Kim H., Abrams G., Byl N., Rosen J. Robotic unilateral and bilateral upper-limb movement training for stroke survivors afflicted by chronic hemiparesis, 2013 IEEE 13th International Conference on Rehabilitation Robotics (ICORR), 2013.

[9] Bergamasco M., Allotta B, Bosio L., Ferretti L., Parrini G., Prisco G.M., Salsedo F., Sartini G. An arm exoskeleton system for teleoperation and virtual environments applications, Proceedings of the 1994 IEEE International Conference on Robotics and Automation, 1994, pages 1449-1454.

[10] Zoss A.B., Kazerooni H., Chu A. Biomechanical Design of the Berkeley Lower Extremity Exoskeleton (BLEEX), IEEE/ASME Transactions on Mechatronics, Vol. 11, No. 2, 2006, pages 128-138.

[11] Banala S.K., Kim S.H., Agrawal S.K., Scholz J.P. Robot Assisted Gait Training With Active Leg Exoskeleton (ALEX), IEEE Transactions On Neural Systems and Rehabilitation Engineering, Vol. 17, No. 1, 2009, pages 2-8.

[12] Jezernik S., Colombo G., Keller T., Frueh H., Morari M. Robotic Orthosis Lokomat: A Rehabilitation and Research Tool, 2003 International Neuromodulation Society, Vol. 6, No. 2, 2003, pages 108-115.

Mateusz Marek Krain: Department of Automation, Biomechanics and Mechatronics, Faculty of Mechanical Engineering, Lodz University of Technology, 1/15 Stefanowski Street, 90-924 Lodz, POLAND (188191@edu.p.lodz.pl). The author gave a presentation of this paper during one of the conference sessions.

Bartłomiej Zagrodny, PhD: Department of Automation, Biomechanics and Mechatronics, Faculty of Mechanical Engineering, Lodz University of Technology, 1/15 Stefanowski Street, 90-924 Lodz, POLAND (bartlomiej.zagrodny@p.lodz.pl)

Jan Awrejcewicz, Professor: Department of Automation, Biomechanics and Mechatronics, Faculty of Mechanical Engineering, Lodz University of Technology, 1/15 Stefanowski Street, 90-924 Lodz, POLAND (jan.awrejcewicz@p.lodz.pl)

Analysis of the nonlinear dynamics of flexible two-layer beams, with account for their stratification

Vadim A. Krysko, Jan Awrejcewicz, Irina V. Papkova, Olga A. Saltykova

Abstract: The mathematical model of a two-layer beam set taking into account the geometric nonlinearity on the basis of well-known kinematic hypotheses of the first (Euler-Bernoulli), the second (Timoshenko) and the third approximations (Reddy-Pelekh-Sheremetyev) is presented. We show also that it is possible to construct mathematical models, when each layer is described by its own hypothesis. Three problems are addressed. Problem 1 - each of beams is described by the first approximation of the kinematic hypothesis. Problem 2 - each of the beams is described by the second approximation. Problem 3 - each of the beams is described by the third approximation. An external spatially distributed harmonic load acts on the beam package. The lamination of the beam structure along the entire length can occur. The stratification will lead to a change in the design algorithm scheme. In order to get reliable results, it is necessary to solve the problem taking into account two types of nonlinearity, i.e. geometric and constructive ones. A lot of attention in the work is paid to the reliability of the results. The methods for calculating such systems as systems with an infinite number of degrees of freedom have been developed. The convergence of the finite differences method is studied and the convergence of Runge-Kutta type methods is investigated. Furthermore, the value of the largest Lyapunov exponent employing three different algorithms (Wolf, Kantz and Rosenstein) is estimated.

1. Introduction

The aim of the work is to study the nonlinear dynamics of the contact interaction of flexible two-layer beams with a small clearance, described by the kinematic hypotheses of the first, second and third approximation. The influence of the inertial component and the theory of the curved normal on the nonlinear dynamics of the beam structure are investigated. It is necessary to determine what is new accounting for deformations associated with transverse forces, and allowance for the inertia of rotation in the non-linear dynamics of beam structures. On one of the beams (beam 1) is subjected to a distributed alternating load, the second beam, comes into motion due to contact with the beam 1.

Owing to complexity of equations governing the non-linear dynamics of two geometrically non-linear beams with a contact interaction, it is impossible to find an exact analytical solution. In general, the problem can be solved using numerical methods. However, the problem regarding reliability of

the obtained results is generated [1]. In many cases errors introduced by numerical computations are identified with chaotic vibrations. Consequently, it is extremely important to determine the truth of the chaotic vibrations that arise during the contact interaction of the beams. It is known that the fundamental characteristics of chaos is associated with sensitivity to the initial conditions.

In this paper, we refer to Gulick [2] definition of chaos. Owing to the definition of chaos given by Gulick, chaotic orbits exist if there is either essential sensitivity to the initial conditions or at least one of the Lyapunov exponents is positive in each point of the considered chaotic domain.

As initial conditions, we will assume: the kinematic hypotheses, the boundary and initial conditions, the number of intervals for integrating beams in the finite difference method, methods for solving the Cauchy problem in the form of Runge-Kutta methods, time step for solving dynamics problems.

To reduce the infinite-dimensional problem to the Cauchy problem, we used the finite-difference method with approximation $O(c^2)$. The parameters of this method and the method itself are remain constant throughout the work.

Well known are the theories of the beams bending, such as the Euler-Bernoulli theory [3] (first approximation), Timoshenko theory [4] (second approximation), Reddy-Pelekh-Sheremetyev theory [5, 6] (third approximation).

In the scientific literature, one can find numerous works devoted to investigation of Euler-Bernoulli [7], Timoshenko [8], Reddy-Pelekh-Sheremetyev [9] beams. But there are no papers devoted to the study of nonlinear dynamics and the contact interaction of beams.

2. Formulation of the problem

The considered structure composed of two beams occupies a 2D space within the R^2 space with the rectangular system of coordinates given in the following way: a reference line, further called the middle line, is fixed in the beam 1, the axis OX is directed z=0 from the left to the right of the middle line, and the axis OZ is directed downwards. In the given system of coordinates, the space Ω is defined in the following way (see Fig. 1): $\Omega = \{x \in [0, a]; -h \leq z \leq h_k + 3h\}, 0 \leq t \leq \infty$.

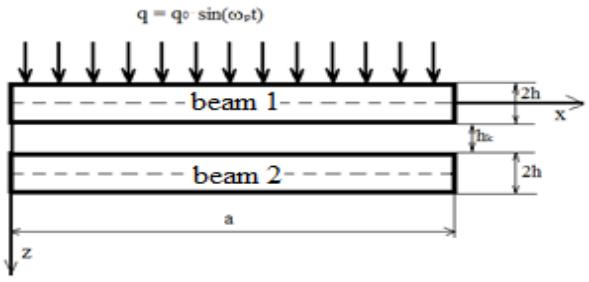

Figure 1. The settlement scheme

Equations of beams motion, as well as the boundary and initial conditions, are obtained from the Hamilton-Ostrogradskiy principle.

The contact pressure is estimated within the Kantor model [10]. The geometric non-linearity is taken in the von Kármán form. The beams are isotropic, elastic, and obey Hook's law. The longitudinal dimensions of beams are larger than their transverse dimensions and the beams have the unit thickness. There is a gap between the beams - h_k. The clearance is less than 0.2h, where h is the height of the beam, i.e. we consider small gaps between the beams.

The Cauchy problem is also solved numerically, and hence solutions essentially depend on both the chosen method and the time step integration. Therefore, in order to achieve reliable results, the Cauchy problem is solved using the Runge-Kutta of the 4th (rk4) and the 2nd (rk2) orders [11], the Runge-Kutta-Fehlberg of the 4th order (rkf45) [12, 13], the Cash-Karp of the 4th order (rkck) [14], the Runge-Kutta-Prince-Dormand of the 8th order (rk8pd) [15] as well as the implicit Runge-Kutta methods of the 2nd (rk2imp) and the 4th (rk4imp) orders.

The spectrum of the Lyapunov exponents has been estimated using three methods based on Kantz [16], Wolf [17] and Rosenstein [18] algorithms. This will ensure the reliability of the obtained numerical results.

3. Mathematical models of the contact interaction of beams described by hypotheses of the first, second and third approximations

The displacements of an arbitrary point of a beam, in the framework of the third-approximation hypothesis, are written as follows:

$$u^z = u + \underline{\underline{z\gamma_x}} + \underline{z^2 u^{\mathrm{T}} + z^3 \gamma^{\mathrm{T}}}\,;\; w^z = w, \tag{1}$$

where γ_x - is the transverse shear function, u^T, γ^T – are the unknown functions, w – is the deflection. We receive system of nonlinear partial differential equations for two Reddy-Pelekh-Sheremetyev beams in the displacements taking into account energy dissipation:

$$\begin{cases} \frac{1}{\lambda^2 63}\left[\frac{4}{5}\frac{\partial^3 \gamma_{xi}}{\partial x^3} - \frac{1}{4}\frac{\partial^4 w_i}{\partial x^4}\right] + k^2 \frac{G_{13}}{E_1}\left[\frac{\partial \gamma_{xi}}{\partial x} + \frac{\partial^2 w_i}{\partial x^2}\right] + \\ \frac{1}{\lambda^2}\left[L_3(w_i,u_i) + L_1(w_i,u_i) + \frac{3}{2}L_2(w_i,w_i)\right] - \\ -(-1)^i K(w_1 - w_2 - h_k)\Psi + q_i(t) - \frac{\partial^2 w_i}{\partial t^2} - \varepsilon_1 \frac{\partial w_i}{\partial t} = 0, \\ \frac{\partial^2 u_i}{\partial x^2} + L_4(w_i,w_i) - \frac{\partial^2 u_i}{\partial t^2} = 0, \\ \frac{204}{315}\frac{\partial^2 \gamma_{xi}}{\partial x^2} - \frac{48}{315}\frac{\partial^3 w_i}{\partial x^3} - 12\lambda^2 k^2 \frac{G_{13}}{E_1}\left[\gamma_{xi} + \frac{\partial w_i}{\partial x}\right] - \frac{\partial^2 \gamma_{xi}}{\partial t^2} = 0, i = 1,2, \end{cases} \tag{2}$$

where: $i = 1,2$ - are the sequence number of beams, $L_1(w_i,u_i) = \frac{\partial^2 w_i}{\partial x^2}\frac{\partial u_i}{\partial x}$, $L_2(w_i,w_i) = \frac{\partial^2 w_i}{\partial x^2}\left(\frac{\partial w_i}{\partial x}\right)^2$, $L_3(w_i,u_i) = \frac{\partial w_i}{\partial x}\frac{\partial^2 u_i}{\partial x^2}$, $L_4(w_i,w_i) = \frac{\partial w_i}{\partial x}\frac{\partial^2 w_i}{\partial x^2}$ - are the non-linear operators, γ_{xi} - is the transverse shear function, w_i, u_i - are the deflection and displacement functions of the beams, respectively, K – is the

coefficient of transverse stiffness of the contact zone.

The equation of motion of the beam element (2) contains a fourth-order derivative, which is extremely important in proving the existence of a solution of the equation and the convergence of various methods for their solution. The hypothesis of the second approximation - the of Timoshenko hypothesis, consists in the fact that tangential displacements are distributed along the beam thickness according to a linear law, i.e. in expression (1) there remain only linear terms, the terms underlined by one line are assumed to be zero.

Equations in displacements for a structure of two beams, in a dimensionless form, where both beams are described by a second approximation model:

$$\begin{cases} \frac{1}{3}\left[\frac{\partial^2 w_i}{\partial x^2}+\frac{\partial \gamma_{xi}}{\partial x}\right]+\frac{1}{\lambda^2} \\ \left[L_1(w_i,u_i)+L_3(w_i,u_i)+\frac{3}{2}L_2(w_i,w_i)\right]- \\ -(-1)^i K(w_1-w_2-h_k)\Psi+q_i(t)-\frac{\partial^2 w_i}{\partial t^2}-\varepsilon_1\frac{\partial w_i}{\partial t}=0; \\ \frac{\partial^2 u_i}{\partial x^2}+L_4(w_i,w_i)-\frac{\partial^2 u_i}{\partial t^2}=0; \\ \frac{\partial^2 \gamma_{xi}}{\partial x^2}-8\lambda^2\left[\gamma_{xi}+\frac{\partial w_i}{\partial x}\right]-\frac{\partial^2 \gamma_{xi}}{\partial t^2}=0; i=1,2. \end{cases} \quad (3)$$

$L_1(w_i,u_i), L_2(w_i,w_i), L_2(w_i,u_i), L_2(w_i,w_i)$ - these are nonlinear operators analogous to those given after the system of equations (2). Differential equations derived from the Timoshenko hypothesis have the highest second partial derivative with respect to x, which sometimes makes the proof the convergence of certain methods difficult. To obtain the Euler-Bernoulli equations, we will assume that the tangential displacements u^z, w^z are distributed linearly along the thickness, and any cross-section normal to the midline before deformation remains after deformation by a straight line and normal to the midline, the height of the section does not change. In expression (1), the zero terms are underlined by one line and replace γ_x by a rotation angle $-\frac{\partial w}{\partial x}$ for the term underlined by two lines. Thus we obtain the Euler-Bernoulli equations.

Equations governing the dynamics of two Euler-Bernoulli beams with respect to displacements and taking into account frictional energy loss (dissipation) are governed by the following PDEs:

$$\begin{cases} \frac{1}{\lambda^2}\left[L_2(w_i,w_i)+L_1(u_i,w_i)-\frac{1}{12}\frac{\partial^4 w_i}{\partial x^4}\right]- \\ -(-1)^i K(w_1-w_2-h_k)\Psi+q_i(t)-\frac{\partial^2 w_i}{\partial t^2}-\varepsilon_1\frac{\partial w_i}{\partial t}=0; \\ \frac{\partial^2 u_i}{\partial x^2}+L_3(w_i,w_i)-\frac{\partial^2 u_i}{\partial t^2}=0;\ i=1,2, \end{cases} \quad (4)$$

where $L_1(u_i,w_i)=\frac{\partial^2 u_i}{\partial x^2}\frac{\partial w_i}{\partial x}+\frac{\partial u_i}{\partial x}\frac{\partial^2 w_i}{\partial x}$, $L_2(w_i,w_i)=\frac{3}{2}\frac{\partial^2 w_i}{\partial x^2}\left(\frac{\partial w_i}{\partial x}\right)^2$, $L_3(w_i,w_i)=\frac{\partial w_i}{\partial x}\frac{\partial^2 w_i}{\partial x^2}$ are the nonlinear operators.

In order to model the contact interaction of the beam within the Kantor model, we introduce the term $(-1)^i K(w_1-w_2-h_k)\Psi$, $i=1,2$ into the equation governing the beams, i - stands for the

beam number. The function is Ψ defined by the formula $\Psi=\frac{1}{2}[1+sign(w_1-h_k-w_2)]$, i.e. if Ψ=1 the beams are in contact $w_1 > w_2 + h_k$, otherwise there is no contact between [10] (see Fig. 1).

By "beam 1" we understand the externally beam loaded, whereas "beam 2" stands for the unloaded beam. We must add boundary and initial conditions to the systems of differential equations (2) – (4). In equations (2) – (4) bars are omitted.

The system of governing PDEs supplemented by boundary and initial conditions is reduced to the counterpart dimensionless form using the following variables:

$$\overline{w}=\frac{w}{2h},\overline{a}=\frac{ua}{(2h)^2},\overline{x}=\frac{x}{a},\lambda=\frac{a}{2h},\overline{q}=q\frac{a^4}{(2h)^4E}, \quad (5)$$

$$\overline{t}=\frac{t}{\tau},\tau=\frac{a}{c},c=\sqrt{\frac{Eg}{\gamma}},\overline{\varepsilon_1}=\varepsilon_1\frac{a}{c},\overline{\gamma_x}=\frac{\gamma_x a}{2h},$$

where: *E* – is the Young's modulus; g – is the gravity of Earth; γ – is the specific gravity of the beam material, *2h* - is the height, *a* - is the length of beams, respectively.

The beam 1 is subjected to the uniformly distributed transverse harmonic excitation of the following form:

$$q = q_0 \sin(\omega_p t), \quad (6)$$

where q_0 stands for the amplitude and ω_p for the frequency of excitation.

The obtained system of non-linear PDEs (2) – (4) is reduced to ODEs using the FDM (Finite Difference Method) with the approximation $O(c^2)$, where c – is a step regarding the spatial coordinate. The Cauchy problem is solved using the Runge-Kutta methods in time.

On the basis of the described algorithms, the program package has been developed, which allows one to solve the given problem with respect to the control parameters $\{q_0, \omega_p\}$. The main attention has been paid to control and avoid the occurrence of penetration of the structural elements. As it has been already pointed out, the studied problems are strongly non-linear, and hence an important question regarding reliability of the obtained results arises. The analysis of the results was carried out using signals, Fourier power spectra, Poincaré pseudo-mappings, phase 2D and 3D portraits, wavelet spectra based on the Gauss 32 mother wavelet. The beam 1 is subjected to the uniformly distributed transverse harmonic excitation (6). Where $q_0 = 5000$, $\omega_p = 5.1$. The beam clearance equals $h_k = 0.1$.

4. Numerical results

4.1. Task 1. Both beams of the packet are described by the kinematic hypothesis of the first approximation

We must add boundary and initial conditions to the system of differential equations (4).

Boundary conditions for case when both ends of the beams are rigidly clamped:

$$w_i(0,t) = w_i(1,t) = u_i(0,t) = u_i(1,t) = \frac{\partial w_i(0,t)}{\partial x} = \frac{\partial w_i(1,t)}{\partial x} = 0, i = 1,2. \quad (7)$$

Initial conditions:

$$w_i(x)_{|_{t=0}} = 0, u_i(x)_{|_{t=0}} = 0, \frac{\partial w_i(x)}{\partial t}_{|_{t=0}} = 0, \frac{\partial u_i(x)}{\partial t}_{|_{t=0}} = 0, i = 1,2. \quad (8)$$

A preliminary study was made of the convergence of the FDM.

We are compared the signals, the Fourier power spectra, the Poincaré pseudo-map, the Gauss 32 wavelet spectra, phase portraits (2D and 3D) for different values of integration intervals *n*=40; 80, 120; 160. It was found that complete coincidence of signals for both beams occurs when n=160. The results were obtained using the 8th order Runge-Kutta method in the modification of Prince-Dormand.

It should be emphasized, that earlier in [19] the convergence of the results for the chaotic state of the system was determined from the convergence of the Fourier power spectra, and convergence with respect to the signal was not required. After obtaining the convergence of the solution by the FDM, was made a comparison of solutions obtained by various methods of Runge-Kutta type. The results are completely the same for the Runge-Kutts of all orders.

The values of the highest Lyapunov exponent, calculated by the methods of Wolff, Rosenstein, and Kants, are compared depending on n. The obtained values result from the computation using the 8th-order Runge-Kutta method. It should be emphasized that different methods of computation of the Lyapunov exponent are needed to obtain reliable/true value and, consequently, reliable estimation of chaos. When using the FDM, for the number of beams partitions n=40, 80, 120; 160 for any mentioned method, the Lyapunov exponents coincide with an accuracy up to the third decimal digit. Furthermore, all of the largest Lyapunov exponents (LLEs) are positive. In what follows we define how the LLEs depend on the method employed for solution of the Cauchy problem. For this purpose, we have computed the Lyapunov exponents using the Wolf, Kantz and Rosenstein algorithms for n=160. On the contrary to the dynamic characteristics, we have not observed full coincidence of the results. However, the difference between the minimum and the maximum of the exponents computed for different Runge-Kutta methods using the Wolf algorithm for the beam 1 is about 0.07, whereas the same done by the Rosenstein and Kantz methods yields the difference of 0.008. Convergence up to the second decimal digit has been observed for each of the computational methods of the LEs computation. It should be noted that all values of the LLE, independently of the employed method of the solution of the Cauchy problem, the beam partition number, and the employed LLE method, are positive.

Based on the analysis of dynamic indicators and the values of LLEs, it can be concluded that the oscillations of the investigated beam structure are chaotic and the revealed chaos is true.

4.2. Task 2. Both beams of the packet are described by the kinematic hypothesis of the second approximation

Let us consider the case when both beams are described by a second-approximation model (the Timoshenko model). We must add boundary (9) and initial (10) conditions to the system of differential equations (3). Both ends of the beams are rigidly clamped:

$$w_i(0,t) = w_i(1,t) = u_i(0,t) = u_i(1,t) = \gamma_{xi}(0,t) = \gamma_{xi}(1,t) = 0, i = 1,2. \quad (9)$$

Initial conditions:

$$w_i(x)_{|_{t=0}} = 0, u_i(x)_{|_{t=0}} = 0, u_i(x)_{|_{t=0}} = 0, \frac{\partial w_i(x)}{\partial t}_{|_{t=0}} = 0, \quad (10)$$

$$\frac{\partial u_i(x)}{\partial t}_{|_{t=0}} = 0, \frac{\partial \gamma_{xi}(x)}{\partial t}_{|_{t=0}} = 0, i = 1,2.$$

Here the bars under the dimensionless parameters are omitted for simplicity.

A preliminary study was made of the convergence of the FDM depending on the $n = 40; 80; 120; 240; 360; 400$.

For n = 40; 80; 120 the deflection is very different from the deflection counted with a large n. Starting with n = 240, deflections for the first beam coincide. For the second beam, the convergence by the number of divisions of the segment is much worse and begins with n = 360. The error between the signals calculated at n = 360 and n = 400 is 3%, but the signals coincide in shape over the entire time interval. The results were obtained using the 8th order Runge-Kutta method in the modification of Prince-Dormand.

The difference in signals does not exceed 2% for beam 2 for different methods of the Runge-Kutta class at the central point of the beams, at the same time. The greatest difference is between the methods of the second and eighth order.

In addition to the convergence of the signals in the center of the beams, let us check the convergence of the solution along the length of the beam. For this purpose, the plots of the deflection of beams were compared at the same instant of time t=500 at n=40; 80; 120; 240; 360; 400. It was revealed that the shape of the median line deflection along the length of the beam completely coincides for beam 1 at n = 240; 360; 400, and for beam 2 with n = 360; 400.

To make a decision on the reliability of the obtained results and the validity of chaotic oscillations, it is necessary to achieve convergence in the spectra of beam power, wavelet spectra, 2D and 3D phase portraits, and the Poincaré section. All the dynamic indices coincided for both beams at n = 400.

Based on the above analysis, we will take it for further research, which will ensure the maximum convergence of the results of beam 1 and beam 2. To solve the Cauchy problem, it is necessary to use the Runge-Kutta methods of the 8th order.

Based on the above analysis, we will take n=400 for further research, which will ensure the maximum convergence of the results of beam 1 and beam 2. To solve the Cauchy problem, it is necessary to use the 8th order Runge-Kutta methods. Let us investigate the convergence of the values of the LLEs, calculated by three different methods-Wolff, Kantz, and Rosenstein. In Table 1 we give the values of the LLEs for different n and for different methods for solving the Cauchy problem.

Table 1. The LLEs calculated for signals obtained in solving the Cauchy problem by various methods of Runge-Kutta type with n=400.

The Runge-Kutta methods	Beam 1			Beam 2		
	Wolff	Rosenstein	Kantz	Wolff	Rosenstein	Kantz
Rk8pd	0,01658	0,05646	0,02191	0,02835	0,04617	0,02363
Rkck	0,01399	0,05528	0,04583	0,02837	0,04583	0,02156
Rkf45	0,01556	0,05035	0,02300	0,02835	0,04321	0,02128
Rk4imp	0,01468	0,04298	0,01922	0,02832	0,03887	0,02051
Rk4	0,01414	0,04228	0,01952	0,02827	0,03911	0,01812
Rk2imp	0,01464	0,03492	0,01520	0,02828	0,03428	0,01752

The LLEs for the first beam are the closest ones by the Rosenstein method, and for the second beam - according to Wolf's method. The convergence of the LE as a function of n is good in the framework of one method. Up to the second decimal place, the values obtained by the Rosenstein method at n = 400 and 360 for the beam 1 are the same. For beam 2, the values of the Lyapunov exponent obtained by the Rosenstein method differ by one-hundredth for the same n. The Kantz method also gives convergence to the second decimal point at n = 400; 360.

In all the cases, the sign of the LLEs is positive, which indicates that the vibrations of beam structure is chaotic.

4.3. Task 3. Both beams of the packet are described by the kinematic hypothesis of the third approximation

We must add boundary (11) and initial (12) conditions to the system of differential equations (2). Both ends of the beams are rigidly clamped:

$$w_i(0,t) = w_i(1,t) = u_i(0,t) = u_i(1,t) = \gamma_{xi}(0,t) = \gamma_{xi}(1,t) = 0,$$
$$\frac{\partial w_i(0,t)}{\partial t} = \frac{\partial w_i(1,t)}{\partial t} = 0;\ \frac{\partial u_i(0,t)}{\partial t} = \frac{\partial u_i(1,t)}{\partial t} = 0; \quad (11)$$
$$\frac{16}{5}\frac{\partial^2 \gamma_{xi}(0,t)}{\partial x^2} - \frac{\partial^3 w_i(0,t)}{\partial x^2} = 0;\ \frac{16}{5}\frac{\partial^2 \gamma_{xi}(1,t)}{\partial x^2} - \frac{\partial^3 w_i(1,t)}{\partial x^2} = 0;$$
$$\frac{136}{315}\frac{\partial \gamma_{xi}(0,t)}{\partial x} - 0.038\frac{\partial^2 w_i(0,t)}{\partial x^2} = 0;\ \frac{136}{315}\frac{\partial \gamma_{xi}(1,t)}{\partial x} - 0.038\frac{\partial^2 w_i(1,t)}{\partial x^2} = 0,\ i=1, 2.$$

Initial conditions:

$$w_i(x)_{|_{t=0}} = 0, u_i(x)_{|_{t=0}} = 0, u_i(x)_{|_{t=0}} = 0, \quad (12)$$

$$\frac{\partial w_i(x)}{\partial t}_{|_{t=0}} = 0, \frac{\partial u_i(x)}{\partial t}_{|_{t=0}} = 0, \frac{\partial \gamma_{xi}(x)}{\partial t}_{|_{t=0}} = 0, i = 1,2.$$

Analogously to the problems described above, the convergence of the results is investigated depending on the number of intervals for the partition of the beam n = 40; 80; 120; 240; 360; 400; 440 and on the method for solving the Cauchy problem. The conclusion about the convergence of the results was made on the basis of the analysis of signals, power spectra, Poincaré pseudo-mappings, phase portraits.

It was found that the coincidence of signals for beam 1 occurs at n = 360, for beam 2 at n = 400. The convergence for different methods of the Runge-Kutta class for the beam 1 is complete, and for beam 2 there are differences between the methods of the 2nd and 4th order from the 8th order method.

Thus, to solve the problem of the contact interaction of two beams described by the kinematic hypothesis of the third approximation, when using the FDM of the second order, the required number of partitions along the spatial coordinate must not be less than 400. As the method for solving the Cauchy problem, the Runge-Kutta method 8-th order in the Prince Dormand modification. For each considered problem, the values of the LLEs were calculated from three different algorithms. All the LLEs are positive, which allows us to speak of the truth of the chaotic oscillations of the studied beam structure.

5. Comparative analysis of the tasks 1-3

In Table 2 we give the main dynamic indicators for each of the described problems. The results obtained by the 8th order Runge-Kutta method in Prince-Dormand modification are presented.

For task 1, the vibrations of the beams are three-frequency, and the frequencies are linearly dependent on the frequencies $\omega_p = 5.1$. The phase portraits and pseudo-Poincare mappings for beams 1 and 2 have significant differences between themselves. For task 2, the Fourier power spectrum of beam 1 has four frequencies with a slight noisy at low frequencies. For the same problem, the power spectrum of beam 2 reflects a greater number of noise frequencies, but the fundamental frequencies are the same as for beam 1. All frequencies are linearly dependent. The greatest number and amplitude of noise frequencies is observed in the case of problem 3. In contrast to problems 1 and 2, on the power spectra of both beams there is the frequency of the first bifurcation $\omega_p/2$. The remaining dynamic characteristics are well correlated with the Fourier power spectra.

Table 2. Dynamic characteristics of beams vibrations.

	beam	Fourier power spectra	3D phase portraits $w(\dot{w};\ddot{w})$	2D phase portraits $w(\dot{w})$	Poincaré pseudo-mappings
n=400; 440, task 3	1	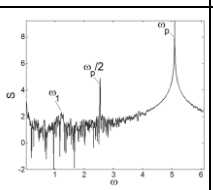	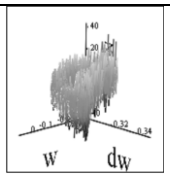	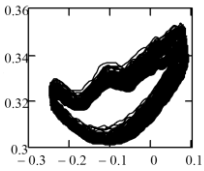	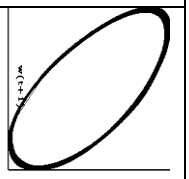
	2	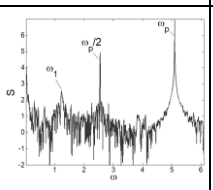	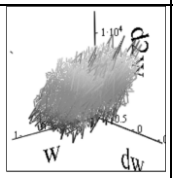	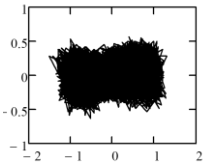	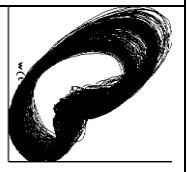
n=360; 400, task 2	1	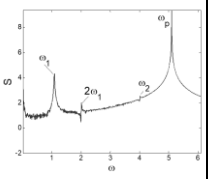	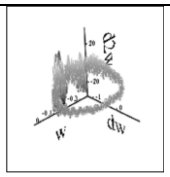	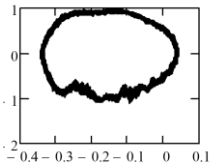	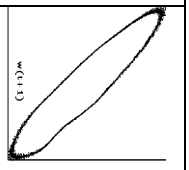
	2	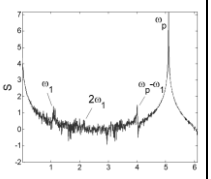	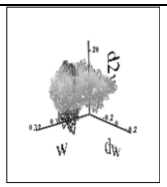	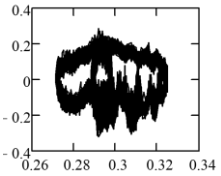	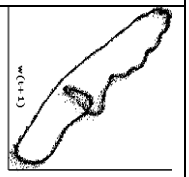
n=120; 160, task 1	1	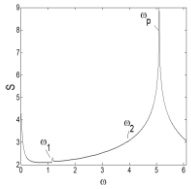	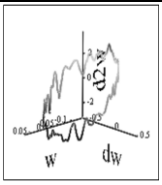	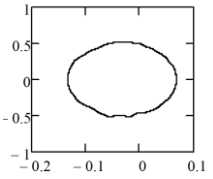	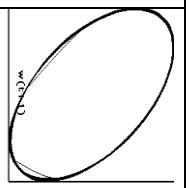
	2	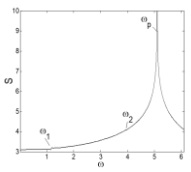	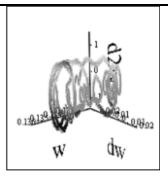	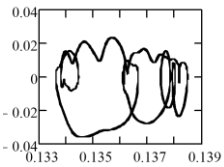	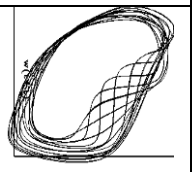

6. Conclusions

The continuous mechanical system cannot be truncated to the system with a finite number of degrees of freedom, but the problem is, indeed, of an infinite dimension.

We have detected, the occurrence of the phase synchronization of beams vibrations for the investigated system, among others. In addition, all frequencies exhibited by beam vibrations are in resonance relation with the excitation frequency.

Regardless of the methods for solving the problem and the hypotheses used at the modeling stage, it can be concluded that the vibrations of the two-layer beam structure are chaotic. The magnitude of the amplitude of the beam vibrations for all problems are of the same order.

It was found that with an increase in the number of partitions, the beam vibrations are regularized.

Acknowledgements

This work has been supported by the Grant RSF № 16-11-10138

References

[1] Ren´e Lozi. Can we trust in numerical computations of chaotic solutions of dynamical systems? *World Scientific Series on Nonlinear Science*, World Scientific, 84, (2013), pp.63-98.

[2] Gulick, D. *Encounters with Chaos*, McGraw-Hill, New York, 1992.

[3] Euler, L. Sur la force des colones. *Memories de L'Academie de Berlin* 13, (1757), pp. 252 – 282.

[4] Timoshenko, S.P. On the correction for shear of differential equation for transverse vibration of prismatic bar. *Philosophical Magazin* 41, (1921), pp. 744-746.

[5] Sheremet'ev, M.P., Peleh, B.L. To the construction of an improved theory of plates. *Inzh.zhurn*. 4 (3) (1964) pp. 34–41 (in Russian).

[6] Reddy, J. N. A refined nonlinear theory of plates with transverse shear deformation. *International Journal of solids and structures* 20 №. 9-10 (1984), pp. 881-896.

[7] Zhigalov, M.V., Pavlov, S.P., Krysko, V.A. Nonlinear Dynamics of Multilayer Beam Structures with Gaps between them taking into Account the Geometrical and Physical Nonlinearities. *International Journal of Applied Engineering Research* 11(21), (2016), pp. 10427-10432.

[8] Awrejcewicz, J., Krysko, V.A., Pavlov, S.P., Zhigalov, M.V. Nonlinear dynamics size-dependent geometrically nonlinear Tymoshenko beams based on a modified moment theory. *Applied Mathematical Sciences*, 11(5), (2017), pp. 237-247.

[9] Krysko, A.V., Awrejcewicz, J., Pavlov, S.P., Zhigalov, M.V., Krysko, V.A. Chaotic dynamics of the size-dependent non-linear micro-beam model. *Communications in Nonlinear Science and Numerical Simulation*, 50, (2017), 16-28.

[10] Kantor, B.Ya. *Contact problems of the nonlinear theory of shells of revolution* Naukova Dumka, Kiev, 1990. (in Rus.)

[11] Süli, E., Mayers, D. *An Introduction to Numerical Analysis*. Cambridge: Cambridge University Press, 2003.

[12] Fehlberg, E. *Low-order classical Runge-Kutta formulas with step size control and their application to some heat transfer problems*. NASA Technical Report 315, 1969.

[13] Fehlberg, E. Klassische Runge-Kutta-Formeln vierter und niedrigerer Ordnung mit Schrittweiten-Kontrolle und ihre Anwendung auf Wärmeleitungsprobleme, *Computing (Arch. Elektron. Rechnen)*, 6, (1970), pp. 61–71.

[14] Cash, J.R., Karp A.H. A variable order Runge-Kutta method for initial value problems with rapidly varying right-hand sides. *ACM Transactions on Mathematical Software* 16, (1990), pp. 201-222.

[15] Dormand, J. R., Prince, P. J. A family of embedded Runge-Kutta formulae, *Journal of Computational and Applied Mathematics*, 6 (1) (1980), pp. 19–26.

[16] Kantz, H. A robust method to estimate the maximum Lyapunov exponent of a time series. *Phys. Lett. A*, 185, (1994), pp. 77-87.

[17] Wolf, A., Swift, J.B., Swinney, H.L., Vastano, J.A. Determining Lyapunov Exponents from a time series *Physica 16 D*, (1985), pp. 285-317.

[18] Rosenstein, M.T., Collins, J.J., Carlo, J. De Luca A practical method for calculating largest Lyapunov exponents from small data sets. *Neuro Muscular Research Center and Department of Biomedical Engineering, Boston University*, 20, (1992).

Vadim A. Krysko, Professor: Department of Mathematics and Modeling, Saratov State Technical University, Politehnicheskaya 77, 410054 Saratov, RUSSIAN FEDERATION (tak@san.ru). The author gave a presentation of this paper during one of the conference sessions.

Jan Awrejcewicz, Professor: Lodz University of Technology, Faculty of Mechanical Engineering, Department of Automation, Biomechanics and Mechatronics, 1/15 Stefanowskego Str., 90-924 Lodz, POLAND (jan.awrejcewicz@p.lodz.pl).

Irina V. Papkova, PhD.: Department of Mathematics and Modeling, Saratov State Technical University, Politehnicheskaya 77, 410054 Saratov, RUSSIAN FEDERATION (ikravzova@mail.ru).

Olga A. Saltykova, PhD.: Department of Mathematics and Modeling, Saratov State Technical University, Politehnicheskaya 77, 410054 Saratov, and Cybernetic Institute, National Research Tomsk Polytechnic University, Lenin Avenue, 30, 634050 Tomsk, RUSSIAN FEDERATION (olga_a_saltykova@mail.ru).

Dynamics of the size-dependent flexible beams embedded into temperature field

Anton V. Krysko, Jan Awrejcewicz, Ilya Kutepov, Vadim A. Krysko

Abstract: The paper studies nonlinear dynamics of Bernoulli-Euler flexible curved beams in the stationary temperature field. The geometric nonlinearity was introduced according to Kármán's model. The effect of the temperature field is taken into account according to the Duhamel-Neumann theory, and no restrictions are imposed on the distribution of the temperature field over the beam thickness. The equations of motion of Bernoulli-Euler flexible beams are obtained from the Ostrogradskii-Hamilton principle taking into account the bending theory of elasticity. The resulting system of partial differential equations, written in terms of displacements, is reduced to the Cauchy problem by the method of finite differences of the second order of accuracy, which is solved by the fourth-order Runge-Kutta method. The temperature field is determined from the solution of the heat equation by the finite difference method. Reliability of the obtained results of the solution is based on the Runge principle. The study is dealing with the reliable determination of the system oscillation mode using a variety of signal analysis methods, such as the Fourier power spectrum, wavelet analysis, phase portrait analysis, Poincaré sections. Determination of a complex mode of the system oscillation does not allow to reliably determine the chaotic mode. To do this, the sign of the highest Lyapunov exponent is determined, and the spectrum of Lyapunov exponents was used to determine the degree of the state of chaos. In order to study the reliability of the obtained sign of the Lyapunov exponent, it was determined by several methods: Wolf, Rosenstein, Kantz, and a neural network method modification. As a result of the study of nonlinear dynamics of size-dependent flexible beams under the effect of the temperature field, depending on the control parameters, we have obtained reliable information on the system oscillation mode. This will prevent cases when chaotic oscillations may arise leading to the failure of MEMS operation.

1. Introduction

Nonlinear phenomena can be studied in the behavior of micro- and nano-mechanical devices. In recent years, more and more studies have been devoted to this topic [1-10]. As one of the first studies, Wang et al. has provided a theoretical analysis and experimental results on the dynamic behavior of the bistable resonator of the microelectromechanical system (MEMS) and has shown the existence of a strange attractor and chaos [11]. Later, De Martini [12], Haghigh, Markazi [13], Aghababa [14] used the version of the Mathieu equation for modeling the regulating equation of MEMS motion and used Melnikov's method, which describes the region of the parameter space where chaos exists. They

also used experimental results and showed chaotic behavior in MEMS. However, the influence of the temperature effect on the operation of MEMS devices is not considered in [11-14]. An important issue is the study of chaos and stability of the system, when studying nonlinear dynamics of mechanical structures [15]. One-dimensional mathematical models of beams, panels of infinite length and shells are constructed in the paper, taking into account the geometric, physical, constructive kinematic nonlinearity and various combinations of these nonlinearities. Many problems were solved by various methods, i.e. the finite differences, Bubnov-Galerkin, Rayleigh-Ritz. The existence of a certain universality of the turbulence transition in the spatial problems of the theory of one-dimensional mechanical structures is shown by analogy with the phenomenon of the universality of the chaos emergence in simple systems. However, the monograph [15] did not consider possible accounting of size-dependent parameters, temperature fields and vibrations. Papers [16-20] deal with the application of the finite element method (FEM), the finite difference method (FDM) to the problems of vibrational gyroscope modeling.

As a rule, nonlinear dynamics typically is aimed on an investigation of a mechanical system with one degree of freedom, which leads to the study of the Duffing-type equation, but does not accurately describe the occurring nonlinear processes. In this paper, a distributed system is considered as a system with an infinite number of degrees of freedom, which most accurately describes the real structure. According to the definition of chaos given by Gulick, chaos essentially depends on the initial conditions and the sign of the spectrum of the Lyapunov exponents. These initial conditions also include the temperature effect, which leads the system to a fundamentally new nature of oscillations, especially at the nano-level. The review [21] considers many papers devoted to small-scale models, however, the issue of studying chaotic dynamics and stability of curved MMS beam elements under the effect of the external load and the temperature field was not considered.

The issue of identifying "true" chaos is extremely important in such problems. This paper is dealing with this issue.

2. Hypotheses

The beam (Figure 1) is a curved body of length L, height h, the beam cross-section is rectangular with a width b, area A, the midline curvature $k_x = 1/R_x$. A beam with boundary Γ occupies the region $\Omega = \{0 < x < L;\ -h/2 < z < h/2\}$.

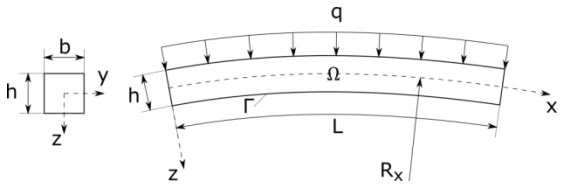

Figure 1. The beam schematic

A mathematical model of the beam is based on the following hypotheses:

- any cross-section normal to the midline before deformation remains a straight line and normal to the midline after deformation, and at the same time the section height does not change;
- the nonlinear relationship between deformations and displacements in the Kármán's form is taken into account;
- the flatness condition is taken due to V.Z. Vlasov [22];
- the beam material is elastic, isotropic and is subject to the Duhamel-Neumann law;
- the thermal conductivity coefficient does not depend on temperature;
- physical properties of the material do not depend on temperature;
- no restrictions are imposed on the distribution of the temperature field over the beam thickness.

Equations of the beam motion, boundary and initial conditions are obtained from the Ostrogradskii-Hamilton energy principle. According to this principle, neighborhood motions are compared that lead the system of material points from the initial position at time t_0 to the final position at time t_1. The following condition satisfied be met for true motions

$$\int_{t_0}^{t_1}(\delta K - \delta\Pi + \delta W)\,dt = 0, \tag{1}$$

where: $K -$ the kinetic energy of the system; $\Pi -$ the potential energy; $W -$ the sum of elementary works of external forces.

For an isotropic homogeneous material, stresses caused by the kinematic parameters included in the strain energy density equation, are determined by the following state equations:

$$\sigma_{ij} = \lambda\varepsilon_{ij}\delta_{ij} + 2\mu\varepsilon_{ij},\ m_{ij} = 2\mu l^2\chi_{ij}, \tag{2}$$

where δ_{ij} – the Kronecker delta, σ_{ij}, ε_{ij}, m_{ij} and χ_{ij} are the components of the classical stress tensor σ, the strain tensor ε, the deviator part of the symmetric momentum tensor of the higher order m and the symmetric part of the curvature tensor χ, respectively; $\lambda = \frac{E\nu}{(1+\nu)(1-2\nu)}$, $\mu = \frac{E}{2(1+\nu)}$ - the Lamè parameters; ν – the Poisson's ratio; l – the independent material length parameter.

After the known conversions, we obtain the resulting equations of motion:

$$\begin{cases} \dfrac{\partial^2 u}{\partial x^2} - k_x \dfrac{\partial w}{\partial x} + L_3(w,w) - \dfrac{\partial N_t}{\partial x} - \dfrac{\partial^2 u}{\partial t^2} = 0 \\ \dfrac{1}{\lambda^2}\left\{\left(-\dfrac{1}{12} + \dfrac{l^2}{4}\right)\dfrac{\partial^4 w}{\partial x^4} + k_x\left[\dfrac{\partial u}{\partial x} - k_x w - \dfrac{1}{2}\left(\dfrac{\partial w}{\partial x}\right)^2 - w\dfrac{\partial^2 w}{\partial x^2}\right] + L_1(u,w) + L_2(w,w)\right\} - \\ - \dfrac{\partial^2 M_t}{\partial x^2} - k_x N_t - \dfrac{\partial}{\partial x}\left\{N_t \dfrac{\partial w}{\partial x}\right\} + q - \dfrac{\partial^2 w}{\partial t^2} - \varepsilon \dfrac{\partial w}{\partial t} = 0, \end{cases} \quad (3)$$

where $L_1(u,w) = \frac{\partial^2 u}{\partial x^2}\frac{\partial w}{\partial x} + \frac{\partial u}{\partial x}\frac{\partial^2 w}{\partial x^2}$; $L_2(w,w) = \frac{3}{2}\left(\frac{\partial w}{\partial x}\right)^2 \frac{\partial^2 w}{\partial x^2}$; $L_3(w,w) = \frac{\partial w}{\partial x}\frac{\partial^2 w}{\partial x^2}$; $-$ the nonlinear operators; $w(x,t)$ – deflection of the element; ϵ – the dissipation coefficient; h - the beam height; L – the beam length; $u(x,t)$ – displacement of the element in the longitudinal direction; M_x^T – the bending moment depending on the temperature; N_x^T – longitudinal force depending on the temperature; t – time; ϑ – bulk weight of the material ; g – the acceleration due to gravity; ρ – density; q – external load. In the special case, in the absence of the temperature and taking $k_x = 0$, equation (3) coincides with equations obtained in [23].

Dimensionless parameters were introduced for the system of equations (3):

$$\bar{w}=\frac{w}{h},\ \bar{u}=\frac{uL}{h^2},\ \bar{x}=\frac{x}{L},\ \bar{z}=\frac{z}{h},\ \ \bar{q}=q\frac{L^4}{h^4E},\ \ c=\sqrt{\frac{Eg}{\rho}},\ \ \bar{\varepsilon}=\frac{\varepsilon L}{c},\ \ \bar{t}=\frac{t}{\tau},\ \ \tau=\frac{L}{c},\ \ \lambda=\frac{L}{h},$$
$$\gamma=\frac{l}{h},\ \ \overline{k_x}=\frac{k_x L^2}{h},\ \ \overline{N_x^T}=\frac{N_x^T L^2}{Eh^3},\ \ \overline{M_x^T}=\frac{M_x^T}{Eh^2},\ \ \bar{T}=\alpha T. \quad (4)$$

In case when the external transverse load is dynamic, the expression for q will be as follows $q = q_0 \sin(\omega_p t)$, where q_0 – the static load, ω_p – the frequency.

The temperature moments and forces M_x^T *and* N_x^T in the system of equations of the beam motion (3), are determined from the following relations:

$$N_x^T = \int_{-1/2}^{1/2} T(x,z)dz\,;\ M_x^T = \int_{-1/2}^{1/2} T(x,z)zdz. \quad (5)$$

As noted above, there are no restrictions on the distribution of the temperature field, and the temperature fields are determined by solving the heat conductivity problem:

$$\nabla^2 T(x,z) = \frac{\partial^2 T(x,z)}{\partial x^2} + \lambda^2 \frac{\partial^2 T(x,z)}{\partial z^2} = 0, \quad (6)$$

with boundary conditions of the first kind:

$$T(x,z)|_\Gamma = g_1(x,z), \quad (7)$$

or conditions of the second kind:

$$\left.\frac{\partial T(x,z)}{\partial n}\right|_\Gamma = g_2(x,z), \quad (8)$$

where $\frac{\partial}{\partial n}$ – the differentiation along the external normal to boundary Γ of the beam.

One of the boundary conditions must be attached to the system of equations (3), corresponding to the method of the beam end fixing, considered in this paper:

$$w(0,t) = u(0,t) = w'_x(0,t) = 0;\ w(1,t) = u(1,t) = w'_x(1,t) = 0, \tag{9}$$

or

$$w(0,t) = u(0,t) = M_x(0,t) = 0;\ w(1,t) = u(1,t) = M_x(1,t) = 0, \tag{10}$$

and the initial conditions:

$$w(x,0) = f_1(x);\ \dot{w}(x,0) = f_2(x);\ u(x,0) = f_3(x);\ \dot{u}(x,0) = f_4(x). \tag{11}$$

A combination of the temperature conditions (7)-(8) at the boundaries of beam Γ allows considering various cases of the temperature effect. In this paper, we simulate the first-type temperature field given by the boundary conditions shown in Table 1 with a graphic interpretation of the temperature field as well. The intensity of the given temperature effect T varies in the range of $0 \le T \le 100°C$. Hereinafter, temperature T is given in dimensional form for steel. The physical characteristics of the material do not change in the studied temperature range. We have adopted the following values for transition to the dimensional temperature values in the main equations: $E = 2{,}06 \times 10^5$ mPa, $\alpha = 12{,}5 \times 10^{-6}$ 1/deg, while temperature $T = \Delta T + T_0$, where $T_0 = 22$℃, and ΔT is the increment $T(x,z)$, determined from the heat conductivity equation (6).

Table 1. Boundary conditions of the heat conductivity equation

Type No.	Boundary condition			Beam sketch in the temperature field
	$T(x,z) = g_1(x,z)$	$z = -1/2$	$0 < x < 1$	
	$T(x,z) = 0$	$z = 1/2$	$0 < x < 1$	
	$T(x,z) = 0$	$x = 1$	$-1/2 < z < 1/2$	
	$T(x,z) = 0$	$x = 0$	$-1/2 < z < 1/2$	

3. Algorithm

The finite difference method (FDM) was used when solving the resulting system of equations (3), as the most effective, relying on earlier studies [24]. For this purpose, a uniform grid with the number of nodes n was superimposed on the beam area. Partial derivatives by spatial coordinates were substituted by central finite-difference approximations. After the introduced substitution, the system of equations (3) is transformed to a system of ordinary differential equations:

$$\begin{cases} \ddot{u} = -\Lambda_x(w)_i\Lambda_{x^2}(w)_i - \Lambda_x(N_T)_i, \\ \ddot{w} + \epsilon\dot{w} = \frac{1}{\lambda^2}\left\{\left(-\frac{1}{12} + \frac{l^2}{4}\right)\Lambda_{x^4}(w)_i + k_x\left[\Lambda_x(u)_i - k_x w_i - \frac{1}{2}(\Lambda_x(w)_i)^2 - \right.\right. \\ -w_i\Lambda_{x^2}(w)_i] + \Lambda_{x^2}(u)_i\Lambda_x(w)_i + \Lambda_x(u)_i\Lambda_{x^2}(w)_i + \\ \left.\left. + \frac{3}{2}(\Lambda_x(w)_i)^2\Lambda_{x^2}(w)_i\right\} - \Lambda_{x^2}(M_T)_i - \Lambda_x(N_T)_i\Lambda_{x^2}(w)_i + q. \end{cases} \quad (12)$$

The difference approximation is also applied to the boundary (9-10) and initial conditions (11). By the method of substitution of variables, system (15) is reduced to the Cauchy problem with respect to the evolutionary variable, solved by the fourth-order Runge-Kutta method. The obtained solution was also compared with the results obtained using the sixth-order Runge-Kutta method. It is established that the results coincide; however, less time is required for the fourth-order Runge-Kutta method calculations, so it was preferable [25].

Partition 10×80 is optimal for the heat conductivity equation. In addition, the numerical solution was compared with the analytical solution obtained by Carslaw and Jaeger in [26] for boundary conditions of the first kind. The order of values obtained as a result of the calculation specified in advance, was used as the optimality criterion. Values of M_x^T and N_x^T were calculated with equations (5) by the Simpson method.

Assumptions were made when solving the problem that correspond to elimination of the conjugation points and increase in the number of grid nodes. At that, both the increase in the total number of nodes of the regular grid, and concentration of nodes near the conjugation points for the irregular grid is possible. The matching conditions at changing boundary conditions for the heat conductivity equation considered in [27] are applied.

4. Numerical experiment

In order to study nonlinear dynamics of the beam, the maximum deflection curves (Fig. 2) were obtained in the beam center $w(0.5, t)$ at time $t \to \infty$, as the dissipation coefficient is assumed to be $\varepsilon = 1$. The following parameters were assumed as the system parameters: frequency $\omega_p = 5$, curvature $k_x = 12$, intensity of the temperature effect $g_1(x, z) = 50$, boundary conditions (9), initial conditions (11).

It follows from the curve that the curved beam, due to the temperature effect, acquires a negative deflection at $q_0 = 0$. Further, as the load increases, the beam becomes unstable. The loss of stability is accompanied by a sharp increase in deflection $w(0.5, t)$ with a small change in the external load q_0 (the Volmir criterion). Two types of the loss of stability were identified: hard for $\gamma = 0$ and $\gamma = 0.3$ at $q_0 = 1{,}6 \times 10^4$ and soft – for $\gamma = 0.5$ at $q_0 = 3{,}8 \times 10^4$. A nonlinear dynamical formulation of the problem made it possible to identify the state of the system at $\gamma = 0.3$, when deflection $w(0.5, t)$ decreases as load q_0 increases.

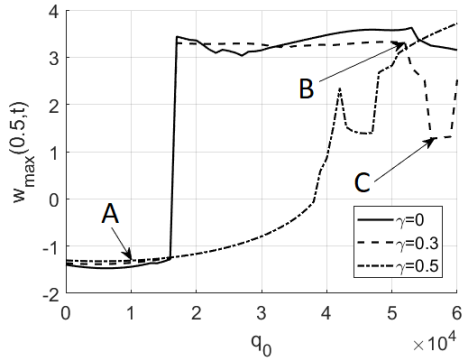

Figure 2. Deflection diagram

The state of the system at the points corresponding to the subcritical – A, the supercritical – B, and the new state C was considered. The following was built for the system state analysis: (Table 2, left to right, top to bottom): a signal, a Fourier power spectrum, a Poincare section, a deflection diagram, a phase portrait and a Morlet wavelet. At $q_0 = 10 \times 10^3$ (A), the signal is harmonic, there is a single frequency $\omega_p = 5$ in the Fourier power spectrum, there is a single point in the Poincare section, the deflection curve is smooth, which corresponds to a small amplitude of oscillations, a single trajectory is shown in the phase portrait, the wavelet corresponds to the Fourier power spectrum. All analysis methods indicate the harmonic mode of the system oscillations and correspond to the stable state of the system.

At $q_0 = 52 \times 10^3$ (B), the signal has an upper and lower envelope, many frequencies are distinguished in the Fourier power spectrum, an attractor is formed in the Poincare section, longitudinal and transverse waves can be seen in the deflection diagram, which indicates an irregular mode of the system oscillations, a lot of close trajectories of a complex shape are in the phase portrait, the wavelet indicates the presence of oscillations at frequencies near $\omega_p = 5$ and $\omega = 1$, but of less power. Thus, it can be asserted that the system is in an unstable state under multifrequency oscillations. Determination of a complex mode of the system oscillations does not allow reliably determining the chaotic mode.

At $q_0 = 56 \times 10^3$ (C), the signal curve shows that another oscillation with the same frequency is present within the oscillation, so there is only one frequency in the Fourier power spectrum, and one point in the Poincare section. The deflection diagram and the trajectory of the beam midpoint in the phase space are of a complex nature, which does not allow unambiguously telling of the state observed in the system.

Table 2. Analysis of the oscillation mode

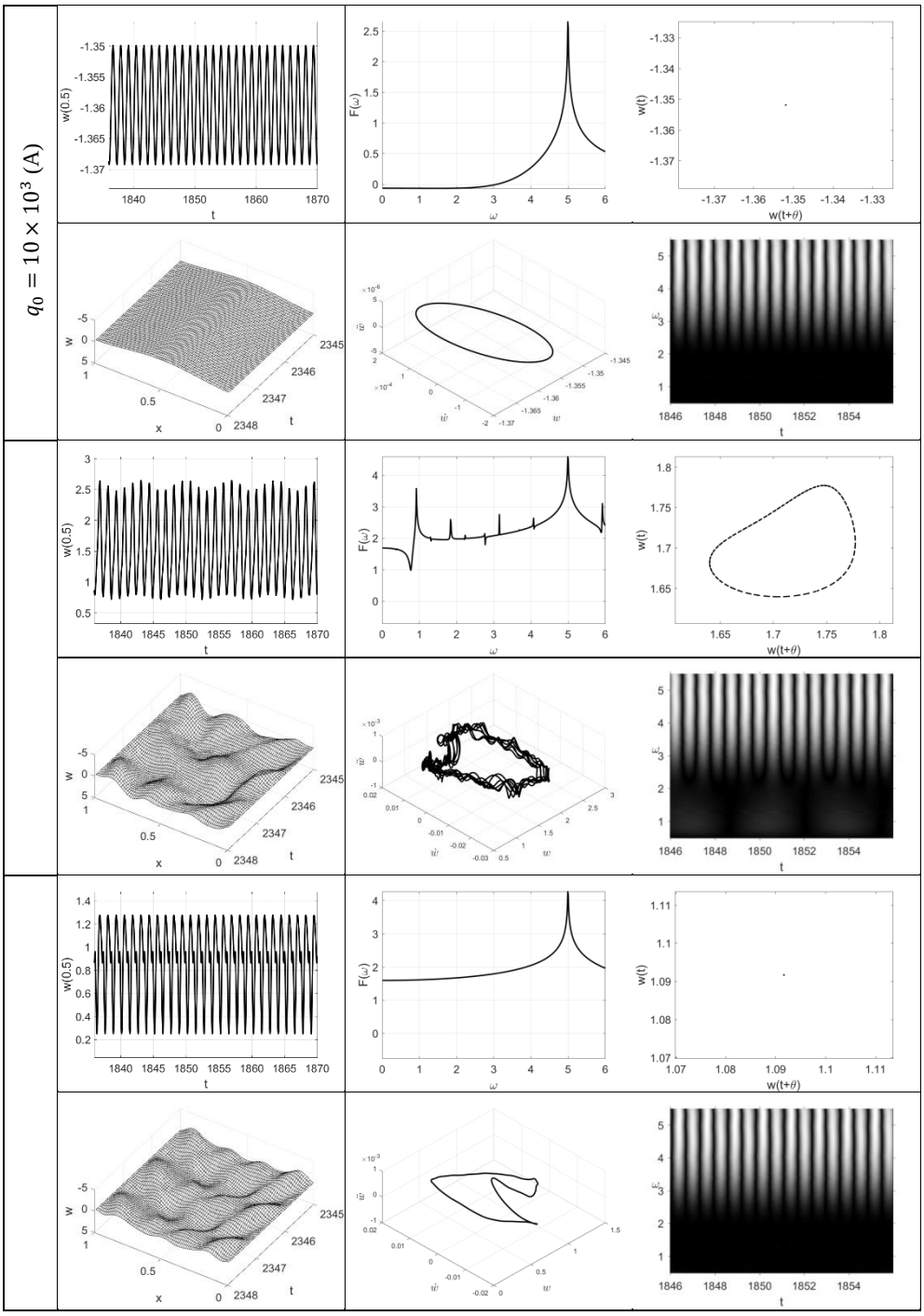

The Lyapunov criterion was used for the additional system state analysis (Table 3). Using the general formulation of the system motion stability problem according to Lyapunov, the system state is considered stable if the higher Lyapunov exponent (Le) is negative and unstable at a positive value.

Table 3. Lyapunov exponents

Load q_0	Algorithm						
				NN			
				1	2	3	4
1×10^3 (A)	-0,00576	-0,00059	-0,00946	-0.00268	-0.42932	-0.42932	-1.89006
52×10^3 (B)	0,00439	0,01451	0,00281	0.00488	-0.38972	-0.38972	-0.57019
56×10^3 (C)	0,00498	-0,00637	-0,00034	-0.00202	-0.39048	-0.42250	-0.42250

The sign of the higher Lyapunov exponent was determined by the modified method of neural networks (NN) [28]. All four Lyapunov exponents have a negative value for point $q_0 = 10 \times 10^3$ (A) and $q_0 = 56 \times 10^3$ (C), which indicates a stable system state. At $q_0 = 52 \times 10^3$ (B), the highest exponent has a positive sign.

To verify reliability of the highest Lyapunov exponent sign determination, the exponents were determined acc. to the algorithms of Wolf [29], Rosenstein [30] and Kantz [31], which gave similar results.

5. Conclusions

1. Dynamics of size-dependent beams in the temperature field was studied.
2. It was established that the value of the scale parameter affects the type of beam stability loss in the temperature field.
3. A reliable assessment of the system state requires the introduction of an additional method, such as the Lyapunov exponent analysis.

Acknowledgments

This work has been supported by the Grant RFBR 16-08-01108a, RFBR 16-01-00721a, as well as the Grant RFBR research project № 16-31-60027.

References

[1] Aldridge J.S. and Cleland A.N. (2005) Noise-enabled precision measurements of a doffing nanomechanical resonator. Phys. Rev. Lett., 94, .

[2] Almog R., Zaitsev S., Shtempluck O., and Buks E. (2006) High intermodulation gain in a micromechanical duffing resonator. Appl. Phys. Lett., 88.

[3] Buks E. and Roukes M.L. (2001) Metastability and the Casimir effect in micromechanical systems. Europhys. Lett., 54, 220.

[4] De Martini B.E., Rhoads J.F., Turner K.L., Shaw S.W., and Moehlis J. (2007) Linear and nonlinear tuning of parametrically excited mems oscillators. J. MEMS

[5] Feng X.L., He R., Yang P., and Roukes M.L. (2007) Very high frequency silicon nanowire electromechanical resonators. Nano Lett., 7, 1953–1959.

[6] Husain A., Hone J., Postma H.W.Ch., Huang X.M.H., Drake T., Barbic M., Scherer, A., and Roukes, M.L. (2003).

[7] Sazonova V., Yaish Y., Ustunel H., Roundy D., Arias T.A., and McEuen P.L. (2004) A tunable carbon nanotube electromechanical oscillator. Nature, 431, 284–287.

[8] Scheible D.V., Erbe A., Blick R.H., and Corso G. (2002) Evidence of a nanomechanical resonator being driven into chaotic response via the ruelle– takens route. Appl. Phys. Lett., 81, 1884–1886.

[9] Zhang W., Baskaran R. and Turner K. (2003) Tuning the dynamic behavior of parametric resonance in a micromechanical oscillator. Appl. Phys. Lett., 82, 130–132.

[10] M. Amabili, S. Carra, R. Garziera, M. Pellegrini, Experiments on nonlinear vibrations of graphite/epoxy composite curved panels, Journal of the Mechanical Behavior of Materials 16 (2005) 287–296.

[11] Wang Y.C. et al. Chaos in MEMS, parameter estimation and its potential application. IEEE transactions on circuits and systems. 1. Fundam Theory Appl 1998;45(10):1013–20.

[12] De Martini B.E. et al. Chaos for a microelectromechanical oscillator governed by the nonlinear Mathieu equation. J Microelectromech Syst 2007;16(6):1314–23.

[13] Haghighi H.S., Markazi A.H. Chaos prediction and control in MEMS resonators. Commun Nonlinear Sci Numer Simul 2010;15(10) : 3091–9.

[14] Aghababa M.P. Chaos in a fractional-order micro-electro-mechanical resonator and its suppression. Chin Phys B 2012;21(10): 100505

[15] Awrejcewicz J., Krysko V.A., Papkova I.V., Krysko A.V. Deterministic Chaos in One-Dimentional Continuous Systems. – Singapur, World Scientific series on Nonlinear Science Series, 2016. – 561 p.

[16] Li G., Aluru N.R. Linear, nonlinear and mixed-mode analysis of electrostatic MEMS. Sensor Actuator A-Phys. 2001, 91, 278-291.

[17] Zhang W.M., Meng G. Nonlinear dynamical system of micro-cantilever under combined parametric and forcing excitations in MEMS. Sensor Actuator A-Phys. 2005, 119, 291-299. Sensors 2010, 10 6168

[18] Adams S.G., Bertsch F.M., Shaw K.A., MacDonald N.C. Independent tuning of linear and nonlinear stiffness coefficients [actuators]. J. Microelectromech. Syst. 1998, 7, 172-180.

[19] Zhang W.H., Baskaran R., Tumer K.L. Effect of cubic nonlinearity on auto-parametrically amplified resonant MEMS mass sensor. Sensor Actuator A-Phys. 2002, 102, 139-150.

[20] Lee S., Kim J., Moon W., Choi J., Park I., Bae D. A multibody-based dynamic simulation method for electrostatic actuators. Nonlinear Dyn. 2008, 54, 53-68.

[21] Thai, H-T., Vo, T.P., Nguyen, T-K., Kim, S-E., A review of continuum mechanics models for size-dependent analysis of beams and plates, Composite Structures (2017), doi: http://dx.doi.org/10.1016/j.compstruct.2017.06.040

[22] Vlasov, V. Z., General Theory for Shells and its Application in Engineering, 1949, Gostekhizdat Publ. Moscow. (translated into English in NACA Technical Translation, 1964)

[23] A.V. Krysko, J. Awrejcewicz, M.V. Zhigalov, S.P. Pavlov, V.A. Krysko Nonlinear behaviour of different flexible size-dependent beams models based on the modified couple stress theory. Part 1. Governing equations and static analysis of flexible beams, International Journal of Non-Linear Mechanics, 93, 2017, 96-105

[24] A.V. Krysko, J. Awrejcewicz, N.A. Zagniboroda, V. Dobriyan, V.A. Krysko, I.E. Kutepov. Chaotic dynamics of flexible Euler-Bernoulli beams. Chaos, 34(4), 2014

[25] J. Awrejcewicz, V.A. Krysko, I.V. Papkova, A.V. Krysko, Deterministic Chaos in One Dimensional Continuous System, World Scientific, Singapore, 2016.

[26] Carslaw H., Jaeger J. Conduction of Heat in Solids. 2 edition. — Oxford University Press, USA, 1959. 510 p.

[27] J Awrejcewicz, VA Krysko, AV Krysko Thermo-dynamics of plates and shells. Springer-Verlag. 2007 777 pages. ISBN: 978-3-540-34261-8.

[28] V. Dobriyan, J.Awrejcewicz, V.A. Krysko etc. On the Lyapunov exponents computation of coupled non-linear Euler-Bernoulli beams. Proceedings of the Fourteenth International Conference on Civil, Structural and Environmental Engineering Computing", Civil-Comp Press, Stirlingshire, UK, Paper 53, 2013.

[29] Wolf A., Swift J.B., Swinney H.L., Vastano J.A. Determining Lyapunov exponents from a time series // Physica. 1985. V. D16. P. 285-317

[30] M. T. Rosenstein, J. J. Collins and C. J. De Luca. A practical method for calculating largest Lyapunov exponents from small data sets. Physica D 65 (1993) 117–134.

[31] H. Kantz. A robust method to estimate the maximal Lyapunov exponent of a time series. Phys. Lett. A 185 (1994) 77–87.

———

Anton V. Krysko, Professor: Department of Applied Mathematics and Systems Analysis, Saratov State Technical University and Cybernetic Institute, National Research Tomsk Polytechnic University, Politehnicheskaya 77, 410054 Saratov, RUSSIAN FEDERATION (anton.krysko@gmail.com), the author presented this contribution at the conference.

Jan Awrejcewicz, Professor: Lodz University of Technology, Faculty of Mechanical Engineering, Department of Automation, Biomechanics and Mechatronics, 1/15 Stefanowskego Str., 90-924 Lodz, POLAND (jan.awrejcewicz@p.lodz.pl).

Ilya Kutepov, Ph.D.: Department of Mathematics and Modeling, Saratov State Technical University, Politehnicheskaya 77, 410054 Saratov, RUSSIAN FEDERATION (iekutepov@gmail.com).

Vadim A. Krysko, Professor: Department of Mathematics and Modeling, Saratov State Technical University, Politehnicheskaya 77, 410054 Saratov, RUSSIAN FEDERATION (tak@san.ru).

Influence of the fixation region of a hip stem on the behaviour of the "bone–implant" system

Ievgen Levadnyi, Dariusz Grzelczyk, Jan Awrejcewicz, Oleg Loskutov

Abstract: In this paper, the stress state of the femoral bone and stem prosthesis is studied using the finite element method, and considering different types of prosthesis fixation in the medullary canal of the femur under action of functional loads. To obtain reliable results of the performed finite element analysis, model generation of both the femur and the endoprosthesis of real size and shape, physico–mechanical properties of the material and the values of the functional load, is employed. The finite element analysis of the stress-strain state shows that for diaphyseal fixation the area of contact between the surface of the stem and the bone is too small. As a result, this type of fixation causes large stresses in the stem what further leads to fatigue fracture of the implant. In the case of diaphyseal fixation type, stress concentration arises in the distal femur and leads to a risk of stress–shielding effect or bone fracture. An increase in the area of contact between the implant and the bone raises the stiffness of the "bone–implant" system, and the values of tensile and compressive stresses in the implant are reduced. For metaphyseal fixation, stress is evenly distributed in bone and no excessive concentrations are observed. In this case, values of stresses in implants do not exceed the endurance limit of the metal of which the implants are made, what ensures a margin of safety. Finally, the presented numerical method can be used to consider the influence of structural changes and clinical technique of installing endoprostheses in the femoral canal on the durability of implants.

1. Introduction

Total hip replacement (THR) is now one of the most effective methods of treatment for patients with severe diseases of the hip joint [1]. It restoring hip function and relieving patients of pain by replacing pathological hip joints with artificial ones. There are about 500,000 THR surgeries in Europe each year, with growing numbers throughout the world [2]. However, despite the wide range of designs in hip arthroplasty, major problems are associated with instability and loosening of the endoprosthesis and development of proximal femur stress–shielding syndrome [3-4]. The fixation may be unstable and leads to loosening of the implant when the relative micromotion between stem and bone interfaces

exceed threshold value. A magnitude of micromotion under 50 μm can be defined for bone ingrowth, from 50 μm to 150 μm as probable bone ingrowth, and larger than 150 μm leads to formation of fibrous tissue that can prevent bone ingrowth [5-6]. At the same time, if in certain areas of the implant the functional load causes stress which exceeds fatigue limit then destruction occurs [7]. Also after the installation, the implant may greatly influence the transmission of the load to the host tissue, what can cause proximal stress-shielding due lack of load or cortical hypertrophy in distal part, due overload, respectively [8-9].

Therefore, in the process of designing implants, efforts should be aimed at solving the aforementioned problems. Even during the most objective physical experiments, it is very difficult to account for differences in mineral density of different specimens. Furthermore, it is impossible to repeat experiments on the same specimen due to total or partial destruction caused by stress and overloading. Currently one of the most effective and informative methods of studying problems of biomechanics is the method of mathematical modeling, and in particular the finite element method (FEM). Using FEM has obvious advantages, such as highly accurate results and the low cost of numerical experiments with the ability to change basic parameters, such as geometry, material properties, forces magnitudes, and it allows us to gain a large range of results that are difficult to measure non-invasively with equipment, including, stress–strain, relative micromotion and contact pressure.

There are many studies that apply finite element analysis to bones or to joints [10-12]. Those studies have reported the stress or strain distributions in various situations. However, to the best of our knowledge, there is small amount of studies aimed on using FEM to analyze the influence of region stem fixation on the behaviour of the “bone–implant” system.

Therefore, in order to improve treatment outcomes and quality of life of patients, the goal of this study was the biomechanical oriented analysis for the choice of optimal implant fixation in case of hip replacement using the finite element modeling of stress-strain state "bone - implant" systems. We hypothesise that proximal fixation would provide the best physiological loading of femur and evenly distribution strain over lateral and medial sides of a bone.

2. Materials and methods

One of the most important stages in the development of endoprostheses is biomechanical rationale of performance and reliability of implants. In this case, the carried out FEM analysis allowed to estimate the stress state of the "femur – implant" system. The influence of conditions fixation of the implant at various levels of the medullary canal of the femur to the stresses occurring in the bone structures and the implant under the action of functional loads have been investigated (Fig. 1). Parameters and dimensions of geometric models of the femoral components corresponded to their real size and shape. In this work, the size and the shape of the ORTAN® (Ukraine) femoral component is used. From the

literature data [13], the value of the components of load (in the case of a human body weight of 700 N) was equal to: Fx=520 N; Fy=177N; Fz=1854N, where: X stands for the front axis; Y–axis is sagittal; and Z is the vertical axis. Also we have taken into account influence forces acting on the surface of the bone during walking. For the numerical calculations was chosen isotropic model of the material for all bodies, with the relevant physical and mechanical parameters. Titanium alloy (Ti6Al4V), having a modulus E = 110 GPa and Poisson ratio ν = 0.3, has been selected as the material for the physical properties of the femoral component of the hip endoprosthesis. The described type of femoral component with collar can be used with distal and proximal fixation types. Distal fixation contributes to jamming the stem in the area of narrowing of the femur medullary canal while proximal fixation supposes fixed in diaphyseal and metaphyseal parts of the femur at the same time. In this work, the distal and proximal fixations of stem are considered (Fig. 1).

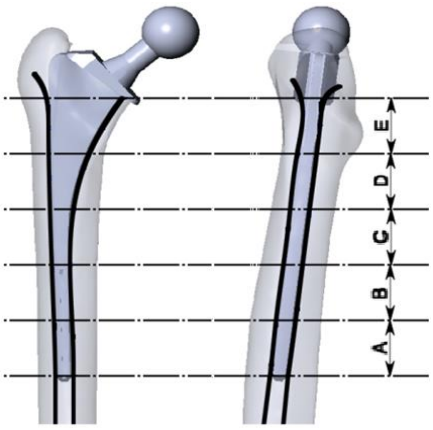

Area of fixation	Types of fixation
DE	by collar
CDE	metaphyseal
BCDE	metaphyseal– diaphyseal
ABCDE	full
ABCD	diaphyseal–metaphyseal
ABC	diaphyseal
AB	diaphyseal
A	diaphyseal

Figure 1. Types of fixation of cemented femoral stem of the prosthesis in different zones of the medullary canal of the femur

Three-dimensional model of the femur has been developed based on the results of computer tomography (CT) scans. The heterogeneous material properties of the femur have been calculated based on the bone density values. The following relationship between the Hounsfield units (HU) of the CT scanner and apparent density (ρ) have been taken: $\rho = 1 + 7.185 \times 10^{-4} \times HU$, Young's modulus is: $E = -388.8 + 5925 \times \rho$ [14]. A total of 20 different bone materials have been assigned for the heterogeneous models. Poisson's ratio ν = 0.3 has been selected for the physical properties of the femur. In this study primary stability of prosthesis is based on pressure between bone tissue and metal and continues during loading with coefficient of friction μ=0.3. For each type of stem fixation, maximum micromotion of the stem in the bone was evaluated using the relative tangential node displacements in the contact surface under maximum loads during gait by equation (1):

$$Micromotion = \sqrt{[CSLIP(x_1, n)]^2 + [CSLIP(x_2, n)]^2} \quad (1)$$

Finally, for finite element analysis in the present study, the three-dimensional geometric model of femur with impant was imported and meshed using ABAQUS software (version 6.14, Dassault Systems, 2015). The FE bone-implant system models used in this study consist of 1100123 tetrahedral elements with maximum length of the edge equals 2 mm.

3. Results and discussion

The purpose of this study is to develop a FEM model for a human femur with stem and to investigate the effects different stem fixations on stress state of system "bone-cement-implant". The strain distribution obtained from the models are compared with each other for evaluating the load-transmit efficiency. Furthermore, the stem micromotion and stress distribution which cause stem loosening and fracture are analysed.

The results showed that the stress state of the stem prosthesis occurs due to the bending moment in the frontal plane and compression forces in the axial direction (Fig. 2). For both bone and implant compressive stress arising on the medial side while tensile stresses arising on the lateral side.

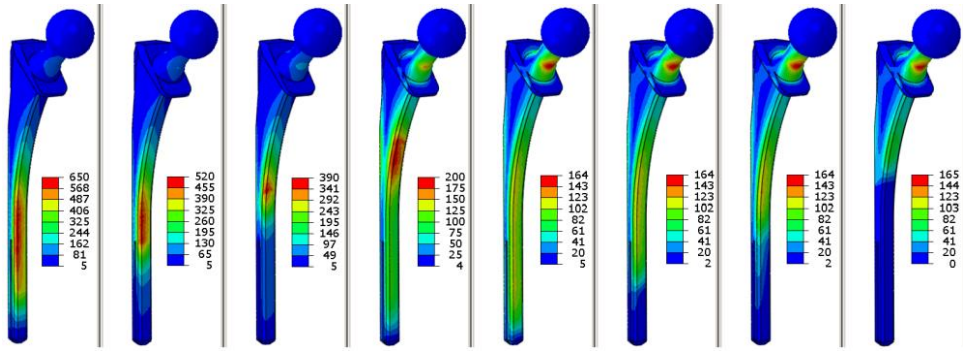

Figure 2. Distribution of equivalent stress on the medial side of the prosthesis in the case of different types of fixation

The results showed that the most unfavorable for the bone is diaphyseal fixation. Since a contact between stem and bone too small, a large level of stress was detected in the distal part of the bone. The latter behavior increases the risk of bone fracture and leads to a proximal stress-shielding effect due loading lack (Fig. 2). Depending on the type of fixation of the implant, the maximum equivalent von Mises stress in the implants varies in the range from 650 to 90 MPa. During calculation, it has been found that for the design of stem endoprosthesis of the hip joint, the most dangerous diaphyseal fixation types are: A, AB, ABC. In these cases, micromotion leads to failure of bone ingrowth (>150 μm) and

can lead implant loosening (Fig. 3). In the latter case, the stresses vary from 650 MPa to 390 MPa. These type of implants and fixations are unacceptable, since stresses occurred in the body stem exceed the limit of durability of the metal, and such loads may imply fatigue fracture of the stem. An increase in the area of contact between the stem reduces bending and the maximum equivalent stresses in the implant. For these types of fixation, our results have shown that the maximum stresses in the elements of the assembly have not exceeded the durability limit of the material, and all elements of the system have been in a state of elastic deformation. Therefore, metaphyseal, metaphyseal–diaphyseal, diaphyseal–metaphyseal types of fixation and fixation using collar guarantee the required safety margin. Also in these cases, except pure collar fixation, micromotion is below the threshold for osseointegration (<150 μm). This indicates that a collar may have importance in preventing implant instability, if close contact between collar and bone is taken. Calculations showed that the metaphyseal-diaphyseal and collar type of fixation of the stem is most acceptable for the femur. In these cases, the tensile stresses and compressing stresses are evenly distributed with the lateral and medial side, beginning from the metaphyseal and ending at the diaphyseal part of the bone (Fig. 3). In these types of fixation an important role plays collar of stem, which helps to normalize the load transfer to the proximal part of femur that eliminates excessive stress concentration in the distal.

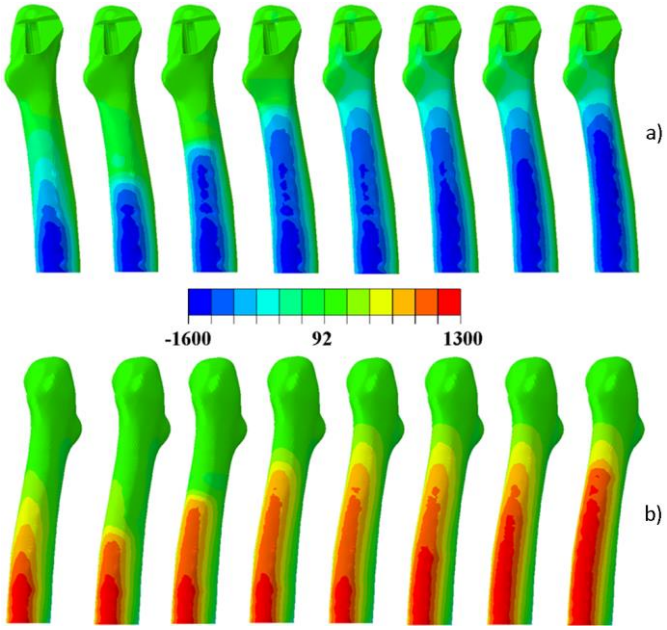

Figure 3. Distribution of compressive (top) and tensile (bottom) strains (in microstain) on the medial and lateral sides of the femur, depending on the type of fixation of the endoprosthesis stem under the action of functional loads.

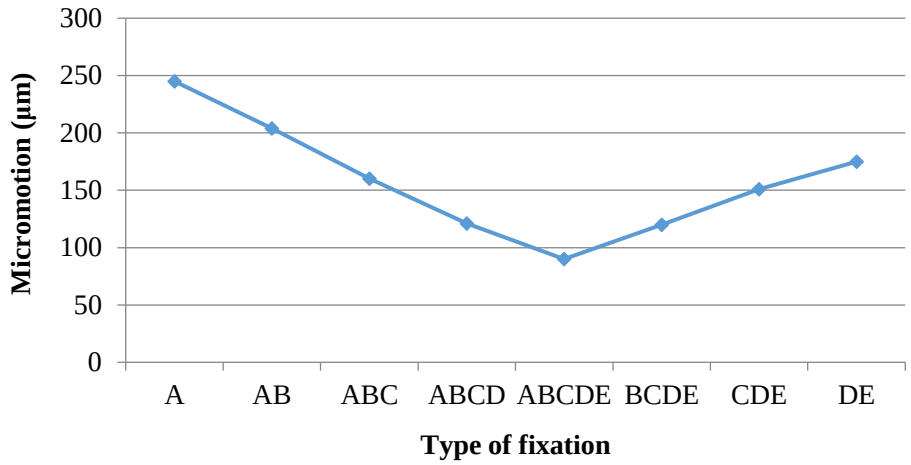

Figure 4. Changes in the maximum micromotion of the implant surface for different variants of implant fixation.

It should be mentioned, however, that in this study had a number of limitations. The material properties in the FE-models were inhomogeneous but isotropic and linear. Nonlinearity and anisotropy might be able to improve predictions. Only the effect of one loading modeled using FE analysis. In reality femur is exposed to numerous other forces in activities of daily living. Here we consider only maximum values of stem micromotions, however, area of these micromotions can also have influence on implant stability.

4. Conclusion

In this research, the biomechanical effect of different stem fixation is analyzed using computational results. The following biomechanical characteristics of the system have been studied: distribution of stresses and micromotions in implants and strain distribution in femur. From the obtained results, it is found that proximal fixation can prevent resorption of the medial femoral neck, decreases the proximal stress shielding and the risk of fracture. Proximal fixation has advantage even in comparison with full fixation of endoprosthesis where there is still a concentration of strains in distal part of femur. However, full fixation can provide better mechanical stability for implants.

Acknowledgments: The work has been supported by the National Science Centre of Poland under the grant OPUS 9 No. 2015/17/B/ST8/01700 for years 2016-2018.

References

[1] Ethgen, O., Bruyère, O., Richy, F., Dardennes, C., Reginster, J.Y. Health–related quality of life in total hip and total knee arthroplasty. A qualitative and systematic review of the literature. *Journal of Bone & Joint Surgery - American Volume*, 86–A (2004), 963–974.

[2] Kelly, M.A., Dalury, D.F., Kim, R.H., Backstein, D. The new arthritic patient and nonarthroplasty treatment options. *Journal of Bone & Joint Surgery - American Volume*, 91 (2009), 40–42.

[3] Wilkinson, J.M., Hamer, A.J., Rogers, A., Stockley, I., Eastell, R. Bone mineral density and biochemical markers of bone turnover in aseptic loosening after total hip arthroplasty. *Journal of Orthopaedic Research*, 21 (2003), 691–696.

[4] Boschin, L.C., Alencar, P.G.C. Stress shielding: radiographic evaluation after long term follow-up. *Revista Brasileira de Ortopedia*, 42 (2007), 290-296.

[5] Pilliar, R.M., Lee, J.M., Maniapoulos, C. Observation of the effect of movement on bone ingrowth into porous-surfaced implants. *Clinical Orthopaedics and Related Research*, 208, (1986), 108–113.

[6] Ramamurti, BS, Orr, TE, Bragdon, CR, Lowenstein, JD, Jasty, M, Harris, WH. Factors influencing stability at the interface between a porous surface and cancellous bone: a finite element analysis of a canine in vivo micromotion experiment. *Journal of Biomedical Materials Research*, 36 (1997), 274-80.

[7] Long, M., Rack, H.J. Titanium alloys in total joint replacement – A materials science perspective. *Biomaterials*, 19 (1998), 1621–1639.

[8] Ritter, M.A., Fechtman, R.W., Distal cortical hypertrophy following total hip arthroplasty. *Journal of Arthroplasty*, 3 (1988), 117-21.

[9] Lim, Y.W., Lee K.H., Bae, S.H., Kwon S.Y., Comparative Analysis of Two Cementless Stems in Total Hip Arthroplasties in Patients with Osteonecrosis of Femoral Head - Summit® Stem and Bencox® Stem. *Journal of the Korean Hip Society*, 24 (2012), 25-31.

[10] Levadnyi, I., Awrejcewicz, J., Goethel, M.F., Loskutov, A. Influence of the fixation region of a press-fit hip endoprosthesis on the stress-strain state of the "bone-implant" system. *Computers in Biology and Medicine*, 84 (2017), 195-204.

[11] Levadnyi, I., Awrejcewicz, J., Gubaua, J.E., Pereira, J.T. Numerical evaluation of bone remodelling and adaptation considering different hip prothesis design. *Clinical Biomechanics*, 2017.

[12] Strafun, S., Levadnyi, I., Makarov, V., Awrejcewicz, J. Comparative Biomechanical Analysis of Stress–Strain State of the Elbow Joint After Displaced Radial Head Fractures. *Journal of Medical and Biological Engineering*. (2017).

[13] Bergmann, G., Deuretzbacher, G., Heller, M., Graichen, F., Rohlmann, A., Strauss, J., Duda, G.N. Hip contact forces and gait patterns from routine activities. *Journal of Biomechanics*, 34 (2001), 859–871.

[14] Peng L., Bai J., Zeng X., Zhou Y., Comparison of isotropic and orthotropic material property assignments on femoral finite element models under two loading conditions. *Medical Engineering & Physics*, 28 (2007), 227–233.

Ievgen Levadnyi, M.Sc. (Ph.D. student): Lodz University of Technology, Faculty of Mechanical Engineering, Department of Automation, Biomechanics and Mechatronics, 1/15 Stefanowski Str., 90-924 Lodz, POLAND (evgenabaqus@gmail.com), the author presented this contribution at the conference.

Dariusz Grzelczyk, Ph.D.: Lodz University of Technology, Faculty of Mechanical Engineering, Department of Automation, Biomechanics and Mechatronics, 1/15 Stefanowski Str., 90-924 Lodz, POLAND (dariusz.grzelczyk@p.lodz.pl).

Jan Awrejcewicz, Professor: Lodz University of Technology, Faculty of Mechanical Engineering, Department of Automation, Biomechanics and Mechatronics, 1/15 Stefanowski Str., 90-924 Lodz, POLAND (jan.awrejcewicz@p.lodz.pl).

Oleg Loskutov, MD-Ph.D: Dnipropetrovsk State Medical Academy, Department of Orthopaedics and Traumatology, Dnipropetrovsk, Ukraine (loskutovae@ukr.net).

Ocean wave energy harvesting of a floating pendulum platform coupled system

Carlos Eduardo Marques, José Manoel Balthazar, Angelo Marcelo Tusset, Rodrigo Tumolin Rocha, Frederic Conrad Janzen, Jeferson José de Lima, Airton Nabarrete

Abstract: This work presents the analysis of an ocean wave energy harvesting system, which consists of a floating ocean platform with a DC motor power generator attached at the platform considering the ocean waves motion to swing the platform in order to convert mechanical energy into electric energy. The mechanical energy is provided by a pendulum which is coupled to the DC generator axis, which will acquire rotational motion due to the vertical excitation of the floating platform, therefore, varying the magnetic flux of the permanent magnets of the DC power motor, generating electric energy. The study of the mass of the pendulum settings and the amplitudes of the ocean wave is important to optimize the power provided by the DC motor, such study that is based on Brazilian's coast characteristics. Therefore, the dynamical behaviour of the system is shown through numerical simulations as well as the efficiency of conversion of the pendulum swings into electricity.

1. Introduction

One of the great challenges of contemporary society is, undoubtedly, the discovery and economically viable exploitation of abundant and renewable energy sources. The global energy crisis is practically a constant, given by the progressive increase of using electrical and electronic devices by the modern humankind.

Researchers of all over the world have focused their efforts exploring new energy sources in the environment, in special, renewable energy sources seeking for the best potential in each kind of available energy source. These energy sources may be provided in thermal way, kinect, magnetic, i.e., such energies that are wasted in the environment. One of these energy sources abundantly available in the world is the ocean wave energy harvesting, which is a source of constant and recent attention. This kind of energy has the advantage of a high-energy density and persistence, being a competitive candidate for energy supply [1-10].

The energy from the oscillations provided by the waves may be extracted by a pendulous system, considering the movement of the waves as an excitation source, for example, in a floating pendulum system. Following this concernment, there are many types of energy conversion from ocean waves in

different categories. One of the most recent concepts in energy extraction from sea waves is the parametric pendulum [11].

The parametric pendulum is recurrently applied in the nonlinear dynamics and introduced in many applications of energy harvesting up to a tuning passive controller. In addition, its use possibilities improvement of energy harvesting in many applications [12-23].

Moreover, many works showed experimental apparatus involving the coupling of the pendulum was built to simulate the energy extraction from the pendulum swing, being possible comparing the experimental to theoretical results [24, 25]. The pendulum was considered up to technologies based on a water-oil integrated transmission systems, which is an application to wave energy harvesting [26, 27].

This work explores the energy harvesting considering the movement of a parametrical pendulum coupled to a floating platform excited by ocean waves. The pendulum is introduced to transfer the vertical oscillation of the floating base platform to rotational oscillations, whose pendulum is part of a DC motor power generator's axis. Therefore, the velocity developed by the pendulum is used to generated electricity by the internal circuit of the DC power generator, i.e., energy proportional to the rotational velocity of the pendulum. The main objective of this work is to maximize the energy harvesting of the system through parametrical analysis of the pendulum's mass and ocean wave amplitudes based on Brazil's coast characteristics, whose characteristics are described in Ref. [28, 29].

This work is organized as follows. Section 1 shows a succinct introduction containing the motivation of keeping this theme in research. Section 2 describes the design of the floating pendulum platform system and its mathematical modelling, developing the equations of motion of the system and the proposal of energy harvesting. Section 3 shows the numerical simulations analyzing the dynamics of the system and energy harvesting with parametrical variations to improve the harvested power. Section 4 presents the conclusions about the analysis carried out in this paper.

2. Physical and mathematical model

The floating pendulum platform, illustrated in Fig. 1, consists of a pendulum coupled to a DC motor power generator, fixed in the floating platform, whose platform is considered floating on the ocean.

The pendulum has a mass m and length l, with rotational angle θ. The DC motor has mass M_2 and the platform mass M_1.

When the platform is floating on the ocean, the buoyancy force of the water fluid pull up the structure, therefore, it can be considered as a non-fixed base directly linked to the platform through a spring with stiffness k, which represents the buoyancy force, and a linear viscous damping of the fluid c.

The generalized coordinate of the vertical motion of the system is represented by Y and θ, respectively, considering the mass of the platform by Y and the angular displacement of the pendulum

by θ. The base is considered with a harmonic displacement represented by $F = A\sin(\omega t)$, where A is the amplitude of the ocean wave, ω is the frequency and t is time.

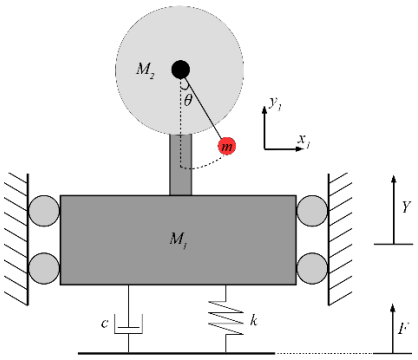

Figure 1. Floating pendulum platform excited by ocean waves simulated by a harmonic displacement

The movement of the pendulum can be considered as in Eq. (1).

$$\begin{aligned} x_1 &= l\sin\theta \\ y_1 &= Y + l(1-\cos\theta) \end{aligned} \tag{1}$$

The kinetic energy of the floating pendulum platform system is represented by the mass of the pendulum, platform and DC motor, as given by Eq. (2).

$$T = \frac{1}{2}(m_1 + m_2)\dot{Y}^2 + \frac{1}{2}m\left(l^2\dot{\theta}^2 + \dot{Y}^2 + 2l\dot{\theta}\dot{Y}\sin\theta\right) \tag{2}$$

The total potential energy of the system is given by the restoration force of the thrust force between the platform and the water-fluid, and the potential gravitational energy of the pendulum, denoted by Eq. (3).

$$V = \frac{1}{2}k(Y-F)^2 + mg\left(Y + l(1-\cos\theta)\right) \tag{3}$$

The Rayleigh-Ritz dissipation function is defined by the linear viscous damping of the water fluid, denote by Eq. (4).

$$D = \frac{1}{2}c\left(\dot{Y} - \dot{F}\right)^2 \tag{4}$$

Therefore, the equations of motion of the system represented in Fig. 1 are obtained by applying the Lagrange's energy method to Eqs. (1) to (4), whose equations of motion are presented in Eq. (5), where the first one represents the platform motion and the second one represents the pendulum motion.

$$M\ddot{Y} + k\left(Y - A\sin(wt)\right) + c\left(\dot{Y} - Aw\cos(wt)\right) + \ldots$$
$$ml\left(\ddot{\theta}\sin(\theta) + \dot{\theta}^2\cos(\theta)\right) + mg = 0 \quad (5)$$
$$ml^2\ddot{\theta} + ml\left(\ddot{Y}\sin\theta + \dot{Y}\dot{\theta}\cos\theta\right) - gml\cos\theta = 0$$

where $M = M_1 + M_2 + m$. In the following subsection, the mathematical modelling of the electrical part of the DC motor is developed.

2.1. DC motor power generator equations

The DC generator model is considered as an RL electric circuit illustrated in Fig. 2, which consists of a load resistance R_{load}, an inductance L, an output voltage e_v, an internal resistance of the motor R_m and an electric current i.

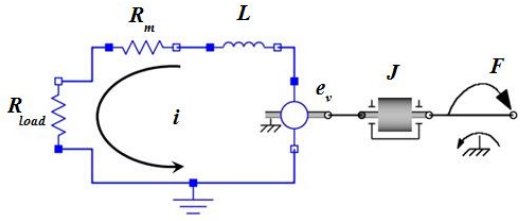

Figure 2. DC motor electric representation

The counter electromotive force generated by a DC generator, when his shaft suffers a torque driven by a force F (Fig. 2) proportional to its angular speed, it is multiplied by a constant known as electromotive force constant k_b [30], therefore, the counter electromotive force is given by Eq. (6).

$$e_v = k_b\dot{\theta} \quad (6)$$

where e_v is the generated output voltage and $\dot{\theta}$ is the angular speed.

By applying the Kirchhoff's voltage law to the circuit of Fig. 2, the equation of motion of the electric circuit is given by Eq. (7).

$$k_b\dot{\theta} = -L\dot{i} - Ri \quad (7)$$

where: $R = R_m + R_{load}$, the electric current is represented by i, and $\dot{i} = \frac{d(i)}{dt}$.

Integrating Eq. (7), an output voltage is obtained which is applied to R_{load}, which can be any kind of load, for example, a battery to be charged.

The electric current provided by the electric circuit has the effect to generate a electromotive torque (which is the motor function). The torque produced by the flux of current is in opposite direction to the torque applied to the motor shaft. This torque can be written as in Eq. (8).

$$F_m = k_t i \tag{8}$$

where k_t is the constant torque and F_m is the generated torque.

The load resistance value has a high impact over the generated torque. The lower the value of R_{load} the higher the current and, consequently, the generated torque may break the pendulum system.

Considering the inclusion of Eq. (7) in Eqs. (5), the governing equations of motion of the floating pendulum platform system coupled to the DC generator is given by Eqs. (9).

$$\begin{aligned} &M\ddot{Y} + k\left(Y - A\sin(wt)\right) + c\left(\dot{Y} - Aw\cos(wt)\right) + ml\left(\ddot{\theta}\sin(\theta) + \dot{\theta}^2\cos(\theta)\right) + mg = 0 \\ &ml^2\ddot{\theta} + ml\left(\ddot{Y}\sin\theta + \dot{Y}\dot{\theta}\cos\theta\right) - gml\cos\theta = b + k_t i \\ &L\dot{i} = -Ri - k_b\theta \end{aligned} \tag{9}$$

Next, a dimensionless process is carried out, resulting in the equations of motion of the system in dimensionless form, given by Eq. (10).

$$\begin{aligned} &y'' + \mu_1 y' + y + \delta_1\left(\theta''\cos\theta + \theta'\sin\theta\right) + G_1 - A_1\cos\Omega\tau - A_2\sin\Omega\tau = 0 \\ &\theta'' + y''\sin\theta + Y'\theta'\cos\theta - G_2\cos\theta - G_3 - \alpha_3 z' = 0 \\ &z' + \alpha_1 z + \alpha_2\theta' = 0 \end{aligned} \tag{10}$$

where

$$\omega = \sqrt{\frac{k}{M}} \quad \tau = \omega t \quad \Omega = \frac{w}{\omega} \quad y = \frac{Y}{l} \quad z = \frac{i}{i_0} \quad \delta_1 = \frac{m}{M} \quad G_1 = \frac{mg}{M\omega^2 l} \quad \mu_1 = \frac{c}{M\omega}$$

$$A_2 = \frac{Acw}{M\omega l} \quad G_2 = \frac{g}{l\omega^2} \quad G_3 = \frac{b}{ml^2\omega^2} \quad \alpha_3 = \frac{k_t i_0}{ml^2\omega^2} \quad \alpha_1 = \frac{R}{L\omega i_0} \quad \alpha_2 = \frac{k_b}{L\omega i_0} \quad A_1 = \frac{A}{l}$$

The electric power can be obtained from Eq. (11).

$$P_e = R_{load} i^2 \tag{11}$$

where P_e is the estimated electrical power, and i is the electric current of the DC motor circuit.

The average electric power will be considered by RMS form in order to analyze the efficiency of the energy generation, according to Eq. (12).

$$P_{e\_rms} = \sqrt{\frac{1}{n}\sum_{j=1}^{n} P_{e\_rms\,j}^{\;2}} \tag{12}$$

Obtaining the governing equations of motion of the full system, in the next sections will be shown numerical simulations to the analysis of the generated power and its improvement.

3. Numerical simulations and discussions

The dynamic analysis of the system was carried out by means of numerical simulations using the Runge-Kutta 4th order integrator with step 0.01. The parameters are shown in Tab. 1.

The parameters of the system were retrieved from Ref. [19], except to the values of the wave amplitude A[m] and frequency w[rad/s]. These values are considered for two situations: the first one is when the amplitude and frequency are maximum, the second one is considered an average value to the amplitude and frequency. Both cases are considered the weather of waves obtained in the period of 1997 and 2009 [32]. The parameters that are in red will be varied along the paper.

Table 1. Parameters of the system

Parameter	Value	Means
M_1 [kg]	200	Platform mass
M_2 [kg]	5	DC Motor mass
m [kg]	Vary	Pendulum mass
c[Ns/m]	80	Water-Fluid damping
l[m]	Vary	Pendulum length
g[m/s^2]	9.81	Gravity Acceleration
k[Nm]	1800	Stiffness of the spring proportional to buoyancy force
R_m[Ohm]	4.57	Internal Resistance of the motor
R_{load}[Ohm]	1.0	Resistance of load
L[H]	0.0032	Inductance of the electric circuit
k_t[Nm/A]	0.23309	Constant torque of the motor
k_b[Vs/rad]	0.23309	Electromotive force constant
A[m]	Vary	Amplitude of ocean waves
w[rad/s]	Vary	Frequency of ocean waves
i_0	1.0	Free dimensionless parameter

Therefore, the next section will analyze the harvested power considering the first case of amplitude and frequency of ocean wave, that is the maximum frequency and amplitude case and described in the next subsection.

3.1. Dynamical and energy harvesting analyses considering maximum frequency and amplitude of excitation

In this first part of numerical simulations, the values of the mass and length of the pendulum are analyzed considering the maximum values of the frequency and amplitude of the ocean waves, seeking the pendulum values that generate the best RMS power given by Eq. (12). The amplitude and frequency are $A = 4.5[m]$ and $w = 1.2712[rad/s]$, respectively [19].

The surfaces of Figs. 3 show the variation of the average RMS harvested power considering the interval of pendulum mass $0.5 \leq m \leq 1.0$ [kg] and length $0.3 \leq l \leq 0.6$ [m]. When the pendulum has mass of $m = 0.8$[kg] and length $l = 0.3$[m], the harvested power is maximum.

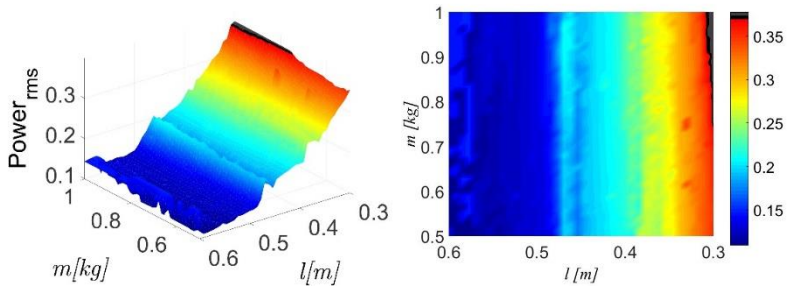

(a) (b)

Figure 3. (a) Surface and (b) coloured contour of the average RMS harvested electric power versus pendulum mass $0.5 \leq m \leq 1.0$ [kg] and length $0.3 \leq l \leq 0.6$ [m], considering $A = 4.5$[m] and $w = 1.2712$[rad/s]

Therefore, considering the mass of the pendulum as $m = 0.8$[kg] and the length $l = 0.3$[m] as a desired region of parameters to harvest energy, and the ocean wave amplitude and frequency are $A = 4.5$[m] and $w = 1.2712$[$rad/$s], the time histories of displacements of the system are shown in Fig. 4, where Fig. 4a shows the displacement of the floating platform, Fig. 4b the angular displacement of the pendulum, Fig. 4c the angular velocity of the pendulum and Fig. 4d the electric current generated by the DC motor.

The behaviour of the platform showed to be periodic with slight motion with high amplitudes. Due to this fact, the pendulum showed rotational motions with a considerably velocity, being possible to harvest, approximately, 0.3763 of amount of RMS power.

To determine the influence of the amplitude and frequency of the ocean waves in the energy harvesting, a variation of these parameters is carried out considering the previous found values of the pendulum $m = 0.8$[kg] and $l = 0.3$[m] because these values are the maximum harvested power registered, as showed in Fig. 3.

Hence, Figs. 5 show the surfaces of the variation of the average RMS harvested power versus the amplitude $0.6 \leq A \leq 4.5$ [m] and frequency $0.5 \leq w \leq 1.8$ [rad/s] of the ocean wave. The maximum harvested power is obtained when $A = 4.5$[m] and $w = 1.8$[rad/s].

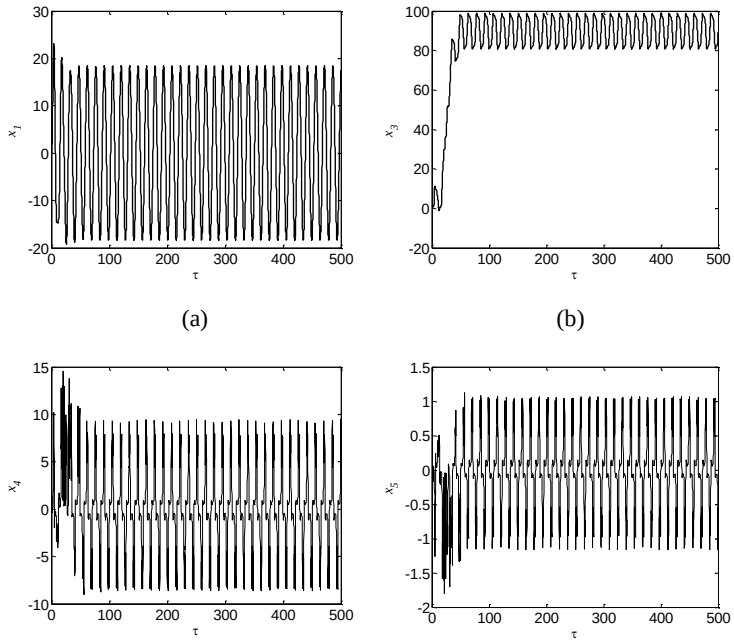

Figure 4. Time histories of (a) floating platform Displacement; (b) angular displacement of the pendulum, (c) angular velocity of the pendulum; (d) electric current of the DC motor; A = 4.5[m], w = 1.2712[rad/s], m = 0.8[kg] and l = 0.3[m]

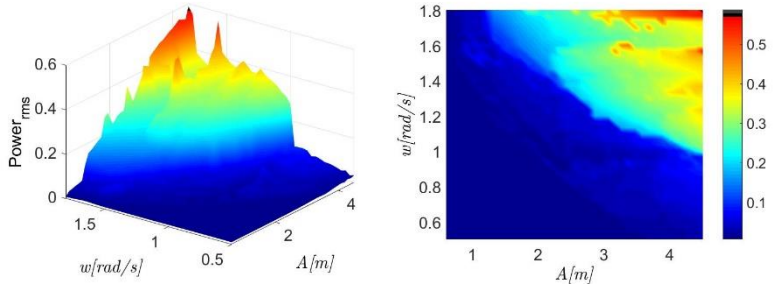

Figure 5. (a) Surface and (b) coloured contour of the average RMS harvested electric power versus ocean wave amplitude $0.6 \leq A \leq 4.5$ [m] and frequency $0.5 \leq w \leq 1.8$ [rad/s], considering m = 0.8[kg] and l = 0.3[m]

Defined the best configuration among the parameters of the pendulum and wave, that are A = 4.5[m], w = 1.8[rad/s], m = 0.8[kg] and l = 0.3[m], the time histories of displacement of the system are shown in Fig. 6, where Fig. 6a shows the displacement of the floating platform, Fig. 6b the angular displacement of the pendulum, Fig. 6c the angular velocity of the pendulum and Fig. 6d the electric current generated by the DC motor.

In this case, the behaviour of the platform showed to be also periodic with slight motion with high amplitudes. However, the pendulum presented very well defined rotational motions with a considerably velocity, increasing the harvested power in comparison to the first analysis, from 0.3763 to 0.5873 of amount of RMS power, approximately.

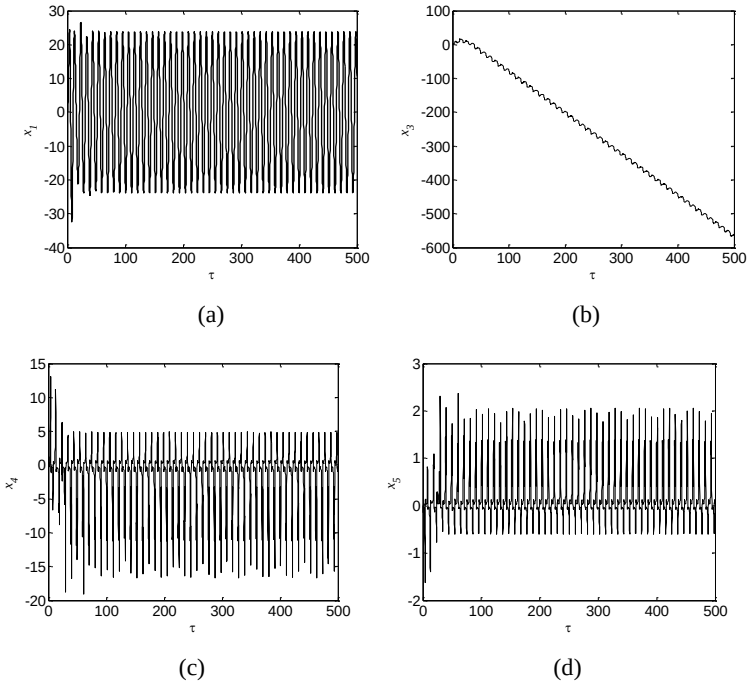

Figure 6. Time histories of (a) floating platform Displacement; (b) angular displacement of the pendulum, (c) angular velocity of the pendulum; (d) electric current of the DC motor; A = 4.5[m], w = 1.8[rad/s], m = 0.8[kg] and l = 0.3[m]

It is worth to mention that the maximum values of amplitude and frequency are obtained in rare ocean situations.

4. Conclusions

This work showed a parametrical analysis of a floating platform with a pendulum coupled to the top end of the structure which is attached to a DC motor shaft in order to harvest energy. General analyses of some essentials parameters were carried out using numerical simulations.

The numerical simulations carried out using the integration method of 4th Runge Kutta showed an optimization of the four most important parameters to improve de energy harvesting, that are the pendulum length and mass, and the ocean waves amplitude and frequency. Two of them showed to be the most sensible with their variation that are the mass and length of the pendulum, as shown in Figs. 3, a minimal change of these parameters induced decrease of increase of harvested power. The amplitude and frequency of ocean wave, not less important than the pendulum configuration, has a foremost importance in the energy harvesting, however, as shown in Figs. 5, the highest amount of harvested power keeps in a smaller region of parameters than in Figs. 3.

Acknowledgments

The authors acknowledge support by CNPq (grant:447539/2014-0) and CAPES, all Brazilian research funding agencies

References

[1] Kong, L. B., Li, T., Hng, H. H., Boey, F., Zhang, T., and Li, S.. Waste Energy Harvesting. Springer, New York, vol 24, (2014), 592 p, 10.1007/978-3-642-54634-1.

[2] Stephen, N. G.. On energy harvesting from ambient vibration. Journal of sound and vibration, 293(1), (2006), 409-425, 10.1016/j.jsv.2005.10.003;

[3] Rocha, R.T.. On saturation phenomenon in energy harvesting based on nonlinear piezoelectric materials coupled to a portal frame foundation with ideal and non-ideal excitations, PhD Thesis, Sao Paulo State University (UNESP), Bauru, SP, Brazil, (2016), Supervisor: José Manoel Balthazar.

[4] Priya, S., and Inman, D. J. (Eds.). Energy harvesting technologies (Vol. 21). New York: Springer, 524, (2009), 10.1007/978-0-387-76464-1.

[5] Abdelkefi, A. Global nonlinear analysis of piezoelectric energy harvesting from ambient and aeroelastic vibrations, PhD Thesis, Virginia Tech, US, (2012), Supervisor: Ali H. Nayfeh.

[6] Litak, G., Friswell, M. I., Kwuimy, C. A. K., Adhikari, S., and Borowiec, M. Energy harvesting by two magnetopiezoelastic oscillators with mistuning. Theoretical and Applied Mechanics Letters, 2(4), (2012), 043009, 10.1063/2.1204309.

[7] Spreemann, D., and Manoli, Y.. Electromagnetic vibration energy harvesting devices: Architectures, design, modeling and optimization, vol 35, (2012), Springer Science & Business Media, 10.1007/978-94-007-2944-5.

[8] Chen, Z., Yu, H., Hu, M., Meng, G., and Wen, C.. A review of offshore wave energy extraction system. Advances in Mechanical Engineering, (2013), 10.1155/2013/623020.

[9] Drew, B., Plummer, A. R., and Sahinkaya, M. N.. A review of wave energy converter technology. Proceedings of the Institution of Mechanical Engineers, Part A: Journal of Power and Energy, 223(8), (2009), 887-902, 10.1243/09576509JPE782.

[10] Falnes, J.. A review of wave-energy extraction. Marine Structures, 20(4), (2007), 185-201, 10.1016/j.marstruc.2007.09.001.

[11] Wiercigroch, M.. A new concept of energy extraction from waves via parametric pendulor. UK Patent pending, (2010).

[12] Wiercigroch, M., Najdecka, A., and Vaziri, V.. Nonlinear dynamics of pendulums system for energy harvesting. In Vibration Problems ICOVP 2011, Springer Netherlands, (2011), 35-42, 10.1007/978-94-007-2069-5.

[13] Xu, X. Nonlinear dynamics of parametric pendulum for wave energy extraction (PhD Thesis, University of Aberdeen), (2005).

[14] Xu, X., and Wiercigroch, M.. Approximate analytical solutions for oscillatory and rotational motion of a parametric pendulum. Nonlinear Dynamics, 47(1), (2007), 311-320, 10.1007/s11071-006-9074-4.

[15] Iliuk, I., Balthazar, J. M., Tusset, A. M., Piqueira, J. R. C., de Pontes, B. R., Felix, J. L. P., and Bueno, Á. M.. A non-ideal portal frame energy harvester controlled using a pendulum. The European Physical Journal Special Topics, 222(7), (2013), 1575-1586, 10.1140/epjst/e2013-01946-4.

[16] De Paula, A. S., Savi, M. A., Wiercigroch, M., and Pavlovskaia, E.. Bifurcation control of a parametric pendulum. International Journal of Bifurcation and Chaos, 22(05), (2012), 1250111, 10.1142/S0218127412501118.

[17] Pavlovskaia, E., Horton, B., Wiercigroch, M., Lenci, S., and Rega, G.. Approximate rotational solutions of pendulum under combined vertical and horizontal excitation. International Journal of Bifurcation and Chaos, 22(05), (2012), 1250100, 10.1142/S0218127412501003.

[18] Marques, C. E., Balthazar, J. M., Rocha, R. T., Tusset, Â. M., and Janzen, F. C.. A PARAMETRIC ANALYSIS OF AN OCEAN WAVE ENERGY HARVESTING SYSTEM. Revista Interdisciplinar de Pesquisa em Engenharia - RIPE, 2(19), (2017), 68-83, ISSN 2447-6102.

[19] Dos Santos, G.P., Tusset, A.M., Piccirillo, V., Marques, C.E., Janzen, F.C., Brasil, R.M.L.R.F., and Balthazar, J.M.. A note on use of a boarded pendulum for generation of electricity. In: 23rd ABCM International Congress of Mechanical Engineering, Rio de Janeiro, Brazil, (2015), 10.20906/CPS/COB-2015-1824.

[20] Rocha, R. T., Balthazar, J. M., Tusset, A. M., Piccirillo, V., and Felix, J. L. P.. Using Saturation Phenomenon to Improve Energy Harvesting in a Portal Frame Platform with Passive Control by a Pendulum. In Dynamical Systems: Theoretical and Experimental Analysis, Springer International Publishing, (2016), 319-329, 10.1007/978-3-319-42408-8_25.

[21] Rocha, R. T., Balthazar, J. M., Tusset, A. M., Piccirillo, V., and Felix, J. L. P.. Comments on energy harvesting on a 2: 1 internal resonance portal frame support structure, using a nonlinear-energy sink as a passive controller. International Review of Mechanical Engineering (IREME), 10(3), (2016), 147-156, 10.15866/ireme.v10i3.8795.

[22] Rocha, R. T., Balthazar, J. M., Tusset, A. M., & Piccirillo, V.. Using passive control by a pendulum in a portal frame platform with piezoelectric energy harvesting. Journal of Vibration and Control, (2017), 1077546317709387.

[23] Nandakumar, K., Wiercigroch, M., and Chatterjee, A.. Optimum energy extraction from rotational motion in a parametrically excited pendulum. Mechanics Research Communications, 43, (2012), 7-14, 10.1016/j.mechrescom.2012.03.003.

[24] Ogai, S., Umeda, S., and Ishida, H.. An experimental study of compressed air generation using a pendulum wave energy converter. Journal of Hydrodynamics, Ser. B, 22(5), (2010), 290-295, 10.1016/S1001-6058(09)60209-2.

[25] Lenci, S., and Rega, G.. Experimental versus theoretical robustness of rotating solutions in a parametrically excited pendulum: a dynamical integrity perspective. Physica D: Nonlinear Phenomena, 240(9), (2011), 814-824, 10.1016/j.physd.2010.12.014.

[26] Lin, Y. G., Tu, L., Zhang, D. H., Liu, H. W., and Li, W.. A study on dual-stroke pendulum wave energy conversion technology based on a water/oil integrated transmission system. Ocean Engineering, 67, (2013), 27-34, 10.1016/j.oceaneng.2013.04.014.

[27] Lasa, J., Antolin, J. C., Angulo, C., Estensoro, P., Santos, M., and Ricci, P.. Design, construction and testing of a hydraulic power take-off for wave energy converters. Energies, 5(6), (2012), 10.3390/en5062030.

[28] Feitosa, A. C.. Morfogenetic Evolution of the north coast of Maranhão`s Island, Rio Claro, UNESP: 210 p (Phd Thesis, in portuguese), (1989).

[29] Carvalho, J.T.. Simulation of energy distribution of ocean waves from the Brazilian`s coast. Master's Thesis, (INPE) Instituto Nacional de Pesquisas, São José dos Campos, Brasil (in portuguese), (2010).

[30] Dorf, R. C., and Bishop, R. H.. Modern control systems ISBN: 978-0136024583, (1998).

Carlos Eduardo Marques, M.Sc. (Ph.D. student): São Paulo State University – Department of Mechanical Engineering, Eng. Luis Edmundo Carrijo Coube Avenue – 1401, 17033-360, Bauru - SP, Brazil (*carlos_e_marques@hotmail.com*).

José Manoel Balthazar, Professor: Aeronautics Technological Institute – Aeronautics Division, Marechal Eduardo Gomes Square – 50, 12228-900, São José dos Campos - SP, Brazil (*jmbaltha@gmail.com*). The author gave a presentation of this paper during one of the conference sessions.

Angelo Marcelo Tusset, Ph.D.: Federal University of Technology – Paraná – Department of Mathematics, Monteiro Lobato Avenue, 84016-410, Ponta Grossa – PR, Brazil (*tusset@utfpr.edu.br*).

Rodrigo Tumolin Rocha, Ph.D.: Federal University of Technology – Paraná – Department of Electronics, Monteiro Lobato Avenue, 84016-410, Ponta Grossa – PR, Brazil (*digao.rocha@gmail.com*).

Frederic Conrad Janzen, Ph.D.: Federal University of Technology – Paraná – Department of Electronics, Monteiro Lobato Avenue, 84016-410, Ponta Grossa – PR, Brazil (*fcjanzen@utfpr.edu.br*).

Jeferson José de Lima, M.Sc. (Ph.D. student): São Paulo State University – Department of Mechanical Engineering, Eng. Luis Edmundo Carrijo Coube Avenue – 1401, 17033-360, Bauru - SP, Brazil (*jefersonjl82@gmail.com*).

Airton Nabarrete, Professor: Aeronautics Technological Institute – Aeronautics Division, Marechal Eduardo Gomes Square – 50, 12228-900, São José dos Campos - SP, Brazil (*nabarret@ita.br*).

Localization and reconstruction of dynamic forces acting on plane structures using displacement transmissibility

Miguel A. A. S. Matos[1], Yoann E. Lage[2], Miguel M. Neves[3], Nuno M. M. Maia[4]

Abstract: The vibration displacement amplitudes at different locations can be related using the Multiple Degree-of-Freedom displacement transmissibility concept, which depends on the position of the applied loads. This relationship between responses at some points is used in this work to develop a methodology in frequency domain that is numerically efficient for the localization and reconstruction of dynamic forces acting upon 2D plane structures, as well as for the identification of local modifications. The methodology is based on a finite element model that is able to characterize the dynamic response along all the structure. The methodology is discussed and tested in examples to illustrate its potential.

1. Introduction

The measurement of the exciting forces applied to a structure is often difficult or impossible to do, at least directly. Being able to identify these exciting forces using only a limited amount of response data is then an option, using as force identification methods.

Those difficulties appear in many situations and have been intensively studied. Several methods using inverse problem solutions are available in the literature. Examples of that are the estimation of operational forces at inaccessible locations of installed machinery [1,2], forces transmitted to the supports [3,4], aerodynamic loads acting upon a rotorcraft blade [5], or to turbine blades [6].

In the direct problem the output of the system (dynamic response) is obtained from the system model and its inputs. The identification problem is based on the inverse of the direct relation, searching for the unknown force that best fits the measured response data.

This interchange in the model comes with a price, the inverse problem is in general ill-posed [4], due to lack of information, e.g., in the responses due to the limitations imposed to the number and location of measurements. Some techniques are known to help overcoming some of these problems, like regularization techniques [4], pseudo-inversion [7], data filtering [8], singular value decomposition (SVD) and Tikhonov regularization [9-11].

In problems where the location of the loads is known, the objective is only the reconstruction of the applied loads, e.g. [12, 13]. In others, the method needs to estimate the location, magnitude and phase of the forces acting on the structure, as in [14]. Methods for frequency or time domain problems with regularization techniques are given in [15-20], generalized inverse of transfer matrices

in [21], finite difference scheme with regularization in [22] and transformation of the deflection data into modal responses, treated as a result of modal forces in [6]. More recently, shape sensing techniques have been presented, estimating the displacement field at every point of the structure through fitting schemes by iterating the applied loads, as described in [23].

The aim of this paper is to propose and test an identification method for harmonic loads in plates, based on the displacement transmissibility concept [24]. Taking a set of measured displacement responses and the dependence of the displacement transmissibility on the set of DOFs where the loads are applied, the applied forces are localized and their amplitude reconstructed using frequency response function (FRFs) matrices. This concept has been explored by some of the authors in the much simpler cases of mass-spring systems [25] and beams [26] (see also [27]). Here, an extension to plate structures is presented, including the procedures to handle the large number of DOFs combinations where loads may be applied. Besides that, an additional novelty is the application of the proposed methodology to identify local mass modifications. Some examples are presented to illustrate the methods and explore their potential.

2. Fundamentals

The dynamic equilibrium equation of a linear viscoelastic structure with *n* DOFs, is given by:

$$\boldsymbol{M}\ddot{\boldsymbol{y}} + \boldsymbol{C}\dot{\boldsymbol{y}} + \boldsymbol{K}\boldsymbol{y} = \boldsymbol{f} \tag{1}$$

where $\boldsymbol{M}$, $\boldsymbol{C}$ and $\boldsymbol{K}$ are the $n \times n$ mass, damping and stiffness matrices of the structure, respectively; $\boldsymbol{y}$, $\dot{\boldsymbol{y}}$, and $\ddot{\boldsymbol{y}}$ are the nodal displacement, velocity and acceleration, respectively and $\boldsymbol{f}$ is the applied load vector. Assuming harmonic excitation, it is easy to obtain the relation between the complex amplitudes of the forces $\boldsymbol{F}(\omega)$ and those of the response $\boldsymbol{Y}(\omega)$, in the frequency domain. Simplifying the notaion,

$$\left(\boldsymbol{K} - \omega^2\boldsymbol{M} + i\omega\boldsymbol{C}\right)\boldsymbol{Y} = \boldsymbol{F} \tag{2}$$

The dynamic stiffness matrix $\boldsymbol{Z}(\omega)$ is then given by:

$$\boldsymbol{Z}(\omega) = \boldsymbol{K} - \omega^2\boldsymbol{M} + i\omega\boldsymbol{C} \tag{3}$$

and the receptance or *FRF* matrix $\boldsymbol{H}(\omega)$ is the inverse of $\boldsymbol{Z}(\omega)$. Simplifying again the notation,

$$\boldsymbol{Y} = \boldsymbol{Z}^{-1}\boldsymbol{F} = \boldsymbol{H}\boldsymbol{F} \tag{4}$$

In classical books, the dynamic displacement transmissibility is introduced as the quotient between the amplitudes (in absolute value) of the transmitted and applied displacements, for single

DOF systems. Recently, the generalization of this concept has been extensively developed (see e.g. [28, 29] and references therein). The generalization is accomplished through the definition of sets of DOFs as illustrated in Fig. 1, with the distinct sets U and K where response amplitudes are measured and the set A where loads can be applied (and that may include DOFs from the other sets).

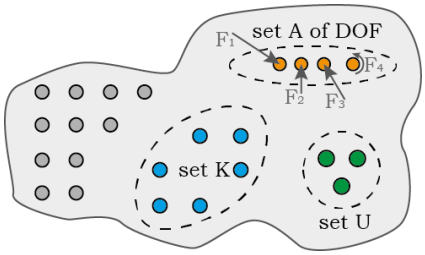

Figure 1. Illustration of the three subdomains of DOFs, namely the sets A, U and K.

From eq. (4) the responses $\boldsymbol{Y}_U$ and $\boldsymbol{Y}_K$ and the applied force amplitudes $\boldsymbol{F}_A$ are related through

$$\begin{aligned} \boldsymbol{Y}_U &= \boldsymbol{H}_{UA}\boldsymbol{F}_A \\ \boldsymbol{Y}_K &= \boldsymbol{H}_{KA}\boldsymbol{F}_A \end{aligned} \tag{5}$$

where $\boldsymbol{H}_{UA}$ is the truncated FRF matrix relating the sets of DOFs U and A. Similarly, $\boldsymbol{H}_{KA}$ relates sets K and A. The transmissibility between the responses $\boldsymbol{Y}_U$ and $\boldsymbol{Y}_K$ is obtained eliminating $\boldsymbol{F}_A$ between eqs. (5), which involves the pseudo-inverse of $\boldsymbol{H}_{KA}$, i.e.,

$$\boldsymbol{Y}_U = \boldsymbol{T}_{UK}^{A}\boldsymbol{Y}_K = \boldsymbol{H}_{UA}\left(\boldsymbol{H}_{KA}\right)^{+}\boldsymbol{Y}_K \tag{6}$$

This pseudo-inversion requires the size of set K to be larger or equal to the size of the set A ($\#K \geq \#A$). Eq. (6) depends on DOFs A, where the loads can be applied, but not on their amplitudes.

3. Methodology

3.1. Force identification method

The proposed methodology requires the knowledge of the response amplitudes of $\tilde{\boldsymbol{Y}}_K$ and $\tilde{\boldsymbol{Y}}_U$ (to be measured at two sets of DOFs, K and U). The sign "~" stands for "measured quantity". The idea relies on the identification of the correct transmissibility matrix $\boldsymbol{T}_{UK}^{A}$, that when applied to $\tilde{\boldsymbol{Y}}_K$ produces an estimated result for $\boldsymbol{Y}_U$ that should correlate with the measured $\tilde{\boldsymbol{Y}}_U$, for the assumed (possible) forces located at the specific set A. When such a correlation happens, it means that the set A has been correctly found. Note that the transmissibility matrix depends only on the location of the loads (set A) but not on their amplitudes. Referring to each possible combination of locations as A_i, one has:

$$\boldsymbol{Y}_U = \boldsymbol{T}_{UK}^{A_i} \tilde{\boldsymbol{Y}}_K \tag{7}$$

where the index i=1,…, refers to the number of combinations of DOFs of A. The resulting $\boldsymbol{Y}_U$ is then compared with the measured $\tilde{\boldsymbol{Y}}_U$, using the following estimation error for each component j:

$$error_j = \sum_{\omega} \left(\log\left|\tilde{Y}_{U_j}\right| - \log\left|Y_{U_j}\right| \right)^2 , \ \mathrm{j} = 1, ..., \text{length of } \left(\tilde{\boldsymbol{Y}}_U\right); \text{ if } \tilde{Y}_{U_j} \neq 0 \text{ and } Y_{U_j} \neq 0. \tag{8}$$

To obtain a scalar value for every single combination A_i, i.e. location DOFs of the assumed forces, the accumulated error of each combination is defined as the norm of the vector $\boldsymbol{\varepsilon} = \boldsymbol{error}$. The correct combination of DOFs A_i is the one with absolute minimum of the accumulated error.

Assuming that the number of loads applied to the structure is not known à priori, the set of possible locations is generated, as in Table 1, starting by combining all the DOFs of the structure in combinations of one force, then in combinations of two force, etc. The number of loads NF is limited by the size of the set K, and $\mathrm{n_p}$ ($\mathrm{n_p} \leq \mathrm{n}$) is the number of maximum nodes where loads may be simultaneously applied.

Table 1. Example of the generation of possible combinations of DOFs for the load location.

Number of loads to search	Combinations for each number of loads	Total number of combinations
1	$(\mathrm{DOF1}), (\mathrm{DOF2}), \ldots (\mathrm{DOFn_p})$	$\mathrm{n_p}$
…	…	…
NF	$(\mathrm{DOF1}, \mathrm{DOF2}, \ldots), \ldots$	$\binom{\mathrm{n_p}}{\mathrm{NF}} = \frac{\mathrm{n_p}!}{\mathrm{NF}!\left(\mathrm{n_p} - \mathrm{NF}\right)}$

For a specific combination A_i, the reconstructed load is obtained from (5) with the values $\tilde{\boldsymbol{Y}}_K$, as:

$$\boldsymbol{F}_{A_i} = \left(\boldsymbol{H}_{KA_i}\right)^{+} \tilde{\boldsymbol{Y}}_K \tag{9}$$

When the combinations involve locations where forces are applied together with other locations without applied forces, the additional locations have, as expected, near-zero force amplitude and a near value of accumulated error is expected. This makes the process less efficient and for this reason the authors propose a modification.

The proposed modification consists of computing both the reconstructed force amplitude for every combination and the root mean square (RMS) in frequency for the loads at each DOF of A_i. When the accumulated error indicates a location where a load has a near zero RMS amplitude, its respective error is artificially increased. This modification improves significantly the efficacy of the

force location method, only at a cost of requiring the matrix multiplication in equation (9), because the pseudo-inverse was previously computed for the transmissibility matrix.

As plates tend to have a larger number of degrees of freedom than simpler systems, it is recommendable as good practice to make the selection of a group of the DOF types, i.e., either the displacements or rotations. This idea results in a smaller number of possible combinations, and less computational time.

3.2. Local mass change identification method

Here, a method is proposed to identify small modifications (reductions or additions) to the original structure. Recalling eq. (1), we may say that $\boldsymbol{M} = \boldsymbol{M}_o + \Delta\boldsymbol{M}$, $\boldsymbol{C} = \boldsymbol{C}_o + \Delta\boldsymbol{C}$, and $\boldsymbol{K} = \boldsymbol{K}_o + \Delta\boldsymbol{K}$, where the subscript "*o*" stands for original system. Eq. (1) becomes:

$$\left(\boldsymbol{M}_o + \Delta\boldsymbol{M}\right)\ddot{\boldsymbol{y}} + \left(\boldsymbol{C}_o + \Delta\boldsymbol{C}\right)\dot{\boldsymbol{y}} + \left(\boldsymbol{K}_o + \Delta\boldsymbol{K}\right)\boldsymbol{y} = \boldsymbol{f} \tag{10}$$

To simplify, let us assume only mass modifications. Eq. (10) turns out to be

$$\boldsymbol{M}_o\ddot{\boldsymbol{y}} + \boldsymbol{C}_o\dot{\boldsymbol{y}} + \boldsymbol{K}_o\boldsymbol{y} = \boldsymbol{f} + \boldsymbol{f}_D \tag{11}$$

where $\boldsymbol{f}_D = -\Delta\boldsymbol{M}\ddot{\boldsymbol{y}}_D$ is the inertia force vector associated to the mass modifications; the subscript "*D*" is due to the fact that the force and acceleration vectors have only non-zero terms at the entries corresponding to the affected DOFs, defining a new set *D*. For harmonic applied forces, $\boldsymbol{f} = \boldsymbol{F}\mathrm{e}^{i\omega t}$ and $\boldsymbol{y} = \boldsymbol{Y}\mathrm{e}^{i\omega t}$. Hence,

$$\left(\boldsymbol{K}_o - \omega^2\boldsymbol{M}_o + i\omega\boldsymbol{C}_o\right)\boldsymbol{Y} = \boldsymbol{F} + \boldsymbol{F}_D \tag{12}$$

where

$$\boldsymbol{F}_D = \omega^2\Delta\boldsymbol{M}\boldsymbol{Y}_D \tag{13}$$

The proposed methodology involves harmonic loads applied at known locations, capable of exciting the displacements at the affected locations. Applying the force identification procedure as in the previous subsection and using the transmissibility matrices of the original structure, new values appear in the force vector, with respect to those affected locations.

The force identification method is used to estimate the additional masses. The amplitude of $\boldsymbol{Y}_D$ can be estimated from the measured $\tilde{\boldsymbol{Y}}_K$ as:

$$\boldsymbol{Y}_D = \boldsymbol{T}_{DK}^{A}\tilde{\boldsymbol{Y}}_K \tag{14}$$

Eq. (13) can be therefore given by:

$$\boldsymbol{F}_D = \omega^2 \Delta \boldsymbol{M} \boldsymbol{T}_{DK}^A \tilde{\boldsymbol{Y}}_K \tag{15}$$

Again, note that the pseudo-inverse involved in the calculation of $\boldsymbol{T}_{DK}^A$ requires that $\#K \geq \#A$.

The local mass identification methodology is a simple extension of the force identification method, as the additional masses act, in fact, as additional forces. It is a three step procedure:

1 - We apply known forces at known locations of the system and look for more forces beyond those ones. The localization procedure will return us the location of the forces that we already know (and thus that can be checked), plus other locations where the new forces due to the additional masses exist;

2 – The reconstruction process is made using eq. (9). This gives us not only the magnitudes of the known forces, but also those of the additional forces;

3 – Finally, the increase or decrease of mass ($\Delta \boldsymbol{M}$) is evaluated from eq. (15).

Within the context of damage identification, this procedure allows for the detection, localization and quantification of the damage.

4. Results and discussion

A free rectangular plate is considered in order to illustrate the application of the proposed method. The properties of the plate are given in Table 2, which is modelled using Reissner-Mindlin shell elements with 4 nodes, each with 6 DOFs (3displacements and 3 rotations), in a 20×20 rectangular mesh. Once the stiffness and mass matrices are assembled (damping is considered as negligible in this case), the code builds the dynamic stiffness matrix $\boldsymbol{Z}$ (equation (3)).

Table 2. Plate properties.

Mass Density - ρ	7850 kg/m^3
Young Elasticity Modulus - E	198 GPa
Thickness - t	3 mm
Width - W	435 mm
Height - H	366 mm

4.1. Numerical verification examples

4.1.1. Single Force Identification

A transversal harmonic load of amplitude 1 N is applied at node 389 of the FE model (see Fig. 2). A frequency range from 1 to 300 Hz is considered and discretized in intervals of 1 Hz. A dynamic

harmonic analysis leads to the dynamic response. Taking or considering the obtained results as "measurements" for this numerical verification, the proposed methodology is used to identify the applied load. Because the force is acting along the axis Oy, only displacement DOFs along this direction are considered at the nodes where the displacements are "measured".

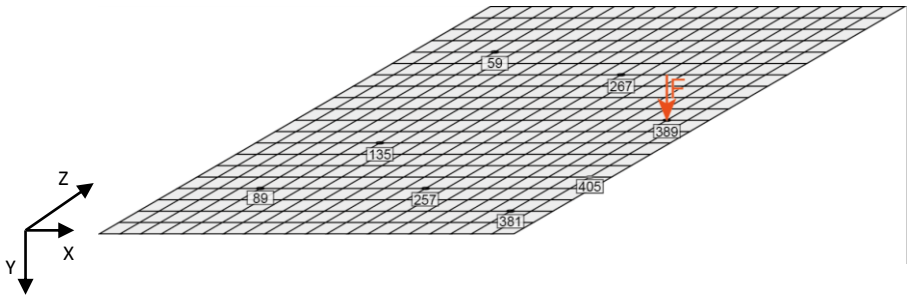

Figure 2. Illustration of the used plate finite element model and representative nodes.

The number of applied forces is considered as unknown, and the search starts by including just one DOF in each combination. The "measured" displacements are $\tilde{Y}_K = \tilde{Y}_{267}$ and $\tilde{Y}_U = \tilde{Y}_{59}$, where Y refers to the displacement along Oy and the subscript to the node, according to Fig. 2. As $\#K = 1$, this set K allows only for the identification of a single applied force. In this case there are 441 possible load locations. The accumulated error, computed from the norm of equation (8) for each combination ID, is plotted in Fig. 3. The minimum value of the error correctly identifies the load, located at node 389.

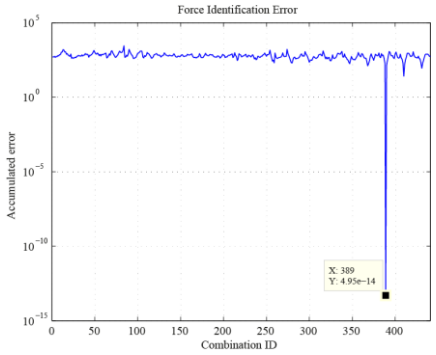

Figure 3. Accumulated error in frequency *vs* force combination for one applied load (#K=1)

After the load reconstruction it is observed that the amplitude of the reconstructed load presents a maximum error of $5 \times 10^{-6}\%$ in this numerical verification. One can observe that until this point, there is no guarantee that the number of loads was indeed correctly predicted. To deal with that

aspect, one considers a new step with a larger set *K*, allowing the maximum number of possible locations to be 2, and use the "measurements" $\tilde{\boldsymbol{Y}}_K = \{\tilde{Y}_{135}, \tilde{Y}_{267}\}^T$ and $\tilde{Y}_U = \tilde{Y}_{59}$. Of course, the number of possible combinations increases significantly, as shown in Table 3. Repeating the procedure for the combinations of two forces, leads to the accumulated error presented in Fig. 4. As presented in Table 4, lower extremes correspond to combinations involving the node 389. This supports the idea that the search can be limited to combinations involving the node located previously.

Table 3. Possible load combinations

Number of forces to search for	Nodes combinations	Combination ID
1	(1), (2), (3),…, (441);	1 to 441
2	(1,2), (1,3), …(440,441);	442 to 97461

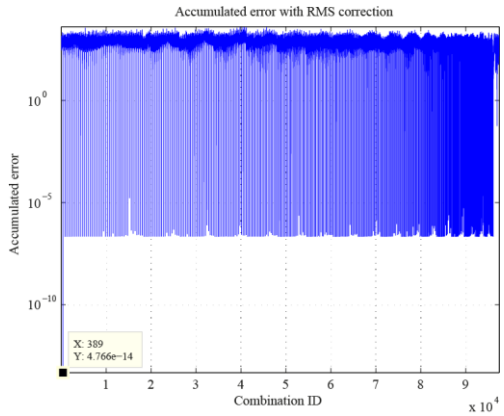

Figure 4. Accumulated error in frequency *vs* force combination when only one load is applied but the search is made for two locations (#K=2)

Table 4. Combinations with minimum accumulated error

Combination ID	Node 1	Node 2	Absolute accumulated error	Load (RMS in frequency) at node 1 [N]	Load (RMS in frequency) at node 2 [N]
389	389	-	4.766×10^{-14}	1.0	-
92753	389	344	4.805×10^{-7}	1.0	4.8×10^{-9}
93879	389	276	4.806×10^{-7}	1.0	1.2×10^{-9}
…	389	…	…	1.0	…

In Fig. 4 one may observe more relative minima besides the correct combination. According to Table 4, all these combinations have the correct node 389 in common, together with another location where the load presents near-zero amplitude (obtained after reconstruction), as concluded from the RMS (in frequency) of the load. As the RMS values at node 2 are all negligible compared with the RMS at node 1, the conclusion is that only the first identified force is being applied, which is the correct situation.

4.1.2. Additional mass identification

Consider the same plate of section 4.1.1, but with a point mass of m_{added} = 0.1 kg at node 89, as illustrated in Fig. 5. Only perpendicular displacements are considered. By the procedure described, one known harmonic load with an amplitude of 2 N is applied at node 59 which is capable of exciting the displacement at the location of the added mass. The unmodified model is used to identify the two forces (#A=2) using the "measured" vectors $\tilde{\boldsymbol{Y}}_K = \left\{\tilde{Y}_{135}, \tilde{Y}_{267}\right\}^T$ and $\tilde{\boldsymbol{Y}}_U = \left\{\tilde{Y}_{257}, \tilde{Y}_{389}\right\}^T$.

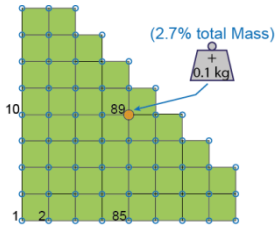

Figure 5. Part of the plate FE model with the added punctual mass at node 89

The accumulated error is plotted in Fig. 6 a), with the minimum at the combination 24338 (nodes 59 (applied load) and 89 (load generated by the additional mass)). The reconstruction of these forces is achieved using eq. (9). The reconstructed amplitude of the second load is presented in Fig. 6 b). The added mass is then obtained from eq. (13):

$$F_{89} = \omega^2 m_{added} Y_{89} \tag{16}$$

where Y_{89} is calculated from eq. (14), using one of the "measured" outputs (nodes 135 and 267) and the transmissibility involving one of those output nodes and node 89, for the applied force at node 59 and zero force at node 89. Note that we can put the force at node 89 as zero because one of the fundamental transmissibility properties is that the transmissibility is invariant with respect to the magnitude of the applied forces. This means that Y_{89} may be calculated (using eq. 14) from:

$$Y_{89} = T^{59}_{89,135} \tilde{Y}_{135} = H_{89,59} \left(H_{135,59}\right)^{-1} \tilde{Y}_{135} \tag{17}$$

or from

$$Y_{89} = T^{59}_{89,267} \tilde{Y}_{267} = H_{89,59} \left(H_{267,59}\right)^{-1} \tilde{Y}_{267} \tag{18}$$

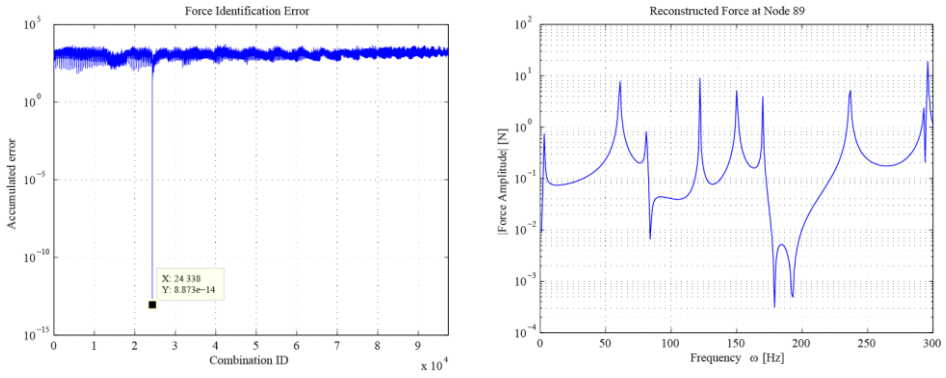

a) b)

Figure 6. Outputs from the force identification procedure to identify the additional mass: a) Accumulated error for every combination; b) Reconstructed amplitude of the additional identified load (at the mass location)

As F_{89} is already known (Fig. 6 b)), the remaining unknown m_{added} can be retrieved from the data using a frequency average, producing an estimate of that value with an error of only $1.2 \times 10^{-7}\%$.

4.2. Experimental validation example

The methodology for force localization was tested experimentally, using a steel plate suspended by nylon strings and with the data given in Table 2. Fig. 7 presents the experimental setup used.

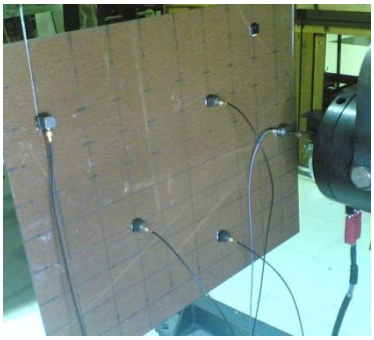

Figure 7. Experimental setup used

To perform the desired experimental tests the following equipment was used: vibration exciter B&K Type 4809; power amplifier B&K Type 2706; accelerometers B&K Type 4508-B; force transducers PCB Piezotronics Model 208C01; and data acquisition equipment B&K Type 3560-C with commercial software Pulse Labshop.

For the proposed identification, the knowledge of the displacement transmissibility matrix is required; this was obtained from the numerical model and the experimental responses were measured

with the described setup. Because it is fundamental that the numerical and the experimental models match as much as possible, the FRFs of the two models were compared; as an example, the FRFs (183,141) are presented in Fig. 8.

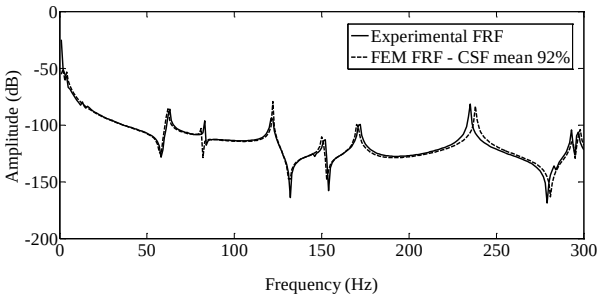

Figure 8. Plot of $FRF_{183,141}$ for the experimental data and for the numerical model.

The quality of the numerical model compared with the experimental one was analyzed using the *Cross Signature Scale Factor* (*CSF*) which gives the correlation function between two *FRF*s amplitudes in the frequency range [1-300] Hz. A mean value of *CSF*=92% was obtained for the $FRF_{183,141}$, which was considered as a good match.

In this experimental case, the plate is submitted to a *multisine* force at node 141 (see Fig. 9). Only two responses are considered: $\tilde{Y}_K = \tilde{Y}_{303}$ and $\tilde{Y}_U = \tilde{Y}_{183}$. Fig. 10 presents the accumulated error curve and, as can be seen, the algorithm identifies the absolute minimum at the combination number 141. This experimental localization of the force was successfully accomplished.

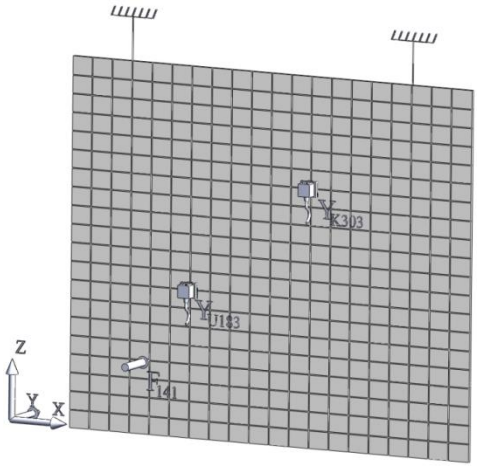

Figure 9. Force and accelerometer positions.

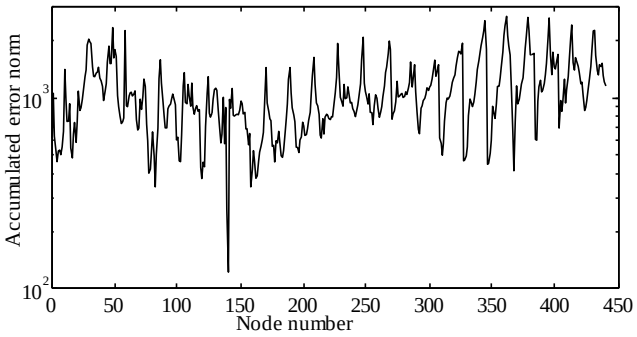

Figure 10. Plot of the accumulated error for every combination.

5. Conclusions

The authors use a transmissibility relation between responses at some points to develop a methodology in frequency domain that shows both numerical and experimental efficiency for the localization and reconstruction of dynamic forces acting upon plate structures.

Although the localization problem could require a high number of runs when the number of possible location of force combinations is high, one should mention that each run (for each force combination) is considered as numerically efficient if in comparison with traditional methods that require full matrices; this is due to the fact that it only requires the transmissibility of the involved DOFs. In this text, the authors also tested the idea of extending the methodology to the location of added masses.

It was also observed that when the combinations involve locations where forces are applied as well as other locations without applied forces, the additional locations have near-zero force amplitude, and a near value of accumulated error, as expected. To deal with some process inefficiency, the authors proposed a modification to the accumulated error of those combinations, consisting of computing the reconstructed force amplitude for every combination and the Root Mean Square (RMS) in frequency for the loads of each DOF of A_i. When the modified accumulated error value indicates a load with near zero RMS amplitude, its respective error is increased. This modification has shown to improve significantly the efficiency of the force localization method, and only at a cost of requiring the matrix multiplication in equation (9), because as one may observe the pseudo-inverse was previously computed for the transmissibility matrix.

It also shown that it was possible to extend the developed procedure to include the identification of structural modifications, namely in the mass, as this can be seen as an applied inertia force. This may be important in the context of the identification of damage, as the procedure allows for the detection, localization and also quantification of a structural modification.

Acknowledgements

The authors thank the Portuguese Science Foundation, FCT, through IDMEC, under LAETA.

References

[1] Mas, P. and Sas, P., Indirect force identification based on impedance matrix inversion: a study on statistical and deterministic accuracy, *Proceedings of 19th ISMA*,(1994), pp. 1049-1065.

[2] Dobson, B. J. and Rider, E., A review of the indirect calculation of excitation forces from measured structural response data, *J. of Mechanical Engineering Science* , 204(2), (1990), pp. 69-75.

[3] Tao, J. S., Liu, G. R. and Lam, K. Y., Excitation Force Identification of an Engine with Velocity Data at Mounting Points, *J. of Sound and Vibration*, 242(2), (2001), pp. 321-331.

[4] Uhl, T., The inverse identification problem and its technical application, *Archive of Applied Mechanics*, 77(5), (2007), pp. 325-337.

[5] McColl, C., Palmer, D., Chierichetti, M., Bauchau, O. and Ruzzene, M., Comprehensive UH-60 loads model validation, *Proceedings of 66th Annual Forum - American Helicopter Society*, (2010), pp. 1531-156.

[6] Vyas, N. S. and Wicks, A. L., Reconstruction of turbine blade forces from response data, *Mechanism and Machine Theory*, 36, (2001), pp. 177-188.

[7] Lage, Y. E., Maia, N. M. M., Neves, M. M., and Ribeiro, A.M.R., A Force Identification Approach for Multiple-Degree-of-Freedom Systems, *Proceedings of the IMAC-XXVIII*, (2010), pp. 53-61.

[8] Ma, C. K. and Ho, C.C., An inverse method for the estimation of input forces acting on non-linear structural systems, *Journal of Sound and Vibration*, 275, (2004), pp. 953-971.

[9] Choi, H.G., Thite, A.N. and Thompson, D.J., A threshold for the use of Tikhnov regularization in inverse force determination, *Applied Acoustics*, 67, (2006), pp. 700-719.

[10] Thite, A.N. and Thompson, D.J., The quantification of structure-borne transmission paths by inverse methods. Part1: improved singular value rejection methods, *Journal of Sound and Vibration*, 264, (2003), pp. 411-431.

[11] Thite, A.N. and Thompson, D.J., The quantification of structure-borne transmission paths by inverse methods. Part 2: use of regularization methods,*" Journal of Sound and Vibration*, 264, (2003), pp. 433-451.

[12] Chang, C. and Sachse, W., Analysis of elastic wave signals from an extended source in a plate," *Journal of the Acoustical Society of America*, 77(4), (1985), pp. 1335-1341.

[13] Michaels, J.E. and Pao, Y.-H., The inverse source problem for an oblique force on an elastic plate," *Journal of Acou*

[14] D'Cruz, J., Crisp, J.D.C., and Ryall, T.G., On the Identification of a Harmonic Force on a Viscoelastic Plate from Response Data, *Journal of Applied Mechanics*, 59, (1992), pp. 722-729.

[15] Liu, J.-J., Ma, C.-K., Kung, I.-C. and Lin, D.-C.,Input force estimation of a cantilever plate by using a system identification technique, *Computer Methods in Applied Mechanics and Engineerin*g, 190, (2000), pp. 1309-1322.

[16] Liu, Y. and Shepard Jr., W.S., An improved method for the reconstruction of a distributed force acting on a vibrating structure, *Journal of Sound and Vibration*, 291, (2006), pp. 369-387.

[17] Jiang, X.Q. and Hu, H.Y. , Reconstruction of distributed dynamic loads on a thin plate via mode-selection and consistent spatial expression," *Journal of Sound and Vibration*, 323, (2009), pp. 626-644.

[18] Voropai, A.V. and Yanyutin, E.G., "Identification of several impulsive loads on a plate," *International Applied Mechanics*, 43(7), (2007), pp. 780-785.

[19] Wang, B.-T., Prediction of Impact and Harmonic Forces Acting on Arbitrary Structures : Theoretical Formulation, *Mechanical Systems and Signal Processing*, 16 (6), (2002), pp. 935-953.

[20] Wang, L., Han, X. and Xie, Y., A New Iterative Regularization Method for Solving the Dynamic Load Identification Problem, *Computer Materials & Continua*, 31 (2), (2012), pp. 113-126.

[21] O'Callahan, J. and Piergentili, F. , Force estimation using operational data," *Proceedings of the 14th International Modal Analysis Conference*, 2768, (1996), pp. 1586-1592.

[22] Pézerat, C. and Guyader, J.L., Force Analysis Technique: Reconstruction of Force Distribution on Plates, *Acustica united with Acta Acustica*, 86, (2000), pp. 322-332.

[23] Chierichetti, M. and Ruzzene, M., Dynamic displacement field reconstruction through a limited set of measurements: Application to plates, *Journal of Sound and Vibration*, 331(21), (2012), pp.4713-4728.

[24] Maia, N.M.M., Silva, J.M.M., Ribeiro, A.M.R., "The Transmissibility Concept in Multi-Degree-of-Freedom Systems," *Mechanical Systems and Signal Processing*, 15 (1), (2001), pp.129-137.

[25] Lage, Y.E., Maia, N.M.M., Neves, M.M., Ribeiro, A.M.R., Force identification using the concept displacement transmissibility, *Journal of Sound and Vibrati*on, 332(7), (2013), pp. 1674-1686.

[26] Neves, M.M., and Maia, N.M.M., Estimation of Applied Forces Using The Transmissibility Concept, *Proceedings of ISMA2010 including USD2010*, (2010), pp. 3887-3897.

[27] Maia, N.M.M., Lage, Y.E., and Neves, M.M., Recent Advances on Force Identification in Structural Dynamics, in *Advances in Vibration Engineering and Structural Dynamics*, InTech, (2012), pp. 103-132.

[28] Maia, N.M.M., Urgueira, A.P.V., and Almeida, R.A.B., Whys and Wherefores of Transmissibility, in *Vibration Analysis and Control - New Trends and Developments*, Dr. Francisco Beltran-Barbajal, InTech, (2011), pp. 197-216.

[29] Lage, Y.E., Neves, M.M., Maia, N.M.M., and Tcherniak, D., Force transmissibility versus displacement transmissibility, *Journal of Sound and Vibration*, 333(22), (2014), pp. 5708-5722.

Miguel A. Matos, 1, M.Sc. (Ph.D. student): DEM, Instituto Superior Técnico, U. Lisboa, Department of Mechanical Engineering, Av. Rovisco Pais, 1049-001 Lisboa, Portugal (miguelsmatos@hotmail.com).

Yoann E. Lage, 2, Ph.D. (Project Leader): Condition and Structural Monitoring, TWI Ltd, Granta Park, Great Abington, Cambridge, CB21 6AL, UK. (yoann.lage@twi.co.uk)

Miguel M. Neves 3, Professor: LAETA, IDMEC, Instituto Superior Técnico Universidade de Lisboa, Av. Rovisco Pais, 1049-001 Lisboa, Portugal. (miguel.matos.neves@tecnico.ulisboa.pt)

Nuno M.M.Maia, 4, Professor: LAETA, IDMEC, Instituto Superior Técnico Universidade de Lisboa, Av. Rovisco Pais, 1049-001 Lisboa, Portugal. (nuno.manuel.maia@tecnico.ulisboa.pt) The author gave a presentation of this paper during one of the conference sessions.

Analysis of the influence of parameters of elastic layer in shock-absorbing holder of helical spring on its dynamic and static properties

Krzysztof Michalczyk, Wojciech Sikora

Abstract: Metal helical springs are widely used in general machines building due to excellent strength and elastic properties, but at the same time they exhibit negligible damping properties which is usually an undesirable feature, especially in suspension systems. One of the methods of increasing damping in support systems based on application of helical springs is the use of a spring holder integrated with the spring by means of elastomeric layer, characterized by high damping properties. The results of numerical analyses of the influence of geometrical and material parameters of elastomeric layer on dynamic and static properties of the spring and holder system are presented in the paper. It is shown that proper selection of these parameters can provide significant vibration energy dissipation whilst maintaining relatively low static stiffness.

1. Introduction

The development of polymer and rubber-like materials processing contributes to increase of application of these materials in many branches of industry. Particularly it refers to general machine building, where these materials are widely used in suspension and vibration isolation systems. High damping, soft materials like rubber are thus applied in suspension systems of rail-vehicles [1], technological vibrating machines [2] or rotational machinery [3]. Their main advantage over metal springs is a significant ability of energy dissipation. However, at the same time they are characterized by different values of dynamic and static stiffness [4]. This feature is unfavorable, especially when low natural vibration frequencies of supported machine are required, as static deflection is directly connected with the natural frequency of the system. For a single degree of freedom system, this relation is given in a well known form [5]:

$$f = \frac{1}{2\pi}\sqrt{\frac{g}{\delta_s}}, \tag{1}$$

where: f – natural frequency of the system in Hz, g – gravitational acceleration, δ_s – static deflection. The dynamic modulus depends on many factors such as: rubber blend, temperature, filling ratio, frequency and amplitude of vibrations. For natural rubbers, unfilled or slightly filled with carbon

black, the dynamic stiffness coefficient – expressed as a quotient of dynamic modulus to static modulus – equals approximately 1, even for vibration frequencies considerably exceeding 100Hz. Thanks to these stable elastic properties, this type of rubber is widely used by companies producing elastic components based on a Neidhart patent [6]. Filled butyl rubber exhibits in turn significant increase in stiffness: in range from 1Hz to 100Hz and temperature 35°C the increase of stiffness amounts to 10 [7]. NBR rubber exhibits about one and a half times increase in stiffness in transition from 0Hz to 1Hz. Further stiffness increase is getting smaller [8]. The increase in stiffness along with the aforementioned factors is accompanied by the increase of damping. The temperature also has a significant influence on stiffness and damping properties of elastomers. For example, for butyl rubber with 40% carbon black and vibration frequency 1Hz an increase of temperature from 20°C to 35°C results in double reduction of damping decrement [7].

The above mentioned features of elastomeric elastic joints cause that in many applications the steel springs are still irreplaceable. In order to increase damping properties of suspension systems basing on helical sprigs two main methods are used. The first one uses Coulomb friction between spring coils and additional elastic elements e.g. [9-11]. The second one uses internal material damping. It is accomplished through the use of high damping elastomeric element connected to the coils of the spring. The element may have a form of a coating covering the spring wire, like solutions shown in [12-14], it may also have a form of an insert between the coils of the spring [15] or another solution is the application of elastomeric material layer between the spring and properly designed spring holder. The last solution presented in [16] is shown in fig.1.

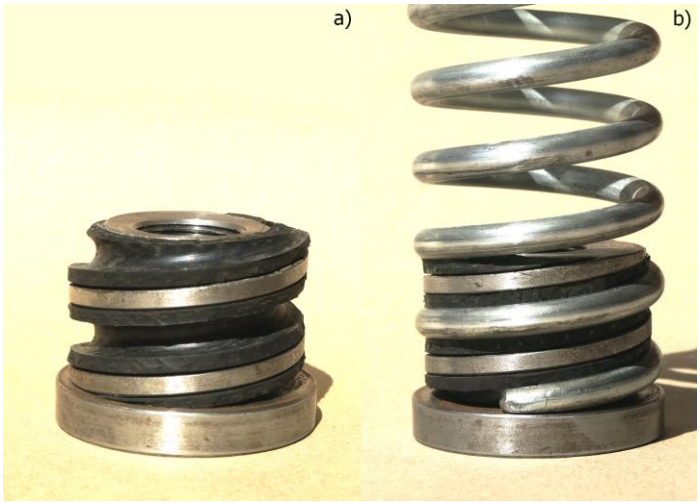

Figure 1. Sketch of the shock-absorbing holder without a spring a), and the holder with the helical spring mounted on it b).

The experimental analysis of the dynamic properties of the discussed construction was presented in [17]. In the cited paper, the discussed construction of the holder was compared with two other conventional variants of the spring holders in terms of damping efficiency of free vibrations of the mass supported on the spring. The experimental studies revealed that application of the shock-absorbing holder allowed to increase damping properties expressed in terms of logarithmic decrement by one order of magnitude – compared with two other holders.

The aim of this study is to define the influence of elastomeric layer parameters on static and dynamic properties of the helical spring – shock absorbing holder system. For this purpose the virtual models of analyzed construction with selected material and geometrical properties of elastomeric insert are developed. Then the series of numerical analyzes are performed to investigate the impact of the above described parameters on static rigidity, energy dissipation ability of the system and natural frequencies in case of clamped-clamped boundary conditions. The conducted analyzes should allow to formulate recommendations useful for the design of such systems.

2. Selection of elastomeric material properties models

As it was mentioned above, rubberlike material exhibit mechanical properties, which are extremely dependant on operating factors such as temperature, frequency, amplitude and character of deformations or history of loading. In spite of this, most material models used to describe the mechanical properties of rubber-like materials do not take into account the effects of speed and load history (Mullins effect) as well as the effects of energy dissipation by means of material damping. These models can be divided into two main groups: phenomenological models such as Polynomial, Mooney-Rivlin, Yeoh, Neo-Hookean, Ogden or Gent model for nearly or fully incompressible materials and Hyperfoam and Blatz-Ko models for compressible materials and models derived on the basis of micromechanical structure of elastomers – like Arruda-Boyce model. Although mentioned models are able to describe nonlinear character of most elastomers, they fail to consider their viscoelasticity. This phenomenon is important for fully understanding behavior of elastomers. It is also the reason behind their damping properties. Therefore, even if one of these models is being used, the problem of introducing damping into calculations remains. Different approach to material modeling was taken in Bergström-Boyce model [18], where elastomeric network is presented as one consisting of two subnetworks. First one is responsible for an ideally elastic part and second for a viscoelastic part of mechanical response. It introduces a time-dependence into the model and therefore allows taking into account also elastic hysteresis due to energy dissipation. In case of Bergström-Boyce model experimental tests used for material parameters estimation have to include load histories of varying strain rates. This, with addition to a large number of material parameters, makes this model troublesome to properly calibrate.

The system consisting of machine element supported on helical springs by means of analyzed shock-absorbing holders can be subjected to loads characterized by wide spectrum of frequencies and amplitudes and also characterized by different load directions. In practice, however, the vibrations of machines supported on helical springs achieve relatively small amplitudes at some initial static loading, caused by for example, the weight of the machine. Small amplitudes of vibrations are accompanied by relatively small deflections of elastomeric elements. In such a case a generally non-linear characteristics of elastomeric material can be linearized without making a significant mistake. Moreover such approach allows one to perform a wider range of numerical analyzes than it would be possible in case of application of nonlinear material models. Commercial finite element analysis software such as ANSYS do not provide any methods dedicated to nonlinear frequency response problems [19]. In the light of the above considerations it was decided to adopt a linear model in further study. It was thus assumed that elastomeric insert has a linear elastic properties and its damping properties are described by material damping model. For the sake of general considerations, the analyzed construction should be investigated for a certain range of material properties of the elastomeric insert. A widely used, general criterion for evaluation of mechanical properties of a rubber is the criterion of the Shore hardness. In literature, empirical relationships between the Shore hardness and elastic moduli can be found. These dependencies give relatively good results for certain ranges of hardness values. The three different dependencies given in [20] - Eq. (2), [21] – Eq. (3), and [22] – Eq. (4) are cited below:

$$E = \frac{0{,}0981\left(56 + 7{,}62336S\right)}{0{,}137505\left(254 - 2{,}54S\right)}, \tag{2}$$

$$S_D = 100 - \frac{20\left(-78{,}188 + \sqrt{6113{,}36 + 781{,}88E}\right)}{E}, \tag{3}$$

$$G = 0{,}086 \cdot 1{,}045^S, \tag{4}$$

where E – the Young's modulus of material in MPa, S – ASTM D2240 Type A durometer hardness and S_D – ASTM D2240 type D hardness, and G – the Shear modulus in MPa. In this study Eq. (2) was applied to find the Young's modulus of elastomeric insert material. Numerical analyzes were performed for the hardness range of the elastomeric insert between 40°ShA and 70°ShA as it is the range of hardness, typical for industrial rubbers. The values of the Young's modulus for rubbers with specified hardness were multiplied by dynamic stiffness coefficient – assumed to be equal to 1,5. The effective elastic modulus E_e values calculated in the manner described above are listed below in the table 1. For rubbers the Poisson's ratio varies from about 0,48 – for highly filled with black carbon blends to 0,5 (within 0,1% error) for non filled blends [23]. Experimental tests presented in [24] showed that for rubber blends made from nitrile rubber, stearin, zinc white, carbon black and

processing additives with hardness between 40°ShA and 70°ShA the Poisson's ratio values were in the range of 0,493 to 0,498. In the present analysis it was thus assumed that the value of the Poisson's ratio is the same for each analyzed rubber models and equals to 0,495.

Table 1. The values of the effective elastic modulus for rubber models.

	40°ShA	50°ShA	60°ShA	70°ShA
E_e [MPa]	2,534	3,684	5,408	8,281

In order to analyze the shock-absorbing holder it is also necessary to determine the strength and damping properties of the rubber models with hardness range specified above. There is a wide variety of rubber-like materials in the market, which differ significantly in performance. In this study the data given in book [22] is used. In cited work, authors divided rubber into eight groups, taking into account seven different material characteristics. According to the classification given by the authors of cited work, rubber blends with the best damping properties exhibit at the same time the lowest tensile strength and vice versa. In addition, the increase of Shore hardness of rubber in each of the eight groups is generally accompanied by an increase in damping. The values of tensile strength σ_T in MPa and the loss factor tanϕ taken from the work cited above and adopted in calculations are presented in the table 2.

Table 2. Tensile strength and the loss factor values adopted in calculations on the basis of [22].

Hardness →	40°ShA		50°ShA		60°ShA		70°ShA	
Group ↓	σ_T	tanϕ	σ_T	tanϕ	σ_T	tanϕ	σ_T	tanϕ
I	17	0,08	19	0,08	20	0,11	20	0,13
II	15	0,09	17	0,09	18	0,12	18	0,15
III	13	0,11	15	0,1	16	0,14	16	0,17
IV	11	0,12	13	0,12	14	0,16	14	0,19
V	9	0,14	11	0,13	12	0,17	12	0,21
VI	7	0,16	9	0,15	10	0,2	10	0,25
VII	5	0,17	7	0,17	8	0,23	8	0,29
VIII	3	0,2	5	0,19	6	0,26	6	0,35

In the calculations following the numerical simulations, the model of internal damping is applied. In order to use damping properties contained in the table 2, the relationship between the loss factor tan ϕ and the specific damping capacity ψ for high damping materials has to be defined. This relationship can be expressed in widely used in literature form:

$$\psi = 2\pi \tan\phi, \tag{5}$$

3. Analyzes preparation

The virtual models of investigated construction were prepared in Design Modeler module of ANSYS Workbench software, version 17.1. Four models with different helical groove diameters in metal parts of holders and outer diameters of elastomeric inserts corresponding to them were prepared. In all cases the parameters of the spring were the same: wire diameter d_w = 5 mm, spring diameter D_s = 50 mm, pitch of the spring h = 20 mm, number of coils n = 9,5. Material properties of the spring and metal parts of the holders were assumed as follows: the Young's modulus E_s = 200000 MPa, the Poisson's ratio ν_s = 0,3 and density ρ_s = 7850 kg/m^3. In order to estimate the efficiency of analyzed system in terms of energy dissipation it is essential to define the damping properties of spring steel. Experimental tests – performed by the authors – of the decay of free vibrations of the system consisting of the mass supported on the spring made of medium carbon steel C45 revealed that for such a system, the logarithmic decrement δ was about 0,001. For weakly damped systems it can be assumed that $\psi \approx 2\delta$. Thus, in this study it is assumed that the specific damping capacity of the spring ψ_s equals 0,002.

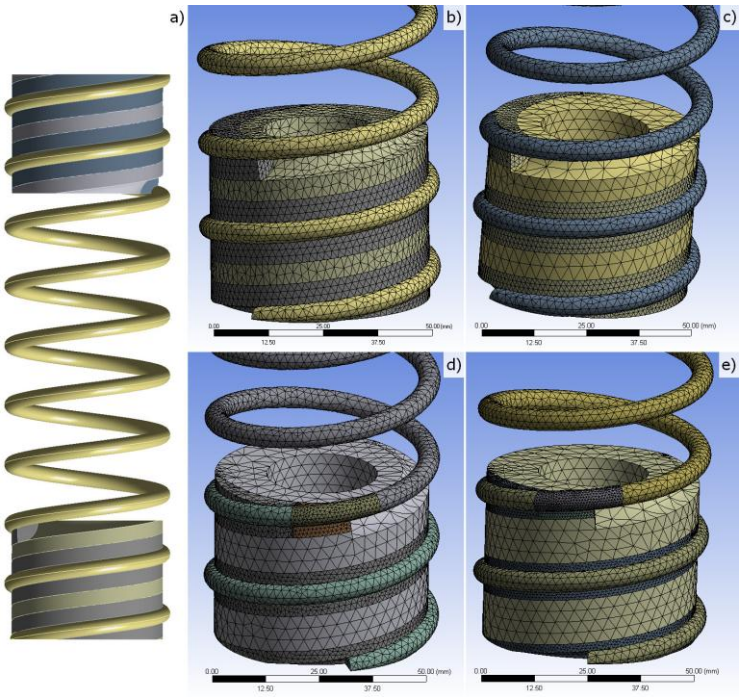

Figure 2. Model of spring-holders assembly a); FE model of assembly with d_e = 15 mm b); FE model of assembly with d_e = 13 mm c); FE model of assembly with d_e = 9 mm d) and FE model of assembly with d_e = 9 mm e).

The height of the holders in each case was equal to 40 mm and the number of the coils of the elastomeric insert was equal to 2. Outer diameters of elastomeric inserts d_e were chosen as $1{,}8d_w$, $2{,}2d_w$, $2{,}6d_w$ and $3d_w$, what equals 9 mm, 11 mm, 13 mm and 15 mm successively. The discretization of models was conducted using 3D higher order 10-node elements SOLID187. The contact pairs between the spring, the elastomeric layer and the holder were modeled as bonded using CONTA174 and TARGE170 elements. The mesh parameters of the helical spring FE models were the same in all simulations. It was assumed that the mesh density should provide 16 nodes on the circumference of the wire, thus the element size was chosen as 1.96 mm. For the elastomeric elements it was assumed that in each case the mesh density should provide 3 layers of elements in radial direction in the area where the spring wire leaves the holder. Fig.2 **a** shows the spring assembly with outer diameter of the elastomeric coating d_e equal 15 mm. In Fig. 2 **b**, **c**, **d**, **e** the models of the part of the assembly for d_e equal to 9 mm, 11 mm, 13 mm and 15 mm respectively are shown. As it can be seen in Fig. 2**d** and **e** the models with d_e equal 9 mm and 11 mm where modified in order to save computing time, whilst maintaining high quality of mesh in critical areas.

4. The results of numerical simulations

A series of nonlinear large deformation static analyzes were performed for each model. The lower surfaces of the bottom holder and the spring were clamped and the upper surfaces of the top holder and the spring were fixed in transversal directions and loaded by displacement in axial direction. The value of the displacement compressing the assembly was equal to 47.5 mm, which corresponds to a quarter of the entire spring length. This value is close to the maximum value of deflection, regarding the spring wire strength. Assuming the allowable shear stress for the spring steel as 500 MPa and only 5.5 out of 9.5 coils are working, the maximum deflection would be equal to 48,6 mm. The analysis showed that, despite a wide range of tested stiffness and geometrical parameters of elastomeric inserts, their influence on rigidity and maximum stress values in the spring wire was ineligible. Fig. 3 shows the characteristics obtained for two extremely different models: the model with the most rigid holder, with rubber hardness of 70°ShA and d_e equal to 9 mm and the model with the softest holder, with rubber hardness of 40°ShA and d_e equal to 15 mm. For every substep of each analysis, the value of the accumulated elastic energy in the spring wire and in the elastomeric inserts was recorded. These values where then used to estimate the energy dissipation capability of the system. The concept of equivalent specific damping capacity ψ_{EQ} was utilized in this purpose. This parameter is defined as

$$\psi_{EQ} = (\psi_s U_s + \psi_e U_e)/(U_s + U_e), \tag{6}$$

where U_s and U_e are maximum elastic energy accumulated in the spring wire and the elastomeric inserts respectively.

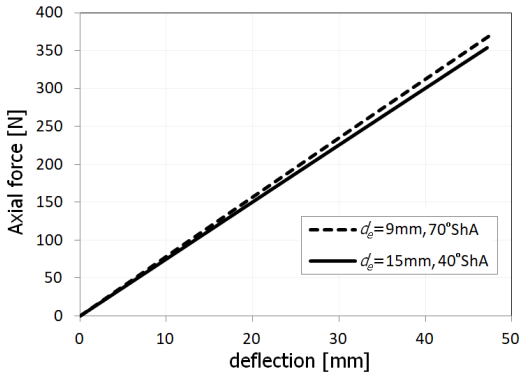

Figure 3. Static characteristics of the spring assemblies: with d_e=15 mm and rubber hardness 40°ShA (continuous line) and with d_e = 9 mm and rubber hardness 70°ShA (dashed line).

Fig. 4 presents the plots of the ratio of the equivalent specific damping capacity ψ_{EQ} to specific damping capacity of the spring steel ψ_s as a function of deflection.

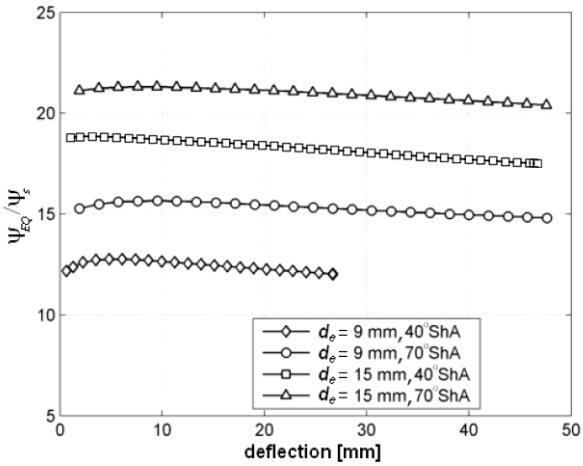

Figure 4. The ratio of equivalent specific damping capacity to specific damping capacity as a function of deflection for four different configurations of the tested systems.

The values of specific damping capacity for rubber elements were calculated using Eq. (5) and the values of loss factor for VIII group of rubbers in table 2. As it can be seen in Fig. 3 and 4 the plots for systems with rubber hardness equal to 40°ShA are not drawn in the whole range of deflections. It is caused by a large deformations of rubber inserts during analyzes, what resulted in lack of solution convergence for higher deflections. It can also be noticed, that the best damping properties exhibits the system with d_e=15mm and 70°ShA. For other, not shown in Fig. 4 configurations, intermediate results were obtained.

For the model shown in Fig. 2 **b** and rubber hardness 40°ShA another static nonlinear analysis was performed, under almost the same conditions as in the first case, but with such a difference that the fixed support was imposed only to the lower surface of the metal part of the bottom holder and the axial displacement was imposed only to the upper surface of the metal part of the top holder. The results of this analysis were almost the same as in the case of the first analysis. It suggests that the spring does not have to rest on additional support, since the mounting in elastomeric insert is sufficient.

Modal analyzes were performed for the two models which characteristics are shown in Fig. 3 under clamped-clamped boundary conditions. Analyzes of the first three natural frequencies have shown that the corresponding frequencies for these two springs did not differ significantly, however the differences where rising along with the number of frequency, achieving about 14% for the third frequency.

5. Conclusions

Analyzes have shown that the application of proposed shock-absorbing holders integrated with helical spring significantly improves the damping properties of the system. For the best tested configuration more than twentyfold increase in damping was achieved compared to the damping of the steel spring itself. Rubbers characterized with higher hardness showed better suitability for use in presented construction. It has also been shown that the changes in elastomeric inserts parameters have inconsiderable effect on the rigidity of the system, maximum reduced stress in the spring wire and first three natural frequencies under clamped-clamped conditions. Further experimental tests are necessary in order to check the application possibilities of the presented solution in terms of its durability.

Acknowledgments

This research was supported in part by PL-Grid Infrastructure. Computations have been performed in ACC CYFRONET AGH.

References

[1] Sebesan, I., Zaharia, N.L., Spiroiu, M.A., Fainus L. Rubber Suspension, a Solution of the future for Railway Vehicles. *Material Plastice*, No.1, 52, (2015), pp. 93-96.

[2] Sikora W., Michalczyk K., Machniewicz T. A study of the preload force in metal-elastomer torsion springs. *Acta Mechanica et Automatica*, vol.10, no.4, (2016), pp. 300-305.

[3] Wodziński, P. Elastic rubber suspension. *Górnictwo i Geoinżynieria*, 31, 4, (2007), pp.107-115.

[4] Arczewski, K., Pietrucha, J., Szuster, J.T. *Vibrations* of Physical *Systems* (in polish). Oficyna Wydawnicza Politechniki Warszawskiej, Warszawa, 2008.

[5] Blevins R.D. *Formulas for Dynamics, Acoustics and Vibration*. John Wiley & Sons, Ltd., 2016.

[6] Neidhart, H. J. *Elastic Joints*, US patent 2 712 742, 1951.

[7] Snowdon J.C. Rubberlike Materials, Their Internal Damping and Role In Vibration Isolation. *Journal of Sound and Vibration*, vol.2, (1965), pp. 175-193.

[8] Rivin, E.I. *Passive Vibration Isolation*. ASME PRESS, New York, 2003.

[9] Kutzbach J.H., Menzel, J.D.I. Antivibrationselement. German patent DE10332637 A1,2005.

[10] Check R.N., Youd J.B., Slade J.E. *Spring damper*. US patent US20080211156 A1, 2008.

[11] Zawilinski D., Dean W.C. *Helical spring damper*. US patent US7871240 B2, 2011.

[12] Nishiyama M., Umetsu C., Kebukawa A., Andoh M. *Beschichtete schraubenfeder*. German patent DE3517900 A1, 1985.

[13] Ukai K., Yano K., Umezawa N., Yamaguchi S., Itoga T.: *Synthetic resin-coated spring and method for making same*. US patent US4753423 A, 1988.

[14] Muzio C. *Coated coil spring, particularly for automotive suspensions and corresponding method of obtaining*. European patent EP1369614 B1, 2005.

[15] Salwiński J., Michalczyk K. *Tubular spring for axial loads*. Polish patent PL219059 B1, 2015.

[16] Michalczyk, J., Michalczyk, K. Coil spring clamp with the shock absorber. Polish patent PL217304B1, 2014.

[17] Michalczyk, K.: The analysis of damping properties of helical spring shock-absorbing holder (in polish). *Przegląd Mechaniczny*, 5, 2012, pp. 21-24.

[18] Bergström, J.S., Boyce, M.C. Constitutive modeling of the large strain time-dependent behavior of elastomers. *Journal of the Mechanics and Physics of Solids*, 46, (1998), pp. 931-954.

[19] Weeger, O., Wever, U., and Simeon, B. Nonlinear frequency response analysis of structural vibrations. Computational Mechanics, 54 (2014), pp. 1477-1495.

[20] Gent, A.N. On the relation between indentation hardness and Young's modulus. *Institution of Rubber Industry -- Transactions*, 34, No.2 (1958), pp. 46–57.

[21] Qi, H.J., Joyce, K., Boyce, M.C. Durometer hardness and the stress-strain behavior of elastomeric materials, *Rubber Chemistry and Technology*, 76, 2(2003), pp. 419–435.

[22] Battermann, W., Köhler, R. *Elastomere Federung, Elastische Lagerungen*. Verlag von Wilhelm Ernst und Sohn, Berlin, 1982.

[23] Pękalak, M., Radkowski, S. *Rubber elastomeric elements* (in polish). PWN, Warszawa, 1989.

[24] Ochelski, S., Bogusz, P., Kiczko, A. Influence of hardness on mechanical properties of elastomers. *Journal of KONES Powertrain and Transport*, vol. 17, no.1 (2010), pp. 317-325.

Krzysztof Michalczyk, Ph.D.: AGH University of Science and Technology, 30 Mickiewicza Avenue, 30-059 Krakow, Poland (*kmichal@agh.edu.pl.edu*). The author gave a presentation of this paper during one of the conference sessions.

Wojciech Sikora, M.Sc. (Ph.D. student): AGH University of Science and Technology, 30 Mickiewicza Avenue, 30-059 Krakow, Poland (*wosikora@agh.edu.pl.edu*).

Model of 4-wheel electric drive vehicle with ESP and ABS system

Tomasz Mirosław, Zbigniew Żebrowski

Abstract: The problem of e-mobility based on electric drive vehicle is very popular. There are several advantages of electric motors over internal combustion engines (ICE) This positive features are not only the lack of poisonous exhausts noise but the torque control over full range as well. Such a feature helps as to use electric motor as the brake, and for 4 wheel drive vehicle as the full electric traction control system. In this paper the concept and model of a 4-wheel drive vehicle is presented. The dynamic 3D model is described with new concept of wheel-surface cooperation which generate longitudinal and lateral forces for tires. The cooperation model is divided into 3 stages: displacement, slip, and attrition of tire, depending on the force generated between road surface and tire. Those forces are conducted though suspension system to the rigid body of vehicle. The vectors of forces act on mass center and are affecting on acceleration or create torques which causes vehicle rotation.

The approach to wheel modeling is easier to be understood and applied for vehicle modelling. As the result the model of vehicle with electric ABS and ESP is presented.

1. Introduction

In the beginning of 20th century the electric and ICE (internal combustion engine) vehicles competed on the market. But the ICE engines had broken their barriers of engine supply with fuel and engine cooling faster and better than electric vehicle overcame their limitation of range and weight.

Today we can observe again the comeback of electric cars on the market of vehicles. Most of the limits are broken. The efficiency of electric motors is over 90%, the capacity of electric cell, efficiency of control units are not technology limitation any more. The newest vehicles of Tesla, BMW, VOLVO are fully electric cars with a satisfying range and an extraordinary comfort of travel and driving.

But we can't say that it is the technology which will be common just after tomorrow. Although the development of electro-mobility is supported by EU governments, politicians who see in this domain the spirit of others domains. The limitation is the price.

Looking at the society development and requirement of pure and ecological environments, the demand of low emission car is the natural consequence of growing and more crowded cities.

Biggest vehicle producers support the trends of low emission ICE, the EU regulations limit the entering old cars into city centers. That all inspires people to buy newer and more expensive cars, but

on the other hand for looking for alternative solution, which could be more ecological than low emission ICE. One of them is the public transport, but the other, more comfortable for people living in the suburbs are electric vehicles, which can be charged from green energy sources like photovoltaic or wind-mils generators. The vehicles dedicated for urban mobility like electric buses or individual cars differ in their requirements to out of cities vehicles.

The car for individual use should be easy to drive and park. But it have to be real car fulfilling all standards of safety: passive and active as well.

2. The concept of 4-wheel drive city car

The concept of a vehicle based on 2 identical driving axles for front and rear with identical electric powertrain, suspension and separated supplying batteries was analyzed. The difference concern only the steering of wheel angles. The rear wheels are blocked and front are steered with a steering wheel. The structure of vehicle is presented in fig. 2.

It could seem to be strange, too expensive solution for a small car. But the idea assumed that one battery would be charged on the board and the second could be replaced.

The second assumption concern the active safety system. The small – short car is less stable than longer one. It seems to be less safe than bigger one. The rear of front drive car has its features and can behave in various ways on the road, especially on the bend. In modern vehicles we have ABS and ESP system which uses the individually controlled brakes keeping the vehicle on a required track.

In the project the assumption is that it can be done by electric motor braking separate front and rear axles.

For analyses of these possibilities the computer model of vehicle was build.

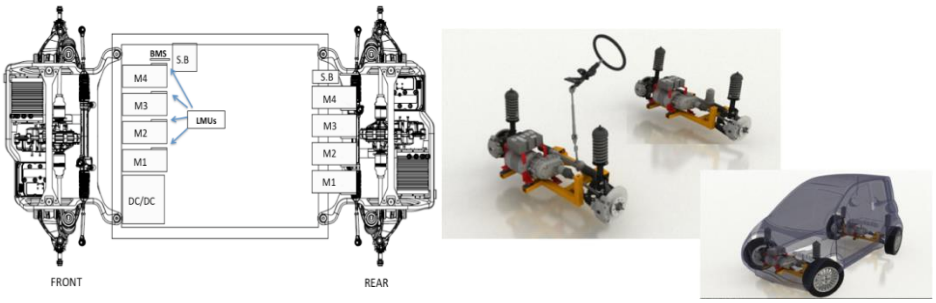

Figure 1. The 4-wheel drive concept according to Free Moby project

3. The principia and analyses for vehicle modelling

In vehicle modelling the following assumptions were made:

- The body (cage) of the vehicle can be treated as a rigid body suspended on four springs with dampers on the wheels.
- The vehicle body rotates around 3 axels changing the loads of the wheels
- The dynamic radius of wheels is constant
- The propelling forces are produced by friction of tires on the road and gravity (the till of road is taken account)
- The steering forces are produced by changing of motor supplying voltage and front wheel turning.
- The wheel can slip, rotate, or stick to the surface.
- The wheel movement friction resistance in two directions (lateral and longitudinal) is the same.
- The tire is modelled in a simplified way as general phenomena's is isometric. The construction specific features are omitted.

4. The model of pneumatic tire

A pneumatic tire is the crucial element in the cooperation of a vehicle with a road. The phenomena which is going on between them decides on vehicle's movement. However the behaviour of the tire is influenced by: temperature of the tire and the road, type of the ground including its moisture content and the most important one i.e. presence of water and loose sand *[5]*. Hence moving layers between the tire and the road arise. The design of a vehicle influences its behaviour: mass distribution, wheel track, toe-in, a way the wheels turn and many others. Despite the fact that many phenomena are known and features influencing the system can be described, there is some disappointment when it comes to the wheel model that would be coherent and backed up with understandable and coherent analysis. Most of the models are based on empirical experiments and observations, often without logical explanation. Although many authors of models base them on Coulomb's model of friction where the force depends on the relative speed of moving and rubbing against each other bodies, at some point they use the model in which the force occurring between a tire and a pavement depends on slip *s [8,10,11,12,13,14,15,16]*.

$$F(s) = N \bullet \mu(s) \tag{1}$$

where: $\boldsymbol{F}$ – propelling force,

$\boldsymbol{N}$ – load (weight of a vehicle),

$\boldsymbol{\mu(s)}$ – friction coefficient depending on slip

Slip does not have any physical representation – it is not possible to measure it and is defined as a result of a mathematical operation:

$$s = 1 - \frac{V}{V_t} \tag{2}$$

where: $\boldsymbol{V}$ – real velocity of a vehicle,

$\boldsymbol{V_t}$ – theoretical velocity (peripheral speed of wheel)

Thus range of the slip for the wheel changes, as said earlier, in the ranges $-\infty < s < 0$ for braking and

$0 < s < 1$ for propelling.

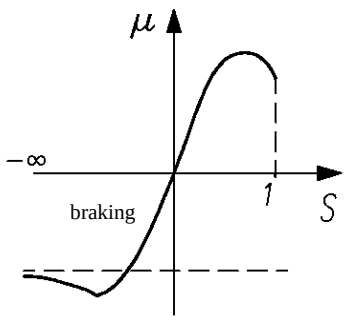

propellin

Figure 2. Diagram of the wheel's slip as a function of the propelling force coefficient *[25]*

5. Characteristic of the most widespread Models of a Wheel

The most popular models that describe cooperation between a tire and a ground are based on the propelling force function depending on a slip *[6,7,10,11,12,14,18,19,20]*.

One of the most common wheel models was developed by Hanse. This model is called "the magic formula". It is written in form:

$$F(s) = d \bullet sin\{c \bullet arctan[b \bullet (1-e) \bullet k + e \bullet arctan(b \bullet k)]\}. \tag{3}$$

Where***:*** ***F(s)*** is the propelling force that depends on s (slip),

b, c, d and ***e*** that represent fitting parameters.

6. Proposition of the model of force generation between wheel and road surface

We can assume that the interaction friction force is generated between a tire and a pavement in the place of their contact and cause the tire blocks displacement. The graphical model is presented in fig. 3 and fig. 4. The wheel is the flexible and resilient with damping element.

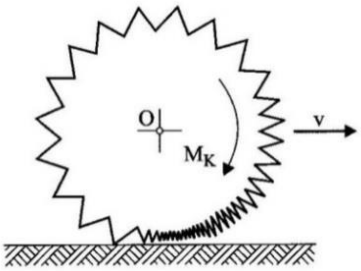

Figure 3. Model of tire deformation [21]

The vehicle propelling force is a result of tyre friction on the road surface. This friction force can be modelled with Columbus model. This force is flowing to the vehicle through deformed by this force tyre. The colobus model is applied for forces lower than critical – attrition force, which above the force is approximately constant.

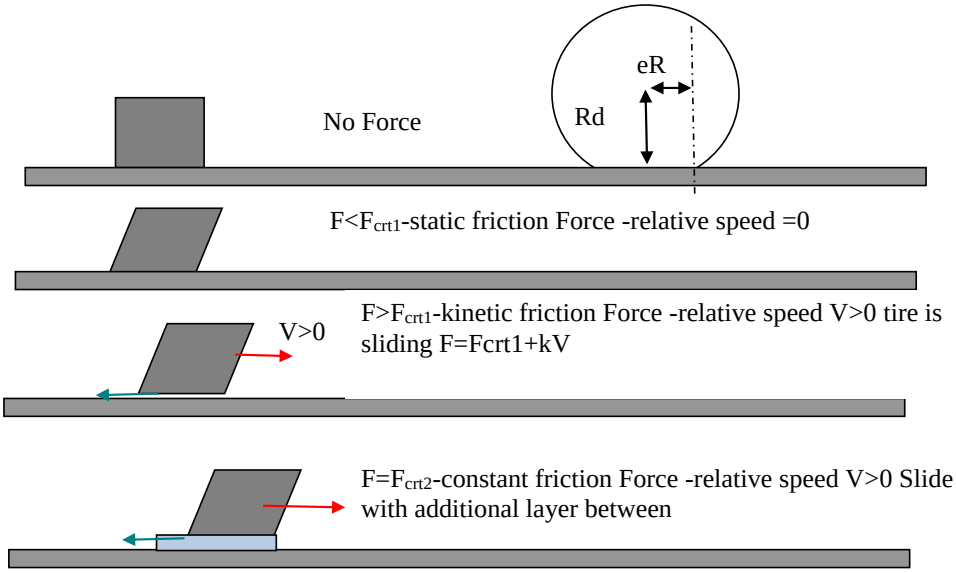

Figure 4. Graphical model of tire block deformation

If we assume that the power flow [27] from engine via wheels and tire to ground is equal:

$P = F_p * v_v$

(4)

Where F_p Is the vehicle propelling force and v_v is the vehicle speed.

The same energy is flowing between tyre and ground.

$P = F_C \Delta V$

(5)

Where the Δv is the relative speed tire to the road surface. Fc is the friction force accordance to Columbus model

$$F_C = K_v \Delta V = k_N N \Delta V$$

(6)

Where the coefficient of Columbus friction in speed relation depends linearly on N-load of tire.

So if we conclude from eq. 1 and eq.3 that:

$F_p = Nk\frac{\Delta V}{v_v} = Nks$

(7)

Where s is the slip defined as $s = \frac{\Delta V}{v_v}$ if take account the nonlinearity we can estimate the propelling force as: $F_p = N\mu(s)$ (eq.1). The Fc is limited by critical value above which the tire is rubbed. It can be characterized by critical slip sm. characterized by critical slip s_m

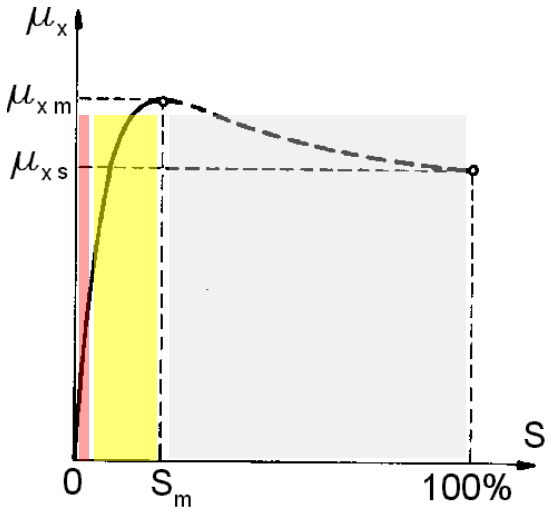

Figure 5. Friction zones: static (red) kinetic (yellow), surface/tire stripping (gray)

The red zone models the deformation of tire without slip, yellow the zone of displacement and slip, and gray one- the slip and rubbed out of tire.

According to the assumption the friction force is isometric, so the zones can be transformed into 2 dimensional system. The Force and zones are referring to the geometrical sum of force and speed vectors, as it is presented in figure.6

According to the assumption the friction does not differ its direction

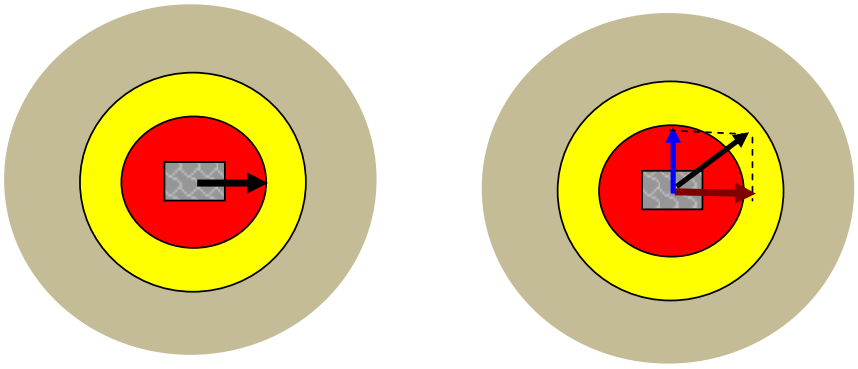

Figure 6. The friction force summing and overcome the border of zones

So the model have to take into account the 2D fiction calculation. It is very important when we model the turning process.

7. The vehicle dynamics model

The vehicle can be treated as the rigid body. The forces generated under the tire act on the centre causing vehicle acceleration in two dimensions. Each “wheel force” can be split out into force laying on the line connecting tire with mass centre Fr and orthogonal Fn. The Fn forces generate rotation torque around vertical axes of vehicle. But if we have four wheels and each generate Fr some torques coming from those forces can compensate each other. The compensated torques give the forces back to the system and they should be summed geometrically like forces Fr and act on mass centre.[21].

We can see that the sum of forces depends on a wheel dislocation, and forces under wheel. When dislocation is symmetric and forces are equal the resultant force acts forward, in other cases can act in various direction.

According to this analyses, sharing the propelling force among axles we can affect the vehicle's movement direction.

Basing on above assumption computer model was built in MATLAB/SIMULIK software.

8. Model description

The general model is presented in fig.7. It consist of a wheel model (green blocks), electric motors (cyan blocks) control unit (yellow block), vehicle kinetics (blue block) external forces (orange block) responsible for gravity ,wind and air speed resistance.

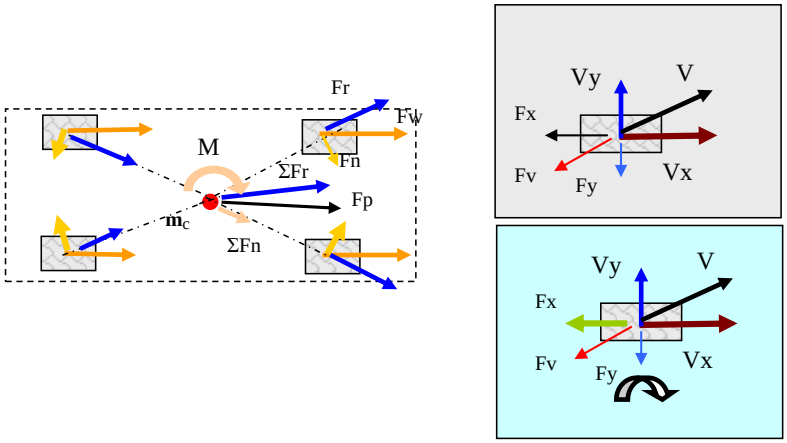

Figure 7. Forces acting for the vehicle

The most interesting part of the model is the wheel and suspension model presented in fig 8 .

In “wheel and suspension” model we have the block of wheel parameters and dimensions where it's dimension, location in reference to mass centre and friction parameter are declared.

Block of force and torque calculation where force and torques values presented in global reference system are recalculated to the reference system joined with vehicle and wheels. It is necessary because the direction of speed and force can be different especially when care is rotating.

The crucial block is the wheel block presented in fig 9. In figure two tracks of a force generation are marked with colours: blue for longitudinal forces, green for lateral forces. In the red the wheel rotation torques and speed are marked. In black the calculation of forces and speed in wheel reference system is presented. The base for force generation is tire deformation represented by Dx and Dy. Between the track we can see the limit blocks which checks the general friction value, and coming out values are proportionally shared between longitudinal and lateral components. The longitudinal forces generate the wheel rotation torques.

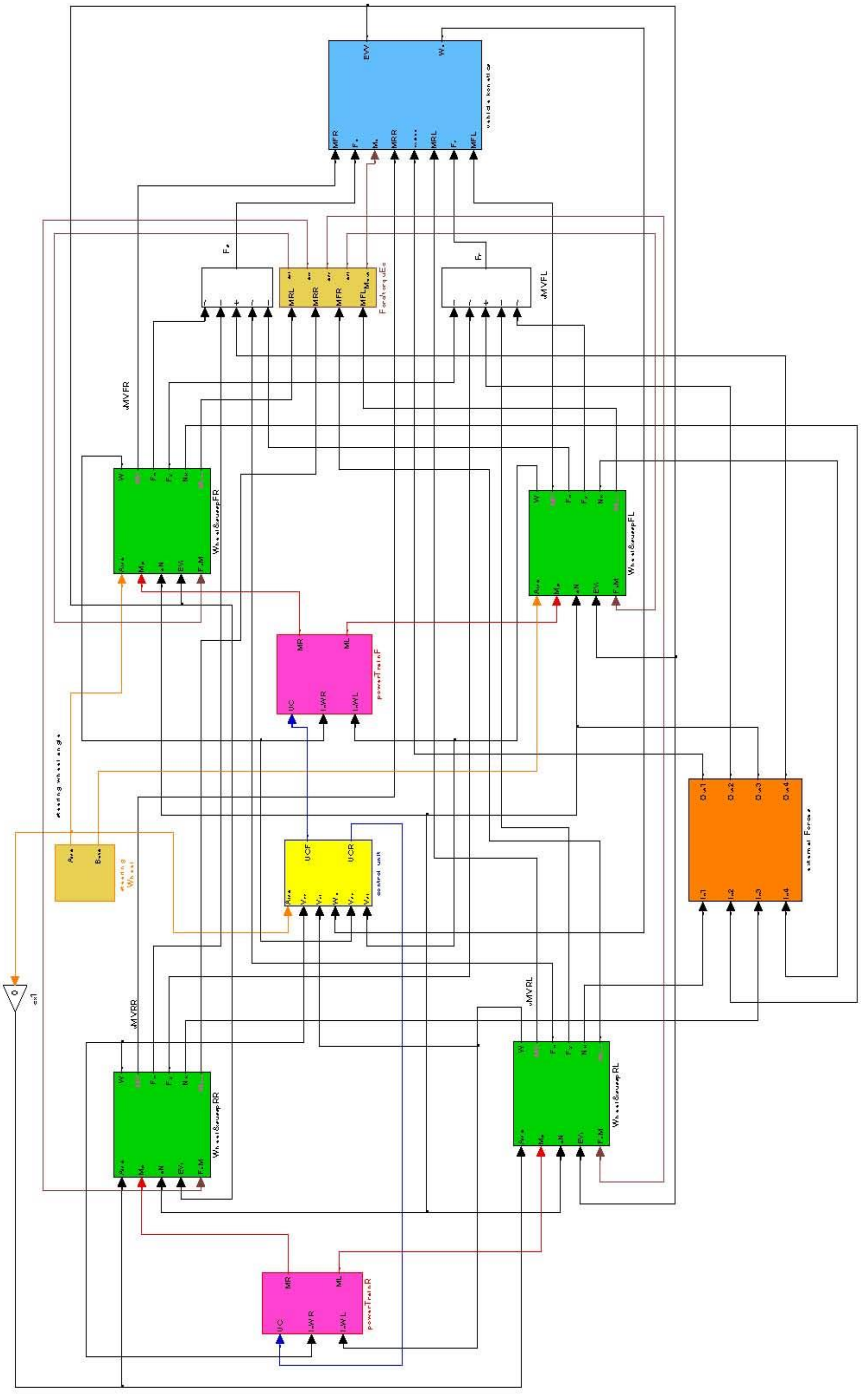

Figure 8. General vehicle model

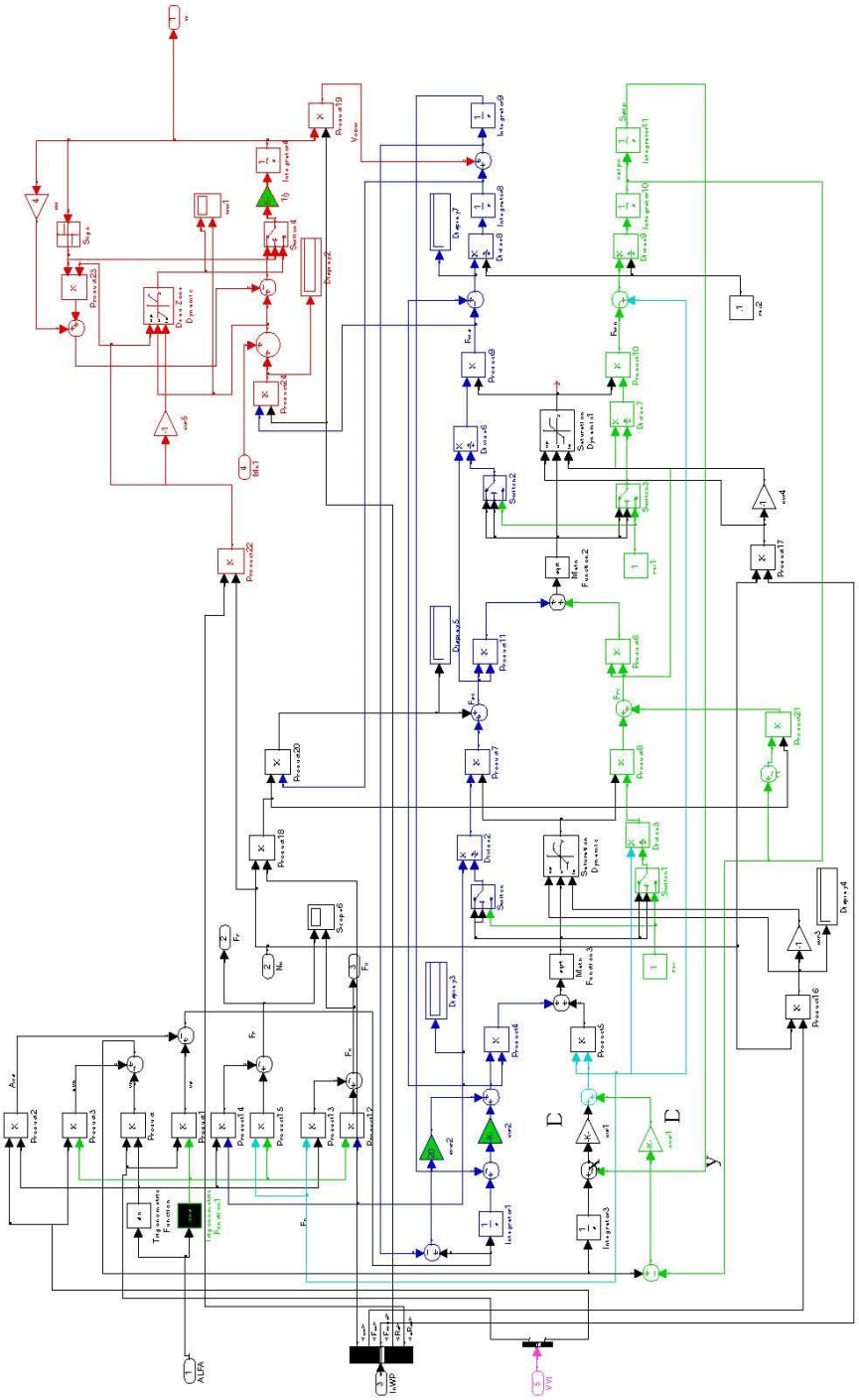

Figure 9. Vheel model

Other blocks are modelled in classical way.

This models were tested and compared with real object tests. Some example of road simulation for bending with growing steering wheel turning are presented in fig.10.

This figure presents the track for vehicle propelled with front axle drive fig. 10a, two axle drive fig.10b, and rear drive fig.10c. We can see that most controllable vehicle is for four wheel drive. In case of only rear axle drive the vehicle relatively early loses the control. Those results reflect real behaviour of vehicle.

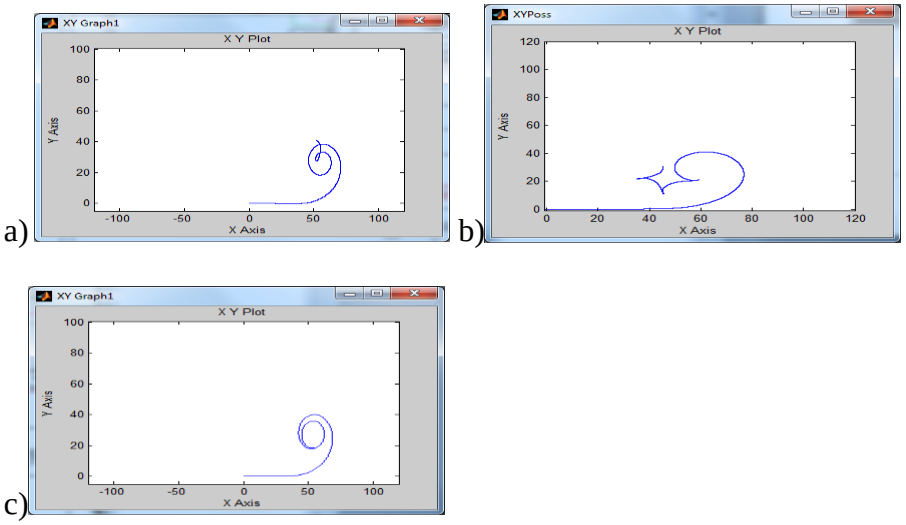

Figure 10. The vehicle trajectory during tests a) for front wheel drive, b) for rear wheel drive, c for 4 wheel drive..

Having such a model some proves of concept of electrical – ABS (e-ABS) and electrical-ESP (e-ESP) were done. The concept is presented in fig 11. The vehicle is pushed on the road side and it starts to rotate in side direction. But the eESP system detects the wheel rotation speed difference and starts to propel front and decrease the speed of rear axle. The vehicle starts to counter rotate and additional force directed to the road appears.

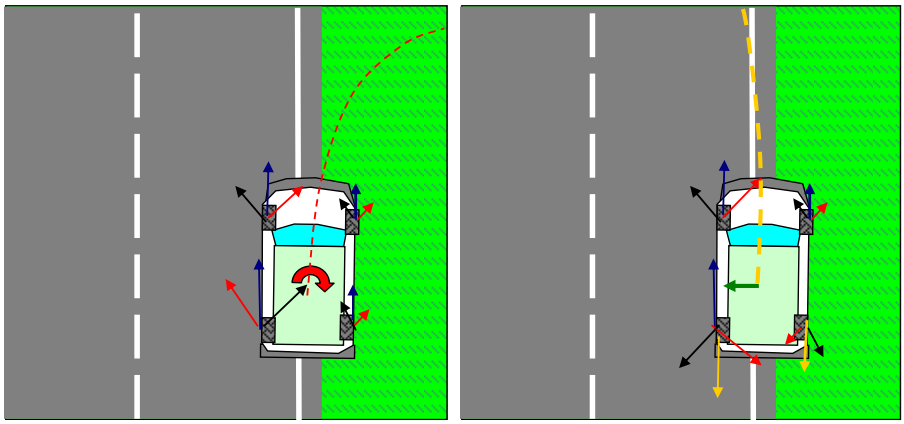

Figure 11. 1 The e-ESP in action on the road side. a) – vehicle without e-ESP b) vehicle with e-ESP.

9. Conclusion

The presented concept of 4-wheel drive urban car has an additional distinguish feature which improves its safety. It enables e-ESP and e-ABS application, improve its stability and traffic controllability.

Presented methodology of a wheel modeling seems to be quite easy to explain and the results are acceptable. The differences between real and simulation tests are only in numbers not in effects. The phenomena going in real are reflected in computer model.

The disadvantage of proposed modeling is the computational time. Presented model of a whole vehicle can't work in real time on a common computer.

After additional tests the model will be optimized for real time application. Probably the real measurement data coming from real vehicle (not calculated in model) will allow to speed up regulator calculation.

Acknowledgments

This paper is the short description of model prepared for ABS and ESP analyses in projects: PLUS MOBY (project ID 605502 FP7-Transport) and FREE MOBY(project ID 608784 FP7-ICT).

References

[1] Roth, Hans (March 2011). Das erste vierrädrige Elektroauto der Welt [The first four-wheeled electric car in the world] (in German). pp. 2–3.

[2] Jump up to: a b Guarnieri, M. (2012). "Looking back to electric cars". Proc.

[3] HISTELCON 2012 - 3rd Region-8 IEEE HISTory of Electro - Technology CONference: The Origins of Electrotechnologies: #6487583. doi:10.1109/HISTELCON.2012.6487583.

[4] Chronologia wydarzeń w upowszechnianiu samochodu elektrycznego. W: Grażyna Jastrzębska: Odnawialne źródła energii i pojazdy proekologiczne. Warszawa: Wydawnictwa Naukowo-Techniczne, 2007, s. 155. ISBN 978-83-204-3250-3

[5] History of Hybrid Vehicles, hybridcars.com, 14 June 2011

[6] Pacejka H. B.: Tyre and vehicle dynamics (2nd ed.). SAE International. (2006).

[7] Pieniążek W.: Obiektywne i subiektywne badania eksperymentalne samochodu osobowego podczas podwójnej zmiany pasa ruchu. Zeszyty instytutu Pojazdów. 2(20)/96

[8] Pokorski J., Szwabik B.: Zmienność współczynnika przyczepności w przekroju poprzecznym i podłużnym drogi. Zeszyty Naukowe Instytutu Pojazdów, 1(40)2001

[9] Bekker M., 1969.: Introduction to terrain-vehicle systems. Michigan Press, An Arbor, USA

[10] Bakker, E. ; Nyborg, L. ; Hans B. Pacejka H. B.: Tyre modelling for use in vehicle dy-namics studies 1987 Jan. Society of Automotive Engineers, Warrendale, PA.

[11] Goriaczkin B.P.: "Theory of Wheel", Moscow 1937.

[12] Grečenko A.: Einflüsse auf die Kraftübertragung von Ackerschlepperreifen. Agrartechnische Kolloquium, Hohenheim, 1989.

[13] Gurkan Erdogan, Tire modelling Lateral and longitudinal Tire Forces Aprill 27, 2009.

[14] Jakliński L., 1999. „Models of pneumatic wheel effecting on the soil" the scientific work Warsaw University of Technology Mechanics edition 175.

[15] Kutzbach D., 1982. Ein Beitrag zur Fahrmechanik der Ackerschleppers-Reifenschlupf, Schleppermasse und Flächenleistung. Grundladen Landtechnik Bd. 32(2).

[16] Mirosław T., Żebrowski Z.: „The steering of front drive switching for wheeled Trac-tors" Mechanical Review 1'01.

[17] Mirosław T., Żebrowski Z.: "Modelling and Simulation of Tractor Differential Mech-anism.; „Mechanical Review" 6'2013.

[18] Pacejka H. B.: The wheel shimmy phenomenon: A theoretical and experimental investigation with particular reference to the nonlinear problem (Analysis of shimmy in pneumatic tires due to lateral flexibility for stationary and no-stationary conditions), Ph.D. Thesis, Delft University of Technology, Delft, 1966.

[19] Pacejka H. B.: Tire and Vehicle Dynamics, Butterworth-Heinemann, Oxford, 2002.

[20] Pacejka H., 2004.: Tyre and Vehicle Dynamics. Elsevier Press

[21] Prochowski L., 2004. "Mechanics of movement" Care Vehicles edition, WKiŁ Warsaw

[22] Pytka J. "Theoretical experimental Study of drive on flexible surface" Lublin Universi-ty of Technology Edition. Lublin 2011

[23] Renius K.T.: Traktoren: Technik und ihre Anwendung. Aufb. – München: BLV Ver-lagsgesellschaft. Frankfurt (Mein)1987.

[24] Schreiber M., Kutzbach H.D., 2007. Comparison of different zero-slip definitions and a proposal to standardize tire traction performance. J. Terramechanics 44.

[25] Zebrowski Z.: The Methodology of wheeled tractor work automation. Scientific Works of Warsaw University of Technology. Mechanics Edition 256 Warsaw 2013

[26] Reimpell J, Betzler J.: Podwozia samochodów. Podstawy konstrukcji. Wydawnictwa

[27] Mirosław T., Żebrowski Z. (2016) The Vehicle Tire Model Based on Energy Flow. In: Awrejcewicz J. (eds) Dynamical Systems: Theoretical and Experimental Analysis. Springer Proceedings in Mathematics & Statistics, vol 182. Springer, Cham

Tomasz Mirosław Ph.D. (Assistant Professor) Warsaw University of Technology Faculty of Automotive and construction Machinery. Institute of construction Machinery Engineering. 84 Narbutta str. 02-524 Warsaw POLAND (tmiroslaw@simr.pw.edu.pl)

Zbigniew Żebrowski Ph.D.. (Professor) Warsaw University of Technology Faculty of Automotive and construction Machinery. Institute of construction Machinery Engineering. 84 Narbutta str. 02-524 Warsaw POLAND (zbigniew.zebrowski@simr.pw.edu.pl)

Influence of pre-stressed zones in beam structures on the modification their modal properties

Milan Naď, Ladislav Rolník, Lenka Kolíková

Abstract: The reduction of harmful effects of vibrations or prevention of their occurrence is one of the important objectives in the design of machine equipment and structures. One of the opportunities how to achieve the desired dynamic behavior for a given structure is to set up or modify its modal properties. Beam structures as one of the fundamental structural element of different machines and structures are considered and modifications of their modal properties are analysed. The application of pre-stressed zones and study of their effect on modal properties (natural frequency, mode shapes) in the beam structures are presented in this paper. The effect of position and magnitude of pre-stressed zone on modal properties of beam structures is investigated.

1. Introduction

The beam structures are a fundamental building elements for many engineering applications. The recent trends tend to the use of lightweight and more flexible beam structures. However, applications of these trends cause problems in beam constructions that become vulnerable to excessive lateral vibrations. These structures are during operating process [1], [5] subjected to the various exciting effects. Very serious problems occur when the frequencies of periodic changes of external loads are close to the values of the tool natural frequencies. As a result of these operating conditions, the resonant states of whole structure are occurring.

It is clear that the dynamical properties of the beam structures are depending on its geometrical parameters and material properties. The beam structure are usually made of homogeneous material and in many cases do not have the required dynamic properties. The beam structures are usually made of homogeneous material and generally do not have to the required dynamic properties. Therefore, the changes are necessary to make in beam structure to meet the requirements to avoid the emergence undesirable dynamic effects. In many cases, it is necessary to eliminate these inconvenient effects by some structural treatments. The techniques of structural modifications [4] which lead to the change of modal properties (natural frequencies, mode shapes) of beam structure is based on application of reinforcing core inserted into beam body and prestressing forces acting in the axial direction of the beam structures.

2. Formulation of the problem

The considered beam structure (see Fig. 1) has the tube shape into which the reinforcing core is inserted. On both side cross sections of core element, the prestressing force effects are applied. The length of core, which is inserted into beam body, is less than the length beam body. The position of the inserted reinforcing core can be changed and then beam structure has three different structural fields. It is clear, that the prestressing forces, the changing the material properties and geometric parameters of reinforcing core induce the change in the distribution of mass and stiffness properties of the modified beam structure [3], which also causes a change in the modal properties. The role of prestressing and reinforcing inner core is to achieve an appropriate modification of distribution of mass and stiffness properties of this beam structure. All this changes also causes a change in the modal properties of given beam structure.

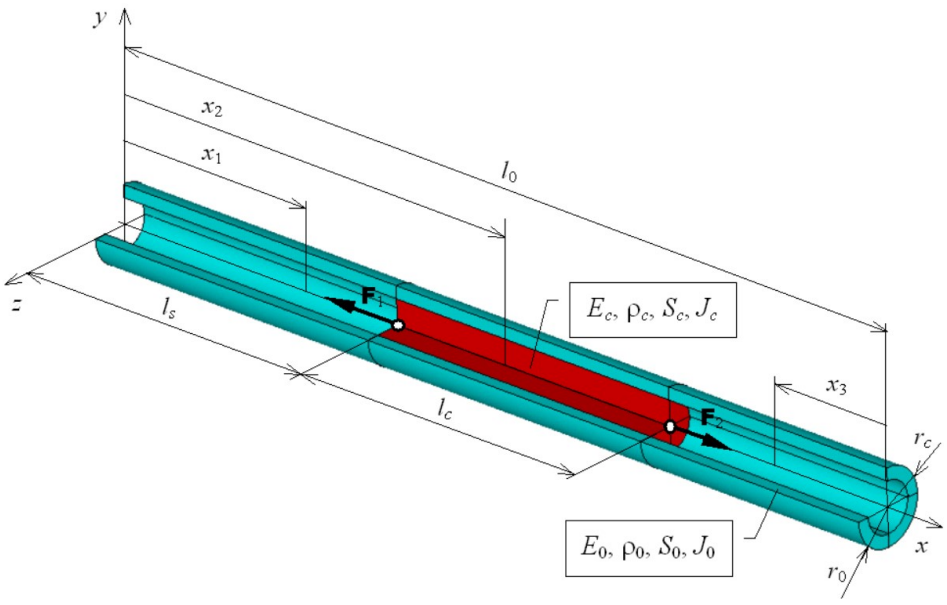

Figure 1. Model of beam structure.

The computational model describing the studied beam structure is based on Euler-Bernoulli beam theory. Two underlying assumptions for the Euler-Bernoulli beam analysis are considered. The first assumption is that the beam is long and slender. In practice, the Euler-Bernoulli theoretical approach is valid when the beam length is minimum 10 times its diameter. Within considered theory, the effects of shear deformation and the rotary inertia are neglected. The Euler-Bernoulli beam theory assumes that the centerline deflection is small and only in the transversal direction.

The following assumptions to the creation of mathematical model of the modified beam structure are considered:

- parts of cross-section of beam structure are lying in plane perpendicular to the neutral axis *x*,
- beam cross-section before and during deformation is assumed as planar,
- cross-sections of basic beam profile and core are symmetrical with respect to both axes *y*, *z*,
- isotropic and homogeneous material properties of the parts of beam structure are considered,
- perfect adhesion at the interface of beam structural parts is supposed.

In accordance with Euler-Bernoulli beam theory, the general equation of motion [2] with axial acting pre-stressed force for each j^{th} segment of beam is written in the form:

$$E_j J_j \frac{\partial^4 w_j(x_j,t)}{\partial x_j^4} - N_j \frac{\partial^2 w_j(x_j,t)}{\partial x_j^2} + \rho_j S_j \frac{\partial^2 w_j(x_j,t)}{\partial t^2} = 0, \tag{1}$$

while in each beam segment, the beam bending stiffness $E_j J_j$ and mass $\rho_j S_j$ are constant. It must be noted that sign minus before force effect N_j is for a tensile load and sing plus is for a compression load.

Introducing the assumed solution $w_j(x_j,t) = W_j(x_j)T(t)$, the Eq. (1) has following form:

$$\overline{W}_j^{VI}(\xi_j) - \alpha_j^2 \overline{W}_j^{II}(\xi_j) - \beta_j^4 \overline{W}_j(\xi_j) = 0, \tag{2}$$

where parameters α_j and β_j are axpressed by:

$$\alpha_j = \sqrt{\frac{N_{r,j}}{E_j J_j} l_0^2} \quad \text{and} \quad \beta_j = \sqrt[4]{\frac{\rho_j S_j}{E_j J_j} l_0^4 \omega_{0m}^2}, \tag{3}$$

and ω_{0m} is natural angular frequency modified beam structure and dimensionless parameters are:

$$\overline{W}_j(\xi_i) = \frac{W_j(x_j)}{l_0}, \qquad \xi_j = \frac{x_j}{l_0}, \qquad \xi_s = \frac{l_s}{l_0}, \qquad \xi_c = \frac{l_c}{l_0}. \tag{4}$$

The eigenvalue problem is:

$$\lambda_{j,k}^4 - \alpha_j^2 \lambda_{j,k}^2 - \beta_j^4 = 0 \tag{5}$$

and eigenvalues are:

$$\lambda_{j,1} = i\eta_{j1}, \qquad \lambda_{j,2} = -i\eta_{j1}, \qquad \lambda_{j,3} = \eta_{j2}, \qquad \lambda_{j,4} = -\eta_{j2}, \tag{6}$$

where:

$$\eta_{j1} = \sqrt{\frac{1}{2}\left[\sqrt{\alpha_j^4 + 4\beta_j^4} - \alpha_j^2\right]}, \qquad \eta_{j2} = \sqrt{\frac{1}{2}\left[\sqrt{\alpha_j^4 + 4\beta_j^4} + \alpha_j^2\right]}. \tag{7}$$

The solution of the Eq. (2) has the following form:

$$\overline{W}_j(\xi_j) = A_{j1}\cos(\eta_{j1}\xi_j) + A_{j2}\sin(\eta_{j1}\xi_j) + A_{j3}\cosh(\eta_{j2}\xi_j) + A_{j4}\sinh(\eta_{j2}\xi_j)\,, \tag{8}$$

where $A_{j1} \div A_{j4}$ are integration constants.

The beam structure (see Fig.1) is fixed on the left edge and on the right edge is free. The boundary conditions are presented in Table 1.

Table 1. Boundary conditions for beam structure (see Fig.1)

$\xi_1 = 0$	$\overline{W}_1(\xi_1)\big\|_{\xi_1=0} = 0$
	$\overline{W}_1'(\xi_1)\big\|_{\xi_1=0} = 0$
$\xi_1 = \xi_s$ $\xi_2 = \xi_s$	$\overline{W}_1(\xi_1)\big\|_{\xi_1=\xi_s} = \overline{W}_2(\xi_2)\big\|_{\xi_2=\xi_s}$
	$\overline{W}_1'(\xi_1)\big\|_{\xi_1=\xi_s} = \overline{W}_2'(\xi_2)\big\|_{\xi_2=\xi_s}$
	$\overline{W}_1''(\xi_1)\big\|_{\xi_1=\xi_s} = \frac{E_2J_2}{E_1J_1}\overline{W}_2''(\xi_2)\big\|_{\xi_2=\xi_s}$
	$\left\{\overline{W}_1'''(\xi_1) - \left(\frac{N_1l_0^2}{E_1J_1}\right)\overline{W}_1'(\xi_1)\right\}\Big\|_{\xi_1=\xi_s} = \frac{E_2J_2}{E_1J_1}\left\{\overline{W}_2'''(\xi_2) - \left(\frac{N_2l_0^2}{E_2J_2}\right)\overline{W}_2'(\xi_2)\right\}\Big\|_{\xi_2=\xi_s}$
$\xi_2 = \xi_s + \xi_c$ $\xi_3 = 1-(\xi_s+\xi_c)$	$\overline{W}_2(\xi_2)\big\|_{\xi_2=\xi_s+\xi_c} = \overline{W}_3(\xi_3)\big\|_{\xi_3=1-(\xi_s+\xi_c)}$
	$\overline{W}_2'(\xi_2)\big\|_{\xi_2=\xi_s+\xi_c} = -\overline{W}_3'(\xi_3)\big\|_{\xi_3=1-(\xi_s+\xi_c)}$
	$\overline{W}_2''(\xi_2)\big\|_{\xi_2=\xi_s+\xi_c} = \frac{E_3J_3}{E_2J_2}\overline{W}_3''(\xi_3)\Big\|_{\xi_3=1-(\xi_s+\xi_c)}$
	$\left\{\overline{W}_2'''(\xi_2) - \frac{N_2l_0^2}{E_2J_2}\overline{W}_2'(\xi_2)\right\}\Big\|_{\xi_1=\xi_s+\xi_c} = -\frac{E_3J_3}{E_2J_2}\left\{\overline{W}_3'''(\xi_3) - \frac{N_3l_0^2}{E_3J_3}\overline{W}_3'(\xi_3)\right\}\Big\|_{\xi_3=1-(\xi_s+\xi_c)}$
$\xi_3 = 0$	$E_3J_3\overline{W}_3''(\xi_3)\big\|_{\xi_3=0} = 0$
	$E_3J_3\left\{\overline{W}_3'''(\xi_3) - \left(\frac{N_3l_0^2}{E_3J_3}\right)\overline{W}_3'(\xi_3)\right\}\Big\|_{\xi_3=1-(\xi_s+\xi_c)} = 0$

$E_1J_1 = E_0J_0$	$E_2J_2 = E_0J_0(1+\Delta_{EJ})$	$E_3J_3 = E_0J_0$
$\rho_1S_1 = \rho_0S_0$	$\rho_2S_2 = \rho_0S_0(1+\Delta_{\rho S})$	$\rho_0S_0 = \rho_0S_0$
$N_1 = -F_1 + F_2$	$N_2 = F_2$	$N_3 = 0$

The intervals for dimensinless parameters ξ_j (j = 1,2,3) are defined as follows:

$$\xi_1 \in \langle 0,\ \xi_s \rangle , \qquad \xi_2 \in \langle \xi_s,\ \xi_s + \xi_c \rangle , \qquad \xi_3 \in \langle 0,\ 1-(\xi_s + \xi_c) \rangle .$$

The parameters $\Delta_{EJ} = \dfrac{E_c J_c}{E_0 J_0}$ and $\Delta_{\rho S} = \dfrac{\rho_c S_c}{\rho_0 S_0}$ characterize the modification of stiffness and mass properties of the beam, where E - Young modulus, ρ - density, S - cross-section area, J - second moment of area (subscript 0 is used for the beam and subscript c is used for the core).

Substituting the solution $\overline{W}_j(\xi_j)$ from the Eq. (8) into the boundary conditions (Table 1), the frequency determinant is created:

$$\begin{vmatrix} \mathbf{A} & \mathbf{B} & \mathbf{0} \\ \mathbf{0} & \mathbf{C} & \mathbf{D} \end{vmatrix} = 0 \quad \Rightarrow \quad \begin{vmatrix} a_{11} & a_{12} & b_{11} & b_{12} & b_{13} & b_{14} & 0 & 0 \\ a_{21} & a_{22} & b_{21} & b_{22} & b_{23} & b_{24} & 0 & 0 \\ a_{31} & a_{32} & b_{31} & b_{32} & b_{33} & b_{34} & 0 & 0 \\ a_{41} & a_{42} & b_{41} & b_{42} & b_{43} & b_{44} & 0 & 0 \\ 0 & 0 & c_{11} & c_{12} & c_{13} & c_{14} & d_{11} & d_{12} \\ 0 & 0 & c_{21} & c_{22} & c_{23} & c_{24} & d_{21} & d_{22} \\ 0 & 0 & c_{31} & c_{32} & c_{33} & c_{34} & d_{31} & d_{32} \\ 0 & 0 & c_{41} & c_{42} & c_{43} & c_{44} & d_{41} & d_{42} \end{vmatrix} = 0 , \tag{9}$$

where the elements of matrices **A**, **B**, **C**, **D** are listed in Appendix.

The parameters η_{j1} and η_{j2} for each segment of beam structure are experessed as follows (supposed for $F_1 = F_2 = F$) :

$$\eta_{11} = \beta_1 , \qquad \eta_{12} = \beta_1 , \tag{10}$$

$$\eta_{21} = \sqrt{\frac{1}{2}\left[\sqrt{\left(\frac{\overline{N}}{1+\Delta_{EJ}}\right)^2 + 4\beta_1^4\left(\frac{1+\Delta_{\rho S}}{1+\Delta_{EJ}}\right)} - \left(\frac{\overline{N}}{1+\Delta_{EJ}}\right)\right]} = \eta_{21}(\beta_1; \Delta_{EJ}, \Delta_{\rho S}, \overline{N}) \tag{11a}$$

$$\eta_{22} = \sqrt{\frac{1}{2}\left[\sqrt{\left(\frac{\overline{N}}{1+\Delta_{EJ}}\right)^2 + 4\beta_1^4\left(\frac{1+\Delta_{\rho S}}{1+\Delta_{EJ}}\right)} + \left(\frac{\overline{N}}{1+\Delta_{EJ}}\right)\right]} = \eta_{22}(\beta_1; \Delta_{EJ}, \Delta_{\rho S}, \overline{N}) \tag{11b}$$

$$\eta_{32} = \beta_1 , \qquad \eta_{31} = \beta_1 , \tag{12}$$

where $\overline{N} = F l_0^2 / E_0 J_0$ is dimensionless axial force. It should be noted that dimensionless axial forces have limitations defined by tensile and buckling conditions, i.e.:

$$N \in (-N_{0,cr}^{buckling}, N_{0,cr}^{tensile}) \quad \Rightarrow \quad \overline{N} \in \left(-\left(\frac{\pi}{\beta}\right)^2, \frac{R_{p0.2}}{E_0}\left(\frac{l_0}{i_0}\right)^2 \right), \tag{13}$$

where β is effective buckling length factor, $R_{p0.2}$ is yield stress, $i_0 = \sqrt{J_0/S_0}$ is radius gyration.

3. Numerical analysis and results

The values of the frequency parameters β_1 for the modified beam structures are obtained by the solution of frequency determinant, the Eq. (9). Using these frequency parameters, the modification function for first natural frequency of vibration the modified beam structure can be expressed. The modification function defined as the ratio of first natural angular frequency of the modified beam structure to first unmodified beam structure is expressed in the form:

$$f_m = 1 + \Delta f_m(\overline{N}, \Delta_{EJ}, \Delta_{\rho S}, \xi_s, \xi_c) = \frac{\omega_{0m}}{\omega_0} = \left(\frac{\beta_1}{\beta_0}\right)^2 . \tag{13}$$

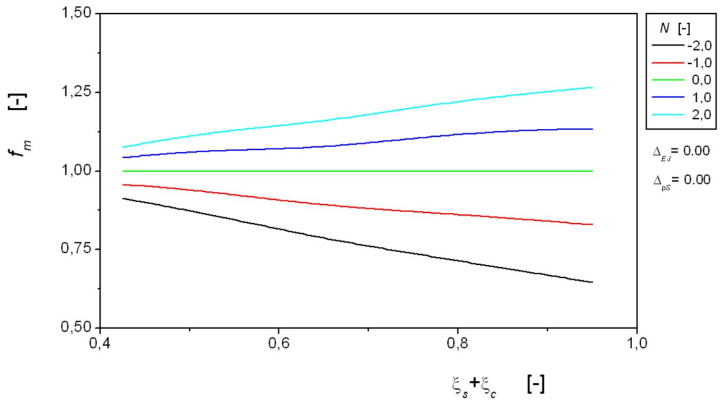

Figure 2. Dependency of modification function f_m on core position ($\Delta_{EJ} = 0.0; \Delta_{\rho S} = 0.0$).

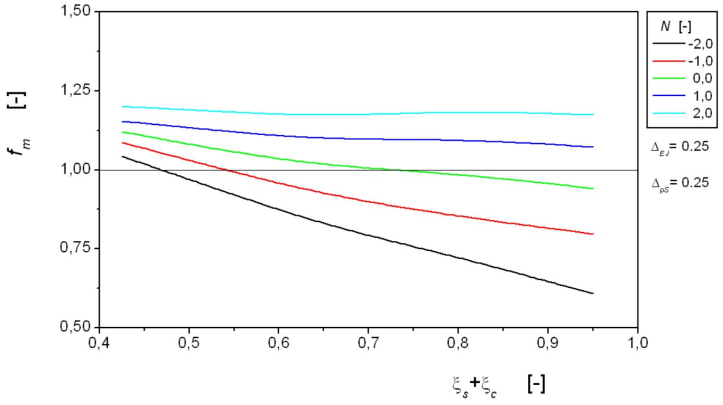

Figure 3. Dependency of modification function f_m on core position ($\Delta_{EJ} = 0.25; \Delta_{\rho S} = 0.25$).

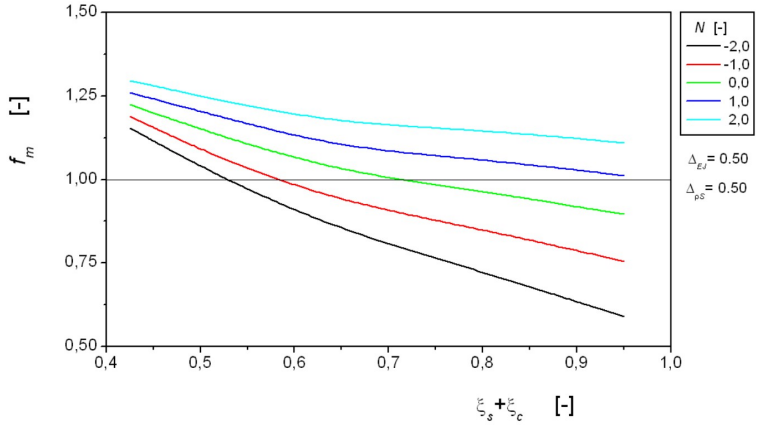

Figure 4. Dependency of modification function f_m on core position ($\Delta_{EJ} = 0.5; \Delta_{\rho S} = 0.5$).

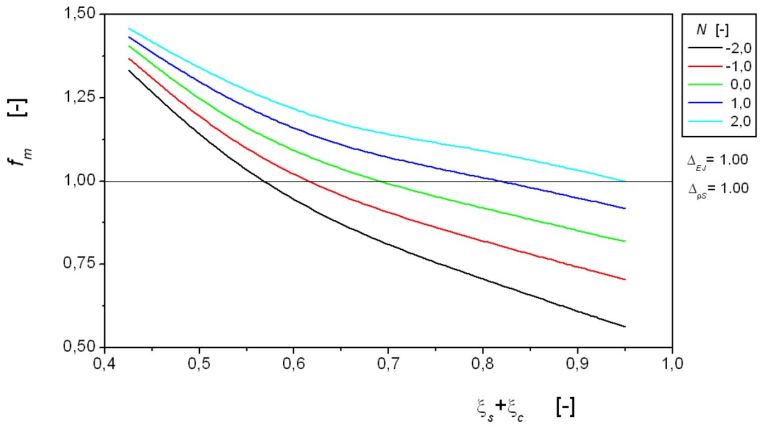

Figure 5. Dependency of modification function f_m on core position ($\Delta_{EJ} = 1.0; \Delta_{\rho S} = 1.0$).

The dependence of modification function of first natural frequency on core location ξ_s ($\xi_c = 0{,}4$) for different modifications parameters $\overline{N}, \Delta_{EJ}, \Delta_{\rho S}$ are shown in Fig. 2 - Fig. 5. If the pressure load is applied in a certain prestressing zone of the beam, the value of the modification function decreases. Contrary to this, in the case of application of tensile prestressing, the modifying function is increasing. The aplication of stiffness and mass modifification (see Fig. 3 - Fig. 5) causes for specified parameters decreasing of the modification function when the value of parameter core position ξ_s is growing.

4. Conclusions

The modification of dynamical properties of clamped beam structure by prestressing force effects and reinforcing core is presented in this paper. Structural modification of the beam structure by tensile, resp. pressure forces and the position and length insertion of the reinforcing core with uniform cross-section provides an effective way to change of the beam structures modal properties. By changing modification parameters $\overline{N}$, Δ_{EJ} , $\Delta_{\rho S}$, ξ_s , ξ_c is possible to achieve a significant modification of natural frequencies of the beam structure (see Fig. 2). The results obtained confirm that this manner of the structural modification of beam offers a very effective tool to the modification of dynamical properties or to the dynamical tuning of the similar beam structures.

Acknowledgments

This work was supported by the poject VEGA 1/1010/16 and project IP MTF 1603/2017.

References

[1] Izrael G., Bukoveczky J., Gulan L., Influence of nonstandard loads onto life of chosen modules of Mobile Working Machines, *Machine Design*, **3** (1), (2011), 13-16.

[2] Meirovitch, L. *Analytical methods in vibrations*, McMillan Company, London, 1987.

[3] Naď M., Rolník L., Čičmancová L. Prediction of changes in modal properties of the Euler–Bernoulli beam structures due to the modification of its spatial properties, *Int. Journal of Structural Stability and Dynamics*, Vol. 17, No. 5 (2017) (13 pages)

[4] Naď M. *Modification of Modal Characteristics of Vibrating Structural Elements*. Scientific Monographs, Köthen, (2010), 92 pages.

[5] Rolník, L. *Structural dynamic modification of lathe tool body.* Ph.D. thesis, Slovak University of Technology in Bratislava, Faculty of Materials Science and Technology, 2015, supervisor - M. Naď

[6] Sága M., Žmindák M., Dekýš V., Sapietová A., Segľa Š., *Selected Methods for the Analysis and Synthesis of Mechanical Systems*. VTS ZU, Zilina, 2009, (in Slovak).

Appendix

$$a_{11} = \cos(\beta_1\xi_s) - \cosh(\beta_1\xi_s) \qquad a_{12} = \sin(\beta_1\xi_s) - \sinh(\beta_1\xi_s)$$

$$a_{21} = -\beta_1\left(\sin(\beta_1\xi_s) + \sinh(\beta_1\xi_s)\right) \qquad a_{22} = \beta_1(\cos(\beta_1\xi_s) - \cosh(\beta_1\xi_s))$$

$$a_{31} = -\beta_1^2\left(\cos(\beta_1\xi_s) + \cosh(\beta_1\xi_s)\right) \qquad a_{32} = -\beta_1^2(\sin(\beta_1\xi_s) + \sinh(\beta_1\xi_s))$$

$$a_{41} = \beta_1^3(\sin(\beta_1\xi_s) - \sinh(\beta_1\xi_s)) \qquad a_{42} = -\beta_1^3(\cos(\beta_1\xi_s) + \cosh(\beta_1\xi_s))$$

$$b_{11} = -\cos(\eta_{21}\xi_s) \qquad b_{12} = -\sin(\eta_{21}\xi_s)$$

$$b_{21} = \eta_{21}\sin(\eta_{21}\xi_s) \qquad b_{22} = -\eta_{21}\cos(\eta_{21}\xi_s)$$

$$b_{31} = \eta_{21}^2(1+\Delta_{EJ})\cos(\eta_{21}\xi_s) \qquad b_{32} = \eta_{21}^2(1+\Delta_{EJ})\sin(\eta_{21}\xi_s)$$

$$b_{41} = -\eta_{21}(\overline{N} + \eta_{21}^2(1+\Delta_{EJ}))\sin(\eta_{21}\xi_s) \qquad b_{42} = \eta_{21}(\overline{N} + \eta_{21}^2(1+\Delta_{EJ}))\cos(\eta_{21}\xi_s)$$

$$b_{13} = -\cosh(\eta_{22}\xi_s) \qquad b_{14} = -\sinh(\eta_{22}\xi_s)$$

$$b_{23} = -\eta_{22}\sinh(\eta_{22}\xi_s) \qquad b_{24} = -\eta_{22}\cosh(\eta_{22}\xi_s)$$

$$b_{33} = -\eta_{22}^2(1+\Delta_{EJ})\cosh(\eta_{22}\xi_s) \qquad b_{34} = -\eta_{22}^2(1+\Delta_{EJ})\sinh(\eta_{22}\xi_s)$$

$$b_{43} = \eta_{22}(\overline{N} - \eta_{22}^2(1+\Delta_{EJ}))\sinh(\eta_{22}\xi_s) \qquad b_{44} = \eta_{22}(\overline{N} - \eta_{22}^2(1+\Delta_{EJ}))\cosh(\eta_{22}\xi_s)$$

$$c_{11} = \cos(\eta_{21}(\xi_s + \xi_c)) \qquad c_{12} = \sin(\eta_{21}(\xi_s + \xi_c))$$

$$c_{21} = -\eta_{21}\sin(\eta_{21}(\xi_s + \xi_c)) \qquad c_{22} = \eta_{21}\cos(\eta_{21}(\xi_s + \xi_c))$$

$$c_{31} = -\eta_{21}^2\cos(\eta_{21}(\xi_s + \xi_c)) \qquad c_{32} = -\eta_{21}^2\sin(\eta_{21}(\xi_s + \xi_c))$$

$$c_{41} = \eta_{21}\left(\frac{\overline{N}}{1+\Delta_{EJ}} + \eta_{21}^2\right)\sin(\eta_{21}(\xi_s + \xi_c)) \qquad c_{42} = -\eta_{21}\left(\frac{\overline{N}}{1+\Delta_{EJ}} + \eta_{21}^2\right)\cos(\eta_{21}(\xi_s + \xi_c))$$

$$c_{13} = \cosh(\eta_{22}(\xi_s + \xi_c)) \qquad c_{14} = \sinh(\eta_{22}(\xi_s + \xi_c))$$

$$c_{23} = \eta_{22}\sinh(\eta_{22}(\xi_s + \xi_c)) \qquad c_{24} = \eta_{22}\cosh(\eta_{22}(\xi_s + \xi_c))$$

$$c_{33} = \eta_{22}^2\cosh(\eta_{22}(\xi_s + \xi_c)) \qquad c_{34} = \eta_{22}^2\sinh(\eta_{22}(\xi_s + \xi_c))$$

$$c_{43} = -\eta_{22}\left(\frac{\overline{N}}{1+\Delta_{EJ}} - \eta_{22}^2\right)\sinh(\eta_{22}(\xi_s + \xi_c)) \qquad c_{44} = -\eta_{22}\left(\frac{\overline{N}}{1+\Delta_{EJ}} - \eta_{22}^2\right)\cosh(\eta_{22}(\xi_s + \xi_c))$$

$$d_{11} = -\left(\cos(\beta_1(1-\xi_s-\xi_c)) + \cosh(\beta_1(1-\xi_s-\xi_c))\right)$$

$$d_{12} = -\left(\sin(\beta_1(1-\xi_s-\xi_c)) + \sinh(\beta_1(1-\xi_s-\xi_c))\right)$$

$$d_{21} = -\beta_1\left(\sin(\beta_1(1-\xi_s-\xi_c)) - \sinh(\beta_1(1-\xi_s-\xi_c))\right)$$

$$d_{22} = \beta_1\left(\cos(\beta_1(1-\xi_s-\xi_c)) + \cosh(\beta_1(1-\xi_s-\xi_c))\right)$$

$$d_{31} = \frac{\beta_1^2}{1+\Delta_{EJ}}\left(\cos(\beta_1(1-\xi_s-\xi_c)) - \cosh(\beta_1(1-\xi_s-\xi_c))\right)$$

$$d_{32} = \frac{\beta_1^2}{1+\Delta_{EJ}}\left(\sin(\beta_1(1-\xi_s-\xi_c)) - \sinh(\beta_1(1-\xi_s-\xi_c))\right)$$

$$d_{41} = \frac{\beta_1^3}{1+\Delta_{EJ}}\left(\sin(\beta_1(1-\xi_s-\xi_c)) + \sinh(\beta_1(1-\xi_s-\xi_c))\right)$$

$$d_{42} = -\frac{\beta_1^3}{1+\Delta_{EJ}}\left(\cos(\beta_1(1-\xi_s-\xi_c)) - \cosh(\beta_1(1-\xi_s-\xi_c))\right)$$

Milan Naď, Associated Professor: Slovak University of Technology, Faculty of Materials Science and Technology, Instutute of Informatics, Automation and Mechatronics, Department of Applied Mechanics and Mechtronics, J. Bottu 25, 917 24 Trnava, Slovak Republic (*milan.nad@stuba.sk*). "The author gave a presentation of this paper during one of the conference sessions."

Ladislav Rolník, Ph.D.: Slovak University of Technology, Faculty of Materials Science and Technology, Instutute of Informatics, Automation and Mechatronics, Department of Applied Mechanics and Mechtronics, J. Bottu 25, 917 24 Trnava, Slovak Republic (*ladislav.rolnik@stuba.sk*)

Lenka Kolíková, Ph.D.: Slovak University of Technology, Faculty of Materials Science and Technology, Instutute of Informatics, Automation and Mechatronics, Department of Applied Mechanics and Mechtronics, J. Bottu 25, 917 24 Trnava, Slovak Republic (*lenka.kolikova@stuba.sk*).

Dynamic properties of pipes in different geometries with pulsating flows in transient states (sweeping up and down) under various temperature conditions

Tomasz Pałczyński,

Abstract: Understanding the dynamic properties of pipes with pulsating flows in transient states (sweeping up and sweeping down) is of great interest for ensuring efficient fluid transportation, including in process plants, the power and chemical industries, in compressed air systems and in automobiles. Pulsating flows can occur during start-stop procedures and due to frequency changes related to the system requirements. In this study, a test rig was prepared to investigate the flow parameters of pipes with pulsating flows, with a wide range of changes in pulsation frequency and intensity, in two directions (up and down). The proposed procedure enables complex analysis of the transient states of pipes with pulsating flows. Three fields were measured: air temperature from 305 K to 343 K and pipe geometry determined by different partially-closed end ratios from 15% to 35%. The experimental results were analyzed in the Matlab environment using the classical Short Fast Fourier Transform and the author's own version of this algorithm. Amplitude frequency characteristics under the influence of two dominant cases (sweeping up and down) were also estimated and compared using relative and absolute values. The results are significant for understanding the transient stages of flow phenomena along pipelines with pulsating flows, with possible industrial applications.

1. Introduction

This work builds on the method for researching instantaneous flow parameters under sine swept constraints proposed in [1]. Its aim was to estimate the amplitude frequency characteristics of pulsating flows in pipes with different air temperatures and pipe geometries. Generally, sweep harmonic constraints enable faster acquisition of whole-spectrum resonance characteristics. Swept input is a natural extension of the classical sinusoidal signal used for dynamic system response testing. It is used in simulations designed to estimate bode characteristics, including in turbomachinery (for spectral and modal analysis of rotors [2]), process and mechanical engineering (sine sweep vibration testing), acoustics [3,4] and automotive engineering (sweeping automotive suspension [5]). The proposed method was used in [6] in an acoustic investigation of pipe flows. Sweeping was limited to only one tone in each sweep step, because of the high level of turbulent noise generated by the mean flow [7]. Multi-reference sine sweep tests are conducted in the aircraft industry for estimating ground vibrations.

Testing time can be minimized and the block size maximized by performing wrapped sweeps, in which the frequency difference between each source is maximized over the full frequency range of the test [8]. However, to the best knowledge of the author, no results have been published for swept inputs and pulsating flows in pipes, and no similar studies to that presented here have been conducted. In particular, this paper investigates the influence of a down- and up-sweep input method on the resulting resonance frequency. The intensity of the sweeping sine frequency process was defined as a sweep rate expressed in [s] units. This describes the number of seconds needed to change the pulsation frequency from 0 Hz to 200 Hz.

2. Research goals

A test rig was prepared to investigate the transitional states of varying pulsation frequencies in pipes. In what follows, the results will be presented of a series of measurements taken during various frequency changes. The main flow parameters evaluated were pressure, temperature and mass flow, measured at three control sections. The test procedure also examined the frequency change domain, in terms of initial and final values. The change in frequency was calculated based on the step function. The amplitude frequency characteristics were estimated using the Curve Fitting function in Matlab software [1]. Estimates were based on second-order inertial elements, and provide quite a good representation of the acquired data [1].

3. Test rig – main assumptions

The following assumptions were made:

- Real measurements taken during transitional states of pulsation frequency changes (from 20 Hz to 180 Hz) in pipes. The main features of the test rig are presented in Figure 1, including the pulse generator (PG) and three control sections (0, K, 3).
- A simplified Simulink model designed to estimate local pulsation amplitude and amplitude-frequency characteristics [1].
- An analysis of the influence of frequency change in a range of amplitudes from 20 Hz to 180 Hz on air pressure during pulsation changes at three control sections.
- Measurements showing resonant frequency changes with increasing and decreasing pulsation frequencies.
- Proposed parameters for estimating second-order inertial elements (the damping coefficient and resonant frequency), to describe the observed phenomena.
- Assessment of the impact of the sine swept constraint on amplitude-frequency characteristics.

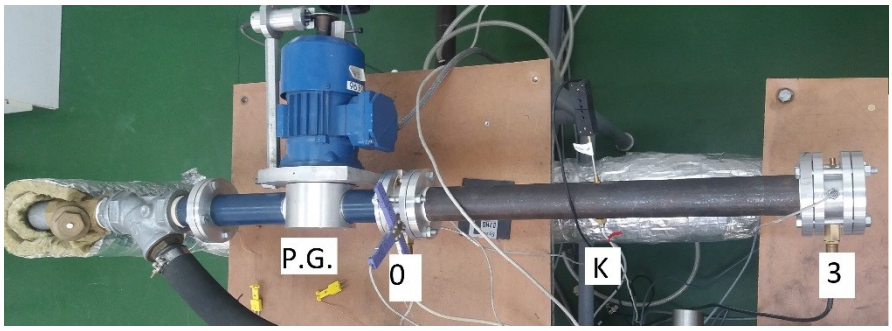

Figure 1. Main elements of the test rig [1]. *P.G. – pulse generator, O,K,3 tested cross sections*

The main parameters are as follows:

- Range of desired values for the frequency of the pulse generator $f = (20 \div 180)$ [Hz].
- Pipe diameter $D_p = 42\ 10^{-3}$[m].
- Pipe length $L_p = 0{,}544$ [m], determined with resonance at 70 Hz and 140 Hz.
- Nozzle diameter $D_n = 10 * 10^{-3}$ [m]. The nozzle is mounted at one end of the pipe, at cross section (3).
- Desired flow temperature $T = 313{,}15$ [K].
- Mean Flow speed $u = 20$[m/s] (mean value).
- Mean Pressure $p = 115000$ [Pa].

Transient and mean values for pressure, temperature and specific mass flow rate were measured at control sections (0) and (3), shown in Figure 4, where the yellow arrows mark the direction of flow. Transient pressure was also measured in section (K), located in the middle of the length of pipe.

Analysis of the dynamic properties of the pipes was performed using the second-order oscillating element as the reference, parametrizing objectively the differences between particular cases. It was thereby possible to approximate the swept frequency probe with a coefficient of determination greater than 95% ($R^2 > 0.95$). Second-order oscillating elements were estimated using equation (1) and the Curve Fitting Tool, with custom equation settings and default 95% confidence bounds:

$$M(f) = \left\{\left[1 - \left(\frac{f}{f_n}\right)^2\right]^2 + \left[\frac{2\zeta f}{f_n}\right]^2\right\}^{-1/2} \tag{1}$$

Where:

$M(f)$ – magnitude of oscillations [-]

f_n – resonance frequency [Hz]

ζ – relative damping coefficient [-]

Experiments were conducted with different intensities of sweeping (sweep rate from 1-9 s), with different diameters of nozzle (Table 1) and at various temperatures (Table 2).

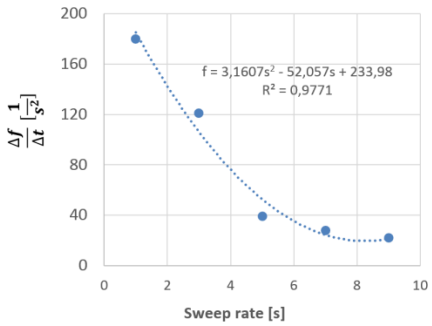

Table 1. Nozzle diameters [$\cdot 10^{-3}\ m$]

7,5	10	12,5	15

Table 2. Temperatures [K]

303	313	323	328	333
335,5	338	341	343	

Figure 2. Frequency increase over time as a sweep rate function

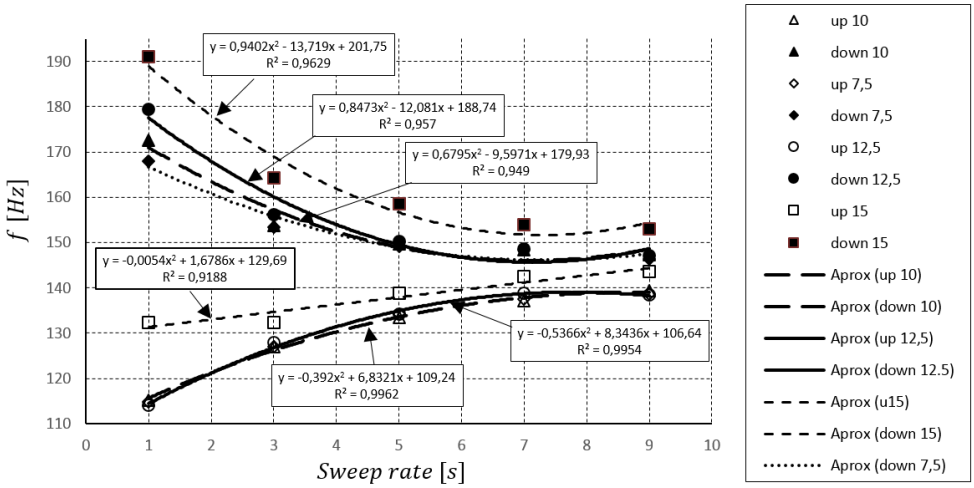

Figure 3. Natural frequency as a sweep rate function for chosen nozzle diameters

The influence on the natural frequency of the chosen nozzle diameters is presented in Figure 3. The results were approximated based on a second-order polynomial fit, with "smile" shaped positive direction factored parabolas representing sweeping down mode and "sad" negative direction factored parabolas representing seeping up mode. Generally, nozzle diameters greater than $15 * 10^{-3}m$ had a noticeable influence on the natural frequency as an function of the sweep rate. The mean natural frequency (at all considered sweeping rates) increased by 6% from 142 Hz to 151 Hz. Irrespective of nozzle diameter, there was noticeable influence on the sweeping rate below 5 s, as discussed in detail in [1].

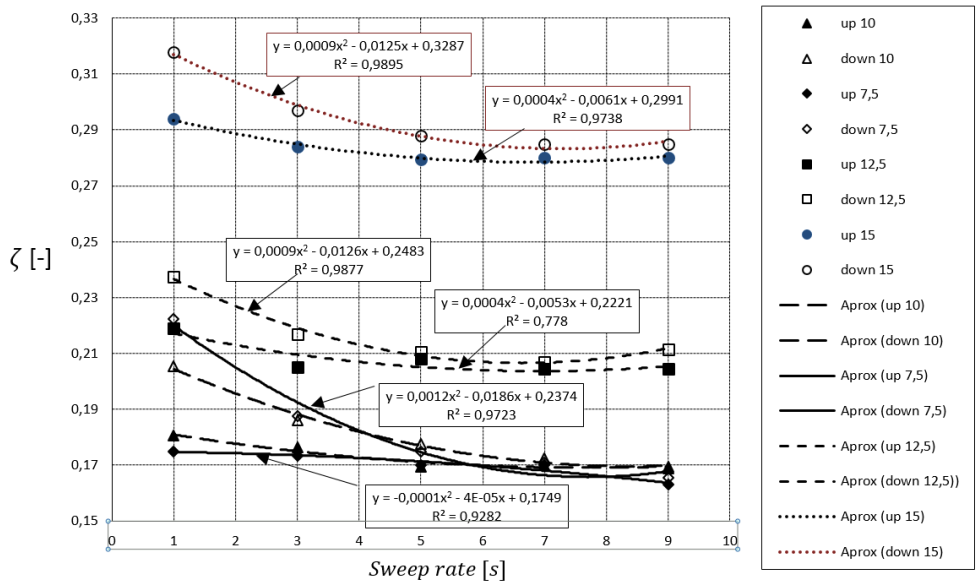

Figure 4. Relative damping coefficient as a sweep rate function for chosen nozzle diameters.

Nozzles with diameters of $7.5 \cdot 10^{-3}\ m$ and $10 \cdot 10^{-3}\ m$ had no influence on the relative damping coefficient. However, as shown in Figure 4, a nozzle with a diameter of $12.5 \cdot 10^{-3}\ m$ had a significant influence on the mean value of the damping coefficient, from 0.177 to 0.212. This was a 20% increase relative to the reference $10 \cdot 10^{-3}\ m$ nozzle. With a nozzle $15 \cdot 10^{-3}\ m$ in diameter, there was an even more significant increase in the mean value of the damping coefficient, from 0.177 to 0.292 – a 65% increase relative to the reference $10 \cdot 10^{-3}\ m$ nozzle.

Much more interesting results were obtained for the influence of temperature on the natural frequency, as shown in Figure 5, and on the relative damping coefficient, presented in Figure 6. The presented meshed graphs were processed using the Curve Fitting Toolbox in the Matlab environment. Polynomial approximation was used with 4 degrees of freedom along both domain axes (temperature and sweep rate). As can be seen, for high sweep rates in both modes (sweeping up – Figure 5a – and down – Figure 5b) there was a quite linear increase in the natural frequency as the temperature increased. In sweeping down mode, the linear increase in the natural frequency due to temperature was rather constant, at approximately 15 Hz (10%), with a sweeping ratio of around 3s. At lower sweep rates (between 1s and 3s) the natural frequency ceased to be temperature dependent.

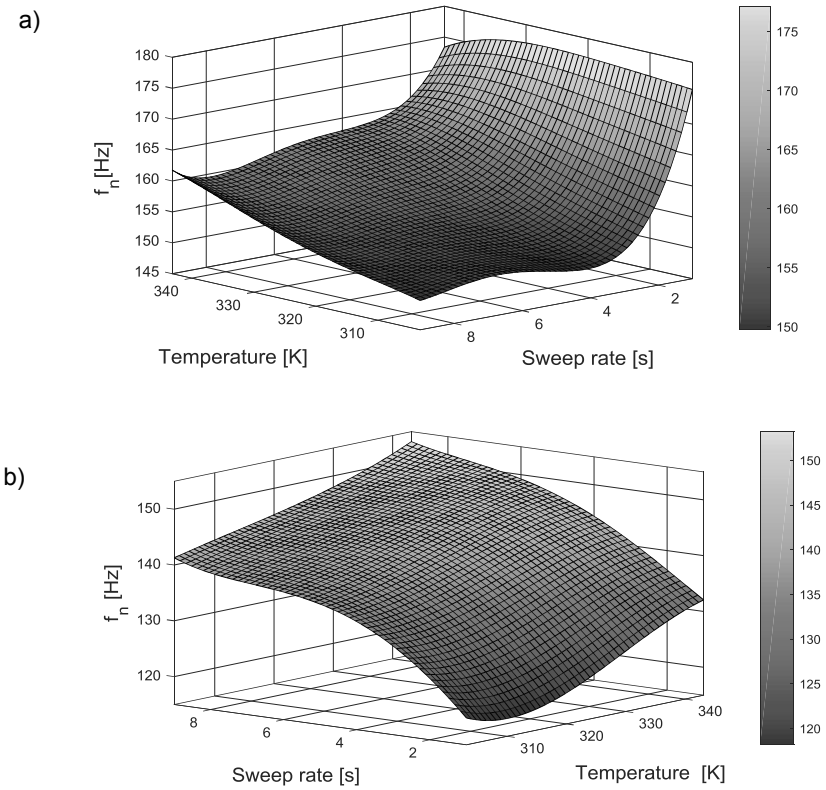

Figure 5. a) Natural frequency of the tested pipe as a function of sweep rate and temperature in sweep down mode b) Natural frequency of the tested pipe as a function of sweep rate and temperature in sweep up mode.

In sweep up mode, natural frequency has a rather linear dependency on temperature, as shown in Figure 5b. It is worth noticing the "sharp dip" at low temperatures and sweep rates.

An increase in the natural frequency was observed, from 140 Hz to 152 Hz (8.6 %). At low sweep rates, there was minimal increase in the natural frequency at medium temperature of around 320 K in sweeping down mode. In sweeping up mode, there was a similar increase in the natural frequency, from 120 Hz to 132 Hz (10%). The changes in the relative damping coefficient due to temperature and in the sweeping rate domain were much more interesting than the variations in natural frequency. Figures 6a and 6b provide an overview of the results, with the relative damping coefficient presented relative to the sweeping rate and air temperature domain.

In sweeping down mode, different monotonous variations were observed due to different sweeping intensities. For high sweep rates (between 5 and 9) there were noticeably decreases in the relative

damping coefficient (from 0.16 to 0.14-15%), due to air temperature increases. At low sweep rates (from 1s to 2s), distinct changes in the damping coefficient were observed. Monotonousness is clearly positive and the relative damping coefficient changed from 0.205 to 0.225, around 10%. In sweeping up mode, there no monotonous sign change was observed. Across the whole range (apart from the middle area) there is a rather constant decrease in the relative damping coefficient of around 8%.

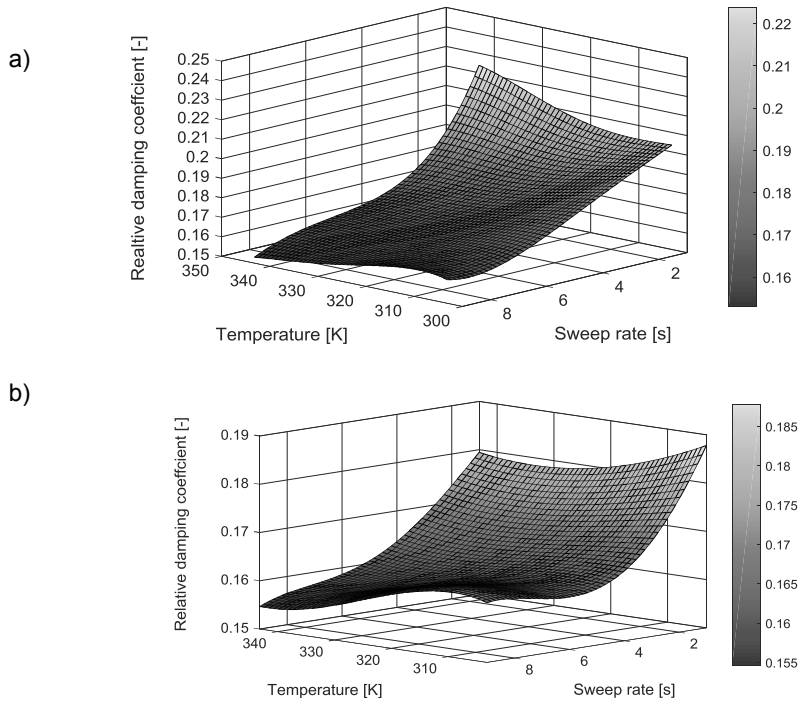

Figure 6. a) Relative damping coefficient as a function of sweep rate and temperature in sweep down mode b) Relative damping coefficient as a function of sweep rate and temperature in sweep up mode.

4. Conclusions

In this study, nozzle diameter and air temperature were found to influence the dynamic properties of pipes supplied with pulsating flows. The results were presented in two ways: polynomial approximation of the influence of the nozzle diameter and three-dimensional maps. It can be used for modeling the control system of the described system. Hybrid modeling of the presented phenomenon is therefore possible, using correction matrixes relating linear dynamics with nonlinear object properties implemented as empirical data. This hybrid modeling method could provide more accurate dynamic models of the existing test stand, including the nonlinear properties of the process.

The approximated polynomial curves and three-dimensional maps elaborated in this study could have applications in process, mechanical and automotive engineering, as well as for turbomachinery. The identified changes in natural frequency and relative damping coefficients could be used to improve the efficiency of machines, including the test system. Understanding the dynamic properties of pipes with pulsating flows can help to prevent damage during start-stop processes. Further research should focus on estimating the resonant frequencies of the tested pipes and developing a hybrid model of the presented system, with a modified equilibrium equation including the influence of different nozzles and air temperatures.

References

[1] Pałczyński, T, Impact of frequency change rate on instantaneous flow parameters in pipes, Advances in condition monitoring of machinery in non-stationary operations, 2017, in press.

[2] Kozanecka D. , Z. Kozanecki, J. Łagodziński, Active magnetic damper in a power transmission system, Communications in Nonlinear Science and Numerical Simulation, Volume 16, Issue 5, May 2011, Pages 2273-2278, ISSN 1007-5704, http://dx.doi.org/10.1016/j.cnsns.2010.04.044.

[3] Farina A., Simultaneous measurement of impulse response and distortion with a swept sine technique, 108th AES Convention, Paris, France, February 2000.

[4] Müller S., Massarini P, Transfer-Function Measurement with Sweeps, J. Audio Eng. Soc., vol.49, pp. 443-471, June 2001.

[5] Konieczny L, Analysis of simplification applied in Vibrating Damping Modelling for Passive Car Shock Absorber, Shock and Vibration, Volume 2016 (2016), Article ID 6182847, 9 pages, http://dx.doi.org/10.1155/2016/6182847.

[6] Kim, Y.-., Kim, S.H., Lim, B.D. et al., Experimental study of acoustic characteristics of expansion chamber with mean flows, KSME Journal (1988) 2: 125. doi:10.1007/BF02953672.

[7] Price, S. M., & Smith, D. R. (1999, September). Sources and remedies of high-frequency piping vibration and noise. In Proc. of the 28th Turbomachinery Symposium (pp. 189-212).

[8] Neapolitano K., Linehan D., Multiple sine sweep excitation for ground vibrations test, Procedings of the IMAC-XXVII February 9-12, 209 Orlando, Florida USA, http://www.ata-e.com/uploads/2009_8.pdf.

[9] Olczyk A, Investigation of the specific mass flow rate distribution in pipes supplied with a pulsating flow, International Journal of Heat and Fluid Flow, Volume 30, Issue 4, August 2009, Pages 637-646, ISSN 0142-727X, http://dx.doi.org/10.1016/j.ijheatfluidflow.2009.02.006.

Tomasz Pałczyński, Ph.D.: Lodz University of Technology, Institute of Turbomachinery, Flow Metrology Division, 219/223 Wółczańska Str., 90-924 Łódź, (*Tomasz.palczynski@p.lodz.pl*). The author presented a version of this paper during one of the conference sessions.

Influence of partially-closed end ratio on dynamic properties of pipes with pulsating flow

Tomasz Pałczyński

Abstract: The partially-closed end ratio has a significant influence on the dynamic properties of pipes supplied with pulsating flows. In many applications (power plants, pipelines, intake and exhaust systems for internal combustion engines), the partially-closed end ratio causes resonance. Depending on the diameter of the nozzle (mounted at the end of the test pipe), and its influence on the transient flow parameters (pressure, temperature, density, speed of sound), there may be significant changes in the dynamic properties of pipes, such as resonant frequencies and the damping coefficient. In this study, experiments were conducted with a relative nozzle diameter of between 3% and 9%. Each measurement series was performed in triplicate. The results were processed in the Matlab environment using Fast Fourier Transforms. The amplitude and phase characteristics, resonant frequencies, damping coefficient and quality of approximation were estimated for each measurement. The empirical coefficients were visualized as 3D maps, including the influence of the partially-closed end ratio on the pulsation dynamics in pipes. Finally, the experimental results were compared with the author's 1D model (based on the method of characteristics). The results are significant both for theoretical understanding of pulsating flows in pipelines and for practical applications in industry.

1. Introduction

The partially-closed end ratio has a significant influence on the dynamic properties of pipes supplied with pulsating flows. In many applications (power plants, pipelines, intake and exhaust systems for internal combustion engines), the partially-closed end ratio causes resonance. Depending on the diameter of the nozzle (mounted at the end of the test pipe) and its influence on the transient flow parameters (pressure, temperature, density, speed of sound), there may be significant changes in the dynamic properties of pipes, such as resonant frequency and the damping coefficient. Pulsating flow implies pulsating pressure, which causes vibrations and noise. It is thus one of the most important problems currently facing industry [1,2,3]. Numerous studies in the literature include mathematical modeling of the dynamics of pipeline systems interacting with a medium [4,5,6,7,8]. In this study, experiments were conducted into the amplitude and phase characteristics, resonant frequencies, damping coefficient and quality of approximation were estimated for pipes supplied with pulsating flows, fitted with relative nozzle diameters of between 3% and 9%. The experimental results were compared with the author's 1D model (based on the method of characteristics).

The method of characteristics is a mathematical technique for solving hyperbolic partial differential equations. It reduces partial differential equations (PDE) into the family of ordinary equations, enabling the integration of a solution from initial data [11]. Such finite difference methods can be divided into two types: implicit and explicit. A first-order of accuracy explicit method was introduced in 1952 by Courant, for use with the Characteristics form of the hyperbolic type PDE. In 1952, Hartee proposed schemes with second-order accuracy and in 1964 Benson proposed a method based on Courant schemes for simulating internal combustion engines and reciprocating compressors. The method compares well with other first-order of accuracy explicit methods and has advantages over them for dealing with boundary conditions.

2. Boundary conditions

Jungowski [9] describes two particular cases of one-dimensional pipe flow, shown in Fig. 1. Gas parameters are presented on two planes: space t = f(x) and stage a=f(u), where *a* is the speed of sound [m/s] and *u* the velocity of flow [m/s] in the direction *x*. Figure 1 shows three areas on the space plane (1,2,3), which are also represented on the stage plane, according to the two basic phases of the valve in section A. The upper index ‘ designates a partially opened valve and “ a partially closed valve.

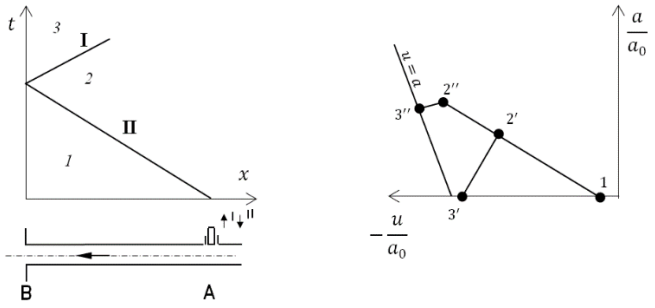

Figure 1. Boundary conditions from Jungowski [9] for unsteady flow through an open-ended pipe.

With subsonic flows, the pressure in the pipe should be equal to the external pressure before and after wave reflection. Figure 2 shows boundary conditions for unsteady flow through a pipe with a partially closed end. A nozzle has been added at the end of pipe. This nozzle can be described as a cross-section area change coefficient, $= \frac{F_n}{F_p}$, where $F_{n,p}$ is the area of the nozzle or pipe cross section [m^2].

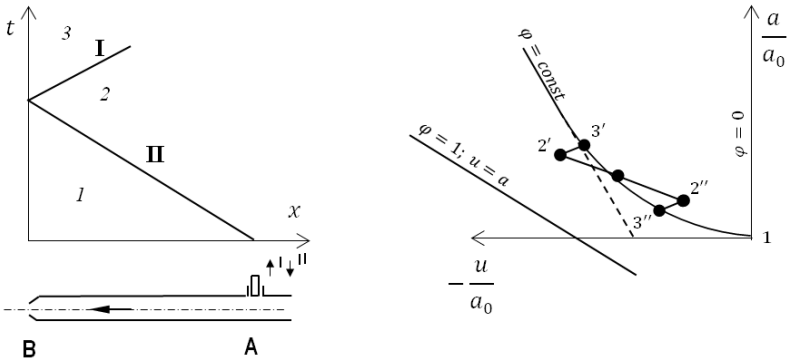

Figure 2. Boundary conditions from Jungowski [9] for pulsating flow through a pipe with a partially-closed end.

For each value of the coefficient, it is possible to draw a line on the state plane showing the boundary conditions and gas state. Moreover, it can be proven that the $\varphi = const$ curve is a straight line for sonic flows and that their extension crosses the centre of the coordinate systems of the state plane. The limit values for φ correspond to open-ended ($\varphi = 1$ from Fig. 1) or completely closed ($\varphi = 0$) pipes. The initial and reflected states must therefore be on the $\varphi = const$ curve. It is worth mentioning that the low-amplitude distortion at the speed of sound is proportional to the cross-section area change coefficient divided into two waves (the wave is reflected from the border of the centres and passed on).

As shown in Fig. 4, there are six unknown quantities: density, speed and pressure at the boundary (i subscript) and throat (t subscript). There are no C^- characteristics, which changes the principles of MOC used previously (Fig. 1). Since there are gases flowing from the pipe, there is no need for entropy correction.

Six equations can be formulated to determine the unknown quantities:

a) Non-dimensional Riemann invariants along the C^+characteristic line:

$$\lambda_{in} = A_i^{n+1} - \frac{\kappa-1}{2} * U_i^{n+1} = A_L^n + \frac{\kappa-1}{2} U_L^n \tag{1}$$

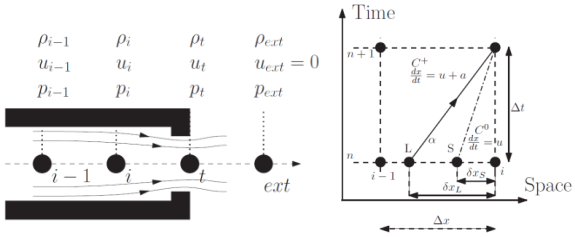

Figure 3. Partially-opened pipe boundary conditions according to the method of characteristics [2].

b) Mass conservation between pipe and the throat:

$$\rho_i^{n+1} * U_i^{n+1} * F_i^{n+1} = \rho_t^{n+1} * U_t^{n+1} * F_t^{n+1} \quad (2)$$

c) Total energy conservation between the pipe and the throat:

$$\left(A_i^{n+1}\right)^2 + \frac{\kappa-1}{2} * \left(U_i^{n+1}\right)^2 = (A_t^{n+1})^2 + \frac{\kappa-1}{2} * (U_t^{n+1})^2 \quad (3)$$

d) Homentropic contraction upstream from the throat:

$$\frac{p_i^{n+1}}{p_t^{n+1}} = \left(\frac{A_i^{n+1}}{A_t^{n+1}}\right)^{\frac{\kappa-1}{2*\kappa}} \quad (4)$$

e) For subsonic flow, the pressure in the throat is equal to the cylinder pressure:

$$p_t^{n+1} = p_{ext} \quad (5)$$

f) Assuming a homentropic contraction downstream from the throat:

$$\frac{p_t^{n+1}}{p_{ext}} = (A_t^{n+1})^{\frac{\kappa-1}{2*\kappa}} \quad (6)$$

3. Test rig – main assumptions

The following assumptions were made:

- Real measurements taken during transitional states of pulsation frequency changes (from 20 Hz to 180 Hz) in pipes. The main features of the test rig are presented in Fig. 1, including the pulse generator (PG) and three control sections (0, K, 3).
- A simplified Simulink model designed to estimate the local pulsation amplitude and amplitude-frequency characteristics [1].
- An analysis of the influence of frequency change in a range of amplitudes from 20 Hz to 180 Hz on air pressure during pulsation changes at three control sections.
- Measurements showing resonant frequency changes with increasing and decreasing pulsation frequencies.
- Proposed parameters for estimating second-order inertial elements (the damping coefficient and resonant frequency), to describe the observed phenomena.
- Assessment of the impact of the sine swept constraint on amplitude-frequency characteristics.

The main parameters were as follows:

- Range of desired values for the frequency of the pulse generator $f = (20 \div 180)$ [Hz].
- Pipe diameter $D_p = 42 \cdot 10^{-3}$[m].
- Pipe length $L_p = 0.544$ [m], determined with resonance at 70 Hz and 140 Hz.
- Nozzle diameters $D_n = 7.5 - 12.5 \cdot 10^{-3}$ [m]. The nozzles were mounted at one end of the pipe, at cross section (3).

- Desired flow temperature $T = 313.15$ [K].
- Mean Flow speed $u = 20$[m/s] (mean value).
- Mean Pressure $p = 115000$ [Pa].

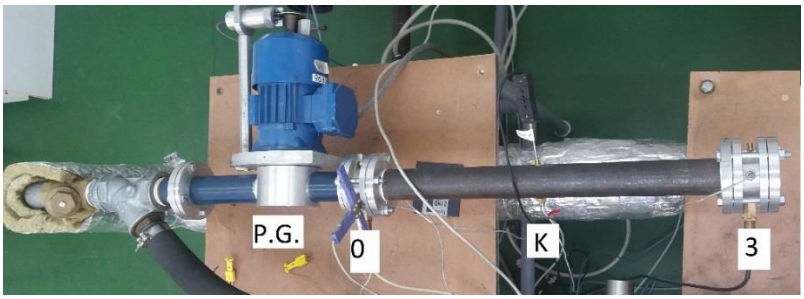

Figure 4. Main elements of the test rig [1]. P.G. – pulse generator, O,K, 3 – tested cross sections

Transient and mean values for pressure, temperature and specific mass flow rate were measured at control sections (0) and (3), shown in Fig. 4. Transient pressure was also measured in section (K), located in the middle of the length of pipe. Analysis of the dynamic properties of the pipes was performed using the second-order oscillating element as the reference, parametrizing objectively the differences between particular cases. It was thereby possible to approximate the swept frequency probe with a coefficient of determination greater than 95% ($R^2 > 0.95$). Second-order oscillating elements were estimated using equation (1) and the Curve Fitting Tool, with custom equation settings and default 95% confidence bounds:

$$M(f) = \left\{ \left[1 - \left(\frac{f}{f_n} \right)^2 \right]^2 + \left[\frac{2\zeta f}{f_n} \right]^2 \right\}^{-1/2} \tag{1}$$

where:

$M(f)$ – magnitude of oscillations [-]

f_n – natural frequency [Hz]

ζ – relative damping coefficient [-]

4. Experimental and simulation results

Experiments were conducted with different nozzles: 7.5 ; 10; $12.5 \cdot 10^{-3} m$ and three inlet radiuses: 4; 5; $6 \cdot 10^{-3} m$. Probes were performed to acquire measurement results with 5 Hz frequency steps. The author's own program for rapid processing of experimental results was used, as presented in [11]. It enables automatic generation of magnitude-frequency characteristics in just a few minutes after test rig measurements. Example results at magnitude p2/p1 in the frequency domain are presented in Figure 5. Points marked with circles represent measurement results. The line shows an approximation of the

measurement results, derived from Eq. 1. Based on the approximation curve, the following were estimated for each test series: natural frequency (146.6 Hz); damping coefficient (0.101) and resonant frequency (145.16 Hz). Resonant frequency was calculated using the equation:

$$f_r = f_n\sqrt{1-\zeta^2} \tag{2}$$

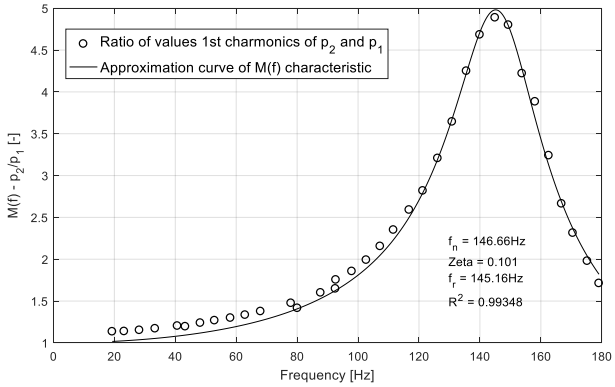

Figure 5. Magnitude p2/p1 in the frequency domain for the nozzle diameter $10 \cdot 10^{-3}m$.

The amplitudes of the oscillation at cross sections 1 and 2 were estimated and the magnitudes p2/p1 calculated. The magnitudes were assigned to the pulse generator frequencies. The coefficient of determination for the magnitude curve approximation is very good $R^2 = 0.99348$. Across the whole spectrum of the processed measurement results, the coefficient of determination was above 95%. This proves that the second-order oscillating element is sufficient for approximating the dynamic states of pulsating flows in pipes with partially-closed ends.

Calculations using the Simulink model (based on the method of characteristics) were performed in parallel with the experimental studies. Sample simulation results are presented in Fig. 6, which shows flow parameters in the time-space domain. The simulation of acoustic phenomena for the initial time steps is clearly visible. The propagating wave is divided into two parts, and is proportional to the cross-section area change coefficient, defined in Fig. 1. The reflected part of the propagating wave has closed-end type boundary conditions. The rest of the falling wave propagates outside the nozzle. Qualitative comparison of the results of the numerical studies revealed a good match with experimental measurements. The assumed cross-section area change coefficient was confirmed as $\varphi = 0.056$. Boundary conditions for the partially-closed end model were verified. Acoustic phenomena were confirmed for the analyzed flows. Nodes and antinodes were found for the standing wave, described in Fig. 6. At resonant frequency pulsations, the pressure nodes were located at the beginning of the pipe. Velocity antinodes can also be seen at the pipe end (cross section 3).

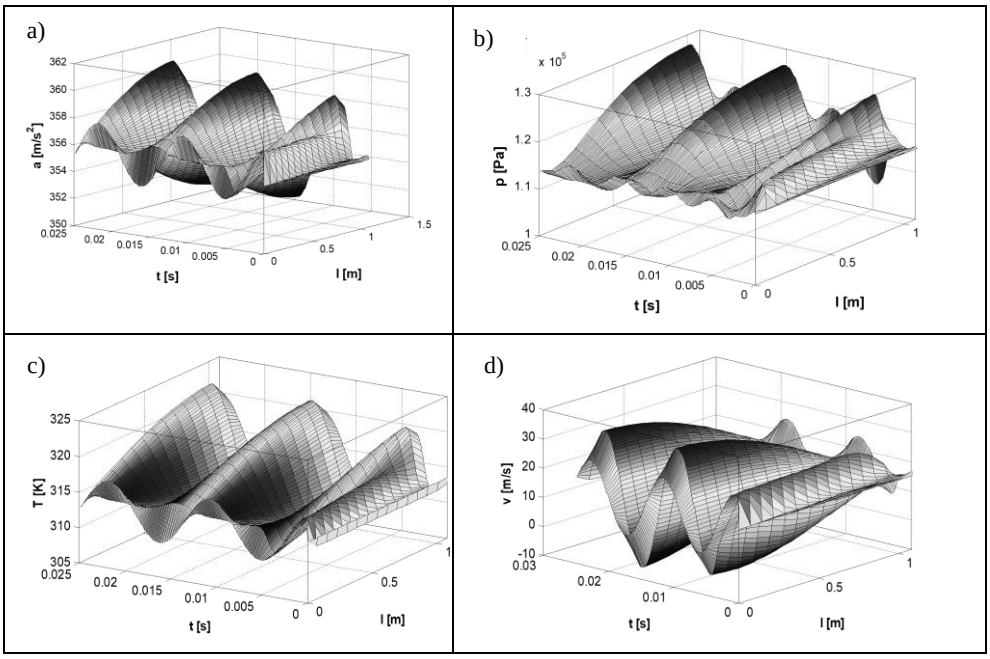

Figure 6. Numerical simulation results for the resonant frequency $f_r = 145.16$ and nozzle diameter $10 \cdot 10^{-3} m$: a) local speed of sound in the time-space domain, b) transient pressure in the time-space domain, c) transient temperature in the time-space domain, d) particle transient velocity in the time-space domain.

It is worth mentioning that the 1D model of pulsating flows through pipes with a partially-closed end correctly takes into account the impact of changes in the nozzle geometry, as one dimensionless coefficient defined as the cross-section area change coefficient. However, this makes it difficult to take into account the impact of the nozzle inlet radius as the cross-section area changes. It is proposed to estimate the (Δd) nozzle diameter correction using the linear coefficient of the impact of the cross-section area change on the relative damping coefficient.

5.1. Experimental and simulation results - discussion

Table 1 shows relative and absolute values for the damping coefficient and resonant frequencies in the cases studied. The first four rows represent the relative damping coefficient of the two particular cases, showing experimental results ("exper.") and simulation results ("calc."). The impact of the nozzle diameter is presented in the first group of three columns and the change in the damping coefficient relative to nozzle diameter $10 \cdot 10^{-3} m$ is shown in parentheses. The impact of the nozzle inlet radius is presented in the second group of three columns. The change in the damping coefficient relative to

the nozzle inlet radius $6 \cdot 10^{-3}m$ is shown in parentheses. The last two rows present the absolute difference between the experimental estimated relative damping coefficient and the reference nozzle inlet diameter $6 \cdot 10^{-3}m$. Corrective nozzle diameters, estimated as the comparable influence on the cross-section area, are presented in the last two rows in parentheses. Resonant frequencies for the studied cases are shown in the fifth row.

Table 1. Relative damping coefficient and resonant frequency (measured and calculated)

	Nozzle diameter $[\cdot 10^{-3}m]$			Nozzle inlet radius $[* 10^{-3}m]$		
	7,5	10	12,5	4	5	6
p3/p1-exper.	0,007 (-78%)	0,0315	0,0830 (163%)	0,0530 (68%)	0,0260 (-17%)	0,0315
p2/p1-exper.	0,0235 (-64%)	0,0650	0,1540 (137%)	0,1010 (55%)	0,0575 (-12%)	0,0650
p3/p1-calc.	0,0120 (-40%)	0,0200	0,0700 (250%)	0,0450 (61%)	0,0250 (-11%)	0,0280
p2/p1-calc.	0,0400 (-33%)	0,0600	0,1650 (175%)	0,090 (50%)	0,0560 (-7%)	0,0600
f_r[Hz]	146,8	149,0	151,9	146,7	146,4	147,2
$\Delta\zeta, (\Delta d)\ [-, (mm)]$	p3/p1-exper.			0,0360 (1,75)	-0,0055 (-0,56)	0
	p2/p1-exper.			0,0170 (0,48)	-0,0075 (-2,34)	0

Figures 7 and 8 provide a graphical interpretation of the results from Table 1. The influence of the nozzle diameter on the relative damping coefficient was estimated for p3/p1 (quotient of pressure pulsation of the third to the first cross-section) and p2/p1 (quotient of pressure pulsation of the second to the first cross section). The nozzle diameter changes were $\pm 2{,}5 \cdot 10^{-3}m$, which makes the cross section area change between -43 % and +56% according to the reference diameter $10 \cdot 10^{-3}m$ (assumed as the reference because all previous research was made for this nozzle). A significant increase in the relative damping coefficient can be noticed, due to the increase in nozzle diameter. Case p3/p1 has much higher values for the relative damping coefficient, compared to the p2/p1 case. This is caused by the flow phenomenon illustrated in Fig. 6b. The amplitudes of the pressure pulsation in the middle length of the tested pipe are lower. The dependence of the square cross-section area on the pipe diameter shows significant asymmetry on the left and right of the value assumed as the reference ($10 \cdot 10^{-3}m$). An increase of 25% ($12{,}5 \cdot 10^{-3}m$) in the nozzle diameter causes almost an almost 150% increase in the relative damping coefficient. A decrease of 25 % ($7.5 \cdot 10^{-3}m$) in nozzle diameter causes an almost 75% decrease in this parameter. Changes in resonant frequencies with changes in nozzle diameter are also significant, with a decrease of around 1% with the smaller nozzle diameter, increasing to 2% with the larger nozzle diameter. The influence of nozzle inlet diameter on the dynamic properties of pipes with pulsating flows is more complicated, and connected to the nozzle construction ratio resulting from fluid mechanics, which is not the main focus of dynamics research. The values for

the relative damping coefficient were calculated with reference to a nozzle inlet diameter of $6 \cdot 10^{-3} m$, well known to the author from previous research.

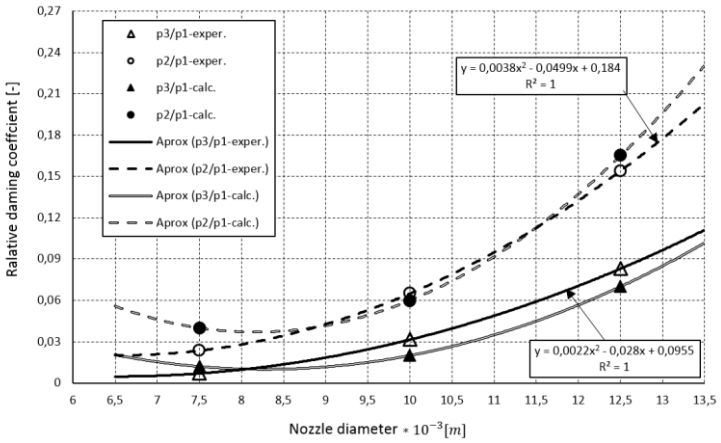

Figure 7. Damping coefficient relative to nozzle diameter (experimental and simulation results).

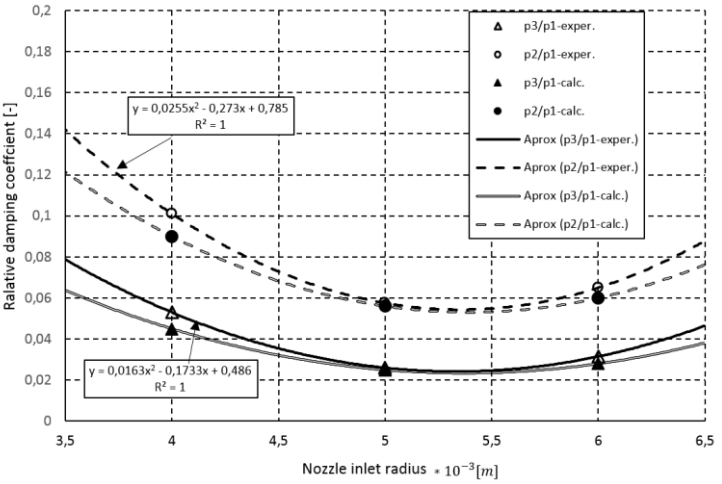

Figure 8. Damping coefficient relative to nozzle inlet radius (experimental and simulation results)

As shown in Fig. 7 and Table 1, a nozzle with an inlet diameter of $5 \cdot 10^{-3} m$ introduced a slight decrease in the dynamic properties of the studied pipes. A nozzle with an inlet diameter of $4 \cdot 10^{-3} m$ caused an almost 50% increase in the relative damping coefficient. Generally, the results of the numerical studies were comparable with the experimental results. The differences identified were caused by the simplicity of the 1D model used, based on MOC.

5. Conclusions

The closed-end ratio has a significant influence on the dynamic properties of pipes supplied with pulsating flows. This paper has presented the results of a quantitative and qualitative investigation into the influence of the diameter and inlet radius of a nozzle mounted at the end of pipes. Numerical modeling and experimental studies were performed in parallel and showed quite close agreement. The results are very important for the mathematical modeling, design and control of pipeline systems interacting with mediums such as compressed air in a wide range of pipeline systems, especially compressed air ducts, internal combustion engine inlets and exhaust systems.

References

[1] He, S. & Jackson, J., 2009. An experimental study of pulsating turbulent flow in a pipe. European Journal of Mechanics B/Fluids, pp. 309-320

[2] Park, J.-I., Adams, D., Ichikawa, Y. & Bayyouk, J., 2004. Frequency response of pressure pulsations and source identification in a suction manifold. Journal of Sound and Vibration 277, pp. 669-690

[3] Dowling, J. & Peat, K., 2003. An algoritm for the efficient acoustic analysis of silencers of any general geometry. Applied Acoustics 65, pp. 211-227

[4] Samuelson R. D. "A second order system model for pneumatic instrumentation lines".IEEE Transactions on Nuclear Science. 1969, Tom 16, 1, pages 271-276

[5] Howel P D *et al* "Mathematical analysis of the dynamic flow characteristic in a damping nozzle for a pressure transmitter"2006 *J. Phys.: Conf. Ser.* **52** 83

[6] Vetter, Gerhard, and B. Seidl. "Pressure pulsation dampening methods for reciprocating pumps." Proc. 10 th Int. Pump Users Symp., Houston Texas. Vol. 19. 1993.

[7] Metwally, M. "Review of Compressible Pulsating Flow Effects on System Performance." 13th International Conference on AEROSPACE SCIENCES & AVIATION TECHNOLOGY, ASAT- 13, May 26 – 28, 2009.

[8] Cyklis P, Młynarczyk P, The Influence of the Spatial Discretization Methods on the Nozzle Impulse Flow Simulation Results, In Procedia Engineering, Volume 157, 2016, Pages 396-403, ISSN 1877-7058,https://doi.org/10.1016/j.proeng.2016.08.382.

[9] Jungowski, W. *Podstawy dynamiki gazów*, WPW, p. 101-105, Warszawa 1972.

[10] Pałczyński T., Rydlewicz W. „ Hybrid Method for Researching Pulsating Flows in Pipes Exemplified with Orifice Application", 2018, Advances in Condition Monitoring of Machinery in Non-Stationary Operations, p. 309-317, Springer.

[11] Pałczyński, T. (2017). A hybrid method of estimating pulsating flow parameters in the space-time domain. *Mechanical Systems and Signal Processing*, *89*, 58-66.

Tomasz Pałczyński, Ph.D.: Lodz University of Technology, Institute of Turbomachinery, Flow Metrology Division, 219/223 Wółczańska Str., 90-924 Łódź, (*Tomasz.palczynski@p.lodz.pl*). The author presented a version of this paper during one of the conference sessions.

CFD predict dynamic properties such as stiffness and damping of long labyrinth seals in axial balance drum for high frequency pump

Adam Papierski, Andrzej Błaszczyk, Mariusz Susik

Abstract: Rotordynamic instability due to fluid flow in seals is a well-known phenomenon that can occur in pumps, steam turbines and compressors. While analysis methods using bulk-flow equations are computationally efficient and can predict dynamic properties fairly well for short seals, they often lack accuracy in cases of seals with complex geometry or with large aspect ratios (L/D above 1.0). This paper presents the linearized rotordynamic coefficients for a liquid seal with complex geometry subjected to incompressible turbulent flow. The fluid-induced forces acting on the rotor are calculated by means of a three-dimensional computational fluid dynamics (3D-CFD) analysis, and are then expressed in terms of equivalent linearized stiffness, damping, and fluid inertia coefficients. The results of rotor dynamic analysis using the coefficients derived from CFD approach

1. Introduction

The current trend in high-performance turbopump design requires more compact and higher power machines with higher efficiencies, which consequently results in higher rotor speeds and tighter clearances. This trend requires a more accurate determination of rotor critical speeds, vibration levels, and the onset of pump instability.

Turbopumps seals interface between rotating parts such as rotors, impeller blades and balance drum and stationary parts such as housings. The seals, used to isolate regions of different pressures, are non-contacting, and allow a leakage flow across. The fluid flow that exists in seals generates reaction forces on the rotor. As a rotor moves away from its nominal operating position, the fluid flow in the seal is altered and reaction forces are generated on the rotor. Knowledge of the type and magnitude of these forces is important when calculating the stability characteristics of the overall rotating system. The reaction forces can be destabilizing e.g. in a labyrinth seal.

Traditional annular seal models are based on bulk flow theory. While these methods are computationally efficient and can predict dynamic properties fairly well for short seals, they lack accuracy in cases of seals with complex geometry or with large aspect ratios (above 1.0). In this paper, the linearized rotordynamic coefficients for a seal with a large aspect ratio are calculated by means of a three-dimensional CFD analysis performed to predict the fluid-induced forces acting on the rotor. As a

seal rotor moves away from its nominal position, the reaction forces generated by the fluid flow can be linked to the rotor displacement, velocity and accelerations using a spring-damper-mass system in 2 directions.

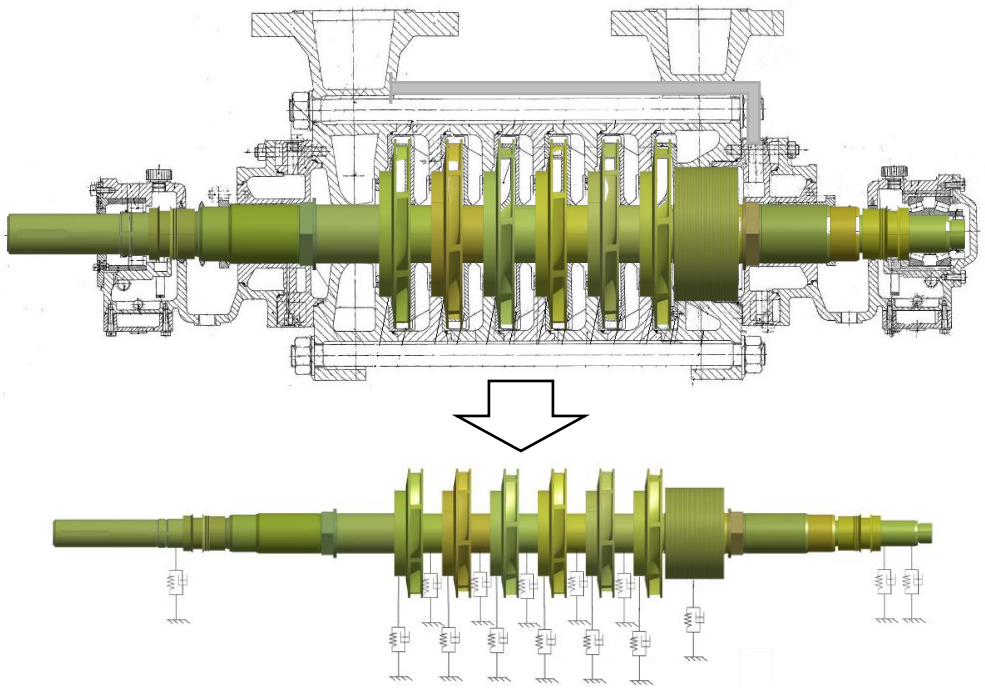

Figure 1. Schematic of horizontal multistage process pump with inline impeller configuration with balance drum for axial force reduce and their rotordynamics model

For the seal configuration shown in Figure 2, the reaction forces F_x and F_y can be linked to the rotor motion using the relation

$$-\begin{bmatrix} F_x \\ F_y \end{bmatrix} = \begin{bmatrix} K_{xx} & K_{xy} \\ K_{yx} & K_{yy} \end{bmatrix} \begin{bmatrix} x \\ y \end{bmatrix} + \begin{bmatrix} C_{xx} & C_{xy} \\ C_{yx} & C_{yy} \end{bmatrix} \begin{bmatrix} \dot{x} \\ \dot{y} \end{bmatrix} + \begin{bmatrix} M_{xx} & M_{xy} \\ M_{yx} & M_{yy} \end{bmatrix} \begin{bmatrix} \ddot{x} \\ \ddot{y} \end{bmatrix} \quad (1)$$

where:

- x, y, $\dot{x}$, $\dot{y}$, $\ddot{x}$, $\ddot{y}$ are the displacements, velocities, and accelerations in the X and Y directions,
- K_{xx} and K_{yy} are the direct and K_{xy} and K_{yx} the cross-coupled stiffness coefficients,
- C_{xx}, C_{yy} and C_{xy}, C_{yx} direct and cross coupled damping coefficients
- M_{xx}, M_{yy} and M_{xy}, M_{yx} the direct and cross-coupled inertia (added mass) coefficients.

Linked in this fashion, the rotor dynamic coefficients can directly be used in the rotor stability calculations.

When the nominal position of the rotor is concentric, the coefficient matrices become simpler and assume a skew-symmetric form with a total of only six distinct coefficients as against twelve for the general case.

$K_{xx} = K_{yy}$; $K_{xy} = -K_{yx}$; $C_{xx} = C_{yy}$; $C_{xy} = -C_{yx}$; $M_{xx} = M_{yy}$; $M_{xy} = -M_{yx}$;

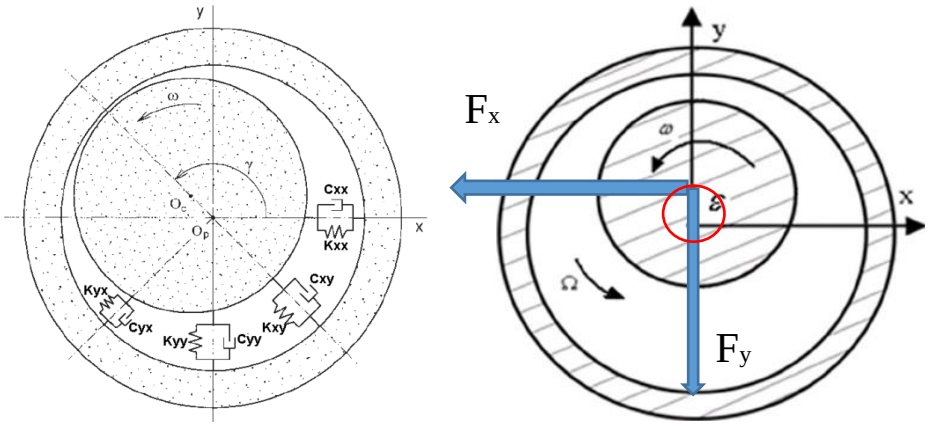

Figure 2. Whirling rotor with small orbit radius ε

Circular whirl orbits of the rotor are applied, assuming that the center of the rotor describes a trajectory expressed as:

$$x = \varepsilon \cos \Omega t \tag{2}$$

$$y = \varepsilon \sin \Omega t \tag{3}$$

Where ε is the eccentricity of the rotor. Replacing derivatives of Eqs.(2) and (3) in Eq. (1), this can then be rewritten in terms of sines and cosines. By selecting the point A(0,ε) in the whirl orbit, illustrated in Fig.2, and using matrix algebra, Eq.(1) is simplified further. As a result, the normal and tangential components of fluid forces acting on the rotor are described by the linearized rotordynamic model as follows:

$$-\frac{F_x}{\varepsilon} = -K_{xy} + C_{xx}\Omega + M_{xy}\Omega^2 \; -\frac{F_x}{\varepsilon} = M_{xy}\Omega^2 + C_{xx}\Omega - K_{xy} \tag{4}$$

$$-\frac{F_y}{\varepsilon} = -K_{yy} + C_{yx}\Omega + M_{yy}\Omega^2 \; -\frac{F_y}{\varepsilon} = M_{yy}\Omega^2 + C_{yx}\Omega - K_{xy} \tag{5}$$

Each of the above equations represents one equation and three unknowns (stiffness K, damping C, mass term M). The dynamic coefficients are evaluated by determining the fluid force components F_x

and F_y, at multiple whirl speeds Ω_i, i=1,2,3,4,5. A curve-fit to the linear second order model is then performed to identify the six unknowns in the equations above, representing the stiffness, damping, and added mass coefficients.

In the CFD simulations the rotor was displaced in a positive Y direction with ε= 0.1 x nominal clearance and the computational model reflected this off-center position of the rotor. The use of a full three-dimensional eccentric CFD model ensured that both minimum and maximum radial clearance is included and, therefore, the pressure variation in circumferential direction that generates fluid excitation forces is taken into account.

2. CFD Prediction of Dynamic Seal Coefficients

To predict dynamic seal properties the selected approach follows many other researchers; a number of interesting publications are cited in the bibliography. The authors consider an idealized model of a rotor with a spinning frequency rotating around the center of the stator on a circular orbit with whirling frequency and orbit radius ε. These model assumptions are shown in Figure 4 /left. This transient problem can be transferred to a stationary one using a rotating relative system as shown in Figure 4 /right. The following boundary conditions are used:

- The gap between rotor and stator is regarded as a rotating-relative system. The relative system rotates with orbit frequency Ω.
- The circumferential velocity of the walls are defined relative to the orbit, i.e., the shaft surface rotates with a frequency $\Omega_{rel} = (\omega - \Omega)$, while the stator surface rotates at $\Omega_{wall} = (-\Omega)$.
- The upstream and downstream parts of the balance drum are defined in a fixed absolute system.
- Using a multiple frame of reference (MFR) software, the flow in all individual parts can be handled as stationary. The coupling between the reference systems can be handled using the so-called “frozen rotor” interface, averaging flow and variables in circumferential velocity.

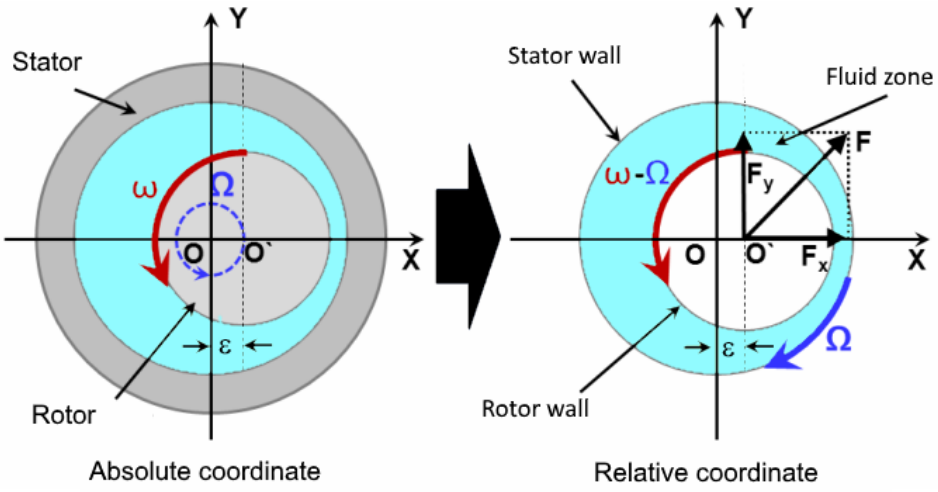

Figure 3. CFD Coordinate Systems for steady-state analysis (Ωt=0)

3. Mesh Generation and Boundary Conditions

The simulation of the flow-through labyrinth seals requires high-quality CFD meshes. In the axial and radial directions extremely high gradients of velocity and pressure occur that must be resolved sufficiently. The need to mesh a complete 360 degree model with an excessive number of nodes with increasing numbers of tips also enforces good grids to minimize computational time to achieve convergence. An example for this mesh refinement is given in Figure 5. Final number of mesh nodes for balance drum gap was 678041 (27120 nodes per 1 of 25 chambers).

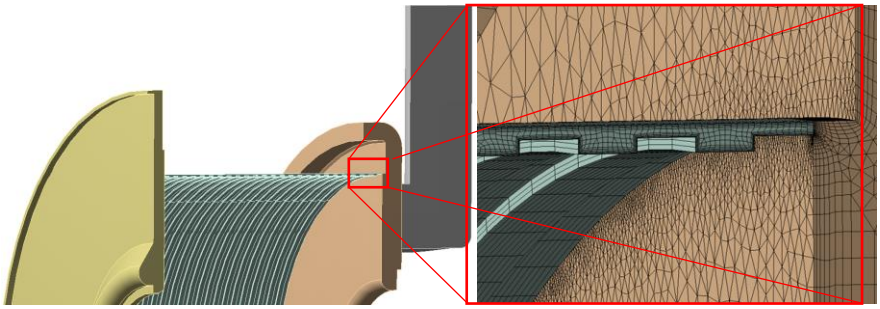

Figure 4. Final mesh for gap of balance drum

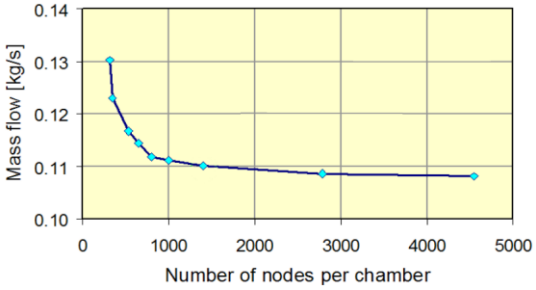

Figure 5. Predicted Mass Flows as Target Function Versus Mesh Density [1]

In [1] authors showed trend of the calculated mass flow throw seal gap versus the number of nodes per chamber (see Fig. 6). 27 120 is the number of nodes that far exceeds the value at which the mass flow is already set.

4. Boundary conditions for CFD calculations

For flow calculation through balance piston it was set following boundary condition (see figure 6) :

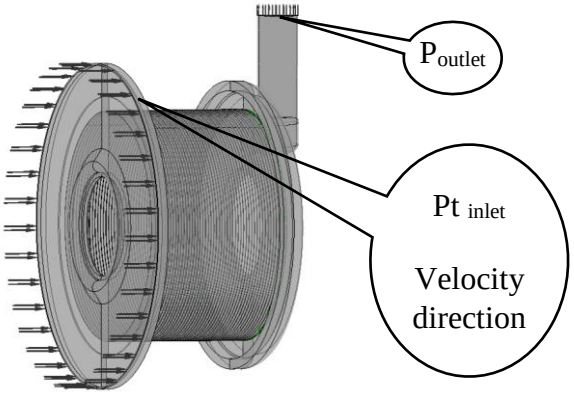

Figure 6. Boundary conditions for stiffness and damping calculations

4.1. Inlet boundary conditions

Total pressure (Pt inlet) and velocity direction at entrance to downstream chamber of last impeller were obtained from result of calculation of all stage pump with ideal centric position of the shaft. In this case is possible to calculate for one passage for every elements of pump like impeller, vanned diffuser and also impeller chamber and seals.

4.2. Outlet boundary condition

Static pressure (P_{outlet}) calculated as pressure in suction pipe increased by pressure loss in connecting pipe between suction pipe and balance chamber. Pressure loss calculated by equation (6)

$$\Delta p = \left(f_t \frac{L}{D} + \sum \xi_i\right) \frac{\rho V^2}{2} \tag{6}$$

where:

f_t –friction coefficients of connection pipe,

L - length of the connection pipe,

D – diameter of the connection pipe,

ρ – density of pumped liquid,

ξ_i – sum of local loss coefficient (bends, entrance, oriffice)

V – liquid velocity in connection pipe calculated from mass flow through balance drum gap

5. Results of calculations

CFD calculations delivers the pressure and velocity distributions field (see figure 7). From pressure field on rotating element (balance drum) it can calculated axial Force (F_z) and parts of radial force (F_x, F_y). Figure 8 show axial force for different balance drum gap. The optimal gap is about 0.7 mm. The residual axial force is transmitted through the support bearing

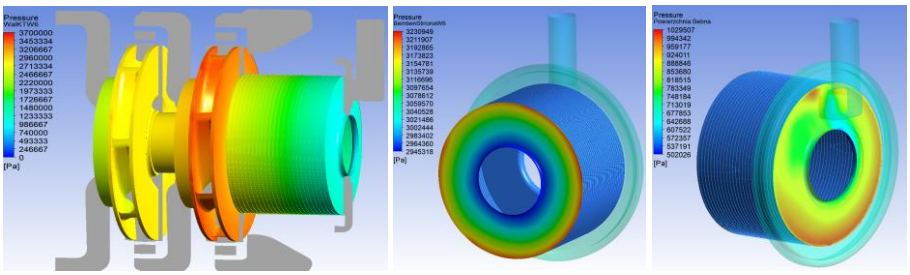

Figure 7. Pressure distributions on rotating element of the pump

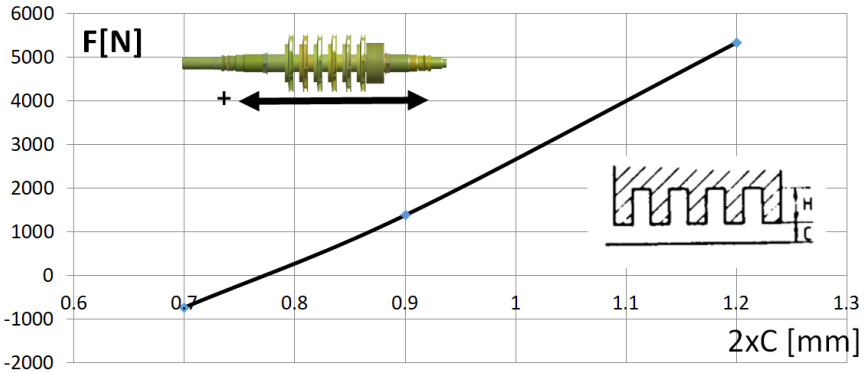

Figure 8. Axial thrust vs balance drum gap (diameter)

Figure 9 show parts of radial force versus 5 orbit frequency Ω. A curve-fit to the linear second order model is then performed to identify the six unknowns in the equations above, representing the stiffness, damping, and added mass coefficients.

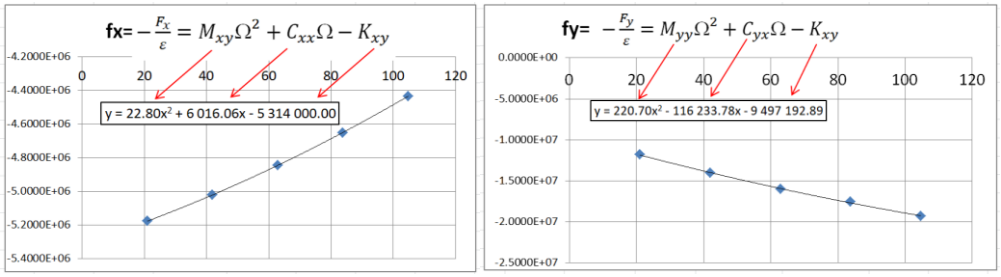

Figure 9. Variation of fluid force components normalized by eccentricity of rotor (estimated from CFD) as function of assumed whirl speeds

The resulting dynamic properties of the seal are listed in follow.

$$[M] = \begin{bmatrix} 220 & 22{,}8 \\ -22{,}8 & 220 \end{bmatrix}; [C] = \begin{bmatrix} 6016 & 116233 \\ -11623 & 6616 \end{bmatrix}; [K] = \begin{bmatrix} 9{,}4927E+06 & 5{,}3140E+06 \\ -5{,}3140E+06 & 9{,}4972E+06 \end{bmatrix}$$

The rest of pump seals dynamics properties was calculated by bulk flow method implemented in lateral rotordynamic analysis computer program XLROTOR@. Critical speed map and its shape obtained from XLROTOR showing figure 10.

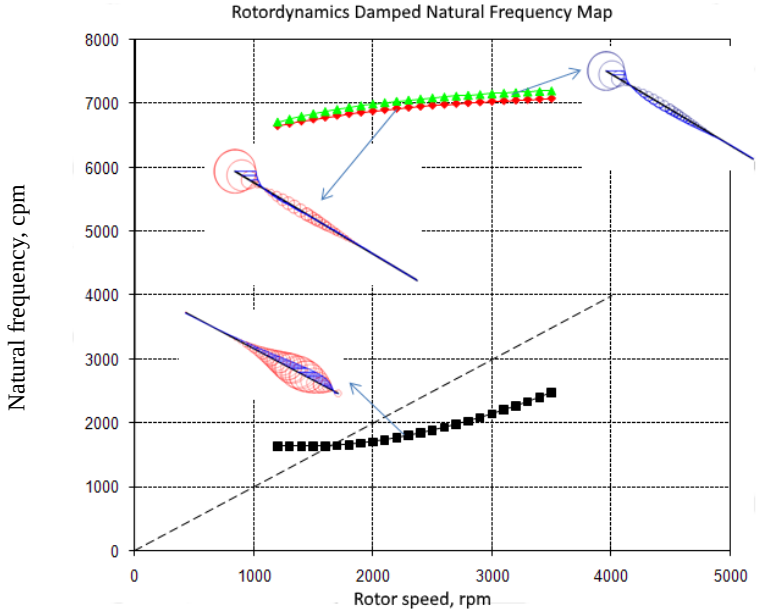

Figure 10. Campbell diagram

6. Conclusions

This paper presented a method to calculate the dynamic properties of circumferentially-grooved seals (balance drum) with large aspect ratios, using CFD as an alternative approach to bulk flow codes. The rotordynamic coefficients were calculated by simulating a rotor that whirls on a circular orbit around the center of the stator. The resulting fluid forces were calculated for five whirl speeds to solve the rotordynamic equations and identify the dynamic properties using a second order curve-fit. The main disadvantage of this method stems in the large computational time and effort required to perform the CFD analysis as compared to the bulk flow analysis, which is frequently used for lateral rotordynamic stability analysis in the industry. However, as the computational power is continuously increasing, it is believed that the CFD technique for modeling fluid forces will become the standard in the industry. Furthermore, the CFD method outlined can be coupled with rotordynamic codes and optimization algorithms to improve the design of rotordynamic systems.

References

[1] Norbert G. Wagner, Klaus Steff, Rainer Gausmann, Marcus Schmidt, Investigations on the dynamic coefficients of impeller eye labyrinth seals, 38th Turbomachinery Symposium (2009)

[2] Alexandrina Untaroiu, Costin D Untaroiu, Paul E Allaire, Numerical Modeling of Fluid-Induced Rotordynamic Forces in Seals With Large Aspect Ratio, Journal of Engineering for Gas Turbines and Power, January 2013

[3] Tae Woong Ha, Bok Seong Choe, Numerical prediction of rotordynamic coefficients for an annular-type plain-gas seal using 3D CFD analysis, Journal of Mechanical Science and Technology 28 (2) (2014), p. 505~511

[4] Alexandrina Untaroiu, Costin D Untaroiu, On the Dynamic Properties of Pump Liquid Seals. Journal of Fluids Engineering · April 2013

[5] Untaroiu, A., Wood, H. G., Dimond, T., and Allaire, P. E., 2008, "Calculation of Dynamic Coefficients for a Magnetically Levitated Artificial Heart Pump Using a CFD Approach," ASME Conf. Proc. IMECE2008, Biomedical and Biotechnology Engineering, Vol. 2, Boston, MA, October 31-November 6, ASME Paper No. IMECE2008-67802, pp. 537–543.

[6] Childs, D. W., and Scharrer, J. K., 1986, "An Iwatsubo-Based Solution for Labyrinth Seals: A Comparison to Experimental Results," ASME J. Eng. Gas Turbines Power, 108, pp. 325–331.

[7] D. Childs, Dynamic analysis of turbulent annular seals based on Hirs' lubrication equation, Journal of Lubrication Technology,105 (1993) 437-444.

[8] D. Childs and J. K. Scharrer, Experimental rotordynamic coefficient results for teeth-on-rotor and teeth-on-stator labyrinth gas seals, Journal of Engineering for Gas Turbine and Power-Transections of the ASME, 108 (4) (1986) 599-604.

[9] Arghir, M., and Freˆne, J., 2004, "A Bulk-Flow Analysis of Static and Dynamic Characteristics of Eccentric Circumferentially-Grooved Liquid Annular Seals," ASME J. Tribol., 126(2), pp. 316–325.

[10] Ha, T. W., and Lee, A. S., 2000, "A Rotordynamic Analysis of Circumferentially-Grooved Pump Seals Based on a Three-Control-Volume Theory," KSME Int. J., 14(3), pp. 261–271.

[11] Black, H. F., 1969, “Effects of Hydraulic Forces in Annular Pressure Seals on the Vibrations of Centrifugal Pump Rotors,” J. Mech. Eng. Sci., 11(2), pp. 206–213.

[12] T.-W. Ha and B. S. Choe, Numerical simulation of rotordynamic coefficients for eccentric annular-type-plain-pump seal using CFD analysis, Journal of mechanical science and technology, 26 (4) (2012) 1043-1048.

[13] G. Kirk and R. Gao, Influence of pre-swirl on rotordynamic characteristics of labyrinth seals, Tribology transactions, 55 (03) (2012) 357-364.

[14] G. G. Hirs, A bulk-flow theory for turbulence in lubricating films, ASME Journal of Lubrication Technology, 105 (1973) 137-146.

[15] William D. Marscher, an end-user’s guide to centrifugal pump rotordynamics, Proceedings of the Twenty-Seventh International Pump Users Symposium September 12-15, 2011, Houston, Texas

Adam Papierski, Associate Professor: Lodz University of Technology Institute of Turbomachinery, 90 - 924 Łódź, 219/223 Wólczańska Street, POLAND (adam.papierski@p.lodz.pl), the author presented this contribution at the conference.

Andrzej Błaszczyk, Professor: Lodz University of Technology Institute of Turbomachinery, 90 - 924 Łódź, 219/223 Wólczańska Street, POLAND (andrzej.blaszczyk@p.lodz.pl).

Mariusz Susik, Ph.D.: Lodz University of Technology Institute of Turbomachinery, 90 - 924 Łódź, 219/223 Wólczańska Street, POLAND (mariusz.susik@p.lodz.pl)

The impact of the shock absorber damage on vehicle control

Krzysztof Parczewski, Henryk Wnęk

Abstract: The article has been analysed the impact of vehicle shock absorber damage on its controlling. The study was conducted on a Class B passenger car for selected road tests. The results of the measurements from road tests obtained for a fully functional and damaged vehicle with different locations of vehicles centre of gravity were compared. The impact of the damaged shock absorber on the change of steering controlling in fixed and dynamically changing conditions has been analysed. Steerage indicators based on the analysis of steerability and vehicle stability were used to evaluate the behaviour of the vehicle. Designated indicators have identified the required change in the range of vehicle steering control and their impact on vehicle active safety.

1. Introduction

Longitudinal, lateral and roll motion of the vehicle are caused by the driver's control of the vehicle. They are dependent on dynamic control characteristics of the vehicle. The driver controls the movement of the vehicle, determines the vehicle track and corrects it in case of deviation from the given track. The driver also predicts the movement and behaviour of the vehicle. Based on this information, the driver decides to take steering wheel maneuverer [5].

2. Factors influencing the dynamic characteristics of vehicle control

On vehicle controls are also influenced by factors that depend on the structure of the vehicle, especially its tires, and the conditions of vehicle tire adhesion to the roadway. Generally they are defined by the notion of dynamic characteristics of the vehicle control. This dynamic characteristic is influenced by:

- steer angles,
- side-slip angles of wheels.

The size of the steer angles is determined by the driver by turning the steering wheel. However, on trajectory of the vehicle has influence factors depends on the structural components and movement of the car, as well as the transmission of forces between the tires and the roadway. As noted above, the factors that affect the trajectory of motion are the steering wheel angle of rotation, tire characteristics, stiffness and damping of vehicle suspension, susceptibility and damping of steering system, wheels geometry, mass distribution and vehicle mass moments of inertia, rolling resistance

and adhesion conditions (tire-road friction) as well as dynamics of the cornering manoeuvre [3,6,7,16].

2.1. Steer angles of wheels

Steer angles of wheels are derived from the value of angle of rotation of the steering wheel, steering gear ratios and its characteristics, and steering system susceptibility and damping. They essentially affect the vehicle motion.

2.2. Wheels side-slip angles

Factors influencing the side-slip angle are related to parameters resulting from the construction of the vehicle and parameters determining its movement. These parameters can be grouped as follows:

- Tire - its rigidity, aspect ratio, tread condition. These parameters mainly affect the tire deflection and its interaction with the roadway, depending on the force acting on the wheel and its tilt angle [9,10,13].
- Suspension - radial and vertical stiffness and characteristics of damping in shock absorbers. Suspension stiffness affects the roll and tilt angles of the vehicle relative to the longitudinal (X) and transverse (Y) axes as well as the forces acting on the axles of the wheels. Torsion of vehicle body has been omitted due to its small impact on vehicle motion [6,7,8,16,18].
- Construction of vehicle - centre of gravity, moments of inertia with respect to vehicle axes X, Y and Z [2,4,12].
- Co-operation of tires with the road - conditions of adhesion between the tire and the road resulting from the type of pavement, its condition (dry, wet), longitudinal and transverse slip of the wheel, rolling resistance. They directly affect the angle of side-slip [2,17,19].
- Vehicle motion parameters - value of steering wheel angle (steer angle), driving speed, longitudinal and lateral acceleration, tilt of the roadway. These parameters characterize the motion and control of the vehicle [1,2].

All the above factors affect the trajectory of motion the vehicle.

Comparison of vehicle control characteristics with fully functional and damaged shock absorber requires to appoint some indicators be used to assess the vehicle's steerability.

3. Assessment methods of steerability of the vehicle

Usually, understeer gradient K_{us}, under the norm ISO 4138 is used to determine the steerability of a vehicle in motion. This relationship allows us to determine the characteristics of the vehicle steer - Equation (1) [18].

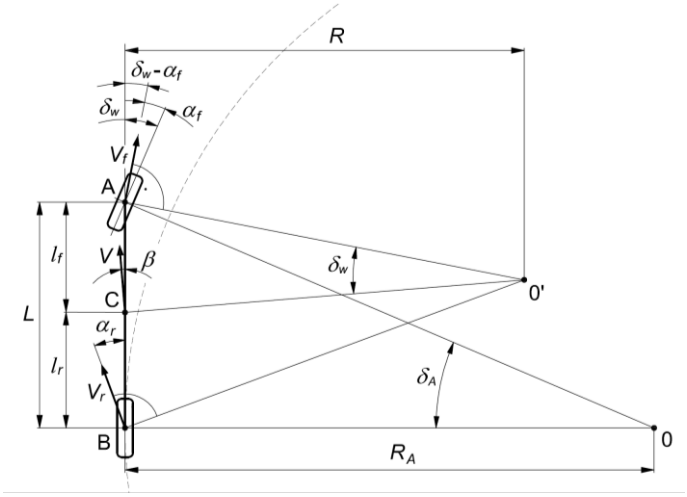

Figure 1. Scheme of motion of a vehicle on a circular track, taking into account and without taking into account, the wheels side-slip angles [18].

The relationships describing the indicators used to evaluate the motion control of the vehicle were presented below [5,6,18,22]:

Understeer gradient

$$K_{us} = \frac{d\delta_w}{da_y} - \frac{d\delta_A}{da_y} = \frac{m}{L}\left(\frac{l_r}{C_{af}} - \frac{l_f}{C_{ar}}\right) \tag{1}$$

Difference in steering angles δ_w - δ_A gradient in steady state conditions

$$A_{ss} = \frac{\delta_w - \delta_A}{a_y} \tag{2}$$

Understeer indicator A_{st}

$$A_{st} = \frac{\alpha_f - \alpha_r}{L \cdot a_y} \tag{3}$$

Yaw rate gain

$$\dot{\psi}_\delta = \frac{\dot{\psi}}{\delta_w} \tag{4}$$

Relationship between the yaw rate and steer angle in steady state conditions

$$\left(\frac{\dot{\psi}}{\delta_w}\right)_{ss} = \frac{v}{L + K_{us} \cdot v^2} \tag{5}$$

Path radius to steer angle ratio

$$\left(\frac{R}{\delta_w}\right)_{ss} \tag{6}$$

For evaluation of the steerability of the vehicle, the indicators determining the deviation from the pre-set trajectory expressed by the difference in steering angles gradient δ_w - δ_A, are used, where δ_w is the average steer angle and δ_A the Ackermann's steer angle (the steer angle of the wheels needed to

drive on these same track in case there are no wheels side-slip of the front and rear axles α_f and α_r). These angles are shown in Figure 1.

The understeer indicator A_{ss} - difference of steer angles to the lateral acceleration ratio - equation (2) was used to evaluate the steerability of the vehicle too. The difference of the side-slip angles between front and rear wheels α_f - α_r, allows you to assess the vehicle's steerability, its tendency to understeer or oversteer, and determine their impact on the vehicle's track. The analyses used the A_{st} indicator, which is the ratio of the difference of the wheels side-slip angles α_f - α_r to the lateral acceleration a_y and the vehicle wheelbase L - equation (3) and the yaw rate gain - ratio of the yaw rate to the steer angle - equation (4). As auxiliary is used the equation (5), to show the relationship between the yaw rate and steer angle, under steady-state conditions (it depends on the vehicle speed, wheelbase and the understeer gradient).

Under the steady state conditions of vehicle motion for the evaluation of steerability was used equations (1-4) and equation (5 and 6) and in the case of sudden change in direction of motion of equations (3-4).

4. Impact of shock absorber damage on steering characteristics of the vehicle

4.1. Testing vehicles in motion

The study was conducted using Class B vehicle (vehicle kerb weight ~ 1000kg, wheelbase ~ 2.3m) [11,15]. Two road tests based on ISO standards [23-28] were used to evaluate the vehicle's steer characteristics: the first test - determining circular driving behaviour of vehicles at steady-state conditions, the second test - attempt consisted of a sudden change of the motion direction, few seconds driving in steady turn and next braking [14,16]. During the first test, the vehicle moved under steady-state conditions at steady speed and constant steer angle (the test was labelled "Circle_Mx"). During the second test, the motion conditions changed dynamically, the vehicle initially moved in a straight line, followed by a turning manoeuvre, and after a few seconds braked (the test was labelled "Corner_Mx"). Vehicle speed at the beginning of braking was about 45 km/h.

These tests are characterized by high lateral acceleration both when driving on a circular track under steady motion conditions and during a sudden change of direction of motion.

Tests were repeated for two centre of gravity positions corresponding to conditions in which only the driver (M1) was in the vehicle and the vehicle was fully loaded (M2). Changing the vehicle load caused the centre of gravity to shift 11.6 centimetres backwards.

During both tests were measured: vehicle speed and track, longitudinal and lateral acceleration, steering wheel angle, tilt and yaw angle, yaw and roll and pitch rates, wheels rotation and brake pedal force and brake pressure on wheels circuits.

For this purpose, the vehicle was equipped with measuring equipment: Correvit S-CE sensor (Corrsys-Datron), measuring steering wheel MSW (Corrsys-Datron), measuring system VBOX3i SL with two GPS antenna and inertial modulus IMU04 (Racelogic), acceleration sensors ADXL203 (Analog Devices), pressure sensors MPX200 (Peltron), brake pedal force sensor CL23 (ZEPWN), incremental encoders with a resolution of 1024 pulses/rev (HEEDS) and gyro sensors CRS03 (Silicon Sensing Systems Japan). Measurement data were recorded at 100Hz in acquisition systems AD-32 [11,12,20] and VBOX Racelogic [21].

4.2. Measurement and evaluation of vehicle steerability

The parameters characterizing the steerability of the vehicle as describing above have been determined, on the basis of the road tests. The results are presented separately for steady-state circular tests and for dynamic change of direction of motion. The tests were carried out on four vehicle conditions: fully functional car with load M1, fully functional car with load M2, damaged car with load M1 (with damaged shock absorber in front suspension) and damaged car with load M2. The faulty shock absorber was mounted in the front right wheel suspension.

The steady-state circular tests

The diagrams below show the comparison of the various indicators for different vehicle states obtained from the measurements during the steady-state circular tests.

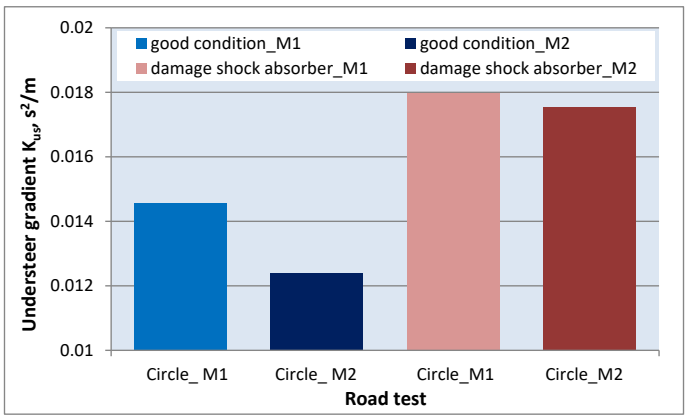

Figure 2. Understeer gradient K_{us} for fully functional and damaged vehicle.

The understeer gradient shown in figure 2 allows you to compare the vehicle with fully functional and with damaged shock absorber in steady-state circular test. The comparison shows that damage of the shock absorber of the front right suspension changes the steerability characteristics of the vehicle. This increases the understeer gradient by more than 25%. Increasing the mass of the vehicle causing the centre of gravity to shift backwards and causes a decrease in the gradient (~ 16%

in a vehicle with a mass of M1 to 3% for a vehicle with a mass of M2). Despite these changes, the vehicle has understeer characteristics in all tested cases.

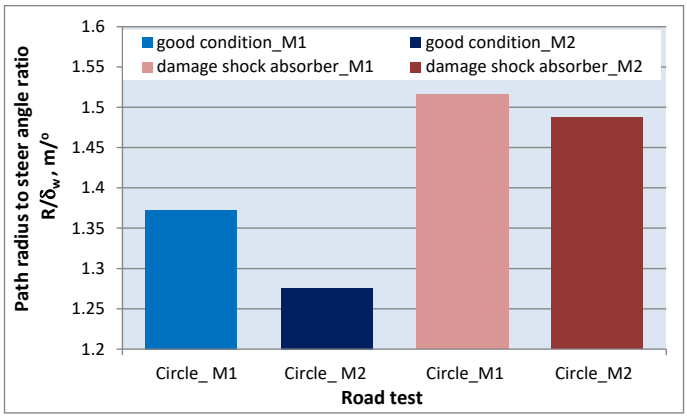

Figure 3. Influence of shock absorber damage on the path radius to steer angle ratio.

Figure 3 shows the change of the vehicle's trajectory radius at fix steering wheel steering angle. For the steering angle of 10° the radius of motion trajectory for the vehicle loaded by driver is 13.7m, after increasing the vehicle load, the radius decreases to 12.75m. Damage of the shock absorber causes that the radius of the track increases to 15.1m and for additionally loaded vehicle up to 14.9m.

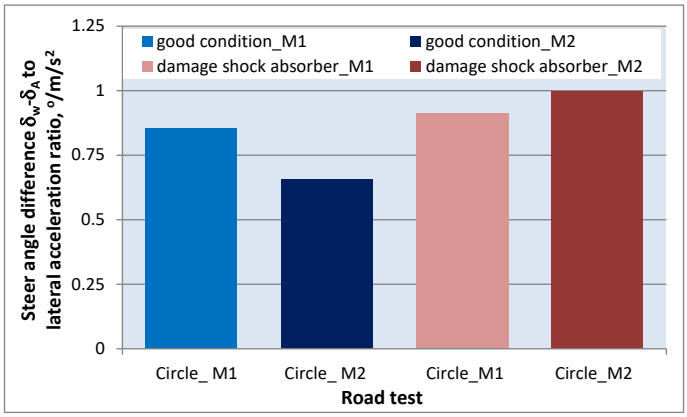

Figure 4. Influence of shock absorber damage on the change of the A_{ss} indicator - difference in steering angles δ_w - δ_A gradient in steady state conditions.

Figure 4 shows the difference between the actual steer angle and the Ackermann angle (δ_w - δ_A) per acceleration unit. For lateral acceleration ~4m/s^2 the actual steer angle of the steered wheels will be greater than the Ackermann angle by ~3.3m. The moving of the gravity centre backwards and increasing the weight of the car will reduce the angles difference to ~2.6°. Damage of the shock

absorber will result in an increase of the angles difference of up to ~3.6° and with increased vehicle weight of up to ~4°.

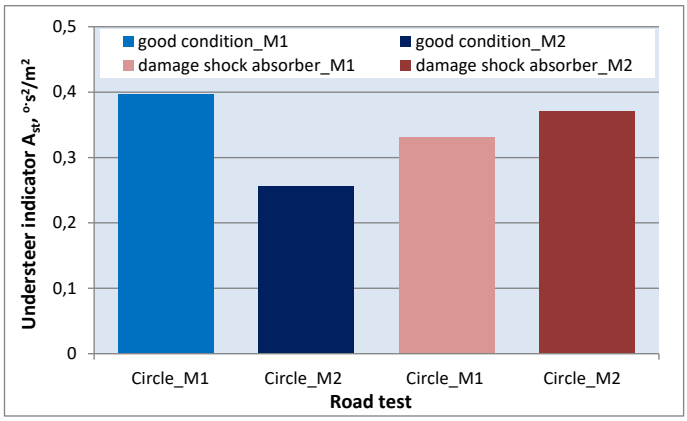

Figure 5. Influence of shock absorber damage on the change of the understeer indicator A_{st} during steady motion on circular path.

The impact of shock absorber damage on values of understeer indicator A_{st} during steady-state circular test is within the range resulting from the change of location the gravity centre. For this reason, it can be considered that damage of the shock absorber has a little impact on the value of this indicator (Fig. 5).

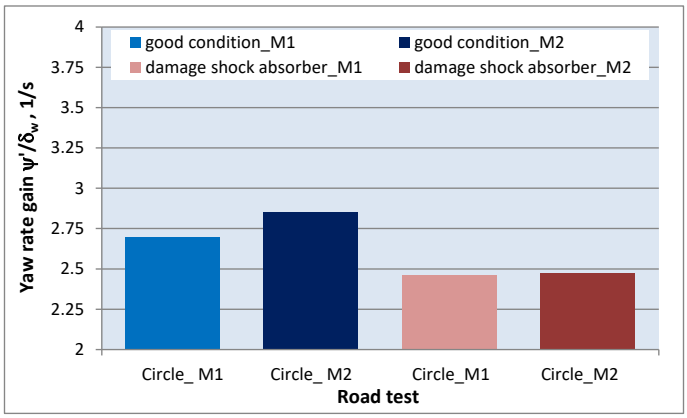

Figure 6. Influence of shock absorber damage on the change of yaw rate gain $\dot{\psi}/\delta_w$ during steady-state motion on circular path.

The yaw rate gain $\dot{\psi}/\delta_w$ during steady-state circular tests, in the event of damage of the shock absorber, is reduced by ~10%. In the case of fully functional vehicle, the change of gravity centre location increases this indicator by 10%, but with a damaged shock absorber, this effect is much smaller (Figure 6).

Test of the dynamic change of the motion direction

Below, on the graphs was shown the comparison of individual indicators for different vehicle states obtained from measurements during the tests of the dynamic change of the motion direction.

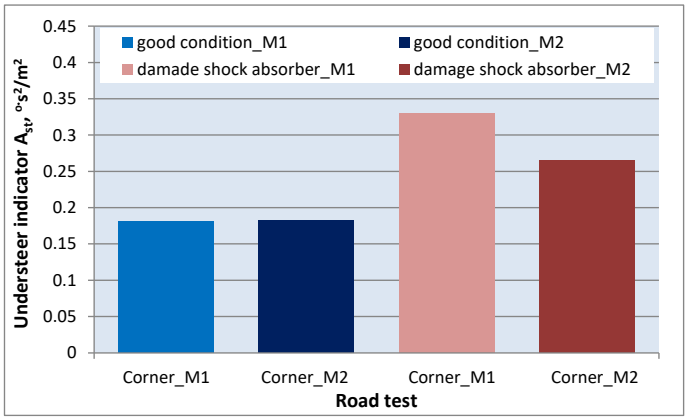

Figure 7. Effect of the shock absorber damage on the understeer indicator A_{sk} during a step input manoeuvre.

Damage of the shock absorber significantly increases the understeer indicator, which means that under the same steering conditions, the difference of side-slip angles in the front and rear axle has increased by ~80% (Figure 7). Shifting the centre of gravity backwards makes improve this relationship - an increase of 50%.

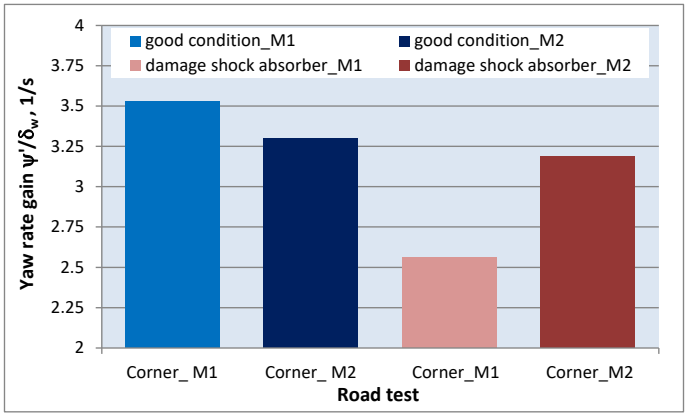

Figure 8. Effect of shock absorber damage on the yaw rate gain $\dot{\psi}_\delta = \frac{\dot{\psi}}{\delta_w}$ during step input manoeuvre.

During dynamic change of the motion direction, in case of the shock absorber damage, the yaw rate gain is reduced by ~30%. In the case of the fully functional vehicle, the change of gravity centre

location reduces this indicator by 10% and with damaged shock absorber, the impact is much higher, the indicator is increased by more than 12% (Figure 8).

4.3. Evaluate the impact of shock absorber damage on the vehicle control

The presented analysis shows that damage of the shock absorber increases the vehicle understeer of ~25%, expressed by the vehicle understeer gradient. This involves with increasing the radius of the vehicle path or the need to increase the steer angle of the steered wheels and thus the angle of rotation of the steering wheel δ up to 18÷22º (greater value for a vehicle loaded only by the driver).

In tables 1 and 2 was shown a comparison of the understeer indicator A_{st} and the yaw rate gain of the vehicle. Table 1 shows the comparison of the understeer indicator of the vehicle $A_{st} = \frac{\alpha_f - \alpha_r}{L \cdot a_y}$ in steady-state driving in a circular path and during a step input manoeuvre.

Table 1. Comparison of the understeer indicator of the vehicle A_{st} in tests

Vehicle condition	Vehicle with driver	Full load
Steady-state circular test		
Fully functional vehicle	0,397	0,255
Damaged vehicle	0,330	0,371
Step input manoeuvre		
Fully functional vehicle	0,180	0,182
Damaged vehicle	0,330	0,264

Table 2 shows the comparison of yaw rate gain of the vehicle $\dot{\psi}_\delta = \frac{\dot{\psi}}{\delta_w}$ during steady-state circular test and step input manoeuvre.

Table 2. Comparison of yaw rate gain of the vehicle in tests

Vehicle condition	Vehicle with driver	Full load
Steady-state circular test		
Fully functional vehicle	2,698	2,853
Damaged vehicle	2,458	2,475
Step input manoeuvre		
Fully functional vehicle	3,777	3,584
Damaged vehicle	2,734	3,125

The comparison shows that during steady-state circular test, the values of the of the understeer indicator, in case of the fully functional and damaged vehicle are not much different from each other. More differences occur during transient motion, when a manoeuvre was performed with a damaged

shock absorber. This increases the understeer of the vehicle and results in a greater angle of the steered wheels (~28° rotation of the steering wheel).

5. Conclusions

The effect of the shock absorber damage on the vehicle control was shown above. Damaged shock absorber was located in the front right wheel suspension. In the carried out tests this wheel was an outer wheel, so more loaded.

The analysis is based on road tests of the car. Vehicle tests were conducted under vehicle motion conditions characterized by large lateral acceleration values simulating vehicle traffic conditions occurring during road accidents.

The shock absorber damage causes increase of angle of rotation of the steering wheel up to 22° (steer angle gain ~ 1.2°) with larger lateral accelerations, during motion in steady-state circular tests. During a step input manoeuvre, this increase is yet greater and may be up to 28° (increment of wheel steer angle ~1.5°).

During steady-state motion with maintain constant of steering wheel rotation angle, occurs the increase of path radius by ~11%, which at the angle of the steering wheel rotation 185°, corresponds to the increase of the radius by 1.4m. This change results in a reduction in the yaw rate under steady-state conditions of ~9% and at a dynamic step input manoeuvre of ~16%. This translates into higher values of the understeer indicator.

This analysis shows that damage of the shock absorber in front right suspension generally results in an understeer characteristics of the vehicle during carried out various manoeuvres. This entails, during drive on a specified curvilinear track, the need to increase the angle of rotation of the steering wheel to 28°.

The presented analysis shows how badly the shock absorber damage affects the vehicle control and how dangerous it is to road users.

Acknowledgments

The authors thank the management of FCA Poland, Tychy Assembling Plant for enabling the vehicle to be tested and for any assistance in their implementation.

References

[1] Abe M.: Vehicle handling dynamics, theory and application, BH, Amsterdam, 2015

[2] Adamiec-Wójcik I., Awrejcewicz J., Grzegożek W., Wojciech St.: Dynamics of articulated vehicles by means of multibody methods, Politechnika Łódzka, Wydział Mechaniczny, Katedra Automatyki, Biomechaniki i Mechatroniki, Dynamical systems, mathematical and numerical approaches; 2015, s. 11-20

[3] Andrzejewski R.: Stabilność ruchu pojazdów kołowych, WNT Warszawa 1997

[4] Gillespie T. D.: Fundamentals of Vehicle Dynamics, SAE, Warrendale, 1992

[5] Grzegożek W.: Modelowanie dynamiki samochodu przy stabilizującym sterowaniu siłami hamowania, Zeszyty Naukowe Politechniki Krakowskiej, Seria Mechanika, monografia 275, Kraków 2000.

[6] Litwinow A.: Kierowalność i stateczność samochodu, WKŁ, Warszawa, 1975. 11-24

[7] Lozia Z., Więckowski D., Żardecki D.: Wpływ luzu i tarcia w układzie kierowniczym na kierowalność samochodu, Zeszyty Naukowe Politechniki Świętokrzyskiej. Nauki Techniczne, 2008/ 8, 89-120.

[8] Lozia Z.: Rollover of the biaxial vehicle (untripped case), Logistyka 4/2014, Poznań

[9] Luty W.: Badania eksperymentalne oraz opis analityczny właściwości ogumienia samochodów, Zeszyty Naukowe Instytutu Pojazdów / Politechnika Warszawska, 1/77, 2010, pp 7-26.

[10] Pacejka H.: Tire and vehicle dynamics, SAE, Warrendale, 2006

[11] Parczewski K, Wnęk H.: Using mobile scaled vehicle to investigate the truck lateral stability, Eskploatacja I Niezawodnosc – Maintanence and Reliability 2013; 4: 414–420

[12] Parczewski K., Wnęk H.: Analiza wpływu parametrów masowych na stateczność ruchu samochodu ciężarowego w oparciu o badania mobilnego modelu pojazdu. Postępy Nauki i Techniki, SIMP; 14 (2012), 208-223.

[13] Parczewski K., Wnęk H.: The tire characteristics of physical models used to investigate vehicles lateral stability, Part D: Journal of Automobile Engineering, London, 2015, Vol. 229(10) 1419–1426, DOI: 10.1177/0123456789123456.

[14] Parczewski K.: Analiza możliwości wykorzystania modelu fizycznego pojazdu do oceny stateczności ruchu pojazdów wielkogabarytowych, Wydawnictwo Akademii Techniczno-Humanistycznej w Bielsku-Białej, Rozprawa naukowa 52/2014

[15] Parczewski K.: Exploration of the shock-absorber damage influence on the steerability and stability of the car motion, Journal of KONES Powertrain and Transport, Vol. 18, No. 3 2011

[16] Pieniążek W.: Wybrane zagadnienia badania stateczności i kierowalności samochodów, Zeszyty Naukowe Instytutu Pojazdów 79 (2010) 3.

[17] Prochowski L., Wach W., Jackowski J., Pieniążek W.: Experimental and model studies on the influence of the run flat tire damage on braking dynamics of the multi-axial special purpose vehicle, Eksploatacja i Niezawodnosc-Maintenance And Reliability, Lublin 2015 Vol. 17 [No] 1, 118-128.

[18] Reński A.: Układy hamulcowe, kierownicze oraz zawieszenia, Oficyna wydawnicza Politechniki Warszawskiej, 1992 Warszawa

[19] Świder P.: Teoria Ruchu Samochodu cz. I, Wydawnictwo Politechniki Krakowskiej, Kraków, 2012. p 143.

[20] Grązіewicz K., Pokorski J.: Układ pomiarowy AD-32 Grapol Electronic, Warszawa, 2015

[21] Racelogic VBOX Manual 2015

[22] Bosch Automotive handbook, 7th edition, John Wiley & Sons, Chichester, 2007, pp. 442-446

[23] ISO 7401 Road Vehicles – Lateral Transient Response Test Method

[24] ISO 4138 Road Vehicles – Steady State Circular Test Procedure.

[25] ISO 14791 (2000) Heavy Commercial vehicles and Articulated Buses. Lateral stability test methods.

[26] ISO 14792 (2003) Heavy Commercial vehicles and Articulated Buses. Steady state circular test.

[27] ISO 14793 (2003) Heavy Commercial vehicles and Articulated Buses. Lateral transient response test methods.

[28] ISO 3888 (2004) Road vehicles. Test procedure for severe line change manoeuvre.

Krzysztof Parczewski, Assistant Professor, PhD: University of Bielsko-Biala/Department of Combustion Engines and Vehicles/Division of Vehicles, Willowa street 2, 43-309 Bielsko-Biala, Poland, (kparczewski@ath.bielsko.pl).

Henryk Wnęk, Ph.D.: University of Bielsko-Biala/Department of Combustion Engines and Vehicles/Division of Vehicles, Willowa street 2, 43-309 Bielsko-Biala, Poland, (hwnek@ath.bielsko.pl).

Impact of diabetes and drug-resistant strains in a fractional order model for TB transmission

Carla M.A. Pinto, Ana R.M. Carvalho

Abstract: We present a fractional order model to assess the impact of diabetes and drug-resistant strains in tuberculosis (TB) transmission. The reproduction number of the model, defined as the 'expected number of secondary cases produced, in a completely susceptible population, by a typical infective individual', is determined. Numerical simulations are performed for biologically relevant parameters and the results are discussed from an epidemiologically point of view. The order of the fractional derivative adds diversity to the patterns of the TB infection.

1. Introduction

Diabetes is a chronic disease which is increasing worldwide. Its prevalence augments significantly with age, and both sexes are at risk of developing it. Diabetic patients have infections more often than non diabetic patients, and the course of infection is also more pronounced, symptomatically. Diabetes is thus associated with defective immunity, higher adherence of microorganisms to diabetic cells, and the presence of micro- and macroangiopathy or neuropathy [7].

Tuberculosis (TB) is caused by the *Mycobacterium tuberculosis* and is generally an infection of the lungs, though it may affect, less commonly, other body parts. TB may be in a latent state, where there are no symptoms of the disease or in an active phase. The classic symptoms of the active TB are chronic cough, with blood-containing sputum, fever, night sweats, and weight loss. TB is one of the top 10 causes of death worldwide. An estimate of 10.4 million people developed active TB and 1.8 million died from the disease, in 2015. Low and middle-income countries are more prone to the spread of TB, with over 95% of TB deaths. Low education, low income, and poor health care systems may explain this scenario. A severe type of TB is associated with the emergence of multi-drug resistant TB strains (MDR-TB). MDR-TB and, more recently, extensively resistant TB (XDR-TB), jeopardize TB control, and rise concerns of a future of non-effective TB drugs [6]. About 15% of adult TB cases are associated with diabetes [19]. Around the world, 70% of diabetics live in countries where TB is endemic [1]. Moreover, insulin-dependent patients are at a two to three

times greater risk of developing TB [8]. Diabetes affects the patient's response to TB treatment, increases the risk of treatment failure, or even possible relapse [4]. The association between diabetes and TB may be the next challenge for global TB control worldwide [1].

Mathematical models have been developed to understand the dynamics of the TB infection and diabetes. In 2012, Moualeu *et al* [9] present a model for TB to analyse the impact of diabetes on the spread of the disease. Numerical results suggest that diabetes promotes TB transmission and progression to active TB. In 2017, Girard *et al* [8] study the fact that migration could undermine control of the impact of TB on the growing diabetes pandemic. They conclude that screening diabetics for active TB and for TB infection, screening for diabetes among migrants, and better access to health care for diabetic patients could help mitigate the effect of diabetes on TB among migrants.

Fractional calculus

Fractional calculus (FC) is a generalization of the integer order calculus. It is first mentioned in the literature in 1695 in a letter exchange between L'Hôpital and Leibniz. Since then, the meaning and methods to compute 1/2-order derivatives or, in general, α-order derivatives, with α non-integer, has been a major research in mathematics. Some well-known mathematicians that have devoted their work to fractional differentiation and integration are Euler, Abel, Liouville, Riemann, Grünwald, Letnikov, Caputo, amongst others [10, 17].

Fractional models have been used in the literature to understand the behavior of epidemiological models, where the integer-order models fail to give a complete explanation [12–14]. Pinto *et al* [11] propose a fractional-order (FO) model for HIV and TB co-infection. They observe that the results from both the integer-order and the FO versions of the model provide biologically feasible results for the coinfection. In 2013, Diethelm [3] proposes a non-integer order mathematical model for the simulation of the dynamics of a dengue fever outbreak. He shows that the numerical results of the model agree very well with real data from dengue fever in Cape Verde islands in 2009. In 2016, Sweilam *et al* [18] propose a fractional order model for TB, which incorporates three strains: drug-sensitive, emerging multi-drug resistant (MDR) and extensively drug resistant (XDR). They use two numerical methods to solve the equations of the model, the standard finite difference method (SFDM) and the nonstandard finite difference method (NSFDM). They conclude that NSFDM preserves the positivity of the solutions, and it is numerically stable in large regions than SFDM.

With the aforementioned ideas in mind, the paper framework is as follows. In Section 2 we introduce the model. We compute the reproduction number of the model and of the TB-only submodel in Section 3, and plot the variation of R_0 for variation of two relevant parameters. Then, in Section 4, we simulate the model for distinct values of the order

of the fractional derivative and biologically reasonable parameters, and discuss the results epidemiologically. Finally, we conclude our work and mention future research headlines.

2. The Model

The model is composed of 10 classes and the population is divided into diabetic (index 2) or non-diabetic (index 1). For each of these groups we have susceptible individuals (S_1 and S_2), exposed to TB (E_1 and E_2), infected with TB (I_1 and I_2), recovered from TB (R_1 and R_2) and infected with the MDR-TB strains (T_{R1} and T_{R2}).

The susceptible non-diabetic individuals are recruited at rate Λ. They become diabetic at rate α_D. If they are infected with TB or with MDR-TB, they became diabetic at rates $\tau\alpha_D$ and $\tau_1\alpha_D$, respectively. Parameters τ and τ_1 are defined such that $\tau, \tau_1 \geq 1$, since diabetic individuals are more infectious than non-diabetics.

Susceptible individuals are infected with TB at rate $\lambda_T = \frac{\beta_T\left(I_1+\epsilon_1 I_2+\epsilon_2\left(T_{R_1}+T_{R2}\right)\right)}{N}$, where β_T is the effective contact rate of the TB and MDR-TB infected individuals, sufficient to transmit infection to susceptible individuals. Parameters ϵ_1 and ϵ_2 are modification parameters, modelling the increased infectiousness of dually infected TB or MDR-TB and diabetes individuals, when compared to TB solely infected ones. The diabetic susceptible individuals are infected with TB at rate $\theta\lambda_T$, where $\theta > 1$, accounts for increasing susceptibility to TB by diabetics. Individuals die from natural causes at rate μ.

The proportions $(1 - p_1)$ and $(1 - p_2)$ are the newly latently TB infected individuals, the first are non-diabetic and the later are diabetic. The recovered individuals may only have partial immunity, and return to the infected state at rates δ_1 or δ_2, for non-diabetic or diabetic cases, respectively. In addition, the recovered individuals who don't return to the active state may be re-infected with TB at rates $\sigma_3(1-\delta_1)\lambda_T$ (non-diabetic) or $\sigma_4(1-\delta_2)\theta\lambda_T$ (diabetic). Parameters σ_3 and σ_4 are reducing factors, since primary infection confers some degree of immunity.

Latently infected individuals develop active TB through endogenous reactivation and exogenous reinfections at rates, $(1 - r_1)k_1$ or $(1 - r_2)k_2$ and $(1 - r_1)\sigma_1\lambda_T$ or $(1 - r_2)\sigma_2\theta\lambda_T$, respectively. Parameters r_1 and r_2 are the rates of chemoprophylaxis, σ_1 and σ_2 are the degrees of immunity given by primary infection. We assume $k_2 > k_1$ given that diabetic individuals tend to develop TB more rapidly than non-diabetic individuals. The non-diabetic and diabetic infected individuals recover from the disease at rates γ_1 and γ_2, respectively. They become resistant to the first line of TB treatment at rates σ_{T1} (non-diabetic) or σ_{T2} (diabetic). The individuals infected with MDR-TB strains recover from tuberculosis at rate a a (non-diabetic) or a_1 (diabetic). The individuals die from TB or diabetes and TB

coinfection at rates d_1 and d_2, respectively.

The nonlinear system of fractional-order differential equations describing the dynamics of the model is:

$$\begin{aligned}
\frac{d^\alpha S_1}{dt^\alpha} &= \Lambda^\alpha - (\mu^\alpha + \alpha_D^\alpha + \lambda_T)S_1 \\
\frac{d^\alpha E_1}{dt^\alpha} &= (1-p_1)\lambda_T S_1 + \sigma_3(1-\delta_1^\alpha)\lambda_T R_1 - (1-r_1^\alpha)(k_1^\alpha + \sigma_1\lambda_T)E_1 - (\mu^\alpha + \alpha_D^\alpha)E_1 \\
\frac{d^\alpha I_1}{dt^\alpha} &= p_1\lambda_T S_1 + (1-r_1^\alpha)(k_1^\alpha + \sigma_1\lambda_T)E_1 + \delta_1^\alpha R_1 - (\mu^\alpha + d_1^\alpha + \tau\alpha_D^\alpha + \gamma_1^a lpha + \sigma_{T1}^\alpha)I_1 \\
\frac{d^\alpha R_1}{dt^\alpha} &= \gamma_1^\alpha I_1 + a^\alpha T_{R1} - \sigma_3(1-\delta_1^\alpha)\lambda_T R_1 - (\delta_1^\alpha + \alpha_D^\alpha + \mu^\alpha)R_1 \\
\frac{d^\alpha T_{R1}}{dt^\alpha} &= \sigma_{T1}^\alpha I_1 - (\tau_1\alpha_D^\alpha + a^\alpha + \mu^\alpha + \delta_2^\alpha)T_{R1} \\
\frac{d^\alpha S_2}{dt^\alpha} &= \alpha_D^\alpha S_1 - (\mu^\alpha + \theta\lambda_T)S_2 \\
\frac{d^\alpha E_2}{dt^\alpha} &= \theta(1-p_2)\lambda_T S_2 + \sigma_4\theta(1-\delta_2^\alpha)\lambda_T R_2 + \alpha_D^\alpha E_1 - (1-r_2^\alpha)(k_2^\alpha + \sigma_2\theta\lambda_T)E_2 - \mu^\alpha E_2 \\
\frac{d^\alpha I_2}{dt^\alpha} &= \theta p_2\lambda_T S_2 + (1-r_2^\alpha)(k_2^\alpha + \sigma_2\theta\lambda_T)E_2 + \tau\alpha_D^\alpha I_1 + \delta_2^\alpha R_2 - (\mu^\alpha + d_2^\alpha + \gamma_2^\alpha + \sigma_{T2}^\alpha)I_2 \\
\frac{d^\alpha R_2}{dt^\alpha} &= \gamma_2^\alpha I_2 + a_1^\alpha T_{R2} - \sigma_4\theta(1-\delta_2^\alpha)\lambda_T R_2 + \alpha_D^\alpha R_1 - (\delta_2^\alpha + \mu^\alpha)R_2 \\
\frac{d^\alpha T_{R2}}{dt^\alpha} &= \sigma_{T2}^\alpha I_2 + \tau_1\alpha_D^\alpha T_{R1} - (a_1^\alpha + \mu^\alpha + \delta_2^\alpha)T_{R2}
\end{aligned} \tag{1}$$

where $\alpha \in (0, 1]$ is the order of the fractional derivative. When $\alpha = 1$, then the model is the integer order counterpart. The fractional derivative of the proposed model is used in the Caputo sense, i.e.:

$$\frac{d^\alpha y(t)}{dt^\alpha} = I^{p-\alpha} y^{(p)}(t), \quad t > 0$$

where $p = [\alpha]$ is the value of α rounded up to the nearest integer, $y^{(p)}$ is the p-th derivative of $y(r)$, I^{p_1} is the Riemann-Liouville fractional integral given by:

$$I^{p_1} z(t) = \frac{1}{\Gamma(p_1)} \int_0^t \left(t - t^{'}\right)^{p_1 - 1} z(t^{'}) dt^{'}$$

3. Reproduction number

The disease-free equilibrium state, P_0, of model (1) is given by:

$$
\begin{aligned}
P_0 &= (S_1^0, E_1^0, I_1^0, R_1^0, T_{R1}^0, S_2^0, E_2^0, I_2^0, R_2^0, T_{R2}^0) \\
&= \left(\tfrac{\Lambda^\alpha}{\mu^\alpha+\alpha_D^\alpha}, 0, 0, 0, 0, \tfrac{\Lambda^\alpha \alpha_D^\alpha}{\mu^\alpha(\mu^\alpha+\alpha_D^\alpha)}, 0, 0, 0, 0\right)
\end{aligned}
$$

System (1) can be written in the following compact form:

$$
\begin{aligned}
x'(t) &= \Gamma + A_x x(t) - \lambda \textstyle\sum_{i=1}^{2} B_i < e_i \mid x(t) > \\
y'(t) &= \lambda \left[\textstyle\sum_{i=1}^{2} \kappa_i < e_i \mid x(t) > + \sum_{i=3}^{6} B_i < e_i \mid y(t) >\right] + A_y y(t)
\end{aligned}
\tag{2}
$$

where $x(t) = (x_1(t), x_2(t))^T = (S_1(t), S_2(t))^T \in \mathbb{R}_+^2$, $y(t) = (y_1(t), y_2(t), y_3(t), y_4(t), y_5(t), y_6(t), y_7(t), y_8(t))^T = (E_1(t), I_1(t), R_1(t), T_{R1}(t), E_2(t), I_2(t), R_2(t), T_{R2}(t))^T \in \mathbb{R}_+^8$, $\Gamma = (\Lambda^\alpha, 0)^T$, $\lambda = \frac{<B|y>}{N}$, $B = (0, \beta_T, 0, \epsilon_2\beta_T, 0, \epsilon_1\beta_T, 0, \epsilon_2\beta_T)$, $B_1 = (1,0)^T$, $B_2 = (0,\theta)^T$, $B_3 = (-\sigma_1(1-r_1^\alpha), \sigma_1(1-r_1^\alpha), 0, 0, 0, 0, 0, 0)^T$, $B_4 = (0,0,0,0,-\theta\sigma_2(1-r_2^\alpha), \theta\sigma_2(1-r_2^\alpha), 0, 0)^T$, $B_5 = (\sigma_3(1-\delta_1^\alpha), 0, -\sigma_3(1-\delta_1^\alpha), 0, 0, 0, 0, 0)^T$, $B_6 = (0,0,0,0,\sigma_4\theta(1-\delta_2^\alpha), 0, -\sigma_4\theta(1-\delta_2^\alpha), 0)^T$, $e_1 = (1,0)$, $e_2 = (0,1)$, $e_3 = (1,0,0,0,0,0,0,0,0)$, $e_4 = (0,0,0,0,1,0,0,0)$, $e_5 = (0,0,1,0,0,0,0,0)$, $e_6 = (0,0,0,0,0,0,1,0)$, $\kappa_1 = ((1-p1), p1, 0, 0, 0, 0, 0, 0)^T$, $\kappa_2 = (0,0,0,0,\theta(1-p_2), \theta p_2, 0, 0)^T$,

$$
A_x = \begin{pmatrix} -(\mu^\alpha + \alpha_D^\alpha) & 0 \\ \alpha_D^\alpha & -\mu^\alpha \end{pmatrix}
$$

$$
A_y = \begin{pmatrix}
-(1-r_1^\alpha)k_1^\alpha - \mu^\alpha - \alpha_D^\alpha & 0 & 0 & 0 & 0 & 0 & 0 & 0 \\
(1-r_1^\alpha)k_1^\alpha & -(\mu^\alpha + d_1^\alpha + \tau\alpha_D^\alpha + \gamma_1^\alpha + \sigma_{T1}^\alpha) & \delta_1^\alpha & 0 & 0 & 0 & 0 & 0 \\
0 & \gamma_1^\alpha & -(\delta_1^\alpha + \alpha_D^\alpha + \mu^\alpha) & a^\alpha & 0 & 0 & 0 & 0 \\
0 & \sigma_{T1}^\alpha & 0 & -(\tau_1\alpha_D^\alpha + a^\alpha + \mu^\alpha + \delta_2^\alpha) & 0 & 0 & 0 & 0 \\
\alpha_D^\alpha & 0 & 0 & 0 & -(1-r_2^\alpha)k_2^\alpha - \mu^\alpha & 0 & 0 & 0 \\
0 & \tau\alpha_D^\alpha & 0 & 0 & (1-r_2^\alpha)k_2^\alpha & -(\mu^\alpha + d_2^\alpha + \gamma_2^\alpha + \sigma_{T2}^\alpha) & \delta_2^\alpha & 0 \\
0 & 0 & \alpha_D^\alpha & 0 & 0 & \gamma_2^\alpha & -(\delta_2^\alpha + \mu^\alpha) & a_1^\alpha \\
0 & 0 & 0 & \tau_1\alpha_D^\alpha & 0 & \sigma_{T2}^\alpha & 0 & -(a_1^\alpha + \mu^\alpha + \delta_2^\alpha)
\end{pmatrix}
$$

In Eq. (2), $< a \mid b >= a^T b$ is the usual inner scalar product. The linear stability of P_0 can be established using the next generation operator method on system (1). Using the same notation as in [2], the matrices F and V, for the new infection terms and the remaining transfer terms, are, respectively:

$$
F = \frac{1}{N_0} \sum_{i=1}^{2} \kappa_i B S_i^0 \qquad V = -A_y \tag{3}
$$

where $N_0 = \frac{\Lambda^\alpha}{\mu^\alpha}$, giving

$$
R_0 = \rho(FV^{-1}) = \frac{1}{N_0} \sum_{i=1}^{2} < B \mid (-A_y)^{-1} \kappa_i > S_i^0 \tag{4}
$$

where ρ represents the spectral radius. The next lemma follows from Theorem 2 of [5].

Lemma 1 *The disease-free equilibrium P_0 of system (1) is locally asymptotically stable whenever $R_0 < 1$ and unstable whenever $R_0 > 1$.*

The threshold quantify R_0 is the basic reproduction number for TB infection in the presence of diabetes. It measures the average number the new TB infections generated by a single infectious in a completely susceptible population. Consequently, the disease-free equilibrium of model (1) is locally asymptotically stable whenever $R_0 < 1$ and unstable if $R_0 > 1$. This means that TB can be eliminated from the community (when $R_0 < 1$) if the sizes of the population of model (1) are in the basin of attraction of P_0.

4. Numerical Results

We simulate the model (1) for different values of the order of the fractional derivative, α. The parameters used in the simulations, based on [9,15,16], are $\Lambda = 667685$, $\mu = 1/53.5$, $\alpha_D = 9/1000$, $\beta_T = 10$, $p_1 = 0.03$, $\sigma_3 = 0.73p_1$, $\delta_1 = 0.0986$, $r_1 = 0$, $\sigma_1 = 0.75p_1$, $k_1 = 0.00013$, $\tau = 1.01$, $\gamma_1 = 0.7372$, $\theta = 2$, $p_2 = 0.06$, $\sigma_4 = 0.71p_2$, $\delta_2 = 0.1$, $\sigma_2 = 0.7p_2$, $r_2 = 0$, $k_2 = 2k_1$, $\gamma_2 = 0.7372$, $\tau_1 = 1.01$, $d_1 = 0.275$, $d_2 = 1.25d_1$, $\epsilon_1 = 1.1$, $\epsilon_2 = 1.1$, $\sigma_T = 0.003$, $a = 0.11$, and the inicial conditions are: $S_1(0) = 8741400$, $E_1(0) = 557800$, $I_1(0) = 20000$, $R_1(0) = 8000$, $T_{R1}(0) = 1000$, $S_2(0) = 200000$, $E_2(0) = 4500$, $I_2(0) = 1800$, $R_2(0) = 200$ and $T_{R2}(0) = 100$.

Figures 1-3 illustrate the behaviour of model (1) for variation of the value of the increased susceptibility to TB due to diabetes, θ. There is an increase of the proportion of exposed and infectious TB individuals with diabetes, with θ. As the epidemic progresses, we also observe higher proportions of TB-solely exposed individuals. Thus, susceptibility to TB impacts the dynamics of TB in diabetics. Similar patterns are present for all values of the order of the fractional derivative, α.

Figures 4-6 suggest that increasing the recruitment of diabetics will increase the prevalence of TB cases, and of MDR-TB infection cases. This means that more hyperglycaemic individuals in the community may increase the prevalence of TB. Thus diabetes must be taken into account in individuals infected with TB in order to control the epidemic. This is particularly important in the case of MDR-TB infected individuals, since these strains jeopardize TB control, and enhance fears of future non-effective TB drugs. The same behaviour is present for all values of the order of the fractional derivative, α.

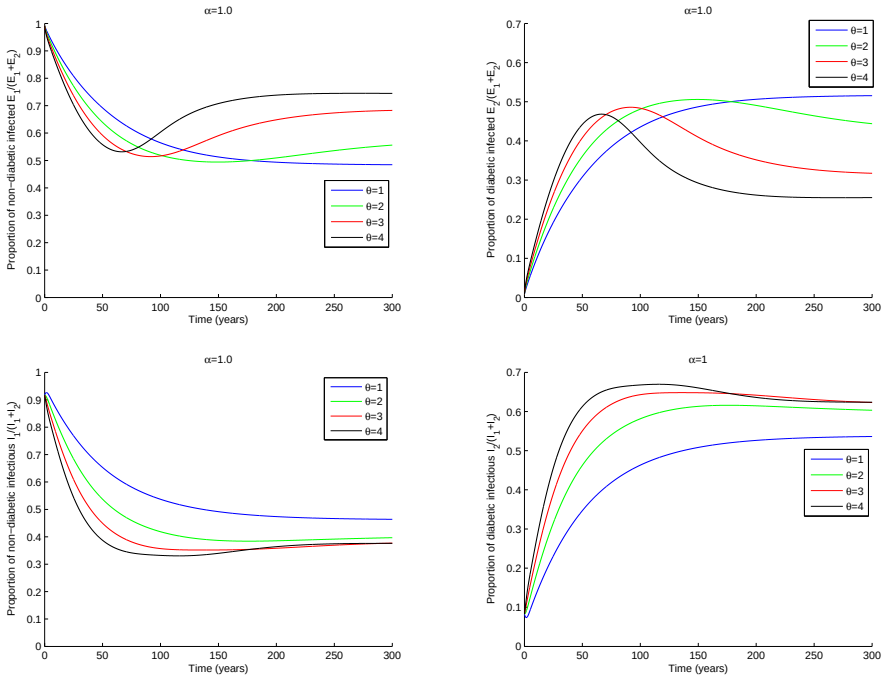

Figure 1. Dynamics of the relevant variables of system (1) for different values of θ, the increased susceptibility to TB due to diabetes, for $\alpha = 1$. Parameter values and initial conditions are in the text, except $\beta_T = 9$ ($\theta = 1$ - $R_0 = 1.0676$, $\theta = 2$ - $R_0 = 1.5623$, $\theta = 3$ - $R_0 = 2.0570$, $\theta = 4$ - $R_0 = 2.5517$).

5. Conclusions

We propose a FO model for TB transmission in the presence of diabetes. We compute the reproduction number of the model. We simulate the model's behaviour for distinct values of the order of the fractional derivative, α, and for biologically reasonable parameters. We observe that the susceptibility to TB, θ, impacts the dynamics of TB in diabetics. Namely, the proportion of exposed and infectious TB individuals with diabetes increases with θ, and, as the epidemic progresses, we also observe higher proportions of TB-solely exposed individuals. The increase in the diabetics recruitment rate, α_D, suggests that the prevalence of TB is higher when more hyperglycaemic individuals are present in the community. Diabetes should thus be taken seriously in control actions for TB infected individuals. The case of MDR-TB infectious with diabetes is even more serious, due to difficulty in treating these resistant strains. The order of the fractional derivative may be used to adjust data from distinct communities. Similar initial factors in distinct communities may produce different

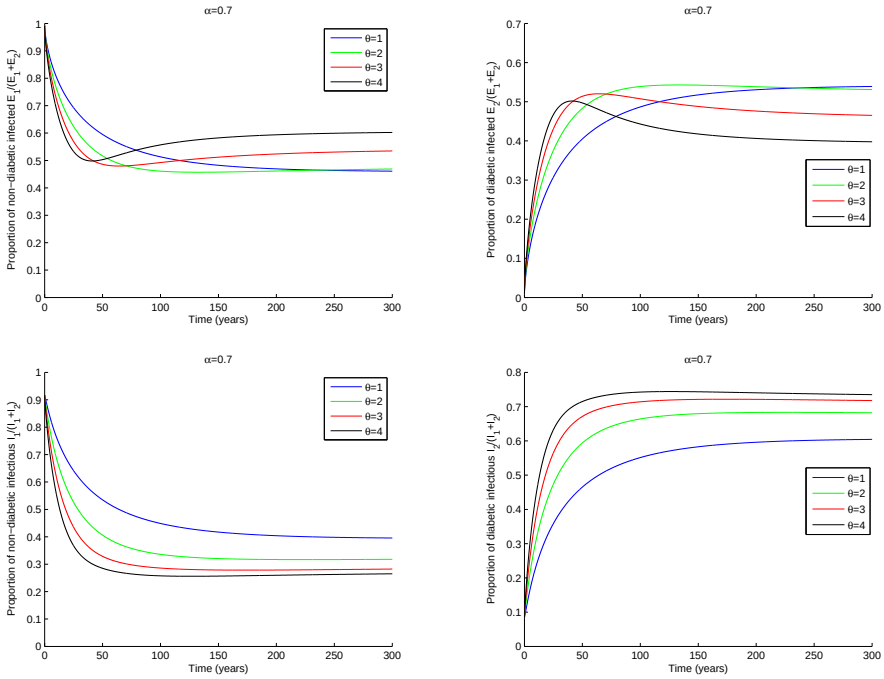

Figure 2. Dynamics of the relevant variables of system (1) for different values of θ, the increased susceptibility to TB due to diabetes, for $\alpha = 0.7$. Parameter values and initial conditions are in the text, except $\beta_T = 9$ ($\theta = 1$ - $R_0 = 1.1173$, $\theta = 2$ - $R_0 = 1.6643$, $\theta = 3$ - $R_0 = 2.2114$, $\theta = 4$ - $R_0 = 2.7584$).

asymptotic behaviours that could be better fitted with a fractional order model.

Acknowledgments

The authors were partially funded by the European Regional Development Fund through the program COMPETE and by the Portuguese Government through the FCT - Fundação para a Ciência e a Tecnologia under the project PEst-C/MAT/UI0144/2013. The research of AC was partially supported by a FCT grant with reference SFRH/BD/96816/2013.

References

[1] Baghaei, P., Marjani, M., Javanmard, P., Tabarsi, P., and Masjedi, M. Diabetes mellitus and tuberculosis facts and controversies. *Journal of Diabetes & Metabolic Disorders 58*, 12 (2013).

[2] Berman, A., and Plemmons, R. *Nonnegative matrices in the mathematical sciences.*

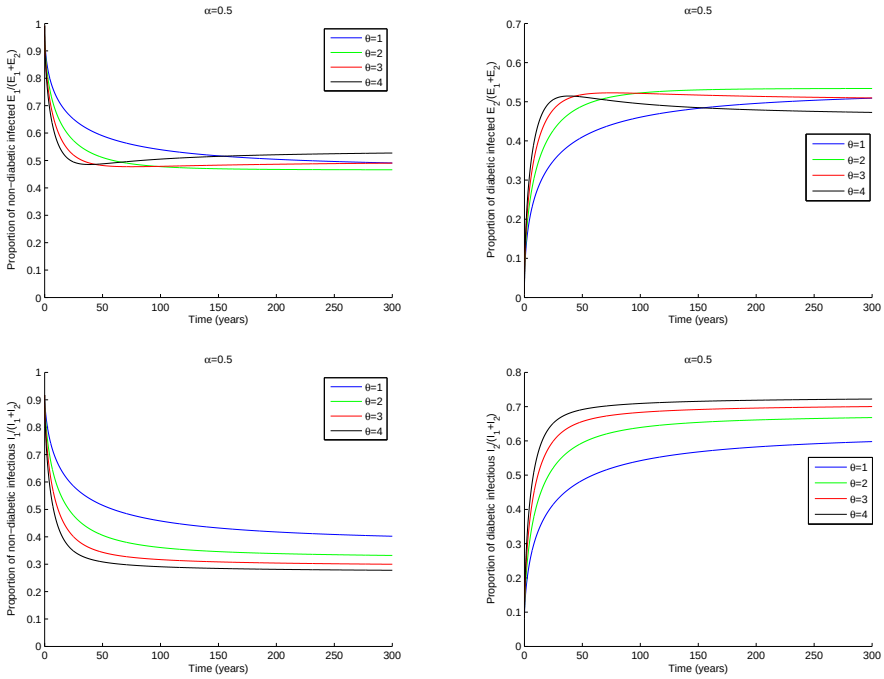

Figure 3. Dynamics of the relevant variables of system (1) for different values of θ, the increased susceptibility to TB due to diabetes, for $\alpha = 0.5$. Parameter values and initial conditions are in the text, except $\beta_T = 9$ ($\theta = 1$ - $R_0 = 1.3735$, $\theta = 2$ - $R_0 = 2.05$, $\theta = 3$ - $R_0 = 2.7265$, $\theta = 4$ - $R_0 = 3.4030$).

SIAM, 1994.

[3] Diethelm, K. A fractional calculus based model for the simulation of an outbreak of dengue fever. *Nonlinear Dynamics" 4*, 71 (2013), 613–619.

[4] Dooley, K., and Chaisson, R. Tuberculosis and diabetes mellitus: convergence of two epidemics. *The Lancet Infectious Diseases 12*, 9 (2009), 737746.

[5] Driessche, P., and Watmough, P. Reproduction numbers and sub-threshold endemic equilibria for compartmental models of disease transmission. *Mathematical Biosciences*, 180 (2002), 29–48.

[6] Gandhi, N., Nunn, P., Dheda, K., Schaaf, H., Zignol, M., Van Soolingen, D., Jensen, P., and Bayona, J. Multidrug-resistant and extensively drug-resistant tuberculosis: a threat to global control of tuberculosis. *Lancet*, 375 (2010), 1830–1843.

[7] Geerlings, S., and Hoepelman, A. Immune dysfunction in patients with diabetes mellitus (dm). *FEMS Immunology and Medical Microbiology*, 26 (1999), 259–265.

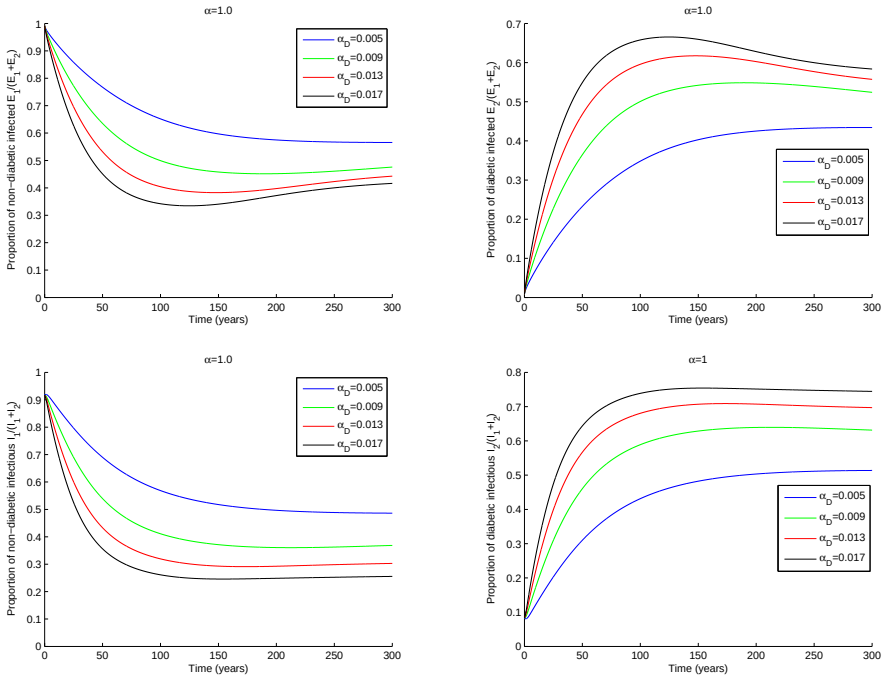

Figure 4. Dynamics of the relevant variables of system (1) for different values of α_D, the recruitment rate of diabetics, for $\alpha = 1$. Parameter values and initial conditions are in the text, except $\beta_T = 8$ ($\alpha_D = 0.005$ - $R_0 = 1.1572$, $\alpha_D = 0.009$ - $R_0 = 1.3887$, $\alpha_D = 0.013$ - $R_0 = 1.56$, $\alpha_D = 0.017$ - $R_0 = 1.6918$).

[8] Girardi, E., Schepisi, M., Goletti, D., Bates, M., Mwaba, P., Yeboah-Manu, D., Ntoumi, F., Palmieri, F., Maeurer, M., and Zumla, A. Ippolito, G. The global dynamics of diabetes and tuberculosis: the impact of migration and policy implications. *International Journal of Infectious Diseases*, 56 (2017), 45–53.

[9] Moualeu, D., Bowong, S., Tewa, J., and Emvudu, Y. Analysis the impact of diabetes on the dynamical transmission of tuberculosis. *Mathematical Modelling of Natural Phenomena 7*, 3 (2012), 117–146.

[10] Oldham, K., and Spanier, J. *The Fractional Calculus: Theory and Application of Differentiation and Integration to Arbitrary Order*. New York, NY: Academic Press,, 1974.

[11] Pinto, C., and Carvalho, A. New findings on the dynamics of hiv and tb coinfection models. *Applied Mathematics and Computation*, 242 (2014), 36–46.

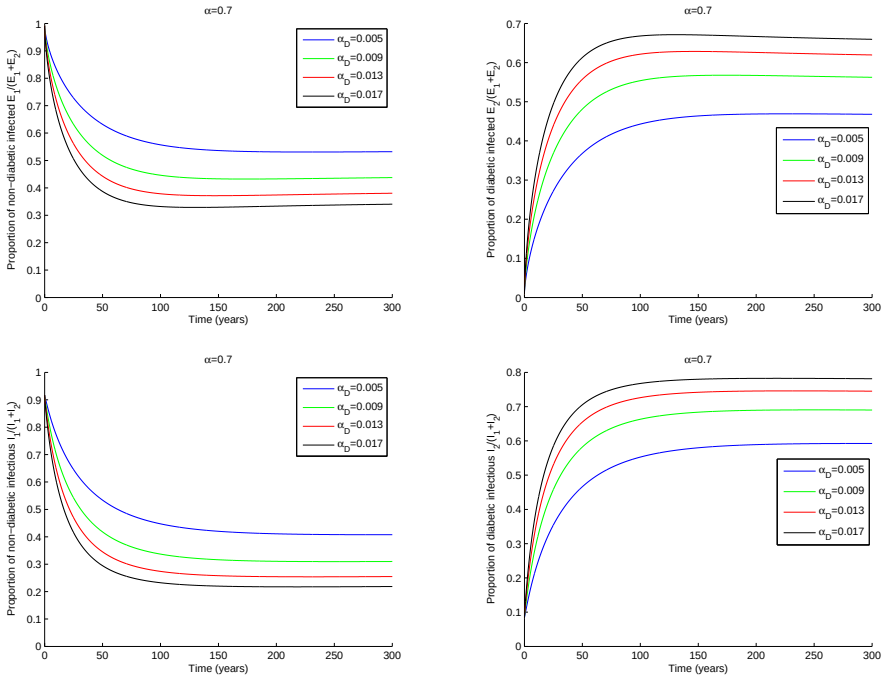

Figure 5. Dynamics of the relevant variables of system (1) for different values of α_D, the recruitment rate of diabetics, for $\alpha = 0.7$. Parameter values and initial conditions are in the text, except $\beta_T = 8$ ($\alpha_D = 0.005$ - $R_0 = 1.3044$, $\alpha_D = 0.009$ - $R_0 = 1.4794$, $\alpha_D = 0.013$ - $R_0 = 1.5973$, $\alpha_D = 0.017$ - $R_0 = 1.6849$).

[12] Pinto, C., and Carvalho, A. Fractional modeling of typical stages in hiv epidemics with drug-resistance. *Progress in Fractional Differentiation and Applications 2*, 1 (2015), 111–122.

[13] Pinto, C., and Carvalho, A. Fractional complex-order model for hiv infection with drug-resistance during therapy. *Journal of Vibration and Control 9*, 22 (2016), 2222–2239.

[14] Pinto, C., and Carvalho, A. The role of synaptic transmission in a hiv model with memory. *Applied Mathematics and Computation*, 292 (2017), 76–95.

[15] Rodrigues, P., Gomes, M., and Rebelo, C. Drug resistance in tuberculosis - a reinfection model. *Theoretical Population Biology*, 71 (2007), 196–212.

[16] Ronoh, M., Jaroudi, R., Fotso, P., Kamdoum, V., Matendechere, N., Wairimu, J., Auma, R., and Lugoye, J. A mathematical model of tuberculosis with drug resistance effects. *Applied Mathematics*, 7 (2016), 13031316.

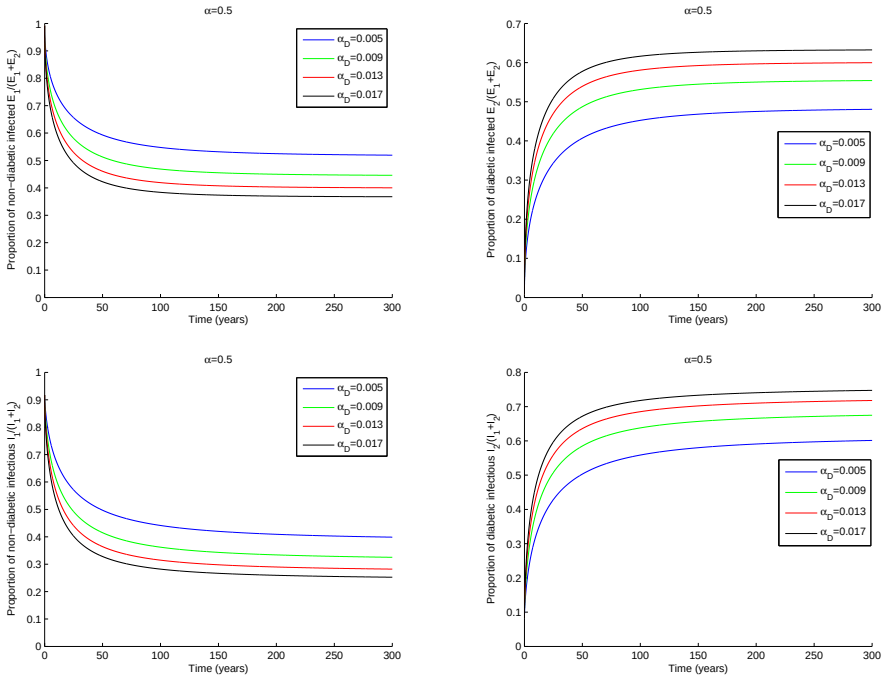

Figure 6. Dynamics of the relevant variables of system (1) for different values of α_D, the recruitment rate of diabetics, for $\alpha = 0.5$. Parameter values and initial conditions are in the text, except $\beta_T = 8$ ($\alpha_D = 0.005$ - $R_0 = 1.68$, $\alpha_D = 0.009$ - $R_0 = 1.8222$, $\alpha_D = 0.013$ - $R_0 = 1.9141$, $\alpha_D = 0.017$ - $R_0 = 1.9815$).

[17] Samko, S., Kilbas, A., and Marichev, O. *Fractional Integrals and Derivatives: Theory and Applications*. London: Gordon and Breach Science Publishers, 1993.

[18] Sweilam1, N., and S.M., A. Comparative study for multi-strain tuberculosis (tb) model of fractional order. *Applied Mathematics & Information Sciences 10*, 4 (2016), 1403–1413.

[19] WHO, W. H. O. The dual epidemic of tb and diabetes. www.who.int/tb.

Carla M.A. Pinto, Ph.D.: School of Engineering, Polytechnic of Porto and Center for Mathematics of the University of Porto, Rua Dr António Bernardino de Almeida 431, 4200-072 Porto, Portugal (*cap@isep.ipp.pt*). The author gave a presentation of this paper during one of the conference sessions.

Ana R.M. Carvalho, M.Sc. (Ph.D. student): Faculty of Sciences, University of Porto, Rua do Campo Alegre s/n, 4169-002 Porto, Portugal (*up200802541@fc.up.pt*).

Influence of plain journal bearing parameters on the rotor nonlinear behaviour

Pavel Polach, Luboš Smolík, Jan Rendl, Michal Hajžman

Abstract: This paper deals with the investigation of the rotor nonlinear behaviour with respect to design parameters of plain journal bearings. The Reynolds equation is solved numerically employing a verified in-house solver based on finite differences. A pressure distribution serves for the calculation of nonlinear bearing forces acting on the rotor. Bearing forces together with the model of a rotating structure form equations of motion of the whole system as a set of ordinary differential equations. The nonlinear rotor behaviour is solved using direct numerical integration of equations of motion, which is a suitable way for the evaluation of possible instabilities with respect to bearing parameters. Obtained numerical results are compared with results calculated using a commercial simulation software.

1. Introduction

Design of supports in rotor dynamics can strongly influence behaviour of a whole rotating system. Since journal bearings are one of the typical solutions in many industrial applications this paper is focused on the investigation of plain journal bearing parameters and their effects on the rotor dynamics performance.

Hydrodynamic forces acting in radial journal bearings can be computed using the Reynolds equation [4]. Basic methods of the solution of this equation are described e.g. in [5, 2]. Another important part of the mathematical modelling of the studied mechanical systems is dynamics of rotating structures [1].

The paper is divided into five sections including Introduction (the first one) and Conclusions (the last one). The second section deals with the Reynolds equation and its solution. The third section describes the general approach for the modelling of rotating systems supported by journal bearings and an alternative modelling approach based on the flexible multibody dynamics. Application and parametric case studies are shown in the fourth section.

2. Modelling of plain journal bearings using the Reynolds equation

The interaction between a journal and a bearing is characterized by hydrodynamic forces, which can be obtained by integrating function $p = p(X, Z, t)$, which describes the pressure

distribution of an oil film in the bearing. Assuming that the geometry of the bearing is given in Fig. 1, the forces acting on the journal are

$$F_{Hy} = -\int_{-\frac{L}{2}}^{\frac{L}{2}} \int_{0}^{2\pi R} p \sin \frac{X}{R} \, \mathrm{d}X \mathrm{d}Z, \quad F_{Hz} = -\int_{-\frac{L}{2}}^{\frac{L}{2}} \int_{0}^{2\pi R} p \cos \frac{X}{R} \, \mathrm{d}X \mathrm{d}Z, \tag{1}$$

where R is the journal radius, L is the bearing length and X and Z are the circumferential and the axial coordinates, respectively.

Pressure field $p = p(X, Z, t)$ is described by the Reynolds equation [4, 5]. Throughout the literature, this equation can be found in many forms respecting various considerations. The approach presented in this paper is based on the form

$$\frac{\partial}{\partial X}\left(\frac{h^3}{\eta}\frac{\partial p}{\partial X}\right) + \frac{\partial}{\partial Z}\left(\frac{h^3}{\eta}\frac{\partial p}{\partial Z}\right) = 6\frac{\partial}{\partial X}\left[h\left(u_1 + u_2\right)\right] + 12\frac{\partial}{\partial t}\left(h\right), \tag{2}$$

which is valid for thin films of constant density and under conditions of laminar flow. $h = h(X, Z, t)$ in (2) is the height of the oil film, η is the dynamic viscosity and u_1, u_2 are circumferential bearing and journal velocities, respectively..

Assuming that the coordinate system (x, y, z) is fixed to the bearing, u_1 is given by angular velocity of the bearing ω_1 and bearing radius R_B as

$$u_1 = -R_B \, \omega_1. \tag{3}$$

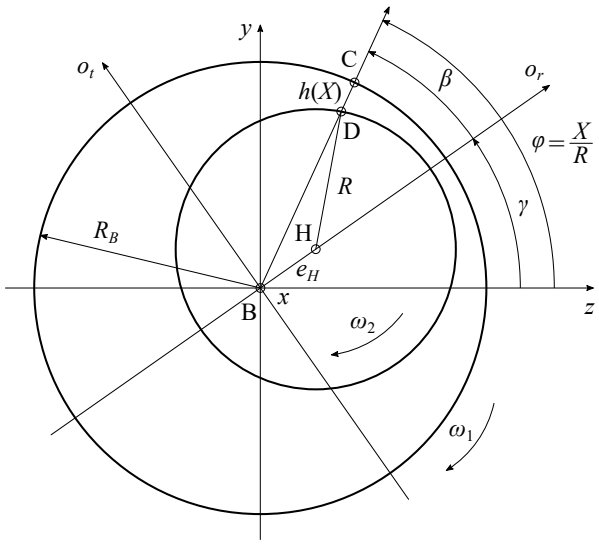

Figure 1. Plain journal bearing

Circumferential velocity of point D $u_{2,D}$ is dependent not only on angular velocity of the journal ω_2 but also on the journal vibrations and can be expressed in the form

$$u_{2,D} = -\dot{z}_H \sin\frac{X}{R} + \dot{y}_H \cos\frac{X}{R} - R\,\omega_2, \tag{4}$$

assuming that $\dot{y}_H$ and $\dot{z}_H$ are vertical and horizontal velocities of point H relative to the (x, y, z) system.

An exact analytical solution of the Reynolds equation (2) is rather difficult to express, so the equation is usually solved numerically. A method based on the finite difference approach is introduced in the article. A surface of the bearing is discretized using an equidistant mesh of nodes with ΔX step in circumferential and ΔZ step in axial direction as shown in Fig. 2.

Partial derivates in (2) can be expressed using central finite differences

$$\frac{\partial p_{i,j}}{\partial X} = \frac{p_{i+1,j} - p_{i-1,j}}{2\Delta X}, \tag{5}$$

$$\frac{\partial^2 p_{i,j}}{\partial X^2} = \frac{p_{i+1,j} - 2p_{i,j} + p_{i-1,j}}{\Delta X^2}, \tag{6}$$

$$\frac{\partial p_{i,j}}{\partial Z} = \frac{p_{i,j+1} - p_{i,j-1}}{2\Delta Z}, \tag{7}$$

$$\frac{\partial^2 p_{i,j}}{\partial Z^2} = \frac{p_{i,j+1} - 2p_{i,j} + p_{i,j-1}}{\Delta Z^2}, \quad \text{where} \quad i = 1, \ldots, M \text{ and } j = 2, \ldots, N-1 \tag{8}$$

where $p_{i,j}$ is the pressure in an inner node (i, j). After introducing expressions (5)–(8) to equation (2), one can obtain

$$a_{i,j}\,p_{i+1,j} + b_{i,j}\,p_{i-1,j} + c_{i,j}\,p_{i,j} + d_{i,j}\,p_{i,j+1} + e_{i,j}\,p_{i,j-1} = f_{i,j}, \tag{9}$$

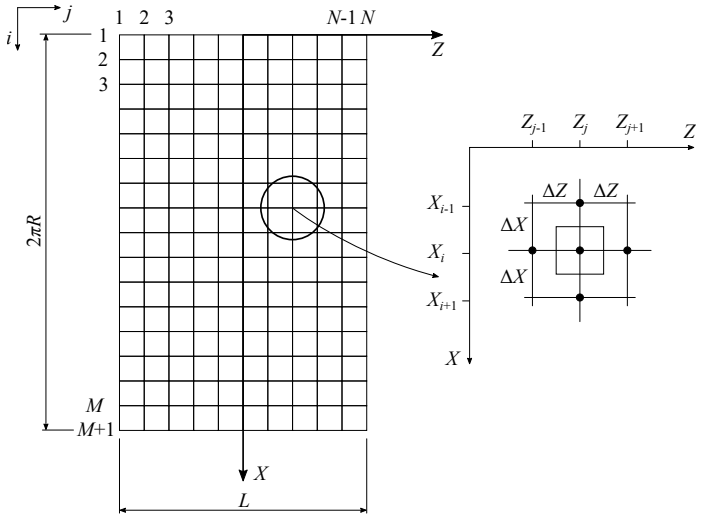

Figure 2. Mesh with nodes for numerical solution

where $a_{i,j}$–$f_{i,j}$ are the coefficients of the linear combination. The system of equations for all inner nodes can be written in the matrix form

$$\mathbf{A}\mathbf{p} = \mathbf{f}, \tag{10}$$

which can be further modified in order to respect boundary conditions [5]. Resulting linear system of equations has symmetric, positive definite and sparse coefficient matrix $\mathbf{A}$.

3. Dynamics of rotors supported by journal bearings

Modelling of thr flexible rotor dynamics is usually based on the finite element method considering the Euler-Bernoulli or Timoshenko beams [1]. The models usually respect continuous mass of rotating shafts and discrete masses characterizing disks or gear wheels. The mathematical model is derived in the form of the second order ordinary differential equation

$$\mathbf{M}\ddot{\mathbf{q}}(t) + (\mathbf{B} + \omega_0\mathbf{G})\,\dot{\mathbf{q}}(t) + \mathbf{K}\mathbf{q}(t) = \mathbf{f}_B\,(\mathbf{q}, \dot{\mathbf{q}}, \omega_0, t) + \mathbf{f}_E(t), \tag{11}$$

where $\mathbf{M}$ is the shaft mass matrix, $\mathbf{B}$ is the damping matrix, $\omega_0\mathbf{G}$ represents gyroscopic effects, $\mathbf{K}$ is the shaft stiffness matrix, $\mathbf{f}_E$ is the general vector of external forces and $\mathbf{f}_B$ is the vector representing bearing forces, which is calculated using the Reynolds equation. The whole mathematical model is derived in the configuration space defined by vector of the generalized coordinates of the shaft $\mathbf{q} = \mathbf{q}(t)$.

General solution of the whole model including hydrodynamic forces can be obtained by means of a direct numerical integration of equation of motion (11) together with the Reynolds equation solution.

Another possibility of the investigation of the nonlinear rotor dynamical behaviour is the utilization of approaches based on the multibody dynamics. Vibrations and global motion of each flexible body are described by a system of differential algebraic equations (DAE) defined by [3]. This alternative modelling approach is implemented in the AVL Excite software, where the Reynolds equation is solved using the finite element method.

4. Application and parametric studies

The above presented mathematical model of the Jeffcott rotor supported by the plain journal bearing was implemented in the in-house MATLAB programme and the AVL Excite software. Parameters of the system are shown in Tab. 1. As can be seen in Tab. 1, the influence of several parameters on rotor behaviours was studied. The varied parameters are rotor speed n, bearing length L, dynamic viscosity η and radial clearance of the bearing c_r.

Parameter		Min. value	Nom. value	Max. value
Rotor mass	m (kg)		3	
Rotor speed	n (rpm)	1000		4000
Length of rotor run up	T (s)		7	
Bearing diameter	D (mm)		47.37	
Bearing length	L (mm)	35.5275	47.37	59.2125
Radial clearance	c_r (mm)	0.675	0.9	1.125
Dynamic viscosity	η (Pa·s)	0.0525	0.07	0.0875
HD mesh size	$M \times N$ (-)		121×21	

Table 1. Parameters of the Jeffcott rotor and journal bearing

The main goal of parametric studies was to explore the dependence of the equilibrium journal eccentricity on the modified Sommerfeld number, which is defined as

$$\sigma = \frac{\eta\,\omega\,L^3\,R}{2\,F\,c_r^2} = \frac{\left(1-\varepsilon^2\right)^2}{\varepsilon\sqrt{16\varepsilon^2+\pi^2\left(1-\varepsilon^2\right)}}, \tag{12}$$

where $F = m\,g$ is the static loading force and $\varepsilon = \sqrt{y_H^2 + z_H^2}/c_r$ is the relative eccentricity. The next goal was to study the onset of a fluid-induced instability. Literature suggests [5] that the fluid-induced instability is characterised by whirl frequency ω_S (rad/s), which is given by

$$\omega_S = \sqrt{\frac{k_{eq}}{m}}, \tag{13}$$

where k_{eq} is the equivalent stiffness of the bearing and m is the rotating mass.

Let us assume that the bearing, that supports the analysed Jeffcott rotor, is linear and displacements y_H and z_H are small and close to the equilibrium position of the journal. The equations of motion of such system are

$$\begin{bmatrix} m & 0 \\ 0 & m \end{bmatrix} \begin{bmatrix} \ddot{y}_H \\ \ddot{z}_H \end{bmatrix} + \begin{bmatrix} b_{yy} & b_{yz} \\ b_{zy} & b_{zz} \end{bmatrix} \begin{bmatrix} \dot{y}_H \\ \dot{z}_H \end{bmatrix} + \begin{bmatrix} k_{yy} & k_{yz} \\ k_{zy} & k_{zz} \end{bmatrix} \begin{bmatrix} y_H \\ z_H \end{bmatrix} = \begin{bmatrix} -m\,g \\ 0 \end{bmatrix}, \tag{14}$$

where k_{ij} and b_{ij} are the linear coefficients of stiffness and damping described in detail in [1]. After a rather lengthy algebraic manipulation, one can derive the solution for small motions (perturbations) Δy_H and Δz_H. Real and imaginary parts of this solution render

$$k_{eq} = \frac{k_{yy}b_{zz} + k_{zz}b_{yy} - b_{zy}k_{yz} - b_{yz}k_{zy}}{b_{yy} + b_{zz}}, \tag{15}$$

$$\omega_S^2 = \Omega_S^2\,\frac{\left(k_{eq} - k_{yy}\right)\left(k_{eq} - k_{zz}\right) - k_{yz}k_{zy}}{b_{yy}b_{zz} - b_{yz}b_{zy}}, \tag{16}$$

where Ω_S is the angular speed, for which the rotating system becomes unstable. Ω_S can be directly expressed after Eqs. (15) and (16) are substituted into Eq. (13).

The results and comparison between the MATLAB and the AVL Excite solutions are shown in composite contour plots in Figs. 3–6. The composite plots consist of three parts:

- a surface plot without isolines depicting the dependency of relative eccentricity ε on independent parameters; each horizontal slice of the plot is in fact a time series of rotor run up,
- a contour plot plot with labelled isolines depicting the dependency of the modified Sommerfeld number σ on independent parameters,
- and a dot-and-dash line, which shows threshold speed n_S at which the linear system becomes unstable; the line is obtained analytically from the Ocvirk solution of the Reynolds equation.

The dot-and-dash line effectively divides all diagrams into two zones: a stable zone on the left side and an unstable zone on the right side of each figure.

In the stable zone, relative eccentricity ε is almost directly proportionate to the modified Sommerfeld number σ in Figs. 3–8. The proportion is less direct for the higher Sommerfeld numbers. When L is modified (see Figs.7 and 6), ε is not proportionate to σ. Such a behaviour is expected because only bearings of the same type and with equal both σ and L/D should perform identically.

The fluid-induced instability arises in the unstable zone. The fully-developed instability is accompanied by high magnitudes of vibrations and preceded by a short transient zone in which the journal oscillates rapidly. The linear model is more conservative as it predicts the onset of the instability at considerably lower speeds. The fact that the shape of a stability line predicted by the nonlinear model does not correspond with the analytically derived dot-and-dash line is also interesting. For this reason, it is necessary to use non-linear model of hydrodynamic lubrication to simulate the fluid-induced instabilities accurately.

5. Conclusions

This work has provided a basic theory for the calculation of nonlinear hydrodynamic forces acting in plain journal bearings. The influence of these nonlinear forces on the rotor behaviour and the system stability was shown. It was documented that even if the nonlinear forces are considered, the bearing performance is reasonably close to a classic linear theory, which is based on the assumption that the bearings of the same type with the equal Sommerfeld numbers and L/D ratios perform identically.

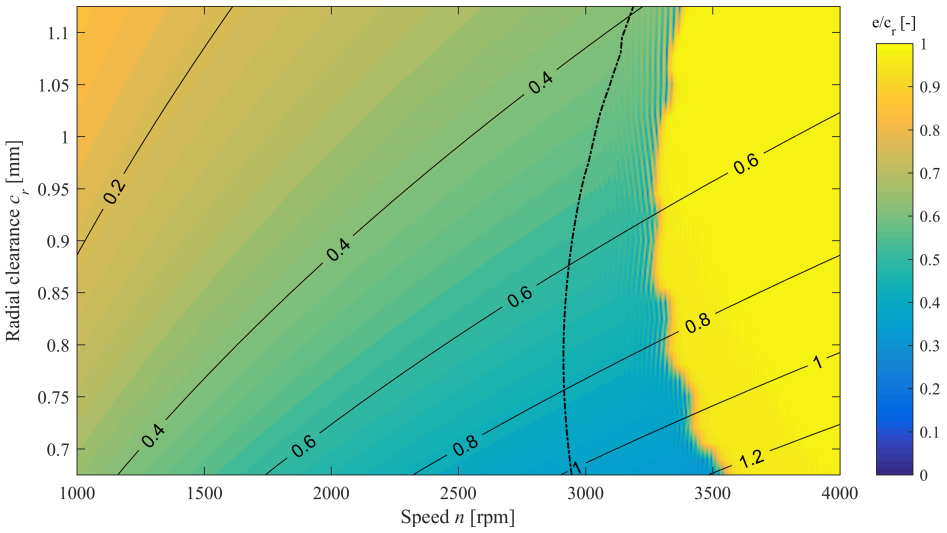

Figure 3. MATLAB – radial clearance

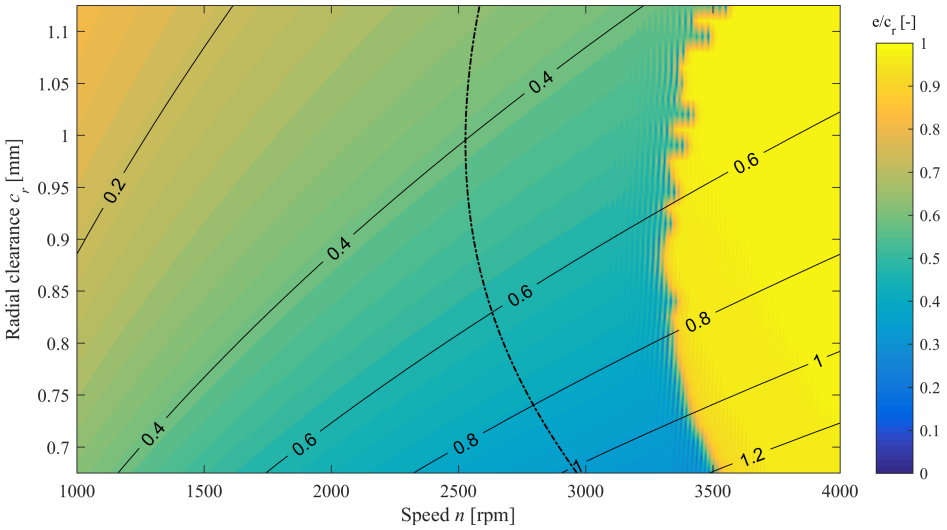

Figure 4. AVL – radial clearance

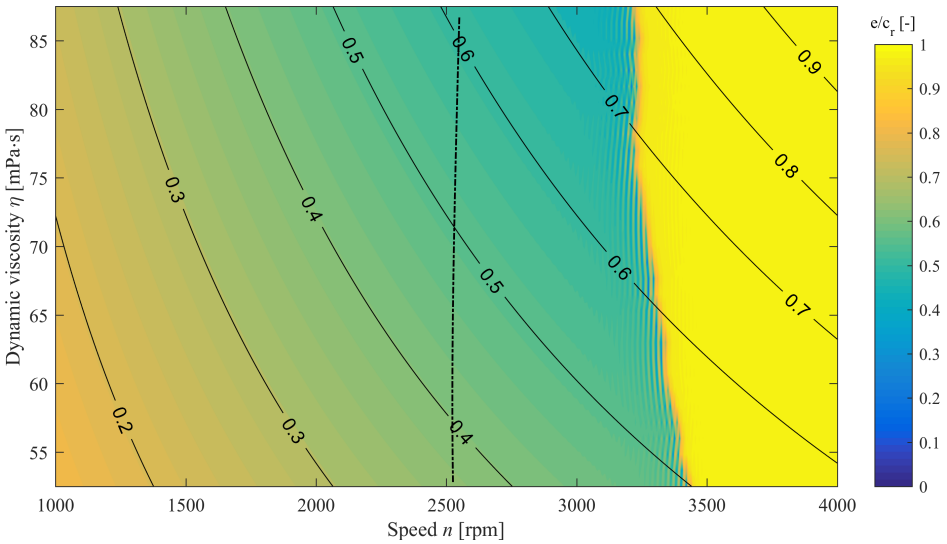

Figure 5. MATLAB – dynamic viscosity

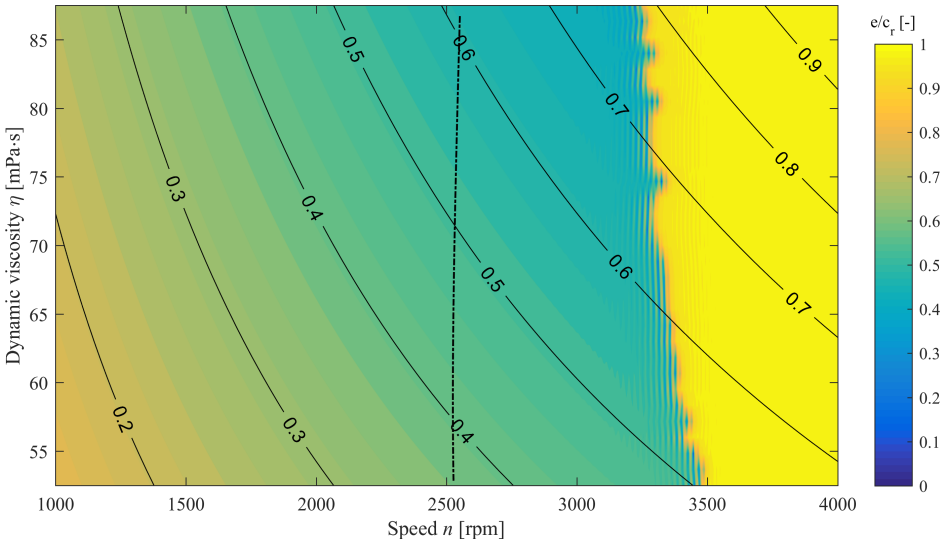

Figure 6. AVL – dynamic viscosity

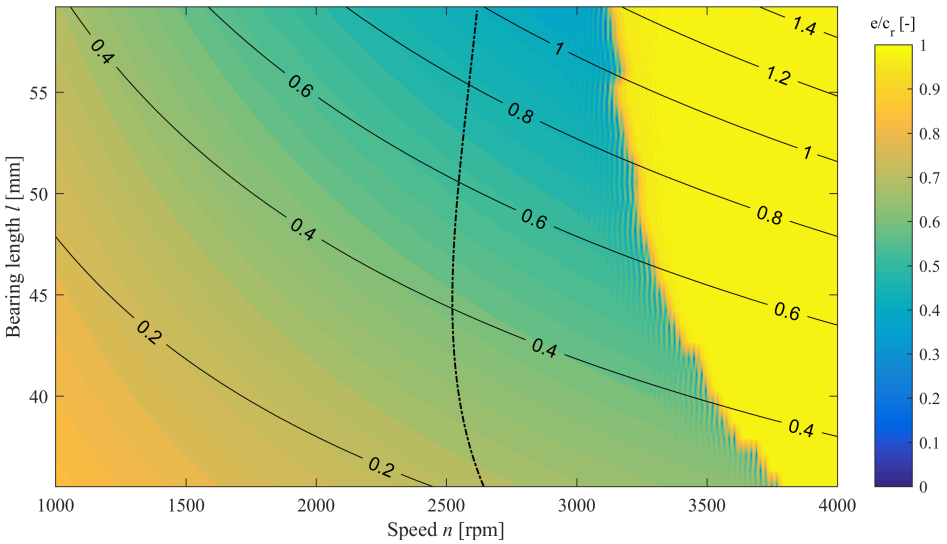

Figure 7. MATLAB – bearing length

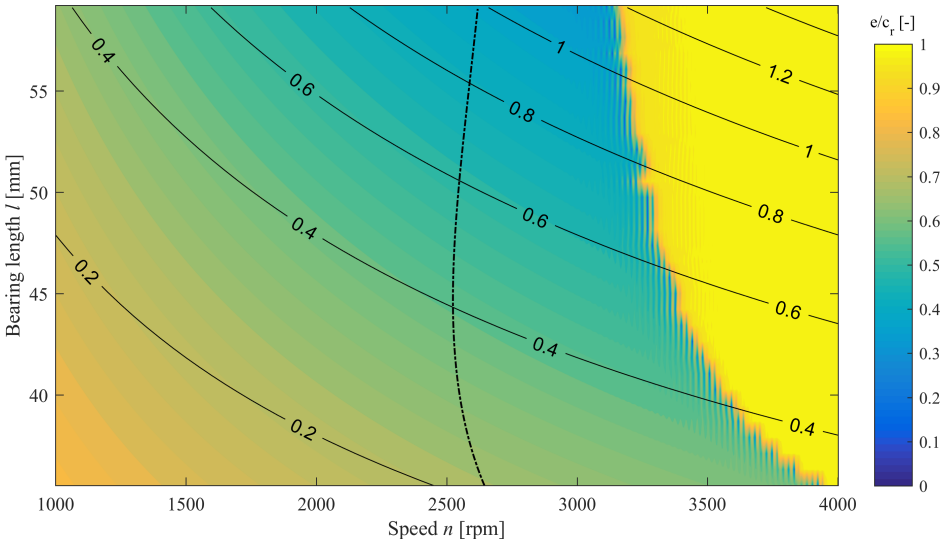

Figure 8. AVL – bearing length

Moreover, the linear theory proved to be far more conservative than the nonlinear approach because a zone in which the system is stable is smaller and of a slightly different shape in the case of the linear theory. This renders the need of the nonlinear analysis for rotor systems operated close to the threshold speed at which a fluid-induced instability is introduced.

Acknowledgments

The paper has originated in the framework of the institutional support for the long-time conception development of the research institution provided by the Ministry of Industry and Trade of the Czech Republic to Research and Testing Institute Plze and solving the project of the Czech Science Foundation No. 17-15915S entitled Nonlinear dynamics of rotating systems considering fluid film instabilities with the emphasis on local effects.

The usage of the AVL Excite software in the framework of the University Partnership Program of AVL List GmbH is greatly acknowledged.

References

[1] Genta, G. *Dynamics of Rotating Systems*. Springer, New York, 2006.

[2] Hori, Y. *Hydrodynamic Lubrication*. Springer, Tokyo, 2006.

[3] Offner, G. Modelling of condensed flexible bodies considering non-linear inertia effects resulting from gross motions. *Proc. IMechE, Part K: J. Multi-body Dynamics 225*, 3 (2011), 204–219.

[4] Reynolds, O. On the theory of lubrication and its application to mr. beauchamp tower's experiments, including an experimental determination of the viscosity of olive oil. *Philosophical Transactions of the Royal Society of London 177* (1886), 157–234.

[5] Stachowiak, G., and Batchelor, A. *Engineering Tribology*. Butterworth-Heinemann, St. Louis, 2014.

Pavel Polach, Ph.D.: Research and Testing Institute Plzen, Tylova 1581/46, 301 00, Pilsen, Czech Republic (*polach@vzuplzen.cz*). The author gave a presentation of this paper during one of the conference sessions.

Luboš Smolík, Ph.D. student: NTIS, Faculty of Applied Sciences, University of West Bohemia, Univerzitni 8, 306 14, Pilsen, Czech Republic (*carlist@ntis.zcu.cz*).

Jan Rendl, Ph.D. student: NTIS, Faculty of Applied Sciences, University of West Bohemia, Univerzitni 8, 306 14, Pilsen, Czech Republic (*rendl@ntis.zcu.cz*).

Michal Hajžman, Ph.D.: Department of Mechanics, Faculty of Applied Sciences, University of West Bohemia, Univerzitni 8, 306 14, Pilsen, Czech Republic (*mhajzman@kme.zcu.cz*).

Modeling and experimental investigation of dynamics of two pendulums elastically coupled and driven by magnetic field

Krystian Polczyński, Grzegorz Wasilewski, Jan Awrejcewicz, Adam Wijata

Abstract: In this work both experimental and simulation results of a study of two physical pendulums coupled through an elastic torsional element are presented. Permanent magnets are attached to the pendulums ends and the system motion is forced by a variable magnetic field with a help of the exciting coils. The electric current signal possesses rectangular shape, and the experimental investigations have been carried out for different frequencies and amplitudes of the current signal (excitation). The derived mathematical model has been validated experimentally taking into account its experimentally confirmed parameters. The magnetic fields interactions have been reduced to the moment of a force based on the experimentally obtained data. A few of the dynamically different cases are studied including the elastically coupled/un-coupled pendulums and the system excitation carried out either by one or two pendulums. Regular and chaotic dynamics of this mechatronic system have been detected, illustrated and discussed.

1. Introduction

In classical mechanics a pendulum (physical or mathematical) is one of the simplest objects of one-degree-of-freedom system, whose motion is governed by a nonlinear differential equation. Technical progress and combination of different branches of technologies yielded possibilities for searching new methods of driving for mechanical systems, and the magnetic forces have recently attracted interest for their employment as the sources for mechanical/mechatronical excitations. It is well known and documented that even simple pendula driven by magnetic field may exhibit a rich dynamic behavior including periodic motions [1], parametric and self-excited oscillations [2], numerous parametric resonances [3], and chaotic behaviors [1, 3, 4].

In a series of papers [1-4] the magnetic field interaction has been simplified to the Gilbert model of magnetic dipole [5]. However, in contrary to the latter investigations the magnetic interaction in our work is expressed as mathematical function based on experimental data, in contrary to the mentioned theoretical model.

2. Experimental rig and electric excitation signal

Fig. 1 presents the setup of the constructed experimental stand. The test stand is equipped with two pendulums marked as (1) and (2). The pendulums are attached to the axes (3) which are hold by rolling bearings. The axes are joined with a cuboid elastic element (4) made of rubber. Pendulum (2)

always has a neodymium magnet (5) (not visible) at the end of the rod. In the case of the pendulum (1), the neodymium magnet can be replaced by a brass element with the same dimensions and mass as the mentioned magnet. Air-core coils (6) (0.022 H inductance) are located below the pendulums. Distance between the coil and the magnet during our experiment was equal to h=0.0016 m (it is possible to regulate this distance). On the axes are also attached wheels (7) used for measurement of static characteristics of the moment of force, that comes from the magnetic interaction. The experimental rig is made of non-magnetic materials like brass, aluminum or polymer composites to reduce its influence on the activated magnetic fields.

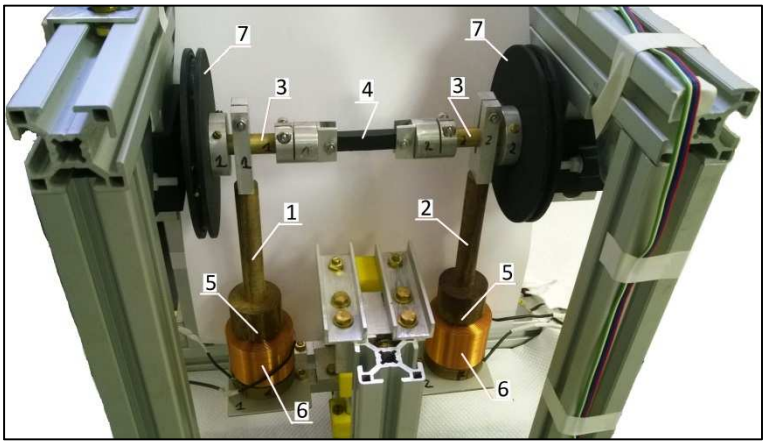

Figure 1. Experimental rig (1 – pendulum, 2 – pendulum, 3 – axis, 4 – elastic element, 5 – neodymium magnet, 6 – air-core coil, 7 – wheel).

Fig. 2 shows a shape of the electric current signal which flows through the coils. The signal can flow through one coil or two coils at the same time. The frequency $\left(f = \frac{1}{\tau}\right)$, duty cycle $\left(w = \frac{\tau_z}{\tau} \cdot 100\%\right)$ and amplitude are controlled. The I_{1a}, I_{2a} denote the amplitudes of the current, where I_{1a} and I_{2a} stand for the pendulum 1 and the pendulum 2, respectively.

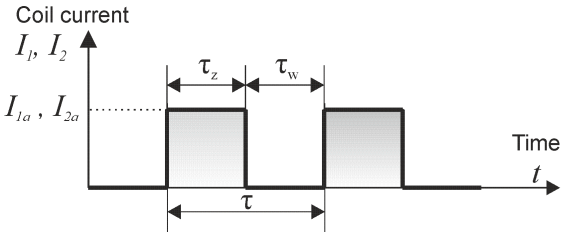

Figure 2. Excitation current signal (τ_z – current ON; τ_w – current OFF; $\tau = \tau_z + \tau_w$ – period; $w = \frac{\tau_z}{\tau} \cdot 100\%$ - duty cycle).

3. Mathematical model

This section describes the mathematical model of the experimental rig presented in section 2. The physical model of the experimental rig is shown in Fig. 3.

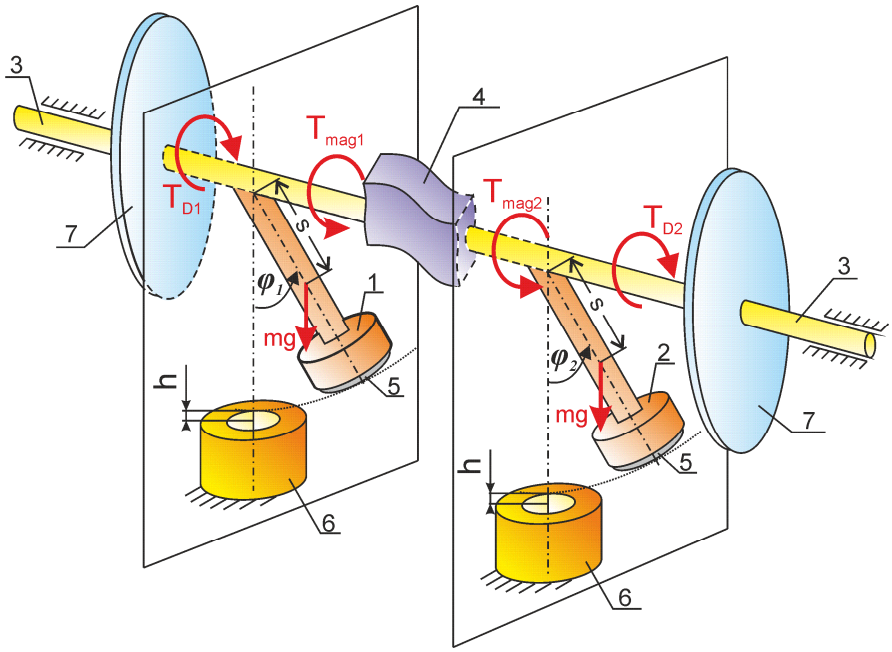

Figure 3. Physical model of the experimental stand.

The mathematical model is created accordingly to the laws of the classical mechanics. It has been developed considering the four torques acting on the each pendulum. General equations of motion of the pendulums are as follows

$$I_1\ddot{\varphi}_1 = T_{mag1} - T_{D1} - mgs \cdot \sin\varphi_1 - k_e(\varphi_1 - \varphi_2), \tag{1}$$

$$I_2\ddot{\varphi}_2 = T_{mag2} - T_{D2} - mgs \cdot \sin\varphi_2 - k_e(\varphi_2 - \varphi_1), \tag{2}$$

where: I_1, I_2 – moments of inertia of the pendulums, T_{mag1}, T_{mag2} – magnetic interaction torques, T_{D1}, T_{D2} – damping torques, mg – weight of the pendulum, s – length between center of mass of the pendulum and the axis of rotation, $k_e(\varphi_1 - \varphi_2)$ – torsional deformation torque of elastic element, where k_e is a stiffness of the element.

Torques T_{D1} and T_{D2} are sum of all damping factors which act on the pendulums during their motions, i.e. we have the

$$T_{D1} = c_1\dot{\varphi}_1 + c_e(\dot{\varphi}_1 - \dot{\varphi}_2) + c_{B1} \cdot sgn(\dot{\varphi}_1)\,,$$

$$T_{D2} = c_2\dot{\varphi}_2 + c_e(\dot{\varphi}_2 - \dot{\varphi}_1) + c_{B2} \cdot sgn(\dot{\varphi}_2)\,, \tag{3}$$

where: $c_1\dot{\varphi}_1, c_2\dot{\varphi}_2$ – the viscous torques, $c_e(\dot{\varphi}_1 - \dot{\varphi}_2)$, $c_e(\dot{\varphi}_2 - \dot{\varphi}_1)$ are the damping torques of the elastic element, $c_{B1} \cdot sgn(\dot{\varphi}_1), c_{B2} \cdot sgn(\dot{\varphi}_2)$ – friction torques of the bearings ($c_1, c_2, c_e, c_{B1}, c_{B2}$ are constant coefficients).

Torques T_{mag1} and T_{mag2} define the magnetic interaction between a coil and a magnet. This interaction depends on the excitation current signal (see Fig. 2) and the moment of magnetic forces:

$$T_{mag1} = M_{mag1} \cdot sgn(I_1),$$

$$T_{mag2} = M_{mag2} \cdot sgn(I_2). \tag{4}$$

During experiments, we observed an interesting phenomenon of a mutual excitation/synchronization of the magnets. When two pendulums are uncoupled and both equipped with the magnets, the magnetic fields of the magnets interact and create some "kind of connection" between the pendulums. Fig. 4 shows this phenomenon for a free swing of pendulum 2.

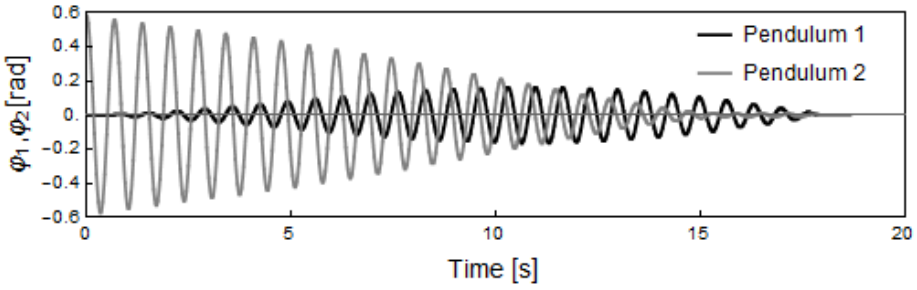

Figure 4. Interaction between pendulums with magnets.

It should be mentioned that though this phenomenon has been demonstrated experimentally, but it requires further experiments and simulations with two pendulums equipped with magnets due to lack of theoretical model of that interaction. This is why in this study we replaced the magnet in pendulum (1) with the brass element (in Eq. 1 we take $T_{mag1} = 0$).

The terms M_{mag1} and M_{mag2} represent the static characteristics of the magnetic forces reduced to the moment of force. The characteristics have been measured for pendulum 2. The way of measuring is schematically shown in Fig. 5.

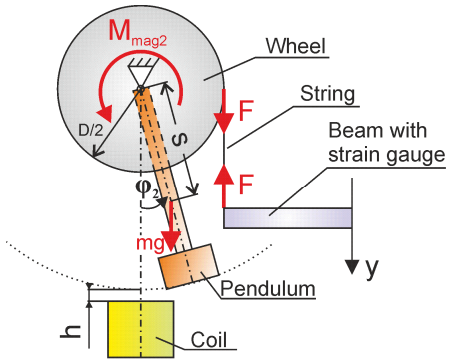

Figure 5. Method of measurement of the static characteristics of the magnetic forces.

The beam with strain gauge moves downward vertically with a constant velocity. The force F and the angle φ_2 are registered and processed by Eq. 5 to achieve

$$M_{mag2} = F \cdot \frac{D}{2} + mgs \cdot \sin\ \varphi_2, \tag{5}$$

where: F – measured force, D – diameter of the wheel.

The measurements have been carried out for two constant values of the coil current: $I_{a2} = 1\ A$ and $I_{a2} = 1.5\ A$. The obtained measurement points are shown in Fig. 6. Particular attention must be paid to the non-zero values of M_{mag2} for a zero angle achieved during the experiment. Though the fitted function should be multivalued for zero angle, however during modeling we have made an assumption that the moment of force is zero for zero angle because there is no moment arm. The experimental non-zero values of M_{mag2} for zero angle is yielded by not high enough resolution of the angle sensor.

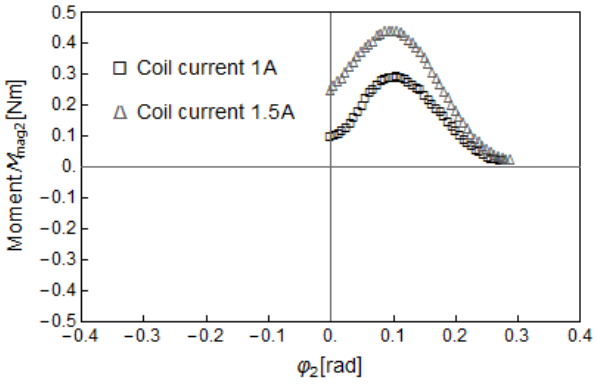

Figure 6. Experimental sets of points regarding the moment M_{mag2}

The obtained set of experimental points can be approximated by the following analytical formula

$$M_{mag2} = \mathrm{a} \cdot \mathrm{sgn}(\varphi) \cdot \exp\left[-\left(\frac{\mathrm{sgn}(\varphi)\cdot\varphi+b}{c}\right)^2\right], \tag{8}$$

where a, b, c are constant parameters being different for each possible values of the current.

It should be explained that the parameters a, b, c appeared in Eq. 8 influence M_{mag2}. Namely, the parameter a is responsible for extreme value of the function (8) for positive angles, whereas $(-b)$ is the argument for its extremum and c is responsible of its shape. For the negative angles, the values of M_{mag2} are symmetrical with respect to the positive angles. The fitted functions and symbolically illustrated a and $(-b)$ parameters are shown in Fig. 7.

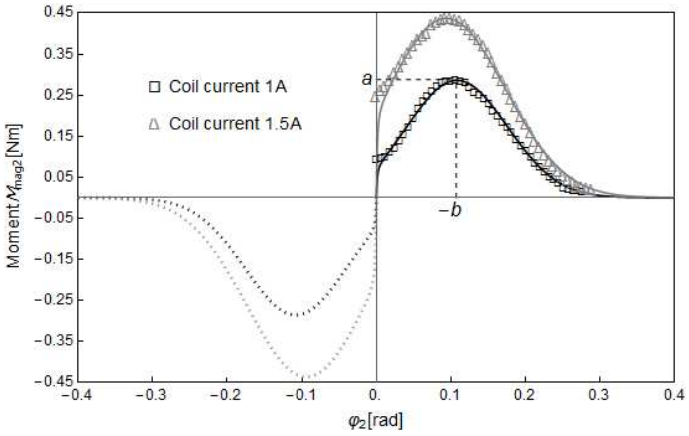

Figure 7. Experimental data versus the analytically approximated functions of the moment M_{mag2}.

4. Experiments versus numerical simulations

This section is aimed on the theoretical and experimental validation of the existence of regular and chaotic dynamics of our mechatronic system. Equations of motion (Eq. 1, 2) are solved numerically using the WOLFRAM MATHEMATICA software. For the purpose of effective simulations signum functions in Eqs. 3, 4 and 8 are replaced by $\frac{2}{\pi}\arctan(\epsilon \cdot x)$, where ϵ is large parameter [6]. That replacement causes that redefined functions and their first derivatives are continuous. The following parameters are fixed: $\epsilon = 10^3$, $I_1 = 6.8025 \cdot 10^{-4}\, kgm^2$, $I_2 = 6.7101 \cdot 10^{-4}\, kgm^2$, $mgs = 0.0578\, Nm$, $k_e = 2.532 \cdot 10^{-4}\, N/m$, $c_1 = 3.1 \cdot 10^{-5}\, Nms$, $c_2 = 7.2 \cdot 10^{-5} Nms$, $c_e = 13.736 \cdot 10^{-5} Nms$, $c_{B1} = 27.523 \cdot 10^{-5} Nm$, $c_{B2} = 27.888 \cdot 10^{-5} Nm$, $I_{a2} = 1A \rightarrow\ a = 0.287684, b = -0.107082, c = -0.095541$, $I_{a2} = 1.5A \rightarrow a = 0.439922, b = -0.092557, c = -0.112422$.

Fig. 8a shows simulation and experimental results of the free vibrations of uncoupled pendulums for the following initial conditions: $\varphi_1(0) = -1.56\, rad$ $(-89.38°)$, $\varphi_2(0) = -0.025\, rad$ $(-1.43°)$,

$\dot{\varphi}_1(0) = 0\frac{rad}{s}$ and $\dot{\varphi}_2(0) = 0\frac{rad}{s}$. Fig. 8b presents time histories of the numerically and experimentally obtained time histories of the excited coupled pendulums, where $I_{a2} = 1A$, $f = 2\ Hz, w = 25\%$. Initial conditions for simulations of the excited coupled pendulums are as follows: $\varphi_1(0) = 0\ rad$, $\varphi_2(0) = 1.75 \cdot 10^{-5}\ rad$ (0.001°), $\dot{\varphi}_1(0) = 0\ rad/s$ and $\dot{\varphi}_2(0) = 0\ rad/s$.

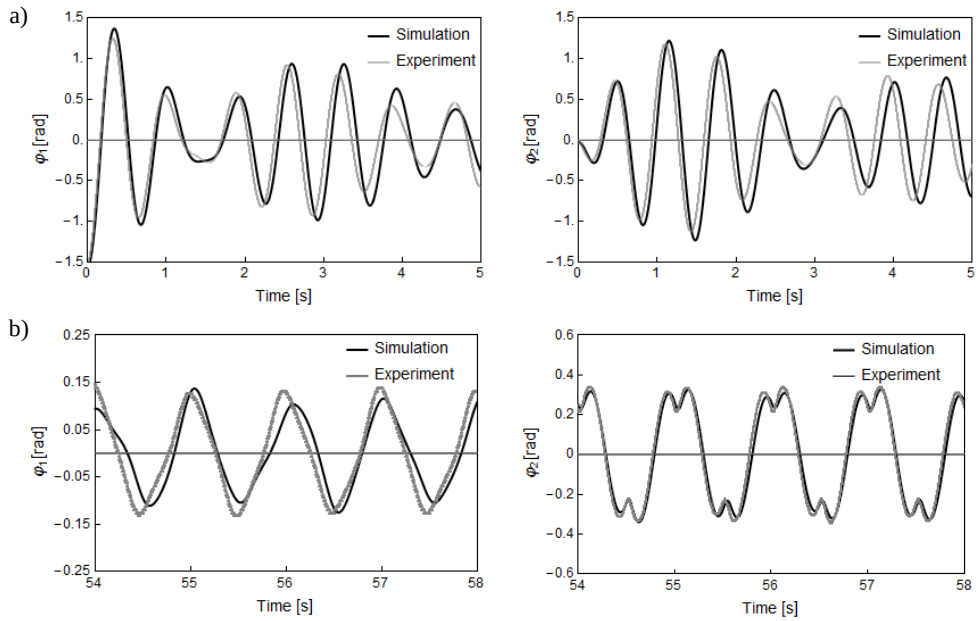

Figure 8. Comparison of simulation and experimental results: a) coupled pendulums – free vibrations, b) coupled pendulums with magnetically excited pendulum (2) ($I_{a2} = 1A, f = 2\ Hz, w = 25\%$).

In the case of regular vibrations, after omitting the transitional process, the coincidence of the numerical and experimental results is clearly visible.

However, the investigated system is very sensitive to small changes of the parameters like the duty cycle *w* and amplitude of the current. We have investigated the system experimentally for three different values of the duty cycle w: 27%, 30% and 33% when the current $I_{a2} = 1A$. We have also carried out the experiments for three amplitudes of the current I_{a2}: 0.5 A, 1 A, 1.5 A when the duty cycle $w = 30\%$. The results of the experiments are shown in the Fig. 9 in the form of bifurcation diagrams. The diagrams are made for increasing (→) frequency in a range 3.4-6 Hz. The system response for changes of the duty cycle plays a key role here. Taking into account Fig. $9a_2$ as a point of reference, one can say that a 3% increase in duty cycle results in significant reduction of chaotic area (represented by clusters of points) while preserving the period-2 motion. The 3% decrease in duty cycle leads to transition of period-2 motion into period-6 motion of the system. The influence of the

current changes is very similar to influence of the duty cycle. As it is seen in Fig. $9a_1$ and $9b_1$, the system motion type is similar and the frequency ranges are located closed to each other. Similarity of behavior has been also detected for the case of different current amplitude $I_{a2} = 1.5\ A$ (Fig. $9b_3$) and $I_{a2} = 1\ A$ (Fig. $9a_3$).

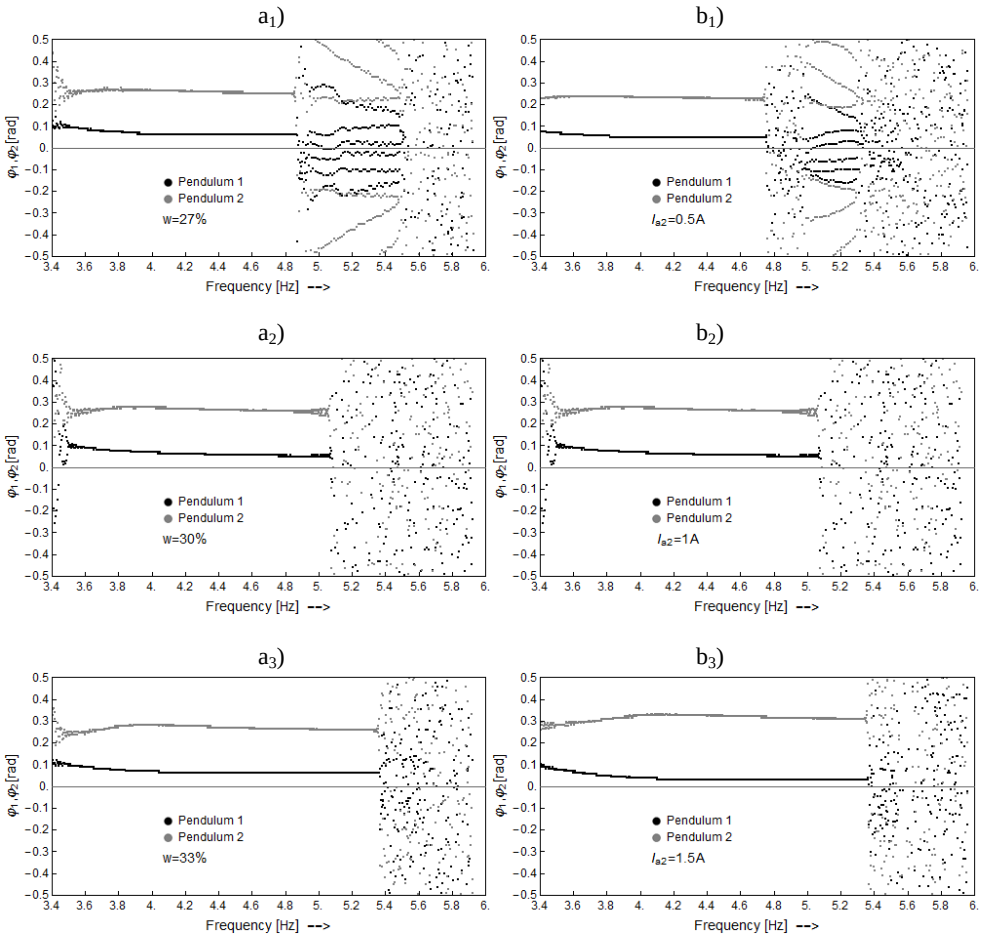

Figure 9. Experimental bifurcation diagrams for increasing frequency:
different duty cycles w for the current $I_{a2} = 1$A (a_1, a_2, a_3);
different amplitudes of the current for the duty cycle $w = 30\%$ (b_1, b_2, b_3).

Owing to the rich dynamics of the system responses we have chosen constant values of the current and duty cycle for a more detailed investigation of the motion. During our observations we have decided that parameters values $I_{a2} = 1A$ and $w = 30\%$ are optimal for thermal conditions of the coil. Our detailed investigation has been started by creating the bifurcation diagrams using numerical

simulations and then verifying them experimentally. The frequency range during simulation and experiment was 1.5-6 Hz. Experimental diagrams were done for linear increasing or decreasing frequency with average velocity $0.12\frac{Hz}{min}$. Figure 10 shows simulation and experiment results for pendulum 2 and for both frequency paths: increase (Fig. 10a, b) and decrease (Fig.10c, d). The simulation and experiment bifurcation diagrams coincide though the motion regions are slightly shifted. Differences between simulation and experiment diagrams can be explained by not sufficiently slow velocity of the frequency during the carried out experiment and by the discrepancies between model of the magnetic interaction and investigated approximation curve.

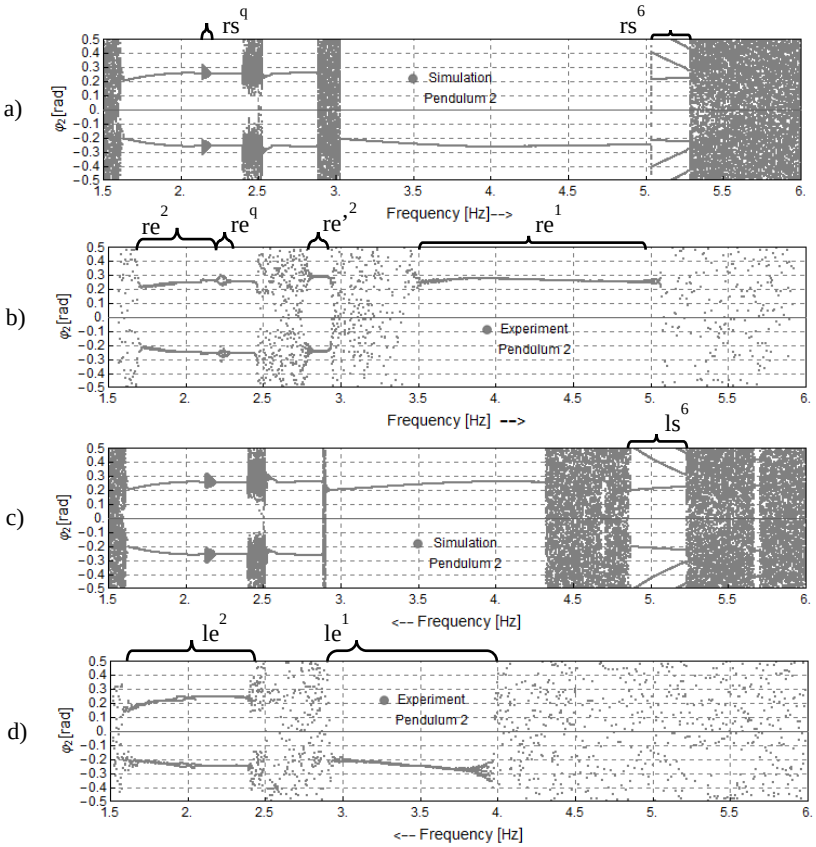

Figure 10. Experimental (laboratory) versus the numerically estimated bifurcation diagrams for the pendulum 2 ($I_{a2} = 1\ A, w = 30\%$).

We can see that direction of frequency path causes that some regions are mutually exclusive, and existence of regular dynamics in a region excludes chaotic behavior. At the same time, character of motion is the same for both pendulums. The system exhibits a few different types of regular motion

(examples labeled in Fig. 10): period-1 (re^1, le^1), period-2 (re^2, re'^2, le^2) and period-6 (rs^6, ls^6). The period-1 motion has two stable states for positive and negative angles (we can see that in both experimental and simulation bifurcation diagrams). The period-6 motion is not visible in experimental diagrams, however we have validated this character of motion after set the constant frequency on 5.1 Hz. Fig. 11 presents simulation and experimental results of the phase plane plots with the Poincaré sections for period-6 motion.

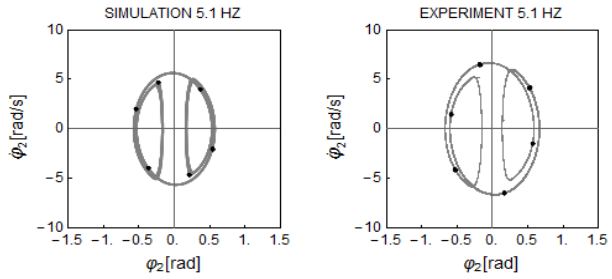

Figure 11. Phase plots with Poincaré sections for 5.1 Hz.

Period-1 and period-2 motions are confirmed by the phase 2D plots and the associated Poincaré maps, as shown in Figures 12, 13.

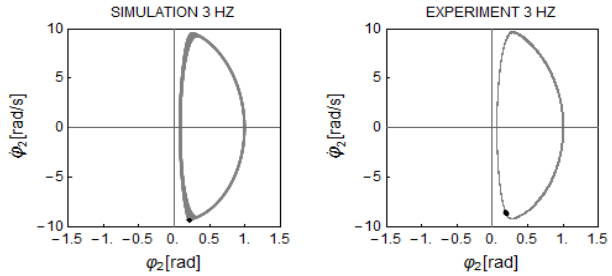

Figure 12. Phase plots with Poincaré sections of period-1 motion for 3 Hz.

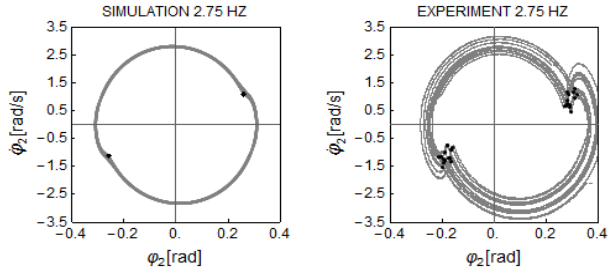

Figure 13. Phase plots with Poincaré sections of period-2 motion for 2.75 Hz

In particular, the sensitivity of the system on the initial conditions yields interesting results for region labeled rs^q (Fig. 10a) and corresponding to it region re^q (Fig. 10b). For earlier studied reasons, the above mentioned regions are shifted relative to each other. Therefore, for further investigations we take the fixed frequencies 2.17 Hz and 2.25 Hz corresponding to the middles of rs^q and re^q regions, respectively. Though in simulation we have achieved three different responses, but only one of them has been validated experimentally (see Fig. 14). Two of them are periodic: period-6 motion which has been observed during experiment (Fig. 14a), period-2 motion (Fig. 14b), whereas the third response presents quasi-periodic orbit (Fig. 14c). The employed initial conditions are as follows: period-2 → $\varphi_2(0) = 0.00052\,rad$ (0.03 °), $\varphi_1(0) = 0\,rad, \dot{\varphi}_1 = \dot{\varphi}_2 = 0\,rad/s$, period-6 → $\varphi_2(0) = 0.0012\,rad$ (0.07 °), $\varphi_1(0) = 0\,rad, \dot{\varphi}_1 = \dot{\varphi}_2 = 0\,rad/s$, quasi-periodicity → $\varphi_2(0) = 1.74 \cdot 10^{-5}\,rad$ (0.001 °), $\varphi_1(0) = 0\,rad, \dot{\varphi}_1 = \dot{\varphi}_2 = 0\,rad/s$.

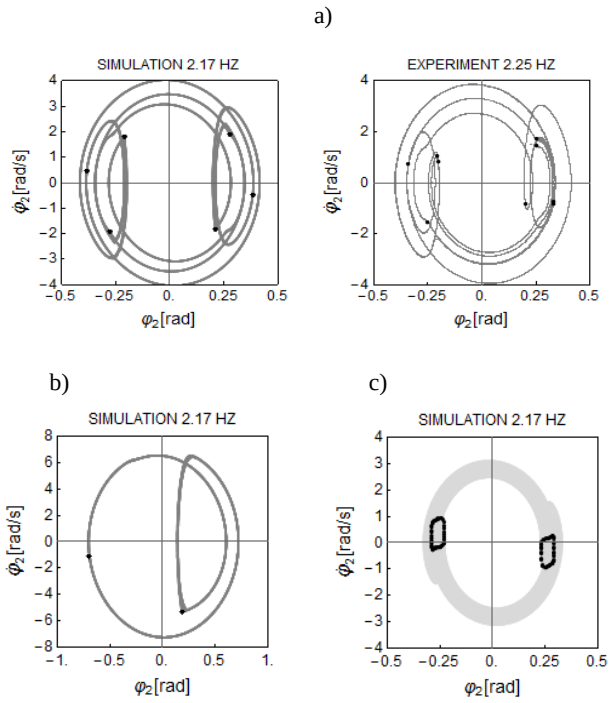

Figure 14. Phase portraits with Poincaré sections for the region rs^q and the corresponding re^q for different initial conditions: a) period-6 motion; b) period-2 motion; c) quasi-periodic motion.

5. Conclusion

The studied system of two pendulums coupled elastically and driven by the magnetic field exhibited rich non-linear dynamical behaviour. We have found numerically and proved experimentally the existence of regular and chaotic motion of the system. We have constructed the bifurcation diagrams,

phase portraits with Poincaré sections by using numerical simulations, and we have validated them experimentally. The simulation results show good agreement with the experimental results. We can observe sensitivity of the system to initial conditions and different values of the control parameters (frequency, amplitude of coil current, duty cycle). Our physical model may serve as a good starting point for modelling of electric motors like steeper motors, which have flexible shaft or are joined through an elastic clutch. It should be mentioned that the influence of control parameters to the system behaviour is not fully examined in this paper, and it stands for further studies. Furthermore, the mathematical model of magnetic interaction also requires a detailed study.

References

[1] Siahmakoun, A., French, V., and Patterson, J. Nonlinear dynamics of a sinusoidally driven pendulum in a repulsive magnetic field. *American Journal of Physics* 65, 393 (1997), 393-400.

[2] Kraftmakher, Y. Demonstrations with a magnetically controlled pendulum. *American Journal of Physics* 78, 532 (2010), 532-535.

[3] Khomeriki, G. Parametric resonance induced chaos in magnetic damped driven pendulum. *Physics Letters A* 380 (2016), 2382–2385.

[4] Tran, V., Brost, E., Johnston, M., and Jalkiod, J. Predicting the behavior of a chaotic pendulum with a variable interaction potential. *Chaos* 23, 033103 (2013), 12 pp.

[5] Griffiths, D. J. *Introduction to Electrodynamics*. Prentice-Hall, New Jersey, 1999.

[6] Wasilewski, G., Kudra, G., Awrejcewicz, J., Kaźmierczak, M., Tyborowski, M., and Kaźmierczak M. Experimental and numerical investigations of a pendulum driven by a low-powered DC motor, in: Awrejcewicz J., Kaźmierczak M., Olejnik P. and Mrozowski J. (eds.) *Dynamical Systems—Mathematical and Numerical Approaches*, TU of Lodz, Lodz, 2015, pp. 579–590.

Krystian Polczyński, B.A. (M.Sc. student): Lodz University of Technology, Faculty of Mechanical Engineering, Department of Automation, Biomechanics and Mechatronics, Stefanowskiego 1/15, 90-924, Lodz, POLAND (*kryst.polczynski@gmail.com*).

Grzegorz Wasilewski, Ph.D.: Lodz University of Technology, Faculty of Mechanical Engineering, Department of Automation, Biomechanics and Mechatronics, Łąkowa 19/21, POLSKA (*grzegorz.wasilewski@p.lodz.pl*).

Jan Awrejcewicz, Professor: Lodz University of Technology, Faculty of Mechanical Engineering, Department of Automation, Biomechanics and Mechatronics, Stefanowskiego 1/15, 90-924, Lodz, POLAND (*jan.awrejcewicz@p.lodz.pl*).

Adam Wijata, M.Sc. (Ph.D. student): Lodz University of Technology, Faculty of Mechanical Engineering, Department of Automation, Biomechanics and Mechatronics, Stefanowskiego 1/15, 90-924, Lodz, POLAND (*adam.wijata@dokt.p.lodz.pl*).

An analysis of dynamics of a truck with a trailer

Adam Przemyk, Szymon Tengler, Andrzej Harlecki

Abstract: Results of an analysis of dynamics of a truck with a trailer are presented in the paper. A mathematical model of a truck with a trailer, constituting a multi-body system was developed by using formalism of Lagrange's equations, based on the joint coordinates and matrices of homogeneous transformations taken from robotics. In the adopted procedure it has been assumed that the modeled system can move over the road with unevenness of a specific shape. Within the computer simulations performed behavior of the modeled system was studied in the road traffic conditions while performing typical road maneuvers, and changing design parameters and load of the trailer. The developed mathematical model can be treated as a virtual prototype of the system in question. According to the authors the proposed method can have practical significance and it can be used in designing the trucks with a trailer. Lots of significant design proposals can be formulated on basis of the results of the performed simulations, and they can become the basis for making real trail prototypes.

1. Introduction

Polish manufacturers of window joinery increase systematically their share in the foreign markets. According to the Trade Analysis Center 13 mil. windows and 8.2 mil. doors were produced in Poland in year 2015 [1]. The share of Poland in the total value of the export of windows and doors on the entire territory of the EU was 21% in 2015 and was the greatest one among all the member countries [1]. A considerable number of vehicles adopted to transport this type of load is needed for the produced windows to be carried. Due to the regulations in force on the maximum permissible length of the vehicle combination (a truck tractor with a semitrailer 16.5 m maximum, a truck with a trailer 18.75m) and relative maneuverability, in the case of transporting loads of large volumes a vehicle combination consisting of a truck and a trailer with a central axle becomes more and more popular. In accordance with the definition provided in Directive 2007/46/EC of the European Parliament [2] a trailer with a central axle is the trailer of which the axles are placed close to a gravity center of a vehicle (at a uniform distribution of load) in such a way that only a slight static vertical load, not exceeding 10% of the maximum trailer weight or 1000 daN load (depending which of these values is lower), is carried to a towing vehicle.

Sometimes in the places of destination the vehicle cannot be unloaded by a forklift due to lack of this equipment. This situation is rather frequent at construction sites. In such situations two solutions are used: a crane mounted on the vehicle or a forklift hooked up to the vehicle or the trailer.
The first solution is practiced mainly in the case of loads which can be transported on the open boxes. The second solution is more frequently used when loads are transported in the closed load boxes (the box covered with a canvas hood or a bodywork with a curtain) – for example transporting windows. The solution with the hooked up forklift is used by such firms as e.g.: EKO-OKNA S.A, BRACIA BERTRAND Sp. z.o.o., the carriers transporting windows of firm OKNOPLAST Sp. z o.o. etc.

Due to its construction (among other things axles placed close to each other and an impact on the vehicle) behavior of the combination can be felt as uncomfortable or even sometimes dangerous in some situations. Drivers describe this behavior as „snaking" of the trailer, „swaying" of the trailer etc., they feel it directly in the vehicle and observe in the mirror. The phenomenon intensifies for un-laden vehicle combination and disappears as vehicles are laden or when the forklift is removed. This phenomenon normally takes place at high speeds of order of 80-90 km/h, a decrease in the speed usually facilitates handling of the combination.

Acc. the technical information of firm Knorr-Bremse, when a trailer pressure on the towing device decreases, or it becomes negative, the trailer can begin to sway from side to side (snaking). This phenomena takes place particularly in the case of combinations: a short truck/a long trailer. In some cases swaying which can be initiated by an input steering signal of a driver or uneven road surface, can become dangerous and may result in overturn" [3].

Legal regulations [4] on a distribution of pressures on the axles and a drawbar stipulate, among other things, the following conditions:
- if a vehicle is laden to the technically permissible maximum weight, the weight per a single axle can exceed neither the technically permissible weight for this axle, the technically permissible weight for a group of axles weight nor the technically permissible maximum weight in the coupling point,
- in the case of the vehicle with flat loading space the above condition must be met for the uniform distribution of load.

Fulfillment of the above conditions does not guarantees proper behavior of a vehicle with partial load, especially, when the load gravity center is shifted far to the back.

2. A dynamic analysis

2.1 An object of investigations

An analysis of the combination of a truck with a trailer and a forklift hooked up at the back of the trailer was made for the vehicles of the most popular body length (7.8m). In the analysis there were

changed selected trailer parameters on which a design engineer/a manufacturer can have an influence at a stage of designing (some parameters such as: adjustments of axle lifting and unloading systems, a change in the trailer drawbar length, adding a lifting system or an unloading system of axles, can be also made in the existing trailers). Fig. 1 presents the combination of a truck with a trailer and markings of main dimensions of the vehicle combination.

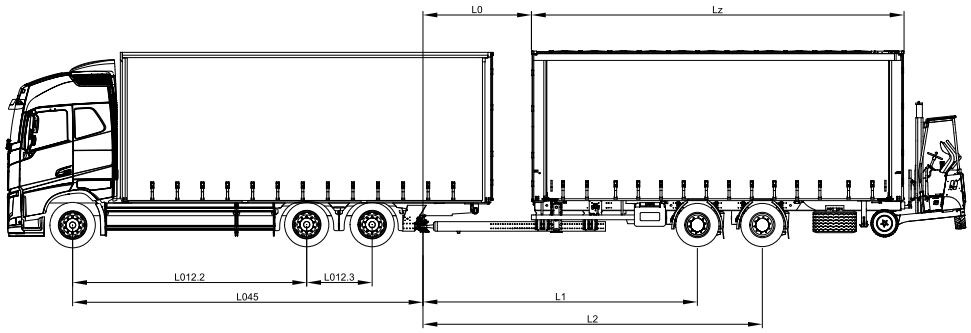

Figure 1. The combination of a truck with a trailer and its main dimensions

In the paper flexibility of the chassis frame of the truck and the trailer was not considered, this flexibility can also have an impact on behavior of vehicles, although the aim of the paper is to indicate designing recommendations regarding the main dimensions of the trailer and systems and mechanisms with which the trailer can be equipped, it has been assumed that the main frame components remain unchanged, and thus its stiffness does not change, whereas a placement and a wheelbase, drawbar length, activation or non-activation of the axle lifting system and changes in its adjustments, activation or non-activation of the axle unloading system and changes in its adjustments, a distribution of heavy components of the trailer (for instance a spare wheel) adding and a distribution of ballast are subject to a change. Those results are used to compare the solutions with each other, and not to indicate a specific value of the oscillation amplitude. It should be remembered that forcing can be both a maneuver of obstacle avoidance and road unevenness, forcings can also occur one after another, overlap etc. All this can cause that oscillation disappearance visible for all trailers in practice will not take place, and in the worst case oscillations will be reinforced quickly what may lead to an accident.

A physical model was made, and then a mathematical model in which elements of the suspension, axles and a cabin were flexible, whereas all other components were treated as rigid bodies. The model consisted of a truck and a central axle trailer with a hooked up forklift coupled to it

Table 1 The main dimensions for different variants of the trailer

Variant	L012.2	L012.3	L045	L0	Lz	L1	L2	x
0	4800	1370	7325	2175	7820	5560	7360	375
1	4800	1370	7325	2175	7820	5560	7360	375
2	4800	1370	7525	1975	7820	5360	7160	375
3	4800	1370	7325	2175	7820	5760	7160	375
4	4800	1370	7325	2175	7820	5560	7360	375
5	4800	1370	7325	2175	7820	5760	7560	575

a)

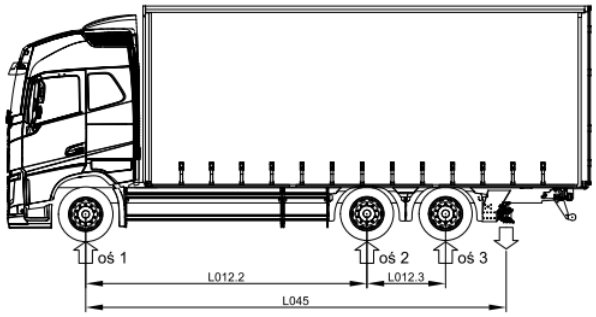

b)

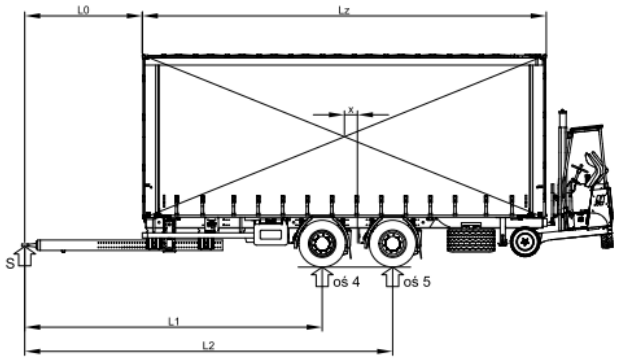

Figure 2. The vehicle and the trailer with the main dimensions marked and the weight distribution on the axles

In the paper the following design variants of the trailer were considered:

0 – A standard trailer, adopted to transport a forklift, an un-laden trailer tends to lift a drawbar and at the same to unload the rear axles of the vehicle. The trailer is towed by the 3-axle vehicle in which the last trailing axle is unloaded, and it does not carry load only it rests on the surface.

1 – The first axle of the trailer unloaded, a greater part of loading is carried by axle 2.

2 – Coupling moved by 200 mm, and the trailer drawbar shortened by 200 mm – length of the combination as in the other variants (the coupling point moved).

3 – Trailer wheelbase decreased by 400 mm and the first axle of the trailer unloaded.

4 – The first axle of the trailer lifted.

5 – The axle arrangement moved by 200 mm backwards, the gravity center of the trailer chassis moved by 150 mm forward.**Table 1** main dimensions for different variants of the trailer are presented. Fig. 2 presents static loads of the vehicle axle and coupling load (S), the position of center of gravity of load and a displacement of the axle center of the trailer in relation to the center of gravity of load are also presented in Fig. 2b. The values of distribution of mass among the axles are presented in Table 2.

Table 2 Distribution of mass among the axles and the mass on the drawbar

Variant	axle 1 [kg]	axle 2 [kg]	axle 3 [kg]	drawbar (S) [kg]	axle 4 [kg]	axle 5 [kg]
0	5766	3507	530	-1129	3765	3958
1	5476	2812	2285	-360	640	6313
2	5828	3423	530	-1149	3720	4025
3	5425	4458	530	-519	640	6472
4	5479	3022	2506	-124	0	6541
5	5345	3167	2662	69	0	6413

2.2 A mathematical model

The multi-body system in question consists of specific sub-assemblies, which were modeled as rigid bodies. Joint coordinates and homogenous transformations were taken in order to determine a position and orientation of those bodies [5]. In the method motion of a particular body is considered in relation to the preceding body, and as a result the entire system is a tree structure (see Figure 3.). The truck frame is the root of this tree in this paper.

The frame model (the body marked by number 1) has six degrees of freedom (three displacement and three rotations), which can be presented by a vector of generalized coordinates: $\tilde{\mathbf{q}}^{(1)} = [\tilde{x}^{(1)} \quad \tilde{y}^{(1)} \quad \tilde{z}^{(1)} \quad \tilde{\psi}^{(1)} \quad \tilde{\theta}^{(1)} \quad \tilde{\varphi}^{(1)}]^T$ – Figure 4. The cabin is also joined with the frame and the cabin can rotate appropriately in relation to it - and its vector of the generalized coordinates has a form of : $\tilde{\mathbf{q}}^{(2)} = \left[\tilde{\theta}^{(2)}\right]^T$. The next bodies connected with the frame are three axles modeled as bodies of two degrees of freedom, thus, their vectors of the generalized coordinates have a form of: $\tilde{\mathbf{q}}^{(k)} = [\tilde{z}^{(k)} \quad \tilde{\varphi}^{(k)}]^T$, $k = 3, 4, 5$. Each axle is equipped with two wheels of which the vector of the generalized coordinates has a form of : $\tilde{\mathbf{q}}^{(k)} = [\tilde{\psi}^{(k)} \quad \tilde{\theta}^{(k)}]^T, k = 6, 7$ (for front steering wheels) and $\tilde{\mathbf{q}}^{(k)} = \left[\tilde{\theta}^{(k)}\right]^T$, $k = 8, \ldots, 11$ for the wheels in the other axles.

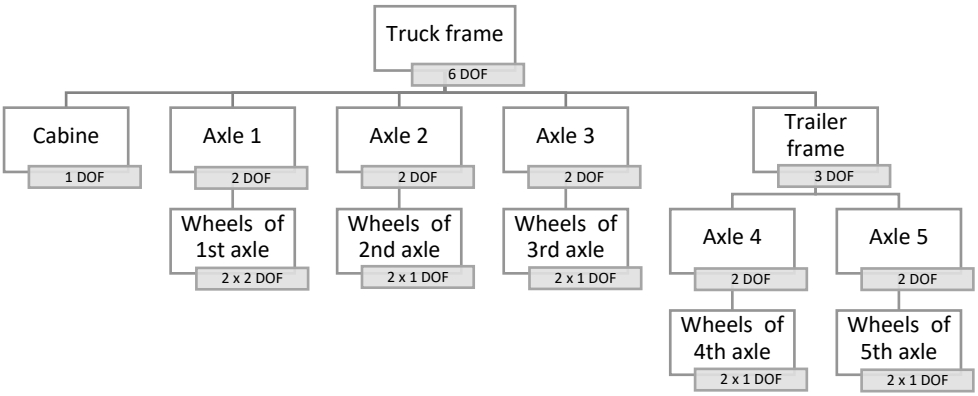

Figure 3. Tree-structure of multi-body system

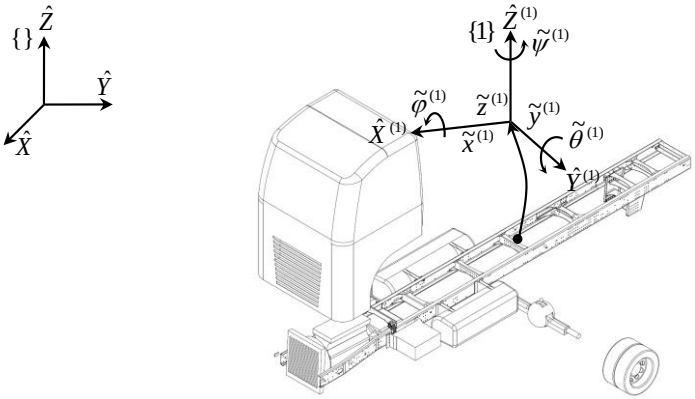

Figure 4. The main truck elements

In the kinematic chain in question the frame also constitutes a root for the body combination which is the trailer (see Figure 5).

The trailer drawbar being its integral part, is joined with the vehicle frame by a spherical pair. Therefore, the trailer frame model has three degrees of freedom (rotations), in relation to the vehicle frame, that is its vector of the generalized coordinates has a form of: $\tilde{\mathbf{q}}^{(12)} = [\tilde{\psi}^{(12)} \quad \tilde{\theta}^{(12)} \quad \tilde{\varphi}^{(12)}]^T$. As in the case of the vehicle, two axles are joined with the trailer frame and their vector of the generalized coordinates has a form of : $\tilde{\mathbf{q}}^{(k)} = [\tilde{z}^{(k)} \quad \tilde{\varphi}^{(k)}]^T$, k=13, 14. Two wheels $\tilde{\mathbf{q}}^{(k)} = \left[\tilde{\theta}^{(k)}\right]^T$ k=15,..,18, are attached to each axel. Load joined with it in a rigid way is also attached to the trailer.

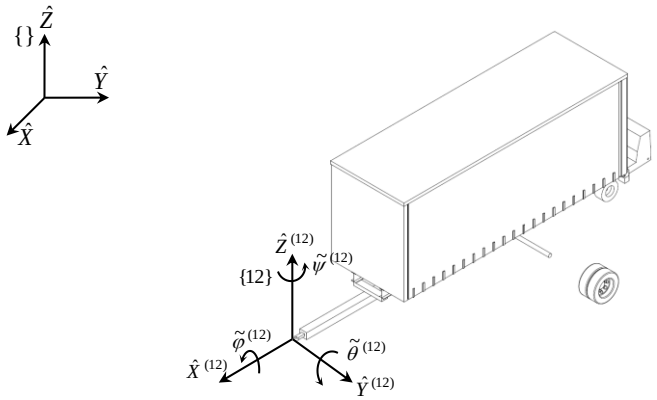

Figure 5. The main elements of the trailer

The vector of the generalized coordinates of the entire combination of the tractor and the trailer has a form of:

$$\mathbf{q} = [\tilde{\mathbf{q}}^{(1)} \quad ... \quad \tilde{\mathbf{q}}^{(18)}]^T . \tag{1}$$

This vector has 32 elements what is a number of degrees of freedom for the system in question.

Equations of vehicle motion have been formulated using Lagrange equations of the second kind [6, 7]:

$$\frac{d}{dt}\frac{\partial E}{\partial \dot{q}_k} - \frac{\partial E}{\partial q_k} + \frac{\partial V}{\partial q_k} + \frac{\partial V_D}{\partial \dot{q}_k} = Q_k \tag{2}$$

where: $E = \sum_{p=1}^{N} E^{(p)}$ - total kinetic energy of the vehicle,

$E^{(p)}$ - kinetic energy of the p-th body,

$V = \sum_{p=1}^{N} V^{(p)}$- total potential energy of the vehicle,

$V^{(p)}$ - potential energy of the p-th body,

$V_D = \sum_{p=1}^{N} V_D^{(p)}$- total energy dissipation function of the vehicle,

$V_D^{(p)}$ - energy dissipation function of the p-th body,

$\dot{\mathbf{q}} = \frac{d\mathbf{q}}{dt} = (\dot{q}_k)_{k=1,\dots,n}$ - vector of generalized velocities of the system,

$\mathbf{Q} = (Q_k)_{k=1,\dots,n}$ - vector of generalized forces of the system,

N - number of bodies of the vehicle,

n - number of generalized coordinates of the vehicle ($n = 32$),

$k = 1, \dots, n$.

In papers [7] there is a detailed description of mathematical modelling which results in a calculation model and dynamic equations of motion in a matrix form written as:

$$\begin{cases} \mathbf{A}\ddot{\mathbf{q}} - \mathbf{\Phi}\mathbf{r} = \mathbf{f} \\ \mathbf{\Phi}^{\mathbf{T}}\ddot{\mathbf{q}} = \mathbf{w} \end{cases} \tag{3}$$

where:

$\mathbf{A}(t, \mathbf{q})$ – mass matrix,

Φ - constraints matrix,

f–ector of external, Coriolis and centrifugal forces,

$\mathbf{r} = [r_1 \quad r_2]^T$ - vector of unknown constraint reactions corresponding to torques acting on front wheels,

$\mathbf{w} = [\ddot{\delta}^{(1)} \quad \ddot{\delta}^{(2)}]^T$ - vector of right sides of constraint equations,

$\delta^{(i)}$ - steering angle of the i-th front wheel.

3. Computer simulations and results

A drive of the empty combination with the forklift was analyzed in all variants. A sudden maneuver of obstacle avoidance which causes oscillations of the combination was initiated while driving.

In the subsequent figures (see Figure 6) time courses of the selected parameters such as a lateral displacement of the trailer, a displacement angle at a level of the frame of the trailer are presented.

a)

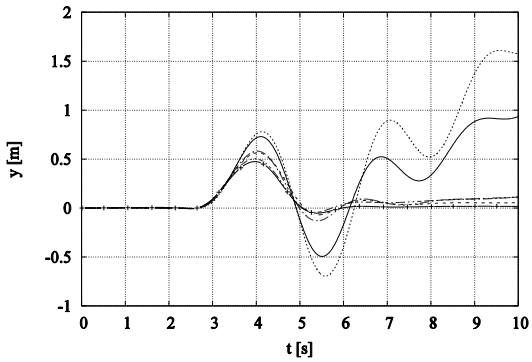

b)

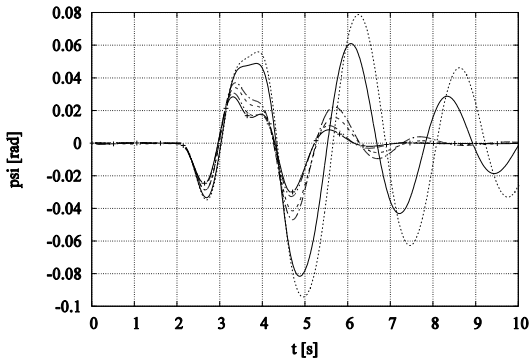

c) 0 1 2 3 4 5

Figure 6. The time courses of the selected parameters, a) a lateral displacement of the trailer center, b) and angular deflection of the trailer in relation to the vertical axis – relative to the truck, c) markings of the designing variants

Variants 0; 2 indicate a clear tendency to snaking, whereas variants 1; 3; 4; 5 do not show such a tendency, after avoiding the obstacle the oscillations disappear quickly. The variants in which the oscillations disappear quickly are characterized by a low level of unloading of the rear axles of the vehicle, value „S" is greater than zero, but not lower than – 500 kg. In the other variants value „S" was below -1000kg. An increase in vertical loading of the drawbar was induced by using the first axle lifted or unloaded in the trailer. Additional relationships can be also noticed.

1. A decrease in the trailer wheelbase increases an oscillation amplitude of the vehicle and impedes driving the combination. Contrary, an increase in the wheelbase should result in improving to drive the vehicle combination.

2. A possible long trailer drawbar should be used and coupling should be mounted as close as possible to the axle. A displacement of the coupling point by 20 0mm backwards can increase the oscillation amplitude of the vehicle frame (a driver's feeling) about 50%, the trailer oscillation about 30%, whereas the trailer displacement in the opposite direction to the maneuver can be greater than the initiating maneuver itself.

3. The best solutions are clearly variants 4 and 5 in which the highest static load of the drawbar occurs simultaneously. Variant 5 shows about half lower amplitude of the secondary displacement than variant 1 and the oscillation disappearance is much quicker.

4. Conclusions

While designing, besides providing the fulfillment of the requirements of the regulations, a placement of the trailer axle and other geometrical dimensions should be selected in such a way that the static load of the drawbar was greater than zero for the trailer loaded only with the forklift. However, it may be difficult or even impossible to meet simultaneously the above postulate and to provide that the maximum permissible load of the drawbar of the loaded trailer is not exceeded, for this reason the dimensions should be so selected in a such a way that loads of the drawbar of the trailer with the forklift is as high as possible, as it has been shown in the performed analysis a slight negative load of the drawbar can provide proper driving of the trailer, although the trailer coupling itself cannot be adjusted to carrying long-term negative vertical loads. In spite of the load distribution an appropriate placement of the coupling point should be also considered, as wide as possible wheelbase of the trailer ought to be used and you should avoid towing of the trailer by a relatively light vehicle – three-axle vehicle are recommended instead of two-axle ones. A size and a type of tires will have an obvious impact on the behavior of the vehicle combination, because greater lateral stiffness can decrease a tendency to snaking. A change in the transverse stiffness of tires can be obtained by a change in the tire pressure.

References

[1] Redakcja Forbes, *Eksportowy rekord polskich producentów okien i drzwi*, http://www.forbes.pl/eksportowy-rekord-polskich-producentow-okien-i-drzwi,artykuly,203240,1,1.html, 2016.

[2] The European Parliament and the Council of the European Union, *Directive 2007/46/EC of the European Parliament and of the Council of 5 September 2007 establishing a framework for the approval of motor vehicles and their trailers, and of systems, components and separate technical units intended for such vehicles,* http://eur-lex.europa.eu/legal-content/EN/TXT/PDF/?uri=CELEX:32007L0046&from=PL.

[3] Knorr-Bremse, *TEBS G2 Roll Stability Program (RSP)*, Doc. No. Y136111 (EN - Rev. 004), http://www.knorr-bremsecvs.com/pl/activeservices/downloadservices/downloaddocumentation_1/downloaddocumentation_1.jsp, September 2016.

[4] Komisja Europejska, *Rozporządzenie Komisji (UE) nr 1230/2012 z dnia 12 grudnia 2012 r, Załącznik 1, część D,* http://eur-lex.europa.eu/legal-content/PL/ALL/?uri=celex:32012R1230.

[5] Craig J.J., *Introduction to Robotics. Mechanics and Control,* Addison-Wesley Publishing Company, Inc.

[6] Grzegożek W., Adamiec-Wójcik I., Wojciech S., *Computer Modeling of Dynamic of Motor Vehicles.* Wydawnictwo Politechniki Krakowskiej, 2003.

[7] Tengler S., *Analysis of Dynamics of Special Vehicles with High Gravity Center*, PhD Thesis, Faculty of Mechanical Engineering and Computer Science, University of Bielsko-Biala, 2012.

Dynamics of planetary gearing box

Ladislav Půst, Luděk Pešek

Abstract: The dynamic properties of planetary gearing boxes are more complicated than those with the single parallel-axes. Therefore the deep dynamic analysis of multi-mesh planetary gearings is very important for reduction of noise and vibration. The frequency and modal spectra are very useful both for the correct design and also for the preparing and evaluation of dynamic measurements.
The presented paper is oriented on the analytical and numerical solution of spectral and modal properties of the plane type of gearing boxes with four planetary subsystems and with fixed planet carrier. The investigated gearing box is connected with a driving motor on the input central sun wheel side and with the braking aggregate on output ring wheel side. Dynamic model of such a transmission system has 20 DOF and is very complicated one with some multiple eigen-frequencies. Corresponding frequency and modal spectra are derived and analyzed.

Keywords: Planetary gearing, flexible pins of planets, frequency and modal spectrum, multiple eigenvalues.

1. Introduction

The principal advantages of planetary gearboxes over parallel shaft gears emerge from the use of multiple planets that allows the load to be divided and transmitted by several tooth contacts. Consequently, the dimensions and weigh would be smaller. On the contrary, the modal and spectral dynamic properties of planet gearboxes are more complicated than that of parallel-axis gear transmission systems and therefore they need deeper dynamic analysis (e.g. [1 - 5]). In order to prevent unequal load sharing on planet stages, floating sun gear and flexible pins of planet gears are applied [6, 7]. Dynamical model of such a gearing system is very complicated also since it has several multiple eigen-frequencies in its spectrum. Therefore the majority of publications are oriented on the specific selected parts (e.g. [8]) and very often on the influence of time variable stiffness in gears contact [9]. The more complex view on the planetary gearboxes is presented in [5].

In this paper, the solution of spectral properties of the plane type of gearings with four planetary subsystems and with fixed planet carrier is presented. It follows the works [10, 11], where the simplified computational models are solved. As the all wheels have helical and sufficiently wide gearings, the fluctuation of teeth contact stiffness over a mesh cycle, considerable in spur gearings, can be neglected. Steady contacts in gearings are asserted by means of preloading due to the constant moment loads on the sun and on outer rig wheels. The planets' carrier is supposed to be fixed.

Application of floating sun wheel, flexible planet pins and also eccentric suspension of ring wheel causes that in addition to the deformations in mesh contact in the direction of tangent to the base circle there is also vertical and horizontal motions of all components. As the gearboxes never work isolated, but they are always included as a subsystem into several-aggregates-set, the mathematical model of driving motor and of braking device have to be added to the mathematical model of planetary gearbox. The variability of dynamic properties of these external aggregates is very wide and therefore in this study only simplified 1DOF models are used. Investigated system is a train of aggregates (Fig. 1) consisting of driving motor (0), gearbox (1, 2, 3) and breaking device (4). The same situation is at the laboratory measurements.

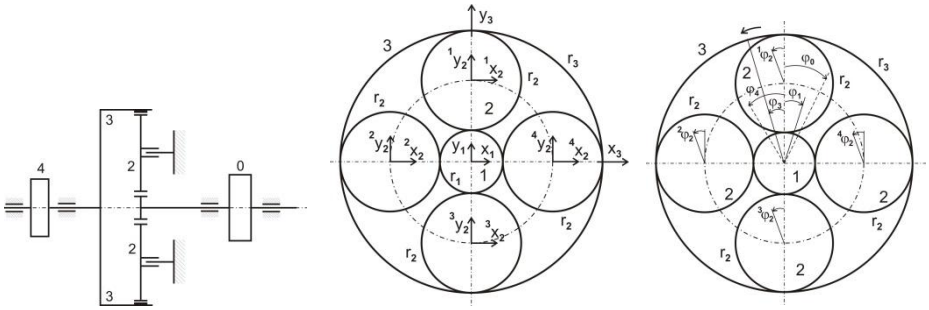

Figure 1. Computational model of tree aggregates system

2. Investigated system - equations of motion

Structure of tree-aggregates system is shown in Fig. 1. The input driving motor (0) and output break- or working-aggregate (4) are modeled by simple torsion 1DOF system. Also the four-planetary gearing set is simplified on the plane motions of all elements. In spite of these simplifications, the mathematical model has 20 DOF, belonging to the 12 translations x_i, y_i (middle subfigure 1) and 8 torsions φ_i (right subfigure 1). Corresponding vector of variables is

$$\mathbf{q} = [\varphi_0\ y_1\ x_1\ \varphi_1\ {}^1y_2\ {}^1x_2\ {}^1\varphi_2\ {}^2y_2\ {}^2x_2\ {}^2\varphi_2\ {}^3y_2\ {}^3x_2\ {}^3\varphi_2\ {}^4y_2\ {}^4x_2\ {}^4\varphi_2\ y_3\ x_3\ \varphi_3\ \varphi_4]^T . \tag{1}$$

The upper indexes in (1) indicate the order of planet wings, bottom indexes mark the type of wheel 0-4. Kinetic energy of such system is

$$T = \frac{1}{2}\begin{bmatrix} \Theta_0\dot{\varphi}_0^2 + m_1(\dot{x}_1^2 + \dot{y}_1^2) + \Theta_1\dot{\varphi}_1^2 + \\ +m_2({}^1\dot{x}_2^2 + {}^2\dot{x}_2^2 + {}^3\dot{x}_2^2 + {}^4\dot{x}_2^2 + {}^1\dot{y}_2^2 + {}^2\dot{y}_2^2 + {}^3\dot{y}_2^2 + {}^4\dot{y}_2^2) + \\ +\Theta_2({}^1\dot{\varphi}_2^2 + {}^2\dot{\varphi}_2^2 + {}^3\dot{\varphi}_2^2 + {}^4\dot{\varphi}_2^2) + m_3(\dot{x}_3^2 + \dot{y}_3^2) + \Theta_3\dot{\varphi}_3^2 + \Theta_4\dot{\varphi}_4^2 \end{bmatrix} \tag{2}$$

and potential energy

$$V = \frac{1}{2}[k_0(\varphi_0 - \varphi_1)^2 + k_1(x_1^2 + y_1^2) + k_{x12}[(x_1 - {}^1x_2 + r_1\varphi_1 - r_2\,{}^1\varphi_2)^2 + (y_1 - {}^2y_2 + r_1\varphi_1 - r_2\,{}^2\varphi_2)^2 +$$
$$+(-x_1 + {}^3x_2 + r_1\varphi_1 - r_2\,{}^3\varphi_2)^2 + ({}^4y_2 - y_1 + r_1\varphi_1 - r_2\,{}^4\varphi_2)^2] + k_{y12}[(y_1 - {}^1y_2)^2 + ({}^2x_2 - x_1)^2 +$$
$$+({}^3y_2 - y_1)^2 + (x_1 - {}^4x_2)^2] + k_c({}^1x_2^2 + {}^1y_2^2 + {}^2x_2^2 + {}^2y_2^2 + {}^3x_2^2 + {}^3y_2^2 + {}^4x_2^2 + {}^4y_2^2) + \quad (3)$$
$$+k_{x23}[(x_3 - r_3\varphi_3 + r_2\,{}^1\varphi_2 - {}^1x_2)^2 + (y_3 - r_3\varphi_3 - {}^2y_2 + r_2\,{}^2\varphi_2)^2 + ({}^3x_2 - x_3 - r_3\varphi_3 + r_2\,{}^3\varphi_2)^2 +$$
$$+({}^4y_2 - y_3 - r_3\varphi_3 + r_2\,{}^4\varphi_2)^2] + k_{y23}[({}^1y_2 - y_3)^2 + ({}^2x_2 - x_3)^2 + ({}^3y_2 - y_3)^2 + ({}^4x_2 - x_3)^2] +$$
$$+k_3(x_3^2 + y_3^2) + k_4(\varphi_4 - \varphi_3)^2].$$

Introducing these expressions into Lagrange equations we get 20 differential equations of motion

$$\Theta_0\ddot{\varphi}_0 + k_0(\varphi_0 - \varphi_1) = 0,$$

$$m_1\ddot{y}_1 + k_1y_1 + k_{x12}[2y_1 - ({}^2y_2 + {}^4y_2) - r_2({}^2\varphi_2 - {}^4\varphi_2)] + k_{y12}[2y_1 - {}^1y_2 - {}^3y_2) = 0,$$

$$m_1\ddot{x}_1 + k_1x_1 + k_{x12}[2x_1 - {}^1x_2 - {}^3x_2 - r_2({}^1\varphi_2 - {}^3\varphi_2)] + k_{y12}[2x_1 - {}^1x_2 - {}^3x_2] = 0,$$

$$\Theta_1\ddot{\varphi}_1 + k_0(\varphi_1 - \varphi_0) + k_{x12}r_1[4r_1\varphi_1 - {}^1x_2 - {}^2y_2 + {}^3x_2 + {}^4y_2 - r_2({}^1\varphi_2 + {}^2\varphi_2 + {}^3\varphi_2 + {}^4\varphi_2)] = 0,$$

$$m_2\,{}^1\ddot{y}_2 + (k_{y12} + k_c + k_{y23})\,{}^1y_2 - k_{y12}y_1 - k_{y23}y_3 = 0,$$

$$m_2\,{}^1\ddot{x}_2 + (k_{x12} + k_c + k_{x23})\,{}^1x_2 + k_{x12}(-x_1 - r_1\varphi_1 + r_2\,{}^1\varphi_2) + k_{x23}(-x_3 + r_3\varphi_3 - r_2\,{}^1\varphi_2) = 0,$$

$$\Theta_2\,{}^1\ddot{\varphi}_2 + (k_{x12} + k_{x23})r_2^2\,{}^1\varphi_2 - k_{x12}r_2(x_1 + r_1\varphi_1) + (k_{x12} - k_{x23})r_2\,{}^1x_2 + k_{x23}r_2(x_3 - r_3\varphi_3) = 0,$$

$$m_2\,{}^2\ddot{y}_2 + (k_{y12} + k_c + k_{y23})\,{}^2y_2 + k_{y12}(-y_1 - r_1\varphi_1) + (k_{y12} - k_{y23})r_2\,{}^2\varphi_2 + k_{y23}(-y_3 + r_3\varphi_3) = 0,$$

$$m_2\,{}^2\ddot{x}_2 + (k_{x12} + k_c + k_{x23})\,{}^2x_2 - k_{x12}x_1 - k_{x23}x_3 = 0,$$

$$\Theta_2\,{}^2\ddot{\varphi}_2 + (k_{y12} + k_{y23})r_2^2\,{}^2\varphi_2 - k_{y12}r_2(y_1 + r_1\varphi_1) + (k_{y12} - k_{y23})r_2\,{}^2y_2 + k_{y23}r_2(y_3 - r_3\varphi_3) = 0, \quad (4)$$

$$m_2\,{}^3\ddot{y}_2 + (k_{y12} + k_c + k_{y23})\,{}^3y_2 - k_{y12}y_1 - k_{y23}y_3 = 0,$$

$$m_2\,{}^3\ddot{x}_2 + (k_{x12} + k_c + k_{x23})\,{}^3x_2 + k_{x12}(-x_1 + r_1\varphi_1) - (k_{x12} - k_{x23})r_2\,{}^3\varphi_2) - k_{x23}(x_3 + r_3\varphi_3) = 0,$$

$$\Theta_2\,{}^3\ddot{\varphi}_2 + k_{x12}r_2(x_1 - r_1\varphi_1) - (k_{x12} - k_{x23})r_2\,{}^3x_2 + (k_{x12} + k_{x23})r_2^2\,{}^3\varphi_2 - k_{x23}r_2(x_3 + r_3\varphi_3) = 0,$$

$$m_2\,{}^4\ddot{y}_2 + (k_{y12} + k_c + k_{y23})\,{}^4y_2 - k_{y12}(y_1 - r_1\varphi_1) - (k_{y12} - k_{y23})r_2\,{}^4\varphi_2) - k_{y23}(y_3 + r_3\varphi_3) = 0,$$

$$m_2\,{}^4\ddot{x}_2 + (k_{x12} + k_c + k_{x23})\,{}^4x_2 - k_{x12}x_1 - k_{x23}x_3 = 0,$$

$$\Theta_2\,{}^4\ddot{\varphi}_2 + (k_{y12} + k_{y23})r_2^2\,{}^4\varphi_2 + k_{y12}r_2(y_1 - r_1\varphi_1) - (k_{y12} - k_{y23})r_2\,{}^4y_2 - k_{y23}r_2(y_3 + r_3\varphi_3) = 0,$$

$$m_3\ddot{y}_3 + k_3y_3 + k_{y23}[4y_3 - ({}^1y_2 + {}^2y_2 + {}^3y_2 + {}^4y_2) + r_2({}^2\varphi_2 - {}^4\varphi_2) = 0,$$

$$m_3\ddot{x}_3 + k_3x_3 + k_{x23}[4x_3 - ({}^1x_2 + {}^2x_2 + {}^3x_2 + {}^4x_2) + r_2({}^1\varphi_2 - {}^3\varphi_2) = 0,$$

$$\Theta_3\ddot{\varphi}_3 + k_4(\varphi_3 - \varphi_4) + k_{x23}r_3[2r_3\varphi_3 + {}^1x_2 - {}^3x_2 - r_2({}^1\varphi_2 + {}^3\varphi_2)] +$$
$$+ k_{y23}r_3[2r_3\varphi_3 + {}^2y_2 - {}^4y_2 - r_2({}^2\varphi_2 + {}^4\varphi_2)] = 0,$$

$$\Theta_4\ddot{\phi}_4 + k_4(\varphi_4 - \varphi_3) = 0.$$

These equations of motion can be written in matrix form

$$\mathbf{M}\ddot{\mathbf{q}} + \mathbf{K}\mathbf{q} = \mathbf{0}\,, \tag{5}$$

where the diagonal inertia matrix **M** has 20 non-zero elements

$$\mathbf{M} = [\backslash\Theta_0, m_1, m_1, \Theta_1, m_2, m_2, \Theta_2, m_2, m_2, \Theta_2, m_2, m_2, \Theta_2, m_2, m_2, \Theta_2, m_3, m_3, \Theta_3, \Theta_4 \backslash], \tag{5a}$$

The full stiffness matrix **K** is of order 20x20 and of great dimension with many complicated expressions (see [11]) unsuitable for presentation in this short contribution. Using adapted program "eig" in system Matlab we get for given **M, K** frequency spectrum of the four-planetary gearbox.

Let us use the parameters of an example of planetary gearbox similar to the high speed planetary gearbox with fixed planet carriers:

Radii $r_0 = 0{,}1$ m, $r_1 = 0{,}06$ m, $r_2 = 0{,}12$ m, $r_3 = 0{,}3$ m, $r_4 = 0{,}1$ m.

Masses $m_1 = 20$ kg, $m_2 = 50$ kg, $m_3 = 250$ kg. (6)

Moments of inertias $\Theta_0 = 0.2$ kgm^2, $\Theta_1 = 0.04$ kgm^2, $\Theta_2 = 0.5$ kgm^2,

$\Theta_3 = 15$ kgm^2, $\Theta_4 = 2$ kgm^2.

Due to the helical and sufficiently wide gearings, the average mesh stiffness can be used:

$k_{12} = 4.0\text{e+}9$ N/m, $k_{23} = 4.2\text{e+}9$ N/m.

Mesh stiffness in the directions of vertical and horizontal axes *x, y* are

$$k_{x12} = k_{12}(\cos(\alpha))^2, \quad k_{x23} = k_{23}(\cos(\alpha))^2,$$

$$k_{y12} = k_{12}(\sin(\alpha))^2, \quad k_{y23} = k_{23}(\sin(\alpha))^2, \tag{6a}$$

where mesh angle $\alpha = 25^o = 5\pi/36 rad$.

The cross stiffness of gearing wheels' axes are $k_1 = 1e+5N/m$, $k_2 = 1.2e+8N/m$, $k_3 = 1.4e+8N/m$ and the torsion stiffness of the external shafts are $k_0 = 6e+5Nm/rad$ and $k_4 = 1e+7Nm/rad$.

3. Eigen-frequencies and eigen-modes.

Introducing these values (6) into motions equations (4) or (5) then by means of special adapted program „eig" (Matlab) we get the set of eigen-frequencies of investigated planetary gearing:

f =(0, 160.9, **180.7, 180.7**, 364.0, 373.0, **568.8, 568.8, 896.0, 896.0**, (7)
1049.3, 1049.3, 1861.7, 2218.2, **2230.3, 2230.3**, 2523.1, **3708.8, 3708.8** 5863.5) Hz.

Due to the structural periodicity of planetary gearboxes, some multiple frequencies occur. The investigated system has 6 double frequencies, which are in (7) bolt written.

The first eigen-frequency has zero value and corresponds to the revolution of the all gearing wheels. The remaining nineteen non-zero eigen-frequencies correspond to the vibrations superposed on this rotation. There exist several twofold frequencies

$$f_3 = f_4 = 180.7\,Hz,\quad f_7 = f_8 = 568.8\,Hz,\quad f_9 = f_{10} = 896.0\,Hz\ ,$$

$$f_{11} = f_{12} = 1049.3\,Hz,\quad f_{15} = f_{16} = 2230.3\,Hz,\quad f_{18} = f_{19} = 3708.8\,Hz\ . \tag{8}$$

The elaborated program in system Matlab ascertains also corresponding modes of vibrations defined by numerical values of all 20 variables of coordinate's vector **q**.

In the simplest case when all the eigen-values are distinct, to each one of them belongs one mode shape orthogonal to the rest of eigen-modes. But there are some multi-fold eigen-frequencies in the planet gearings frequency spectrum, which need special mode shape procedure (see e.g. [1, 2]).

For transformation of these numerically described modes into clear, well-arranged graphical presentation of eigen-modes of gearings box, which is a complicated multi-body system, we have elaborated computational program "emode20DOFxx"in system Matlab. The output of this program are figures of modes, where the torsion amplitudes of wheels are drawn by inclinations of bolt vertical diameters, shifts of axes are pictured by thin dashed lines connecting the axis zero position with displaced one. Dashed lines draw also the contact deformations in gearings meshes. Bold dashed lines are used for expression of external aggregates torsion amplitudes.

Following figures shown the modes of the lowest 12 eigen-frequencies.

The Fig. 2 shows the situation at revolution. The displacements drawn by thick lines give distribution of displacements or velocities of points on wheels. As displacements at rotation with constant velocity increase over all limits, the small deformations in tooth contacts are negligible and therefore this mode shape is connected in all eight mesh contacts. The displacements of wheels centres are also negligible as well as torsion deformations of shafts among all three aggregates. Angle of inclination of thick wheel diameter to the radius is proportional to the corresponding angular velocity.

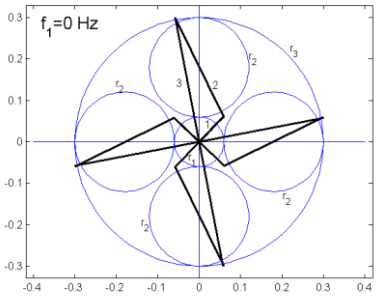

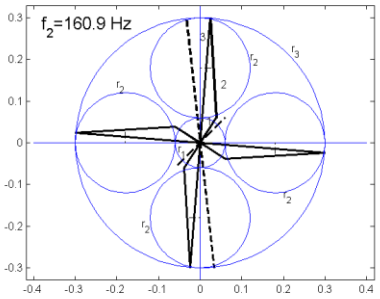

Figure 2. System revolution

Figure 3. Lowest eigen-frequency

The mode in Fig. 3 belongs to the lowest eigen-frequency. All wheels vibrate and the knot of vibration is in shaft between ring wheel and output aggregate, deformations of mesh contacts are again negligible.

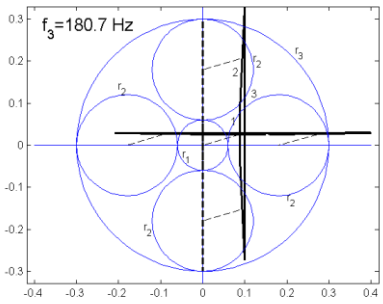

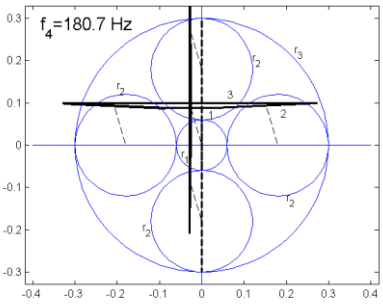

Figure 4. Mode of twofold frequency

Figure 5. Mode of twofold frequency

Modes in figures 4 and 5 belong to the twofold eigen-frequency $f_3 = f_4 =$ 180.7 Hz. Sun and ring wheels vibrate only transversally without rotation and therefore the external aggregates do not move. The main deformations are realized in wheels' axes supports, All wheels vibrate roughly parallel, directions of these vibrations are orthogonal.

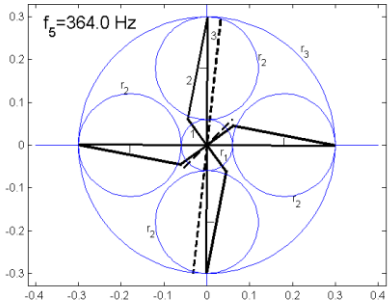

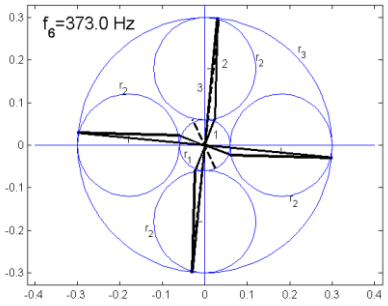

Figure 6. Singular eigen-frequency

Figure 7. Singular eigen-frequency

Next two natural frequencies are singular. The planetary gearing set vibrates similarly as at frequency $f_2 = 160.9$ Hz with very small deformations in mesh contacts. Both external aggregates, sun and ring wheels vibrate torsional. The mode in Fig. 6 at $f_5 = 364.0$ Hz has two knots: First on between input motor and gearing box, second one between gearing box and output aggregate. The mode in Fig. 7 at $f_6 = 373.0$ Hz has only one knot between input motor and gearing box.

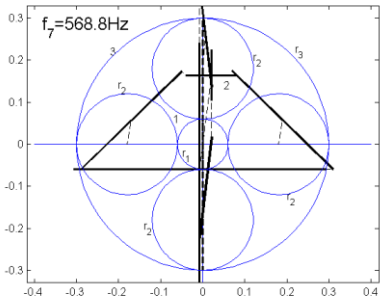

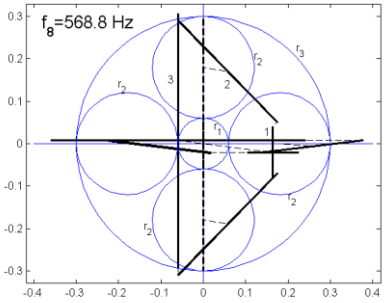

Figure 8. Mode of twofold frequency

Figure 9. Mode of twofold frequency

Modes in Fig. 8 and 9 belong to the further twofold eigen-frequency $f_8 = f_9 =$ 568.8 Hz. The contact deformations in mesh gearings are here important. Both modes are orthogonal and quasi-symmetric to the vertical (Fig. 8) or horizontal (Fig. 9) axis.

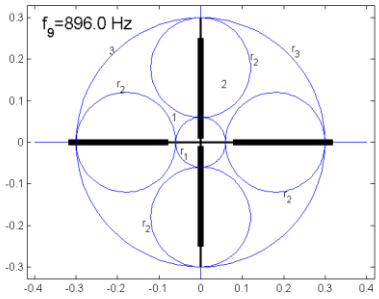

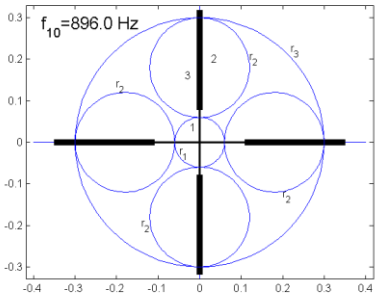

Figure 10. Mode of twofold frequency

Figure 11. Mode of twofold frequency

The couple of modes shown in Fig. 10 and 11 belong also to twofold eigen-frequency $f_{10} = f_{11} =$ 896.0 Hz. They have very simple forms only with radial vibrations of planets, without any torsion motion. The extreme position of planets is highlighted by thicker lines. Odd and even planets vibrate in opposition in Fig. 10, parallel in Fig. 11. High of eigen-frequencies are given by planet's pin stiffness and radial stiffness in mesh gearings.

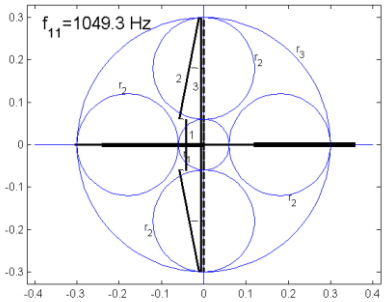

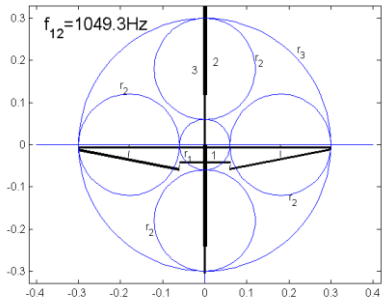

Figure 12. Mode of twofold frequency

Figure 13. Mode of twofold frequency

The more general type of modes is shown in Fig. 12 and 13 belonging to the again twofold eigen-frequency $f_{12} = f_{13} =$ 1049.3 Hz. Both modes are symmetric either to the horizontal (Fig. 12) or vertical (Fig. 13) axis.

4. Conclusions

n this paper spectral and modal spectra of a three aggregates system modelling dynamic properties of real application of planetary gearbox in technical praxis are analyzed. The investigated gearing box is four planetary type with the fixed planets' carrier. All gearing wheels are supposed to be solid, elastically supported bodies with general plain motions. The mesh contacts in gearings are computed

as elastic and constant with neglecting the time fluctuation of teeth contact stiffness as in the helical and sufficiently wide gearings is this fluctuation very small.

Both external aggregates –the driving motor connected with sun gear wheel and the output brake connected with ring gear wheel – are modelled by one DOF torsion systems. Together with planetary gearbox is such a mathematical model of this three aggregates system described by 20 linear differential equations. By means of elaborated programs in "Matlab" language, the corresponding frequency and modal spectra were ascertained for parameters of a high-speed gearing train. There is one zero and six twofold eigen-frequencies in obtained 20 elements of frequency spectrum.

Zero eigen-frequency corresponds to the revolution of all gearing wheels. The remaining elements in frequency spectrum give natural frequencies of the three aggregates gearing train. Modal spectra belonging to these frequencies and obtained as modal matrix in digital form had to be transformed into clear visual figures. However, due to limited extend only 12 lowest modes can be presented in this contribution. It is shown that two similar but orthogonal modes belong to every twofold eigen-frequency.

There exist also modes where sun and/or ring wheels do not vibrate. This property means that at laboratory experimental research, these frequencies cannot be excited by forced vibration of sun or ring shafts. In addition, these frequencies do not depend on properties of external driving and braking aggregates and do not change in the all gearing box applications.

Analysis of modes prove that the lower eigen-frequencies are influenced mainly through stiffness of wheels axes supports and torsional stiffness of input and output shafts. On the contrary, the mesh stiffness gears contact influence mainly the high frequency modes.

Acknowledgments

This work has been supported by the project of the IT ASCR AVOZ2076919 "Experimental and theoretical research of planetary gearing with fixed planet carrier".

References

[1] Cooley Ch., G., Parker, R., G.,: A Review of Planetary and Epicyclic Gear Dynamics and Vibrations Research, AMR, 66,2014, 040804-1-15

[2] Peeters J., Vandepitte D., Sas P., Flexible multi-body model of a three-stage planetary gearbox in a wind turbine. Proc. ISMA 2004, p. 3923 – 3941

[3] Parker R. G., A physical explanation for the effectiveness of planet phasing to suppress planetary gear vibration, JSV 236 2000, No. 4, p. 561 – 573

[4] Zeman. V., Internal dynamics of stereostatic planet gear box with double-helical gearings, (in Czech), Strojnícky Časopis 20, 1969 No. 3, p. 249 –266

[5] R. August, R. Kasuba, J. L. Frater, A. Pintz: Dynamics of planetary gear train. NASA-CR-3793 Report, June 1984

[6] CaiChao Zhu, a kol.: Effect of flexible pin on the dynamic behaviours of wind turbine planetary gear drives. JMES 227(1) p. 74-86

[7] Yanabe, S., Yoshino, M., Self-centring Characteristics of floating sun gear in a star-type planetary gear train, Proc. 10th congress on TMM, Oulu, Finland 1999, pp. 2386 - 2391

[8[Lin Xu, Kai Liu, Yahui Cui, Peiyuan Meng: Dynamic analysis of planetary gear train withTwo degrees of freedom, Proc. 2nd International Conferenceon machinery, materials Engineering, chemical Engineering and Biotechnology (MMECEB 2015), Chongqing, China, 2015, Atlantis Press, p.896-901

[9] Hortel, M., Škuderová, A., Houfek, M.,: Linear time heteronymous damping in nonlinear parametric systems. Applied Mathematical Modelling, 40(2016) p. 10038-10051

[10] Půst, L. Pešek, L. Radolfová, A., Free vibration frequency spectrum of four-planetary gearing box, Int. Conference on the Theory of Machines and Mechanisms, Liberec, 2016, s. 161-167

[11] Půst, L., Pešek, L., Radolfová, A.,: Frequency and modal spectra of planet gearing box Wikov, (in Czech), Report IT ASCR Z-1571/17 Prague, 2017

[12] Newland, D., E.,: Mechanical vibration analysis and computation, Longman ST., Singapore, 1989

[13] Collatz, L.: Eigenwertaufgaben mit Technischen Anwendumgen, Akademische Verlagsgesellshaft, Leipzig, 1949

Ladislav Pust, Ludek Pesek,

Institute of Thermomechanics, ASCR, Prague, CR.

Flutter running waves in turbine blades cascade

Ladislav Půst, Luděk Pešek, Miroslav Byrtus

Abstract: The existence of flutter running waves has been often observed at experimental investigation of turbine blades cascade. The presented paper is an attempt to explain origin and behavior of running flutter waves in the rotating blade cascade excited by steam flow from the stationary bladed disk. One of the possibly reasons for existence of running waves are the running periodic forces from steam wakes due to different numbers of blades of stationary and rotating wheels. On a computational model of turbine disk with 10 blades there are shown properties – velocities, directions and modes – of these forced running waves. Interaction of this kind of forced excitation with aero-elastic self-excitation – flutter – causes origin of flutter running waves. These flutter waves will be analyzed in the paper for several kinds and combinations of aero-elastic self-excitations.

1. Introduction

Dynamic properties of blades cascades in turbines excited by the external periodic forces or by aero-elastic effects of flowing gas – flutter – have been intensively studied during the several last decades (e.g. [1-3]). Relating to this, the existence of running waves was observed and mentioned. Main attention has been given to running waves in connection with origin of classical flutter. From the broad number of publications oriented on the flutter phenomenon and running waves in cascades let us mention e.g. [4-6]. Some methods of analytical solution of blades vibration with flutter phenomenon are presented in [4, 5, 7]. Dynamic properties of closed 10 blades bundle modelling turbine blades wheal are analyzed in the conference publications [8-10], where the blades are modelled as systems with one DOF. Due to the different numbers of blades of stationary and of rotating wheels the running waves forced by the wakes from the stationary cascade exist. These forced running waves can entrain aero-elastic self-excited oscillations and cause origin of the flutter running waves. The influence of friction dampers between blades on the blade bundle dynamics considering as a non-smooth system is investigated in [11].

The presented article tries to improve this analysis by modelling of blades as systems with two DOF – translation and pitching. This improvement of dynamic bladed wheal model enables to investigate better the properties of vibration's processes in real turbine. In order to study the behavior of bladed cascade in the unstable regions, the simple Van der Pol expression for description of self-excitation forces are used.

2. Investigated system

The computing model of turbine wheel with ten blades with the simplest type of linear connections between neighbouring blades is shown in Fig. 1.

This connection between blades realized by means of Voigt-Kelvin model with paralleled connected spring (stiffness k_1 [kgs^{-2}]) and damping element with coefficient b_1 [kgs^{-1}] enables (at least approximately) modelling of both elastic and damping properties of disc as well as elastic and damping properties of shroud.

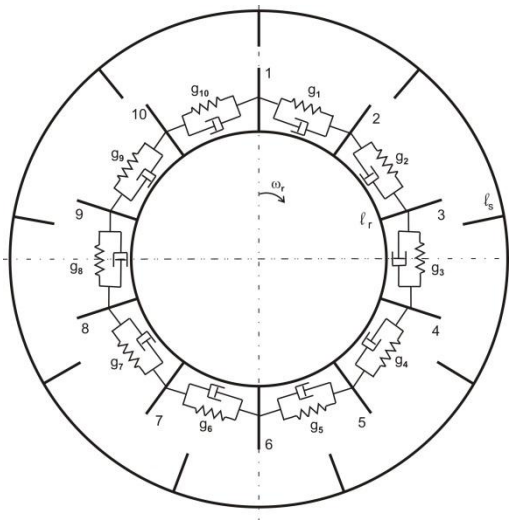

Figure 1. Turbine wheel with ten blades and linear connections between neighboring blades. Stator cascade with nine blades.

Turbine blades are in this Figure graphically presented by simple lines. The more detail displays of one blade with pitch and transition motion is in Fig. 2.

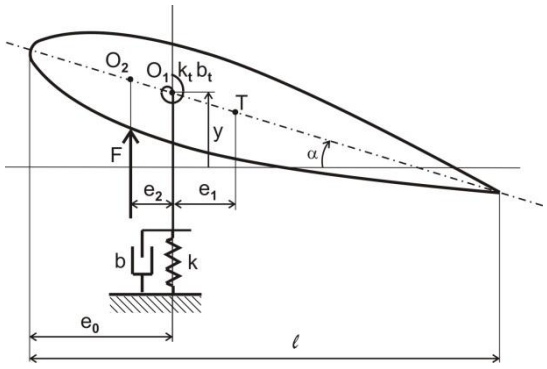

Figure 2. Dynamic model of blade.

This 2 DOF profile is capable of demonstrating aero-elastic phenomena. The center of mass *m* is designated as *T*. Corresponding moment of inertia is *I*. Flexural axis of this profile is labelled by O_1 and the transitional stiffness in vertical direction *y* is *k*. Parallel to the elastic force acts also viscous damping force with coefficient *b*. Pitch spring stiffness around this flexural axis is k_t. This stiffness is again parallel connected by a damping moment with torsional damping coefficient b_t. The vertical aerodynamic force *F* acting on the blade in direction *y* is shifted in distance e_2 into point O_2. There is also an aero-elastic moment $M_e = F e_2$ acting around the flexural axis O_1 and oriented to increase of pitch angle α.

3. Free motion equations of one blade

Equations of free vibration of a singular blade without any aerodynamic influences can be classically constructed using expressions for potential energy $V = 1/2(ky^2 + k_t\alpha^2)$ and for kinetic energy $T = 1/2(m(\dot{y} - e_1\dot{\alpha})^2 + I\dot{\alpha}^2$. Equations of motion are than obtained by inserting the expressions of both energies into Lagrange equation $\frac{\partial}{\partial t}(\frac{dT}{d\dot{q}}) + \frac{dV}{dq} = 0$, where $q = [y\ \alpha]$. So we get

$$m(\ddot{y} - e_1\ddot{\alpha}) + ky = 0,$$
$$I\ddot{\alpha} - me(\ddot{y} - e_1\ddot{\alpha}) + k_t\alpha = 0. \quad (1)$$

These motion equations can be rearranged into another form of two equations

$$m\ddot{y} + \frac{k_t m e_1}{I}\alpha + (k + \frac{k m e_1^2}{I})y = 0, \quad (1a)$$
$$I\ddot{\alpha} + k_t\alpha + k e_1 y = 0,$$

or into matrix form

$$M\ddot{q} + Kq = 0, \quad (2)$$

where mass matrix is $M = \begin{bmatrix} m & 0 \\ 0 & I \end{bmatrix}$ and stiffness matrix $K = \begin{bmatrix} k + k m e_1^2 / I & k_t m e_1 / I \\ k e_1 & k_t \end{bmatrix}$. (2a)

Eigen-frequencies of singular undamped blade, computed in the following examples for blade's mass, stiffness and damping coefficient for translation *y* and for tilting α

m=0.18 kg, k=100000 kgs^{-2}, b=2 kgs^{-1}, I=0.000025 kgm^2, k_t=0.1 kgm^2s^{-2}, e_1=0.005 m,
bt=0.0005 kgm^2s^{-2}/rad (3)

are $\Omega_1 = 179.87\,rad/s,\ \Omega_2 = 750.47\,rad/s.$

4. Motion equations of blade's cascade

The sector of blade's cascade is shown in Fig. 3. The blades' interconnections stiffness and damping in g_i are $k_1 = 1000 kgs^{-2}$ and b_1=0.2 kg/s. These viscous-elastic connections between neighboring blades can express properties of connections in blade-shroud, dynamic properties of damping wires or compliance of turbine disk.

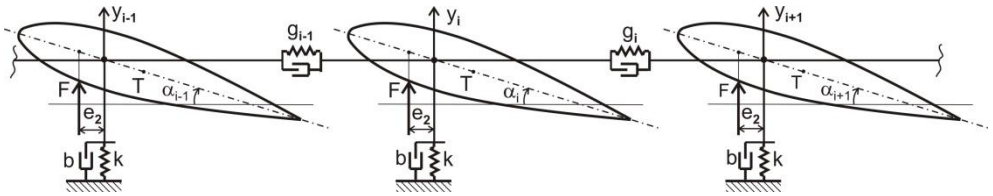

Figure 3. Section of blade cascade

The aerodynamic forces F act on the blades in points O_2 in distance of e_2=0.005m from the elastic axes O_1. There are two types of these aerodynamic forces:

1) The velocity of steam flowing from the stator cascade has periodic profile due to the stator blades distortion and the wakes of flow from the stator blades produce forced vibration of the rotating blades. Different blades' number of rotating and of stator wheels (Fig. 1) causes the phase delays of excitation forces produced by these wakes.

2) Steam flowing through the rotating blade-cascade, where each blade has two DOF (y, α) can cause decrease of damping and aero-elastic instability - rise of flutter. Exact mathematical model of this aero-elastic phenomenon is very complicated; therefore we will use in this study the Van der Pol model, described by equation

$$G = -\mu(1-(y/r)^2)\dot{y}\,, \tag{4}$$

where G is the aerodynamic force, $y, \dot{y}$ are general displacement and velocity, r is displacement of blade at which the aerodynamic force changes its sign, μ gives intensity of this non-linear damping.

This negative self-exciting force G is compensated by positive structural damping with coefficient b (3). Self-excited oscillations can arise if $\mu > b$, but it needs an initial impulse for its expansion.

4.1. Running forced vibration

The blades in the rotating bladed row are excited by external periodic forces arising at the rotation of bladed wheel with l_r = 10 blades in the spatially periodical flow of steam from the stator blade cascade with another number l_s of blades: $l_r \neq l_s$. Periodic force exciting the i-th blade by the wakes of steam-flow can be simplified on the first harmonic component $F_{0i}\cos(\omega t-(i-1)\Delta\varphi)$, where the

excitation frequency ω depends on the wheel rotation: $\omega_r = \omega / l_r$. The phase delay $\Delta\varphi$ of harmonic excitation forces depends on the ration l_s / l_r of rotor and stator blades' numbers according following relation:

$$\Delta\varphi = 2\pi(1 - \frac{l_s}{l_r}) . \qquad (5)$$

Equations of these forced vibrations, described by the motion y of the elastic axis and angle α, are

$$m\ddot{y}_i + \frac{k_t m e_1}{I}\alpha_i + (k + \frac{k m e_1^2}{I})y_i + b\dot{y}_i + g_i - g_{i+1} = F_{0i}\cos(\omega t - (i-1)\Delta\varphi), \qquad i = 1,..,10 , \qquad (6)$$
$$I\ddot{\alpha}_i + k_t\alpha_i + b_t\dot{\alpha}_i + k e_1 y_i = e_2 F_{0i}\cos(\omega t - (i-1)\Delta\varphi),$$

where $g_i = k_1(y_i - y_{i-1}) + b_1(\dot{y}_i - \dot{y}_{i-1}) \qquad i = 1,..,10$ (6a)

are viscous-elastic connections among blades and for the closed cascade $g_{11} = g_1$. This connecting element can model both elastic properties of disc as well as of damping properties of shroud or of damping wires, etc. Response curves of such a bladed system are further computed for parameters (3) similar to parameters of a bladed disk, measured in laboratory of IT ASCR. The inter-blades connections with viscous-elastic Voigt-Kelvin model g_i have parameters

$k_1 = 10000$ kgs^{-2}, $b_1 = 0.2$ kgs^{-1}. (7)

Response curves are calculated as non-stationary with amplitude of external excitation $F_0 = 1$ kgms^{-2} and at the very small constant angular acceleration $d\omega / dt = 10 rad / s$. Such non-stationary curves are practically identical with the stationary curves. If the numbers of blades of stationary and rotating disk are the same ($l_s = l_r$), there it is no phase shift $\Delta\varphi = 0$ and the blade cascade vibrates with the so-called umbrella mode.

The phase shift is non-zero $\Delta\varphi \neq 0$ at different numbers of blades of stationary and rotating disk ($l_s \neq l_r$). This causes running wave in the blade cascade. The relative vibrations among neighbouring blades occur in such case and the inter-connection stiffness k_1 increases resonance frequency. The phase shifts of wake's exciting forces in system with 9 stationary blades ($l_s / l_r = 0.9$) are $\Delta\varphi = \pi / 5$. Dynamic behaviour of blades' cascade is shown in Fig. 4, where vibrations of elastic centres y are shown in Fig. 4a and vibrations of mass centres $y_T = y - e_1\alpha$ are in Fig. 4b. The time records of first blade's vibrations (i=1) are bold drawn and the time records of tenth blade's vibrations (i=10) are drawn in upper dashed bold lines. The vibration of eleventh blade is not drawn, because it is in the closed cascade identical with the first blade.

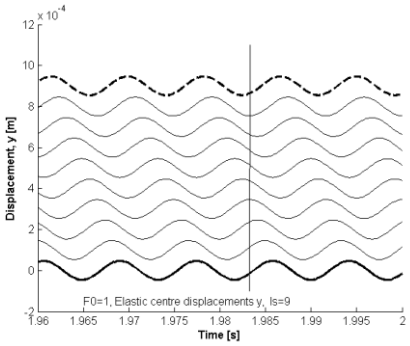

Figure 4a. Displacements y

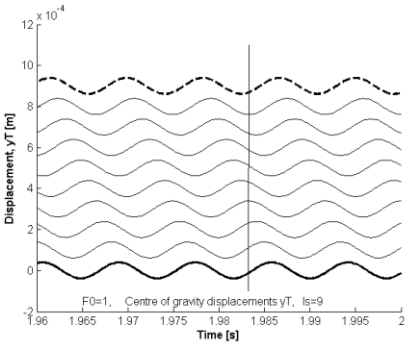

Figure 4b. Displacements $y_T = y - e_1\alpha$

The mode of vibration can be obtained by cutting this set of response curves at constant time see e.g. vertical lines in Fig. 4. Corresponding modes of elastic and mass centers displacements y, $y_T = y - e_1\alpha$ are drawn in Fig. 5a. Difference between both curves is proportional to the angle α.

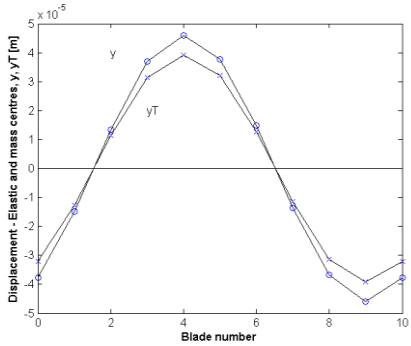

Figure 5a. Mode at $\Delta\varphi = \pi / 5$

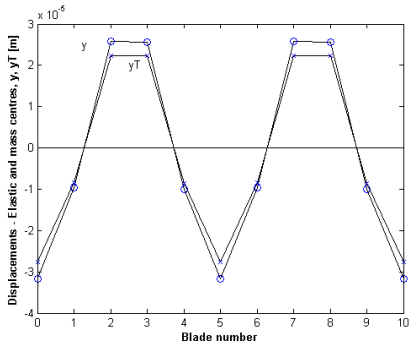

Figure 5b. Mode at $\Delta\varphi = 2\pi / 5$

Similar properties has also vibration of rotating disk with $l_s = 8$ blades excited by wakes of gas flow from the stationary disk with $l_s = 8$ blades, as it is presented in Fig. 6a and 6b, where the relative phase shift among neighbouring blades is $\Delta\varphi = 2\pi / 5$. Modes of elasticity centre displacements y and of mass centre $y_T = y - e_1\alpha$ are drawn in Fig. 5b. Difference between both curves is again proportional to the angle α.

The difference between both cases is also in the two times smaller velocity of running waves in the case of system with $l_s = 8$ than of system with $l_s = 9$.

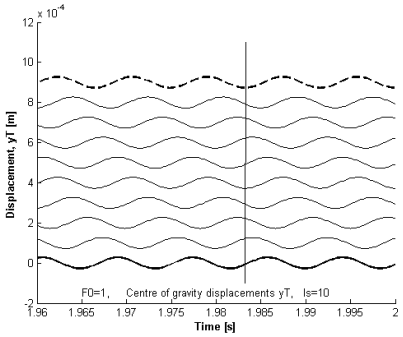

Figure 6a. Displacement *y*.

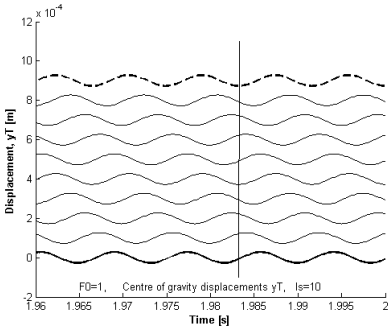

Figure 6b. Displacements $y_T = y - e_1\alpha$

5. Self-excited vibrations – flutter

The flowing steam through the rotating blade cascade produces besides mentioned periodic forced vibration also aero-elastic self-exciting forces resulting into dangerous vibrations – flutter. . These both sources of excitation interact mutually and the running waves of forced vibration initiate also the flutter running waves. Forced and flutter types of vibrations are synchronised and run with the same velocity and in the same direction.

There are two important types of aero-elastic forces: First one acting on individual blades and controlled by only one blade's motion parameters and the second one with the interaction forces between neighboring blades and controlled by parameters of relative motion of both blades. Using the Van der Pol model of self-excitation forces, then these forces are expressed by equations

$$F_{ei} = -\mu(1-(y_i / r)^2)\dot{y}_i \quad \text{or} \quad F_{ei,i+1} = -\mu(1-((y_i - y_{i+1}) / r)^2)(\dot{y}_i - \dot{y}_{i+1}) \ . \tag{8}$$

Only the first type of aero-elastic forces (8) is applied in this contribution. Differential equations describing complex motion of blade cascade are

$$\begin{aligned} &m\ddot{y}_i + \frac{k_t m e_1}{I}\alpha_i + (k + \frac{k m e_1^{\,2}}{I})y_i + b\dot{y}_i + F_{ei} + g_i - g_{i+1} = F_{0i}\cos(\omega t - (i-1)\Delta\varphi), \quad i = 1,.....,10, \\ &I\ddot{\alpha}_i + k_t\alpha_i + b_t\dot{\alpha}_i + e_1 F_{ei} + k e_1 y_i = e_2 F_{0i}\cos(\omega t - (i-1)\Delta\varphi), \end{aligned} \tag{9}$$

where $g_0 = g_{10}$.

Response curves are computed in the following examples for the same parameters (3) and (7) used for the forced vibration. Parameters of Van der Pol model (8) are:

$$\mu = 3,\ r = 0.009,\ e_2 = 0.005 \ . \tag{9a}$$

Amplitude of external wakes force is F_0=1 N with frequency $\omega = 750\,rad/s$.

Two damping forces act on each blade. One of these forces is positive structural damping with coefficient b = 2 kgs^{-1}, the second one is negative aero-elastic damping with coefficient μ. Self-excited oscillation can arise if $\mu > b = 2$, but it needs an initial impulse e.g. random noise for its expansion. At numerical simulation, if no random noise is applied and also no external wake force exists (F_0=0), then no self-excited oscillation arises, in spite of high negative total damping coefficient $b - \mu < 0$. However, when the wakes of steam flowing from the stator blade cascade at amplitude F_0=1N excites rotating blades, then these impulses initiate increase of self-excited vibrations. Even very small running forced vibrations excite the flutter vibrations and cause that both types of vibrations are synchronized and run with the same velocity and in the same direction. It is shown in Fig. 7a (backward running flutter of vibration *y*) and in Fig. 7b (backward running flutter of vibration y_T). Modes of flutter vibrations, obtained by cutting the response curves set along the vertical lines, are seen in Fig. 8a. The mode of forced vibration, source of flutter origin provocation, is drawn as well (F0=1, $\mu = 0$, $l_s / l_r = 0.9$).

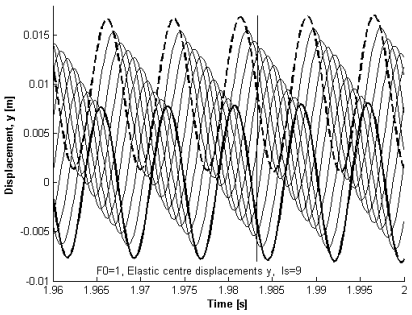

Figure 7a. Displacements *y*

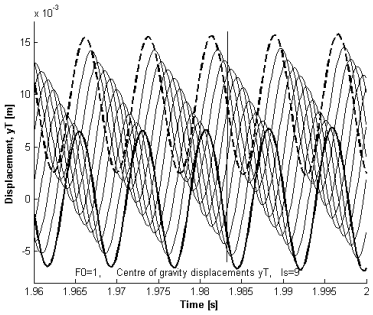

Figure 7b. Displacements $y_T = y - e_1\alpha$

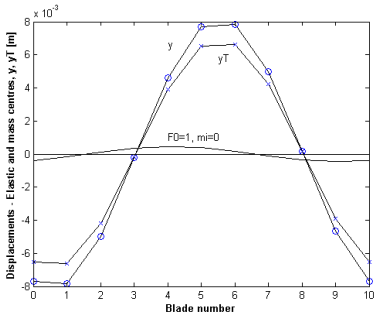

Figure 8a. Mode at $\Delta\varphi = \pi / 5$

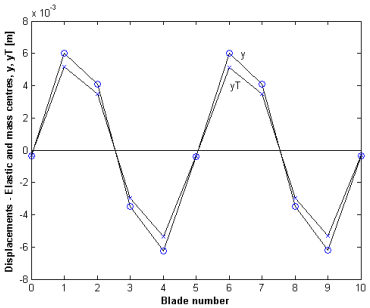

Figure 8b. Mode at $\Delta\varphi = 2\pi / 5$

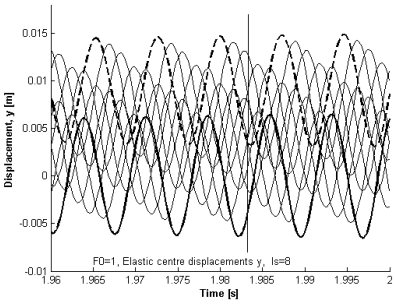

Figure 9a Displacements y

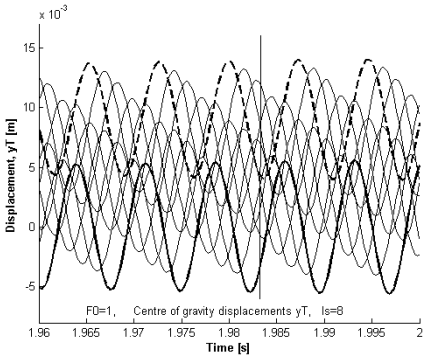

Figure 9b. Displacements $y_T = y - e_1\alpha$

Flutter properties in bladed system with blades' ratio $l_s / l_r = 0.8$ are presented in Fig. 8b, 9a, 9b. Most of the general dynamic properties of this bladed system are the same as in the previous case. Twice greater phase shift $\Delta\varphi = 2\pi / 5$ causes twice smaller slope of response curves set (see Fig. 9), twice smaller velocity of flutter running waves and two-wave mode on periphery (Fig. 8b). Amplitudes of flutter waves are up to 0.008 m. yet only very small distribution for their origin and excitation is sufficient – forced running vibrations with amplitude 4e-4 m, – which is 20-times smaller, than flutter amplitude.

6. Conclusion

The presented paper deals with investigation and ascertaining of conditions for origin of flutter running waves in turbine. The flutter self-excitation that is very complicated aero-elastic phenomenon is here realized by a simple Van der Pol model. The main advantage of this model, in comparison to the other self-excitation models used in literature, there it is its ability to describe dynamic behavior of investigated system in the whole range of instability region due to the amplitude increase restriction.

The forced running waves excited by the wakes of flow from the stator blades at different blades' number of stator and rotor cascades were computed for two bladed systems: rotating wheel with 10 blades and stator wheels with 9 or 8 blades. The set of response curves, backward running waves and modes of forced vibrations were ascertained.

After including the flutter self-excitation expressions into mathematical model, the synchronized flutter running waves with the similar properties as forced waves were determined. It is shown that

the very small disturbances from the stator wakes suffice for origin and synchronization of running flutter waves.

Acknowledgement

This work has been supported by the grant project of the Czech Science Foundation No 16-04546S "Aero-elastic couplings and dynamic behavior of rotational periodic bodies".

References

[1] Rao J.S., Turbomachine Blade Vibration, Wiley Eastern Limited, New Delhi, 1991

[2] Tobias S.A. & Arnold R.N., The Influence of Dynamical Imperfection on the Vibration of Rotating Disks, Proc. Inst. Mech. Engrs, 171, Edinburgh, 1957, p. 669-690

[3] Yan Li-Tang & Li Qi-Han, Investigation of Travelling Wave Vibration for Bladed Disk in Turbomachinery, in: Proc. 3rd Int. Conf. on Rotordynamics– IFToMM (Lalanne M., ed.), Lyon, 1990, p.133-135

[4] Kielb R.E., Barter J., Chernysheva O., Fransson T., Flutter of low pressure turbine blades with cyclic symmetric modes: A preliminary design method," Journal of Turbomachinery-transactions of the ASME 126, 2004, pp. 306-309

[5] Schlaefli D., Experimentalle Untersuchung der instationaeren Stroemung in oszillierenden Ringgittern (in German), Ph.D. Thesis, EPFL Lausanne, 1989

[6] Rzadkowski R., Gnesin V., A 3D Inviscid self-excited vibration of the last stage turbine blade row," Journal of Fluids and Structures 23, 2007, pp. 858-873

[7] Yan Li-Tang, Li Qi-Han, Investigation of Travelling Wave Vibration for Bladed Disk in Turbomachinery, Proceedings of the 3rd International. Conference on Rotordynamics– IFToMM (Lalanne, M., ed.), Lyon, 1990, pp.133-135.

[8] Půst L., Pešek L., Running excitation of blades bunches, Proceedings DYNAMESI 2014, IT ASCR, 2014, Prague, pp. 45-52.

[9] Půst L., Pešek L., Interaction of self-excited and delayed forced excitation on blade bunch, Proceedings of VETOMAC XII, Warszaw, Poland, 2016, pp. 139-148.

[10] Půst L., Pešek L., Modelling of running waves in turbine blades cascade, Proceedings of Dynamesi 2017, Cracow (Poland), IT ASCR, 2017, pp. 95-102.

[11] Byrtus M., Hajšman M., Púst L., Non-smooth modelling of a periodic structure with contact-friction and aero-elastic coupling, ENOC 2017 Conference proceedings, June 25-30, 2017, Budapest, Hungary

Ing. Ladislav Pust, DrSc., Institute of Thermomechanics, CAS, Dolejskova 5, 18200 Prague 8, Czech Republic. He gave a presentation of this paper during one of the conference sessions. (pust@it.cas.cz)

Ing. Ludek Pesek, CSc., Institute of Thermomechanics, CAS, Dolejskova 5, 18200 Prague 8, Czech Republic. (pesek@it.cas.cz)

Ing. Miroslav Byrtus, Ph.D. University of West Bohemia, FAV, Universitni 8, 30614 Plzen, Czech Republic. (mbyrtus@rice.zcu.cz)

Dynamics and effectiveness of Villari effect in magnetostrictive composite beam in the presence of magnetic field

Andrzej Rysak

Abstract: In investigations of systems with active magnetostrictive element, the presence of an external homogeneous bias magnetic field is generally assumed. Contrary to this, in this paper are reported tests results of a bimorph magnetostrictive-aluminum beam, vibrating in the non-homogeneous bias field. By comparing the results obtained under different conditions of the system operation, the influence of combined effects of the non-linear beam stress and non-homogeneous external magnetic field on the dynamics of the Villaria phenomenon was assessed.

1. Introduction

Although the MS phenomenon was discovered by James Joule in 1842 and the reverse phenomenon by Emilio Villari in 1865, the research of both these effects and their applications still are continuing. Testing of systems and equipment in which materials with a giant MS effect are used are increasingly common and require adequate theoretical support. Therefore, models that consider the coupled magnetoelastic properties of highly MS materials are of great importance.

From among many can be mentioned such theoretical approaches as micromechanical characterization [1], the implementation of the mean field theory and the resulting from it the hysteresis model of Jiles-Artheros [3–5], the extension of this model by adding rotation of magnetic moments in the MS material [2], or Preisach hysteresis model [9]. The multilayer beam constructions are very attractive for practical applications as they can in parallel improve the efficiency of different combined effects and are relatively easy to produce. Kumar *et al.* [7] investigated the possibility of using such beams as active elements. They tested the possibility to control of the bimorph (Al - MS) beam by the magnetic field of the coil, set at different beam axial locations. The system was analysed by finite element method and in experiment the active control was applied for different vibration modes. Wang and Yuan [10] have analysed the energy harvesting system, where the active element was a beam built as a laminate joining multiple layers of amorphous Metglas giant MS material. Metglas layers were prepared in such a way that their mechanical properties were better than piezoelectrics, while the bias magnetic field needed for effective system operation was reduced. In turn,

the hybrid MS-piezoelectric system for energy harvesting was developed and analyzed by Lafont et al. [8]. They built and tested very efficient energy harvesting system based on the MFC/Terfenol-D/MFC multilayer beam. During the 90 degree rotation, the MS layer caused the tension of MFC covers, which resulted in high voltage generated by MFC patches even at very slow rotation. A device similar to considered in the current study was analysed by Jin-Hyeong Yoo and Flatau in paper [6]. In this paper bimorph MS-aluminium beam was tested as the efficient energy harvesting system. In their system two magnets was fixed to both beam ends to provide a magnetic biass field through the galfenol element. This approach, assuming a constant and homogeneous bias magnetic field, is common in both the theoretical considerations and the experimental studies of MS systems.

In practice, it is often difficult to maintain homogeneous bias field throughout the whole MS element. Therefore, the question arises how does a non-homogeneous magnetic field influence on the dynamics of the hybrid system with the active MS element? Here, to answer this question, we report the results of the experimental investigations of a bimorph beam with a built-in MS element and with applied a non-homogeneous magnetic field. In the vibrating beam, non-hmoogeneous magnetic field combines with non-homoogeneous stress. As a result, both mechanical and magnetic nonlinearities can influence the dynamics of the system. The layout of the paper is as follows: section 2 describes the construction of the tested beam and the measuring system scheme. The next section presents selected measurement results. In the last one, the most important conclusions have been drawn.

2. Experiment

2.1. Hybrid double beam system

The device under test was a galfenol-Al bimorph with attached tip mass having the form of an Al tube. A slightly longer Al beam was attached to the galfenol MS beam. The Al tube was fixed at the end of the Al beam, so that the axis of the tube is perpendicular to the beam surface. The tube wall thickness is 1 mm. Piezo element (MFC) was glued to the double beam area with the highest bending. In the same part of the double beam, the pick-up coil was wound. The coil wire diameter is 0.3 mm and the number of windings $N = 510$. The sketch of the beam is presented in Fig. 1 a and b. The most important dimensions of the examined system are listed in Tab. 1.

2.2. Scheme of the experiment

The tests were done in two series for different measurement settings: A and B. In both series, the voltages generated by the coil and the piezo patch were recorded. In current studies, only the coil voltage induced by the Villari effect is analysed. In setting A, the acceleration

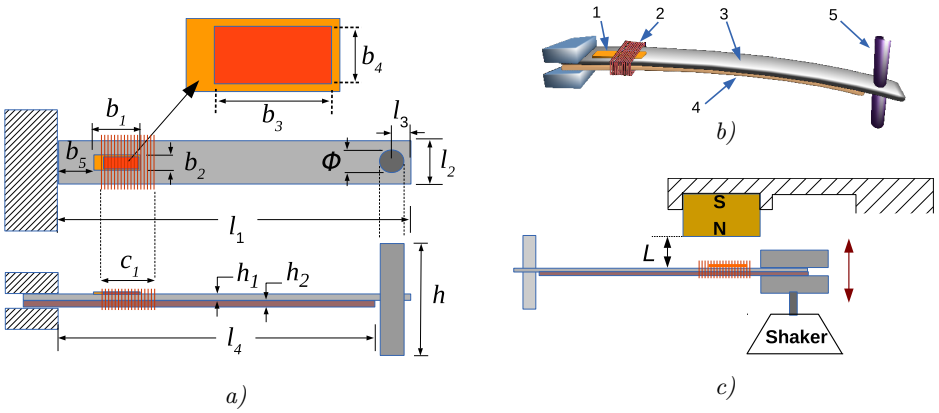

Figure 1. Figure a) - scheme of the beam, dimensions are listed in tab. 1; figure b) - construction of the beam, elements are listed in Tab. 1; figure c) - experiment configuration - the beam oscillating in the presence of the magnetic field, L - magnet position

Table 1. The most important dimensions of the tested device

beam dimensions $[mm]$		beam construction
$b_1 = 19$	$l_1 = 169$	1 - piezo patch
$b_2 = 6$	$l_2 = 20$	2 - coil
$b_3 = 13$	$l_3 = 8$	3 - Al beam
$b_4 = 5$	$l_4 = 150$	4 - galfenol beam
$b_5 = 11$	$h = 58$	5 - Al pipe (tip mass)
$c_1 = 20$	$h_1 = 1.5$	
$\phi = 12$	$h_2 = 1.6$	

excitation amplitude was 0.5 g, and the acceleration of the system was measured by the accelerometer at the end of the beam. In the next study, a sitting B was used in which the vibrations of the beam handle were measured by a reference laser vibrometer. In this measurement series the excitation amplitude was 1 g. The schemes of the both experimental settings are presented in Fig. 2. In all experiments the frequency was varied with a constant rate in the range of 30 to 60 Hz.

3. Results

The primary result obtained for a single measurement is the plot of the peaks of the absolute values of the coil voltage versus frequency dependency. An example of such a result obtained in series A for $L = 19.4$ mm is shown in Fig. 3. As the frequency changes linearly over time,

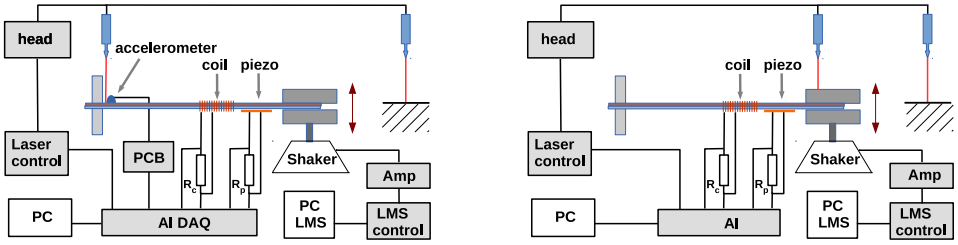

a) *b)*

Figure 2. a) - the scheme of the experiment for the measurement series A. The amplitude of the excitation acceleration was 0.5 g. In this series, the acceleration of the end of beam was measured by accelerometer and PCB conditioning system. b) - measurement system used in the measurement series B. The amplitude of the excitation acceleration was 1 g and the real vibration of the device handle were measured by the laser reference system

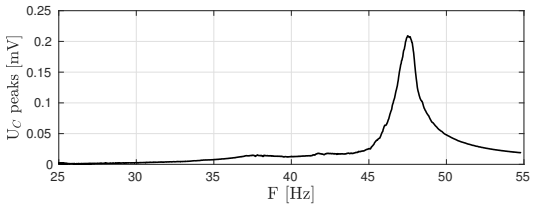

Figure 3. Maximal voltage generated in the coil for different magnet locations in the B series of measurements

changing the F axis to t does not change it qualitatively. After specifying the height of the U_c peak for each measurement of the series, the dependency between the height of the peak and the location of the magnet was plotted (Fig. 4a). As can be noticed, increasing the intensity

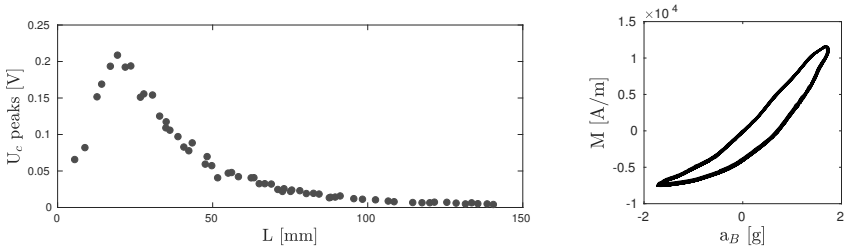

a) *b)*

Figure 4. Maximal voltage generated in the coil for different magnet locations in the A series of measurements (a). The hysteresis loop calculated for the case with $L = 19.4\ mm$ (b)

of the magnetic field and its non-homogeneity (by moving magnet closer) does not increase monotonically the magnitude of the average magnetization in the coil area under resonance conditions (high and nonlinear stress). The resonance peak U_c after reaching the maximum value for $L = 19.4\ mm$ reduces with the further decrease of L. This is inconsistent with studies in which the magnetic field is homogeneous and constant over time (e.g. [6]). Figure 4b shows the hysteresis loop drawn for a short time period from the resonance area, for the measurement with magnet location $L = 19.4\ mm$ (Location of the magnet for which the highest value of the U_c peak was recorded in series A). A distinct hysteresis of magnetization is noticeable, but the shape of the loop indicates that both relations are smooth with a clear phase shift. The shape of the presented hysteresis loop, plotted for the narrow time interval in the resonance area of U_c, is characteristic for the all A-series measurements in the resonance conditions. Bearing in mind that in this series the acceleration was measured at the end of the beam (Fig. 2a), the shape of the hysteresis loop shows that in all measurements of this series the beam vibrated in the first mode. Figure 5 shows how the peak height was changing with the location of the magnet for all B-series measurements. Qualitatively, the

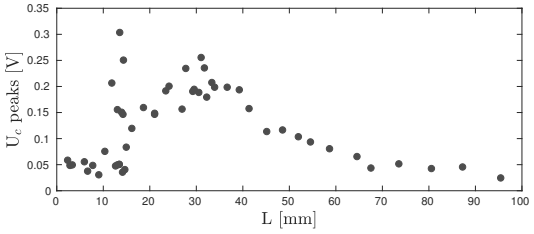

Figure 5. Maximal voltage generated in the coil for different magnet locations in the B series of measurements

U_c peak varies with L in the similar way as in the A measurement series. However, in this series the maximum amplitude of magnetization occurs for $L = 31\ mm$ and in addition, very high values of U_c peaks appear in the narrow range of L between 11 and 13 mm. Unlike in the A series, the hysteresis loop changes when the magnet changes its position. Hysteresis loops for selected magnet locations are shown in Fig. 6. For the case d) the dependence of the both functions on frequency (ie time) is shown in Fig. 7. As was explained in Sec. 2.2, the velocity of the beam handle movement was measured in B-series experiments. Based on this, the beam handle acceleration was calculated by differentiation. The shape of the relation $a(F)$ shows that for the higher amplitude of the acceleration and for the magnet location corresponding to highest Uc peaks some disturbances of beam handle acceleration appears. This could be the result of violent magnetic interferences between the MS beam

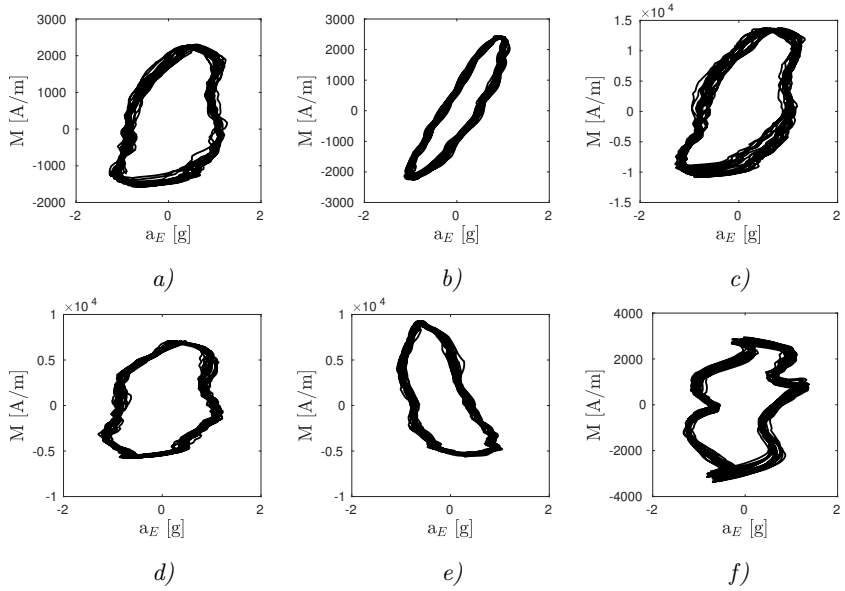

Figure 6. The hysteresis loops $M(a)$ of the resonance area calculated for the results obtained in the B series for: $L = 80.6\ mm$ (a), $L = 41.4\ mm$ (b), $L = 31.1\ mm$ (c), $L = 16.2\ mm$ (d), $L = 13.6\ mm$ (e), $L = 6.0\ mm$ (f)

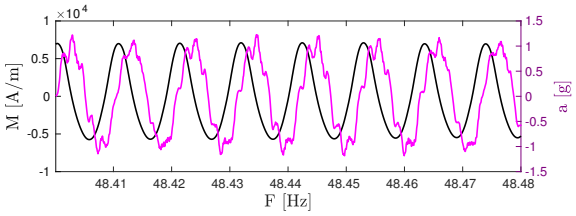

Figure 7. Frequency (ie time) dependences of the average magnetization and acceleration for the d) case of the B series of measurements($L = 13.6\ mm$). The acceleration y-axis (magenta) is placed on the right side of the plot

and the external magnetic field. Since in Fig. 7 the $M(F)$ curve is approximately sinusoidal and $a(F)$ is clearly not, then some general conclusions can be drawn from the comparison of the two curves. The shape of $a(F)$ shows that in the case of high excitation amplitude ($1\ g$) and strong magnetic coupling (low L values), the mode of the beam vibration changes into a more complex one. This is due to the heterogeneity of the stiffnes coefficient along the MS beam caused by the combination of two effects: the interaction of non-homogeneous magnetic field and non-homogeneous mechanical stress resulting from beam deflection. The

regular shape of the magnetization curve is due to the approximate homogeneity of the local magnetic field and stress in the pick-up coil area.

The next figure shows how the oscillations' amplitude of the coil voltage varies with frequency for the three selected magnet locations. As can be deduced from the graph, moving

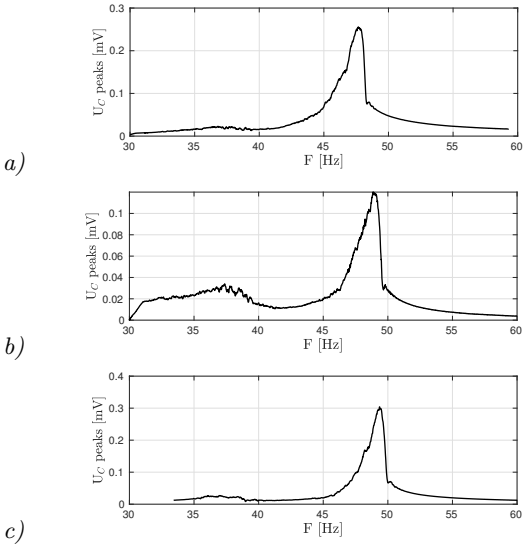

Figure 8. The coil voltage peaks function draw for the three results obtained in the B series: $L = 31.1\ mm$ (a)-[c], $L = 16.2\ mm$ (b)-[d], $L = 13.6\ mm$ (c)-[e]

the magnet closer to the beam increases its rigidity what in effect shifts the resonance frequency to the higher values.

4. Conclusions

This paper presents the experimental results of the dynamics of the bimorph $Al\text{-}MS$ beam with tip mass, immersed in the external non-homogeneous magnetic field. For the amplitude of excitation 0.5 g, the magnetization peak changes non-monotonically along with the location L of the magnet, showing the maximum value for $L = 19.4\ mm$. For all measurements of this series the hysteresis loop in the resonance area are similar in shape and are smooth. After increasing the excitation amplitude up to 1 g, the optimal distance L increases to 31 mm. Additional narrow L range appears with large values of U_c peaks. A more detailed analysis of the curves $a(t)$ and $M(t)$ shows that in this experimental regime additional periodic magnetization oscillations occur. Their frequency is six times the frequency of excitation. Related to them magnetic interactions cause effect similar to impacts, periodically disturbing

the handle of the shaker.

Acknowledgments

This work was supported by the Polish National Science Center under the grant Agreement No. DEC-2013/11/D/ST8/03308.

Literatura

[1] Brown, W. F. *Magnetoelastic Interactions.* Springer-Verlag, Berlin, Germany, 1966.

[2] Dapino, M. J., C., S. R., and B., F. A. Structural magnetic strain model for magnetostrictive transducers. *IEEE Transactions on Magnetics 36*, 3 (2000), 545–556.

[3] Jiles, D. C. *Introduction to Magnetism and Magnetic Materials.* Chapman and Hall, New York, 1991.

[4] Jiles, D. C., and Atherton, D. L. Theory of ferromagnetic hysteresis. *Journal of Magnetism and Magnetic Materials 61* (1986), 48–60.

[5] Jiles, D. C., Thoelke, J. B., and K., D. M. Numerical determination of hysteresis parameters for the modeling of magnetic properties using the theory of ferromagnetic hysteresis. *IEEE Transactions on Magnetics 28*, 1 (1992), 27–35.

[6] Jin-Hyeong Yoo, and Flatau, A. B. A bending-mode galfenol electric power harvester. *Journal of Intelligent Materials, Systems and Structures 23*, 6 (2012), 647–654.

[7] Kumar, J. S., Ganesan, N., Swarnamani, S., and C., P. Active control of beam with magnetostrictive layer. *Computers & Structures 81* (2003), 1375–1382.

[8] Lafont, T., Gimeon, L., Delamare, J., Lebedev, G. A. andZakharov, D. I., B., V., Cugat, O., Galopin, N., Garuio, L., and Geoffroy, O. Magnetostrictive-piezoelectric composite structures for energy hasrvesting. *Journal of Micromechanics and Microengineering 22* (2012), 094006.

[9] Restorff, J. B., Savage, H. T., Clark, A. E., and Wun-Fogle, M. Preisach modeling of hysteresis in terfenol-d. *Journal of Applied Physics 67*, 9 (1996), 5016–5018.

[10] Wang, L., and Yuan, F. G. Vibration energy harvesting by magnetostrictive material. *Smart Materialsand and Structures 17* (2008), 045009.

Andrzej Rysak, Ph.D.: Lublin University of Technology, Faculty of Mechanical Engineering, Nadbystrzycka 36, PL-20-618 Lublin, Poland (*a.rysak@pollub.pl*). The author gave a presentation of this paper during one of the conference sessions.

Elastically mounted double pendulum in flow

Yury D. Selyutskiy, Andrei P. Holub, Marat Z. Dosaev, Rinaldo Garziera

Abstract: An elastically mounted double-link aerodynamic pendulum is considered. It is assumed that the flow acts only upon the second link of the system. Conditions of asymptotic stability of the trivial equilibrium (when both links are stretched along the flow) are obtained. Limit cycles are studied that arise in the system for a certain range of values of parameters. Experiments with such pendulum are performed in the wind tunnel of the Institute of Mechanics of Lomonosov MSU, where parameters of periodic motions are registered for different wind speeds, and different locations of the wing with respect to the second link. It is shown that experimental data is in qualitative agreement with results of numerical simulation.

1. Introduction

Systems of rigid bodies that move under the combined action of elastic forces and aerodynamic (or hydrodynamic) load are called aeroelastic systems and are of great interest from the point of view of basic research and applications (especially in the areas of aerospace and civil engineering). Intensive study of such systems started in 30^{th} of the last century, but even now it is far from being completed, which is due to quite sophisticated nature and high nonlinearity of forces acting upon the bodies from the part of the medium.

The majority of works consider a body (wing-like or bluff), which is an elastically mounted in flow in such a way that it has one rotational, and one translational degree of freedom. In this situation, the interplay between elastic and aerodynamic forces, under certain circumstances, can lead to appearance of oscillations or chaotic motions. Some questions of description and control of such oscillations for wings are discussed in [1-3]. Dynamics of bluff bodies in flow is studied, in particular, in [4-5].

Generally speaking, such oscillations are considered as undesired, because they can lead to destruction of structures. On the other hand, presence of flow-induces oscillations means that such systems can be used as converters of flow energy. Taking into account the continuous increase in load upon ecological systems of the Earth, the need to extend the scope of use of renewable energy, in particular, energy of moving media, in order to convert it into electricity or other forms of useful power, becomes more and more urgent. This stimulates looking for new variants of design of devices suitable for this purpose.

The most wide-spread wind- and hydro power plants convert the motion of the air or water into rotational motion of the working element (vertically or horizontally installed turbine).

However, different groups of researchers develop other types of devices to convert the flow energy [6-10]. In these installations, the working element performs an oscillatory motion instead of rotational one. An important task during development of such energy conversion systems is selection and analysis of mechanical systems that could be used as working elements for them.

Double pendulum in gravity field shows a wide variety of oscillatory regimes, including chaotic ones (e.g., [11], [12]). High nonlinearity of aerodynamic load allows expecting that dynamics of double pendulum in flow would be also rich enough for this object to be suitable for use as a flow energy converter. In the present paper, we investigate some feature of its behavior.

2. Mathematical model of the system

Consider a double aerodynamic pendulum that represents a double pendulum, the second link of which carries a thin wing with symmetrical airfoil. The entire system is placed in flow with the constant speed V and mounted in such a way that both axes of the pendulum are vertical. Unlike [11], we assume that both joints of the pendulum are equipped with linear spiral springs.

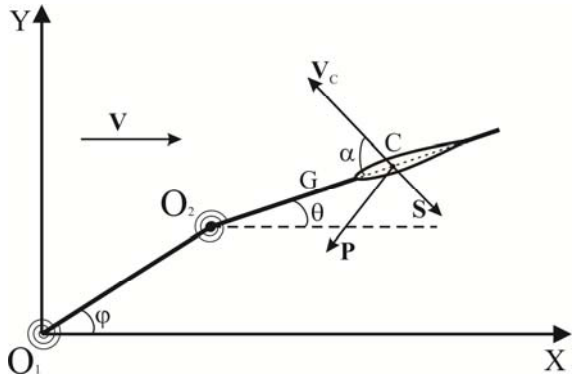

Figure 1. Double aerodynamic pendulum in elastic mounting (top view).

Introduce the reference system O_1XY, the abscissa of which is directed along the wind speed. Choose the angle φ between this axis and the first link and the angle θ between this axis and the second link as generalized coordinates. Assume that springs are stress-free when both these angles are zero, i.e., links are oriented “along the flow”.

In order to describe the aerodynamic load upon the wing, we use the quasi-steady approach. In this model, it is assumed that the aerodynamic load upon the wing depends only upon the instantaneous state of motion of the system. Then this load can be decomposed into the drag force S and lift force P applied in the center C of the wing chord, and aerodynamic torque M_z about this point.

The drag force is directed along the airspeed V_C of the point *C*, and the lift force is perpendicular to it. Then the mentioned components of the aerodynamic load can be represented in the following form:

$$S = \frac{1}{2}\rho\sigma V_C^2 C_d(\alpha), \quad P = \frac{1}{2}\rho\sigma V_C^2 C_l(\alpha), \quad M_z = \frac{1}{2}\rho\sigma b V_C^2 C_m(\alpha). \tag{1}$$

Here ρ is the air density, σ is the characteristic wing area, b is the wing chord, $C_d(\alpha)$ and $C_l(\alpha)$ are the dimensionless drag and lift coefficients, correspondingly, $C_m(\alpha)$ is the dimensionless torque coefficient, α is the instantaneous angle of attack, i.e. the angle between V_C and the wing chord. As the wing airfoil is symmetric, the following relations hold: $C_d(\alpha) = C_d(-\alpha)$, $C_l(\alpha) = -C_l(-\alpha)$, $C_m(\alpha) = -C_m(-\alpha)$.

The angle of attack and V_C are defined by the following equations:

$$\begin{aligned} V_C\cos\alpha &= V\cos\theta + L_1\dot{\varphi}\sin(\varphi-\theta) \\ V_C\sin\alpha &= V\sin\theta + L_1\dot{\varphi}\cos(\varphi-\theta) + R\dot{\theta} \end{aligned}. \tag{2}$$

Here *R* is the distance between the inter-link joint and the point *C*, L_1 is the length of the first link.

Taking into account the above stated, the equation of motion look as follows:

$$\begin{aligned} &\left(J_1 + mL_1^2\right)\ddot{\varphi} + mL_1L_2\cos(\theta-\varphi)\ddot{\theta} - mL_1L_2\sin(\theta-\varphi)\dot{\theta}^2 = \\ &= -\frac{\rho\sigma V_C L_1}{2}C_d(\alpha)\left(V\sin\varphi + L_1\dot{\varphi} + R\cos(\theta-\varphi)\dot{\theta}\right) + \\ &+ \frac{\rho\sigma V_C L_1}{2}C_l(\alpha)\left(-V\cos\varphi + R\sin(\theta-\varphi)\dot{\theta}\right) - K_1\varphi + K_2(\theta-\varphi) \\ &\left(J_2 + mL_2^2\right)\ddot{\theta} + ml_1l_2\cos(\theta-\varphi)\ddot{\varphi} + mL_1L_2\sin(\theta-\varphi)\dot{\varphi}^2 = \\ &= -\frac{\rho\sigma V_C R}{2}C_d(\alpha)\left(V\sin\theta + R\dot{\theta} + L_1\cos(\theta-\varphi)\dot{\varphi}\right) + \\ &+ \frac{\rho\sigma V_C R}{2}C_l(\alpha)\left(-V\cos\theta + L_1\sin(\theta-\varphi)\dot{\varphi}\right) + \frac{\rho\sigma V_C^2 b}{2}C_m(\alpha) - K_2(\theta-\varphi) \end{aligned} \tag{3}$$

Here J_1 is the moment of inertia of the first link with respect to the fixed axis, J_2 is the central moment of inertia of the second link, m is mass of the second link, L_1 is the first link length, L_2 is the distance between the inter-link joint and the center of mass of the second link, $K_{1,2}$ are stiffness coefficients of springs installed in the first and the second joints, correspondingly.

In order to non-dimensionalize the system, we introduce the non-dimensional time $\tau = V_0 t/b$ (where V_0 is a certain characteristic speed) and the following dimensionless parameters:

$$u = \frac{V}{V_0},\ u_C = \frac{V_C}{V_0},\ j_{1,2} = \frac{2J_{1,2}}{\rho\sigma b^3},\ \mu = \frac{2m}{\rho\sigma b},\ l_{1,2} = \frac{L_{1,2}}{b},\ r = \frac{R}{b},\ k_{1,2} = \frac{2K_{1,2}}{\rho\sigma V_0^2 b}$$

Equations (2) и (3) take the following form (dot denotes derivative with respect to τ):

$$\begin{aligned} &u_C \cos\alpha = u\cos\theta + l_1\dot{\varphi}\sin(\varphi-\theta) \\ &u_C \sin\alpha = u\sin\theta + l_1\dot{\varphi}\cos(\theta-\varphi) + r\dot{\theta} \end{aligned} \tag{4}$$

$$\begin{aligned} &\left(j_1 + \mu l_1^2\right)\ddot{\varphi} + \mu l_1 l_2 \ddot{\theta}\cos(\theta-\varphi) - \mu l_1 l_2 \dot{\theta}^2 \sin(\theta-\varphi) = \\ &= -u_C l_1 C_d(\alpha)\left(u\sin\varphi + l_1\dot{\varphi} + r\dot{\theta}\cos(\theta-\varphi)\right) + \\ &+ u_C l_1 C_l(\alpha)\left(-u\cos\varphi + r\dot{\theta}\sin(\theta-\varphi)\right) - k_1\varphi + k_2(\theta-\varphi) \\ &\left(j_2 + \mu l_2^2\right)\ddot{\theta} + \mu l_1 l_2 \ddot{\varphi}\cos(\theta-\varphi) + \mu l_1 l_2 \dot{\varphi}^2 \sin(\theta-\varphi) = \\ &= -u_C r C_d(\alpha)\left(u\sin\theta + r\dot{\theta} + l_1\dot{\varphi}\cos(\theta-\varphi)\right) + \\ &+ u_C r C_l(\alpha)\left(-u\cos\theta + l_1\dot{\varphi}\sin(\theta-\varphi)\right) + u_C^2 C_m(\alpha) - k_2(\theta-\varphi) \end{aligned} \tag{5}$$

Equations (4)-(5) form a closed system that defines the dynamics of the pendulum.

3. Equilibrium positions and limit cycle oscillations

Symmetry of the airfoil implies that the system (4)-(5) has a trivial fixed point: $\varphi \equiv 0$, $\theta \equiv 0$. This means situation when both links are oriented “along the flow”. Actually, these equations can also have other fixed points that correspond to “oblique” equilibrium positions. The number of such equilibria increases, as stiffness of springs decreases (or as the wind speed increases). However, here we restrict ourselves to analysis of the “along the flow” equilibrium only.

Equations of motion linearized in the vicinity of this equilibrium look as follows:

$$\begin{aligned} &\left(j_1 + \mu l_1^2\right)\ddot{\varphi} + \mu l_1 l_2 \ddot{\theta} = -u l_1 C_{d0}\left(u\varphi + l_1\dot{\varphi} + r\dot{\theta}\right) - u^2 l_1 C_l^{\alpha}\left(u\theta + l_1\dot{\varphi} + r\dot{\theta}\right) - \\ &\qquad - k_1\varphi + k_2(\theta-\varphi) \\ &\left(j_2 + \mu l_2^2\right)\ddot{\theta} + \mu l_1 l_2 \ddot{\varphi} = -u(r-r_0)\left(C_l^{\alpha} + C_{d0}\right)\left(u\theta + r\dot{\theta} + l_1\dot{\varphi}\right) - k_2(\theta-\varphi) \end{aligned} \tag{6}$$

Here $C_{d0} = C_d(0)$, $C_l^{\alpha} = C_l'(\alpha)\big|_{\alpha=0}$, r_0 is the distance from C to the front focus of the wing: $r_0 = C_m^{\alpha}/\left(C_l^{\alpha} + C_{d0}\right)$, and, $C_m^{\alpha} = C_m'(\alpha)\big|_{\alpha=0}$. Assume that the distance between the inter-link joint and the front edge of the wing is always positive and, hence, $r - r_0 > 0$.

Criteria of asymptotic stability of this equilibrium are rather cumbersome in general case. So, we discuss in more detail some special cases.

First, consider the pendulum without springs: $k_1 = k_2 = 0$. Take into account the fact that, for thin wings, the drag coefficient is small at small angles of attack: $C_{d0} << 1$.

Then one can readily write down the following approximation formulae for two roots of the characteristic polynomial:

$$\lambda_{1,2} = \pm iu\sqrt{\frac{C_{d0}(r-r_0)}{j_1(r-r_0)-\mu l_1^2(l_2-r+r_0)}} -$$
$$-u(r-r_0)l_1\frac{j_1(r-r_0)-j_2l_1-\mu l_1(l_2+l_1)(l_2-r+r_0)}{\left(j_1(r-r_0)-\mu l_1^2(l_2-r+r_0)\right)^2}C_{d0}+o(C_{d0})$$

The other two roots are derived from the following equation with the accuracy up to $o(1)$:

$$\left(j_1\mu l_2^2+j_2\mu l_1^2+j_1j_2\right)\lambda_{3,4}^2+uC_l^{\alpha}\left(\mu l_1^2(l_2-r)(l_2-r+r_0)+j_1r(r-r_0)+j_2l_1^2\right)\lambda_{3,4}+$$
$$+u^2C_l^{\alpha}\left(j_1(r-r_0)-\mu l_1^2(l_2-r+r_0)\right)=0$$

Let the following inequality be satisfied:

$$j_1(r-r_0)-j_2l_1-\mu l_1(l_2+l_1)(l_2-r+r_0)>0 \tag{6}$$

Then one can easily show that real parts of all λ_{1-4} are negative, and the equilibrium in question is asymptotically stable. And, vice versa, if (9) is not met, then this equilibrium is unstable.

Condition (6) is satisfied for large enough r. Thus, if the wing is installed at far from the inter-link joint, the "along the flow" equilibrium is asymptotically stable. In the same time, the inequality (9) is not met for r close to r_0, and instability takes place.

Now we analyze the influence of stiffness coefficients upon the stability.

Under assumptions made here, the boundary of the stability domain in the parameter space can be represented in the following structural form:

$$A_2(k_1-k_{11})(k_1-k_{12})=0 \tag{7}$$

Here:

$$A_2=\left(C_l^{\alpha}\right)^2u^2l_1^2r(r-r_0)\left(j_2+\mu l_2(l_2-r)\right)\left(j_2+\mu l_2(l_2-r+r_0)\right)$$

$$k_{11}=\frac{k_2(l_1+r-r_0)\left(j_1(r-r_0)-j_2l_1-\mu l_1(l_1+l_2)(l_2-r+r_0)\right)}{l_1(r-r_0)\left(j_2+\mu l_2(l_2-r+r_0)\right)}$$

$$k_{12} = \frac{C_l^{\alpha} u^2 l_1 \left(j_1 r (r - r_0) + j_2 l_1^2 + \mu l_1^2 (l_2 - r)(l_2 - r + r_0) \right)}{l_1 r \left(j_2 + \mu l_2 (l_2 - r) \right)} +$$
$$+ \frac{k_2 (l_1 + r) \left(j_1 r - j_2 l_1 - \mu l_1 (l_1 + l_2)(l_2 - r) \right)}{l_1 r \left(j_2 + \mu l_2 (l_2 - r) \right)}$$

For $r > j_2/\mu l_2 + l_2 + r_0$, values k_{11} and k_{12} are negative, $A_2 > 0$, hence, asymptotic stability takes place for any physically meaningful values of stiffness coefficients. For $j_2/\mu l_2 + l_2 < r < j_2/\mu l_2 + l_2 + r_0$, the coefficient A_2 is negative. This means that (7) will be smaller than zero for large enough k_1 (for any k_2), so that the considered equilibrium will be unstable. If the second spring is absent ($k_2 = 0$), and the moment of inertia of the second link is sufficiently large, $j_2 > \mu r_0^2/4$, then the "along the flow" equilibrium is unstable for $r_0 < r < j_2/\mu l_2 + l_2$, if the stiffness of the first spring satisfies the following condition:

$$0 < k_1 < \frac{C_l^{\alpha} u^2 l_1 \left(j_1 r (r - r_0) + j_2 l_1^2 + \mu l_1^2 (l_2 - r)(l_2 - r + r_0) \right)}{l_1 r \left(j_2 + \mu l_2 (l_2 - r) \right)}$$

Note that this range increases as the wind speed grows.

When the "along the flow" equilibrium becomes unstable, oscillations arise in the system. In order to investigate them, numerical simulation was performed using the following values of parameters: $j_1 = 10$, $j_2 = 10$, $m = 10$, $l_1 = 1$, $l_2 = 1$, $r = 1.2$, $u = 1$. Aerodynamic characteristics of a standard NACA0015 airfoil were used [12].

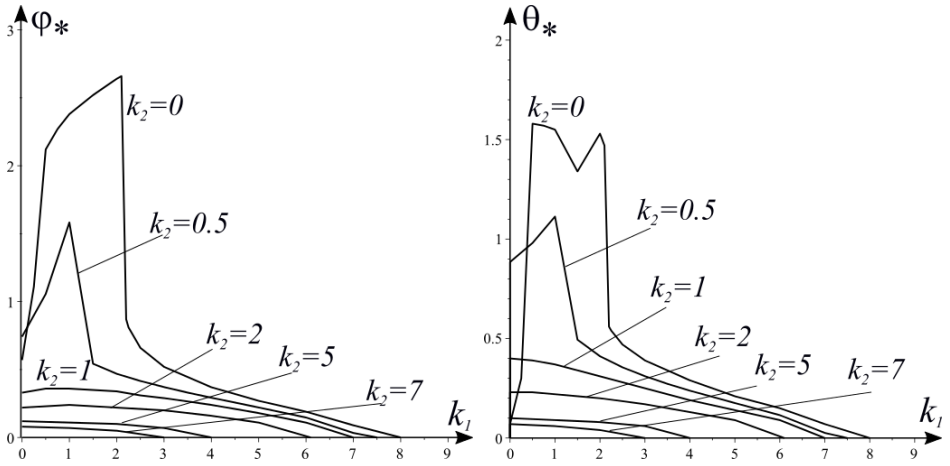

Figure 2. Amplitudes of oscillation of pendulum links depending on stiffness coefficients.

In Fig. 2 there are shown dependences of amplitudes φ_*, θ_* of the first and the second link, correspondingly, on the stiffness coefficients.

Note that, while the second spring, generally speaking, has a stabilizing action upon the system, the increase in the stiffness of the first spring can lead to significant growth of the amplitude of oscillations of the pendulum.

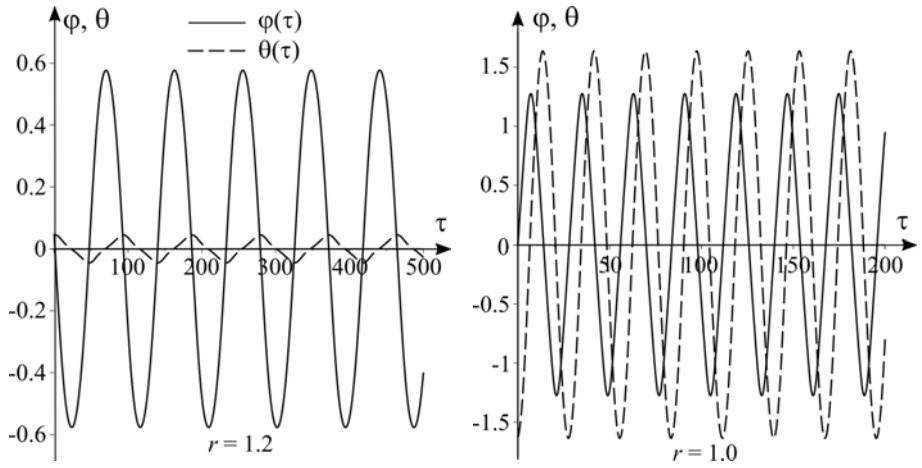

Figure 3. Limit cycles arising for different values of *r*.

If there no springs, in the system there exist two types of limit cycles. The corresponding time dependences of angles of revolution of links are shown in Fig. 3 (solid line for the first link, and dashed one for the second). In the first cycle (existing for larger *r*), the amplitude of the first link is relatively large, while the second link makes rather small angle with the flow. In cycles of the other type, which appear for smaller *r*, both links oscillate with large amplitudes (and θ_* can be larger than φ_*). In the range of small *r* oscillations become irregular.

4. Experimental study

In order to study the dynamics of the aerodynamic pendulum, a series of experiments was performed. Tests were carried out in the subsonic wind tunnel A10 of the Institute of Mechanics of the Lomonosov Moscow State University (diameter of the cross-section of the working area is 0.8 m).

Links of the pendulum are manufactured as pin-jointed frames made of wire (Fig. 4). The wing is made of synthetic foam, has a standard NACA0015 airfoil, and can be fixed in different positions with respect to the second link.

Tests were performed at different values of the flow speed (from 4 to 18 mps) and different distances between the center point of the wing and the inter-link joint (from 8 to 14 cm). Positions of pendulum link were registered using the high speed camera.

Mass and inertial parameters of the system and aerodynamic characteristics of the wing are such that condition (6) of asymptotic stability of the “along the flow” equilibrium is not met.

Figure 4. Double aerodynamic pendulum in wind tunnel.

In Fig. 5a, experimental dependence of amplitudes φ_*, θ_* of oscillations of pendulum links upon the flow speed is shown; in Fig. 5b, dependence of the frequency ω_* of these oscillations on V is shown. Black color in Fig. 5a denotes amplitudes of the first link, and grey color, amplitudes of the second link. Different symbols correspond to different positions of the wing.

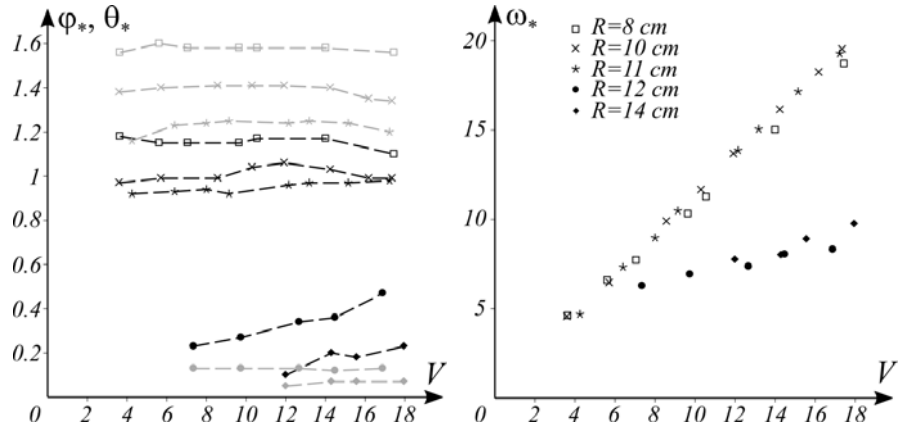

Figure 5. Amplitudes and frequency of oscillations vs. wind speed

Evidently, two different types of limit cycles exist in different ranges of parameter r (that is, different distances from the wing to the first link). For relatively small r, amplitude of oscillations of both links practically practically doesn’t depend upon the wind speed and slightly decreases as r gets

larger. Amplitude of the first link is smaller than that of the second link. Frequency of oscillations grows linearly with V, and the coefficient of proportionality doesn't depend on r. Cycles of this type qualitatively correspond to cycles obtained in numerical simulation and shown in Fig. 3b.

For larger values of r, another type of cycles appears, where φ_* is is larger than θ_*. It should be noted that φ_* increases, as the wind speed increases (which can be due to the influence of damping in the first joint in the range of small angles). Frequency of oscillations in these cycles is considerably lower than in cycles of the first type. Cycles of the second type qualitatively correspond to cycles shown in Fig. 3a.

5. Conclusions

Dynamics of a double aerodynamic pendulum in elastic mounting is considered. Conditions of asymptotic stability of the "along the flow" equilibrium are obtained. Influence of position of the wing and of coefficients of structural stiffness upon the stability is discussed.

Limit cycles are studied that arise in the system for a certain range of values of parameters. Dependence of their amplitude on coefficients of stiffness is analyzed.

Experiments with such pendulum are performed in the wind tunnel of the Institute of Mechanics of Lomonosov MSU, where parameters of periodic motions are registered for different wind speeds, and different locations of the wing with respect to the second link. It is shown that experimental data is in qualitative agreement with results of numerical simulation.

Acknowledgments

The work is partially supported by RFBR (projects No. 15-01-06970, 16-31-00374, 17-08-01366).

References

[1] Strganac, T.W., Ko. J., Kurdila, A.J. Identification and Control of Limit Cycle Oscillations in Aeroelastic Systems. *J. of Guidance, Control, and Dynamics* 23, 6 (2000), pp. 1127-1133.

[2] Dimitriadis, G., Li, J. Bifurcation behavior of airfoil undergoing stall flutter oscillations in low-speed wind tunnel. *AIAA Journal* 47, 11 (2009), pp. 2577–2596.

[3] Gao, M., Cai, G. Robust fault-tolerant control for wing flutter under actuator failure. *Chinese Journal of Aeronautics* 29, 4, (2016), pp. 1007-1017.

[4] Mannini, C., Marra, A.M., Bartoli, G. VIV-galloping instability of rectangular cylinders: Review and new experiments. *J. of Wind Engineering and Industrial Aerodynamics* 132 (2014), pp. 109–124.

[5] Xu, K., Ge, Y., Zhang, D. Wake oscillator model for assessment of vortex-induced vibration of flexible structures under wind action. *J. of Wind Engineering and Industrial Aerodynamics* 136 (201), pp. 192–200.

[6] Jones K.D., Davids S.T., Platzer M.F. Oscillating-wing power generation // 3rd ASME/JSME Joint Fluids Engineering Conference, 1999, pp. 1-6.

[7] Isoc, T.; Leach, F.; Bobean, C.; Pavel, V.; Vadan, I.: Study and design of a wing oscillating wind system // Advanced Topics in Electrical Engineering (ATEE), 2011 7th International Symposium, 2011, pp.1-4.

[8] Barrero-Gil, A., Pindado, S. Avila, S. Extracting energy from vortex-induced vibrations: a parametric study. *Appl. Math. Model.* 36, 7 (2012), pp. 3153–3160.

[9] Klimina, L.A., Samsonov, V.A., Hwang, S.S., Lin, K.H., Lin, C.H. Application of the Poincare-Pontryagin theorem to analysis of a dynamical model of a wind powered car // 2016 International Conference Stability and Oscillations of Nonlinear Control Systems (Pyatnitskiy's Conference), IEEE, 2016, pp. 1–3.

[10] Abdelkefi, A. Aeroelastic energy harvesting: A review. *International Journal of Engineering Science* 100 (2016), pp. 112–135.

[11] Zhou, Z., Whiteman, C. Motions of a double pendulum. *Nonlinear Analysis: Theory, Methods & Applications* 26, 7 (1996), pp. 1177-1191.

[12] Awrejcewicz, J., Sendkowski, D. Geometric analysis of the dynamics of a double pendulum. *J. of Mechanics of Materials & Structures* 2, 8 (2007), pp. 1421-1430.

[13] Dosaev, M.Z., Selyutskiy, Yu.D. On dynamics of double pendulum in airflow. *Proc. of the 6th EUROMECH Nonlinear Dynamics Conference* (2008), 4 p.

[14] Sheldahl, R.E.; Klimas, P.C. Aerodynamic Characteristics of Seven Symmetrical Airfoil sections Through 180 Degree Angle of Attack for Use in Aerodynamic Analysis of Vertical Axis Wind Turbines. *Sandia National Laboratories: Albuquerque, NM, USA* (1981), 118 p.

Yury Selyutskiy, Ph.D.: Lomonosov Moscow State University, Institute of Mechanics, Michurinsky prosp. 1, 119192, Moscow, Russia (*seliutski@imec.msu.ru*). The author gave a presentation of this paper during one of the conference sessions.

Andrei Holub: Lomonosov Moscow State University, Institute of Mechanics, Michurinsky prosp. 1, 119192, Moscow, Russia (*holub.imech@gmail.com*).

Marat Dosaev, Ph.D.: Lomonosov Moscow State University, Institute of Mechanics, Michurinsky prosp. 1, 119192, Moscow, Russia (*dosayev@imec.msu.ru*).

Rinaldo Garziera, Professor: University of Parma, via Università, 12 - I 43121 Parma, Italy (*rinaldo.garziera@unipr.it*).

Nonlinear effects in dynamics of micromechanical gyroscope

Roman Starosta, Grażyna Sypniewska-Kamińska, Jan Awrejcewicz

Abstract: Resonant sensors basing on microstructures and belonging to microelectromechanical systems (MEMS) have been developed in recent years. The paper deals with dynamics of micro-gyroscope being a sensor designed for measuring the angular displacement. Such device is used for the attitude control of a moving object. Vibration of the basic measuring element suspended on a set of two pivoted and mutually orthogonal axes is the object of our study. One coordinate of the angular velocity of the support can be measured by the MEMS system. Since a resonance phenomenon is the desirable state of work of this sensor, the elastic properties of the support should be appropriately designed. Therefore, it is important to consider also the nonlinear behaviour of the system. It is assumed that the elastic features of the sensor suspension are weakly nonlinear. The equations of motion of the micromechanical sensor have been derived using the Lagrange formalism. The approximated solutions obtained using multiple scales method allow to investigate the resonant behaviour of the system.

1. Introduction

Gyroscopes are present in a broad range of engineering systems such as air vehicles, automobiles, and satellites to track their orientation and control their path. Besides the directional gyroscopes there are variety kinds of gyroscopes (e.g. mechanical, optical and vibrating) that are being used to measuring the angular velocity. The critical part of the conventional mechanical gyroscope is a wheel spinning at a high speed. Therefore, conventional gyroscopes although accurate are bulky and very expensive and they are applicable mainly in the navigation systems of large vehicles, such as ships, airplanes, spacecrafts, etc.

Progress in micromachining technology embraces the development of the miniaturized gyroscopes with improved performance and low power consumption that allow the integration with electronic circuits. Their manufacturing cost are also significantly lower [1–2]. Such type of gyroscopes belongs to broad class of microelectromechanical systems (MEMS). Practically, any device fabricated using photo-lithography based techniques with micrometer scale features that utilizes both electrical and mechanical functions could be considered as MEMS.

The operating principle of vibrating gyroscopes is based on the transfer of the mechanical energy among two vibrations modes via the Coriolis effect which occurs in the presence of

a combination of rotational motions about two orthogonal axes. The drive mode is mainly generated employing the electrostatic actuation mechanism.

In the present work, we conduct an analysis of dynamics of a MEMS gyroscope. This micro device is a torsional resonator. Resonance is the desirable state of work of this sensor, so the elastic properties should be appropriately matched. Designing the resonator, only linear elasticity is taken into account. There arises the question what is the significance of the nonlinear properties of resilient resonator elements. Therefore, we propose the mathematical model describing motion of the MEMS gyroscope taking into account the nonlinear effects generated by the elastic properties of the suspension elements. The main objective of the paper is to obtain and to examine the resonant responses of the considered system.

2. Description of micromechanical gyroscope

MEMS gyroscope, whose scheme is presented in Fig. 1, with the sensing plate suspended on a set of two pivoted and mutually orthogonal axes is studied. The active gimbal is supported by two torsional connectors that are anchored to the substrate and designate the drive axis, so that the gimbal oscillates only about this axis. The sensing plate is linked to the gimbal via two torsional joints determining the sense axis and allowing to oscillate about this axis independent from the gimbal position. Both the sensing plate and the gimbal are treated further as rigid bodies.

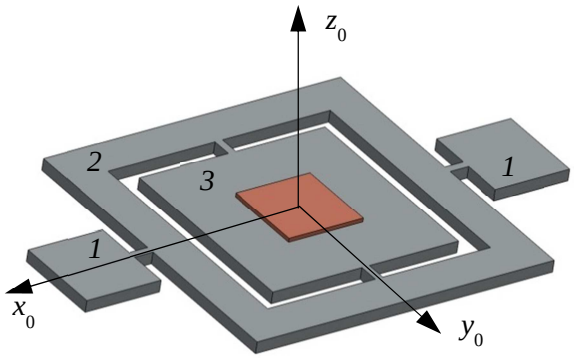

Figure 1. Micromechanical gyroscope suspended on a set of two pivoted and mutually orthogonal pivot axes; 1 – anchor, 2 – gimbal, 3 – sensing plate.

The kinematics of the gyroscope is best to understand by introducing three reference frames shown in Fig. 2. They have the common origin at the point O. In the frame F_0 with the coordinate system $Ox_0y_0z_0$ the anchors are motionless. The frame F_1 with the coordinate system $Ox_1y_1z_1$ is fixed to the intermediate pivoted support, whereas the frame F in which it is assumed the coordinate system $Oxyz$ is rigid connected with the sensing plate. The frame F_1 which can oscillate about the drive axis

x_0 is presented in position rotated by Φ counterclockwise, and the frame F oscillating around the sense axis y_1 is shown in position being a result of the rotation by Θ, also counterclockwise.

The substrate, in general, can rotate about a fixed pivot axis. Let as assume that its angular velocity $\mathbf{\Omega}_z$ projected on the axes of the frame F_0 is $\mathbf{\Omega}_z = [0,0,\Omega_z]^T$ where Ω_z is to be measured.

The absolute gimbal angular velocity $\mathbf{\Omega}_1$ is a superposition of the substrate rotation and own rotation about the drive axis. Projecting it onto the axes of the frame F_1, we obtain

$$\mathbf{\Omega}_1 = \left[\dot{\Phi}, \Omega_z \sin\Phi, \Omega_z \cos\Phi\right]^T. \tag{1}$$

The absolute angular velocity $\mathbf{\Omega}$ of the sensing plate written in the reference frame F and being a result of the substrate motion, gimbal rotation and own rotation about y-axis is

$$\mathbf{\Omega} = \left[-\Omega_z \cos\Phi \sin\Theta + \cos\Theta\dot{\Phi}, \Omega_z \sin\Phi + \dot{\Theta}, \Omega_z \cos\Phi \cos\Theta + \dot{\Phi}\sin\Theta\right]^T. \tag{2}$$

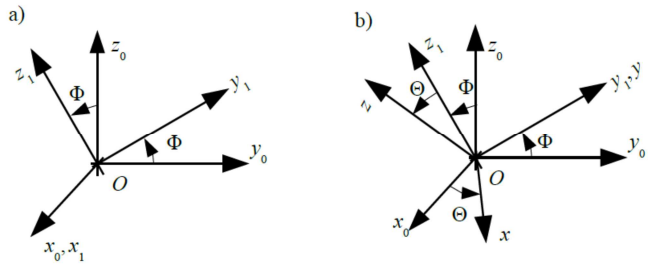

Figure 2. The angles of rotation Φ and Θ: (a) the rotation of F_1 by Φ about x_0-axis; (b) The rotation of F_2 by Θ around y_1.

3. Equations of motion

The considered microsystem has two degrees of freedom in motion with respect to the substrate. The rotation angles Φ(t) and Θ(t) are assumed to be the general coordinates. The point O that is the mass center both of the sensing plate and the gimbal is constantly at rest. The axes of reference frames F_1 and F are the principal axes of inertia of the gimbal and the plate, respectively. Therefore, the inertia tensors of each of the gyroscope part related to these axes are of diagonal form independent of the current system configuration. Let I_x, I_y and I_z denote moments of inertia of the gimbal about its principal inertia axes x_1, y_1 and z_1, whereas J_x, J_y and J_z stands for the principal moments of inertia of the senor plate i.e. with respect to the axes x, y and z. In other words, the inertia tensors of both gyroscope parts we can write as $\hat{\mathbf{I}} = diag(I_x, I_y, I_z)$ and $\hat{\mathbf{J}} = diag(J_x, J_y, J_z)$.

The kinetic energy of the system is a sum of two quadratic forms

$$T = \frac{1}{2}\left(\boldsymbol{\Omega}_1^T . \hat{\mathbf{I}} . \boldsymbol{\Omega}_1 + \boldsymbol{\Omega}^{\mathrm{T}} . \hat{\mathbf{J}} . \boldsymbol{\Omega}\right). \tag{3}$$

Substituting formulas (1) and (2) into equation (3), we get

$$T = \frac{1}{2}\left(I_z\Omega_z^2(\cos\Phi)^2 + I_y\Omega_z^2(\sin\Phi)^2 + I_x\Theta^2\right) + \tag{4}$$
$$\frac{1}{2}\left(J_x\left(\Omega_z\cos\Phi\sin\Theta - \Phi\cos\Theta\right)^2 + J_z\left(\Omega_z\cos\Phi\cos\Theta + \Phi\sin\Theta\right)^2 + J_y\left(\Omega_z\sin\Phi + \Theta\right)^2\right).$$

Taking into account that the system mass center *O* is immovable and assuming that the elastic properties of all torsional connectors are nonlinear of cubic type, we can write the potential energy as follows

$$V = \frac{1}{2}k_{11}\Phi^2 - \frac{1}{4}k_{12}\Phi^4 + \frac{1}{2}k_{21}\Theta^2 - \frac{1}{4}k_{22}\Theta^4, \tag{5}$$

where k_{11}, k_{12} and k_{21}, k_{22} are elastic coefficients of the outer and the inner torsional connectors respectively.

The viscous effects of gas, which is confined between the rotating surfaces and the immovable ones, play the primary role in damping mechanism. The system is excited by the driving electrostatic torque $M_0 \sin(P\,t)$ applied to the drive gimbal.

The governing equations have been derived using Lagrange's equations of the second kind. Due to expected small values of angles Φ and Θ, we assume linear approximation of the trigonometric functions, whose arguments are these angles, making the equations of motion simpler of the following form

$$(I_x + J_x)\Phi + k_{11}\Phi - k_{12}\Phi^3 + C_1\Phi + (I_z - I_y + J_z - J_y)\Omega_z^2\Phi - (J_x + J_y - J_z)\Omega_z\Theta + \tag{6}$$
$$2(J_z - J_x)\Theta\Theta\Phi = M_0\sin(P\,t),$$

$$J_y\Theta + k_{21}\Theta - k_{22}\Theta^3 + C_2\Theta + (J_z - J_x)\Omega_z^2\Theta + (J_x + J_y - J_z)\Omega_z\Phi + (J_z - J_x)\Omega_z\Theta^2\Phi + \tag{7}$$
$$(J_x - J_z)\Theta\Phi^2 = 0,$$

where C_1 and C_2 are the damping coefficients.

It is convenient to transform the governing equations into the nondimensional form. For this purpose we introduce the dimensionless time $\tau = t\,\omega_1$ and the following dimensionless parameters:

$$p = \frac{P}{\omega_1},\ \omega_z = \frac{\Omega_z}{\omega_1},\ f_0 = \frac{M_0}{(I_x + J_x)\omega_1^2},\ c_1 = \frac{C_1}{(I_x + J_x)\omega_1},\ c_2 = \frac{C_2}{J_y\omega_1},\ \alpha_1 = \frac{k_{12}}{(I_x + J_x)\omega_1^2},$$

$$\alpha_2 = \frac{k_{22}}{J_y \omega_1^2},\ j_1 = \frac{I_z + J_z - I_y - J_y}{I_x + J_x},\ j_2 = \frac{J_z - J_x - J_y}{I_x + J_x},\ j_3 = \frac{J_y + J_x - J_z}{J_y}, \tag{8}$$

$$j_4 = \frac{2J_z - 2J_x}{I_x + J_x},\ w^2 = \frac{\omega_2^2}{\omega_1^2},$$

where $\omega_1 = \sqrt{\frac{k_{11}}{I_x + J_x}}$, $\omega_2 = \sqrt{\frac{k_{21}}{J_y}}$.

The dimensionless form of the governing equations takes the following form

$$\phi + \left(1 + j_1 \omega_z^2\right)\phi - \alpha_1 \phi^3 + c_1 \phi + j_2 \omega_z \vartheta + j_4 \vartheta \vartheta \phi = f_0 \sin\left(p\tau\right), \tag{9}$$

$$\vartheta + \left(w^2 + \left(1 - j_3\right)\omega_z^2\right)\vartheta - \alpha_2 \vartheta^3 + c_2 \vartheta + \left(1 - j_3\right)\omega_z \vartheta^2 \varphi + \left(j_3 - 1\right)\vartheta \varphi^2 + j_3 \omega_z \varphi = 0, \tag{10}$$

where functions $\varphi(\tau)$, $\vartheta(\tau)$ correspond to the dimensional general coordinates $\Phi(t)$ and $\Theta(t)$.

Equations (9) and (10) are supplemented with the proper initial conditions

$$\varphi(0) = \varphi_0,\ \dot{\varphi}(0) = \omega_0,\ \vartheta(0) = \vartheta_0,\ \dot{\vartheta}(0) = \varpi_0. \tag{11}$$

From the viewpoint of the gyroscope applications, the main resonance is the most important state of its work. Ideally, it is desired to utilize resonance in both the drive and the sense modes in order to attain the maximum possible response gain and sensitivity. This is typically achieved by properly designing and if needed tuning the resonant frequencies of the drive and the sense in order to their equalizing. This is why we have assumed that $\omega_2 = \omega_1$ (i.e. w=1). Angular velocity of the substrate ω_z is usually much lower than angular frequencies of the movable gyroscope elements. Therefore, in order to deal with this case of the resonance we take

$$p = 1 + \sigma, \tag{12}$$

where σ plays a role of the detuning parameter.

4. Approximate analytical solution

The method of multiple scales (MSM) has been used to solve of the problem (9) – (11) taking into account the main resonance condition. Since a few of the parameters are assumed to be small, after introduction of the so-called small/perturbation parameter ε the following relations are employed:

$$c_1 = \tilde{c}_1 \varepsilon^2,\ c_2 = \tilde{c}_2 \varepsilon^2,\ w_z = \tilde{w}_z \varepsilon,\ f_0 = \tilde{f}_0 \varepsilon^3,\ \sigma = \tilde{\sigma} \varepsilon^2. \tag{13}$$

According to MSM, three time scales are introduced that are defined in the following manner: $\tau_0 = \tau$ is the "fast" time, whereas $\tau_1 = \varepsilon\tau$ and $\tau_2 = \varepsilon^2\tau$ serve as the "slow" times [3]. The derivatives with respect to time τ are calculated in terms of the new time scales as follows

$$\begin{aligned}\frac{d}{d\tau} &= \frac{\partial}{\partial\tau_0} + \varepsilon\frac{\partial}{\partial\tau_1} + \varepsilon^2\frac{\partial}{\partial\tau_2},\\ \frac{d^2}{d\tau^2} &= \frac{\partial^2}{\partial\tau_0^2} + 2\varepsilon\frac{\partial^2}{\partial\tau_0\partial\tau_1} + \varepsilon^2\left(\frac{\partial^2}{\partial\tau_1^2} + 2\frac{\partial^2}{\partial\tau_0\partial\tau_2}\right) + o\left(\varepsilon^3\right).\end{aligned} \tag{14}$$

The solution of the initial-value problem (9) – (11) is searched in the form of the power series regarding the small parameter ε:

$$\varphi(\tau;\varepsilon) = \sum_{k=1}^{k=3}\varepsilon^k\phi_k\left(\tau_0,\tau_1,\tau_2\right) + O(\varepsilon^4), \qquad \vartheta(\tau;\varepsilon) = \sum_{k=1}^{k=3}\varepsilon^k\theta_k\left(\tau_0,\tau_1,\tau_2\right) + O(\varepsilon^4). \tag{15}$$

Then, relations (13) – (14) are introduced into equations of motion (9) - (10). In this way, the small parameter appears in the mathematical model. After rearranging the equations with respect to the powers of the small parameter, we get a system of equations which are to be satisfied in order to guarantee satisfaction to the original equations. They are as follows:

- the equations of the first order approximation

$$\frac{\partial^2\phi_1}{\partial\tau_0^2} + \phi_1 = 0, \tag{16}$$

$$\frac{\partial^2\theta_1}{\partial\tau_0^2} + \theta_1 = 0; \tag{17}$$

- the equations of the second order approximation

$$\frac{\partial^2\varphi_2}{\partial\tau_0^2} + \varphi_2 = -2\frac{\partial^2\varphi_1}{\partial\tau_0\partial\tau_1}, \tag{18}$$

$$\frac{\partial^2\theta_2}{\partial\tau_0^2} + \theta_2 = -2\frac{\partial^2\theta_1}{\partial\tau_0\partial\tau_1}; \tag{19}$$

- the equations of the third order approximation

$$\begin{aligned}&\frac{\partial^2\varphi_3}{\partial\tau_0^2} + \varphi_3 = -2\frac{\partial^2\varphi_1}{\partial\tau_0\partial\tau_2} - 2\frac{\partial^2\varphi_2}{\partial\tau_0\partial\tau_1} - \frac{\partial^2\varphi_1}{\partial\tau_1^2} + \alpha_1\varphi_1^3 - c_1\frac{\partial\varphi_1}{\partial\tau_0} -\\ &j_4\theta_1\frac{\partial\theta_1}{\partial\tau_0}\frac{\partial\varphi_1}{\partial\tau_0} - j_2\omega_z\frac{\partial\theta_1}{\partial\tau_0} + f_0\sin\left(\tau_0 + \tau_2\sigma\right),\end{aligned} \tag{20}$$

$$\frac{\partial^2\theta_3}{\partial\tau_0^2}+\theta_3=-2\frac{\partial^2\theta_1}{\partial\tau_0\partial\tau_2}-2\frac{\partial^2\theta_2}{\partial\tau_0\partial\tau_1}-\frac{\partial^2\theta_1}{\partial\tau_1^2}+\alpha_2\theta_1^3-c_2\frac{\partial\theta_1}{\partial\tau_0}- \tag{21}$$
$$j_3\theta_1\left(\frac{\partial\varphi_1}{\partial\tau_0}\right)^2-j_3\omega_z\frac{\partial\varphi_1}{\partial\tau_0}+\theta_1\frac{\partial\varphi_1}{\partial\tau_0}.$$

System (16) – (21) is solved recursively, i.e. solution of equations (16) – (17) is substituted into equations (18) – (19), and then their solution into equations (20) – (21). The solution contains unknown complex functions $B_1(\tau_1,\tau_2)$ and $B_2(\tau_1,\tau_2)$. The values of generalized coordinates are to be bounded, therefore all secular terms should be eliminated what leads to conclusion that $B_1(\tau_2)$ and $B_2(\tau_2)$ do not depend on the time scale τ_1 and satisfy the solvability condition:

$$-j_4\overline{B}_1B_2^2-iB_1\tilde{c}_1-\frac{1}{2}ie^{i\tau_2\tilde{\sigma}}f_0+3B_1^2\overline{B}_1\tilde{\alpha}_1-i\,j_2B_2\tilde{\omega}_z=2i\frac{dB_1}{d\tau_2}, \tag{22}$$

$$2(1-j_3)B_1\overline{B}_1B_2+(j_3-1)B_1^2\overline{B}_2-iB_2\tilde{c}_2+3B_2^2\overline{B}_2\tilde{\alpha}_2-i\,j_3B_1\omega_z=2i\frac{dB_2}{d\tau_2}. \tag{23}$$

The functions $B_1(\tau_2)$ and $B_2(\tau_2)$ can be determined from the solvability conditions (22) – (23), but it is more preferably to introduce their real representations as follows

$$B_1(\tau_2)\to\frac{\tilde{a}_1(\tau_2)}{2}e^{i\psi_1(\tau_2)},\qquad B_2(\tau_2)\to\frac{\tilde{a}_2(\tau_2)}{2}e^{i\psi_2(\tau_2)}, \tag{24}$$

where $a_1=\varepsilon\tilde{a}_1$, $a_2=\varepsilon\tilde{a}_2$ and ψ_1,ψ_2 are real-valued functions and denote amplitudes and phases of the general coordinates φ and ϑ.

After substituting (24) into (22) – (23) and separating real and imaginary parts, we obtain the modulation equations which can be transformed to more suitable autonomous form by introducing modified phases as follows

$$\psi_1(\tau_2)=\tau_2\tilde{\sigma}-\Psi_1(\tau_2),\quad \psi_2(\tau_2)=\tau_2\tilde{\sigma}-\Psi_2(\tau_2)\ \text{ and }\ \sigma=\varepsilon^2\tilde{\sigma}. \tag{25}$$

Substituting expressions (24) and (25) into the solvability conditions (22) – (23) and returning to the initial denotations according to (13), the modulation equations in autonomous form are obtained

$$a_1\frac{\partial\Psi_1}{\partial\tau}=a_1\sigma-\frac{1}{8}j_4a_1a_2^2\cos(2(\Psi_1-\Psi_2))+\frac{1}{2}j_2\omega_za_2\sin(\Psi_1-\Psi_2)+\frac{1}{2}f_0\sin(\Psi_1), \tag{26}$$

$$\frac{\partial a_1}{\partial\tau}=-\frac{1}{2}c_1a_1-\frac{1}{8}j_4a_1a_2^2\sin(2(\Psi_1-\Psi_2))-\frac{1}{2}j_2\omega_za_2\cos(\Psi_1-\Psi_2)-\frac{1}{2}f_0\cos(\Psi_1), \tag{27}$$

$$a_2\frac{\partial\Psi_2}{\partial\tau}=a_2\sigma+\frac{1-j_3}{4}a_1^2a_2+\frac{3}{8}\alpha_2a_2^3+\frac{1}{8}(j_3-1)a_1^2a_2\cos(2(\Psi_1-\Psi_2))-\frac{1}{2}j_3\omega_z a_1\sin(\Psi_1-\Psi_2), \quad (28)$$

$$\frac{\partial a_2}{\partial\tau}=-\frac{1}{2}c_2a_2-\frac{1}{2}j_3\omega_z a_1\cos(\Psi_1-\Psi_2)+\frac{1-j_3}{8}a_1^2a_2\sin(2(\Psi_1-\Psi_2)). \quad (29)$$

There is no possibility to solve analytically the modulation equations (26) – (29). The final form of the analytical solution of the original problem (9) – (11) is obtained after substituting solutions of equations (16) – (21) into power series (15):

$$\varphi=a_1\cos(\tau+\psi_1)-\frac{1}{32}\alpha_1a_1^3\cos(3(\tau+\psi_1))-\frac{1}{32}j_4a_1a_2^2\cos(3\tau+\psi_1+2\psi_2), \quad (30)$$

$$\vartheta=a_2\cos(\tau+\psi_2)-\frac{1}{32}\alpha_2a_2^3\cos(3(\tau+\psi_2))+\frac{1-j_3}{32}a_1^2a_2\cos(3\tau+2\psi_1+\psi_2), \quad (31)$$

where a_1, a_2, ψ_1 and ψ_2 satisfy modulation equations (26) – (29).

Taking into account some special case of parameters discussed in [4], i.e. $j_4=0$, $j_2=-1$ and $j_3=1$, the amplitude-frequency response functions are obtained analytically. They follow

$$9a_2^6\alpha_2^2+48a_2^4\alpha_2\sigma+a_2^2(16c_2^2+64\sigma^2)=16a_1^2w_z^2, \quad (32)$$

$$9a_1^8\alpha_1^2+48a_1^6\alpha_1\sigma+2a_1^4(8c_1^2-9a_2^4\alpha_1\alpha_2-24a_2^2\alpha_1\sigma+32\sigma^2)-16a_1^2a_2^2(\sigma(3a_2^2\alpha_2+8\sigma)-2c_1c_2)+ a_2^4(16c_2^2+(3a_2^2\alpha_2+8\sigma)^2)=16a_1^2f_0^2. \quad (33)$$

The derived formulas (32) – (33) offer a well-judged analysis of the influence of parameters on the steady state vibration of the gyroscope sensing plate.

5. Results

Here are presented some exemplary graphs concerning motion of the gyroscope near resonance. Calculations are performed for the following fixed dimensionless parameters: $\omega_z=6.64\times10^{-5}$, $f_0=4.37\times10^{-7}$, $c_1=c_2=3.98\times10^{-5}$, $\alpha_1=\alpha_2=1$, $j_1=-1.6\times10^{-16}$, $j_2=-1$, $j_3=1$, $j_4=0$. The latter correspond to values of real-world structure [4]. Time histories of the generalized coordinates φ and ϑ, according to (30) – (31), are presented in Fig. 3.

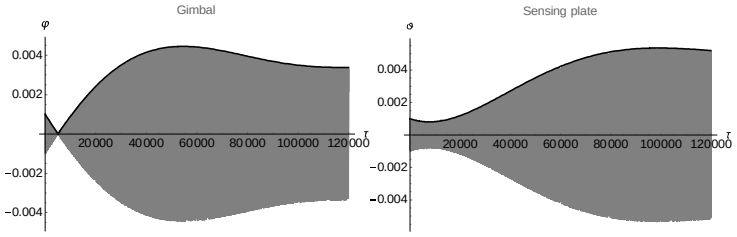

Figure 3. Time histories of the vibration.

The thick black line in Fig. 3 describe amplitude modulation yielded by equations (26) – (29). It should be emphasized that the approximate analytical solution satisfies the governing equations (9) – (10) with a high accuracy (the absolute errors Δ_1 and Δ_2 are reported in Fig. 4).

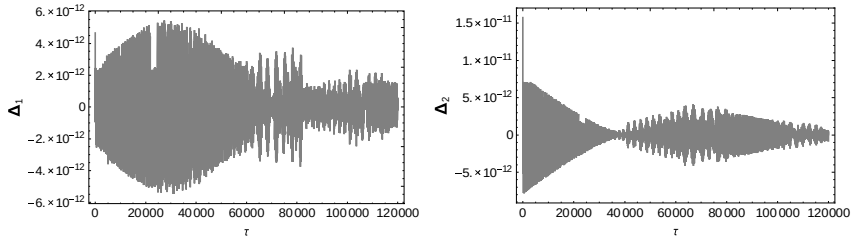

Figure 4. Absolute errors exhibited by the governing equations for the approximate analytical solution.

The employed analytical methodology and computational approach is suited to engineers dealing with MEMS. Namely, we have used the optimized numerical algorithm implemented in Wolfram Mathematica™. However, in the latter case the error of satisfaction of the equation of motion is five orders of magnitude larger in comparison to our described analytical solutions.

The amplitude curves for steady state motion obtained with the help of eq. (32) – (33) are presented in Fig. 5 for the same data as before.

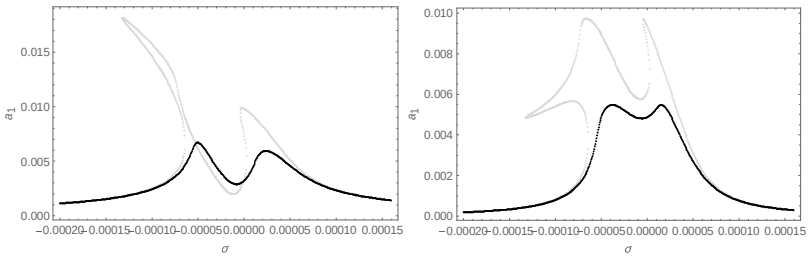

Figure 5. Amplitude of steady state vibration vs. detuning parameter: grey line – small damping $c_1 = c_2 = 2.2\times10^{-5}$; black line – large damping $c_1 = c_2 = 4.0\times10^{-5}$

For small value of the damping coefficients several regimes of steady-state amplitudes are possible. On the other hand, for properly large damping coefficients, the amplitudes versus time create the unique functions.

6. Conclusions

The mathematical model describing dynamics of some class of micromechanical gyroscope has been derived and presented in dimensionless form. The approximate analytical solution of the governing equations has been obtained using multiple scale method in time domain in the case of main resonance. The analytical solution presented in compact form gives opportunity to study behavior of the system for wide range of parameters. The asymptotic solution is very accurate.

The analytical form of the amplitude-frequency dependence allows to qualitative and quantitative analysis of the steady-state motion of the system. The results show, among others, that value of damping coefficients may violate uniqueness of the solution and influence the duration of the transient states.

Acknowledgments

This paper was financially supported by the grant of the Ministry of Science and Higher Education in Poland realized in Institute of Applied Mechanics of Poznan University of Technology (DS-PB: 02/21/DSPB/3493).

References

[1] Williams C.B., Shearwood C., Mellor P.H., Mattingley A.D., Gibbs M.R., Yates R.B., Initial fabrication of a micro-induction gyroscope, Microelectron. Eng. 30 (1996) 531–534.

[2] Jin L., Zhang H., Zhong Z., Design of a lc-tuned magnetically suspended rotating gyroscope, J. Appl. Phys. 109 (2011) 07E525–07E525–3.

[3] Awrejcewicz J., Krysko V. A.: *Introduction to Asymptotic Methods*, Boca Raton, Chapman and Hall, 2006.

[4] Merkuriev I.W, Podalkov W.W.: Study of nonlinear dynamics of a micromechanical gyroscope. Pproceedings of the IV International School –NDM “Nonlinear Dynamics of Machines”, 82-91, IMASH RAS, Moscow 2017 (in Russian)

Roman Starosta, Ph. D: Poznań University of Technology, Institute of Applied Mechanics, ul. Piotrowo 3, 60-965 Poznań, Poland (*roman.starosta@put.poznan.pl*). The author gave a presentation of this paper during one of the conference sessions.

Jan Awrejcewicz, Professor: Technical Universityof of Łódź, Department of Automatics and Biomechanics, ul. Stefanowskiego 90-924, Łódź, Poland (*awrejcew@p.lodz.pl*).

Grażyna Sypniewska-Kamińska, Ph. D: Poznań University of Technology, Institute of Applied Mechanics, ul. Piotrowo 3,60-965 Poznań, Poland, (*grazyna.sypniewska-kaminska@put.poznan.pl*).

Stimulation of nerve endings via medical device

Antonin Svoboda, Josef Soukup

Abstract: In this article is solved problem of stimulating of nerve endings of patients after spin injury via vibro-generator. Was developed mechanism of vibrations which can able change amplitude and fervency and vibration. Here is published solution of construction mechanism, results of experimental measuring and optimization of construction. Next is described use in practice. During the development of the structure, was paid great attention to the safety of the mechanism, the device is powered on the battery. This solution eliminates the deficiencies of similar devices used in the world, powered from the network (110 - 230 V). The success rate of vibrator use, in patients is ranges between 60-80%.

1. Introduction

According to available information, and clinical test have mechanisms to induce ejaculation reflex for the collection of genetic material (sperm) in affected males for several years. These methods proved to be reliable with relatively high efficiency [1]. As the most effective method of obtaining genetic material in men can be called surgical sperm collection. This method is performed under general anesthesia, which limits patient. Performance is preceded by internal examination, ECG, blood biochemistry and other examinations according to the patient's condition. Behind this method it is then electrostimulation, which again is performed under general anesthesia by electrical stimulation of the prostate. This method, however, requires a great practical experience of the doctor, as it can cause a burn or burns intestine of the patient. At least stressful method for the patient is vibrostimulation. The doctor or also informed patient stimulates via vibration nerve endings in the penis prescribed amplitude and frequency [4]. After injury of spine are medical doctors ready to help tetraplegic and paraplegic patients return them back normal or near normal life. Most man patients after injury of spine are no able to have got children and family. This status is for most men traumatic and stressful [4]. At least stressful method for the patient is vibro-stimulating. The doctor or also informed patient vibration stimulates nerve endings in the penis specified amplitude and frequency. To induce ejaculation is after approximately eleven minutes of stimulation, but it is necessary to observe the procedure three series of stimulation after three minutes and a minute break between every three minutes. Another way to evokes reflection in paraplegics and another way in tetraplegic. Paraplegic person is paralyzed legs, and then the person tetraplegic paralyzed on all four limbs. This method describes ways to return back to

life without minimum patient's stresses. One of no stress method is vibro-stimulating of nerve paths [1]. Our developed mechanism is generating vibrations – amplitude and frequencies between effective ranges. After consultations injury doctor specialists, we can presuppose amplitude of the range between 1 – 3 mm and frequencies between 80 – 100 Hz. For optimal frequency and amplitude, we can take information from doctor's injury and convalescence specialists. Finally, we can make a proposal optimal frequency and amplitude [1]. For the best solution we can mark range between 80 – 120 Hz and 1 – 4 mm [2]. To achieve the desired frequency, range between 80 – 120 Hz, it is necessary to convert frequency to DC engine speed:

$$f = \frac{n}{T}\ [Hz] \Rightarrow n = f \cdot T \Rightarrow n = f \cdot 60 \tag{1}$$

Where is *f* – frequency, *n* – DC engine speed, *T* – time

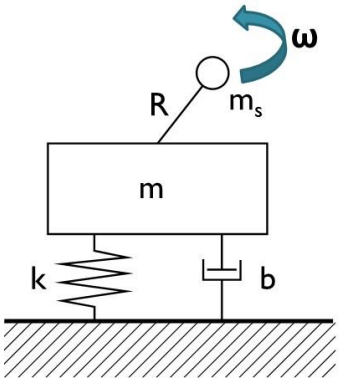

Figure 1. Forced damped vibration system with one degree of freedom

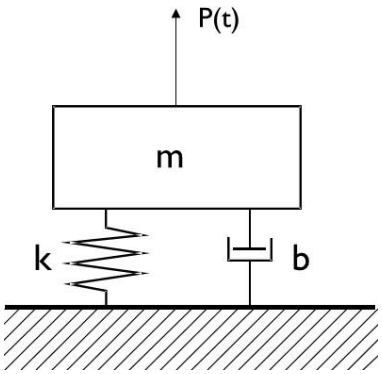

Figure 2. Forced damped vibration system with one degree of freedom

Where is ms - weight of particles, m – weight, R – eccentricity, ω – angular velocity, b – coefficient of shock absorber, k – stiffness of the spring

Equation of motion,

$$m\ddot{x} + b\dot{x} + kx = P(t), \tag{2}$$

where is x – the displacement from the static equilibrium of position, $P(t)$ – the excitation of power
Another form of motion of equation from angular frequency

$$\omega^2 = \frac{k}{m}, \tag{3}$$

Harmonic oscillation is characterized by harmonic waveforms

$$y = y_0 \sin(2\pi f) = y_0 \sin \omega\, t, \tag{4}$$

$$a = \frac{dv}{dt} = -\omega^2 \;\; y_0 \sin \omega\, t \; = a_0 \sin \omega\, t, \tag{5}$$

$$v = \frac{dy}{dt} = y_0\, \omega \cos \omega, \tag{6}$$

where is ω – angular velocity, y_0 – amplitude of displacement, a_0 – amplitude of acceleration
t – time

2. Methods of mechanism solution

The mechanism was designed in several variants. Solution can be effective via analytics method, method of final points and experimental measurement. For the best solution can be mark experimental measurement. For making these test of experimental measurement was designed vibro-generator in several variants. In all variants was used electrical engine SPEED 400 with maximum 12000 rpm and powered between 6 – 12 Vols. For our needs are effective rpm between 4800 – 7200 @ 3,32 – 4,81 Volts.

Crank mechanism Figure 1 is very hard for production in this very small sizes. Is necessary to take into consideration more difficult assembly of mechanism and device [2].

Advantages: Precisely adjustable amplitude shift crankshaft, separation of amplitude from frequency - with increasing of the engine speed (frequency) is the amplitude constant. Disadvantages: Miniature parts of the crank mechanism - higher demands on production and assembly [5].

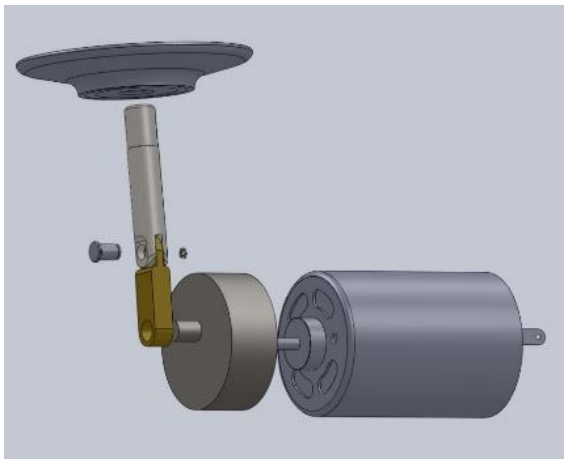

Figure 3. Crank mechanism

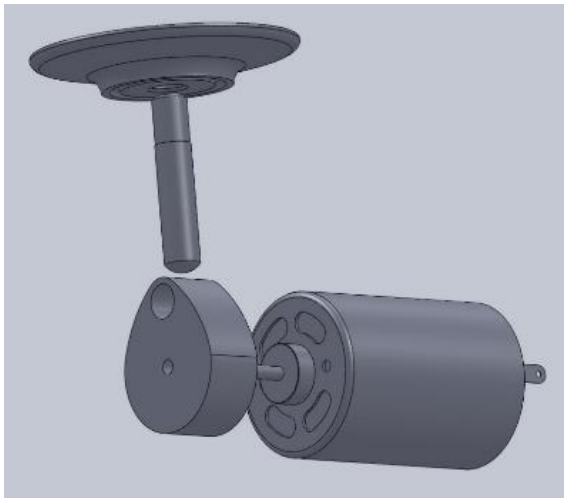

Figure 4. Construction with the cam

A cam mechanism Figure 4 provides the distinct advantage the simplicity of design [7], the lower cost of the assembly apparatus, than the variants with the crank mechanism [3]. Advantages: Simplicity of design - lower assembly costs and assembly of device mechanism. Disadvantages: Complicated of cam production, noise. When using a cam mechanism, it is necessary to take into account unbalance cam which causes the vibration of the whole mechanism. In this case, unbalance works in favour of the final oscillation amplitudes, but to the detriment of engine bearings and the entire device. At the prescribed speed in the range 4800 – 7200 rpm occurs due to imbalance even more options, so-called own auto oscillations [3].

Eccentric is probably the simplest design of solution, bringing in low manufacturing costs. Experimental measurements with eccentric showed higher noise of the device. Advantages: Simplicity of design. Disadvantages: Higher load of engine's bearings, noise.

Unbalance Figure 4 and Figure 5 is the simplest solution, however, the fundamental problem depending engine speed (frequency) vs. amplitude. Advantages: Simplicity of design. Disadvantages: Higher load of engine's bearings, frequency dependence of the amplitude.

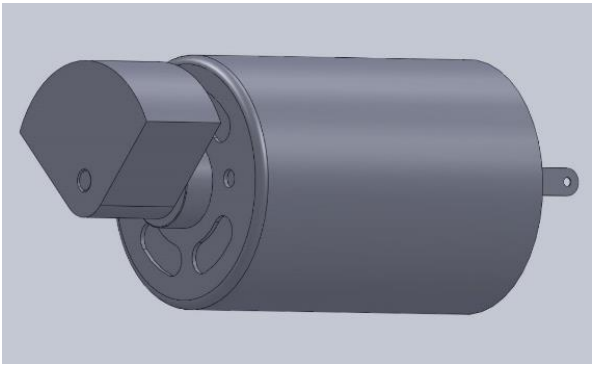

Figure 6. Construction with the unbalance

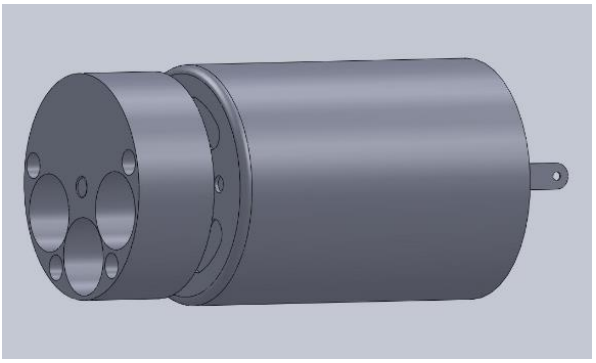

Figure 7. Constructions with drilled unbalance holes are simpler from a manufacturing point of view

3. Result

By experimental measurements were found maximum values of amplitude at frequency. In the future, these results will be used for the final design of the device for generating vibrations. Unbalance method was verified in the laboratory Figure 6. DC engine was powered by a stabilized source and were measured engine rpm, the electric current (A) and frequency (Hz).

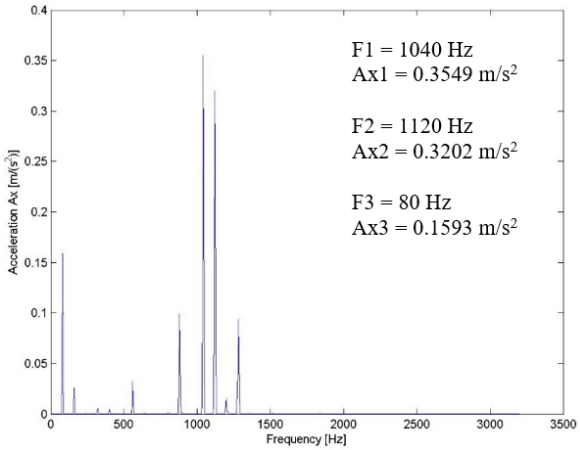

Figure 9. Acceleration in the x direction – measurements at speed 4800 rpm

In Figure 9 was achieve the maximum of acceleration value 0.3549 m/s^2 in frequency 1040 Hz via 4800 rpm of DC engine. These values were recalculated to amplitude and later theoretically confirmed via Lagrange numerical mathematics method.

In Figure 10 was achieve the maximum of acceleration value 9.1390 m/s^2 in frequency 172 Hz via 5160 rpm of DC engine. These values were recalculated to amplitude and later theoretically confirmed via Lagrange numerical mathematics method.

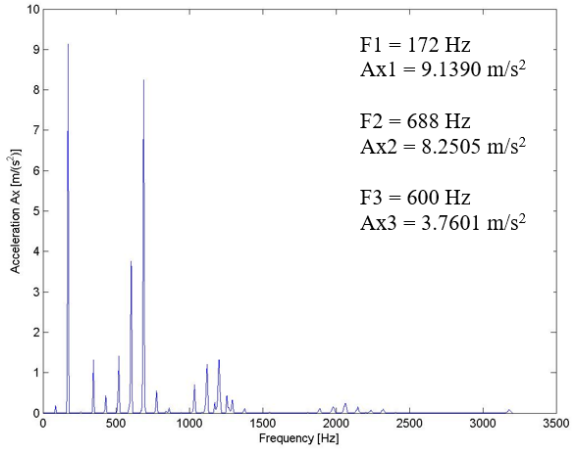

Figure 10. Acceleration in the x direction – measurements at speed 5160 rpm

In Figure 11 was achieve the maximum of acceleration value 0.3892 m/s^2 in frequency 52 Hz via 3060 rpm of DC engine. These values were recalculated to amplitude and later theoretically confirmed via Lagrange numerical mathematics method.

In Figure 11 was achieve the maximum of acceleration value 0.3892 m/s^2 in frequency 52 Hz via 3060 rpm of DC engine. These values were recalculated to amplitude and later theoretically confirmed via Lagrange numerical mathematics method.

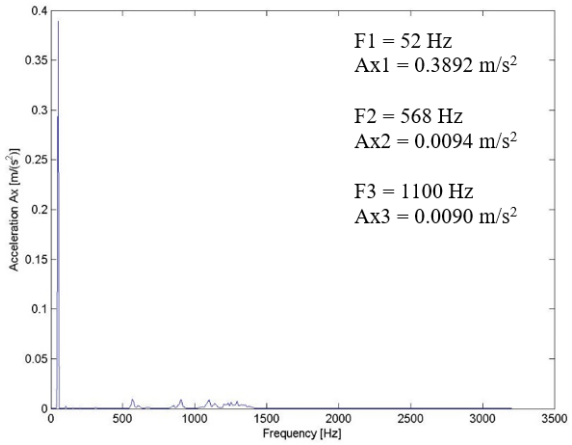

Figure 11. Acceleration in the x direction – measurements at speed 3060 rpm

4. Conclusions

For measurement of vibrations was designed special stand. In all cases of tests were used the same engine SPEED 400 powered by stabilized source. RPM was taken via laser sensor and vibration was measured via accelerometer. All measurement results were recalculating from acceleration to amplitude and was used numerical method Lagrange for verify this values. Next were processed via software MATLAB and converted to MS-EXCEL. In these methods described above were compared vibration exciter suitable mechanism design. Was selected the most appropriate method of construction equipment. This method was experimentally verified in laboratory. It will also be developed by the cheapest method of production and assembly device for vibration excitation and stimulation of nerve endings and paths. The result of this work will be quality and cheap device for stimulating a man patients.

ACKNOWLEDGEMENT

J. E. Purkyne University in Usti nad Labem, Faculty of Production Technology and Management for support of this project from SGS grant.

5. References

[1] Šrámková, T., *Poruchy sexuality u somatických nemocných a jejich léčba*, Grada Publishing, Praha, 2013.

[2] Dejl, Z. *Konstrukce strojů a zařízení I*. Spoje. Montanex, Ostrava, 2000.

[3] Vejrosta, V. *Konstrukce zdravotnických přístrojů*, Česká společnost pro zdravotnickou techniku, June 1995

[4] Prim., MD., Marta Vachová, *Verbal presentation doctor of neurology*, Head of neurology department hospital Teplice, 2014

[5] Juliš, K., Brebta R. a kol. *Mechanika I. – Statika a kinematika*, SNTL Praha, 1986

[6] Brebta R., Půst L., Turek F., *Mechanické kmitání*, Sobotáles, Praha, 1994

[7] Benaroya H., *Mechanical vibration*, Marcel Dekker, N.Y., 2004

[8] Svoboda, A., *Mechanický přístroj pro stimulaci nervových drah*, Diplomová práce, Fakulta výrobních technologií a managementu UJEP v Ústí nad Labem, Ústí n. L., 2015, 53 str.

Experimental investigation of a human-like rib cage model subjected to an impact load

Olga Szymanowska, Bartłomiej Zagrodny, Wojciech Kunikowski, Jan Awrejcewicz, Paweł Olejnik

Abstract: This work continues some experimental investigations of a human-like rib cage subjected to an impact load. The construction of the experimental rig is based on a Hybrid III thorax calibration test stand. Impact velocity reaches 4 m/s and the 23 kg impact mass. The elastic impact subsystem consists of a rigid disc, the initial velocity of which is initiated by a pre-tensioned spring of very high stiffness. Time characteristics of force and deflection responses of the investigated model constitute a reference properties in identification of the human-like rib cage. Another aim of this work is to obtain biologically compatible parameters, like stiffness and damping of the artificial chest, by fitting a proper material that will in an average degree imitate properties of internal organs of the human chest. All measurements presented in the work were collected with the use of the NI DAQ system. Chest deflection was captured by measuring the angle between the sides of an isosceles triangle. The triangle was mounted between the sternum and the vertebral column, and the angle was captured with a potentiometer. In addition, an accelerometer was used to record the acceleration of the impacting mass.

1. Introduction

A thoracic (or rib) cage is an extremely important part of a human body. It encloses organs such as the heart, lower respiratory tract or oseophagus as well as a part of main arteries. Rib cage injuries are thus very dangerous to health and their consequences are often fatal. One of the most threatening causes of thorax injuries are vehicle collisions during which a human is subjected to a frontal impact to the steering wheel, which leads to deflection of the rib cage resulting in rib fractures and damage to internal organs. According to statistical analysis, chest injuries are still a major cause of morbidity and mortality of car accidents victims and one of the most common contact points associated with possible severe injury is the steering wheel ([1,2]) . Therefore, numerous studies on the dynamical response of the thorax to the anterior impact play an important role in the research aimed at minimizing the effects of car accidents.

As for the basic aspects of anatomy of the thoracic cage, it is formed by the sternum (located in the anterior part of the rib cage) connected by means of twelve ribs with the vertebrae of the spinal column located in the posterior part (Figure 1). The ribs differ in length and are separated from each other by eleven intercostal spaces filled with the intercostal muscles and membranes. Ribs 1-7 (called

'true') are directly attached to both sternum and vertebrae via costal cartilage while the remaining ribs are called 'false'. Ribs 8-10 are connected with vertebrae in the posterior part and are indirectly attached to the sternum via costal cartilages of the ribs above them. Furthermore, ribs 11 and 12 are called 'floating' as there is no connection between them and the sternum.

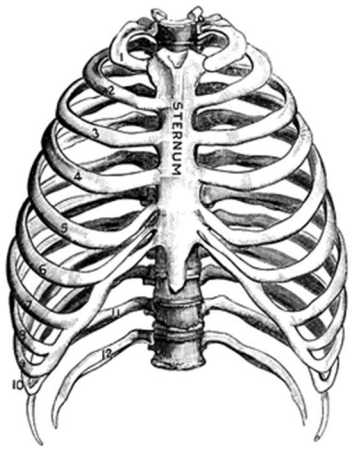

Figure 1. Anatomy of a thoracic cage
(Copyright: Florida Center for Instructional Technology; Source: Albert F. Blaisedell *Our bodies and How We Live* (Boston: Ginn &, 1904) 28).

Among tools to investigate reaction of a human body to impact forces, one can distinguish Anthropomorphic Test Devices (ATD), called also dummies. They are mechanical surrogates of a human that are mainly used in simulated vehicle impacts (crash tests). ATDs are designed in a way to represent the shape, size and mass of the human body as well as to mimic its reaction to various collision conditions, which is recorded by numerous sensors. The results of the tests performed with the use of dummies are employed to evaluate restraint systems [3]. Although numerical representations of ATDs have become popular in the recent years due to relatively low cost of numerical studies, mechanical representations are still used to simulate human response to impacts. Usually, Hybrid III or its proposed successor, THOR, are investigated.

The present paper comprises the results of an experimental study to investigate the effect of a frontal impact load acting on a model imitating a human thoracic cage (rib cage). The model is a simple ATD consisting of a rib cage filled with a foam. The ATD can be treated as biofidelic with respect to the human thorax geometry and stiffness. The study extends the investigations presented, for instance, in [4].

The paper is organized into sections consecutively presenting the investigated experimental stand and the results followed by a comprehensive discussion on the results reliability and, eventually, general conclusions to the study.

2. Materials and methods

2.1. Experimental stand

All the experiments were conducted on an experimental rig fulfilling the requirements of National Highway Traffic Safety Administration (NHTSA) as well as European New Car Assessment Programme (EuroNCAP) protocols for dummies used in crash tests. The construction of the stand has been partially based on the calibration/certification stand used with Hybrid III dummies while the geometry of the model of the thoracic cage is similar to the one of a THOR dummy [5].

The main elements of the stand considered in the present paper (Figure 3) include a thorax, a 15-cm-diameter 23.4 kg rigid disk impactor (mimicking the impactor used in [6,7]) and a spring loaded release mechanism. The thorax comprises twelve polyurethane ribs and 17 vertebrae (which constitute the thoracic and lumbar spine), positioned in a way following the natural shape of the spinal column. It is filled with an elastic foam acting both as body tissues and the air filling the airways. Since the main intention is to study the response of the thorax, the remaining parts of the body, such as arms, head or lower limbs, have been replaced with appropriate counterweights so as the total mass and inertia distribution are maintained. Horizontal movement of the dummy (to the back/front) is allowed by a bearing trolley moving along two guideways.

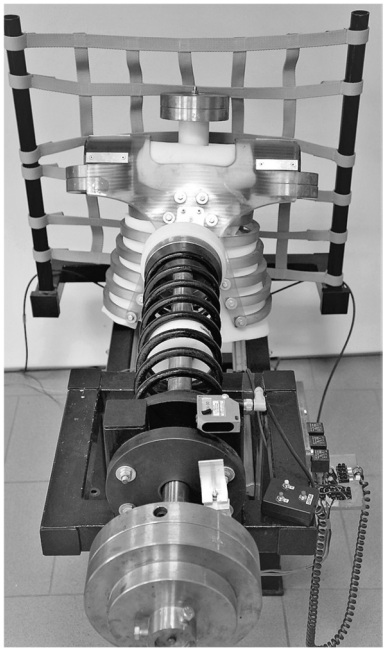

Figure 2. Experimental stand consisting of a thorax, an impactor and a spring loaded release mechanism

Despite stiffness of the thorax is non-linear with respect to chest compression depth and varies individually [8], it can be assumed that the relationship is linear in the considered range of the compression depth. Thus, stiffness of the filler was chosen in a way to ensure the total stiffness of the system falling in the range 20-150 N/cm (200-1500 N/m), as given in [8] based on the data collected during hospital/ambulance cardiopulmonary resuscitation (CPR) for non-intubated patients. Stiffness of the thorax was investigated following the methodology outlined in [9] for the case of the hub loading condition.

Overall, the construction of the rig ensures its biofidelity with respect to mass, anthropometry, geometry, and dynamic response in comparison to human chest and standards mentioned above. The detailed parameters of the thorax can be found in Table 1. The experimental values of stiffness, equal to 84 and 142.3 N/cm for the thorax without and with the filler, respectively, are comparable with the values obtained in [9], i.e., 54.1 and 99.4 N/cm, respectively (eviscerated and denuded cases).

Table 1. Characteristics of the investigated thorax

Parameter		Value
Mass [kg]	Arm (each)	4.5
	Lower body (below pelvis)	40
	Head	5
Chest breadth (4th rib/8th rib) [mm]		205/200
Stiffness (rib cage) [N/cm]		84
Stiffness (rib cage with the filler) [N/cm]		142.3

In the experiment, the spring is compressed and then released causing rapid translocation (movement) of the load, which eventually performs a frontal (anterior) impact to the centre of the chest model (approximately the 4^{th} intercostal space) (Figure 4). One can investigate reaction of the thorax to impacts at different velocities (up to 4m/s), which is possible by controlling the spring loaded release mechanism comprising a linear actuator powered by a DC motor, i.e. a crossed helical gear).

The experimental rig is also supplemented with deflection sensor, accelerometer and laser distance meter (Figure 5), which are described further (in “Data collection and signal processing” section).

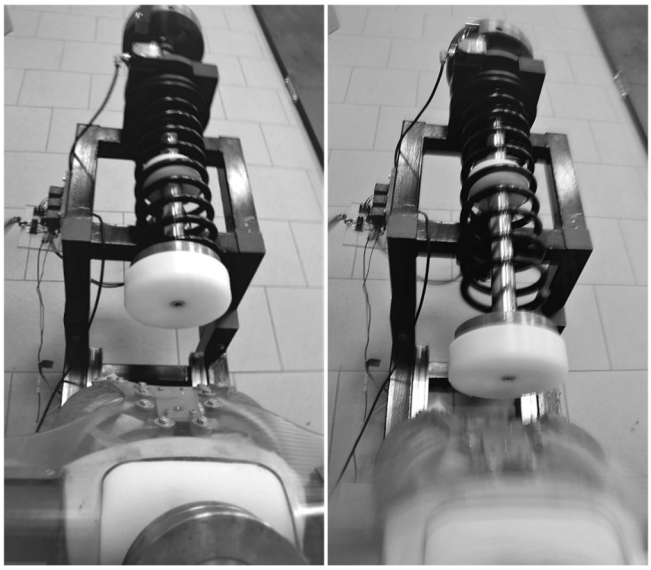

Figure 3. The system before (left) and right after (right) the impact to the chest

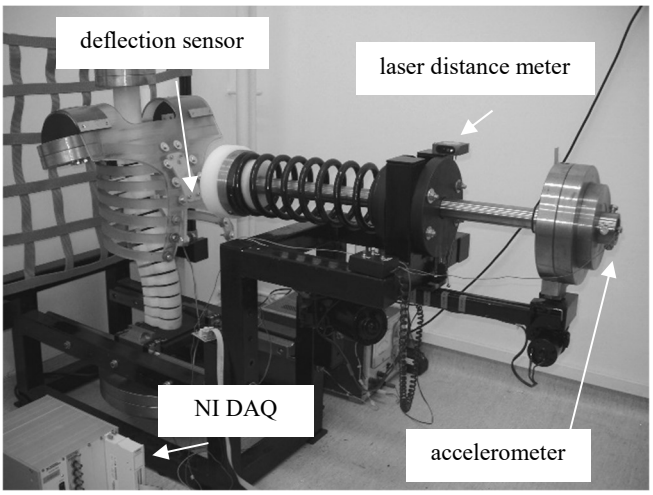

Figure 4. The measurement system (rib case before filling with a foam)

2.2. Data collection and signal processing

Data collection was carried out with the aid of the National Instruments DAQ system while the data were processed in a dedicated LabVIEW routine. The program allows for simultaneous collection of three analogue signals. Furthermore, the user can set arbitrary values of parameters of signal processing (filtration) and save the processed data to a file. The block diagram of the program is depicted in Figure 5 .

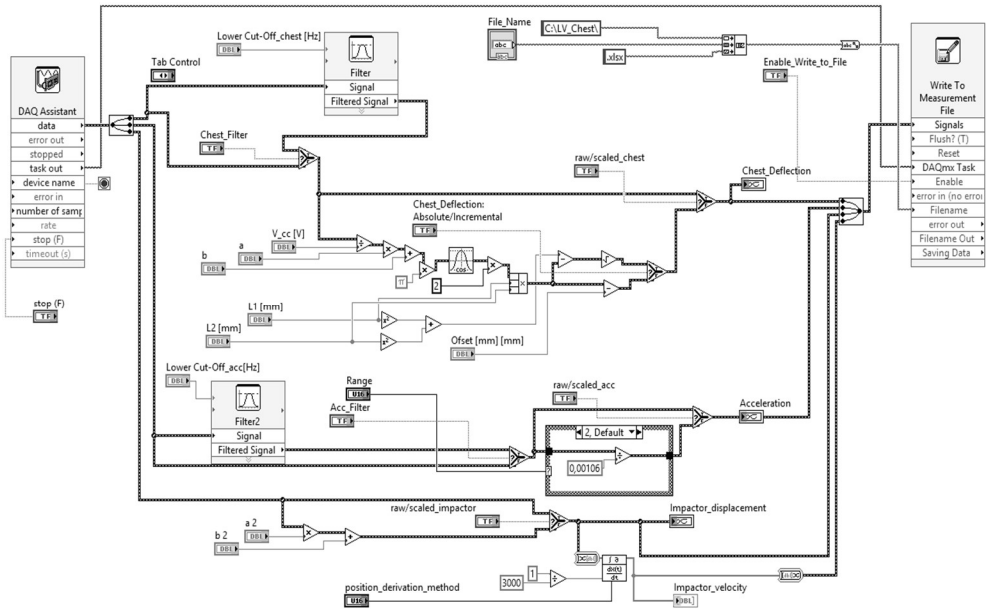

Figure 5. The employed LabVIEW routine

Measurements of the chest deflection were conducted using a custom V-shaped (compression depth) sensor placed inside the thorax. The sensor uses a potentiometer to measure voltage corresponding to the length of the base of an isosceles triangle, the legs of which are attached to the sternum and thoracic vertebrae (both at the level of the impactor), respectively, while the potentiometer is placed at the vertex angle (see Figure 6). Dynamical force of the impactor was found by capturing the data from a piezoelectric Dytran® 3220B accelerometer installed at the impactor and paired to a SVAN 912AE vibration analyser. To obtain velocity of the impactor at the time of its impact to the thorax, a Sensopart® FT 50 RLA-40 laser distance meter was employed.

Figure 6. Custom chest deflection sensor

The signal processing procedure started with separation of signals of the above-mentioned sensors from one array containing all the data into three arrays. Then, as the signals contain a wide range of frequencies and it is known that components of higher frequencies (caused, for instance, by linear bearings of impactor guides) play no significant role in the study and mainly introduce noise to the signals, the signals presented in "Results" section were filtered with a Butterworth low-pass filter with a cutoff frequency of 100 Hz (deflection) and 400 Hz (acceleration/dynamical force), respectively. In the next step, all data presented in terms of time-varying voltage were transformed into units of acceleration, displacement and deflection, respectively, by adequate linear transformations. Then, signal from the distance meter was differentiated with respect to time.

The processed data were eventually used to construct deflection-time, acceleration-time and velocity-time plots, which present the response of the thorax to the given impact conditions.

3. Results

3.1. Experimental results

This section comprises the plots presenting the dependence of thorax deflection, acceleration of the impactor as well as displacement and velocity of the impactor on time. All signals considered in the present paper (Figures 7-12) were measured at the sampling rate of 3 kHz. The trial numbers given in plot titles correspond to different loading conditions. Namely, trial 1 was conducted for spring compression corresponding to the impactor motion at 1 m/s, trial 2 - at 2 m/s and trial 3 - at 3 m/s (at the moment of impact to the thorax).

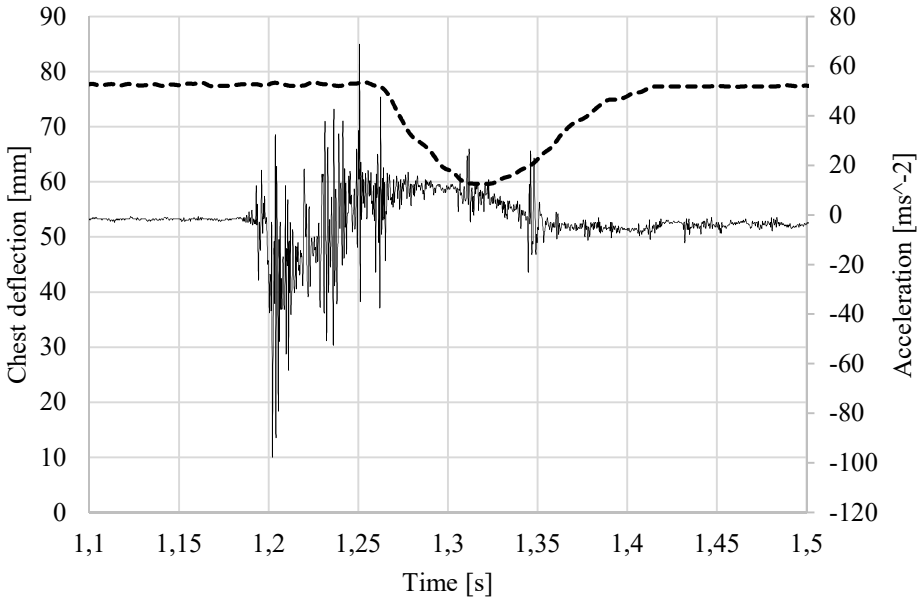

Figure 7. Chest deflection (dashed curve) and impactor acceleration (solid) vs. time for trial 1

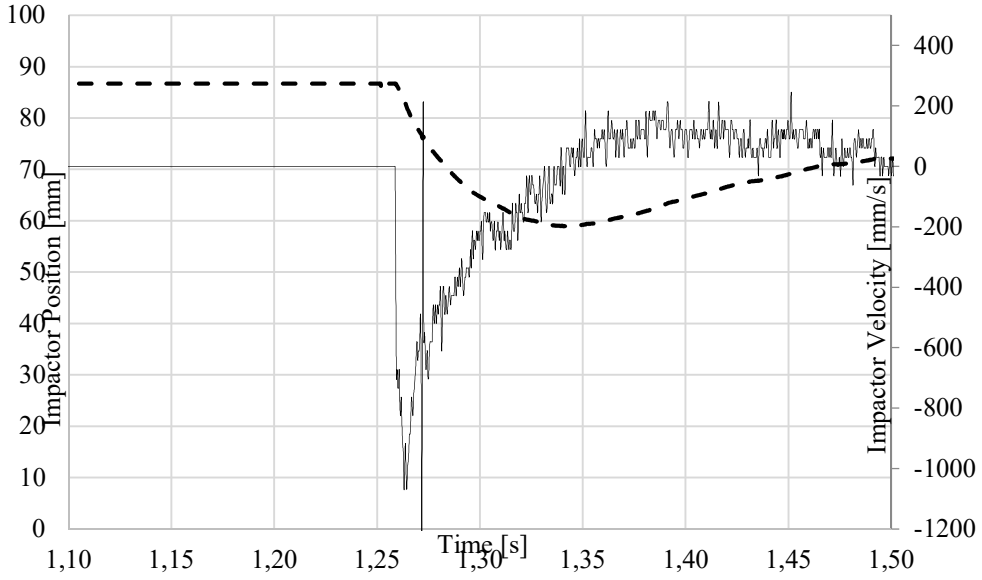

Figure 8. Impactor position (dashed) and impactor velocity (solid) vs. time for trial 1

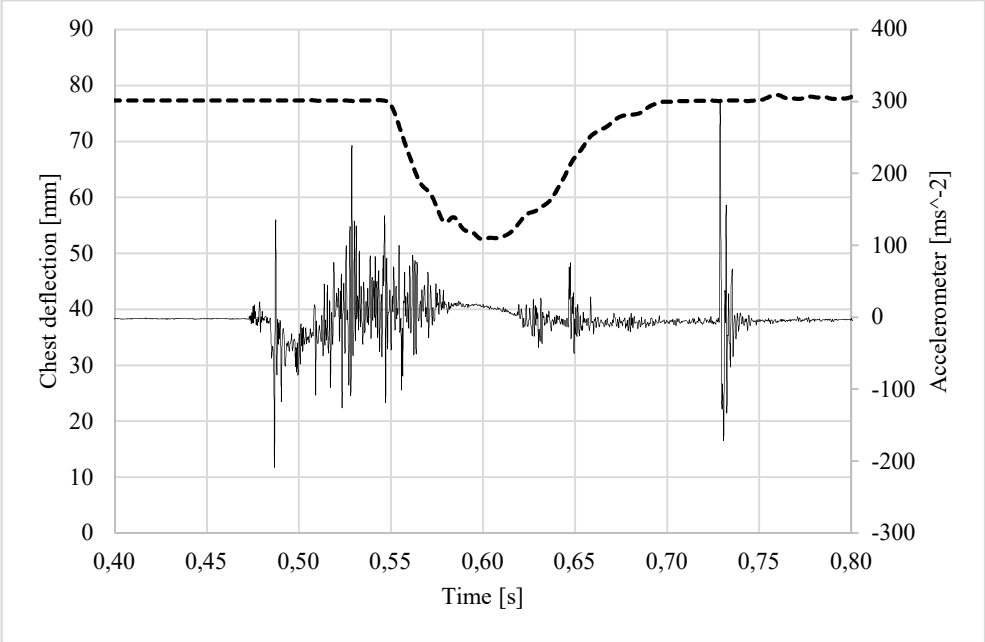

Figure 9. Chest deflection (dashed curve) and impactor acceleration (solid) vs. time for trial 2

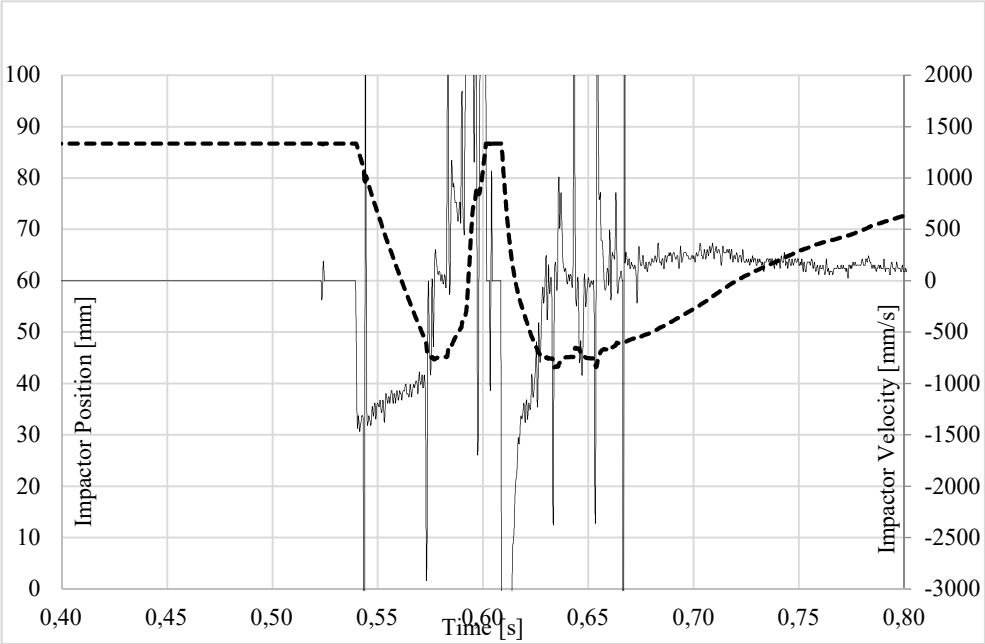

Figure 10. Impactor position (dashed) and impactor velocity (solid) vs. time for trial 2

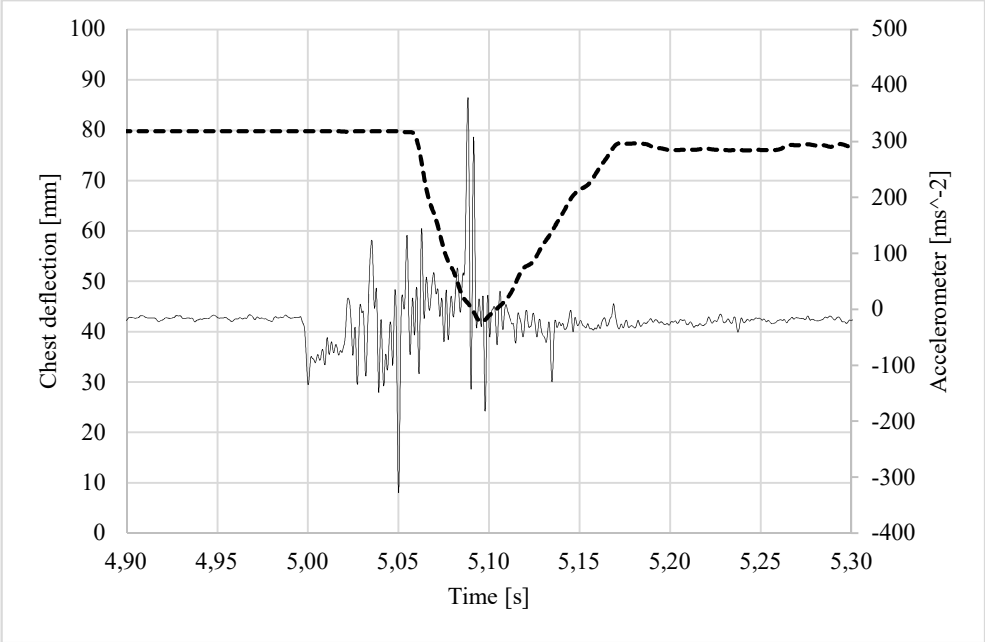

Figure 11. Chest deflection (dashed curve) and impactor acceleration (solid) vs. time for trial 3

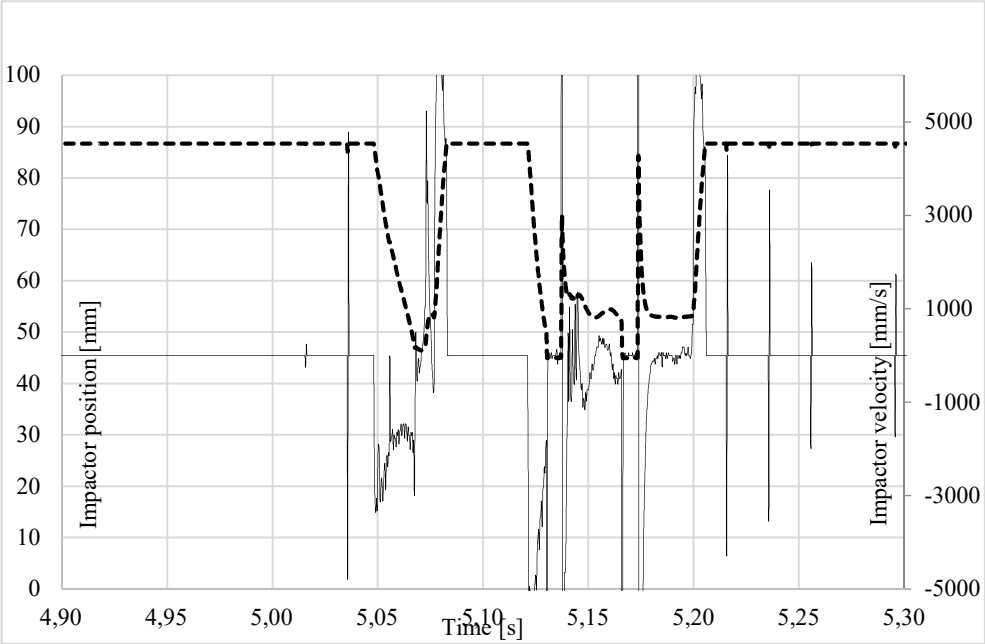

Figure 12. Impactor position (dashed) and impactor velocity (solid) vs. time for trial 3

4. Discussion and conclusions

Nowadays the Finite Element Modelling methods are widely used for vehicle crash simulation. Despite the ever-growing precision of the above-mentioned models, the numerical data must be compared with a practical experiment. Often the artificial ATD are replaced with real human corpses what raises many problems, partly due to ethical aspects of such a procedure.

With this in mind, the need for an apparatus resembling as closely as possible the real thoracic cage becomes apparent. The laboratory stand presented in this work provides coincident parameters with much more expensive, professional ADT's.

The study does not regard the influence of seatbelts and airbags during the impact. Those devices are planned to be incorporated to the laboratory stand during course of future work.

With the increase in the impact strength (which is dependent on the impact velocity and initial spring deflection), a larger deflection of the thoracic cage is observed as well as is the increase in time needed for the cage to return to its initial dimensions. In spite of incorporating a low-pass filter, the accurate value of acceleration at the moment of impact cannot be read reliably. Due to this issue, the real value of impact force and its evolution was not studied.

References

[1] R. Nirula, F.A. Pintar, Identification of vehicle components associated with severe thoracic injury in motor vehicle crashes: A CIREN and NASS analysis, Accid. Anal. Prev. 40 (2008) 137–141. doi:10.1016/j.aap.2007.04.013.

[2] R. Cuerden, R. Damm, C. Pastor, An estimation of the costs and benefits of improved car to car compatibility on a national and European scale, VC Compat Growth Proj. GRD2-2001-50083, Deliv. D24. (2006).

[3] H.J. Mertz, Anthropomorphic Test Devices, in: A.M. Nahum, J.W. Melvin (Eds.), Accid. Inj., Springer, NY, 2002: pp. 72–88. doi:https://doi.org/10.1007/978-0-387-21787-1_4.

[4] J. Awrejcewicz, B. Łuczak, Calibration of the new human thorax model for low impact loading rates (in Polish), J. KONES Powertrain Transp. 14 (2007) 7–14.

[5] T. Shams, N. Rangarajan, J. McDonald, Y. Wang, G. Platten, C. Spade, P. Pope, M. Haffner, Development of THOR NT: Enhancement of THOR Alpha-The NHTSA Advanced Frontal Dummy, in: Proc. 19th Int. Tech. Conf. Enhanc. Saf. Veh., Washington, D.C., 2005.

[6] C.K. Kroell, D.C. Schneider, A.M. Nahum, Impact Tolerance and Response of the Human Thorax, in: Proc. 15th Stapp Car Crash Conf., 1971: pp. 84–134. doi:10.4271/710851.

[7] C.K. Kroell, D.C. Schneider, A.M. Nahum, Impact Tolerance and Response of the Human Thorax II, Stapp Car Crash Conf. (1974) 383–457. doi:741187.

[8] A.E. Tomlinson, J. Nysaether, J. Kramer-Johansen, P.A. Steen, E. Dorph, Compression force-depth relationship during out-of-hospital cardiopulmonary resuscitation, Resuscitation. 72 (2007) 364–370. doi:10.1016/j.resuscitation.2006.07.017.

[9] R. Kent, Frontal thoracic response to dynamic loading: The role of superficial tissues, viscera and the rib cage, Int. J. Crashworthiness. 13 (2008) 289–300. doi:10.1080/13588260801933725.

Olga Szymanowska, M.Sc. (Ph.D. student): Department of Automation, Biomechanics and Mechatronics, Faculty of Mechanical Engineering, Lodz University of Technology, 1/15 Stefanowski Street, 90-924 Lodz, POLAND (*olga.szymanowska@dokt.p.lodz.pl*).

Bartłomiej Zagrodny, Ph.D.: Department of Automation, Biomechanics and Mechatronics, Faculty of Mechanical Engineering, Lodz University of Technology, 1/15 Stefanowski Street, 90-924 Lodz, POLAND (*bartlomiej.zagrodny@p.lodz.pl*).

Wojciech Kunikowski, M.Sc. (Ph.D. student): Department of Automation, Biomechanics and Mechatronics, Faculty of Mechanical Engineering, Lodz University of Technology, 1/15 Stefanowski Street, 90-924 Lodz, POLAND (*wojciech.kunikowski@dokt.p.lodz.pl*).

Jan Awrejcewicz, Professor: Department of Automation, Biomechanics and Mechatronics, Faculty of Mechanical Engineering, Lodz University of Technology, 1/15 Stefanowski Street, 90-924 Lodz, POLAND (*jan.awrejcewicz@p.lodz.pl*).

Paweł Olejnik, Associate Professor: Department of Automation, Biomechanics and Mechatronics, Faculty of Mechanical Engineering, Lodz University of Technology, 1/15 Stefanowski Street, 90-924 Lodz, POLAND (*pawel.olejnik@p.lodz.pl*). The author gave a presentation of this paper during one of the conference sessions.

Distributed Multi-population Genetic Algorithm to improve driver's comfort

Szymon Tengler, Kornel Warwas

Abstract: A solution of the task how to select the optimal parameters of a sub-assembly of a driver's seat of a special vehicle with a high gravity center will be presented in this paper. In the analyzed vehicle there were twelve sub-assemblies. The vehicle was modeled with use of joint coordinates, and homogenous transformations. Equations of motion were derived from Lagrange equations of the second kind. An aim of optimization is to select appropriate values of damping factors of a driver's seat sub-assembly to provide the best possible driving comfort. The optimization aim is to minimize a functional determining vertical acceleration of a driver's seat. There was made own implementation of an algorithm called Distributed Multi-Population Genetic Algorithm, based on genetic algorithms with floating coding of genes in the chromosome of the client-server architecture. The proposed method is based on a possibility of processing lots of populations at the same time within formation exchange between the populations. A particular iteration of the procedure consists of standard genetic operators: a natural selection, one-point crossing, uniform mutation and a data exchange in the grid. Results of numerical calculations for a vehicle driving at a different velocity through an obstacle in a form of a bump will be presented in the paper.

1. Introduction

At a time of the automobile race aiming at procuring both new clients and maintaining current ones there are important elements which have a direct impact on feelings of passengers of a vehicle. Driving comfort of a driver is one of the key elements in this scope. A comfort improvement can have a significant influence on both effective time of vehicle use and a level of operator tiredness. It is particularly important in the case of articulated and special vehicles in which an operator spends daily on average from a few to over a dozen hours [21]. A lot of research deals with human-seat interaction [8, 17]. In these works authors focus on accurate modelling of human body with the seat contact. The presented research deals with truck drivers considering travel time factor and designing best possible alternatives of driver's seat shape. In order to achieve this objective they used the aid of ergonomics and advanced design tools like CAD CAE and FEM. As it is shown in [13, 20] the comfort improvement of a driver and passengers is frequently identified with modifications of the vehicle sub-assemblies. In this case researchers do not include the human body interaction but they focus on

changes and improvements in the vehicle elements such as suspension, and those systems are commonly called an active or semi-active suspension [20, 22]. Works in this scope usually deal with reducing the vibrations present in those sub-assemblies. It can be achieved in different ways, and use of a supporting system is one of them. Those systems have to be calibrated properly to operate correctly. Constructing a test stand is usually connected with high costs and in the first stage of tests it is not justified. An application of virtual models and computer modeling allow reducing the costs and verifying basic assumptions. Optimization is particularly useful in this scope [6, 15, 28]. A virtual model and optimization results are grounds for use of the dedicated drivers of the existing systems or implementing new active elements into the standard equipment of a vehicle in a next stage. It is difficult to select an appropriate optimization method for a specific issue and it usually requires knowledge of a domain expert. The classical optimization methods result in the local optima and in the case of a vehicle, that is a multi-component system with open kinematic chains of a tree structure, they are often replaced with the methods originating from computational intelligence [1, 5, 26]. Evolutionary algorithms of different varieties are normally used [2, 12, 24]. These methods are less susceptible to the local minima and a selection of a start point, although their weak point is that they indicate only an approximate optimum value [18]. An application of the hybrid methods which join the selected features of the classical and evolutionary methods seems to be justified [27]. Then, we obtain the results which meet the basic assumptions of the defined problem. Another approach consisting in use of the evolutionary methods solving a problem at the same time an exchanging information about the best adapted individuals, was used in this paper. In such a way the populations growing independently can exchange the genetic material which is kept in the main store. In the literature this method is known as Multi-Population Genetic Algorithm [4, 10, 14] and it is used in different scientific disciplines. As an example in the work [23] the authors used the Multi-Population Genetic Algorithm for Unmanned Aerial Vehicles Path Planning. In paper [29] this method was used for optimizing the Train-Set Circulation Plan Problem, and in [7] for solving Dynamic Shortest Path Routing Problems in Mobile Ad Hoc Networks. Regardless of a field authors agree that use of many populations with emigration of the best individuals after each generation, contributes significantly to productivity growth and it enables to obtain better matching of the resultant population. In this paper use of this method for solving the issue of selecting the optimum values of damping of a special vehicle seat while driving through the obstacle in a form of a speed bump on basis of proprietary computer programs in the heterogeneous environment (C++/C# Microsoft .NET), is presented. Fundamentals of the mathematical model of the object in question are presented, the optimization task is defined and the computation results are presented for a different number of individuals in the population. The computation results were compared with the results obtained by the classical genetic algorithm.

2. Model of investigation

An object of testing is a rescue fire-fighting vehicle being an example of a special vehicle with a high gravity center. In the analyzed vehicle there were ten sub-assemblies identified such as: a frame, a cabin, a driver's seat, a body, an engine, a front and rear axle and wheels (fig. 1).

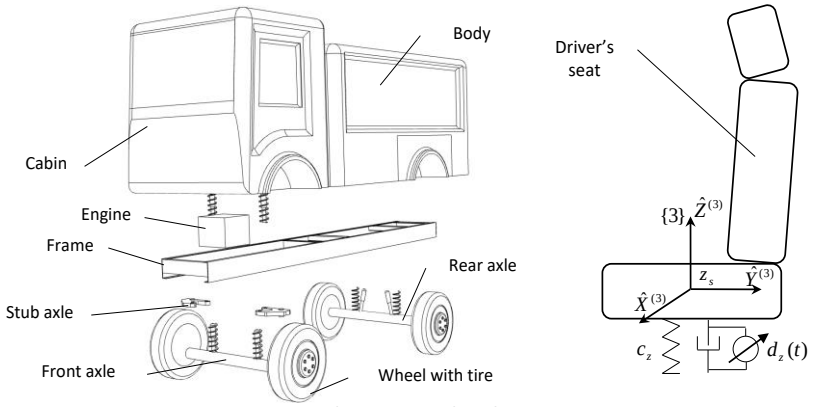

Figure 1. Parts of the rescue fire-fighting vehicle.

Joint coordinates and homogenous transformations were used to determine a position and orientation of these bodies in the three-dimensional space [25]. At such a way of modeling motion of each body (except for the base body), is determined in relation to a preceding body, and this motion is described by the generalized coordinates assumed appropriately. The vector of the generalized coordinates of vehicle has the following form:

$$\mathbf{q} = \left[\mathbf{q}_f^T \quad \mathbf{q}_c^T \quad \mathbf{q}_s^T \quad \mathbf{q}_b^T \quad \mathbf{q}_{a,1}^T \quad \mathbf{q}_{a,2}^T \quad \mathbf{q}_{w,1}^T \quad \mathbf{q}_{w,2}^T \quad \mathbf{q}_{w,3}^T \quad \mathbf{q}_{w,4}^T\right], \tag{1}$$

where:

$\mathbf{q}_f = [x_f \quad y_f \quad z_f \quad \psi_f \quad \theta_f \quad \varphi_f]^T$ -vector of generalized coordinates of frame,

$\mathbf{q}_c = [\theta_c]$ - vector of generalized coordinates of cabin,

$\mathbf{q}_s = [z_s]$ - vector of generalized coordinates of driver's seat,

$\mathbf{q}_b = [\emptyset]$ - vector of generalized coordinates of vehicle body fixed to frame,

$\mathbf{q}_{a,i} = [z_{a,i} \quad \varphi_{a,i}]^T$ - vector of generalized coordinates of front and rear axles,

$\mathbf{q}_{w,i} = [\psi_{w,i} \quad \theta_{w,i}]^T$ - vector of generalized coordinates of front wheels ($i = 1,2$),

$\mathbf{q}_{w,i} = \left[\theta_{w,i}\right]$ - vector of generalized coordinates of rear wheels ($i = 3,4$),

x_i, y_i, z_i - mass center coordinates of i-th body,

$\psi_i, \theta_i, \varphi_i$ - rotation angles of the i-th body.

Equations of vehicle motion have been formulated using Lagrange equations of the second kind [3, 25, 26]. After transformations dynamic equations of motion of the i-th sub-system of the vehicle can be written in the general form:

$$\mathbf{A}^{(i)}\ddot{\mathbf{q}}^{(i)} = \mathbf{f}^{(i)} \tag{2}$$

where:

$\mathbf{A}^{(i)}$ - mass matrix,

$\mathbf{f}^{(i)}$ - vector of external, Coriolis, centrifugal and gravity forces.

Therefore, equations of motion of the particular sub-system of the vehicle can be described as follows:

- sub-system 1 (frame - F, front axle - AF, stub axle - SA, front wheels - WF)

$$\mathbf{A}^{(1)} = \begin{bmatrix} \mathbf{A}_{F,F}^{(1)} & \mathbf{A}_{F,AF}^{(1)} & \mathbf{A}_{F,SA}^{(1)} & \mathbf{A}_{F,WF}^{(1)} \\ \mathbf{A}_{AF,F}^{(1)} & \mathbf{A}_{AF,AF}^{(1)} & \mathbf{A}_{AF,SA}^{(1)} & \mathbf{A}_{AF,WF}^{(1)} \\ \mathbf{A}_{SA,F}^{(1)} & \mathbf{A}_{SA,AF}^{(1)} & \mathbf{A}_{SA,SA}^{(1)} & \mathbf{A}_{SA,WF}^{(1)} \\ \mathbf{A}_{WF,F}^{(1)} & \mathbf{A}_{WF,AF}^{(1)} & \mathbf{A}_{WF,SA}^{(1)} & \mathbf{A}_{WF,WF}^{(1)} \end{bmatrix}, \mathbf{q}^{(1)} = \begin{bmatrix} \tilde{\mathbf{q}}^{(1)} \\ \tilde{\mathbf{q}}^{(4)} \\ \tilde{\mathbf{q}}_{SA}^{(1)} \\ \tilde{\mathbf{q}}_{WF}^{(1)} \end{bmatrix}, \mathbf{f}^{(1)} = \begin{bmatrix} \mathbf{f}_{F}^{(1)} \\ \mathbf{f}_{AF}^{(1)} \\ \mathbf{f}_{SA}^{(1)} \\ \mathbf{f}_{WF}^{(1)} \end{bmatrix},$$

where: $\tilde{\mathbf{q}}_{SA}^{(1)} = \begin{bmatrix} \tilde{\psi}^{(6)} \\ \tilde{\psi}^{(7)} \end{bmatrix}$, $\tilde{\mathbf{q}}_{WF}^{(1)} = \begin{bmatrix} \tilde{\theta}^{(1)} \\ \tilde{\theta}^{(2)} \end{bmatrix}$,

- sub-system 2 (frame - F, rear axle - AR, rear wheel - WR)

$$\mathbf{A}^{(2)} = \begin{bmatrix} \mathbf{A}_{F,F}^{(2)} & \mathbf{A}_{F,AR}^{(2)} & \mathbf{A}_{F,WR}^{(2)} \\ \mathbf{A}_{AR,F}^{(2)} & \mathbf{A}_{AR,AR}^{(2)} & \mathbf{A}_{AR,WR}^{(2)} \\ \mathbf{A}_{WR,F}^{(2)} & \mathbf{A}_{WR,AR}^{(2)} & \mathbf{A}_{WR,WR}^{(2)} \end{bmatrix}, \mathbf{q}^{(2)} = \begin{bmatrix} \tilde{\mathbf{q}}^{(1)} \\ \tilde{\mathbf{q}}^{(5)} \\ \tilde{\mathbf{q}}_{WR}^{(2)} \end{bmatrix}, \mathbf{f}^{(2)} = \begin{bmatrix} \mathbf{f}_{F}^{(2)} \\ \mathbf{f}_{AR}^{(2)} \\ \mathbf{f}_{WR}^{(2)} \end{bmatrix},$$

where $\tilde{\mathbf{q}}_{WR}^{(2)} = \begin{bmatrix} \tilde{\theta}^{(3)} \\ \tilde{\theta}^{(4)} \end{bmatrix}$,

- sub-system 3 (frame - F, cabin - C, driver seat - S)

$$\mathbf{A}^{(3)} = \begin{bmatrix} \mathbf{A}_{F,F}^{(3)} & \mathbf{A}_{F,C}^{(3)} & \mathbf{A}_{F,S}^{(3)} \\ \mathbf{A}_{C,F}^{(3)} & \mathbf{A}_{C,C}^{(3)} & \mathbf{A}_{C,S}^{(3)} \\ \mathbf{A}_{S,F}^{(3)} & \mathbf{A}_{S,C}^{(3)} & \mathbf{A}_{S,S}^{(3)} \end{bmatrix}, \mathbf{q}^{(2)} = \begin{bmatrix} \tilde{\mathbf{q}}^{(1)} \\ \tilde{\mathbf{q}}^{(2)} \\ \tilde{\mathbf{q}}^{(3)} \end{bmatrix}, \mathbf{f}^{(2)} = \begin{bmatrix} \mathbf{f}_{F}^{(3)} \\ \mathbf{f}_{C}^{(3)} \\ \mathbf{f}_{S}^{(3)} \end{bmatrix}.$$

In papers [11, 25, 26] there is a detailed description of mathematical modeling which results in a calculation model and dynamic equations of motion in a matrix form written as:

$$\begin{cases} \mathbf{A}\ddot{\mathbf{q}} - \mathbf{\Phi}\mathbf{r} = \mathbf{f} \\ \mathbf{\Phi}^{\mathbf{T}}\ddot{\mathbf{q}} = \mathbf{w} \end{cases} \tag{3}$$

where:

$$\mathbf{A}=\begin{bmatrix}\mathbf{A}_{F,F}^{(1)}+\mathbf{A}_{F,F}^{(2)}+\mathbf{A}_{F,F}^{(3)} & \mathbf{A}_{F,AF}^{(1)} & \mathbf{A}_{F,SA}^{(1)} & \mathbf{A}_{F,WF}^{(1)} & \mathbf{A}_{F,AR}^{(2)} & \mathbf{A}_{F,WR}^{(2)} & \mathbf{A}_{F,C}^{(3)} & \mathbf{A}_{F,S}^{(3)}\\ \mathbf{A}_{AF,F}^{(1)} & \mathbf{A}_{AF,AF}^{(1)} & \mathbf{A}_{AF,SA}^{(1)} & \mathbf{A}_{AF,WF}^{(1)} & \mathbf{0} & \mathbf{0} & \mathbf{0} & \mathbf{0}\\ \mathbf{A}_{SA,F}^{(1)} & \mathbf{A}_{SA,AF}^{(1)} & \mathbf{A}_{SA,SA}^{(1)} & \mathbf{A}_{SA,WF}^{(1)} & \mathbf{0} & \mathbf{0} & \mathbf{0} & \mathbf{0}\\ \mathbf{A}_{WF,F}^{(1)} & \mathbf{A}_{WF,AF}^{(1)} & \mathbf{A}_{WF,SA}^{(1)} & \mathbf{A}_{WF,WF}^{(1)} & \mathbf{0} & \mathbf{0} & \mathbf{0} & \mathbf{0}\\ \mathbf{A}_{AR,F}^{(2)} & \mathbf{0} & \mathbf{0} & \mathbf{0} & \mathbf{A}_{AR,AR}^{(2)} & \mathbf{A}_{AR,WR}^{(2)} & \mathbf{0} & \mathbf{0}\\ \mathbf{A}_{WR,F}^{(2)} & \mathbf{0} & \mathbf{0} & \mathbf{0} & \mathbf{A}_{WR,AR}^{(2)} & \mathbf{A}_{WR,WR}^{(2)} & \mathbf{0} & \mathbf{0}\\ \mathbf{A}_{C,F}^{(3)} & \mathbf{0} & \mathbf{0} & \mathbf{0} & \mathbf{0} & \mathbf{0} & \mathbf{A}_{C,C}^{(3)} & \mathbf{A}_{C,S}^{(3)}\\ \mathbf{A}_{S,F}^{(3)} & \mathbf{0} & \mathbf{0} & \mathbf{0} & \mathbf{0} & \mathbf{0} & \mathbf{A}_{S,C}^{(3)} & \mathbf{A}_{S,S}^{(3)}\end{bmatrix} \quad -$$

mass matrix,

$\mathbf{q}=\begin{bmatrix}\tilde{\mathbf{q}}^{(1)} & \tilde{\mathbf{q}}^{(4)} & \tilde{\mathbf{q}}_{SA}^{(1)} & \tilde{\mathbf{q}}_{WF}^{(1)} & \tilde{\mathbf{q}}^{(5)} & \tilde{\mathbf{q}}_{WR}^{(2)} & \tilde{\mathbf{q}}^{(2)} & \tilde{\mathbf{q}}^{(3)}\end{bmatrix}^T$ - vector of generalized coordinates of the system,

$\mathbf{\Phi}=\begin{bmatrix}\mathbf{0} & \mathbf{0} & 0 & 1 & \mathbf{0} & \mathbf{0} & \mathbf{0} & \mathbf{0} & \mathbf{0}\\ \mathbf{0} & \mathbf{0} & 1 & 0 & \mathbf{0} & \mathbf{0} & \mathbf{0} & \mathbf{0} & \mathbf{0}\end{bmatrix}^T$ - constraints matrix,

$\mathbf{f}=\begin{bmatrix}\mathbf{f}_F^{(1)}+\mathbf{f}_F^{(2)}+\mathbf{f}_F^{(3)} & \mathbf{f}_{AF}^{(1)} & \mathbf{f}_{SA}^{(1)} & \mathbf{f}_{WF}^{(1)} & \mathbf{f}_{AR}^{(2)} & \mathbf{f}_{WR}^{(2)} & \mathbf{f}_C^{(3)} & \mathbf{f}_S^{(3)}\end{bmatrix}^T$ - vector of external, Coriolis and centrifugal forces,

$\mathbf{r}=[r_1 \quad r_2]^T$ - vector of unknown constraint reactions corresponding to torques acting on stub axles connected with the wheels,

$\mathbf{w}=\begin{bmatrix}\ddot{\psi}_{w,1} & \ddot{\psi}_{w,2}\end{bmatrix}^T$ - vector of right sides of constraint equations,

$\psi_{w,i}$ - steering angle of the *i*-th front wheels.

The details of the procedure which lead to form equation (3) with description of elements in matrix **A**and vector **f**are presented in [25]. The dedicated models of road surface and own authors algorithms to determine position of contact point of tire with road surface where acting reaction forces, have been used [25]. To obtain these reactions tire model Fiala was used [9].

3. Optimization task

The main aim of optimization is to select proper vehicle parameters to provide the best possible driving comfort. In the issue in question the decisive variables determine the damping coefficients of the driver's seat sub-assembly in the discrete time moments:

$$\mathbf{d}=[d_1 \quad \ldots \quad d_1 \quad \ldots \quad d_{n_d}]^T \tag{4}$$

where:

d_i- value of driver's seat damping coefficient,

n_d- number of the discrete timestamps.

Spline functions of the first degree were used to obtain a continuous function of the decisive variables. Additionally, inequality constraints determining the minimum and maximum values of the damping coefficients were considered:

$$d_{min} \leq d_i \leq d_{max} \tag{5}$$

These constraints were taken into account in the optimization task by the external penalty function [18, 19], of which value was added to the objective function minimized:

$$\zeta_i(\mathbf{d}) = \begin{cases} 0 & \text{for} \quad g_i(\mathbf{d}) \leq 0 \\ C_{1,i} e^{C_{2,i} g_i(\mathbf{d})} & \text{for} \quad g_i(\mathbf{d}) > 0 \end{cases} \tag{6}$$

where:

$g_i(\mathbf{d}) \leq 0$ dla $i = 1, \ldots, n_g$ -the inequality constraint defined on basis of (5),

n_g -a number of the inequality constraints,

$C_{1,i}$, $C_{2,i}$- weights selected empirically.

In the optimization process there were separate analyses made in which the following Root Mean Quad (RMQ) of the driver seat acceleration were minimized:

$$\Omega(\mathbf{d}, \ddot{\mathbf{q}}) = \frac{C}{t_e} \sqrt[4]{\int_0^{t_e} \left[\ddot{\tilde{z}}^{(3)}(t)\right]^4 dt} + \sum_{i=1}^{n_g} \zeta_i(\mathbf{d}) \rightarrow \min \tag{7}$$

where:

C- weight selected empirically,

t_e- simulation duration.

The problem was solved by the Genetic Algorithm (GA) and Distributed Multi-population Genetic Algorithm (DMPGA). In both method the real-value representation of genes in the chromosome was used [16]. Additional selection, one-point crossover and uniform mutation have been used as genetic operators [16, 27]. The domain of the evolution methods is to find the global extreme in the state space. The classical methods are characterized by determining the extremum in a more precise way, however, they are prone to local extrema and strongly depend on a starting point. An important element deciding about the selection of the specific optimization method is its convergence. Since pseudo-random numbers are used the computational intelligence methods should be executed a few times to achieve the desired solution accuracy. It is connected with prolongation of computation time which in the case of the dynamic optimization where in each step of the optimization procedure the dynamic equations of motion should be integrated in the entire time interval, is usually long. Use of parallel and distributed computing is one of the possibilities to shorten computing time. Since there is an easy access to the computing units having the multi-core processors the parallel computing can be made on the common use units without using the dedicated computing centers. The discussed method of the modification of the classic genetic algorithm consists in using resources of a single unit for

parallel computing in which calculations of lots of populations making parallel computing are made. The populations after each generation exchange the data with each other in a form of the best individuals (fig. 2a).

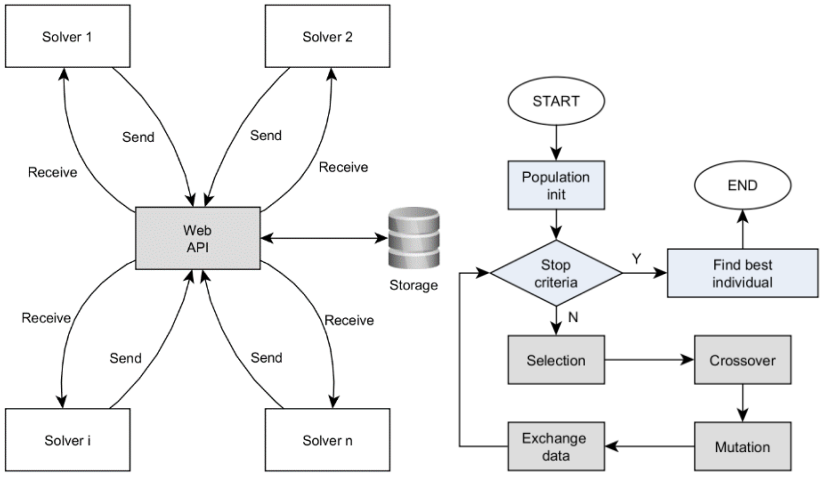

a) b)

Figure 2. DMPGA a) general architecture, b) flowchart.

Such an approach allows better matching of population to be obtained in each computing node and is an additional form of entering a new genetic material into the population. From the genetic point of view the presented method can be called a new additional genetic operator being a complement of the classical operators (fig. 2b). In the presented approach the computations can be moved to the additional computing units being the nodes of the computing luster using possibilities of distributed computing. In this article a comparison of the genetic algorithm in the classical form and its variation (DMPGA) activated on one computing unit with use of lots of instances of the computing application. The results of the numerical simulations performed for the selected road case and a comparison of the results obtained while conducting the numerical simulations for an objective function and the decisive variables are presented further in the article.

4. Calculation results

A case in which a vehicle driving with a constant velocity drives over an obstacle in a form of speed bumps of 0.06 m height is presented in fig. 3.

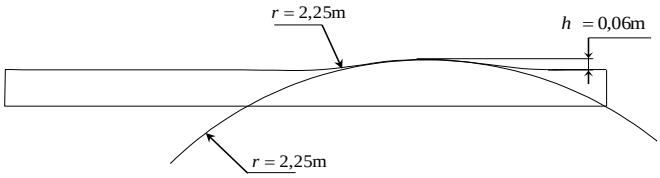

Figure 3. The profile of the analyzed speed bump.

An object of the investigation was to determine the optimal coefficients providing a reduction of the driver's seat vibrations while performing the maneuver. In the numerical simulations it has been assumed that the maneuver lasted 3 sec. in which the vehicle drove over the obstacle (the speed bump) with the front and rear wheels. Constant velocity equal to 10 km/h, provided by controlling the driving torque moments using PID regulator [25], was assumed. The physical parameters of the vehicle necessary to perform the simulation were taken from work [25]. The driver model was accounted in the calculations and dynamic equations of motion as additional mass of 80 kg weight joined with the driver's seat. The constant step Runge-Kutta method of 4-th order [19] was used to integrate equations of motion in each optimization step. The minimal and maximal values of the damping coefficients being inequality constraints were taken $d_{z,min} = 10$ Ns/m and $d_{z,max} = 4000$ Ns/m, respectively. The mathematical model, the mechanism of generating dynamic equations of motion, appropriate integration methods and optimization algorithms were recorded in the proprietary computer program in C++ using the techniques of object-oriented programming. The server was also storage of the data made in technology ASP.NET Web API with use of language C#. The calculations were made on one computing cluster node with use of two parallel activated instances of an application performing optimization computing and sending the results to the global store. The calculations were made for a variable number of the individuals in the population (from 10 to 50). The DMPGA computing results were compared with the results obtained by the classical genetic algorithm [27].

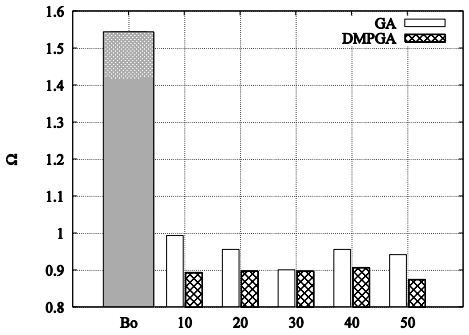

Figure 4. Values of the objective function for both GA and DMPGA.

In fig. 4 values of the objective function are presented for the calculations by methods GA, DMPGA, including the reference value without optimization. The following conclusions can be drawn by analyzing fig. 4:

- optimization with use of the DMPGA method allowed obtaining a lower value of the objective function than in the case of GA use ,
- in majority of cases the value obtained of the objective function is lower than while using the classical optimization method (e.g. Variable Metric Method), including the hybrid methods [27],
- An application of the DMPGA method even on the single node of the computing cluster, due to use of the parallel computing, does not cause computing time prolongation.

Furthermore, owing to the genetic material exchange between the parallel populations the computations by the DMPGA method:

- are characterized by a great repeatability,
- are less susceptible to a number of individuals in the population,
- enable to obtain better results in the case of a single activation of calculations than an equivalent number of separate activations of the classical genetic algorithm.

Courses of the decisive variables for (a) the best and the worst (b) computing result are presented in fig. 5.

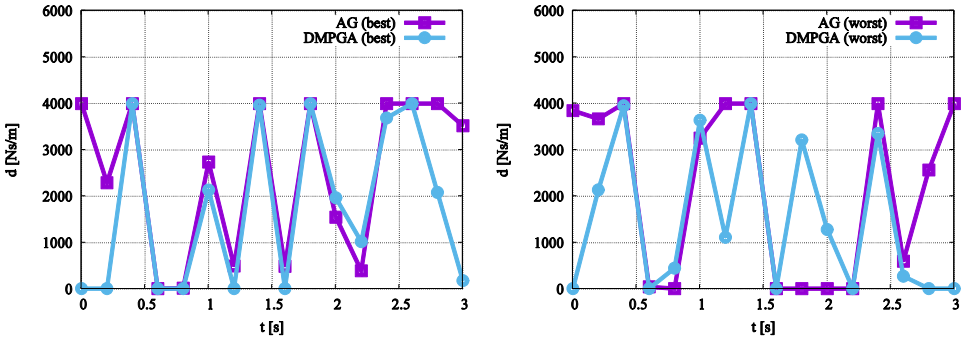

a) b)

Figure 5. Courses of the decisive variables (damping) of the driver's seat obtained in the optimization process.

Big differences between the courses of the decisive variables can be noticed in the show examples. In spite of the differences in the values and the decisive variable courses the subsequent figures show that their usage in the sub-assembly of an active suspension of the seat driver yields desirable effects. Courses of the driver's seat acceleration for the best (a) and the worst (b) result of the minimized functional are presented in fig 6.

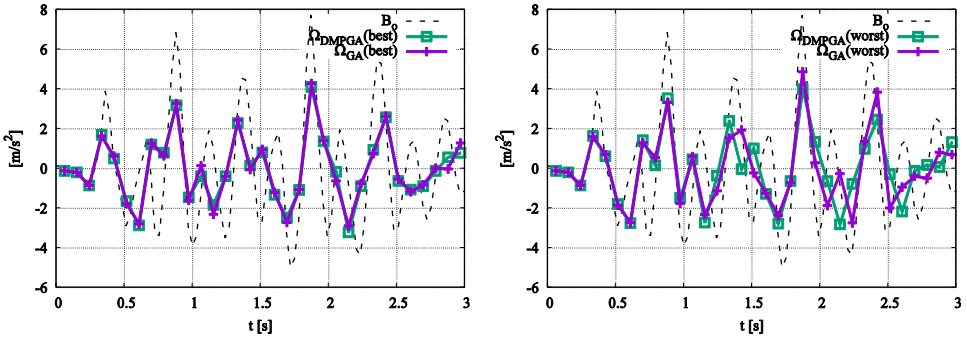

a) b)

Figure 6. Courses of the driver's seat acceleration of the optimization.

The courses presented in fig. 6 confirm that the results obtained by the DMPGA method casus an increase in comfort of a driver while performing a maneuver. In the case of the best result a significant difference can be noticed comparing to the course with use of the GA classical method.

5. Conclusions

The article presents a solution of selecting the parameters of active damping of the driver's seat using the dynamic optimization, by integrating an equation of motion of the vehicle in each iteration. The DMPGA method, consisting in combining the results obtained from the evolution method with sharing best chromosomes with other populations was used in the calculations. It facilitated to find the global minimum of the objective function by using features of these optimization methods. The results indicate that use of the distributed method enabled to obtain better results than use of the presented GA methods run separately one by one. According to the authors any improvement is important in this type of issues due to their complexity and has a direct influence on driver's feeling of comfort. The calculations were made for the selected road maneuver with the obstacle in a form of the speed bump. The numerical analyses also indicate that with an increase in the acceleration caused by road unevenness, the dynamical optimization conducted properly can improve significantly driving comfort of a driver. The use of the method in question does not have an impact on worsening of the optimization process efficiency, it leads to acceptable results, even in the case of using a few individuals in the population. Furthermore, it can be implemented even on personal computers without using the dedicated computing clusters. It should be emphasized that the performed studies deal with one road maneuver and a shape of the speed bump. However, authors conducted a number of other simulations taking into account the different types of road unevenness and speed. The presented procedure algorithm is universal and can be applied in other vehicle sub-assemblies and multi-body systems. In this article the presented algorithm improves significantly driving comfort of a

special vehicle driver, although due to long time of calculations it can be used only to verify the existing controllers.

References

[1] Abbas W., Abouelatta O., El-Azab M., M. El-Saidy, Megahed A., *Genetic algorithms for the optimal vehicle's driver-seat suspension design*, Journal of Mechanics Engineering and Automation 1, 2011, 44-52.

[2] Abbas W., Abouelatta O., El-Azab M., Megahed A.*Genetic algorithms for the optimal vehicle's driver-seat suspension design*, Ain Shams Journal of Engineering Physics and Mathematics, Vol. 2, 2009, pp. 17-29.

[3] Adamiec-Wójcik I., Awrajcewicz J., Grzegożek G., Wojciech S., *Dynamics of articulated vehicles by means of multibody methods*, Dynamical systems : mathematical and numerical approaches, 2015, pp. 11-20.

[4] Alshraideh M., Tahat L.*Multiple-Population Genetic Algorithm for Solving Min-Max Optimization Problems*, International Review on Computers and Software (I.RE.CO.S.), Vol. 10, N. 1, 2015, pp. 9-19.

[5] Augustynek K., Warwas K., An application of PSO method in a motion optimization of a passenger car, Modelowanie Inżynierskie, Vol. 27 No. 58, 2016, pp. 5-12.

[6] Augustynek K., Warwas K. *Real-time drive functions optimisation of the satellite by using MLP and RBF neural network*, Dynamical systems : control and stability, 2015, pp. 53-64.

[7] Cheng H., Yang S. *Multi-population Genetic Algorithms with Immigrants Scheme for Dynamic Shortest Path Routing Problems in Mobile Ad Hoc Networks*, EvoApplications 2010: Applications of Evolutionary Computation, 2010, pp. 562-571.

[8] Chimote K., Gupta M.*Integrated Approach Of Ergonomics And Fem Into Truck Drivers Seat Comfort*, 1st International and 16th National Conference on Machines and Mechanisms, IIT Roorkee, 2013, pp. 183-188.

[9] Fiala E.*Leteral forces at the rolling pneumatic tire*, Technische Hochschule, 1954.

[10] Gong D., Zhou Y., Multi-population Genetic Algorithms with Space Partition forMulti-objective Optimization Problems, IJCSNS International Journal of Computer Science and Network Security, VOL.6 No.2A, 2006, pp. 52-57.

[11] Grzegożek W., Adamiec-Wójcik I., Wojciech S.*Komputerowe Modelowanie Dynamiki Pojazdów Samochodowych*, Wydawnictwo Politechniki Krakowskiej, 2003.

[12] Gupta R., Sonawane V., Sudhakar D. *Optimization of vehicle suspension system using genetic algorithm*, International Journal of Mechanical Engineering and Technology (IJMET), Vol. 6, 2015, pp. 47-55.

[13] Holen P., Thorvald B.*Possibilities and limitations with distributed damping in heavy vehicles*,Vehicle System Dynamics Supplement 41, 2004, pp. 172-181.

[14] Kommenda M., Affenzeller M., Kronberger G., Burlacu B., Winkler S. *Multi-Population Programming with Data Migration for Symbolic Regression*, Computational Intelligence and Efficiency in Engineering System, Springer, Chapter 6, 2015.

[15] Lozia Z., Zdanowicz P.*Optimization of damping in the passive automotive suspension system with using two quarter-car models*, Scientific Conference on Automotive Vehicles and Combustion Engines (KONMOT 2016), Vol. 148, No. 1, 2016.

[16] Michalewicz Z., *Genetic Algorithms + Data Structures = Evolution Programs*, Springer Science & Business Media, 2013.

[17] Mircheski I., Kandikjan T., Sidorenko S., *Comfort analysis of vehicle driver's seat through simulation of the sitting process*, Tehnički vjesnik 21, 2014, pp. 291-298.

[18] Paulavičius R., Žilinskas J.*Simplicial Global Optimization*, Springer-Verlag New York, 2014.

[19] Press W., Teukolsky W., Vetterling S., Flannery W. B.*Numerical Recipes 3rd Edition: The Art of Scientific Computing*, Cambridge University Press, Cambridge, 2007.

[20] Rao K., Kumar S.*Modeling and Simulation of Quarter Car Semi Active Suspension System Using LQR Controller*, Proceedings of the 3rd International Conference on Frontiers of Intelligent Computing: Theory and Applications (FICTA), Springer-Verlag, 2015, Vol. 1, pp. 441-448.

[21] Sammonds G., Fray M., Mansfield N.*Overall car seat discomfort onset during long duration driving trials*, Advances in Physical Ergonomics and Human Factors Part II, AHFE Conference Books, 2014, pp. 25-35.

[22] Savaresi S., Poussot-Vassal C., Spelta C., Sename O., Dugard L. Semi-Active Suspension Control Design for Vehicles, Elsevier Ltd., 2010.

[23] Silva M., Silva J., Motta Toledo C., Williams B. *A Hybrid Multi-Population Genetic Algorithm for UAV Path Planning*, 16 Proceedings of the Genetic and Evolutionary Computation Conference 2016, pp. 853-860.

[24] Song C., Zhao Y., Wang L.*Design of active suspension based on genetic algorithm*, Conference on Industrial Electronics and Applications, 2008, pp. 162-167.

[25] Tengler S.*Analiza dynamiki samochodów specjalnych o wysoko położonym środku ciężkości*, PhD Thesis, Faculty of Mechanical Engineering and Computer Science, University of Bielsko-Biala, 2012.

[26] Warwas K., *Analiza i sterowanie ruchem pojazdów wieloczłonowych z uwzględnieniem podatności elementów*, PhD Thesis, Faculty of Mechanical Engineering and Computer Science, University of Bielsko-Biala, 2009.

[27] Warwas K., Tengler S. *A hybrid optimization method to improve driver's comfort*, 2017 IEEE International Conference on INnovations in Intelligent SysTems and Applications, 2017, pp. 73-78.

[28] Warwas K, Tengler S. *Dynamic Optimization of Multibody System Using Multithread Calculations and a Modification of Variable Metric Method*, ASME. J. Comput. Nonlinear Dynam. 2017;12(5):051031-051031-9. doi:10.1115/1.4037104.

[29] Zhou Y., Zhou L., Wang Y., Yang Z., Wu J. *Application of Multiple-Population Genetic Algorithm in Optimizing the Train-Set Circulation Plan Problem*, Hindawi, Volume 2017 (2017), Article ID 3717654 (14 pages), https://doi.org/10.1155/2017/3717654.

Szymon Tengler, Ph.D.: University of Bielsko-Biała, Bielsko-Biała Department of Computer Science and Engineering, Willowa 2, 43-00 Bielsko-Biala, Poland (*stengler@ath.bielsko.pl*).

Kornel Warwas, Ph.D.:University of Bielsko-Biała, Bielsko-Biała Department of Computer Science and Engineering, Willowa 2, 43-00 Bielsko-Biala, Poland (*kwarwas@ath.bielsko.pl*).

Dynamics and control of a truck-mounted crane with flexible jib

Andrzej Urbaś, Adam Jabłoński, Jacek Kłosiński, Krzysztof Augustynek

Abstract The load oscillations carried by crane devices have a significant influence on their work. Especially oscillations which remain after working motion of the crane are undesirable. The mathematical model for dynamics analysis of a truck-mounted crane is presented in the paper. The proposed model is used to control problem of a crane. The dynamics equations of motion are derived from the Lagrange equations using the formalism joint coordinates, homogeneous transformation matrices. The flexibility of a jib and friction in joints are taken into account in the dynamics model. The rigid finite element method is applied to modeling of the flexible links of the crane. Friction in the joints are modelled by means of the LuGre friction model. The numerical results obtained from following control system of a selected working motion of the crane are presented in the paper. The working motion assures the minimization of the tangent component of the load oscillations. In proposed control model this component is compared with assumed set point value. The obtained controlling error is used to compensate driving torques.

Nomenclature

g	–	acceleration of gravity
$m^{(c,p)}$	–	mass of link p
$m^{(l)}$	–	mass of load l
n_{dof}	–	number of generalised coordinates describing the motion of the crane
$n_{dof}^{(l)}$	–	number of generalised coordinates describing the motion of link l with respect to reference system
n_{dr}	–	number of drives
n_l	–	number of links
n_s	–	number of supports
$s^{(d,p)}, d^{(d,p)}$	–	stiffness and damping coefficient of drive p
$s^{(r)}, d^{(r)}$	–	stiffness and damping coefficient of the hoist rope
$s_\alpha^{(s,i)}, d_\alpha^{(s,i)}$	–	stiffness and damping coefficient of support i in α direction
$t_{dr}^{(d,p)}$	–	driving torque of link p
$t_f^{(d,p)}$	–	friction torque in revolute joint
$\mathbf{r}_P^{(c,p)}$	–	vector of position of point P defined in the local coordinate system of link c, p
$\mathbf{H}^{(c,p)}$	–	pseudo-inertia matrix of link c, p

$\mathbf{T}^{(c,p)}$ – homogeneous transformation matrix from the local coordinate system of link p to reference system

$$\mathbf{T}_i^{(c,p)} = \frac{\partial \mathbf{T}^{(c,p)}}{\partial q_i^{(c,p)}}\ ,\ \mathbf{T}_{i,j}^{(c,p)} = \frac{\partial \mathbf{T}_i^{(c,p)}}{\partial q_j^{(c,p)}} = \frac{\partial^2 \mathbf{T}^{(c,p)}}{\partial q_i^{(c,p)} \partial q_j^{(c,p)}}$$

Friction parameters

$\sigma_0^{(d,i)}, \sigma_1^{(d,i)}, \sigma_2^{(d,i)}$ – stiffness, damping and viscous friction coefficients

$\mu_s^{(d,i)}, \mu_k^{(d,i)}$ – static and kinetic friction coefficients

$z^{(d,i)}$ – deflections of bristles which model the flexibility of the contact surfaces

γ – coefficient which describes the geometry of the contact surfaces

PID controller parameters

$k_p^{(d,p)}, k_i^{(d,p)}, k_d^{(d,p)}$ – proportional, integral, and derivative coefficients

$c_t^{(l)}, c_n^{(l)}$ – tangent and normal component of the load swing

$T^{(l)}, \omega^{(l)}$ – period and natural circular frequency of the load swing

1. Introduction

The sway angle of the transferred load during and after the crane's movement is a major hindrance to work, as it can also pose a danger to persons standing in its vicinity. Furthermore, the residual sway at the end of the working motion lengthens the waiting period for the positioning or foundation of the load and can cause damage to the crane or nearby machinery, installation and/or other cargo.

In cranes in which the load is moved in plane motion, e.g. gantries, a properly chosen control method provides limitation to the sway angle during motion and allows to stop the load at the point of destination. Such a control method consists of three phases: the first phase of acceleration, during which the crane load gains speed through movement – the phase ends when both the load and the point of its suspension move in the same direction at the same speed; the second phase, in which the load, along with the entire crane, are moving uniformly; and the third phase, which is a reversal of the first phase (Kłosiński 2005, Sorensen et al. 2007, Kuo and Kang 2014). A method providing a small positional error in the absence of external interference, such as a strong wind burst, can also be used to control the movements, which are a combination of plane motions, e.g. the associated movements of the bridge and the trolley of the crane.

Other methods of motion control of cranes are also used Lee et al. (2006), e.g. using both closed and open control systems (Singhose et al. 2006), taking into account the changing load weight (Lew and Halder 2003), and other parameters of the model (Moradi and Vossoughi 2015, Zhang et al. 2016, Ermidoro et al. 2016) also using control formulas based on fuzzy logic (Trabia et al. 2008, Janusz and Kłosiński 2008, Wu et al. 2016) and neural networks (Toxqui and Li 2006). In control systems, an important role is played by full identification of the crane's mathematical model and the correct

selection of the controller settings; for the fuzzy controller (FLC), a properly formulated rulebase and membership functions have been adopted.

However, the issue is more complicated in the case of a crane's rotation motion, e.g. in slewing crane control, as additional restrictions occur during various stages of movement or to control the crane (Kłosiński 2005, Uchiyama et al. 2013). It is often impossible to completely eliminate the sway angle at the end of the movement as a result of the centrifugal forces and the Coriolis force.

A mathematical model of a truck-mounted crane is presented in this paper, in which the load movements are done by using the slewing motion of the jib, luffing motion and lifting/lowering motion. The flexibility of the truck chassis and the friction in the joints are both taken into account. Numerical studies were conducted to demonstrate the impact of different control strategies and different model parameters on the size of the sway angle, both during movement and after its completion. Identifying the model is the starting point to select a controller and the movement control strategy.

The paper is a continuation of the authors' work (Urbaś 2017, Urbaś et al. 2016) in modeling the dynamics of truck-mounted and grab cranes when taking into account the flexibility of the crane's support, drives and hoist system. The effect of friction on the dynamics of the crane by using different models of friction, including Dahl and LuGre, is also analysed (Awrejcewicz and Olejnik 2005).

2. Mathematical model of the system

Fig.1 shows a simplified model of a crane built of three links ($n_l = 3$). The truck-mounted crane's chassis ($\mathrm{link}1$) is fixed to the ground via four flexible supports $(n_s = 4)$. It is assumed that the crane's links are driven directly by two flexible motors placed in the joints ($n_{dr} = 2$), modelled as driving torques $\mathbf{t}_{dr}^{(d,p)}\Big|_{p=2,3}$. Friction in the joints is taken into account by using the LuGre model (Åström and Canudas-de-Witt 2008).

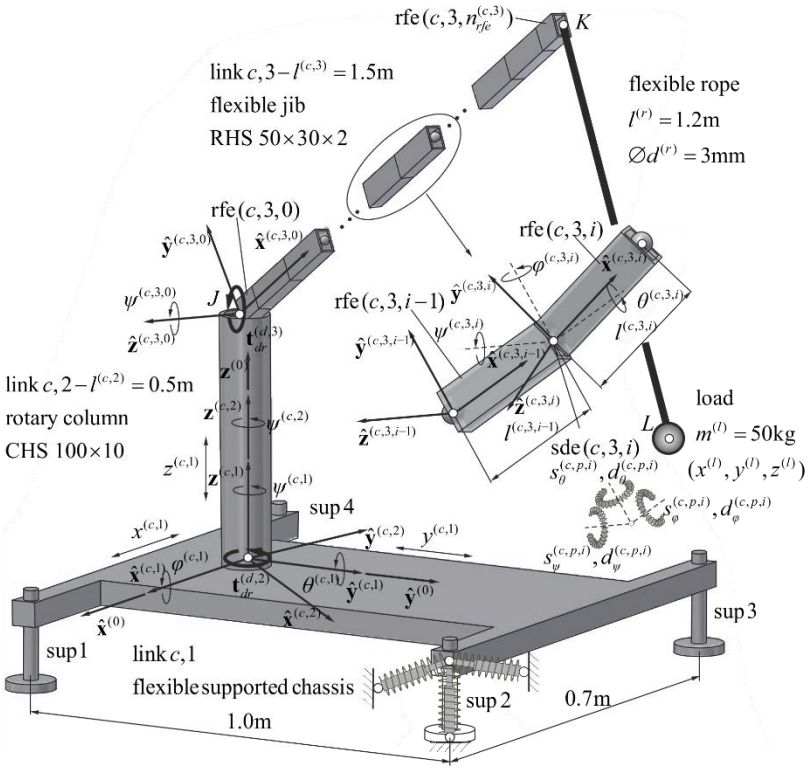

Fig. 1. Model of flexible supported crane

The mathematical model allows to take into account the flexibility of the crane's jib ($\text{link}\,c,3$). Discretisation of the link was made by using the rigid finite element method (Kruszewski et al. 1999) in a modified formula (Wittbrodt et al. 2013) – Fig. 2. In the first stage (primary division), the link is divided into five sections $(n_{div}^{(c,3)}=4)$ of equal length $d^{(c,3)}=\dfrac{l^{(c,3)}}{n_{div}^{(c,3)}}$. The spring-damping features of the link are concentrated in the middle of each segment in the form of a rotational spring-damping element ($n_{sde}^{(c,3)}=4$). As a result of the second stage of discretisation (secondary division), six rigid elements ($n_{rfe}^{(c,3)}=5$) of length $l^{(c,3,i)}=\begin{cases} d^{(c,3)}\big|_{i=1,\ldots,n_{rfe}^{(c,3)}-2} \\ 0.5d^{(c,3)}\big|_{i\in\{0,n_{rfe}^{(c,3)}-1\}} \end{cases}$ interconnected by means of spring-damping elements were obtained.

The formalism of the joint coordinates and homogeneous transformation matrices (Craig 1989) is used to describe the crane's link motions.

The vector of the generalised (joint) coordinates is defined in the following form:

$$\mathbf{q} = \begin{bmatrix} \mathbf{q}^{(c)} \\ \mathbf{q}^{(l)} \end{bmatrix}, \tag{1}$$

where:

$\mathbf{q}^{(c)}$ – vector of generalised coordinates describing the motion of the crane's links,

$\mathbf{q}^{(l)} = q_j^{(l)}{}_{\,j=1,\ldots,n_{dof}^{(l)}} = \begin{bmatrix} x^{(l)} & y^{(l)} & z^{(l)} \end{bmatrix}^T$ – vector of generalised coordinates describing the load's motion.

The motion of link p is defined by vector:

$$\mathbf{q}^{(c,p)}\Big|_{p=1,\ldots,n_l} = q_j^{(c,p)}{}_{\,j=1,\ldots,n_{dof}^{(c,p)}} = \begin{bmatrix} \mathbf{q}^{(c,p-1)} \\ \tilde{\mathbf{q}}^{(c,p)} \end{bmatrix} = \begin{bmatrix} q_j^{(c,p-1)}{}_{\,j=1,\ldots,n_{dof}^{(c,p-1)}} \\ \tilde{q}_j^{(c,p)}{}_{\,j=1,\ldots,n_{dof}^{(c,p)}} \end{bmatrix}, \tag{2}$$

where:

$$\mathbf{q}^{(c,0)} = \varnothing,\ \tilde{\mathbf{q}}^{(c,1)} = \begin{bmatrix} x^{(c,1)} & y^{(c,1)} & z^{(c,1)} & \psi^{(c,1)} & \theta^{(c,1)} & \varphi^{(c,1)} \end{bmatrix}^T,\ \tilde{\mathbf{q}}^{(c,2)} = \begin{bmatrix} \psi^{(c,2)} \end{bmatrix},$$

$$\tilde{\mathbf{q}}^{(c,3)} = \begin{bmatrix} \tilde{\mathbf{q}}^{(c,3,0)^T} & \cdots & \tilde{\mathbf{q}}^{(c,3,i)^T} & \cdots & \tilde{\mathbf{q}}^{(c,3,n_{rfe}^{(c,3)})^T} \end{bmatrix}^T,\ \tilde{\mathbf{q}}^{(c,3,0)} = \begin{bmatrix} \psi^{(c,3,0)} \end{bmatrix},$$

$$\tilde{\mathbf{q}}^{(c,3,i)} = \begin{bmatrix} \psi^{(c,3,i)} & \theta^{(c,3,i)} & \varphi^{(c,3,i)} \end{bmatrix}^T.$$

The homogeneous transformation matrix from the local coordinate system of link p to the reference system is determined according to the relationship:

$$\mathbf{T}^{(c,p)}\Big|_{p=1,\ldots,n_l} = \mathbf{T}^{(c,p-1)}\tilde{\mathbf{T}}^{(c,p)}, \tag{3}$$

where: $\mathbf{T}^{(c,0)} = \mathbf{I}$,

$$\tilde{\mathbf{T}}^{(c,1)} = \begin{bmatrix} \mathrm{c}\psi^{(c,1)}\mathrm{c}\theta^{(c,1)} & \mathrm{c}\psi^{(c,1)}\mathrm{s}\theta^{(c,1)}\mathrm{s}\varphi^{(c,1)} - \mathrm{s}\psi^{(c,1)}\mathrm{c}\varphi^{(c,1)} \\ \mathrm{s}\psi^{(c,1)}\mathrm{c}\theta^{(c,1)} & \mathrm{s}\psi^{(c,1)}\mathrm{s}\theta^{(c,1)}\mathrm{s}\varphi^{(c,1)} + \mathrm{c}\psi^{(c,1)}\mathrm{c}\varphi^{(c,1)} \\ -\mathrm{s}\theta^{(c,1)} & \mathrm{c}\theta^{(c,1)}\mathrm{s}\varphi^{(c,1)} \\ 0 & 0 \end{bmatrix}$$

$$\begin{bmatrix} \mathrm{c}\psi^{(c,1)}\mathrm{s}\theta^{(c,1)}\mathrm{c}\varphi^{(c,1)} + \mathrm{s}\psi^{(c,1)}\mathrm{s}\varphi^{(c,1)} & x^{(c,1)} \\ \mathrm{s}\psi^{(c,1)}\mathrm{s}\theta^{(c,1)}\mathrm{c}\varphi^{(c,1)} - \mathrm{c}\psi^{(c,1)}\mathrm{s}\varphi^{(c,1)} & y^{(c,1)} \\ \mathrm{c}\theta^{(c,1)}\mathrm{c}\varphi^{(c,1)} & z^{(c,1)} \\ 0 & 1 \end{bmatrix},$$

$$\tilde{\mathbf{T}}^{(c,2)} = \begin{bmatrix} \mathrm{c}\psi^{(c,2)} & -\mathrm{s}\psi^{(c,2)} & 0 & 0 \\ \mathrm{s}\psi^{(c,2)} & \mathrm{c}\psi^{(c,2)} & 0 & 0 \\ 0 & 0 & 1 & 0 \\ 0 & 0 & 0 & 1 \end{bmatrix}, \tilde{\mathbf{T}}^{(c,3,0)} = \begin{bmatrix} \mathrm{c}\psi^{(c,3,0)} & -\mathrm{s}\psi^{(c,3,0)} & 0 & 0 \\ 0 & 0 & -1 & 0 \\ \mathrm{s}\psi^{(c,3,0)} & \mathrm{c}\psi^{(c,3,0)} & 0 & l^{(c,3,0)} \\ 0 & 0 & 0 & 1 \end{bmatrix},$$

$$\tilde{\mathbf{T}}^{(c,3,i)}\Big|_{i=1,\ldots,n_{rfe}^{(c,3)}} = \begin{bmatrix} \mathrm{c}\psi^{(c,3,i)}\mathrm{c}\theta^{(c,3,i)} & \mathrm{c}\psi^{(c,3,i)}\mathrm{s}\theta^{(c,3,i)}\mathrm{s}\varphi^{(c,3,i)} - \mathrm{s}\psi^{(c,3,i)}\mathrm{c}\varphi^{(c,3,i)} \\ \mathrm{s}\psi^{(c,3,i)}\mathrm{c}\theta^{(c,3,i)} & \mathrm{s}\psi^{(c,3,i)}\mathrm{s}\theta^{(c,3,i)}\mathrm{s}\varphi^{(c,3,i)} + \mathrm{c}\psi^{(c,3,i)}\mathrm{c}\varphi^{(c,3,i)} \\ -\mathrm{s}\theta^{(c,3,i)} & \mathrm{c}\theta^{(c,3,i)}\mathrm{s}\varphi^{(c,3,i)} \\ 0 & 0 \end{bmatrix}$$

$$\begin{bmatrix} \mathrm{c}\psi^{(c,3,i)}\mathrm{s}\theta^{(c,3,i)}\mathrm{c}\varphi^{(c,3,i)} + \mathrm{s}\psi^{(c,3,i)}\mathrm{s}\varphi^{(c,3,i)} & l^{(c,3,i)} \\ \mathrm{s}\psi^{(c,3,i)}\mathrm{s}\theta^{(c,3,i)}\mathrm{c}\varphi^{(c,3,i)} - \mathrm{c}\psi^{(c,3,i)}\mathrm{s}\varphi^{(c,3,i)} & 0 \\ \mathrm{c}\theta^{(c,3,i)}\mathrm{c}\varphi^{(c,3,i)} & 0 \\ 0 & 1 \end{bmatrix}.$$

The equations of motion were derived by using the Lagrange equations of the second kind and algorithms presented in monographs (Jurevič 1984, Wittbrodt et al. 2013):

$$\begin{aligned} \dot{\mathbf{z}} &= \mathbf{LuGre}\ t, \mathbf{q}^{(c)}, \mathbf{z}\ , \\ \mathbf{M}\ddot{\mathbf{q}} &= \mathbf{e} + \mathbf{f}_s + \mathbf{t}_{dr} - \mathbf{t}_f , \end{aligned} \tag{4}$$

where:

$$\mathbf{LuGre}_{i\ \ i=1,2} = \dot{q}_j^{(c)} \left(1 - \frac{\sigma_0^{(d,i+1)} z^{(d,i+1)} \operatorname{sgn}\ \dot{q}_j^{(c)}}{\mu_k^{(d,i+1)} + \ \mu_s^{(d,i+1)} - \mu_k^{(d,i+1)}\ \exp\left(- \left(\frac{\dot{q}_j^{(c)}}{\dot{q}_{S,j}^{(c)}} \right)^{\gamma} \right)} \right),$$

$$\mu^{(d,i+1)} = \sigma_0^{(d,i+1)} z^{(d,i+1)} + \sigma_1^{(d,i+1)} \dot{z}^{(d,i+1)} + \sigma_2^{(d,i+1)} \dot{q}_j^{(c)},$$

$$\mathbf{M} = \begin{bmatrix} \mathbf{M}^{(c)} & \mathbf{0} \\ \mathbf{0} & \mathbf{M}^{(l)} \end{bmatrix},\ \mathbf{M}^{(c)} = \begin{bmatrix} \mathbf{M}_{1,1}^{(c)} & \cdots & \mathbf{M}_{1,j}^{(c)} & \cdots & \mathbf{M}_{1,n_l}^{(c)} \\ \vdots & \ddots & \vdots & \iddots & \vdots \\ \mathbf{M}_{i,1}^{(c)} & \cdots & \mathbf{M}_{i,j}^{(c)} & \cdots & \mathbf{M}_{i,n_l}^{(c)} \\ \vdots & \iddots & \vdots & \ddots & \vdots \\ \mathbf{M}_{n_l,1}^{(c)} & \cdots & \mathbf{M}_{n_l,1}^{(c)} & \cdots & \mathbf{M}_{n_l,n_l}^{(c)} \end{bmatrix},$$

$$\mathbf{M}^{(l)} = \operatorname{diag}\ \ m^{(l)}, m^{(l)}, m^{(l)}\ \ ,$$

$$\mathbf{M}_{i,j}^{(c)} = \sum_{p=\max\{i,j\}}^{n_l} \mathbf{M}_{i,j}^{(c,p)},\ \mathbf{M}_{i,j}^{(c,p)}\Big|_{i,j=1,\ldots,p} = \ m^{(c,p)}_{n_{dof}^{(c,i-1)}+k, n_{dof}^{(c,j-1)}+l\ \ \substack{k=1,\ldots,\tilde{n}_{dof}^{(c,i)} \\ l=1,..,\tilde{n}_{dof}^{(c,j)}}},$$

$$m_{i,j}^{(c,p)} = \operatorname{tr}\ \ \mathbf{T}_i^{(c,p)} \mathbf{H}^{(c,p)}\ \ \mathbf{T}_j^{(c,p)\ \ T}\ \ ,$$

$$\mathbf{e} = \begin{bmatrix} \mathbf{e}^{(c)} \\ \mathbf{e}^{(l)} \end{bmatrix},\ \mathbf{e}^{(c)} = \begin{bmatrix} \mathbf{e}_1^{(c)} \\ \vdots \\ \mathbf{e}_i^{(c)} \\ \vdots \\ \mathbf{e}_{n_l}^{(c)} \end{bmatrix},\ \mathbf{e}^{(l)} = \begin{bmatrix} 0 \\ 0 \\ m^{(l)} g \end{bmatrix},\ \mathbf{e}_i^{(c)} = -\sum_{p=i}^{n_l} \mathbf{h}_i^{(c,p)} + \mathbf{g}_i^{(c,p)}\ \ ,$$

$$\mathbf{h}_i^{(c,p)}\Big|_{i=1,\ldots,p} = \left(h^{(c,p)}_{n_{dof}^{(c,i-1)}+k} \right)_{k=1,\ldots,\tilde{n}_{dof}^{(c,i)}},$$

$$h_i^{(c,p)} = \sum_{m=1}^{n_{dof}^{(c,p)}} \sum_{n=1}^{n_{dof}^{(c,p)}} \operatorname{tr}\ \ \mathbf{T}_i^{(c,p)} \mathbf{H}^{(c,p)}\ \ \mathbf{T}_{m,n}^{(c,p)\ \ T}\ \ \dot{q}_m^{(c)} \dot{q}_n^{(c)},$$

$$\mathbf{g}_i^{(c,p)}\Big|_{i=1,\ldots,p} = \left(g^{(c,p)}_{n_{dof}^{(c,i-1)}+k} \right)_{k=1,\ldots,n_{dof}^{(c,i)}},\quad g_i^{(c,p)} = m^{(c,p)} g \mathbf{j}_3 \mathbf{T}_i^{(c,p)} \mathbf{r}_{C^{(c,p)}}^{(c,p)},$$

$$\mathbf{f}_s = \begin{bmatrix} \mathbf{f}_s^{(c)} \\ \mathbf{f}_s^{(l)} \end{bmatrix}, \mathbf{f}_s^{(c)} = \mathbf{f}_s^{(c,s)} + \mathbf{f}_s^{(c,l_f)} + \mathbf{f}_s^{(c,r)}\ ,\ \mathbf{f}_s^{(c,s)} = \begin{bmatrix} -\left(\dfrac{\partial E_{p,s}^{(s)}}{\partial \tilde{\mathbf{q}}^{(c,1)}} + \dfrac{\partial R^{(s)}}{\partial \dot{\tilde{\mathbf{q}}}^{(c,1)}} \right)^T & \mathbf{0} \end{bmatrix}^T ,$$

$$\mathbf{f}_s^{(c,l_f)} = \begin{bmatrix} \mathbf{0} & -\left(\dfrac{\partial E_{p,s}^{(l_f)}}{\partial \tilde{\mathbf{q}}^{(c,3)}} + \dfrac{\partial R^{(l_f)}}{\partial \dot{\tilde{\mathbf{q}}}^{(c,3)}} \right)^T & \mathbf{0} \end{bmatrix}^T ,$$

$$\mathbf{f}_s^{(c,r)} = \left[-\left(\frac{\partial E_{p,s}^{(r)}}{\partial \mathbf{q}^{(c)}} + \frac{\partial R^{(r)}}{\partial \dot{\mathbf{q}}^{(c)}} \right) \right]^T , \mathbf{f}_s^{(l)} = \left[-\left(\frac{\partial E_{p,s}^{(r)}}{\partial \mathbf{q}^{(l)}} + \frac{\partial R^{(r)}}{\partial \dot{\mathbf{q}}^{(l)}} \right) \right]^T ,$$

$$\left(\frac{\partial E_{p,s}^{(s)}}{\partial \tilde{\mathbf{q}}^{(c,1)}} + \frac{\partial R^{(s)}}{\partial \dot{\tilde{\mathbf{q}}}^{(c,1)}} \right) = \sum_{i=1}^{n_s} \left(\ \mathbf{U}^{(s,i)\ T} \mathbf{S}^{(s,i)} \mathbf{U}^{(s,i)} \tilde{\mathbf{q}}^{(c,1)} + \ \mathbf{U}^{(s,i)\ T} \mathbf{D}^{(s,i)} \mathbf{U}^{(s,i)} \dot{\tilde{\mathbf{q}}}^{(c,1)} \right),$$

$$\mathbf{U}^{(s,i)} = \left[\begin{array}{ccc:ccc} 1 & 0 & 0 & 0 & z^{(s,i)} & -y^{(s,i)} \\ 0 & 1 & 0 & -z^{(s,i)} & 0 & x^{(s,i)} \\ 0 & 0 & 1 & y^{(s,i)} & -x^{(s,i)} & 0 \end{array} \right],$$

$$\mathbf{S}^{(s,i)} = \text{diag}\ \ s_x^{(s,i)}, s_y^{(s,i)}, s_z^{(s,i)}\ \ , \mathbf{D}^{(s,i)} = \text{diag}\ \ d_x^{(s,i)}, d_y^{(s,i)}, d_z^{(s,i)}\ \ ,$$

$$\left(\frac{\partial E_{p,s}^{(l_f)}}{\partial \tilde{\mathbf{q}}^{(c,3)}} + \frac{\partial R^{(l_f)}}{\partial \dot{\tilde{\mathbf{q}}}^{(c,3)}} \right) = \mathbf{S}^{(c,3)} \tilde{\mathbf{q}}^{(c,3)} + \mathbf{D}^{(c,3)} \dot{\tilde{\mathbf{q}}}^{(c,3)},$$

$$\mathbf{S}^{(c,3)} = \text{diag}\ \ \mathbf{S}^{(c,3,1)}, \ldots, \mathbf{S}^{(c,3,n_{rfe}^{(c,3)})}\ \ , \mathbf{S}^{(c,3,i)} = \text{diag}\ \ s_\psi^{(c,3,i)}, s_\theta^{(c,3,i)}, s_\varphi^{(c,3,i)}\ \ ,$$

$$\mathbf{D}^{(c,3)} = \text{diag}\ \ \mathbf{D}^{(c,3,1)}, \ldots, \mathbf{D}^{(c,3,n_{rfe}^{(c,3)})}\ \ , \quad \mathbf{D}^{(c,3,i)} = \text{diag}\ \left\{ d_\psi^{(c,3,i)}, d_\theta^{(c,3,i)}, d_\varphi^{(c,3,i)} \right\},$$

$$\frac{\partial E_{p,s}^{(r)}}{\partial q_j^{(c)}} + \frac{\partial R^{(r)}}{\partial \dot{q}_j^{(c)}} = \delta^{(r)} \left(s^{(r)} \frac{e^{(r)}}{l^{(r)}} \mathbf{r}_{KL}^T + d^{(r)} \dot{\mathbf{r}}_{KL}^T \right) \mathbf{J}\mathbf{T}_j^{(c,3)} \mathbf{r}_K^{(c,3)},$$

$$\frac{\partial E_{p,s}^{(r)}}{\partial q_j^{(l)}} + \frac{\partial R^{(r)}}{\partial \dot{q}_j^{(l)}} = -\delta^{(r)} \left(s^{(r)} \frac{e^{(r)}}{l^{(r)}} \mathbf{r}_{KL}^T + d^{(r)} \dot{\mathbf{r}}_{KL}^T \right) \mathbf{j}_j,$$

$$\mathbf{r}_{KL} = \mathbf{J}\ \ \mathbf{r}_K^{(0)} - \mathbf{r}_L^{(0)}\ \ , l^{(r)} = \sqrt{\mathbf{r}_{KL}^T \mathbf{r}_{KL}}, \ e^{(r)} = l^{(r)} - l_0^{(r)}, \ \delta^{(r)} = \begin{cases} 1, & e^{(r)} > 0 \\ 0, & e^{(r)} \le 0 \end{cases},$$

$$\mathbf{J} = \left[\begin{array}{c:c:c:c} 1 & 0 & 0 & 0 \\ 0 & 1 & 0 & 0 \\ 0 & 0 & 1 & 0 \end{array} \right] = \begin{bmatrix} \mathbf{j}_1 \\ \mathbf{j}_2 \\ \mathbf{j}_3 \end{bmatrix}, \ \mathbf{t}_{dr} = \begin{bmatrix} \mathbf{0} & t_{dr}^{(d,2)} + \delta t_{dr}^{(d,2)} & t_{dr}^{(d,3)} + \delta t_{dr}^{(d,3)} & \mathbf{0} \end{bmatrix}^T,$$

$$t_{dr}^{(d,p)} = -\left(\frac{\partial E_{p,s}^{(d,p)}}{\partial q_j^{(c)}} + \frac{\partial R^{(d,p)}}{\partial \dot{q}_j^{(c)}}\right) = -\ s^{(d,p)}\ \ q_{dr,j}^{(c)} - q_j^{(c)}\ \ + d^{(d,p)}\ \ \dot{q}_{dr,j}^{(c)} - \dot{q}_j^{(c)}\quad ,$$

$$q_{dr,j}^{(c,p)} = \begin{cases} q_{in,j}^{(c,p)} + \dfrac{at^3}{(T^{(c,p)})^3} - \dfrac{15at^4}{(T^{(c,p)})^4} + \dfrac{6at^5}{(T^{(c,p)})^5}, & \text{for } t \le T^{(c,p)} \\ q_{fin,j}^{(c)}, & \text{for } t > T^{(c,p)} \end{cases}, \quad a = q_{fin,j}^{(c,p)} - q_{in,j}^{(c,p)},$$

$$\delta t_{dr}^{(d,p)} = k_p^{(d,p)} e_\alpha^{(l)} + k_i^{(d,p)} \int_0^t e_\alpha^{(l)} \mathrm{d}t + k_d^{(d,p)} \frac{\mathrm{d}e_\alpha^{(l)}}{\mathrm{d}t},$$

$$e_\alpha^{(l)}\Big|_{\alpha \in\ t,n} = w_\alpha^{(l)}(t) - c_\alpha^{(l)},\ w_\alpha^{(l)}(t) = \begin{cases} -A_\alpha^{(l)} \sin \omega^{(l)} t, & t \le 0.5T^{(l)} \\ 0, & 0.5T^{(l)} < t \le 1.5T^{(l)} \\ A_\alpha^{(l)} \sin \omega^{(l)}\ \ t - 1.5T^{(l)}\ , & 1.5T^{(l)} < t \le 2T^{(l)} \\ 0, & t > 2T^{(l)} \end{cases}$$

$$T^{(l)} = 2\pi\sqrt{\frac{l^{(r)}}{g}},\ \omega^{(l)} = \frac{2\pi}{T^{(l)}},\ \mathbf{t}_f = \left[\mathbf{0} \quad t_f^{(d,2)} \quad t_f^{(d,3)} \quad \mathbf{0}\right]^T.$$

Dynamics equations of motion have been integrated using constant step-size Runge-Kutta 4th order method.

3. Numerical results

The parameters of the drives, supports and PID controller settings are presented in Tables 1,2 and 3 respectively.

Table 1. Parameters of the drives and friction

dr p		2	3
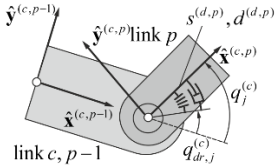	$s^{(d,p)}$[N mrad^{-1}]	10^5	
	$d^{(d,p)}$[N msrad^{-1}]	$7 \cdot 10^2$	
	$q_{in,j}^{(c,p)}$[°]	0	30
	$q_{fin,j}^{(c,p)}$[°]	90	60
	$\mu_s^{(d,p)}$	0.2	
	$\mu_k^{(d,p)}$	0.1	

	$\dot{q}_{S,j}^{(c)}[\mathrm{rads}^{-1}]$	10^{-3}
	$\sigma_0^{(d,p)}[\mathrm{Nmrad}^{-1}]$	10^3
	$\sigma_1^{(d,p)}[\mathrm{Nmsrad}^{-1}]$	5
	$\sigma_2^{(d,p)}[\mathrm{Nmsrad}^{-1}]$	0
	γ	2

Table 2. Parameters of the supports

$\sup i$	1	2	3	4
$x^{(s,i)}$[m]	0.35	0.35	−0.35	−0.35
$y^{(s,i)}$[m]	−0.325	0.625	0.625	−0.325
$z^{(s,i)}$[m]	−0.23			
$l_{\alpha,0}^{(s,i)}\big\vert_{\alpha\in x,y,z}$ [m]	0			
$s_\alpha^{(s,i)}\big\vert_{\alpha\in x,y}$ [$\mathrm{N\,m^{-1}}$]	10^4			
$s_z^{(s,i)}$[$\mathrm{N\,m^{-1}}$]	10^6			
$d_\alpha^{(s,i)}\big\vert_{\alpha\in x,y}$ [$\mathrm{Ns\,m^{-1}}$]	10^2			
$d_z^{(s,i)}$[$\mathrm{Ns\,m^{-1}}$]	10^3			

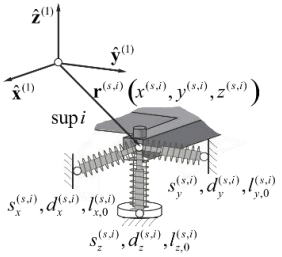

Table 3. Parameters of the PID controller

jib	friction	symbol	$k_p^{(d,2)}$	$k_i^{(d,2)}$	$k_d^{(d,2)}$	$A_t^{(l)}$[m]
rigid	omitted	rig	10^5	10	10^3	
	included	rig_f	10^7	0	10^3	0.06
flexible	omitted	flex	10^{-2}	10^{-2}	10^{-4}	

In simulations dynamics of the crane with rigid links without friction (rig) and with friction in joints (rig_f) are analysed. In the case when jib's flexibility is taken into account friction in joints is omitted (flex). Time courses of tangent and normal components of the load position obtained for all analysed cases are presented in Fig. 2. Fig. 3 presents time courses of driving torques realizing assumed time course of the tangent component of the load position. The driving torque of the second link ($t_{dr}^{(d,2)}$) contains correction of torque ($\delta t_{dr}^{(d,2)}$) resulting from PID controller.

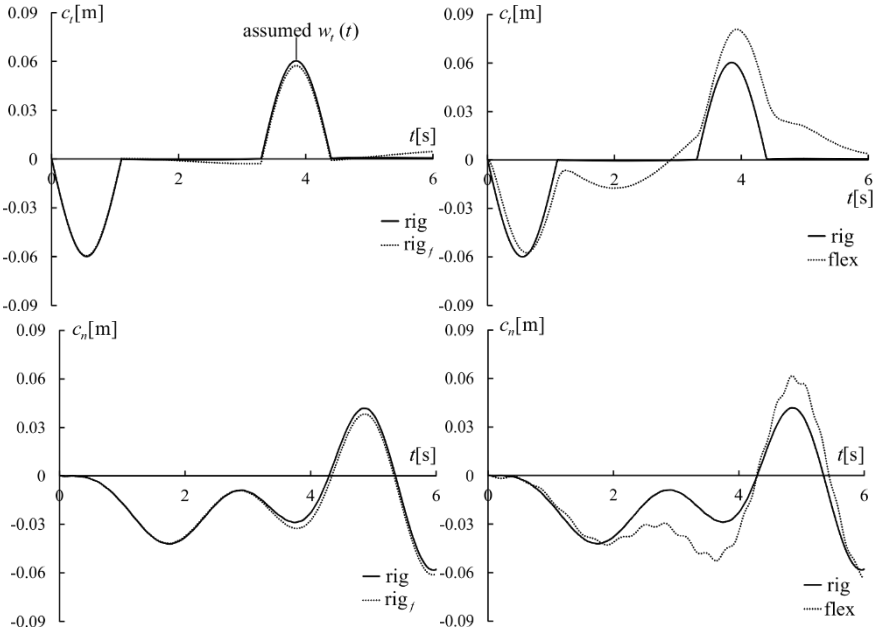

Fig. 2. Time courses of tangent and normal component of the load position

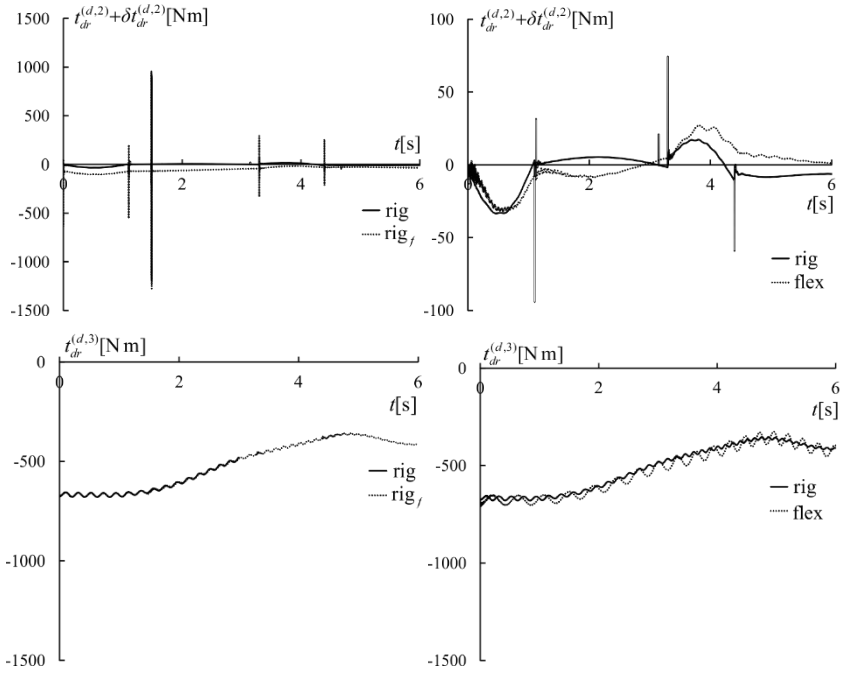

Fig. 3. Time courses of driving torques

The numerical calculations show that PID controller can be used in order to compensate influence of friction in joints and jib's flexibility on load motion. It can be observed significant impulses in time courses of driving torques when friction is taken into account. Better results of control are obtained when jib's flexibility is omitted.

4. Conclusions

The paper presents a mathematical model of a truck-mounted crane which was designed for dynamics analysis. The model takes into account the flexibility of the crane's support, one of the links, the drives and friction in the joints. The rigid finite element method was used for discretisation in order to take into account the flexibility of the link. The friction coefficients were determined by using the LuGre model. The results of the numerical calculations show that PID controller can be applied to control load motion for different crane's models. The control of crane with rigid links and friction in joints gives better results than those with flexible links. According to the authors, the model presented here of a truck-mounted crane and the results of the numerical simulations can aid in the design process of these devices, especially in the selection of drive systems and control methods.

References

[1] Åström, K.J., Canudas-de-Witt, C.: Revisiting the LuGre model. IEEE Control Systems Magazine, Institute of Electrical and Electronics Magazine 28(6), 101–114 (2008)

[2] Awrejcewicz, J., Olejnik, P.: Analysis of Dynamic Systems With Various Friction Laws. Applied Mechanics Reviews 58(6), 389–411 (2005). doi:10.1115/1.2048687

[3] Craig, J.J.: Introduction to robotics. Mechanics and control. Addison-Wesley Publishing Company, Inc. (1989)

[4] Ermidoro, M., Cologni, A.L., Formentin, S. Previdi, F.: Fixed-order gain-scheduling anti-sway control of overhead bridge cranes. Mechatronics 39, 237–247 (2016)

[5] Janusz, J., Kłosiński, J.: Fuzzy controlling of a mobile crane ensuring stable work. Acta Mechanica Slovaca 3-C, 215–222 (2008)

[6] Jurevič, E.I. (ed.): Dynamics of robot control. Nauka, Moscow (1984) (in Russian)

[7] Kłosiński, J.: Swing-free stop control of the slewing motion of the mobile crane. Control Eng. Pract. 13, 451–460 (2005)

[8] Kruszewski, J., Sawiak, S., Wittbrodt, E.: The rigid finite element method in dynamics. Science and Technical Publishers, Warsaw (1999) (in Polish).

[9] Kuo, TY.T., Kang, SC. J.: Control of fast crane operation. Automation in Construction 42, 25–35 (2014)

[10] Lee, H.H., Liang, Y., Segura, D.: A sliding-mode anti-swing trajectory control for overhead cranes with high-speed load hoisting. J. Dyn. Syst. Meas. Control-Trans. ASME 128, 842–845 (2006)

[11] Lew, J.Y., Halder, B.: Experimental study of anti-swing crane control for a varying load. Proceedings of American Control Conference, V. 2, 1434–1439, Denver, Colorado, USA, 4-6 June 2003

[12] Moradi, H., Vossoughi, G.: State estimation, positioning and anti-swing robust control of traveling crane-lifter system. Applied Mathematical Modelling 39, 6990–7007 (2015)

[13] Sorensen, K.L., Singhose, W., Dickerson, S.: A controller enabling precise positioning and sway reduction in bridge and gantry cranes. Control Eng. Pract. 15, 825–837 (2007)

[14] Singhose, W., Lawrence, J., Sorensen, K., Kim, D.: Applications and educational uses of crane oscillation control. FME Trans. 34, 175–183 (2006)

[15] Toxqui, R., Yu, Li, X.: Anti-swing control for overhead crane with neural compensation. Proceedings of the International Joint Conference on Neural Networks, Vancouver, BC, Canada 16-21 July 2006

[16] Trabia, M.B., Renno, J.M., Moustafa, K.A.F.: Generalized design of an anti-swing fuzzy logic controller for an overhead crane with hoist. J. Vib. Control. 14, 319–346 (2008)

[17] Uchiyama, N., Ouyang, H., Sano, S.: Simple rotary crane dynamics modeling and open-loop control for residual load sway suppression by only horizontal boom motion. Mechatronics 23, 1223–1236 (2013)

[18] Urbaś, A.: Computational implementation of the rigid finite element method in the statics and dynamics analysis of forest cranes. Applied Mathematical Modelling 46, 750–762 (2017). doi.org/10.1016/j.apm.2016.08.006

[19] Urbaś, A., Stanclik, G., Kłosiński, J., Harlecki, A.: Dynamics analysis of a truck-mounted crane with the LuGre friction model in the joints. Vibrations in Physical Systems 27, 391–398 (2016)

[20] Wittbrodt, E. Szczotka, M., Maczyński, A., Wojciech, S.: Rigid Finite Element Method in Analysis of Dynamics of Offshore Structures. Ocean Engineering & Oceanography (2013)

[21] Wu, T.S., Karkoub, M., Yu, W.S., Chen, C.T., Her, M.G., Wu, K.W.: Anti-sway tracking control of tower cranes with delayed uncertainty using a robust adaptive fuzzy control, Fuzzy Sets and Systems 290, 118–137 (2016)

[22] Zhang, M., Ma, X., Rong, X., Tian, X., Li, Y.: Error tracking control for underactuated overhead cranes against arbitrary initial payload swing angles. Mechanical Systems and Signal Processing 84, 268–285 (2016)

A. Urbaś: University of Bielsko-Biala, Department of Mechanical Engineering Fundamentals
43-309 Bielsko-Biala, Willowa 2, Poland, e-mail: aurbas@ath.bielsko.pl

A. Jabłoński: University of Bielsko-Biala, Department of Mechanical Engineering Fundamentals
43-309 Bielsko-Biala, Willowa 2, Poland, e-mail: ajablonski@ath.bielsko.pl

J. Kłosiński: University of Bielsko-Biala, Department of Mechanical Engineering Fundamentals
43-309 Bielsko-Biala, Willowa 2, Poland, e-mail: jklosinski@ath.bielsko.pl

K. Augustynek: University of Bielsko-Biala, Department of Computer Science and Automatics
43-309 Bielsko-Biala, Willowa 2, Poland, e-mail: kaugustynek@ath.bielsko.pl

Features of low-channel sEMG and FMG control systems for the biomechatronic solution of human fingers replacement

Kostiantyn Vonsevych, Mikhail Bezuglyi, Jerzy Mrozowski, Jan Awrejcewicz

Abstract: An important role in construction of human hand plays the presence of fingers, which provides the most precise and delicate tasks. As consequence, in the case of their loss, even partial replacement of some function needs the application of multiple biomechatronic systems. The most modern solution that can be implemented as natural analogue is a bionic prosthesis. It usually consists of few individual modules such as electronic feedback and controlling units, mechanical parts etc. Construction of such prosthesis should have a biomimetic size, view and as more as possible amount of DoF. When the controlling unit, which is actually the "artificial brain" of the system, should be portable and have an appropriate level of accuracy. In general, a successful implementation of these modules needs a cumbersome or multi-channel hardware that makes a final device expensive or large and non-mobile. The one-channel sEMG and three-channels FMG controlling units based on ANN method of signal classification could be a possible partial solution to the described problem. ANN with well-organised structure and correctly selected TDF parameters of measured EMG signal can allow to produce a unit with classification rate more than 87% and 96% even with 6 types of provided movements. Joint use of such "artificial brain" in prostheses with microcontrollers based hardware can make it an enough portable for artificial fingers and now is studing in the research provided by authors.

1. Introduction

Everyday human makes a big amount of actions and activities, in a significant amount of which a presence of hand, wrist and fingers plays the key role. There are a lot of grips, grasp and individual finger movements that are frequently used in a daily activity and rehabilitation exercises [1]. They include full movements of the hand, digit flexion and extension, some combination of the finger movement etc. For example, such tasks like drinking, or some gestures from sign language that can be used in activities of daily living (ADL) includes various types of hands movement [2; 3]. According to the literature, there are several hand grasps and movements which is using more frequently in ADL [4-6], but anyway it is obvious that the loss of a limb has a significant negative impact on the person.

The possible decision that can help to partially replace the function of the health hand is the using of different types of modern bionic prostheses devices. The technology of upper extremity bionic devices, robotic multi-dexterous hands such as Bebionic3, Touch Bionics i-Limb, Otto Bock's Michelangelo hand, and others which are commercially available in the last decade [6], makes this task

more realistic. However, despite the fact of advances in prosthesis technologies, the significant challenges remains in prosthetic design and control for them to be well accepted and integrated into daily life [7]. One of the difficulty is that the increased complexity of prosthesis also makes the new challenge of effectively controlling these devices, their reliability and integrated user-friendly control interfaces without misclassification of the user's intentions and unplanned movements [6-7].

Nowadays, the technology for recognizing hand and finger gestures is significantly improved and except of the prosthetic control have an active implementation as a subject of research in various fields, such as robotic telemanipulation of rehabilitation, assistive devices, virtual reality or human–computers interaction [4; 8]. One of the common challenges in all of these fields is to develop the control interface of an automated assistive device for providing an operation in a more precise human-like manner as also as improving the wearability of such devices for monitoring. In addition to efficiency, the realization of these purposes allows to decrease the discomfort and embarrassment of the patient that has to take a rehabilitation procedure for long periods [4; 9].

In modern prosthetic control, there are various interfacing devices and techniques for controlling prostheses with various efficiencies of control which is usually can be categorized into vision devices, inertial sensors, data gloves, and muscle or neural activities sensor based technologies [[7;8]]. Each of these categories has some features. For example in a case of tasks like prosthesis control, where motor control is needed, the using of internal sensors or data gloves is not always possible and largely relies on the position of the sensors, accelerometers and gyroscopes attached to a user's wrist and fingers. So, as a consequence, in many prosthesis applications the using of direct biological control, i.e., utilizing a human physiological signal, is more desirable and natural [4; 9].

The most established noninvasive technique to record and analyze body part movements is by measuring the electrical activities of the corresponding skeletal muscles. This technique is called surface electromyography (sEMG) and in general, before its next implementation, requires of amplifying and filtering, rectification and smoothening of the signal, measured at the time of procedure for making it useful for the next calculations and for the possibility of their using in classification units of prosthetic devices. The technique of surface electromyography has been extensively investigated in decipher of hand gestures and it classified the different types of grasp and actively used for movement pattern recognition and classification of some complex hand movements as also as individual finger movements [8-11]. However, despite the fact that this technique has been widely used for hand and finger movement prediction, there are some disadvantages that is limiting their practical use in medical applications and creates a large inconsistency between laboratory results and those observed in realistic clinical setting [7; 9; 15]. As an example of such disadvantages can be highlighted: 1) Sensitivity of sEMG signals to noise caused by electrode displacement, poor contact, sweat or skin impedance; 2) Decline of performance of sEMGs due to change of user's hand position or muscle fatigue; 3) Necessity

of placement of the sEMG electrodes on a specific muscles, which requires work preparation and previous knowledge of the muscle anatomy; 4) Necessity of feature extraction in order to achieve optimal training results, which can be a challenging and time-consuming procedure [4; 6; 7; 9].

That is why there is a recent interest in the development of more easy-to-use approaches to classify and predict the finger and hand movements. One of such approaches is using a less researched method of Force Myography (FMG). FMG, which is also referred to as residual kinetic imaging (RKI), Topographic force mapping (TFM), or muscle pressure mapping (MPM), is a technique which utilizes force resisting sensors surrounding a limb to register the volumetric changes of the underlying musculotendinous during muscle activities and according to, [6] can be effectively used for real prosthesis implementation even with commercial devices [1; 6; 7; 9; 10; 12].

As a sensitive element in the FMG methods can be used Force Sensing Resisters (FSR) [2; 7; 10; 12], Filament Strain Sensors (FSS) [4] or Resistance strain gages (RSG) [3] with different shapes and amount of sensors in a measurement array. In this case, FSR is a polymer thick film (PTF), which exhibits decreasing resistance as increasing force, is applied to the active area. [1; 8; 9]. An FSS it is a sensors, fabricated by using a mixture of thermoplastic and nano-conductive particles; this blend is extruded into small filaments of diameter 0.7 mm and length of 1.5 cm [4]. And an RSG are based on electrical resistance sensors which usually embedded in a transparent flexible wristband, covering the entire measuring zone [7]. Amount of pressure sensors depends from each specific research and in general varying from 8 to 128 channels (for so-called high-density force myography (HD-FMG) [7; 13].

Studies show that FMG similarly to the sEMG, are able to successfully classify different grasps types, predict the strength of a grip, detect some positions of the wrist and elbow related movements, have a possibility to predict the different finger gestures, or for example, to detect upper-extremity movements in a task as drinking a glass of water. It can be effectively utilized for rehabilitation applications, to control prosthetic devices as also as in the creation of human-machine interfaces and industrial robots, as well as the creation of monitoring systems for some rehabilitation programs [5; 7; 9; 10; 12].

Compared to sEMG, FMG technique is relatively unexplored and less standardized, but has several potential advantages as 1) Insensibility to external electrical interference or sweating; 2) It does not require the same level of signal processing required in EMG datasets; 3) It is more easy-to-use, affordable alternative to other muscle activity tracking methods, an experimental prototype for which can costs less than US $50 [1; 12; 14].

However, it is also should be taken into account some limitations of this method, among which can be highlighted: 1) The measurement efficiency depends on the type of used sensor; 2) In the most of situations, systems based on FSRs requires a close contact with the skin of a user to ensure that the

movements can be detected. [4; 12]; 3) According to the literature, on the accuracy of FMG based hand and finger movements recognition have an influence such factor, as: position of the hand in a space during the measurement [7; 14], the placement of measurement sensors on forearm region [12], the force exertion level while measurement procedure, as also as providing the minimum grasping force needed for a grasp classification with an acceptable accuracy [8].

In the field of work with sEMG signal it is usually calculating some Features of sEMG signal which in general can divide into four main categories for achieving of signal classification good results: time domain features (TDF), time-series domain (TSD), frequently of the spectral domain (FD) and time-frequency domain (TFD) [15; 16]. One of the most popular categories of characteristics is a time domain features that can give a high classification ability without using complex mathematical equations. A set of TDF-features can include different characteristics and in general, takes into account mean absolute value (MAV), integral absolute value (IAV), standard deviation (SD), variance (VAR), wavelength (WL), root mean square (RMS) or Willison amplitude (WAMP). In the case of FMG in order to determine the state of a hand, most of the research has focused on the classification of the raw FMG signal (i.e. instantaneous FMG samples). However, given the temporal nature of force generation during grasping, the use of temporal feature extraction techniques may yield an increased accuracy of measured signals classification [5]. TDF-features which are using for classification of sEMG signal can be also implemented in this method simultaneously with features like an RMS, waveform length, autoregressive coefficient, linear fit (LF), parabolic fit (PF) etc [6; 10].

Usually, feature extraction of FMG and sEMG signals carried out on time intervals with define lengths that depend on the type of provided movement and in general takes values from 32 to 300ms. Besides, the data movement is usually normalized before the feature extraction and classification of the measured signal. For data normalization can be used different methods such as scaling, based on minimum and maximum values, standardization using standard deviation (z-score normalization), and normalization by maximum value of some label parameter [1; 4; 7; 14]

There are many machine-learning methods, which can be used for classification of FMG or sEMG signals with the purpose of their next implementation for gesture recognition in control units of bionic prosthetic devices. The most popular methods used to the classification of hand movements are Support Vector Machines (SVM), Fuzzy and Neuro-Fuzzy Systems, Artificial Neural Networks (ANN) and Linear Discriminant Analysis (LDA) [1; 2; 7; 10; 17; 18]. Each of these methods can give a different level of classification accuracy depending on the number and quality of input parameters and usually depends on specific research.

As it was said earlier, there are many factors that influents on the classification of hands and finger movements and accuracy of user-friendly algorithms of prosthesis control. In the most of situations for the achievement of a high results, the classification systems requires different parameters, as also a big

amount of measuring channels in the devices, which can vary from 2 to 8 for sEMG and from 8 to 128 for FMG controlling devices. Despite the fact that increasing of measuring channels increases an accuracy of controlling module of prosthesis devices, it also makes the final devices more complex and expensive. That fact also can make a final system cumbersome and not portative, which is very significant for prosthesis implementation (especially for wrist and fingers prosthesis). In this study, we propose two methods of finger movements classification based on low-channels sEMG and FMG measured systems and machine learning technologies.

2. Methods

For providing an experiment in that research the control group of 10 healthy volunteers (in age from 10 to 50 years old) were invited to provide the set of 6 gestures. The gender of the measured subject includes Male and Female persons. All invited volunteers were informed about the process of research and signed the contest form with the questionnaire before an experiment. The form in questionnaire includes questions about some anthropometric data (mass, weight and body structure etc.) and clarifying questions about the state of the skin and availability of previous trauma in a zone of providing measurement. Each volunteer was comfortably sat on a chair in front of a desk, both of standard height and depth, and was informed by experimenter about the process of measurement and types of providing gestures, with sufficient time to practice in it, if it was needed.

As the set of researched movements in this article have been proposed different types of fingers flexion and extension. It consists of four individual finger movements (pinky, ring, middle and index), in which only one finger is activated and causes muscle activity in a muscle group related to this finger, called A1-A4. An activated finger moved from starting position (relaxed hand laying on a table with an open palm facing up) to the point of reaching the inner surface of the palm and the same way back. And two combined finger movements B1 and B2, which activated multiple muscles and include the simultaneous movement of three fingers (pinky, ring and middle) for a gesture of B1 and four fingers (pinky, ring, middle and index) for a gesture of B2 according to the principle described for A1-A4 gestures above. Each of provided movements repeated 5 times in the same time interval.

For providing a research two types of measurement devices were used by authors. The first one is the device for measuring sEMG signal based on MyoWare sEMG module from Advancer technologies. This is one-channel sEMG module created especially for the possibility of it direct use with ADC of microcontroller, which gives the possibility to work with RAW sEMG signal as also as with already rectified and integrated sEMG signal.

Myoware has embedded electrode snaps right on the sensor board itself, replacing the need for advanced cables and having a wide supply voltage range from 2.9 to 5.7V that makes it very comfortable for portative use. In the scheme of the sEMG measurement device were also included

Microcontroller Atmega 16 (Atmel Corporation) and HC-12 SI446 UART-RF module. The short sEMG device work algorithm has as follows: after the power supplying and turning the device on, the sEMG signal is measuring by MyoWare module and goes to an analogue-digital converter (ADC) of microcontroller Atmega 16.

In a microcontroller, the received signal is transformed to the appropriate level of voltage amplitude based on the reference voltage of microcontroller and MyoWare module. On the next step, the certain level of amplitude is transferred to UART-RF module for their next use in a special customized visual software on PC. Herewith, the delay between transferring of each portion of information is 1ms, a Baud Rate of UART is 9600 bod and the working frequency of microcontroller and ADC is 2 MHz and 500 kHz respectively. As measuring sensors for the MyoWare module were used F-55 surface Ag-AgCl electrodes from the SkinTact Company.

The second device (Fig. 1a) used in this research is FMG measuring bracelet based on three FSR 400 Short force-sensing resistors by Interlink Electronics, microcontroller Atmega 16 and HC-12 SI446 UART-RF module. FSR 400 are polymer thick, film based sensors with large sensitivity range (0.2N–40N), which exhibits resistance in the result of the force applied to the active area and have an almost linear transfer function for small forces (0N–15N) [19]. Three sensors FSRs (included in an electric circuit of amplifying taken from the datasheet) were placed on 2 cm apart from each other supported by two soft and one firm thin layers of soft tape and plastic sheet respectively (Fig.1.b,c). The total length of the strap was approximately 30 cm. The FMG bracelet device work algorithm was the same as in sEMG device, with the same parameters of Microcontroller, ADC and Baud Rate of UART described above, however with the different amount of input ADC channels, which was equal to three.

The principle of sEMG and FMG measuring devices placement shown in Fig.2. Both devices placed simultaneously on the left forearm of the volunteer. Where measuring electrodes for sEMG placed on Flexor Digitorum Superficial muscle (on the same distance N from the elbow joint in alignment with the length of a forearm) and the ground electrode was placed on the elbow bone of the same hand.

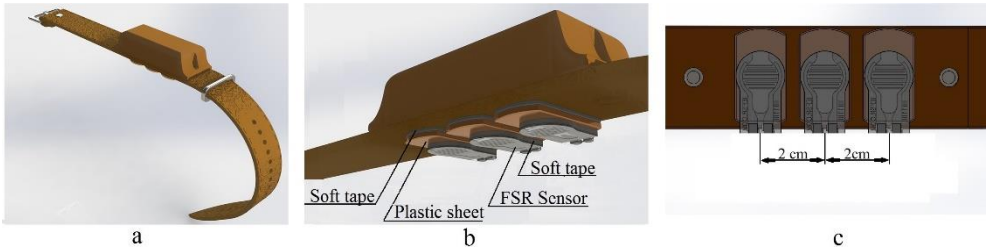

Figure 1. FMG bracelet and the principle of three FSR 400 sensors placement.

In the case of FMG measuring devices, based on works [4; 14], authors proposed hypotheses that FSR sensors can be implemented for measuring a pressure, caused by movement of muscle tendons which responsible for moving the respective fingers. As consequences, FMG bracelet with FSR measuring sensors was placed on the anterior wrist zone of a forearm on the distance that equal approximately 2 cm respectively for the length of forearm (Fig. 2).

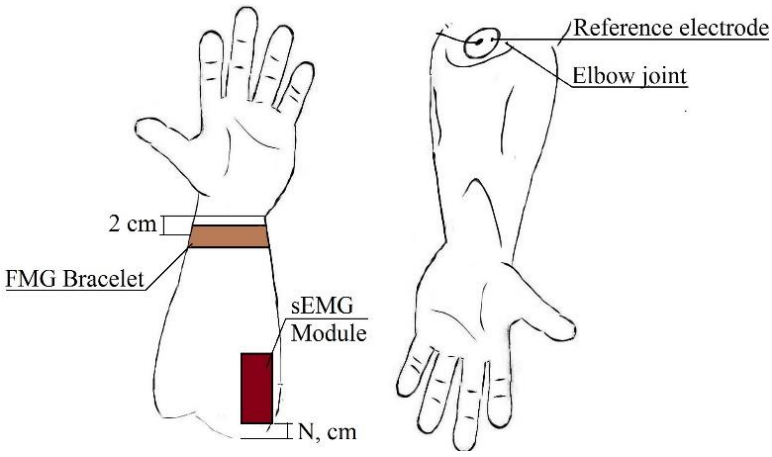

Figure 2. sEMG and FMG measuring devices placement principles

Both types of signals from the FSRs and sEMG sensors were synchronized and recorded using special created visual software (Fig.3) on the working laptop. The created software gives a possibility to show the measured signals in a real-time mode and to show the type of provided movement and create a short-form database (with a sequence number of subject, his name, age and gender) which include text files with received measured data.

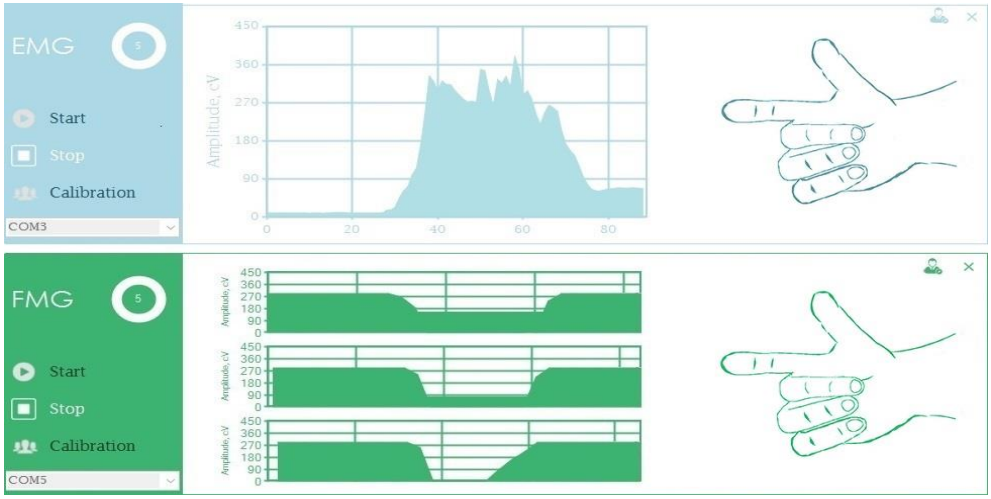

Figure 3. Visual software and example of measured sEMG and FMG signals received by them

3. Features and methods of classification

For both the sEMG and FMG approach methods of feature extraction were the same. The measured data were firstly normalized and only after that, the relevant features of signals were extracted. For FMG signal was used the method of Min-Max normalization [20], and sEMG data were normalized by maximum amplitude value of B1 movement. The dataset has been divided into five time-windows. These time-windows includes data from each trial for a selected type of movements which were described before. The width of the window consisting of 50 points and was equal to 50ms.

As empirical parameters of sEMG signals were used four-time domain features: Integral (Int), Peak (P), Variance (VAR) and Mean Absolute Deviation (MAD) [21]. For FMG signals parameters were the same, instead of the value of Peak (P) which was not included like an input of the model. In this case, the integral – it is a trapezoidal integration of chosen sample that allows to calculate the area under the measured signal. The peak – it is a maximum value of measuring amplitude for the sample in a chosen window. The variance and mean absolute deviation – that is the features, which allows to measure of by how much the value in the sample are likely to differ from their mean.

In this study was used the ANN method of sEMG and FMG signals classification to identify 6 different types of movement described above. ANN model was designed using Matlab's Neural Network Toolbox, for estimation the No/Yes confirmation category (0 or 1, respectively) for each type of movement based on the empirical parameters (inputs) listed above. For the possibility of the correct comparing of proposed low-channel measurement systems in this work, ANN classification model was used for classification of two types of input data: data from one-channel sEMG and three-channel FMG systems. The set of input data used for classification of signals consist of 765 samples for training and

135 for testing in the case of one-channel sEMG and 2295 samples for training and 405 for testing for three-channels FMG.

For this study were tested different ANN models with different amount of hidden units and training error goals. The final testing ANN structures were feed-forward ANN's, with layers and scaled error correction conducted via the Levenberg–Marquardt back-propagation algorithm. The first layer consisted of a set of independent variables, which included 4 input units for sEMG signals and 9 input units for FMG signals. The second layer of a proposed model called hidden layer (HL) and consisted of 40 hidden units (HU) for sEMG and 30 HU for FMG. The last layer consisted of 6 output units, representing the estimated decision about confirmation category to each type of movement. The hidden and output units summed incoming weighted connections and processed an outgoing activation signal with a sigmoidal transfer function in the hidden units and a pure linear transfer function in the output units. Back-propagated error correction of the synaptic weights and biases was also conducted using the Levenberg–Marquardt algorithm. In this study, the networks were trained using a training error goal (E) of 0.001 and the training continued until the error goal was met, or until the network had run for 1000 epochs. The training proportion was set at 0.85 and the remaining data (15 %) were used to test the ANN performance with data that were different from those used in the training.

4. Results and discussion

This study sought to demonstrate the ability of an ANN model to accurately recognize types of finger movements based on TDF-features of signals measured by low-channel sEMG and FMG systems. The results of provided a classification of one-channel sEMG and three-channel FMG systems by using a proposed (and described above) ANN classification models are shown in Fig. 4. The effectiveness of categorization was measured by the ROC (receiver operating characteristic) value calculated for each system. Specifically, the ROC value is calculated as the area under a curve, which is generated from the specificity and sensitivity results of multiple diagnostic testing sessions. Specificity is defined as the proportion of false-positives (movements categorized to one finger, when they are in fact of another finger). Sensitivity is defined as the proportion of true positives (movements appropriately categorized).

Comparing with the results achieved in authors study in the articles [10] have shown that 8 measuring channels for both sEMG and FMG methods can successfully predict elbow, forearm and wrist positions with accuracies of 84.3%, 82.4% and 71.0% using FMG and 75.4%, 83.4% and 92.4% accuracies for predicting the same respective positions using sEMG. In a study [7] authors used 16 x 8 (128 FSR sensors) to recognize eight gestures: wrist flexion, wrist extension, supination, pronation, open hand, power grip, pinch grip and rest. Each performed from nine different positions ranging from [-90°, 90°] and classified with an accuracy of 90% using ANN model. Also, in the research [9] thumb

and middle and index fingers movements prediction were studied using an array of 8 FSRs with resulting correlation coefficient of 0,96.

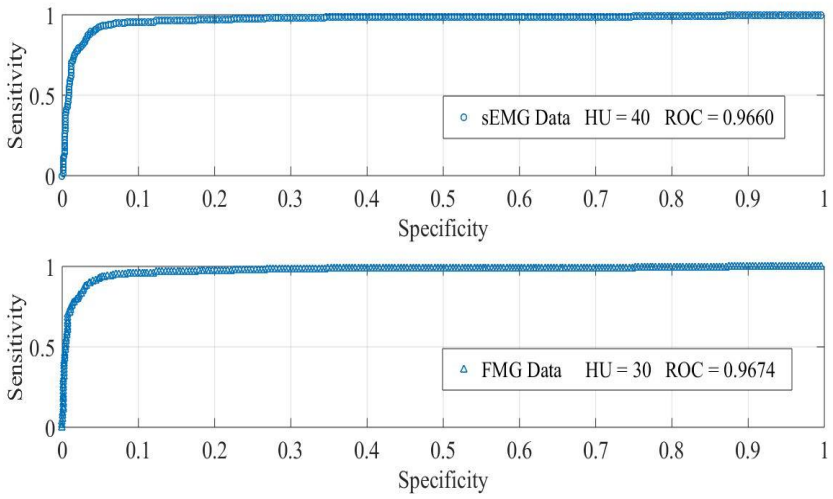

Figure 4. ROC curves of sEMG and FMG data classification accuracy

The methods proposed by author instead of used microcontroller, were based on measuring one-channel sEMG and three-channel FMG measuring devices simultaneously with simple ANN model of classification. The classification accuracy is relatively high and ranged from 96,60% for sEMG signals and 96.74% FMG respectively. As a continuation of this research the sample set and pattern of recognized motions should be increased as also as the one-channel FMG-system with the different bigger type of measuring sensor should be tested. Moreover, the achievement results should be tested in accordance with the spatial arrangement of measuring systems and the forces of fingertip compression during research [7; 8] as described in the related articles discussed above in the text.

5. Conclusions

In this article have been proposed two types of low-channels measurement devices of biological signals, which together with relatively simple ANN model of classification could allow to recognize different finger movements and can be implemented as control units in biomechatronic solution for human fingers replacement. Reviewed devices based on sEMG and FMG signals measurement techniques and with one and three measurement channels respectively. The ANN model used in this research were trained with error goals of E=0.001 and consisted of the HL=1 hidden layer and HU=40 hidden units for sEMG signals and HU=30 for FMG respectively. According to the results described in section 4, we can observe that ROC values of classification accuracy for multi-channel FMG measurement system

are higher approximately on 8% in comparing with the single sEMG system. Despite the fact that multi-channel FMG system has a higher accuracy, both systems can be equally effectively used for measurement and next classification of different single and complex movements of human fingers and can be implemented into high mobility fingers prostheses for the creation of low-cost and effective bionic and biomechatronic systems.

Moreover, the hypothesis about using the FMG device for measuring of tendons movements was also confirmed by authors and the increase of training data samples for classification sample can improve the further classification accuracy of proposed technologies.

References

[1] Jiang X, Merhi LK, Xiao ZG, Menon C. Exploration of Force Myography and surface Electromyography in hand gesture classification. Med Eng Phys. 2017, 41, 63-73.

[2] Xiao ZG, Menon C. Towards the development of a wearable feedback system for monitoring the activities of the upper-extremities. J Neuroeng Rehabil. 2014, 11 (1), 2.

[3] Ng HW, Jiang X, Merhi L, Menon C. Investigation of the Feasibility of Strain Gages as Pressure Sensors for Force Myography. 2015, 261-270.

[4] Ferrone A, Maita F, Maiolo L, et al. Wearable band for hand gesture recognition based on strain sensors. Biomed Robot Biomechatronics (BioRob), 2016 6th IEEE Int Conf. 2016, 1319-1322.

[5] Sadarangani GP, Menon C. A preliminary investigation on the utility of temporal features of Force Myography in the two-class problem of grasp vs. no-grasp in the presence of upper-extremity movements. Biomed Eng Online. 2017, 16 (1), 59.

[6] Cho E, Chen R, Merhi L-K, Xiao Z, Pousett B, Menon C. Force Myography to Control Robotic Upper Extremity Prostheses: A Feasibility Study. Front Bioeng Biotechnol. 2016, 4 (March), 1-12.

[7] Rasouli M, Chellamuthu K, Cabibihan JJ, Kukreja SL. Towards enhanced control of upper prosthetic limbs: A force-myographic approach. Proc IEEE RAS EMBS Int Conf Biomed Robot Biomechatronics. 2016, 2016-July, 232-236.

[8] Jiang X, Merhi LK, Xiao ZG, Menon C. Exploration of Force Myography and surface Electromyography in hand gesture classification. Med Eng Phys. 2017, 41, 63-73.

[9] Kadkhodayan A, Jiang X, Menon C. Continuous Prediction of Finger Movements Using Force Myography. J Med Biol Eng. 2016, 36 (4), 594-604.

[10] Xiao ZG, Menon C. Performance of Forearm FMG and sEMG for Estimating Elbow, Forearm and Wrist Positions. J Bionic Eng. 2017, 14 (2), 284-295.

[11] Ferrone A, Maita F, Maiolo L, et al. Wearable Band for Hand Gesture Recognition based on Strain Sensors. IEEE RAA/EMBS Int Conf Biomed Robot Biomechatronics. 2016, 2016-July, 4-7.

[12] Back P. Pilot study on strategies in sensor placement for robust hand/wrist gesture classification based on movement related changes in forearm volume. Healthc Innov Point-Of-Care Technol Conf. 2016, 46-49.

[13] Radmand A, Scheme E, Englehart K. High-density force myography: A possible alternative for upper-limb prosthetic control. J Rehabil Res Dev. 2016, 53 (4), 443-456.

[14] Xiao ZG, Menon C. Counting Grasping Action Using Force Myography: An Exploratory Study With Healthy Individuals. JMIR Rehabil Assist Technol. 2017, 4 (1), e5.

[15] Безуглий М, Клочко Т, Тимчик Г. Розробка класифікатора засобів моніторингу біотехнічних об ′єктів. Вісник НТУУ «КПІ» Приладобудування збірник наукових праць. 2003, 26, 131-138.

[16] Micera S, Carpaneto J, Raspopovic S. Control of Hand Prostheses Using Peripheral Information. IEEE Rev Biomed Eng. 2010, 3 ,48-68.

[17] Strazzulla I, Nowak M, Controzzi M, Cipriani C, Castellini C. Online Bimanual Manipulation Using Surface Electromyography and Incremental Learning. IEEE Trans Neural Syst Rehabil Eng. 2016, 4320 (c), 1-1.

[18] Gailey A, Artemiadis P, Santello M. Proof of concept of an online EMG-based decoding of hand postures and individual digit forces for prosthetic hand control. Front Neurol. 2017, 8(February), 7.

[19] Connan M, Ramírez ER, Vodermayer B, Castellini C. Assessment of a wearable forceand electromyography device and comparison of the related signals for myocontrol. Front Neurorobot. 2016, 10(NOV), 1-13.

[20] Raschka S, Vahid M. Python Machine Learning Second Edition. Second. UK: Packt Publishing Ltd, Birmingham B3 2PB, 2017.

[21] Vonsevych K, Bezuglyi M, Haponiuk A. INFORMATION-MEASURING SYSTEM OF MYOGRAPH OF BIONIC LIMB PROSTHESIS. Perspect Technol devices. 2017;10(1):32-37.

Kostiantyn Vonsevych, M.Sc. (PhD Student): National Technical University of Ukraine “Igor Sikorsky Kyiv Polytechnic Institute”, Faculty of Instrumentation Engineering, Department of Instrument Making, Prosp Peremohy 56 str, 03-056 Kyiv, Ukraine (wonsewych@gmail.com). The author gave a presentation of this paper during one of the conference sessions.

Mikhail Bezuglyi, Associate Professor: National Technical University of Ukraine “Igor Sikorsky Kyiv Polytechnic Institute”, Faculty of Instrumentation Engineering, Department of Instrument Making, Prosp Peremohy 56 str, 03-056 Kyiv, Ukraine (mikhail_bezuglyy@ukr.net).

Jerzy Mrozowski, Professor: Lodz University of Technology, Faculty of Mechanical Engineering, Department of Automation, Biomechanics and Mechatronics, 1/15 Stefanowski Str., 90-924 Lodz, Poland (jerzy.mrozowski@p.lodz.pl).

Jan Awrejcewicz, Professor: Lodz University of Technology, Faculty of Mechanical Engineering, Department of Automation, Biomechanics and Mechatronics, 1/15 Stefanowski Str., 90-924 Lodz, Poland (jan.awrejcewicz@p.lodz.pl)

Energy based composite damping modelling

Mario Wuehrl, Matthias Klaerner, Lothar Kroll

Abstract: Both, composite materials with either anisotropic layers, like fibre-reinforced polymers, or isotropic layers like metal or simple polymer layers offer a high potential in lightweight design applications. However, the thin structures react delicately to vibrations due to their high stiffness to mass ratio. In general, the damping of these composite materials is estimated using volumetric based averaging. However, thin structures show primary out of plane loads, for which the main strain energy is stored in the outer layers. As the damping of a material is a dissipation of strain energy under cyclic load, we assume that the outer layers contribute more to the complete composite damping making a volumetric mean value insufficient. In detail, the strain energy is varying not only by thickness but locally distributed among the whole part. The presented approach uses the FEA-based strain energy distribution to estimate the overall damping of the composite. This leads to an energetic averaged damping for each specific deformation state. The new model can be applied for modal damping of different mode shapes or amplitude dependent damping for nonlinear materials. As an example, the damping of a hybrid composite with steel face sheets and a very thin shear sensitive plastic core is estimated for different stress states. Furthermore, the applicability of this modelling approach is discussed for composites with anisotropic layers.

1. Introduction

Composite structures such as fibre reinforced plastics (frp) or metal plastic composites (mpc) tend to be sensitive to vibrations and thus to structure borne sound radiation. Especially frp offer a unique range of adjustable material properties by numerous influencing parameters such as fibre and matrix material, fibre volume content, textile structure of fabrics, fibre orientation and layup. Moreover, mpc offer the possibility of a highly shear sensitive core, in which the vibration energy dissipates [3]. For anisotropic frp materials the damping prediction by basic assumptions as the rule of mixture or micro mechanics is not suitable due to the missing fibre-matrix interactions. Thus, damping in such materials can not only be described as a material property and has to be treated as complex relation between material properties, the layup and the deformation characteristics including all boundary conditions [2].

Laminate properties are usually based on the classic laminate theory and hence imply perfect bonding between all plies, no strains or stresses out of plane, linear elastic behaviour and small deformations. The notation used here is number subscripts (1, 2, or 12) for the principal material directions of a lamina as well as letter subscripts (x, y, or xy) for the global laminate coordinates. Hence, the normal direction of the laminate is equally 3 and z. For anisotropic materials the characterisation of the elastic and damping properties of multi-layered composite beams is done by three basic deformation modes: longitudinal - fibre direction, transverse to the fibre direction and transverse shear deformations (Adams et al. 1994), resulting in three specific damping capacities ($\psi_1, \psi_2, \psi_{12}$), which is the basis for the well-known Adams Bacon model [1]. Moreover, it is based on identical elastic behaviour for tension and compression for low stress amplitudes. The damping capacity can be described as

$$\psi = \frac{E_{diss}}{E_{pot}} \tag{1}$$

with the total energy dissipated per vibration cycle

$$\Delta E_{diss} = \int_V \psi \sigma \epsilon dV. \tag{2}$$

While frp damping is predicted with an anisotropic model already based on strain energy, for isotropic materials a volumetric average for the damping is used. This volumetric average damping is often referred as structural damping. This structural damping is based on the assumption that damping forces are proportional to the forces caused by stressing the structure and opposed to the velocity [5]. Structural damping is intended to represent frictional effects in the material such as viscous behaviour. For different stress states, this structural damping remains the same and is assumed equal for all elements of a material. Especially for multi-material-systems, such as mpc, the different materials are not stressed equally. Under dynamic tension for example, the main stress occurs in the face sheets. Therefore, the new approach averages the damping of the materials of a mpc by their strain energy density distribution for a specific load case or mode shape.

2. Strain energy based damping modelling

The strain energy E can be calculated using the strain ϵ, the stress σ and the Volume V of any element in a material.

$$E_{pot} = \frac{1}{2} V \sigma \epsilon \tag{3}$$

Both load case depended values in 3 have six independent components and thus, the strain energy as well as the strain energy density U

$$U = \frac{E_{pot}}{V} = \frac{1}{2}\sigma\epsilon \tag{4}$$

are expressed in six components [4]:

$$\begin{aligned} U &= \frac{1}{2}(\sigma_{11}\epsilon_{11} + \sigma_{22}\epsilon_{22} + \sigma_{33}\epsilon_{33} + \sigma_{12}\epsilon_{12} + \sigma_{23}\epsilon_{23} + \sigma_{13}\epsilon_{13}) \\ &= \frac{1}{2}(U_{11} + U_{22} + U_{33} + U_{12} + U_{23} + U_{13}) \end{aligned} \tag{5}$$

With the YOUNGS modulus E and HOOKE'S Law

$$E = \frac{\sigma}{\epsilon} \tag{6}$$

the quadratic increase of the strain energy density with increasing load can be pointed out:

$$U = \frac{1}{2}E\epsilon^2 = \frac{1}{2}\frac{\sigma^2}{E}. \tag{7}$$

We further use the mean strain energy density

$$\overline{U} = \frac{E_{pot}}{V} = \overline{U}_{11} + \overline{U}_{22} + \overline{U}_{33} + \overline{U}_{12} + \overline{U}_{13} + \overline{U}_{23}. \tag{8}$$

In figure 1 the stress, strain and strain energy in x-direction are shown for a specimen under tension.

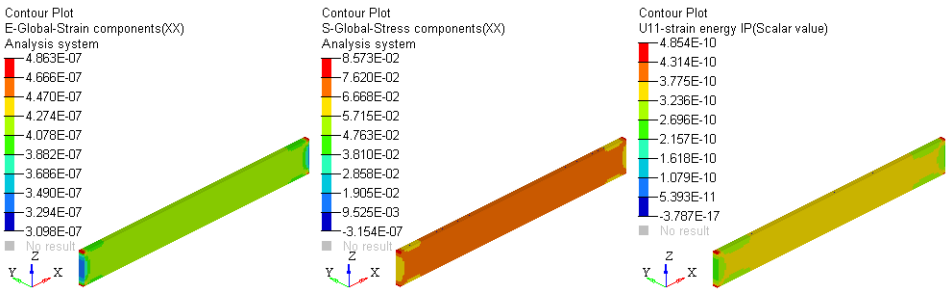

Figure 1. Strain, stress and strain energy in x-direction for a specimen under tension

3. Comparison for a metal-plastic composite

For the presented study the strain energy based damping approach is compared to the conventional volumetric averaging. The mpc consists of three layers, two face sheets with 0.75 mm thickness and a 0.05 mm thick polymer core. Assuming a damping of 0.1 for the core and 0.001 for the face sheets the volumetric mean value for the mpc can be calculated with:

$$D_{vol} = \frac{V_{core}}{V_{tot}} D_{core} + \frac{V_{facesheets}}{V_{tot}} D_{facesheets} \tag{9}$$

This damping is conventionally assumed for all load cases in static simulations or mode shapes in steady state dynamics.

The strain energy approach is shown for two different static load cases. First a specimen under pure longitudinal tension is shown in figure 2. In this case, the main strain energy occurs in the face sheet and the U_{11} component is dominant.

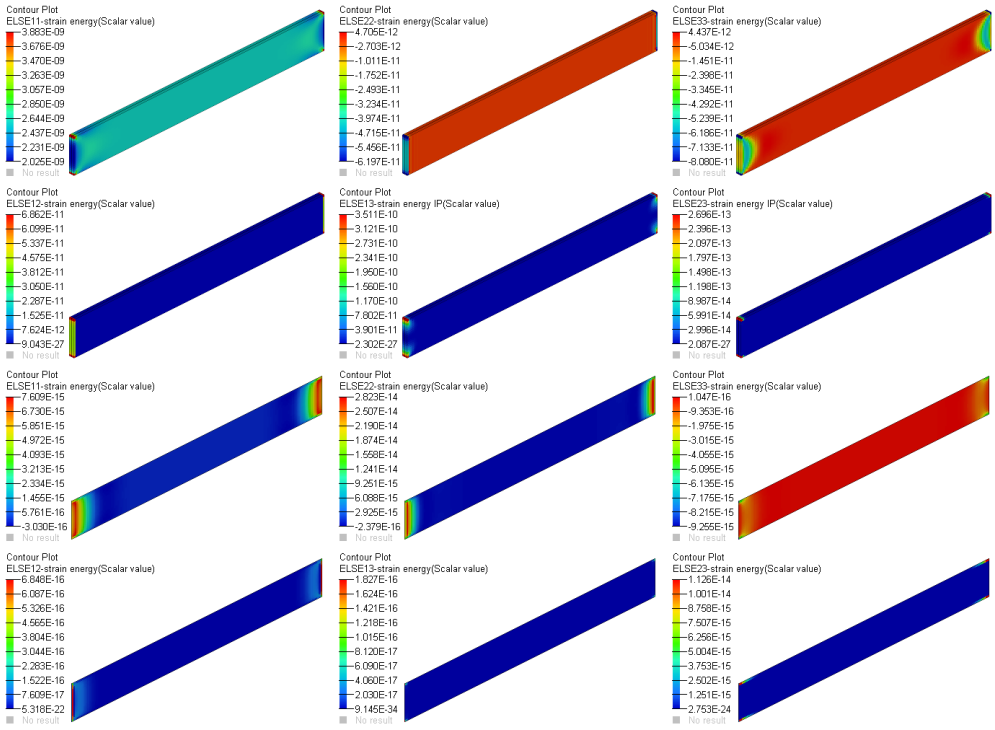

Figure 2. Strain energy distribution for longitudinal tension (facesheet in line 1 and 2, core in line 3 and 4

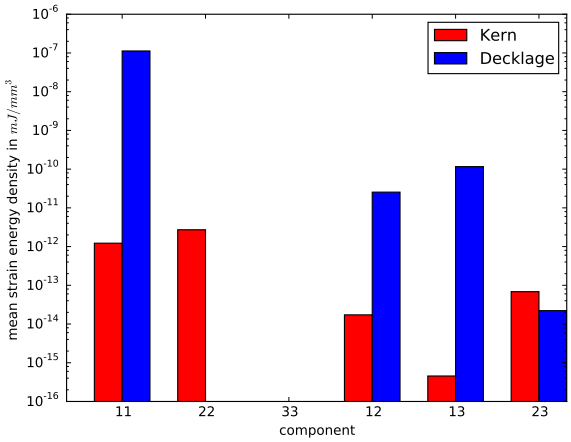

Figure 3. Mean strain energy density for tension

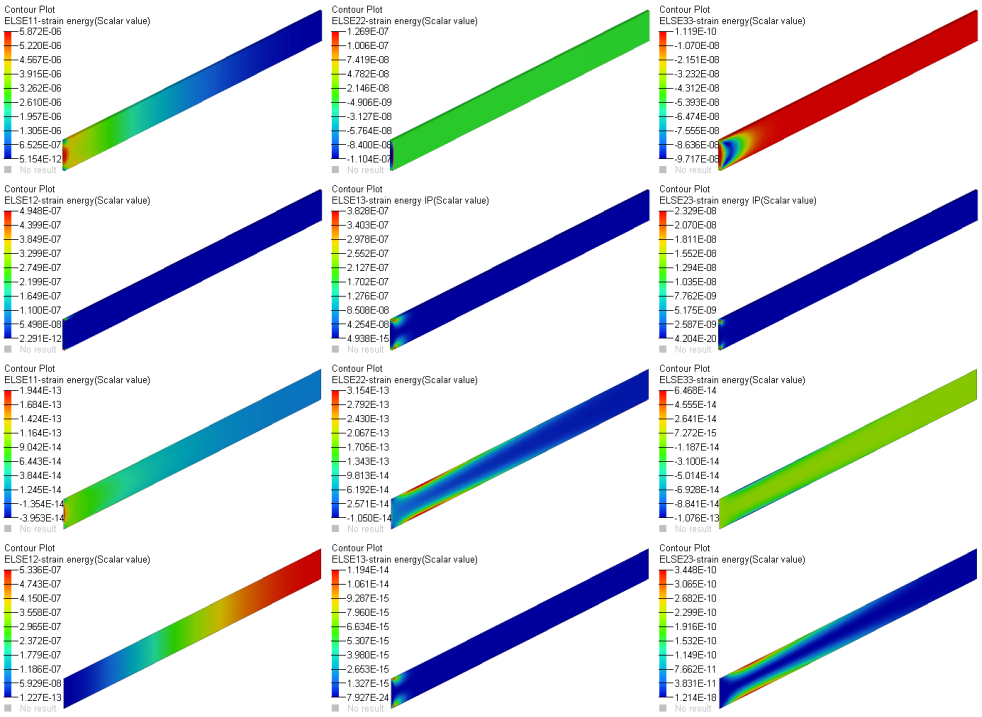

Figure 4. Strain energy distribution for a cantilever beam(facesheet in line 1 and 2, core in line 3 and 4

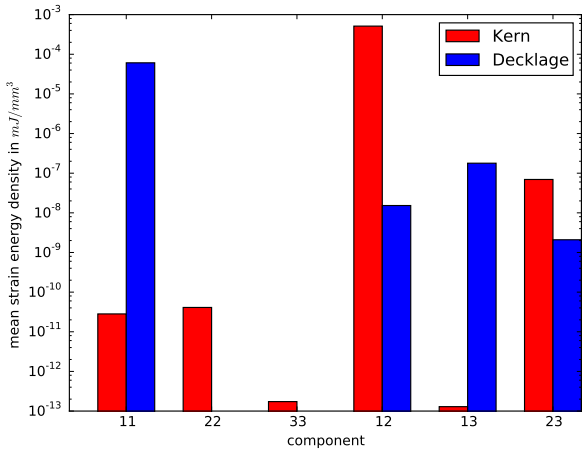

Figure 5. Mean strain energy density for a cantilever beam

The second static load case is a cantilever beam, for which the strain energy distributions are shown in fig. 4. For the face sheets, the dominant strain energy occurs in the x-direction, while for the core the main energy component is shear in the xy-plane (s. figure 5). For the mean strain energy density, this means that 89.411% of it occur in the core material.

So, different load cases result in a different strain energy and strain energy density distribution and thus, not all components of the mpc store and dissipate the same amount of energy, making the volumetric average insufficient. The strain energy density based average of the damping can be calculated using the following formulation:

$$D_{SE} = \frac{\overline{U}core}{\overline{U}total} D_{core} + \frac{\overline{U}facesheet}{\overline{U}total} D_{facesheet} \tag{10}$$

Using the shown strain energy damping modelling, the damping for the tension load case is 0.001 and 0.089 for the cantilever beam, making it a more realistic approach than the conventional volumetric average damping with 0.004 for all load cases. For steady state dynamics, this strain energy based damping has to be evaluated for each mode shape and thus different mode shapes will have different damping.

Regarding the mean strain energy densities over all elements, 99.997% occur in the face sheets (s. fig. 3)

4. Damping modelling of different types of composites

To discuss the damping modelling of different composite materials an overview of the materials is given in fig. 6. For a single isotropic material system the damping has only one

value.

$$\psi = \psi_1 = \psi_2 = \psi_{12} \tag{11}$$

Materials such as mpc consist of more than one material and thus, for each isotropic material one damping value is needed. For a symmetric isotropic composite like discussed in chapter 3 two damping values have to be determined. However, it is often not possible to characterize the core material itself due to its low thickness and low strength. Therefore, special test methods have to be used in which the main fraction of the load occurs in the core material. Hence, a material with N isotropic components needs N specific damping capacities.

Composites with orthotropic properties such as frp materials offer different stiffness longitudinal and transverse to the fiber direction. With the assumption that all shear damping components are equal and that the laminate is thin, so no damping in normal direction is present, the damping of such materials is described by three values $(\psi_1, \psi_2, \psi_{12})$.

If the composite consists of more than one material and an anisotropy is present, the damping of such a composite gets even more complex with three components for anisotropic layers and one for the isotropic layer. The presented strain energy density based damping modelling for isotropic materials offers the potential to model the isotropic layers with a similar approach as the anisotropic layers modelled with the Adams Bacon model.

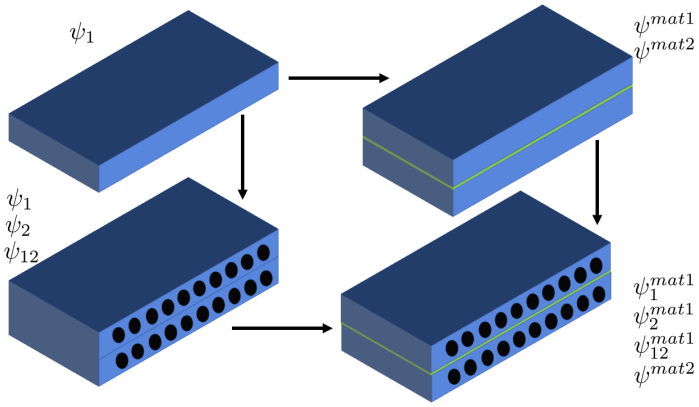

Figure 6. Scheme for the increasing complexity of damping models

5. Conclusions

Conventional approaches for the damping of isotropic materials are different to anisotropic materials . While anisotropic materials are described by taking the strain energy of the ma-

terial into account, isotropic materials are normally averaged using the volumetric average. Thus, for isotropic materials the damping is independent of the energy distribution. Especially for steady state dynamic simulation with different mode shapes the energy distribution between the materials of the composite changes significantly, making a volumetric average insufficient for damping modelling.

The strain energy density based modelling presented, also offers the ability to model nonlinear material properties such as amplitude depended damping, therefore further studies address the layer-wise strain energy related experimental characterisation. An FEA-based design of experiment will be further implied using the mean strain energy per component as a criterion rating the amplitudes for the description of an amplitude dependent behaviour.

Acknowledgments

The paper arose in the context of the project DFG-KR 1713/18-1 *Schallabstrahlung bei nichtlinearem und lokal variierendem Dämpfungsverhalten von Mehrlagenverbunden* as well as the Federal Cluster of Excellence EXC 1075 *MERGE Technologies for Multifunctional Lightweight Structures* supported by the Deutsche Forschungsgemeinschaft (DFG). Financial support is gratefully acknowledged.

References

[1] Adams, R. D., and Bacon, D. G. C. Effect of fibre orientation and laminate geometry on the dynamic properties of cfrp. *Journal of Composite Materials 7* (1973), 402–428.

[2] Maheri, M. R. The effect of layup and boundary conditions on the modal damping of frp composite panels. *Journal of Composite Materials 45*, 13 (2011), 1411–1422.

[3] Ross, D., Ungar, E. E., and Kerwin, E. M. I. I. Damping of plate flexural vibrations by means of viscoelastic laminae. In *Structural Damping* (Oxford, 1960), J. E. Ruzicka, Ed., Pergamon Press, pp. 49–87.

[4] Saad, M. H. *Elasticity - Theory, Application and Numerics*, second edition ed. Academic Press, 2009.

[5] SIMULIA. *Abaqus 6.14-1 Analysis User's Guide.*

Mario Wuehrl, B.Sc.: Chemnitz University of Technology, Institute of Lightweight Structures, 09107 Chemnitz, Germany (*mario.wuehrl@mb.tu-chemnitz.de*). The author gave a presentation of this paper during one of the conference sessions.

Matthias Klaerner, Dipl.-Ing.: Chemnitz University of Technology, Institute of Lightweight Structures, 09107 Chemnitz, Germany (*matthias.klaerner@mb.tu-chemnitz.de*).

Lothar Kroll, Univ.-Prof. Dr.-Ing. habil. Prof. E. h. Prof.: Chemnitz University of Technology, Institute of Lightweight Structures, 09107 Chemnitz, Germany (*lothar.kroll@mb.tu-chemnitz.de*).

Nonlinear acoustic metamaterials: Editable dynamics

Tianzhi Yang, Zhiguang Song

Abstract: Acoustic metamaterials with specifically designed lattices can manipulate acoustic/elastic waves in unprecedented ways. Whereas there are many studies that focus on passive linear lattice, with non-reconfigurable structures. In this letter, we present the design, theory and experimental demonstration of an active nonlinear acoustic metamaterial, the dynamic properties of which can be modified instantaneously with reversibility. By incorporating active and nonlinear elements in a single unit cell, a real-time tunability and switchability of the band gap is achieved. In addition, we demonstrate a dynamic editing capability for shaping transmission spectra, which can be used to create the desired band gap and resonance. This feature is impossible to achieve in passive metamaterials. These advantages demonstrate the versatility of the proposed device, paving the way toward smart acoustic devices, such as logic elements, diode and transistor.

1. Introduction

Metamaterials are man-made composites that control waves in ways that are not available in nature materials, resulting in exotic behavior [16, 21]. The acoustic metamaterials can manipulate waves with wavelengths much larger than the structure features of the system and have been successfully applied for acoustic wave cloaking [5, 22, 35], imaging [30], wavefront modulation [31, 32], and vibration control [14, 15, 18, 20, 28, 34]. The extraordinary ability of acoustic metamaterials is bestowed by band gaps, within which elastic/acoustic waves experience strong attenuation. Band gaps are typically generated from two main mechanisms, namely Bragg scattering [23] and local resonance [17]. In most acoustic metamaterials, local resonance is the main mechanism. However, most acoustic metamaterials comprise passive building blocks, such as internal resonator, which limits the tunability during operation. As once fabricated, their structures modification is generally difficult, making it hard to be reconfigured beyond their design.

Soft metamaterials are very promising for overcoming this difficulty, which have recently received increased attention due to their unusual properties [4,26,27]. When these structures are subjected to external load, remarkable phase transitions can be switched in a sudden but controlled manner. It is expected that such media can offer new opportunities for the manipulation of elastic wave and sound in a smart manner. Nevertheless, as local instability

(buckling) is required in this strategy, the large plastic deformation may occur, leading to an irreversible, relatively slow tunability. Moreover, this strategy often requires additional facilities to apply continuous external pressure during operation, inherently limiting their practical application. In this letter, we demonstrate an acoustic metamaterial that has a real-time reconfiguration ability. On the other hand, some active acoustic metamaterials have been presented to circumvent these limitation [1–3, 9–11, 24, 29, 33]. Nevertheless, most of the active acoustic metamaterials are based on linear internal resonator [1, 2, 9–11, 24, 29, 33], which exhibits relatively narrow operation frequency range. Although a nonlinear acoustic metamaterial device was theoretically presented in Reference [19], there is no experimental demonstration in the literature known to the authors. In this letter, we combine both active and nonlinear elements in a single metamaterial device. Specially, some unexplored phenomena like real-time, programmable, reconfigurable band gaps, and transition dynamics, are unveiled.An electric-controlled programmable acoustic metamaterial. (a) The device comprises 10 unit cells and fabricated using 3D-printer and. Each cell is connected by an independent switch and the whole acoustic materials is controlled by a digital controller. (b) Close-up of a single unit cell comprising a square frame, two curved beam and a pair of electromagnets

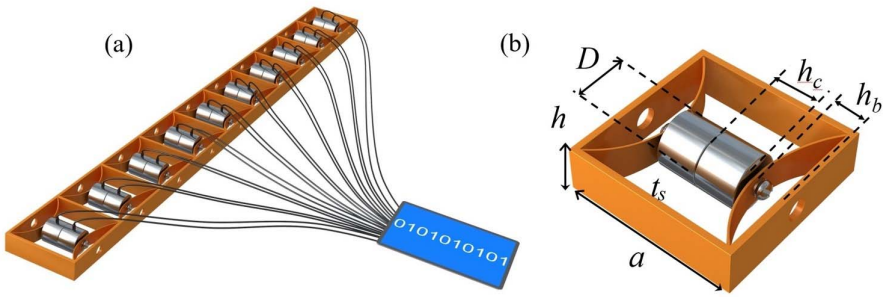

Figure 1. An electric-controlled programmable acoustic metamaterial. (a) The device comprises 10 unit cells and fabricated using 3D-printer and. Each cell is connected by an independent switch and the whole acoustic materials is controlled by a digital controller. (b) Close-up of a single unit cell comprising a square frame, two curved beam and a pair of electromagnets

Figure 1 (a) shows a 1D acoustic metamaterial with ten periodic unit cells is fabricated out of Polylactic Acid (PLA, with Youngs modulus is E_s=3.5 Gpa, Poisson ratio $\mu_s = 0.36$, mass density $\rho_s = 1250\ kg/m^3$) using a 3D-printer (Replicator 2X, MakerBot). Each unit cell comprises of two nonlinear internal resonators fixed in a 3D-printed square frame with

a lattice constant $a = 65.1$ mm, wall thickness $t_s = 2.2$ mm and height h=20 mm. Figure 1 (b) shows a typical implementation of a unit cell. A pair of cylindrical electromagnets (radius R=10 mm, height h_c=15 mm and mass m =20 g) are arranged with a gap of 1.1 mm and mounted on the two curved beams, acting as two independent nonlinear internal resonators. Each unit cell is connected to a switch and powered by a DC current supply. Therefore, each internal resonators can be controlled individually and continuously.

2. Device Design

The curved beam is the key element to support nonlinear stiffness. In the undeformed configuration, it has width $w_b = 20$ mm, thickness t_b=1 mm and height h_b=16 mm. In Figure 2(a) we report experimental measurements of deformation to displacement relation of a single curved beam. The stiffness value can be calculated through the slope in this figure i.e. $k = dF/dx$. It is seen that the stiffness value monotonically increases with the applied force, exhibiting a strongly hardening nonlinear property. Moreover, the stiffness value significantly alters at 0.32 mm. To rapidly switch between high and low stiffness, electrically switched electromagnets are adopted to generate the required deformation in a instants way. When the circuit is turned off, the two electromagnets are separated and the undeformed stiffness is measured as $k_un \approx 7900$ N/m. In contrast, when the circuit is turned on, the two electromagnets are attached and each nonlinear curved beam has a displacement 0.55 mm, yielding a significantly large stiffness value: $k_de \approx 59000\ N/m$. Here we use ON and OFF to denote the deformed and undeformed configurations, behaving as coding elements of 0 and 1, as shown in Figure 2(b). By coding the elements as 0000., 1100, and 1111., some interesting dynamical behavior may be achieved. Next, we numerically investigate the propagation of acoustic wave through the acoustic metamaterial. With a long wavelength assumption, the proposed 1D acoustic metamaterial could be modeled as a sandwich beam with internal resonators. Therefore, the Timoshenko beam theory with internal resonators is used to analysis wave propagation. The equation of motion for transverse vibration for OFF state can be expressed as [6–8]

$$\begin{aligned} GA(w'' + \varphi') - \rho A\ddot{w} + \frac{k_{un}}{a}(v_1 - 2w - v_2) &= 0 \\ EI\varphi'' - GA(w' + \varphi) - \rho I\ddot{\varphi} &= 0 \\ -\frac{m_1}{a}\ddot{v}_1 - \frac{k_{un}}{a}(v_1 - w) &= 0 \\ -\frac{m_2}{a}\ddot{v}_2 + \frac{k_{un}}{a}(w - v_2) &= 0) \end{aligned} \tag{1}$$

in which the EI, GA, I, A are bending rigidity, transverse shear rigidity, rotary inertia,

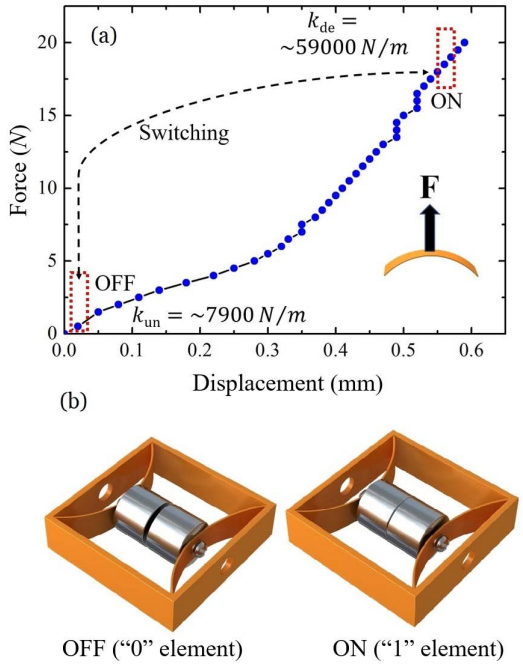

Figure 2. Simulated dispersion and measured frequency-dependent transmission for the samples. Both numerical Fig. 3 (a) and (c) and experimental Fig. 3 (b) and (d) results are shown. The gray regions in in each subplot highlight the band gap

and mass of the beam per unit length, respectively. w denotes the transverse displacement of the beam, denotes the rotation of the cross section, v_1 and v_2 are the oscillating displacement of the mass m_1 and m_2, respectively. (v_3 denotes the oscillating displacement of the attached resonator). In our case presented here, $m_1 = m_2 = 20\ g$. The effective material parameters of the acoustic metamaterial can be analyzed based on cellular solids theory [12, 25]:$E = E_s(t_s/a)$, $= 2_s(t_s/a)$, $\mu = \mu_s(t_s/a)$, $G = E/2(1+\mu)$. For the ON state, the equation of motion for the deformed internal resonator becomes

$$\begin{aligned} GA(w'' + \varphi') - \rho A\ddot{w} + \frac{2k_{de}}{a}(v_3 - w) = 0 \\ EI\varphi'' - GA(w' + \varphi) - \rho I\ddot{\varphi} = 0 \\ \frac{m_1+m_2}{a}\ddot{v}_3 + \frac{2k_{de}}{a}(v_3 - w) = 0 \end{aligned} \tag{2}$$

in which v_3 is the displacement of the two attached electromagnets, which behaviors like a single resonator. The displacement function can be assumed as

$$
\begin{aligned}
w(x,t) &= \hat{w}e^{i(qx-\omega t)} \\
\varphi(x,t) &= \hat{\varphi}e^{i(qx-\omega t)} \\
v_n(x,t) &= \hat{v}_n e^{i(qx-\omega t)}
\end{aligned} \tag{3}
$$

in which $n = 1, 2, 3$. in which $\hat{w}$, $\hat{\psi}$, and $\hat{v_n}$ are coefficients of displacement amplitude. The dispersion relation between the wave number q and frequency can be obtained by substituting Eq. (3) into Eqs. (1) and (2), respectively. Figure 3 (a) shows the simulated dispersion relation between the first-three frequency branches. The dimensionless wave number is defined as $\bar{q} = aq$. It is seen that a band gap appears between f=67-250 Hz in OFF state, within which strong elastic wave attenuation takes place. Differently, for the ON state, the acoustic wave in this range are allowed to propagate through the metamaterial, as seen in Figure 3(c).

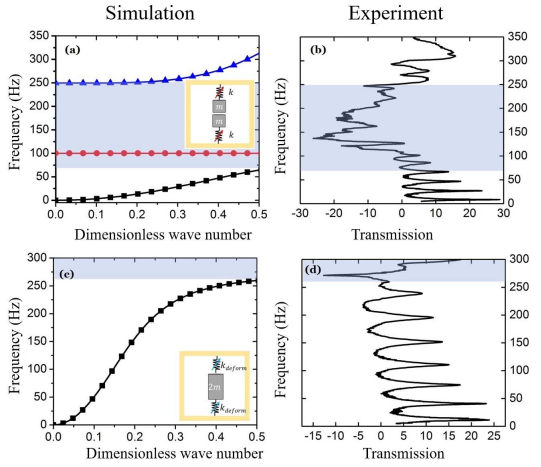

Figure 3. A 3D-printed unit cell.aMeasured force-displacement relation of a curved beam. The effective stiffness can be calculated from the slope of the curve. Inset shows the curved beam is subjected to an applied force F. bThe attached and detached configuration of a single unit cell

To validate the numerical simulation, we experimentally test the dynamic response of the fabricated sample. To measure the transmission response, elastic wave is harmonically excited through the metamaterial using an electrodynamic shaker (ETS type MPA409). Two tri-axial accelerometers (Brüel & Kjær type 4528-B) are adhesive-bonded to the bottom and top surfaces of the beam. Both the input and output signal are recorded by a dynamic

signal analyzer (LMS SCADAS), which also provides input signal to the shaker. Figure 3 (b) shows the experimentally measured normalized transmission spectra for the OFF state. It shows in Figure 3(c) that the transmission is characterized by a drop of 25 dB for f=75-80 Hz, which is in close agreement with the numerical simulation. In contrast, the measured results in Figure 3(d) shows the acoustic wave can propagate through the metamaterials in this frequency range, indicating that the proposed device can be used as an acoustic switch, whose response is rapidly controlled.

We next demonstrate the real-time programmable response of the acoustic metamaterial device. We note that the programmable, static mechanical metamaterials were presented in Reference [13], our purpose is to force the metamaterial to generate a dynamic programmable response during operation.

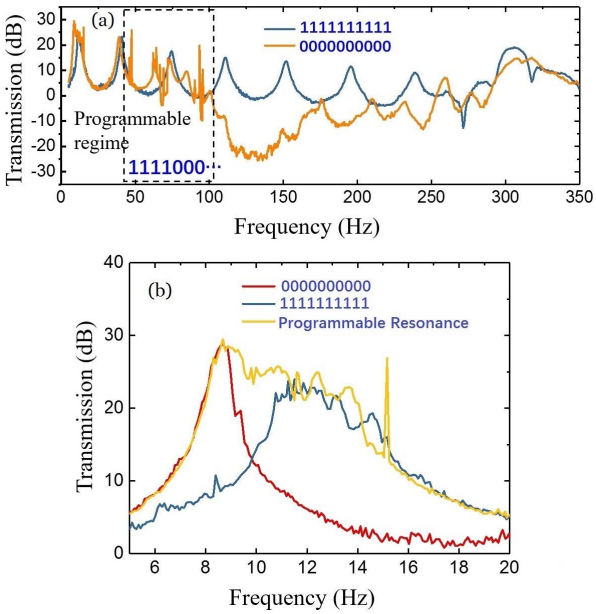

Figure 4. Real-time programmable dynamics during operation: (a) Programmable band gap. The dark-blue line denotes the transmission of the metamaterial with ten switched on unit cells. The orange line denotes the transmission with a dynamic switching process. The switching regime is shown in the dashed rectangle. (b) Programmable resonance. The dark blue and red lines indicate the first resonance when switched on and off, respectively. The yellow line denotes the dynamic switching during operation between the two states

As shown in Figure 4(a), we first switch on all the ten unit cells and then start to

shake the metamaterial, sweeping from 5 Hz to 350 Hz. Then we gradually switch off the ten units during the sweeping process (within frequency f=5-100 Hz). The orange line in Figure 4(a) shows the corresponding programmable transmission spectra with a sequence of impulse, which are induced by detaching of the electromagnets. The continuous switching shapes the metamaterial to generate a remarkably different transmission spectra, as shown in blue line. Eventually, a band gap appears between f=105-260 Hz, suggesting that the band gap is switchable during operation. Bides band gap switching, we next demonstrate the dynamic editing ability for resonance behavior. For reference, we measure the transmission spectra between 5-20 Hz, within which the first resonance occurs, as shown in Figure 4(b). The blue and red lines denote the ON and OFF resonance, respectively. Starting from ON state, we shake the metamaterial and sweep the frequency from 5 Hz. At 8.3 Hz, the spectra reach a peak value (the first nature frequency). At this value, we turn off all the unit cells gradually. Eventually, we found that an intermediate resonance (orange line) is created, which is different from either the ON and OFF states. Furthermore, this new resonance curve has a wider frequency range and bridges the two states. This feature is impossible to achieve in passive metamaterial devices, providing an interesting feature of our metamaterial: the ability to edit transmission spectra as desired, which was not reported before. By controlling and designing more complex logic operation, more interesting functionalities may be achieved. We expect this finding can inspire new applications such as broad band vibration/noise isolation or energy harvesting.

3. Conclusions

In conclusion, we report on the design, fabrication and experimental demonstration of the first nonlinear acoustic metamaterial, which has the ability to reversibly, and rapidly manipulate acoustic waves. The proposed acoustic metamaterial can switch on and off the propagation of acoustic waves. Our results show the electrically triggered deformation can control the nonlinear stiffness of internal resonators in an easier way, offering an alternative solution to implement nonlinear acoustic metamaterial. We expect that it can find applications including low-frequency vibration isolation, sound filter, and digital programmable materials.

Acknowledgments

The authors are grateful to the Alexander von Humboldt Foundation for offering fellowships to Dr. T-Z. Yang and Dr. Z.G. Song to carry out their research at Darmstadt University of Technology, Germany. T-Z. Yang acknowledges the support of National Science Foundation of China (Nos. 11672187)

References

[1] Akl, W., and Baz, A. Multi-cell active acoustic metamaterial with programmable bulk modulus. *Journal of intelligent material systems and structures 21*, 5 (2010), 541–556.

[2] Baz, A. The structure of an active acoustic metamaterial with tunable effective density. *New Journal of Physics 11*, 12 (2009), 123010.

[3] Bergamini, A., Delpero, T., Simoni, L. D., Lillo, L. D., Ruzzene, M., and Ermanni, P. Phononic crystal with adaptive connectivity. *Advanced Materials 26*, 9 (2014), 1343–1347.

[4] Bertoldi, K., and Boyce, M. Mechanically triggered transformations of phononic band gaps in periodic elastomeric structures. *Physical Review B 77*, 5 (2008), 052105.

[5] Brun, M., Guenneau, S., and Movchan, A. B. Achieving control of in-plane elastic waves. *Applied Physics Letters 94*, 6 (2009), 061903.

[6] Chen, J., and Huang, Y. Wave propagation in sandwich structures with multiresonators. *Journal of Vibration and Acoustics 138*, 4 (2016), 041009.

[7] Chen, J., Sharma, B., and Sun, C. Dynamic behaviour of sandwich structure containing spring-mass resonators. *Composite Structures 93*, 8 (2011), 2120–2125.

[8] Chen, J.-S., and Sun, C. Dynamic behavior of a sandwich beam with internal resonators. *Journal of Sandwich Structures and Materials* (2011), 1099636210391124.

[9] Chen, Y., Huang, G., and Sun, C. Band gap control in an active elastic metamaterial with negative capacitance piezoelectric shunting. *Journal of Vibration and Acoustics 136*, 6 (2014), 061008.

[10] Degraeve, S., Granger, C., Dubus, B., Vasseur, J. O., Thi, M. P., and Hladky, A.-C. Tunability of bragg band gaps in one-dimensional piezoelectric phononic crystals using external capacitances. *Smart Materials and Structures 24*, 8 (2015), 085013.

[11] Fleury, R., Sounas, D. L., Sieck, C. F., Haberman, M. R., and Alù, A. Sound isolation and giant linear nonreciprocity in a compact acoustic circulator. *Science 343*, 6170 (2014), 516–519.

[12] Gibson, L. J., and Ashby, M. F. *Cellular solids: structure and properties*. Cambridge university press, 1999.

[13] Haghpanah, B., Salari-Sharif, L., Pourrajab, P., Hopkins, J., and Valdevit, L. Multistable shape-reconfigurable architected materials. *Advanced Materials 28*, 36 (2016), 7915–7920.

[14] Huang, G., and Sun, C. Band gaps in a multiresonator acoustic metamaterial. *Journal of Vibration and Acoustics 132*, 3 (2010), 031003.

[15] Huang, H., Sun, C., and Huang, G. On the negative effective mass density in acoustic metamaterials. *International Journal of Engineering Science 47*, 4 (2009), 610–617.

[16] Leonhardt, U. Optical conformal mapping. *Science 312*, 5781 (2006), 1777–1780.

[17] Liu, Z., Zhang, X., Mao, Y., Zhu, Y., Yang, Z., Chan, C. T., and Sheng, P. Locally resonant sonic materials. *science 289*, 5485 (2000), 1734–1736.

[18] Ma, G., Yang, M., Xiao, S., Yang, Z., and Sheng, P. Acoustic metasurface with hybrid resonances. *Nature materials 13*, 9 (2014), 873–878.

[19] Manimala, J. M., and Sun, C. Numerical investigation of amplitude-dependent dynamic response in acoustic metamaterials with nonlinear oscillators. *The Journal of the Acoustical Society of America 139*, 6 (2016), 3365–3372.

[20] Matlack, K. H., Bauhofer, A., Krödel, S., Palermo, A., and Daraio, C. Composite 3d-printed metastructures for low-frequency and broadband vibration absorption. *Proceedings of the National Academy of Sciences* (2016), 201600171.

[21] Pendry, J. B., Schurig, D., and Smith, D. R. Controlling electromagnetic fields. *science 312*, 5781 (2006), 1780–1782.

[22] Popa, B.-I., Zigoneanu, L., and Cummer, S. A. Experimental acoustic ground cloak in air. *Physical review letters 106*, 25 (2011), 253901.

[23] Sánchez-Dehesa, J., Garcia-Chocano, V. M., Torrent, D., Cervera, F., Cabrera, S., and Simon, F. Noise control by sonic crystal barriers made of recycled materials. *The Journal of the Acoustical Society of America 129*, 3 (2011), 1173–1183.

[24] Sugino, C., Leadenham, S., Ruzzene, M., and Erturk, A. An investigation of electroelastic bandgap formation in locally resonant piezoelectric metastructures. *Smart Materials and Structures 26*, 5 (2017), 055029.

[25] Wang, A.-J., and McDowell, D. In-plane stiffness and yield strength of periodic metal honeycombs. *Journal of engineering materials and technology 126*, 2 (2004), 137–156.

[26] Wang, P., Casadei, F., Shan, S., Weaver, J. C., and Bertoldi, K. Harnessing buckling to design tunable locally resonant acoustic metamaterials. *Physical review letters 113*, 1 (2014), 014301.

[27] Wang, P., Zheng, Y., Fernandes, M. C., Sun, Y., Xu, K., Sun, S., Kang, S. H., Tournat, V., and Bertoldi, K. Harnessing geometric frustration to form band gaps in acoustic channel lattices. *Physical Review Letters 118*, 8 (2017), 084302.

[28] Wang, Y.-F., Wang, Y.-S., and Su, X.-X. Large bandgaps of two-dimensional phononic crystals with cross-like holes. *Journal of Applied Physics 110*, 11 (2011), 113520.

[29] Wang, Z., Zhang, Q., Zhang, K., and Hu, G. Tunable digital metamaterial for broadband vibration isolation at low frequency. *Advanced Materials 28*, 44 (2016), 9857–9861.

[30] Xie, B., Tang, K., Cheng, H., Liu, Z., Chen, S., and Tian, J. Coding acoustic metasurfaces. *Advanced Materials* (2016).

[31] Xie, Y., Wang, W., Chen, H., Konneker, A., Popa, B.-I., and Cummer, S. A. Wavefront modulation and subwavelength diffractive acoustics with an acoustic metasurface. *arXiv preprint arXiv:1406.6306* (2014).

[32] Zhao, J., Li, B., Chen, Z. N., and Qiu, C.-W. Redirection of sound waves using acoustic metasurface. *Applied Physics Letters 103*, 15 (2013), 151604.

[33] Zhou, W., Wu, Y., and Zuo, L. Vibration and wave propagation attenuation for metamaterials by periodic piezoelectric arrays with high-order resonant circuit shunts. *Smart Materials and Structures 24*, 6 (2015), 065021.

[34] Zhu, R., Liu, X., Hu, G., Sun, C., and Huang, G. A chiral elastic metamaterial beam for broadband vibration suppression. *Journal of Sound and Vibration 333*, 10 (2014), 2759–2773.

[35] Zigoneanu, L., Popa, B.-I., and Cummer, S. A. Three-dimensional broadband omnidirectional acoustic ground cloak. *Nature materials 13*, 4 (2014), 352–355.

Tianzhi Yang, Ph.D.: Tianjin University, department of Mechanics, 300072, Tianjin, China (*yangtz@me.com*). The author gave a presentation of this paper during one of the conference sessions.

Experimental verification of modeling contact phenomena in living structures using example of an implant-bone system

Marcin Zaczyk, Ph.D. Eng., Prof. Danuta Jasińska-Choromańska, D.Sc. Ph.D. Eng.

Abstract: The work presents modeling of contact phenomena in living structures. Selected ways of numerical modeling of phenomena at the boundary of two materials by means of FEM methods are discussed. The work focuses on phenomena related to living structures and their mutual interactions. Using an example of an implant-bone system, various techniques of modeling contact phenomena are compared and referred to experimental results. The study reveals the main features of the selected modeling techniques, e.g. complexity of creating the model, time-consumption of computation, reliability of the obtained results. The obtained results proved that the most advantageous method is the one that makes it possible to regard interactions as numerical values, without an excessive generation of the finite elements (the grid) at the materials boundary.

1. Introduction

Modern medicine relies on engineering solutions in order to create procedures of a healing process in a more precise way. The engineering solutions can be found first of all while planning a reconstruction of an injured human motor system. The related works generate a lot of biomechanical phenomena that are to be modeled in an engineering manner in order to make it possible to analyze phenomena, which occur within the considered system as well as related phenomena taking place even before the surgery [1,2,3,4,5,6]. Results of experiments related to biomechanical properties of living structures having an artificial material implanted inside, are widely used in research pertaining to surgical fixation of bone fractures as well as in processes of repairing damaged joints using bone implants [10,11,12]. Accuracy of the obtained results is of a crucial importance with regard to a future surgery. In order to eliminate risks connected with a failure of a surgery, an initial study is performed by the way of launching computer simulation, mainly based on FEM techniques. The form and complexity of the created model directly influence accuracy of the obtained results. It is striven for a simplicity of creating the computer model of the biomechanical phenomena that occur in living structures, including the contact phenomena; yet, at the same time, the obtained results should reconstruct the real phenomena that occur in the living structures, making it possible to simultaneously analyze particular medical cases. Currently, there are available many techniques of modeling the contact problems for bodies deformable over a large range and slides. The fist approach to modeling a contact of deformable bodies was undertaken by Hallquist in 1985 and then by

Wriggers in 1990, due to convective coordinates connected with the contact surface, after regularization of the boundary conditions by a method of enhanced Lagrangian multipliers [9]. Among the problems that are of crucial importance for the development of medicine and related sciences, the contact problems belong to a group of difficult problems [7,8,9]. A high degree of complication of the contact problems in the case of systems containing a living structure, results from many factors, including nonlinearity (both geometrical as well as of constitutive models), material properties of a living structure (featuring orthotropism or materials regarded viscoelastic), problems that occur at the discretisation level [13,14,15]. The present increase of computing power and development of such computer techniques as FEM results in the fact that solving these difficult problems became more effective and is used more and more often while dealing with biomechanical problems. It was attempted to show a practical application of computer FEM methods, using a simplified modeling of contact problems in simulations that yield results comparable with outputs of simulations based on complicated contact models regarding most of the contact conditions related to the real object, among which we can name kinematics of the contact, friction occurring between the bodies, measure of elasticity of the bodies, constitutive connections, magnitude of deformation of these bodies.

2. Materials

The presented considerations are related to simplified techniques of modeling contact phenomena in a medium consisting of two different materials; one of them has traits of a living structure (it is able to grow, to remodel and to adapt due to the surrounding conditions, it is able to regenerate) and the other is an artificial material in quasi-static study. An example of such medium is an implant-bone system, where the bone has traits of the living structure and the implant corresponds to the artificial material.

Figure 1. Image of the contact geometry at the boundary of a living structure and an artificial material: a steel rod mounted within a bone – magnification of 200x

Another example may be a connecting element mounted within a tree, where the tree has traits of the living structure and the connecting element in a form of a screw or a nail plays the role of the artificial material.

Figure 2. Image of the contact geometry at the boundary of the living structure and the artificial material: a steel screw mounted within a tree – magnification of 200x

In the considered medium, at the boundary of two materials, there take place a lot of phenomena of mechanical and biological character. Some of them are as follows:

- phenomena taking place at the boundary between an isotropic and orthotropic body, at a considerable spread of the material properties,
- phenomenon of occurrence of large displacements within the medium at the boundary of different materials,
- phenomenon of occurrence of large displacements, accompanied by deformation of the surface that is more deformable – in the considered case, it is the surface of the material that is mechanically weaker,
- occurrence of friction phenomenon (Coulomb) at the boundary of two materials - one isotropic and the other of a orthotropic character,
- interaction of a living structure with an artificial material on the border line between static and kinetic friction,
- possibility of destruction of the weaker element,
- possibility of delamination of the medium at the boundary of two materials,
- possibility of dynamic strain and adaptation of the living structure in a biological way to interactions of the external conditions.

The aforementioned phenomena illustrate complexity of the mutual interaction of living structures with an artificial material. Despite many options while modeling contact phenomena by means of engineering tools for FEM simulation, it is difficult to find a technique, which would make it possible to precisely, yet in a simple way, regard all these phenomena taking place within the

considered medium. Limitations due to the accepted technique of solving the task may generate some problems connected with the following:

- large disproportion in values of so-called material constants describing strength of particular materials, the medium is composed of,
- possibility of occurrence of large displacements at the boundary of finite elements and breaking continuity of the model structure, what makes it necessary to introduce a continuity index of the model in order to ensure appropriate discretisation of the whole model,
- possibility of a degradation of the weaker element - in case of a contact, where the finite elements of the weaker material overlap each other,
- possibility of occurrence of a local interpenetration of finite elements within the medium,
- possibility of delamination of an element - in case of a contact, where a local breaking of the continuity of the model takes place, what results in appearance of a clearance, a gap between elements describing the living structure and elements describing the artificial material.

A limitation in FEM techniques is also a contact algorithm, in which both contact surfaces are treated equally despite the fact that in computations one of them plays the role of the inferior surface and the other the superior surface. A contact that takes place between the living structure and the artificial material is a problem, where inequality conditions appear both at the level of geometry, material properties, as well as the structure of the contact surfaces. Because of searching for the most simple form of modeling the contact between living structures and an artificial material, it was accepted that the most convenient form was a contact realized between the surfaces, disregarding at the same time a contact at the nodes level. Creation of the contact at the level of the nodes requires to perform a toilsome work that consists in isolation of the boundary nodes and assigning for them appropriate mating parameters. The following table presents selected techniques of modeling the contact that were analyzed.

Table 1. Selected techniques of modeling the contact in the case of living structures mating with an artificial material

Description of the contact type	Schematic of contact operation	Advantages	Disadvantages
Contact employing damping-elastic elements		- implemented algorithms in FEM software, - no need to define the superior and inferior	- necessity of experimental determination of the damping and elasticity constants in the

	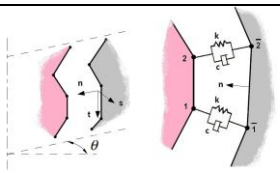	surface	medium at the boundary of two materials, - necessity of appropriate compression of the grid at the border of two different materials in the medium
Contact based on so-called slide lines	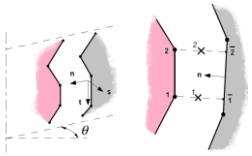	- implemented algorithms in FEM software, - simple discretisation of the model,	- necessity of determining the superior and inferior surface, - necessity of appropriate compression of the grid at the border of two materials in the medium
Contact based on so-called bio-layer with Gaussian point	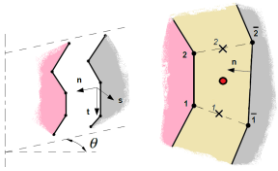	- elimination of problems related to disproportion of material properties in the contact, - no need to appropriately compress the grid at the border of two materials in the medium	- necessity of formulating an algorithm for the bio-layer
Contact based on contact index	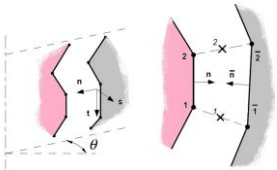	- simple discretisation of the model, - no need to appropriately compress the grid at the border of two materials in the	- necessity of experimental determination of the contact index, which defines correlation of the interaction

	medium, - no need to define the superior and inferior surface.

3. Method

An analysis related to capabilities of a simplified modeling of contact phenomena for living structures being in contact with an artificial material is presented. An aspect of the analysis concerning the modeling techniques was complication of proceedings while modeling as correlated to quality and reliability of the obtained results. The analysis consisted in a qualitative evaluation of realization of the proceedings versus amount of the necessary input data. A complement of the performed simulations was an experiment on real objects, where the considered contact took place. The analyses and the experimental study were performed for contact phenomena taking place at the boundary between the implant mandrel and the bone, accepting that the bone is the living structure and the implant is the artificial material. Accepting the contact at the boundary between the implant mandrel and the bone seems to be justified since it is one of the most difficult to be modeled. The difficulties result from an asymmetry of the osseous structure, diversified material traits and the related biological phenomena. The works consisted in elaboration of a geometry of a 3D model in a form of a "solid", having a structure of the cortical and trabecular bone specified, and in simplification of the implant structure. Then, a grid of finite elements of "hibrid" type was generated over the model prepared in this way. Such approach eliminates many errors while creating the grid in objects featuring a complex geometry. The boundary conditions as well as material properties for the models were the same in all the considered cases.

Table 2. Material properties used in the model for the first object obtained experimentally

Component of the 3D model	Kind of the material	Material properties used in the model	
Part representing the artificial material	Isotropic (cobalt alloy according to ISO 5832_12)	Modulus of elasticity	200 GPa
		Poisson ratio	0.3
Part representing the living structure - the cortical bone	Orthotropic	Modulus of elasticity Z	16 GPa
		Modulus of elasticity XY	9.5 GPa

	Poisson ratio	0.4
Part representing the living structure - the trabecular bone	Orthotropic	Modulus of elasticity Z 1.3 GPa
		Modulus of elasticity XY 1.1 GPa
		Modulus of elasticity XY 0.5

A lot of computer simulations were launched for the model created in such way, where only the technique of modeling the contact at the boundary of the living structure and the artificial material was changed, applying a modeling technique according to Table 1.

4. Results

The performed computer FEM simulations as well as experimental study were focused on determining value of displacement of the artificial material (i.e. fragment of the mandrel) with respect to an adjacent fragment of the living structure (i.e. bone). Such decision resulted from the fact that it was possible to determine this parameter directly, both in the computer simulations as well as in the experimental study. Such approach made it possible to eliminate errors resulting from determination of parameters indirectly. The following table presents values of displacements obtained owing to simulations based on models implementing different techniques of modeling the contact phenomena at the boundary between a living structure and an artificial material.

Table 3. Values of the strain obtained for particular types of shape of the implant mandrel

Applied load	Contact employing damping-elastic elements	Contact based on so-called slide lines	Contact based on so-called bio-layer	Contact based on contact index	Data obtained experimentally using a real model
Pa	The obtained displacements between materials in the object [mm]				
707	0.470	0.564	0.613	0.632	0.613
848	0.564	0.620	0.615	0.634	0.618
990	0.658	0.645	0.617	0.636	0.619
1131	0.752	0.729	0.626	0.6386	0.622
1273	0.846	0.817	0.628	0.641	0.625

5. Statistical analysis

All the simulation studies were launched using the same object featuring the same number of finite elements within the model, being equal to 5.552, and number of nodes of 12.508. The original contact surface at the boundary of the living structure and the artificial material was the same in each model. For each of the created models, a number of simulation was launched, changing only value of the load in the boundary conditions and recording displacements of the elements describing the living structure with respect the artificial material. Parameters accepted in the model (described in Table 1) were determined experimentally, investigating properties of the bone structure on the basis of density of the osseous tissue.

In order to determine properties of the living structures, 18 real objects were studied for this purpose. The real density of the cortical bone was of ca. 1.9 g/cm^3, and density of the trabecular bone from 0.14 to 1.1 g/cm^3. On the basis of the determined real density of the osseous tissue, an equivalent Young modulus was determined during the experiment. The equivalent Young modulus of the osseous preparation was determined using Keller equation. A basis for determination of the other properties of the bone structure were experiments performed by M. Nordin. For particular measured quantities, their standard deviations were scaled down/up. Results of these measurements were processed using the Mann-Whitney U test, in order to determine the absolute value of parameters, which were used for determination of material conditions while creating the simulation models.

6. Conclusions

The performed analyses and experimental study prove that despite the fact that there are so many possibilities of modeling the contact phenomena, yet universal tools implemented in the software for FEM simulation do not reconstruct in a satisfactory way the phenomena that take place in the real objects. The considered description of the contact at the boundary of a living structure and an artificial material is connected with significant spread of results, whereas universal models reveal an increasing spread with respect to the reference point, created for the models. It turned out that among the analyzed contact models, the most convenient one was the model based on bio-layer and the model with an assigned value of the contact index of a living structure and an artificial material. Models based on elastic elements and so-called slide lines revealed the biggest deviations with respect to reference values obtained experimentally.

7. Discussion

One attempted to find a simplified method of modeling the contact phenomena at the boundary of a living structure mating with an artificial material, concluding that it is possible to use the existing

algorithms implemented in the software designed for modeling the contact. However, only such algorithms should be selected, which implement such description of the contact that is the closest to the phenomena taking place within the real object. Living structures themselves are problematic while modeled because of their complex geometry, variable local biomechanical properties and a possibility of manifold reaction to the conditions of external interactions [9,10,13,15] The accepted simplifications in the geometry result in smaller errors than in the case of an inappropriate contact model. Thus, a key issue is description of the contact itself. As results from the performed analyses and experiments, dedicated techniques of modeling the contact in the case of living structures mating with an artificial material, by means of such methods as bio-layers algorithm or the contact index determining interactions of the material, increase reliability of the obtained results. A hardship related to this modeling method is a necessity of experimental determination of parameters describing mutual interaction in order to determine contact indexes or a relevant algorithm. Despite the difficulty, an advantage of the methods is a possibility of eliminating a compression of the grid at the boundary of the contact and thus shortening the computation time, while the process of creating the model is aimed at reconstruction of the geometry and setting simplified boundary conditions. Despite the simplification while modeling many phenomena of a biomechanical character related to living structures, it is still possible to obtain correct results using universal tools for modeling the contact.

References

[1] Alonso J., Lamarca R., Marti-Valls J. The Pain and Function of the Hip (PFH) Scale A Patient-Based Instrument for Measuring Outcome After Total Hip Replacement. Orthopedics. Dec 2000; vol. 23 No 12: 1273-1278

[2] Billsten M., Sernbo I., Ornstein E., Rogmark C., Johnell O. The incidence and mortality of hip fractures in two regions of southern Sweden 1992-1997. Current Orthopaedics. 2000: 182-188

[3] Childs L.M., Pashalis E.P., Xing L., et al. In vivo Ranksignaling blockade using the receptor activator of NK-kappaB Fc effectively prevents and ameriolates wear debris-inducted osteolysis via osteoclast depletion without inhibiting osteogenesis. J Bone Miner Res. 2002; 17(2): 192-199

[4] Francis R.M., Baillie S.P., Chuck A.J., Crook P.R., Daymond T., Dunn N., Fordham J.N., Kelly C., Rodgers A. Management of osteoporosis in patients with hip fractures. QJM. 2000 Aug; 93 (8): 501-506

[5] Harpal S. Khanuja, MD; Samik Banerjee, MS(Orth), MRCS(Glasg); Deepak Jain, MS(Orth); Pivec R., MD; Michael A. Mont, MD, Short Bone-Conserving Stems in Cementless Hip Arthroplasty, J Bone Joint Surg Am, 2014 Oct 15; 96 (20): 1742 -1752

[6] Gregory K. Deirmengian, MD; Zmistowski B., BS; Joseph T. O'Neil, BA; William J. Hozack, MD, Management of Acetabular Bone Loss in Revision Total Hip Arthroplasty, J Bone Joint Surg Am, 2011 Oct 05; 93 (19): 1842 -1852

[7] Kovacs J. A., Chacón P., Cong Y., Metwally E. and Wriggers W. Fast rotational matching of rigid bodies by fast Fourier transform acceleration of five degrees of freedom, Acta Crystallographica Section D structural Biology, 2003: 1371-1376

[8] Kusserow A., Fisklscherer A., Kreuz P. K., Importance of a distal centralizer in experimental malpositioning of cemented stems. A biomechanical study on human femora. Arch Med Sci 6. 2015 1324-1329

[9] Neto G.A., Pimenta P.M., Weigger J. A master-surface to master-surface formation for beam to beam contact. Part II Frictional interaction, Computer Methods in Applied Mechanics and Engineering, 1985, vol. 51: 107-137

[10] Uklejewski R.,Rogala P., Winiecki M.,Mielúńczuk J., Augúściński A., Berdychowski M. Engineering of Biomaterials, , Polish Society for Biomaterials in Cracow, Vol. 11, dec.2008:32-33

[11] Schmolz W., Gordon D.R., Shields A.J., Kirkwood D. Grigoris P. The effect of stem geometry on stresses within the distal cement mantle in total hip replacement. Technol Health Care 2000; 8: 67-73

[12] Rocco P. Pitto M.D., Koessler M. Kuehle J.W. Comparison of Fixation of the Femoral Component without Cement and Fixation with Use of a Bone-Vacuum Cementing Technique for the Prevention of Fat Embolism During Total Hip Arthroplasty. A Prospective, Randomized Clinical Trial, J Bone Joint Surg Am, 1999 Jun; 81: 831 -43

[13] Sumner D.R. Turner T.M. Urban R .M. Galante J.O. Remodeling and ingrowth of bone at two years in a canine cementless total hip-arthroplasty model J Bone Joint Surg Am, 1992 Feb; 74 (2): 239 -250

[14] Smith S.W. Estok D.M. 2nd, Harris W.H. Total hip arthroplasty with use of second-generation cementing techniques. An eighteen-year-average follow-up study. J Bone Joint Surg Am 1998; 80: 1632-40

[15] Zaczyk M**.** Jasińska-Choromańska D. Selected Mechanical Properties of the Implant-Bone Joint, Recent Technological and Scientific Advances, Springer-Verlag Berlin Heidelberg, , 2011: 691-695

Marcin Zaczyk, Ph.D. of Warsaw University of Technology and Faculty of Mechatronics, Institute of Micromechanics and Photonics, 8 Św. A. Boboli St., 02-525 Warsaw, Poland (*m.zaczyk@mchtr.pw.edu.pl*). The author gave a presentation of this paper during one of the conference sessions.

Danuta Jasińska-Choromańska, prof Ph.D., D.Sc. of Warsaw University of Technology and Faculty of Mechatronics, Institute of Micromechanics and Photonics, 8 Św. A. Boboli St., 02-525 Warsaw, Poland (*danuta@mchtr.pw.edu.pl*).

Bionic movement algorithms implemented in mechatronic robots

Bartłomiej Zagrodny, Cezary Miśkiewicz, Krystian Polczyński, Jan Awrejcewicz

Abstract: This paper addresses the problem of bionic movement algorithms of two types of limbless species: serpentes and geometridae. Bionic aspects seem to play important role in the processes of designing and development of new mechatronic systems and in modeling of their movement patterns. Evolution of the biological systems and resulting benefits cannot be neglected as the nature has created a lot of very complicated but specialized and effective systems. This gives an opportunity to observe, examine, modeling, and design via adjustable mechatronical systems. In this work we are presenting a way of implementation undulatory and inch-worm like movement locomotion algorithms based on examples of the manufactured two different robots.

1. Introduction

Bionics is a relatively new branch of science, however mankind has a tendency to mimic or copy the biological solutions probably at the beginning of our civilization development. This trend is visible in all fields of our life and we are in habit of looking for solutions to complex problems from different fields of science, engineering and daily life in the surrounding us nature [1]. It is quite popular to introduce naturally occurring behaviors in designing, construction and control of new mechatronics devices [2, 3]. In this work we are focusing on construction and implementation of the bionic movement algorithms in two types of robots. They are inspired by snake and inchworm and can serve as examples of transfer of living organisms structure and movement algorithms to the mechatronic structures. The movement patterns applied in this study were created on the basis of Hirose [4] and Saito et al. [5] results with assumption, that generated control signals can be treated as simplified Central Pattern Generator signals [6].

We begin with a short introduction to a biological aspect of the snake motion. Among the limbless animals there is a wide diversity of the movement patterns but, in general, the possibility of movement is caused by friction force created between the body and the ground. One of the examples of the limbless animals are serpents. Different movements patterns are not only caused by their structure (size), but also by environment, way of hunting, available space for movement and types of barriers they have to overcome [10]. Therefore, in the case of snakes, we can differentiate the following types of motion: serpenoid, concertina, rectilinear or sidewinding (see Fig. 1) [7]. The belly scales occurring in varied shapes depending on the natural animals natural environment [9] stand for useful tools helping with increasing the friction force (friction coefficient) in an intended direction of movement [8].

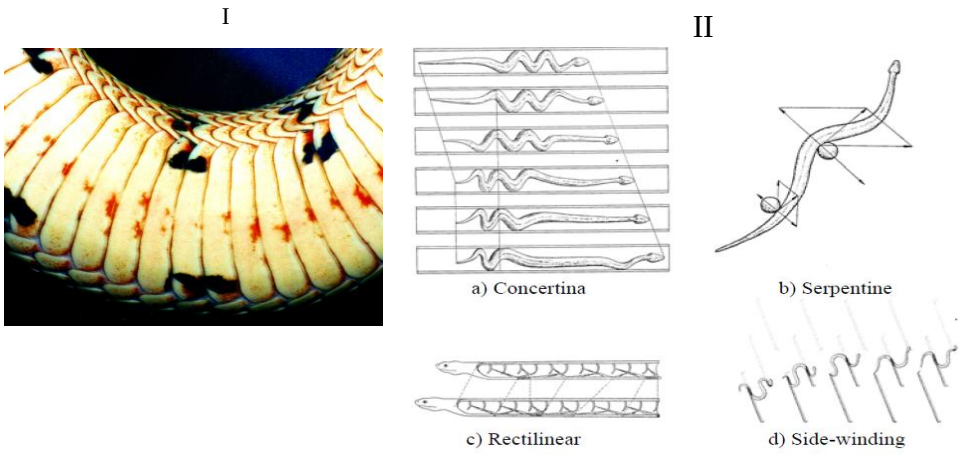

Figure 1. Snake appearance and main gaits of snakes. I – Belly scales of snake, II – Types of movement: a) Concertina, b) Serpentine, c) Rectilinear, d) Side-winding [7]

The inchworms also known as *Geometridae* caterpillars belong to a multispecies group [11]. Dimension of their body length is rather small and fluctuates from 10 to 50 mm. Significant role in caterpillar movement play prolegs, thanks to them the inchworms can attach to the ground [12]. Fig. 2 presents four phases of inchworm movement.

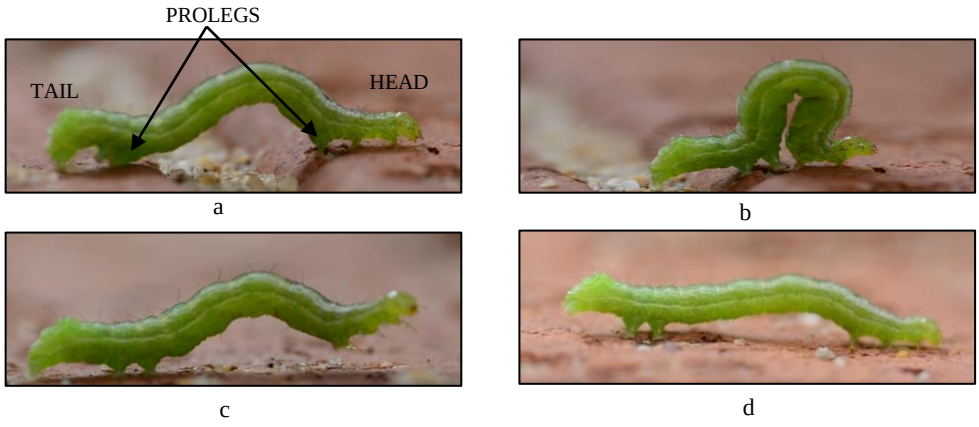

Figure 2. Four phases of inchworm movement [14]: a) Thorax part with head is attached to the ground by prolegs; b) Thorax part with tail is lifted upward and attracted to head; c) Thorax part with tail is attached to the ground by prolegs; d) Thorax part with head is lifted and shifted to forward direction.

When inchworm wants to change the direction of motion, it stops in the position shown in Fig. 2c and turns thorax part with head to new direction. It should be pointed out that the angle of turning is limited, as a result this type of species cannot turn back in one step.

2. Mechanical structure of biology inspired robots

This subsection includes examples of the snake robot and the inch-worm robot. Presented in this study snake-robot (Fig. 3) was designed and constructed by authors. It consists of eleven segments printed at 3D printer from durable acrylonitrile butadiene styrene (ABS) material. Six of them are able to move in vertical and five in horizontal plane. They are placed alternately, what allowed to achieve the rotation angle up to 40˚ for each of the joints. This construction of 0.97 m length and 1.7 kg weight is powered by servomotors with maximum torque of 1.32 Nm placed in each of the segments. Its remote control is realized by means of the microcontroller (programmable Arduino M0) located in the tail-segment of the robot.

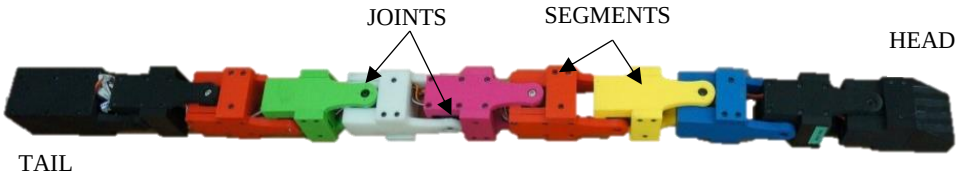

Figure 3. Horizontal view of the designed snake robot

The designed inch-worm robot (Fig. 4) consists of four segments printed on the 3D printer from ABS material with total length of 0.32 m and total weight of 0.53 kg. Its first (head) and last (tail) segments are additionally equipped with suction cups acting as the prolegs. Suction cups are connected to ejectors which using compressed air to produce vacuum pressure, allowing robot to attach to the ground. Two middle segments allow lifting non-attached segment and attracting/repulsing it. In the tail there is located stepper motor which can rotate the robot and change its motion direction. Servomotors are used for drive. The main simplifications of the proposed model, in comparison to the real inch-worms are exhibited by its much bigger size and significantly decreased number of the segments.

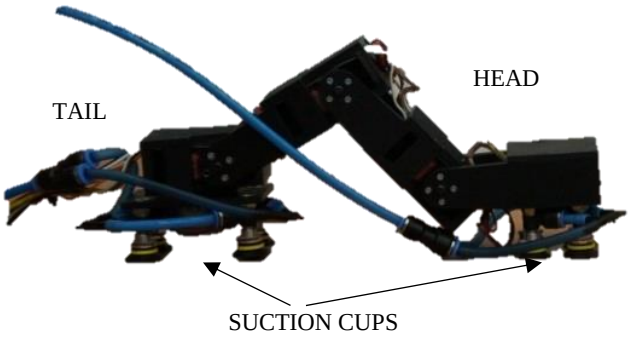

Figure 4. Horizontal view of the inchworm robot

3. Motion algorithm of two designed mechatronic robots

3.1 Snake robot algorithm

One of the most popular mathematical models of snake motion, describing its kinematics, has been created by Hirose [4]. The model assumes that the snake body is represented by continues curve and the coordinates are expressed by the following two equations:

$$x(s) = \int_0^s \cos[a \cdot \cos(b\sigma) + c\sigma]\, d\sigma,$$

$$y(s) = \int_0^s \sin[a \cdot \cos(b\sigma) + c\sigma]\, d\sigma, \quad (1)$$

where: s – length from start of the curve, a – parameter describing an undulation, b – parameter describing a frequency, c – parameter describing a deflection of curve.

The curve governed by two parametric equations (1) is called serpenoid curve. Fig. 5 presents influence of parameters *a*, *b* and *c* for the shape of serpenoid curve.

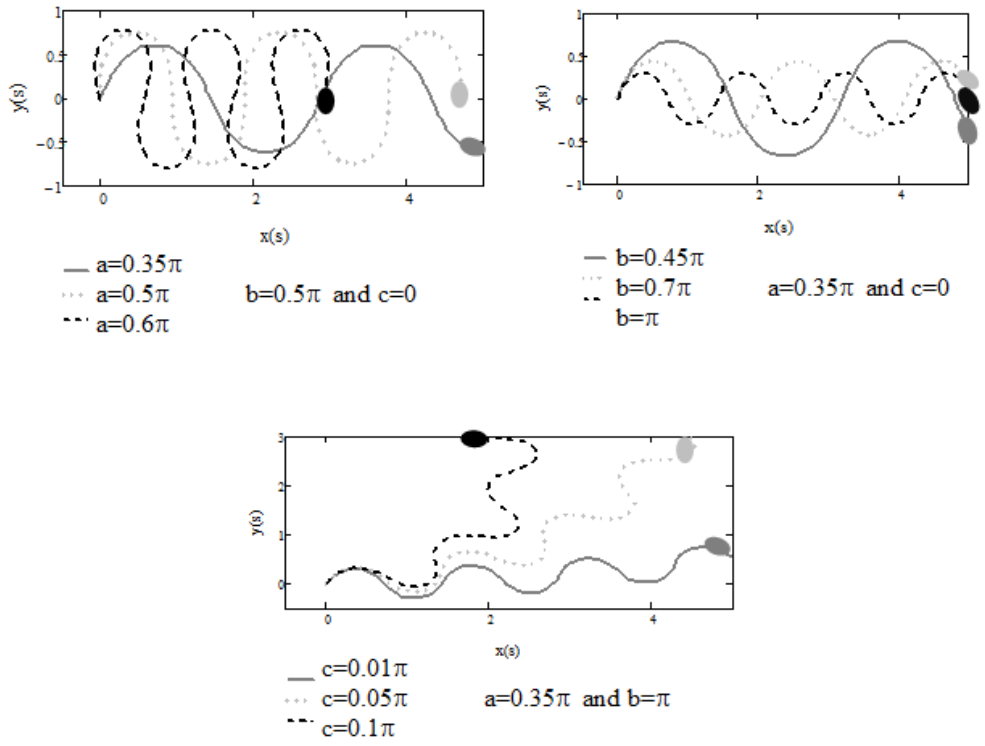

Figure 5. Shape of serpenoid curve for different parameters, (black dot denotes head of the snake).

Increasing of the parameter *a* implies increase of curvature of the serpenoid, while the parameter *b* is responsible for the period of the serpenoid and parameter *c* for the direction of the curve propagation.

To enable application in a microcontroller, the algorithm (1) can be simplified to achieve a sinusoid function [8]. Equations of angles in joints for the snake robot are as follows

i. Motion in a vertical plane (see Fig. 6) is described by the function

$$\xi_i(t) = A_\xi \sin\left(\frac{2\pi}{T}\cdot t + \psi_i\right) + \gamma, \tag{2}$$

ii. Motion in a horizontal plane is governed by the following formula

$$\Omega_i(t) = A_\Omega \sin\left(\frac{2\pi}{T}\cdot t + \omega_i\right) + \delta, \tag{3}$$

where: i – number of joint, ξ_i, Ω_i – angles of rotation in i-th joint for each segment, t – time, A_ξ, A_Ω – amplitudes, T – period, ψ_i, ω_i – phase shift for next link, γ, δ – vertical shift.

Scheme model of the snake robot in vertical plane is shown in Fig. 6.

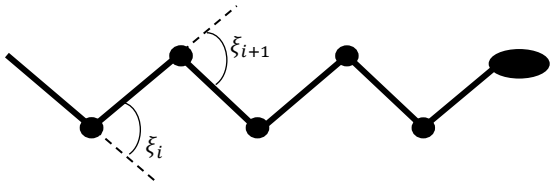

Figure 6. Model of the snake robot in vertical plane

In Fig. 7 examples of the changing angles in joints during snake-robot horizontal motion are presented. As it can be observed, signals have the same amplitudes and periods but they are shifted in phase for different segments, what creates a proper intersegmental coordination during their movement.

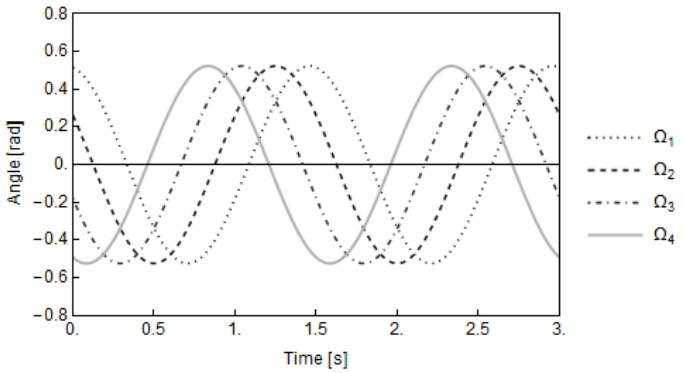

Figure 7. Control signals for serpentine motion for *i*-th segment

3.2 Inch-worm robot

Inchworm robot can move only in a vertical plane but the scheme model of the movement pattern is generated in the same way as for the snake robot in vertical plane (Fig. 6). The main difference is that a number of segments is limited to four. In contrary to the previous case, the algorithm is not continuous function but discrete changing sequence of the values of the angles in joints [13]. These sequences of angle values are shown in Fig 8. One can see that the values have sinusoid trend and oscillate above zero, the periods and phase shifts are the same for all of them but the amplitudes are different. It also creates a proper intersegmental coordination. Because the discrete algorithm of angle in joint has the

sinusoid trend, it can be replaced by a continuous function expressed by modified Eq. 2 with a positive vertical shift. Fig. 9 shows sinusoidal wave fitting to angle values generated during the robot motion.

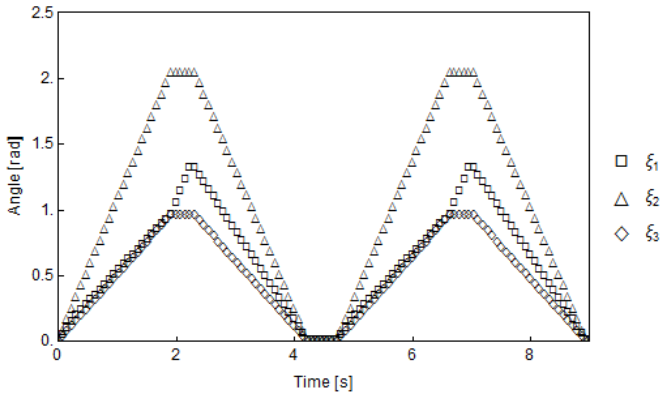

Figure 8. Discrete angle values in joints for the inchworm robot for the *i*–th segment

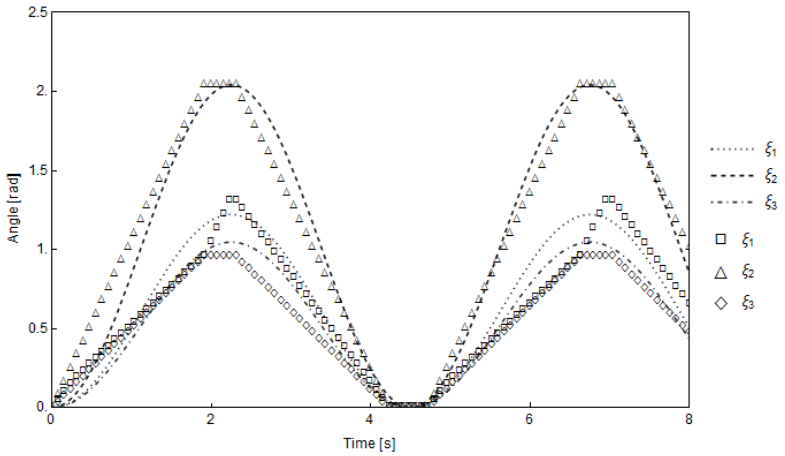

Figure 9. Curve fitting to discrete algorithm of the inchworm motion.

The angle signals are generated by microcontroller and send to servomotors located in rotation nods (joints).

4. Implementation of discrete algorithm

The results of the motion algorithms implementation are presented in a form of comparison of the real pictures which were done during motion recording versus the corresponding theoretical computation of the robots behavior. Coordinates of joint points for snake-robot have been obtained according to

equations 2, 3, while for inch-worm robot according to Eq. 2 with the parameters chosen after curve fitting (Fig. 10). Theoretical results were plotted in global coordinates. Table 1 contains parameters of implemented algorithm for both robots. In case of snake robot the parameters have been defined experimentally.

Table 1. Motion parameters of discrete algorithm implemented in control algorithms

Snake robot		Inchworm robot
Vertical plane	Horizontal plane	Vertical plane
$A_\xi = 30°,\ T = 1.5\ s,\ \psi_1 = 160°,\ \psi_2 = 210°,\ \psi_3 = 320°,\ \psi_4 = 410°,\ \psi_5 = 500°, \gamma = 0°$	$A_\Omega = 30°, T = 1.5\ s, \omega_1 = 100°,\ \omega_2 = 150°,\ \omega_3 = 200°, \omega_4 = 250°, \delta = 0°$	$A_{\xi 1} = 32°,\ A_{\xi 2} = 58.5°,\ A_{\xi 1} = 27.°,\ T = 4.5\ s,\ \psi_1 = 270°,\ \psi_2 = 270°,\ \psi_3 = 270°,\ \gamma_1 = 35°,\ \gamma_2 = 58.5°,\ \gamma_3 = 30°$

Differences between theoretical and experimental results are caused mainly by a lack of precision in the servomotors, friction and dynamic processes. Also a control unit does not have a positive coupling, what yields lack of repeatability of movement cycles and what generates it differences between experimental and theoretical results. Implementation results are shown in Fig. 10 and Fig. 11 for the snake robot and in Fig. 12 for the inchworm robot.

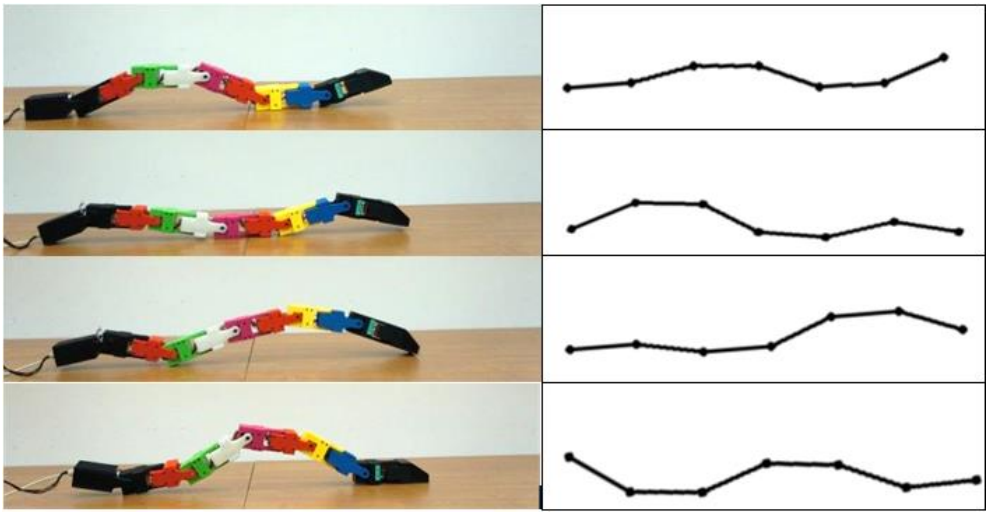

Figure 10. Snake robot motion – vertical plane

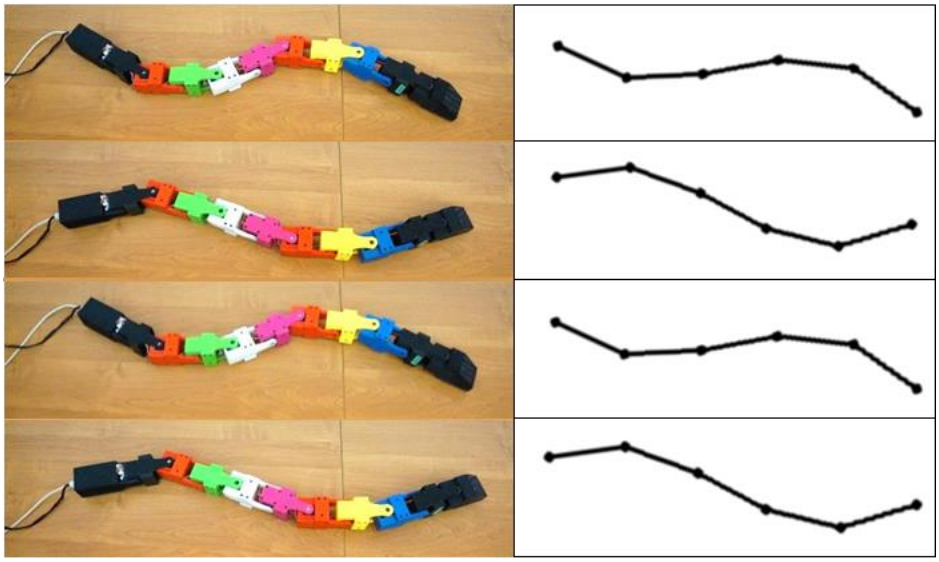

Figure 11. Snake robot motion – horizontal plane

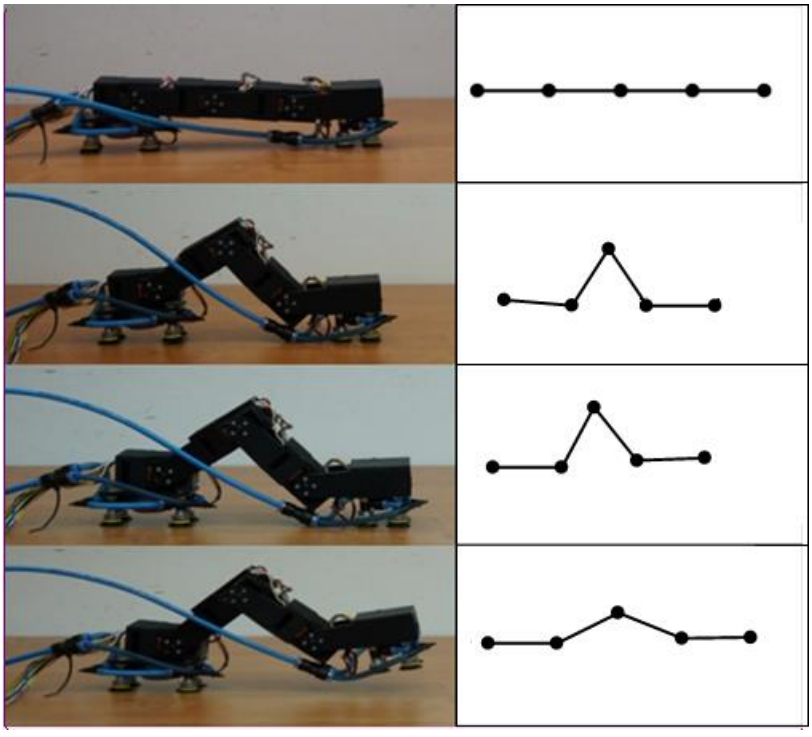

Figure 12. Inchworm robot motion – vertical plane

It was observed that for the uneven surfaces, decrease in the amplitude A_ξ results in shifting the mass center closer to the ground which implies stabilization of the robot. Main problem which occurred during realization of the motion of the snake robot is a sliding phenomenon appearing for the serpentine movement. In order to eliminate this harmful effect it is possible to apply material with directed friction force and/or increase the weight of segments.

The main disadvantage of the inchworm robot is its requirement of the smooth ground surface, as in other case the suction cups cannot create an underpressure, and hence a further motion is not possible. However, the robot can climb even on perpendicular wall if the surface of the ground is enough smooth and the vacuum pressure is high enough (see Fig. 13). There is also an option for replacing the suction cups by electromagnets, which allows the robot to move on ferromagnetic surfaces.

Figure 13. Climbing of inch-worm robot on the glass plate

5. Concluding remarks

Two unique bionic robots with which are able to imitate limbless animals: a snake and an inchworm are presented. Moreover, a control algorithm with proper parameter was implemented. Theoretical results were verified with experiments. It is assumed, that these robots can be useful as an inspection robots there, where is no room for wheeled or tracked vehicles. The main contribution of this paper is:

1. Presentation of movement algorithms creation for specific mechanisms.
2. Implementation of created algorithms to the robots control unit.

3. Comparison of theoretical results with robots behavior
4. Verification of the robots movement and its comparison to the biological structures movement abilities.

Moreover, it can be observed, that the robots dynamics have to be taken under consideration and this will be the subject of further study. Also some improvements in construction is necessary for a better imitation of the living animals like segments range of motion or stability control.

Acknowledgements:

We thank Miss Magdalena Jastrzębska for text improvements and the fruitful discussions.

References

[1] Vincent, J.F.V., Bogatyreva, O. A., Bogatyrev, N.R., Bowyer A., Pahl A.K., Biomimetics: its practice and theory. Journal of Royal Society Interface 2006 3, 471-482

[2] Li Y., Li B., Ruan J., Rong X., Research of Mammal Bionic Quadruped Robots: a Review, in 5th International Conference on Robotics, Automation and Mechatronics, Qiundao, China, (2011), 166-171,

[3] Dario, P., Sandini, G., Aebischer P., Robots and Biological Stsrems: Towards a New Bionics?, NATO ASI Series (F) Computer and System Science, vol. 102, Springer, 1989

[4] Shigeo H., Biologically Inspired Robots: Snake-Like Locomotion and Manipulators, Oxford University Press, 1993

[5] Saito, M., Fukaya, M. and Iwasaki, T. Modeling, analysis, and synthesis of serpentine locomotion with a multilink robotic snake. IEEE Control Systems Magazine, 22(1), 64-81.

[6] Hooper, Scott L. (1999–2010). "Central Pattern Generators". Encyclopedia of Life Sciences. John Wiley & Sons

[7] Dehghani, M. and Mahjoob, M. A Modified Serpenoid Equation for Snake Robots. 2008 IEEE International Conference on Robotics and Biomimetics, (2009), 1647-1652.

[8] Maity, A., Majumder, S., and Ghosh, S. An Experimental Hyper Redundant Serpentine Robot. 2010 IEEE International Conference on Systems Man and Cybernetics (SMC-2010), 3180-3185.

[9] O'Shea, M., Venomous Snakes in the World, Princeton University Press, 2006.

[10] Bartoszek, J. Robowąż – nowy trend w robotyce mobilnej. Pomiary automatyka i robotyka, R.16, Nr 2/2012, 254-259.

[11] Gaston K. Scoble M. Crook A. Patterns in species description: a case study using the Geometridae (Lepidoptera) 6/1995, 225-237.

[12] Kotay. K, Rus. D, The inchworm Robot: A Multi – Functional System, „Autonomus Robots”; Autonomous Robots, 8/2000, 53-69.

[13] Wang. W, Wang. K, Zhang. H, Crawling gait realization of the mini – modular climbing Caterpillar robot, „Progress in Natural Science", 25.07.2009, 1821-1829.

[14] Frames from film „Inchworm: Geometridae Caterpillar" available in Internet, https://www.youtube.com/watch?v=rcIbT6F0U1w, Access at 18.07.2017

Bartłomiej Zagrodny, Ph.D.: Lodz University of Technology, Faculty of Mechanical Engineering, Department of Automation, Biomechanics and Mechatronics, Stefanowskiego 1/15, 90-924, Lodz, POLAND (bartlomiej.zagrodny@p.lodz.pl), the author presented this contribution at the conference.

Cezary Miśkiewicz, B.A. (M.Sc. student): Lodz University of Technology, Faculty of Mechanical Engineering, Department of Automation, Biomechanics and Mechatronics, Stefanowskiego 1/15, 90-924, Lodz, POLAND (cezary.miskiewicz@edu.p.lodz.pl).

Krystian Polczyński, B.A. (M.Sc. student): Lodz University of Technology, Faculty of Mechanical Engineering, Department of Automation, Biomechanics and Mechatronics, Stefanowskiego 1/15, 90-924, Lodz, POLAND (*kryst.polczynski@gmail.com*).

Jan Awrejcewicz, Professor: Lodz University of Technology, Faculty of Mechanical Engineering, Department of Automation, Biomechanics and Mechatronics, Stefanowskiego 1/15, 90-924, Lodz, POLAND (*jan.awrejcewicz@p.lodz.pl*).

Effects of mild hallux valgus on forefoot biomechanics during walking: a finite element analysis

Yan Zhang, Jan Awrejcewicz

Abstract: Hallux valgus (HV) is a common foot deformity characterized by progressive lateral deviation of the hallux with medial deviation of the first metatarsal. In this study, foot models of a normal subject and a mild HV hallux valgus patient were developed to evaluate the effects of mild HV on forefoot biomechanics during walking. Three-dimensional finite element model of a normal foot and a mild HV foot were constructed. Finite element analysis was conducted in ANSYS Workbench 17.0. The biomechanical performances were compared at three gait instants, first-peak, mid-stance, and second-peak. The equivalent stress on five metatarsals increased while the resultant joint force and the contact pressure of the first metatarsophalangeal joint (MTP) decreased in mild HV foot in comparison of normal foot. At push-off instant, the normal foot presented a concentrated pressure under the more distal portion of the metatarsal and the hallux, while the HV foot exhibited a more evenly distributed pattern with concentrated pressure under more proximal location of the metatarsal and the hallux. The predicted alternations in joint loading and plantar pressure distribution pattern of the HV foot indicated that HV feet may have deficient capability of body weight transfer at the first MTP during walking.

1. Introduction

Hallux valgus (HV) is one of the most common foot deformities with the high prevalence of 23% in adult and 35.7% in elderly population [1]. It is characterized by the progressive subluxation and valgus angulation of the first metatarsophalangeal joint in combination with pronation of the proximal phalanx. Increasing HV severity often induces problems of foot pain [2], metatarsalgia [3], and balance defects [4]. More and more elderly people complain instability and risk of falling, particularly when walking on irregular terrain [2]. In addition, the deformity of foot structure is very likely to impair these biomechanical functions. The fact is that there is no scientific data so far to evidence this speculation and to completely explain the painful phenomenon in HV feet. Research on biomechanical behaviour of the deformed foot should be carried out to provide fundamental and systematic knowledge for the development of podiatrics and orthopaedics.

The metatarsal bones act as a unit in the forefoot to provide a broad plantar surface for load bearing. Various in vivo studies that evaluated risks at metatarsals regarding to HV have focused on potential overloading and altered weigh bearing pattern by plantar pressure measurements. Increased forefoot

plantar pressure has been evidenced in HV feet; however, debate remains in the forefoot regions where the alternation occurs. Bryant et al. [5] suggested that peak pressure of HV foot increased significantly under the first, second and third metatarsal heads compared with normal foot. Plank [6] also observed a medial shift of peak pressure in HV patients. On the contrary, there is research reporting increased load on lateral metatarsals [7]. Koller et al. [8] assessed the plantar pressure of HV feet of different grades and concluded a positive correlation between HV grade and peak pressure of the fifth metatarsal head.

FE model is capable of simulating complicated boundary and loading conditions and predicting the internal stress/strain in the foot complex. As the deformities of the complex foot structures increase the challenge in the modeling process, few studies concern FE models of deformed foot. It is of high significance to take insight into the biomechanical behavior of HV foot which is an increasingly prevalent foot deformity, particularly in the elderly population. Using FE method to develop numerical models of the deformed feet is an important step in the investigation of foot kinematical and mechanical manifestation during locomotion. This study aimed to establish an enhanced approach to predicting injury risk and evaluating biomechanical function efficiency of HV deformed foot. Knowledge of this project could improve the understanding of the underlying mechanisms of structural mechanical problems and abnormal gait pattern of mild HV feet.

2. Method

The three-dimensional models of the normal foot and the HV foot were reconstructed from computer tomography (CT) images of a 26-year old female (height: 165cm; weight: 51kg) and a 29-year old female (height: 163cm; weight: 54kg) respectively. Both participants had no other musculoskeletal pathology, pain, or lower limb injury or surgery within the past 12 months.

The coronal CT images were obtained with a space interval of 2 mm without weight-bearing. The images were segmented using MIMICS 16.0 (Materialise, Leuven, Belgium) to obtain the boundaries of the skeleton and the soft tissue. The geometry of the skeletal components and the soft tissue were processed using Geomagic Studio 2013 (Geomagic, Inc., Research Triangle Park, NC, USA) to smooth the uneven surface caused by the stacking of the medical images. Each surface component was then imported into Solidworks 2016 (SolidWorks Corporation, Massachusetts, USA) individually to form solid parts. To ensure the alignment of the exterior surfaces of the assembled model, cartilages were created using Boolean operations by subtracting one bony object with the adjacent one to connect the two bones and fill the cartilaginous spaces. The encapsulated soft tissue was subtracted from the whole foot volume by the bony and cartilaginous structures. The whole foot model consisted of 28 foot bony segments, including tibia, fibula, talus, calcaneus, cuboid, navicular, three cuneiforms, five metatarsals and 14 phalanges. Link elements that have only tension function capability were used to simulate

ligaments bearing the tension load. A total number of 76 ligaments and five plantar fascia were included and defined by connecting corresponding anatomical locations on the bones by reference to an anatomy book [9]. HyperMesh 13.0 (Altair Engineering Inc., Hyperworks, America) was used for mesh generation. Each bony and cartilaginous component and the soft tissue were partitioned based on the anatomical structure and were meshed as Hexahedral dominant elements. The FE package ANSYS Workbench 17.0 (ANSYS, Inc., Canonsburg, USA) was used for subsequent analysis. Automated surface-to-surface contact algorithm in ANSYS Workbench was used to simulate the interaction of the surfaces of the cartilaginous and bony structures. All the bones and cartilages were bonded to the encapsulated soft tissue.

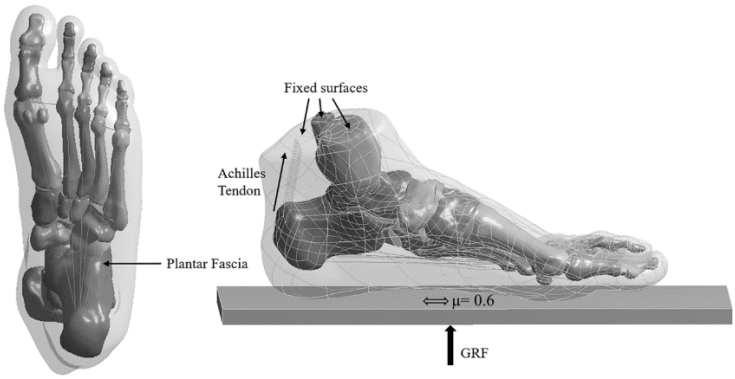

Figure 1. The three-dimensional finite element model and the application of boundary and loading conditions.

All the materials except for the soft tissue were considered isotropic and linearly elastic with material properties obtained from previous literature [10, 11]. The two material constants of Young's modulus E and Poisson's ratio ν were given to describe the elasticity. The encapsulated soft tissue was set as nonlinear hyperelastic material which was defined as Moonley-Rivlin model. The element types and material properties used are listed in Table 1 and Table 2.

Table 1 Material properties and mesh element types for the foot model components.

Component	Element Type	Young's Modulus (MPa)	Poisson's Ratio	Cross-section Area (mm^2)
Bone	Hexahedral solid	7300	0.3	-
Cartilage	Hexahedral solid	1	0.4	-

Ligaments	Tension-only spar	260	0.4	18.4
Plantar Fascia	Tension-only spar	350	0.4	58.6
Plate	Hexahedral solid	17000	0.4	-

Table 2 The element type and coefficients of the hyperelastic material used for the encapsulated soft tissue.

Element Type	C10	C01	C20	C11	C02	D1	D2
Hexahedral solid	0.08556	-0.05841	0.03900	-0.02319	0.00851	3.65273	0.00000

Stance phase was simulated by applying GRF and tibial inclination. The input data were originated from the gait experiment of the same participant. Three instants were extracted in the following percentage stance phase: 0% (heel-strike), 27% (GRF first peak), and 75% (GRF second peak). The percent-age maximum voluntary contraction of muscles corresponding to these instants were adopted [12] and multiplied by their maxi-mum force [13] for the calculation of muscle forces at the selected instants. The superior surfaces of the encapsulated soft tissue, distal tibia and distal fibula were fixed. The foot-ground interaction was simulated as a foot-plate system (Fig. 1). The plate was assigned with an elastic property to simulate the concrete ground support. The interaction between the foot plantar surface and the superior surface of the plate was simulated as contact with friction. The coefficient of friction was set to 0.6 [14]. Five equivalent force vectors representing the Achilles tendon force were applied over the area of the posterior extreme of the calcaneus.

The numerical model was validated by comparing plantar pressure obtained from computational simulation in FE software and experimental measurement by a Novel emed pressure platform (Novel, Munich, Germany) in standing position. For FE simulation of balanced standing, vertical GRF of half-body weight was applied at the inferior surface of the plate; and the force of Achilles tendon force was estimated as 50% of the force acting on the foot [11]. The validated models were then used for FE analysis on forefoot biomechanics.

3. Results

Three-dimensional FE models were validated by plantar pressure measurement. This method was commonly used in the validation of finite element foot model [11]. Fig. 2 shows the comparison of

predicted plantar pressure of the normal foot with experimental results. The predicted peak pressure and the pressure distribution pattern were generally agreeable with those from measurement. The peak pressure from numerical models and experimental measurement was 0.141MPa and 0.135MPa respectively, and both located at the heel region.

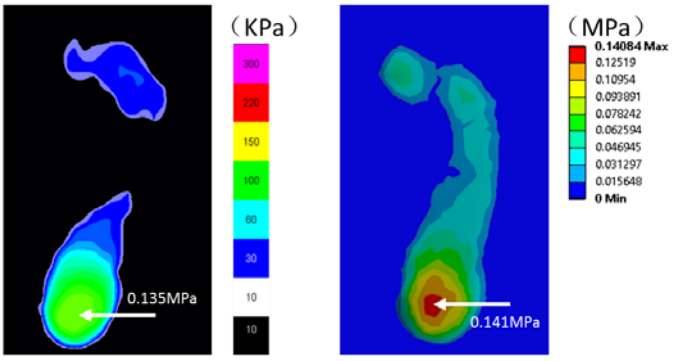

Figure 2. Comparison of the plantar pressure between experimental measurement and computational prediction in balanced standing position.

Previous experimental results advocated medial or lateral shift of forefoot plantar pressure due to HV deformity. As to von-Mises stress at the five metatarsals, stress distribution remains unchanged. The metatarsals of the HV foot sustained higher von-Mises stress (Fig. 3). It is possible to speculate that the increased metatarsal stress may cause metatarsalgia while weight bearing. The most obvious increasing of von-Mises stress at the first metatarsal indicates that this metatarsal is more susceptible to injury, such as stress fractures [15] and pain. The first metatarsal should be expected to avoid sustaining high stress during weight bearing in view of the first ray deformity. This is very likely to be associated with medial arch collapse which is often thought to supervene with hallux valgus [16].

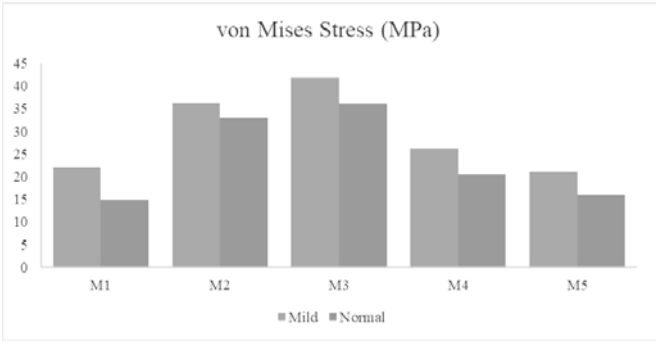

Figure 3. Comparison of von-Mises stress at five metatarsals between normal and hallux valgus foot.

Contact pressure of MTP joints was lower in HV foot (Fig. 4). Also, the resultant joint force of the first MTP showed lower magnitude compared to that of normal foot (Fig. 5). The decreased joint loading may imply the impairment of load bearing and transfer function of the first MTP joint in gait. In agreement with this speculation, Zhang et al. [17] found weakened windlass mechanism in HV foot during initial push-off. In contrast to the location of central bottom on the cartilage for the normal foot, it shifts to medial bottom for the HV foot, which may aggravate the symptom of "painful bunion" which is one of the most common complaints among HV patients [18]. Moreover, the component joint force in the medial-lateral direction presented to be opposite between HV and normal foot. The HV foot shows lateral reaction force at the first MTP joint during balanced standing, suggesting that loading of body weight alone could predispose the patient to the risk of developing HV deformity.

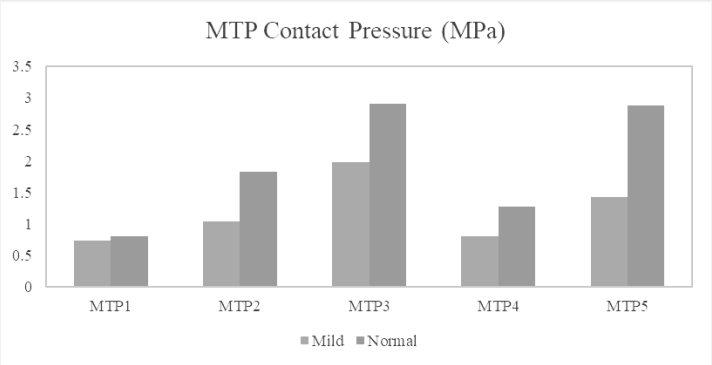

Figure 4. Comparison of contact pressure at the first metatarsophalangeal joint between normal and hallux valgus foot.

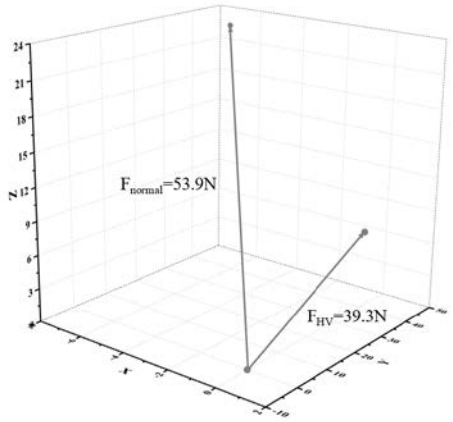

Figure 5. Comparison of joint force at the first metatarsophalangeal joint between normal and hallux valgus foot.

The ratio of peak plantar pressure between the hallux and the first MTP indicates different plantar pressure pattern between normal foot and mild HV foot. The ratio is 1.8 and 2.1 for the normal foot and HV foot respectively, which suggests that the normal foot exhibited a concentrated pressure closer to distal portion of the metatarsal, by contrast, the HV foot presented a more evenly distributed pattern with concentrated pressure at a more proximal location. This reinforces the notion of impaired windlass function in gait due to hallux valgus.

The FE models in this study were based on some simplifications and assumptions. First, cortical and cancellous bone was considered as a single homogeneous component with linear elastic properties. Second, this study created a representative single-subject model of a mild hallux valgus foot. The foot structure, such as arch height and toe deformity, may vary among hallux valgus feet; therefore, the presented data should be considered as a first rough approximation. Third, although hallux valgus is prominently characterized by skeletal deformity, it is also thought to be associated with ligamentous laxity and hypermobility of the first metatarsophalangeal joint [19]. For further study, the material properties of soft tissues should be assumed based on patient-specific model.

4. Conclusions

The first initiative of this project is to develop deformed FE models of a mild HV foot and a HV foot. Furthermore, since hexahedral elements were indicated to provide a more accurate and efficient foundation in structural analysis, all solid parts in this research will be initially meshed into hexahedral elements rather than tetrahedral elements that are commonly relied on in mesh generation of human foot models so far. Moreover, instead of simulating the main bone interactions as contacting deformable bodies, this research will initially create cartilaginous volumes using Boolean operations by subtracting the adjacent bones to fill the spaces between the bones.

Generally, the equivalent stress on five metatarsals increased while the resultant joint force of the first MTP decreased in HV foot in comparison of normal foot. At push-off instant, the normal foot presented a concentrated pressure under the more distal portion of the metatarsal and the hallux, while the HV foot exhibited a more evenly distributed pattern with concentrated pressure under more proximal location of the metatarsal and the hallux. The predicted alternations in joint loading and plantar pressure distribution pattern of the HV foot indicated that HV feet may have deficient capability of body weight transfer at the first MTP during walking.

References

[1] S. Nix, M. Smith, B. Vicenzino, Prevalence of hallux valgus in the general population: a systematicreview and meta-analysis. *J Foot Ankle Res* 3, 1 (2010), 1-9.

[2] Menz, H.B., Lord, S.R. Gait instability in older people with hallux valgus. *Foot Ankle Int* 26, 6 (2005), 483-489.

[3] Waldecker, U. Metatarsalgia in hallux valgus deformity: a pedographic analysis. *J Foot Ankle Surg* 41, 5 (2002), 300-308.

[4] Menz, H.B., and Lord, S.R. The contribution of foot problems to mobility impairment and falls in community‐dwelling older people, *J Am Geriatr Soc* 49, 12 (2001), 1651-1656.

[5] Bryant, A.P., Tinley, P., Singer, K. Plantar pressure distribution in normal, hallux valgus and hallux limitus feet. *The foot* 9, 3 (1999), 115-119.

[6] Plank, M. The pattern of forefoot pressure distribution in hallux valgus. *The foot* 5, 1 (1995) 8-14.

[7] Hurn, S.E., Vicenzino, B., Smith, M.D., Functional impairments characterizing mild, moderate, and severe hallux valgus. *Arthrit Care Res* 67, 1 (2015), 80-88.

[8] Koller, U., Willegger, M., Windhager, R., Wanivenhaus, A., Trnka, H.J., and Schuh, R. Plantar pressure characteristics in hallux valgus feet. *J Orthop Res* 32, 12 (2014), 1688-1693.

[9] Platzer, W., and Kahle, W. *Color Atlas and Textbook of Human Anatomy: Locomotor system, Color Atlas and Textbook of Human Anatomy.* New York, 2002.

[10] Wu, L. Nonlinear finite element analysis for musculoskeletal biomechanics of medial and lateral plantar longitudinal arch of Virtual Chinese Human after plantar ligamentous structure failures. *Clin Biomech* 22, 2 (2007), 221-229.

[11] Cheung, J.T.M., Zhang, M., Leung, A.K.L., and Fan, Y.B. Three-dimensional finite element analysis of the foot during standing—a material sensitivity study. *J Biomech* 38, 5 (2005), 1045-1054.

[12] Perry, J., and Burnfield, J.M. Gait analysis: normal and pathological function. Slack, New Jersey, 1993.

[13] Arnold, E.M., Ward, S.R., Lieber, R.L., and Delp, S.L. A model of the lower limb for analysis of human movement. *Ann Biomed Eng* 38, 2 (2010), 269–79.

[14] Yu, J., Cheung, J.T.M., Fan, Y., Zhang, Y., Leung, A.K.L., and Zhang, M. Development of a finite element model of female foot for high-heeled shoe design. *Clin Biomech* 23, (2008), S31-S38.

[15] Keyak, J.H., and Rossi, S.A. Prediction of femoral fracture load using finite element models: an examination of stress-and strain-based failure theories. *J Biomech* 33, 2 (2000), 209-214.

[16] Glasoe, W.M., Nuckley, D.J., and Ludewig, P.M. Hallux valgus and the first metatarsal arch segment: a theoretical biomechanical perspective. *Phys Ther* 90, 1 (2010), 110.

[17] Zhang, M., and Fan, Y.B. *Computational Biomechanics of the Musculoskeletal System.* CRC Press, 2014.

[18] Piqué-Vidal, C., Solé, M.T., and Antich, J. Hallux valgus inheritance: pedigree research in 350 patients with bunion deformity. *J Foot Ankle Surg* 46, 3 (2007), 149-154.

[19] Perera, A., Mason, L., and Stephens, M. The pathogenesis of hallux valgus. *J Bone Joint Surg Am* 93, 17 (2011), 1650-1661.

Yan Zhang, M.Sc. (Ph.D. student): Lodz University of Technology, Department of Automation, Biomechanics and Mechatronics, Stefanowskiego 1/15, 90-924 Lodz, Poland (*zhangyannbu@gmail.com*).

Jan Awrejcewicz, Professor: Lodz University of Technology, Department of Automation, Biomechanics and Mechatronics, Stefanowskiego 1/15, 90-924 Lodz, Poland (*jan.awrejcewicz@p.lodz.pl*).

INDEX OF AUTHORS